

Green Energy and Technology

Juan M. Coronado
Fernando Fresno
María D. Hernández-Alonso
Raquel Portela *Editors*



Design of Advanced Photocatalytic Materials for Energy and Environmental Applications

 Springer

Green Energy and Technology

For further volumes:
<http://www.springer.com/series/8059>

Juan M. Coronado · Fernando Fresno
María D. Hernández-Alonso
Raquel Portela
Editors

Design of Advanced Photocatalytic Materials for Energy and Environmental Applications

 Springer

Editors

Juan M. Coronado
Institute IMDEA Energía
Móstoles
Madrid
Spain

María D. Hernández-Alonso
Renewable Energy Division
CIEMAT
Madrid
Spain

Fernando Fresno
Laboratory for Environmental Research
University of Nova Gorica
Nova Gorica
Slovenia

Raquel Portela
Institute of Catalysis and Petrochemistry
CSIC
Madrid
Spain

ISSN 1865-3529

ISSN 1865-3537 (electronic)

ISBN 978-1-4471-5060-2

ISBN 978-1-4471-5061-9 (eBook)

DOI 10.1007/978-1-4471-5061-9

Springer London Heidelberg New York Dordrecht

Library of Congress Control Number: 2013937604

© Springer-Verlag London 2013

This work is subject to copyright. All rights are reserved by the Publisher, whether the whole or part of the material is concerned, specifically the rights of translation, reprinting, reuse of illustrations, recitation, broadcasting, reproduction on microfilms or in any other physical way, and transmission or information storage and retrieval, electronic adaptation, computer software, or by similar or dissimilar methodology now known or hereafter developed. Exempted from this legal reservation are brief excerpts in connection with reviews or scholarly analysis or material supplied specifically for the purpose of being entered and executed on a computer system, for exclusive use by the purchaser of the work. Duplication of this publication or parts thereof is permitted only under the provisions of the Copyright Law of the Publisher's location, in its current version, and permission for use must always be obtained from Springer. Permissions for use may be obtained through RightsLink at the Copyright Clearance Center. Violations are liable to prosecution under the respective Copyright Law. The use of general descriptive names, registered names, trademarks, service marks, etc. in this publication does not imply, even in the absence of a specific statement, that such names are exempt from the relevant protective laws and regulations and therefore free for general use.

While the advice and information in this book are believed to be true and accurate at the date of publication, neither the authors nor the editors nor the publisher can accept any legal responsibility for any errors or omissions that may be made. The publisher makes no warranty, express or implied, with respect to the material contained herein.

Printed on acid-free paper

Springer is part of Springer Science+Business Media (www.springer.com)

*For a successful technology, reality must
take precedence over public relations,
for Nature cannot be fooled*

Richard Feynman
US physicist and Nobel Laureate
(1918–1988)

Preface

No doubt, the possibility of performing chemical processes as complex as bacteria inactivation or CO₂ conversion into fuels, without the concurrence of high pressures or elevated temperatures, and using light as the only energy source, is fascinating not only from an engineering point of view, but also from a fundamental perspective. Yet, and perhaps more importantly, it touches deeply our scientific curiosity and even our esthetic feelings. In this way, photocatalysis can be very appealing in a whimsical sense, and we think that the readers can find by themselves clear examples of that in the images and schemes displayed through this book. All these reasons, from the obvious technological relevance to the subjective psychological allure, may justify the great success of this area of research, which currently represents a very significant part of the contributions to the journals in the environmental, energy, materials, and physicochemical fields. Our motivation to write this book is also rooted in these premises.

In contrast with other textbooks about photocatalysis, the present one is focused on materials. Accordingly, molecular aspects, which are gaining relevance but are still a relatively small branch of photocatalysis, are only indirectly considered in this book. From our understanding, this can be the right time for a monograph on photocatalysis from a material science angle because, although a variety of photoactive solids have always been assayed for different purposes, the preponderance of TiO₂ has been challenged in the last years with the exploration of a number of new photocatalytically active materials. Furthermore, in order to enhance the efficiency of these processes, a variety of morphological and chemical modifications of diverse semiconductors have been obtained by means of increasingly sophisticated routes. As a consequence, the already long list of photocatalysts phases and their modifications is increasing day by day. Under this situation, a guide is necessary to deal with the huge amount of information currently available. A valuable road-map should allow finding the common principles lying behind the diversity of materials, but also delimiting the imprecise border between the contrasted results and the most speculative studies or those mainly based on wishful thinking. Some excellent reviews have already addressed, total or partially, the description of this huge number of photocatalysts, and these papers constitute a constant reference through the present book. However, the approach chosen here differs from those articles published in academic journals in three main aspects: (i)

it does not intend to be exhaustive, but to remark the most promising and extensively investigated systems; (ii) it adopts a more integrated view, by considering most of the photocatalysts globally and in connection with other technologies; (iii) although the information provided is of interest for the specialist, the less-experienced scientists can easily follow the text as well. This has been made possible by including some general chapters to establish a common background for those readers interested in photocatalysis from different perspectives and with different skills. In any case, although some references to other chapters are frequently included to facilitate the comprehension of the themes exposed, each chapter can be read independently. As a consequence of the selfconsistency of the different chapters, certain degree of overlapping occurs because, as it is usually the case in science and technology, frontiers between topics are blurred, and classifications cannot be immutable without becoming fully artificial. We hope that the readers will find the organization of this book useful.

Our direct experience as researchers in the field of photocatalysis is rich, but, obviously, it is limited and partial. Therefore, apart from some aspects such as style, organization, or selection of materials, this book does not pretend to provide a personal account of photocatalysis, but it is conceived as a chronicle of the advances in this technological field. Consequently, this work is necessarily based on the experience outlined in hundreds of articles and reviews by many scientists, as it is acknowledged in the ample bibliography of each chapter. Therefore, although we are the only responsible of any possible error unconsciously introduced in the text, we are fully in debt with all these innumerable authors, many of them specifically mentioned throughout the text, for their remarkable contributions. Accordingly, we would like to express here our recognition and admiration for the efforts of all these scientists, colleagues, and mentors, to get more efficient photocatalytic processes and a progressively better understanding of the mechanisms operating at molecular scale. Finally, we would like to highline that the short historical notes included, in particular in [Chap. 1](#), intend to be a tribute to the pioneering researchers who helped to create this new technological reality.

Publication of this book has been possible by the kind assistance and infinite patience of Springer Editorial. Equally crucial has been the collaboration of the following colleagues and friends who have been so kind (or naïve) to agree to participate in this enterprise: Dr. Silvia Suárez, who has authored [Chaps. 9](#) and [12](#); Dr. Sergio García-Rodríguez, author of [Chap. 6](#); and Dr. Victor A. de la Peña O'Shea, author of [Chap. 10](#). Furthermore, we have personally acquired, working on photocatalysis, an enormous debt of gratitude with our introducers and guides to this wonderful field: Prof. Marc A. Anderson and Dr. Isabel Tejedor-Tejedor, of the University of Wisconsin at Madison (USA), and Emeritus Professor Javier

Soria from the Catalysis Institute of CSIC in Madrid (Spain). Finally, but no less importantly, we would like to thank our couples, friends, and family for their support. We fully appreciate their generosity in accepting to share our limited time with this endeavor.

Fernando Fresno
María Dolores Hernández-Alonso
Raquel Portela
Juan M. Coronado

Contents

1	A Historical Introduction to Photocatalysis	1
	Juan M. Coronado	
2	Photons, Electrons and Holes: Fundamentals of Photocatalysis with Semiconductors.	5
	Juan M. Coronado	
3	Environmental Applications of Photocatalysis	35
	Raquel Portela and María Dolores Hernández-Alonso	
4	Turning Sunlight into Fuels: Photocatalysis for Energy	67
	María Dolores Hernández-Alonso, Raquel Portela and Juan M. Coronado	
5	The Keys of Success: TiO₂ as a Benchmark Photocatalyst	85
	Juan M. Coronado and María Dolores Hernández-Alonso	
6	Alternative Metal Oxide Photocatalysts	103
	Sergio García-Rodríguez	
7	The New Promising Semiconductors: Metallates and Other Mixed Compounds.	123
	Fernando Fresno	
8	Chalcogenides and Other Non-oxidic Semiconductors	157
	Fernando Fresno	
9	Single-Site Photocatalysts: Photoactive Species Dispersed on Porous Matrixes	171
	Silvia Suárez	

10 The Role of Co-catalysts: Interaction and Synergies with Semiconductors.	195
Victor A. de la Peña O'Shea	
11 Shaping Photocatalysts: Morphological Modifications of Semiconductors	217
María Dolores Hernández-Alonso	
12 Immobilised Photocatalysts	245
Silvia Suárez	
13 Metal Doping of Semiconductors for Improving Photoactivity . . .	269
María Dolores Hernández-Alonso	
14 Non-metal Doping for Band-Gap Engineering	287
Raquel Portela	
15 Heterojunctions: Joining Different Semiconductors	311
Fernando Fresno	
16 Sensitizers: Dyes and Quantum Dots	329
Fernando Fresno and María Dolores Hernández-Alonso	
17 Future Perspectives of Photocatalysis	345
Juan M. Coronado, María D. Hernández-Alonso, Fernando Fresno and Raquel Portela	

Chapter 1

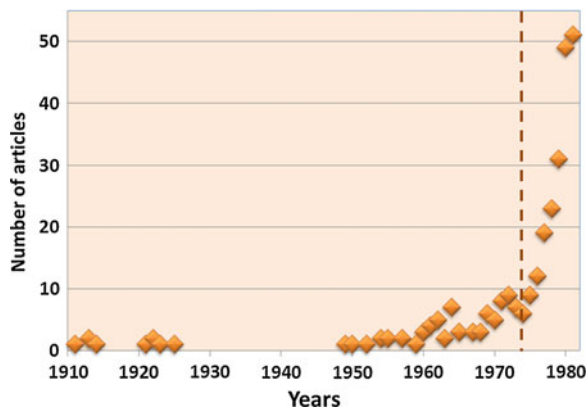
A Historical Introduction to Photocatalysis

Juan M. Coronado

As early as in 1911, 76 years after Berzelius coined the word *catalysis*, the term *photocatalysis* appeared in several scientific communications. In Germany, Eibner incorporated this concept in his studies on the effect of the illumination of ZnO on the bleaching of Prussian blue (Eibner 1911). Contemporaneously, the term photocatalysis achieved additional relevance when it was displayed in the title of a few articles dealing with the degradation of oxalic acid under illumination in the presence of uranyl (UO_2^+) salts (Bruner and Kozak 1911; Landau 1913). These pioneering experiments, performed by recognized scientists in France and Germany, explored the unusual photochemical properties of this cation of the actinide element, and they laid the foundations of the actinometric measurements, which are used even now for determining the flux of photons in photochemical reactions. However, nowadays this process is not usually described as photocatalytic, despite the fact that it implies the absorption of light by the uranyl ions in solution and their interaction in an excited state with the organic species to yield CO_2 and water. After those seminal reports, the interest on these processes decayed for almost a decade and the following reference in the literature was published in 1921. In this work, (Baly et al. 1921) studied the production of formaldehyde under visible light, using colloidal uranium salts and ferric hydroxides as catalysts. Shortly after, the group of Baur at the ETH of Zurich reported that the irradiation of a ZnO suspension promoted the reduction of Ag^+ salts to Ag^0 (Baur and Perret 1924). A few years later, the influence of rutile in the light-induced aging of paints and fabrics was recognized (Keidel 1929). Following this research line, (Doodeve and Kitchener 1938) investigated for the first time the ability of TiO_2 to act as photosensitizer for bleaching dyes in the presence of oxygen in the late 1930s. This work reported that UV absorption produces active oxygen species on the TiO_2 surface, causing the discoloration of organic chemicals by photooxidation,

J. M. Coronado (✉)
Institute IMDEA Energía, Avenida de Ramón de la Sagra, 3
28935 Móstoles, Madrid, Spain
e-mail: juanmanuel.coronado@imdea.org

Fig. 1.1 Annual evolution of the number of articles of Scientific Citation Index (SCI) publications related to photocatalysis from 1910 to 1981. The *dashed line* marks the publication of the seminal article of Fujishima and Honda. However, it is important to note that such work is not included in these data because it does not contain the term “photocatalysis” (data obtained from ISI web of knowledge)



although TiO_2 itself remains unchanged after the process. Therefore, some of the basic features of heterogeneous photocatalysis were already discovered during these early investigations. However, in the absence of practical applications, these processes were as much a curiosity and, frequently, an annoying drawback of inorganic pigments. Consequently, the interest on these characteristics of semiconductors almost faded in the following decades, as it can be appreciated in Fig. 1.1. Nevertheless, some topics related to the interaction of semiconductors with adsorbed molecules, like the mechanism of photosensitization in the presence of dyes molecules or the effect of gases on photoconductivity, were investigated in the late 1950s by the group of Terenin at the University of St. Petersburg (Terenin 1955; Serpone 2012). However, the opportunities of using these photoactive materials to induce chemical transformations continued to be overlooked at that time. In the 1960s, this situation started to change slowly when a Russian group headed by Filimonov (1964) began to explore the odds of using materials such as ZnO or TiO_2 for isopropanol photooxidation. In parallel, different Japanese groups studied the heterogeneous photooxidation of organic solvents in the presence of ZnO (Kato and Mashio 1964; Ikekawa et al. 1965). Simultaneously, in Germany, Doerffler and collaborators observed the promotion of carbon monoxide oxidation over illuminated ZnO (Doerffler 1964). The interest on the photocatalytic oxidation processes continued in the early 1970s with the work by Teichner’s group on the partial oxidation of paraffins and olefins over TiO_2 (Formenti et al. 1970), whereas Tanaka and Blyholde (1970) studied the photocatalytic decomposition of nitrous oxide.

At that point, this technology was ready for a change of paradigm, and this step forward was prompted, at least partly, by the economic situation at the beginning of the 1970s decade. In 1973, crude prices, traditionally stable, skyrocketed

suddenly due to the embargo of the organization of Arab Petroleum Exporting Countries (OAPEC), and for the first time the future scarcity of oil became a serious concern. This *oil crisis* led to an unprecedented impulse of the research in alternative energy sources so as to overcome the dependence on petroleum. In those economically convulse times, two Japanese researchers, Fujishima and Honda (1972), reported in an article in *Nature* the electrochemical photolysis of water using a rutile electrode exposed to near-UV light and connected to a platinum counter electrode through an electrical load. This apparently modest work opened up a new world of possibilities for the production of clean hydrogen using abundant and inexpensive water and sunlight. Accordingly, this report is still immensely popular as it can be inferred from the number of citations that it accumulates, approaching 6,500 by the end of 2012. However, the influence of this article was not immediate, and up to late 1970, water splitting basically lied on the side of photoelectrochemistry. This started to change when Nozik (1977), at that time working for Allied Chemical Corporation, evidenced that external potential was not required to split the water molecule and the photoactivity could be boosted if a noble metal (e.g., Pt) was incorporated. Subsequent investigations by Wagner and Somorjai (1980) compared the photogeneration of H_2 over platinized $SrTiO_3$ single crystals with and without potential. In a similar study, Sakata and Kawai (1981) reported the production of H_2 and CH_4 upon irradiation of Pt/ TiO_2 suspensions in aqueous ethanol with high quantum efficiency: ca. 38 %.

The influence of Fujishima's work was also important to consolidate the preponderance of TiO_2 among photoactive materials because its stability in aqueous solution was established under a wide range of pH and external potentials. Therefore, the relevance of this semiconductor progressively increased with works such as that of Bickley et al. who tested the photooxidation of isopropanol on rutile TiO_2 (Bickley et al. 1973). In a similar way, it is worth to highlight the pioneering studies by Bard's group at the University of Texas, which showed that cyanide (CN^-) could be efficiently photooxidized to cyanate (CNO^-) in alkaline conditions and in the presence of TiO_2 and oxygen (Frank and Bard 1977).

Therefore, it seems clear that photocatalysis, along its already centennial history, has acquired knowledge from very different disciplines. Evidently, photochemistry, catalysis and, to a lesser extent, semiconductor physics have historically shaped our understanding of this phenomena, which depends on the solid interactions with radiation but also on surface reactivity. Interestingly, photoelectrocatalysis, as a closely related process, has contributed enormously to boost energetic applications, and both technologies have growth intertwined. Most recently, nanotechnology has provided new exciting possibilities for the development of more efficient and sophisticated photocatalytic materials, although it has also brought new concerns related to the toxicity of nanostructured solids. Although it was once considered a problem for promoting the discoloration of paints and dyes, photocatalysis progressively has evolved to become a well-established technology, which holds the promise of many environmentally friendly solutions for the society demands.

References

- Baly ECC, Heilbron IM, Barker WF (1921) Photocatalysis. Part I. The synthesis of formaldehyde and carbohydrates from carbon dioxide and water. *J Chem Soc* 119:1025–1035
- Baur E, Perret A (1924) The action of light on dissolved silver salts in the presence of zinc oxide. *Helv Chim Acta* 7:910–915
- Bickley RI, Munuera G, Stone FS (1973) Photoadsorption and photocatalysis on rutile surface. II. Photocatalytic oxidation of isopropanol. *J Catal* 31:398–407
- Bruner L, Kozak J (1911) Information on the photocatalysis I the light reaction in uranium salt plus oxalic acid mixtures. *Z Elektrochem Angew P* 17:354–360
- Doerfler W, Hauffe K. (1964) Heterogeneous photocatalysis I. Influence of oxidizing and reducing gases on the electrical conductivity of dark and illuminated zinc oxide surfaces. *J Catal* 3:156–170
- Doodeve CF, Kitchener JA (1938) The mechanism of photosensitization by solids trans. *Faraday Soc* 34:902–912
- Eibner A (1911) Action of light on pigments I. *Chem-Ztg* 35:753–755
- Filimonov VN (1964) Photocatalytic oxidation of gaseous isopropanol on ZnO + TiO₂. *Dokl Akad Nauk SSSR* 154(4):922–925
- Formenti M, Juillet F, Teichner SJ (1970) Controlled photooxidation of paraffins and olefins over anatase at room temperature. *C R Seances Acad, Sci Ser C* 270C:138–141
- Frank SN, Bard AJ (1977) Heterogeneous photocatalytic oxidation of cyanide ion in aqueous solutions at titanium dioxide powder. *J Am Chem Soc* 99:303–304
- Fujishima A, Honda K (1972) Electrochemical photolysis of water at a semiconductor electrode. *Nature* 238:37–38
- Ikekawa A, Kamiya M, Fujita Y, Kwan T (1965) Competition of homogeneous and heterogeneous chain terminations in heterogeneous photooxidation catalysis by ZnO. *Bull Chem Soc Jpn* 38:32–36
- Kato S, Mashio F (1964) Titanium dioxide-photocatalyzed oxidation. I. Titanium dioxide photocatalyzed liquid phase oxidation of tetralin, *Kogyo Kagaku Zasshi* 67:1136–1140
- Keidel E (1929) The fading of aniline dyes in the presence of titanium white. *Farben-Zeitung* 34:1242–1243
- Landau M (1913) Le phénomène de la photocatalyse. *Compt Rend* 156:1894–1896
- Nozik AJ (1977) Photochemical diodes. *Appl Phys Lett* 30(11):567–570
- Sakata T, Kawai T (1981) Heterogeneous photocatalytic production of hydrogen and methane from ethanol and water. *Chem Phys Lett* 80:341–344
- Serpone N, Emeline AV, Horikoshi S, Kuznetsov VN, Ryabchukh VK (2012) On the genesis of heterogeneous photocatalysis: a brief historical perspective in the period 1910 to the mid-1980s. *Photochem Photobiol Sci* 11:1121–1150
- Tanaka KI, Blyholde G (1970) Photocatalytic and thermal catalytic decomposition of nitrous oxide on zinc oxide. *J Chem Soc D-Chem Comm* 18:1130
- Terenin AN (1955) The desorption of adsorbed gases from metals and semiconductors, and their adsorption under the influence of light. *Probl Kinet Katal* 8:17–33
- Wagner FT, Somorjai GA (1980) Photocatalytic and photoelectrochemical hydrogen production on strontium titanate single crystals. *J Am Chem Soc* 102:5494–5502

Chapter 2

Photons, Electrons and Holes: Fundamentals of Photocatalysis with Semiconductors

Juan Manuel Coronado

Although not all the heterogeneous photocatalysts are semiconductors, as it will be discussed extensively in [Chap. 9](#), this type of solids represents, by far, the most representative and widely investigated photoactive materials. For that reason, it is important to gain some elementary insight into the physicochemical properties of the semiconductors, in order to understand the ultimate basis of their behaviour. Accordingly, the fundamentals of the electronic structure of semiconductors, as well as the mechanism of their interaction with light, will be accounted for in this chapter. However, in contrast to other applications of semiconductors, surface characteristics are paramount for establishing the efficiency of photocatalysts. This fact connects with the second pillar of photocatalysis: the surface reactivity, which implies the interaction between photogenerated charge carriers and adsorbed species. Nevertheless, it is also important to keep in mind that differences in photocatalysis with thermally activated, conventional catalysis are not irrelevant, and they must be recalled when designing materials with improved performance. On the other side, there is also a strong link between photocatalysis and electrochemistry, which, as it was mentioned in the previous chapter, is rooted in the historical development of these functional materials, but is also correlated with the redox nature of the processes discussed here. All these aspects are conveniently described in this chapter, which also outlines the parameters used for determining the efficiency of photocatalytic materials.

J. M. Coronado (✉)
Institute IMDEA Energía, Avenida de Ramón de la Sagra, 3
28935 Móstoles, Madrid, Spain
e-mail: juanmanuel.coronado@imdea.org

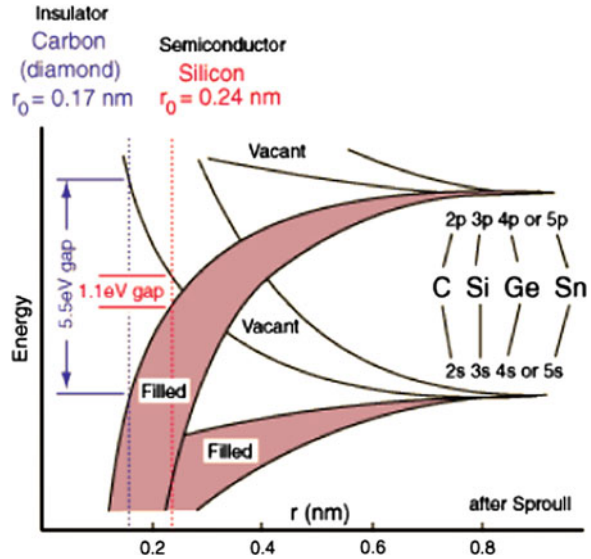
2.1 Bonds and Bands: The Electronic Structure of Semiconductors

Semiconductors constitute a family of materials with huge technological relevance. In fact, the information revolution, which started with the first computers in the second half of the twentieth century, and it is still unfolding with the development of even more complex networks for data transmission and storage, relies on the exploitation of the archetypical semiconductor material: silicon (Nelson 2003). This is the basic constituent of current transistors and diodes in any kind of electronic devices from computers to cell phones. In the field of energy, the photovoltaic (PV) cells, in a similar way to photocatalysts, take advantage of the interaction of light with semiconductors for electrical power generation. Nowadays, these devices constitute one of the most promising technologies for the exploitation of renewable technologies, and solar PV farms are currently taking off as a large-scale supplier of power in certain Western countries such as Germany, Portugal or Spain (Campoccia et al. 2009). Considering this technological success, a straightforward question arises: What is special about semiconductors? The key to the answer is the particular electronic structure of these solids, which is the topic of this section.

2.1.1 Metals, Semiconductors and Insulators

When two atoms are brought together to form a molecule, their atomic orbitals are shared to yield bonding (low energy) and antibonding (high energy) molecular orbitals. Valence electrons occupy the new orbitals in such a way that the energy of the systems is minimized, and this means, in a typical case, that only the bonding orbitals are filled. If the number of atoms which constitute the molecule increases, the number of molecular orbitals will grow progressively (Duffy 1990; Hoffmann 1989). At the same time, the energy difference between discrete levels of the same character (bonding or antibonding) will diminish gradually. Similarly, the energy difference from the highest bonding to the lowest antibonding orbital will slightly decrease, but it will stay comparatively large (see Fig. 2.1). In the limit, if the amount of atoms implied in bonding approaches the Avogadro's number, as it occurs in conventional solids, the energy levels of the electrons contributing to bonding will develop a virtual continuum of energy levels known as *valence band* (VB). In the same way, the more energetic antibonding orbitals will merge to form a continuous band of unoccupied states called *conduction band* (CB). At this point, there are two possible situations, as sketched in Fig. 2.1, either the unoccupied or the occupied states will merge together in more electronic levels than bonding electrons, or, alternatively, a void band with no available energy states will develop between the occupied and unoccupied levels. The first situation corresponds to metallic bonding, which is typical of relatively weak and not

Fig. 2.1 Schematic representation of the energy levels in the elements of the carbon group as a function of the interatomic distance, r . Reproduced with permission from Georgia State University 2011 (<http://hyperphysics.phy-astr.gsu.edu/hbase/hframe.html>)



directional interactions between atoms of the same kind, while the second type of materials, more common in phases with directional covalent bonds, can correspond to either semiconductor or insulating solids, depending on the magnitude of the forbidden band (Duffy 1990; Hoffmann 1989).

An important parameter for establishing the electronic properties of a solid is the Fermi level, which is related to the chemical potential of the electrons, and it can be defined as the highest unoccupied level at the temperature of absolute zero (Georgia State University 2011; Hoffmann 1989; Nelson 2003). Thus, in the case of a metal at 0 K, all the positive charge carriers will be allocated in the states of lower possible energy and the Fermi level will correspond to the less energetic empty state; however, for semiconductors, this level is situated within the forbidden band, and consequently, it does not correspond to any real energy state. As it will be discussed later, since the presence of impurities affects the electronic distribution, it can cause remarkable shifts in the Fermi level.

Distinction between materials of different electronic characteristics is a question of grade, as it can be appreciated in Table 2.1, and often, frontiers are established in a rather arbitrary manner. Thus, solids with a band gap exceeding 4 eV are usually considered as electrical insulators. On the other extreme, some solids of small band gap, such as Ge (0.74 eV), are sometimes referred to as semimetals (Nelson 2003). Nevertheless, in general, there is a clear-cut difference in the properties of metallic and semiconductor materials. Metals are very good electronic and thermal conductors, because as these materials possess a continuous range of energy states, electrons can move freely through the solid. However, increasing the temperature is detrimental for electrical conductivity (as opposed to thermal conductivity), because the increment of the vibration of the lattice (i.e. phonons) opposes resistance to the movement of electrons. The dependence of the

Table 2.1 Approximate values of band gaps and resistivity at room temperature of some materials of different electronic characteristics (Georgia State University 2011; Nelson 2003; Duffy 1990)

Material	Diamond	Mica	GaAs	Si (intrinsic)	Ge	Fe	Cu
Type	Insulator	Insulator	Semiconductor	Semiconductor	Semiconductor	Metal	Metal
Band gap (eV)	5.5	-	1.42	1.11	0.74	0	0
Resistivity ρ (Ωm)	10^{12}	9×10^{13}	10^6	3×10^3	5×10^{-1}	1×10^{-7}	1.7×10^{-8}

semiconductor resistivity on the temperature is more complex, but for intrinsic semiconductors at relatively high temperatures (<400 K), conductivity shows an exponential increment with temperature. This is due to the fact that as a consequence of thermal activation, some electrons can leap to the conduction band. According to the Boltzmann approximation, the density of electrons in the conduction band, n_i , can be estimated by the following equation (Nelson 2003):

$$n_i^2 = N_c N_v e^{-E_g/k_B T} \quad (2.1)$$

where N_c and N_v are the density of states of the conduction and valence bands, respectively, E_g is the band-gap energy, K_B is the Boltzmann constant, and T represents the temperature. Besides, from this formula, it can be deduced that at a given temperature, the larger the band-gap energy, the lower the conductivity is, since the number of carriers depends exponentially on the inverse of band-gap energy.

2.1.2 Some Hints of Quantum Theory of Band Structure

In order to determine the energy levels of a solid, as in the case of molecules, we need to solve the Schrödinger's equation for the whole polyatomic system. However, as crystalline solids possess a periodic arrangement of atoms, this implies that bonding electrons are also submitted to a period potential, and this fact should also be introduced in the calculations. This is the approach of the tight-binding model, which was developed in 1928 by the Swiss-born physicist Felix Bloch, and is frequently utilized for describing the electronic structure of solids (Duffy 1990; Hoffmann 1989). As the lattice becomes sufficiently large to be taken as infinite and the electrons are delocalized throughout the whole solid, the probability density must be affected by the periodicity. To fulfil these conditions, the wave function of the electrons must simultaneously consider the mobility of the electrons and the periodic array of atoms in the crystals. Mathematically, this requires a wave function ψ of the type

$$\Psi(k, r) = u_i(r) e^{ik \cdot r} \quad (2.2)$$

which is known as Bloch function. The factor $u_i(r)$ ¹ corresponds to the wave function of the atom i placed at the distance r , and $e^{ik \cdot r}$ is a plane wave similar to that used for describing free electrons. In this last term of the Eq. 2.2, the parameter k accounts for the translational symmetry and it is an appropriate quantum number, which is related to the linear momentum of electrons. As periodicity implies repetition, k can only range from 0 to $\pm\pi/a$, where a accounts

¹ Implicitly, the effective-mass approximation is adopted here (see Sect. 2.3), because the weak dependence of $u_i(r)$ with k is neglected.

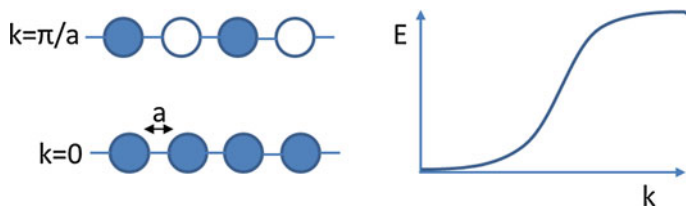


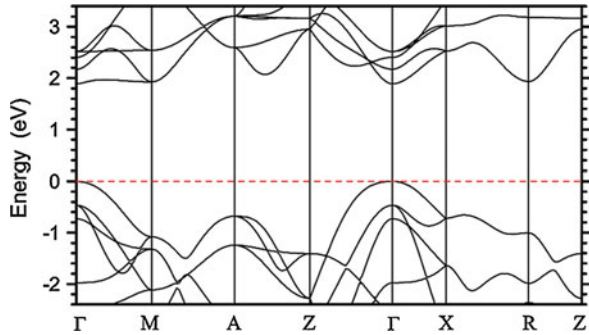
Fig. 2.2 Diagram of the energy variation with k for a one-dimensional homoatomic chain (Adapted from Hoffmann 1989)

for the unit cell spacing. Within these limits, k can take as many values as a number of atoms are implied in the bonding. The variation of energy, $E(k)$, with k for each wave function is what engenders the system of bands. This can be illustrated by considering the simplest possible case of a one-dimensional homoatomic crystal (Hoffmann 1989; Duffy 1990), which is schematically represented in Fig. 2.2. As it is shown in this graph, when k is zero, then the associated wave has a wavelength,² λ , equal to infinite, and all the atoms in the lattice present a bonding character. This situation represents the maximum energy gain over free atoms, and consequently, it represents the bottom of the valence band. On the contrary, if k is now equal to π/a , λ becomes $2a$. In energy terms, this situation corresponds to the interaction between atoms separated by $2a$, which is clearly the less favourable case, with no bonding interaction between the chain of atoms, and it represents the top of the valence band. For values of k between 0 and π/a , a variable number of atoms participate in bonding, generating all possible intermediate energy states and, accordingly, giving rise to the continuum of states of the valence band. The same reasoning can be applied to the antibonding orbitals to explain the development of the conduction band, although in this case maximum interaction corresponds to minimum energy. On the other hand, the width of the bands depends on the degree of overlapping between atomic orbitals. Thus, if the orbitals are highly localized in the atoms, then the bands are narrow and the mobility of the electrons is limited. On the contrary, if the overlapping between neighbour atoms increases, so does the dispersion or width of the band.

Obviously, this oversimplified vision ignores not only the existence of different types of atoms or the three-dimensional structure of solids, but also the contribution of the different types of orbitals to the configuration of the band structure. In this respect, it is worth noting that direction is also a crucial factor for correlating k and $E(k)$. Thus, the value $k = \pi/a$ defines the Brillouin zone boundary in a particular direction, but when this limit is taking in all the relevant directions, it generates a polyhedron in the reciprocal space. These geometric bodies delineate the possible values of k . For the sake of simplicity, what is usually represented is the variation of energy in certain important directions designated with capital

² This wavelength derives from the Broglie relationship, $\lambda = h/p$, where h is the Heisenberg constant and p is the momentum.

Fig. 2.3 The band structure of bulk TiO_2 in the rutile phase along some symmetry directions of the Brillouin zone. Reproduced with permission from Migas et al. (2010). Copyright American Chemical Society



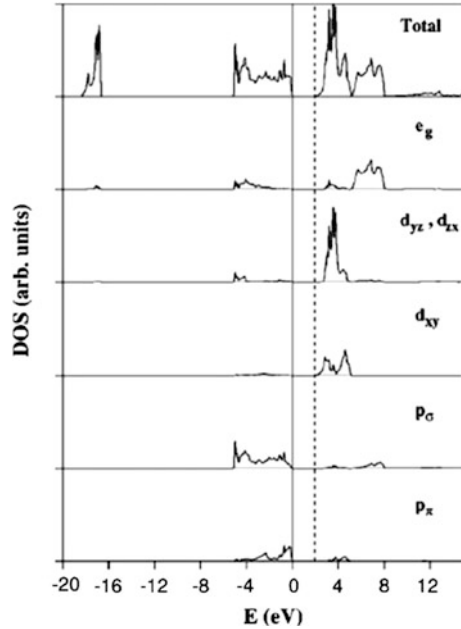
Greek letters starting from the origin, which is denoted by Γ . A simple example of this is represented in Fig. 2.3 in a two-dimensional graph.

Apart from the position of the energy levels, another important aspect that needs to be defined is the number of electrons that can be allocated to each band. According to the Pauli's exclusion principle, each state can be only occupied by two electrons with different spin orientations. As in crystals, energy levels are defined by k ; thus, in cubic lattices, it is found that there are $(1/2\pi)^3$ levels per unit crystal volume (Nelson 2003). Considering that energy depends on k , it is possible to define a density of states, DOS, as the number of states within an energy interval. In general, DOS is proportional to the inverse slope of the $E(k)$ versus k curve. These transformations are represented in the real space, in contrast to those of the Brillouin zone, which are plotted in the reciprocal space (Hoffmann 1989), as it can be appreciated in Fig. 2.4. The computer calculation of DOS for a given semiconductor frequently allows establishing the relative contribution of atomic orbitals to these states, providing an intuitive picture of the chemical bonding established on the solid. This is known as "projection" of the DOS. In this way, narrow bands represent more localized states with increasing atomic properties, as opposed to wider bands which allow the delocalization of electrons through the entire semiconductor mass. On the other hand, it is important to emphasize that filling of these levels by available electrons obviously establishes the lowest occupied level, and thus, it defines the electronic characteristics of the solid such as the Fermi level.

2.1.3 Classifying Semiconductors

The degree of overlapping between different types of orbitals depends on their direction and symmetry, and therefore, variation of energy with k adopts a different form for each band. As a consequence, the separation of the top of the VB and the bottom of the CB depends on this quantum number. According to this, two distinct scenarios can be envisaged, as it is schematically shown in Fig. 2.5; the minimum band gap is observed for the same value of k , or, alternatively, the smallest

Fig. 2.4 Total and projected density of states (DOSs) of the anatase TiO₂ structure with the contribution of the different orbitals. The *top* of the valence band (the vertical *solid line*) is taken as the zero of energy. The vertical *dashed line* indicates the conduction band minimum. Reproduced with permission from Asahi et al. (2000). Copyright American Physical Society



separation corresponds to two different k values. The first case defines direct semiconductors, while the second one accounts for indirect semiconductors. Such division implies important differences in the optical behaviour of these materials. In order to make the electronic transition allowed, indirect energy jumps require coupling with the phonons of the solid. Thus, electronic transitions involving a change in k have lower probability to occur than those with no change in k (Duffy 1990; Nelson 2003). Accordingly, indirect semiconductors such as silicon are poorer absorbers than direct-type materials such as GaAs. Typically, optical spectra of direct semiconductors show a sharp onset when wavelength approaches band-gap energy, while a more gradual increase is expected for indirect semiconductors. Therefore, as it is illustrated in Fig. 2.5b, the type of semiconductor could be distinguished from their UV–vis spectra by considering the presence or absence of some “tailing” before the step-like band-gap absorption. In practice, this classification is not so straightforward, because other phenomena, such as impurities or superficial states in large surface area materials, also result in a less marked optical transition. As a consequence, identification of the type of semiconductor using exclusively optical spectra is frequently difficult or even misleading.

More rigorously, the band gap of a semiconductor can be estimated from optical measurements using the equation that relates the absorption coefficient, $\alpha(\lambda)$, with the variation in energy ($E = h\nu$):

$$\alpha(\lambda) = B(h\nu - E_g)^n (h\nu)^{-1} \quad (2.3)$$

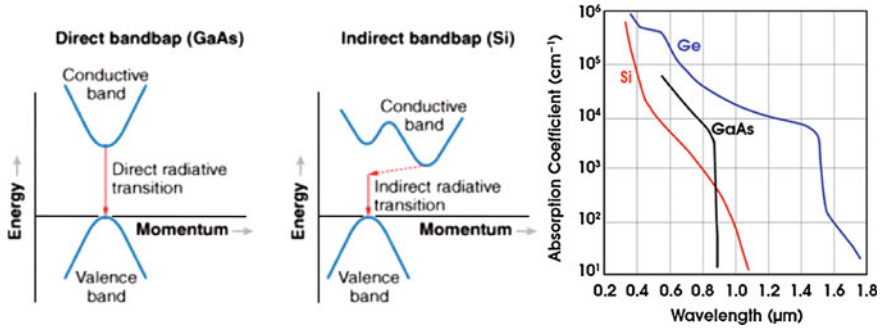


Fig. 2.5 *Left* Schematic showing the interband transition in direct (GaAs) and indirect (Si) semiconductors. *Right* Optical absorption spectra for silicon, gallium arsenide and germanium are shown. Note the gallium arsenide steep direct absorption edge at about 0.87 μm . Adapted from Miller (2007). Copyright Photonic Spectra

where the exponent n equals $\frac{1}{2}$ or 2 for direct and indirect semiconductors, respectively, B is a constant, and E_g is the band-gap energy (Fernandez-Garcia et al. 2004). Thus, from the extrapolation of the linear range of the plot of $B(h\nu - E_g)^n$ versus $h\nu$, the E_g can be obtained as the intersect with the abscise axis.

Up to now, only pure semiconductors have been considered, but the presence of impurities, either artificially added or intrinsically present, has a significant influence on modulating the electronic properties of these materials (Duffy 1990; Nelson 2003). Electronic industry requires extremely high-purity silicon with foreign atom content lower than one in 10^6 . This type of materials, virtually pure, is known as *intrinsic semiconductors*. However, many technological applications may require the introduction of a small and finely controlled amount of impurities to tune the electronic properties of the material (e.g. conductivity). This process is referred to as *doping* and results in the creation of additional electronic levels. These states, if the density of dopant atoms is low, are localized because chemical differences preclude effective bonding with the other atoms of the semiconductor lattice. Nevertheless, if the impurity states occur within the band gap, they have a remarkable influence on the Fermi level and, therefore, on the relative concentration of negative (electrons) and positive (holes) carriers (Nelson 2003).

At this point, there are two different situations to be considered, as schematically depicted in Fig. 2.6. If dopants have extra valence electrons to share with adjacent atoms, as in the archetypical case of phosphorus-doped silicon, they act as donors and the semiconductor is called n-type. As a consequence of the presence of such additional electrons, which are placed in localized states, the Fermi level is shifted to higher energy. As additional electrons are loosely bound, they can be easily ionized. Thermal activation can provide the energy, typically a few meV, required to promote the electrons to the conduction band. Consequently, in n-type semiconductors, the density of electrons is increased, and accordingly, they become the majority carriers, while holes are the minority ones. With respect to

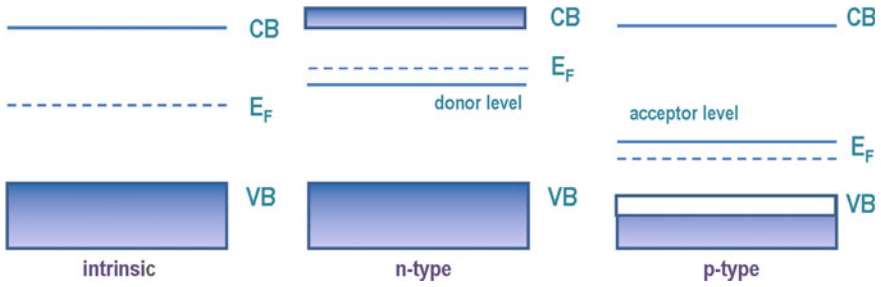


Fig. 2.6 Band diagram for intrinsic, p-type and n-type semiconductors

the intrinsic case, the total density of carriers is increased, and more interestingly, it can be modulated by changing the dopant concentration. In this way, provided that impurity atoms are fully ionized and its concentration is larger than that of the intrinsic carriers, the density of electrons is approximately equal to that of heteroatoms (Nelson 2003). Thus, considering that conductivity, σ , is given by

$$\sigma = q(\mu_n n + \mu_p p) \quad (2.4)$$

where q is the charge of the carrier, and n and p are the concentrations of positive and negative carriers, respectively, and μ is the mobility; it becomes obvious that increasing the carrier density rises conductivity. On the other hand, charge carrier transport in a semiconductor can be conveniently described by the effective-mass approximation (EMA). In this approach, carriers can be treated as semiclassical particles, in such a way that the larger the effective mass of the particle (relative to that of a free electron), m^* , the more localized it is and the less likely it is to move through the lattice. This approach allows to use the Newton's mechanics for charge particles in electromagnetic field, and it can be derived from neglecting the dependence of the $u_i(r)$ with k in the Bloch function (Eq. 2.2).

The counterpart of donor doping is the incorporation of acceptor atoms to create a p-type semiconductor. This is the case, for example, of the incorporation of a trivalent atom such as boron or nitrogen in silicon. In contrast to the former case, the additional energy levels created by the dopant are lacking electrons to complete bonding with neighbour atoms, and consequently, they trap electrons and generate holes in the valence bands. Therefore, in this case, the Fermi level is displaced to lower energy and the majority carriers are holes, in a density roughly equal to the concentration of acceptor atoms (Nelson 2003).

If the concentration of dopants, either donors or acceptors, increases, the number of states rises accordingly, and this can lead to a decrease in the band gap of the semiconductor. This fact can be visualized as a “tailing” of the absorption edge in the optical spectra. Heavy doping (density of heteroatoms $>10^{19} \text{ cm}^{-3}$) increases the intrinsic carrier density. However, in general, the density of defect sites will also grow accordingly, and because they act as recombination centres, the efficiency of the semiconductor for photoexcitation is deteriorated. Consequently, doping level is

usually kept low, typically between 10^{15} and 10^{18} cm^{-3} for silicon. In addition, self-doping is also possible such as in the case of TiO_2 where the presence of some Ti^{3+} centres originates n-type conductivity (Henderson 2011).

2.2 The Photoexcitation Process

In the early 1800s, Christian von Grotthus and John Draper formulated the first law of photochemistry, which states that only the light absorbed by a substance can produce a photochemical change (Ohtani 2010). Photocatalysis is not an exception to this general principle, and therefore, photons of energy larger than the band gap must be absorbed to initiate any chemical transformation. Although this may be seen as an obvious statement, it implies that if the spectrum of the light source does not match closely the electronic structure of the semiconductor, many photons may be lost without any productive interaction with the solid. Consequently, the selection of the excitation source affects critically the energetic efficiency of the process. Considering that the sunlight is the ideal excitation source for environmental reasons, the search of semiconductors with the adequate band gap is a crucial concern of many researchers on photocatalysis, as it is widely discussed in the following chapters.

Although the most relevant process for the semiconductor photochemistry is band-gap excitation, other events take place simultaneously upon illumination, as it is schematically shown in Fig. 2.7. Solids reflect a certain proportion of light (as high as 30–40 % in silicon films). Besides, photons can be scattered by semiconductors without any energy gain or loss, as extensively occurs in white powders of TiO_2 and ZnO . On the other hand, irradiation can also promote electrons from localized states, and it can also cause the relaxation of an electron to the valence band by the stimulated emission of a photon.

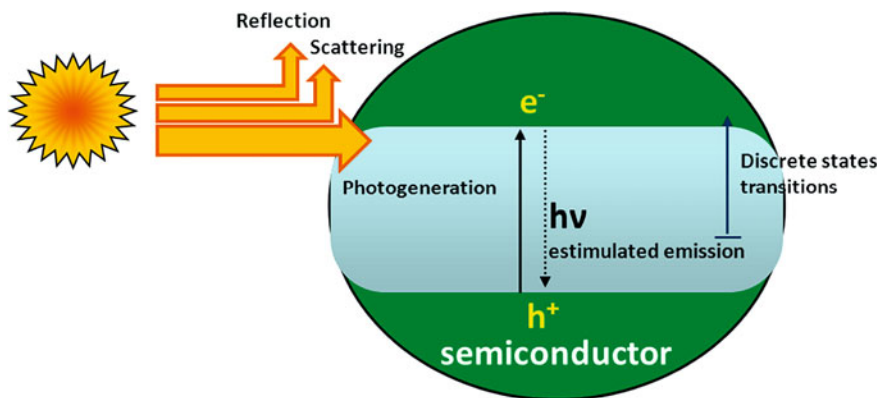


Fig. 2.7 Schematic of the main types of interaction of light with a semiconductor

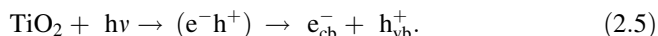
phenomena must be considered as they affect the efficiency of the photogeneration process, which cause the separation of electrons and holes, and is the primary event in the photocatalytic phenomena.

The absorption coefficient, α , can be related to the imaginary part of the refractive index of the semiconductor (Nelson 2003), and it accounts for the attenuation of light intensity when it goes through a solid. If the material is homogeneous, the Beer–Lambert law can be applied, and therefore

$$I(x) = I_0 e^{-\alpha x} \quad (2.5)$$

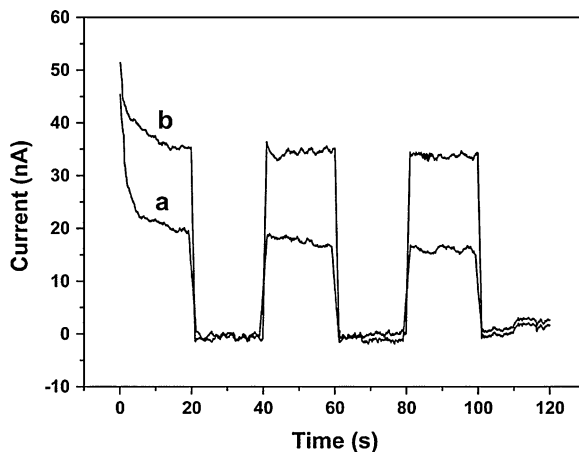
where x refers to the thickness of the material and I_0 refers to the light intensity. The value of α depends on the nature of the semiconductor, but, in general terms, as it has been mentioned in the previous section, in indirect semiconductors, it is lower and rises more smoothly when decreasing wavelength than in direct ones. An example of this can be observed in Fig. 2.5b.

Charge separation in semiconductors is a very rapid event, which occurs in the femtoseconds scale (Hoffmann et al. 1995). In the case of TiO_2 , excitation is usually thought to occur through an excitonic state, where the electron is bound as a quasi-particle to the hole, prior to charge separation (Henderson 2011) according to



However, the stability of the exciton state varies with the nature of the semiconductor, and in general, it is difficult to characterize. In the case of semiconductors with high dielectric constant, such as TiO_2 , separation is facilitated because carriers moving away from each other are screened by the lattice. Photogenerated charge separation can be measured by different techniques, among which the most direct is photoconductivity monitoring, an example of which is shown in Fig. 2.8, although an increase in the featureless background of the infrared spectrum (Drude absorption) has also been observed upon irradiation of TiO_2 (Thompson and Yates 2006).

Fig. 2.8 Example of the photocurrent responses of ZnO with two different morphologies: nanotubes (a) and nanorods (b) irradiated with 340 nm UV light under a 200 mV bias. Reproduced with permission from Guo et al. (2009). Copyright American Chemical Society



On the other hand, trap centres, such as Ti^{3+} in TiO_2 , play a very relevant role in the carrier dynamics because they provide localized states, which can be thermally or radiatively excited. Finally, it is important to note that if the energy of the incident photons overpasses that of the band gap, the excess of energy is transferred to the carriers as kinetic energy. However, due to the interactions with the lattice, this excess of energy is quickly released as heat or, in other words, by phonon excitation (Nelson 2003). Therefore, illumination with light of shorter wavelength than the band gap is inefficient because it does not increase the density of charge carriers and part of the photons' energy is lost as heat. Another important consequence of this rapid thermal decay is that the redox potential of the charge carriers is fixed by the band gap and is basically independent of the photon wavelength. Nevertheless, in the case of holes, thermalization is not so rapid and some enhancement of the whole oxidation capacity has been reported for photons with energy in excess of band gap (Henderson 2011).

Once the photoinduced separation of electrons and holes occurs, these charge carriers can promote redox reactions if they are transferred from the bulk of the semiconductor to adsorbed species with donor or acceptor properties. This phenomenon is the central event of the photocatalytic process, and it will be discussed in detail in the next section. However, the separation of electrons and holes is only stable for tens of nanoseconds before they annihilate each other in the process known as *recombination*. The two major types of recombination are radiative (photoluminescence) and non-radiative energy release. Although the actual contribution of each process may be difficult to assess, the proportion of radiative versus non-radiative recombination events in TiO_2 is generally believed to be skewed towards the latter, especially in the case of rutile (Henderson 2011). However, in other semiconductors such as ZnO, photoluminescence is more relevant (Guo et al. 2009). Photoluminescence generally occurs at sub-band-gap energies due to carrier relaxation (thermalization), and for anatase, the timescale is typically in the order of nanoseconds.

In contrast to radiative recombination, which is due to intrinsic physicochemical characteristics of the semiconductor, non-radiative recombination in trap states can be limited by carefully engineering the materials properties, so as to reduce the density of defects. This process can be explained by the Shockley–Read–Hall model for non-radiative recombination (Thompson and Yates 2006; Nelson 2003), which describes the capture of mobile electrons and/or holes at trap centres within the semiconductor. Once trapped, the electron or hole is then annihilated via recombination with, respectively, holes from the valence band or electrons from the conduction band, as schematically depicted in Fig. 2.9. The nature of recombination sites varies, but they are usually described as defect centres that form localized states within the band gap. At this point, it is worth to point out that trap sites are distinct than recombination sites because the former preferentially capture only one type of carrier, either electron or hole, while the latter interact with both leading to their obliteration. This is so because the time for thermal activation of the trapped electron or hole is much shorter than the time

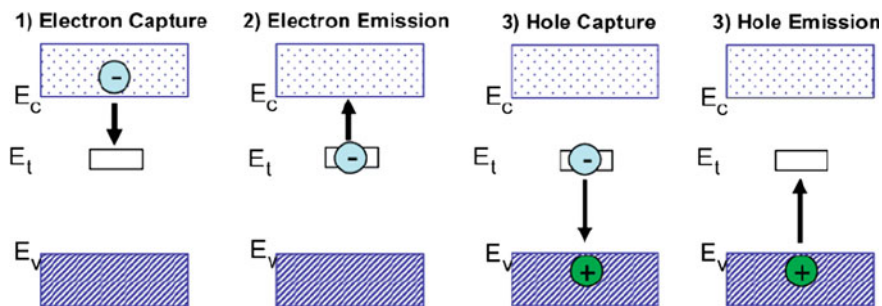


Fig. 2.9 Schematic diagram showing the four electronic transition processes that may occur for the charge carrier recombination according to the Shockley–Read–Hall model. Reproduced with permission from Shockley and Read (1952). Copyright from American Physical Society

required for capturing a carrier of opposite charge. Therefore, traps slow carriers down but do not remove them.

The Shockley–Read–Hall mechanism assumes that the semiconductor is non-degenerate and that the density of trap sites is relatively small compared to the majority carrier density in the material. Thus, for TiO_2 single crystals, the concentration of hole-trapping sites was estimated to correspond to about 3×10^{-5} for each atomic site in the crystal (Thompson and Yates 2006). Even so, recombination is a very important phenomenon since it has been estimated that 85 % of all excitation events lead to recombination after 10 ns of illumination. The kinetics of recombination depends on the density of e^-/h^+ pairs and the presence of electron scavenger or donors, but it frequently follows a second order on the concentration of charge carriers (Henderson 2011).

2.3 Charge Carrier Dynamics at Interfaces

In order to prompt chemical transformations, photogenerated charge carriers must reach the surface and be transferred to adsorbed species. For this to occur, first electrons and holes must travel through the solid avoiding recombination and they must be trapped by acceptor and donor molecules, respectively, as schematically shown in Fig. 2.10 (Linsebigler et al. 1995). The semiconductor can donate electrons to reduce an electron acceptor (pathway 5), whereas a hole can migrate to the surface where an electron from a donor species can combine with it (pathway 6). These events constitute the core of the photocatalysis process, as they trigger the formation and/or the breaking of molecular bonds required for chemical transformations. These electronic transferences require the interaction between conduction and valence bands with the localized states of the adsorbed molecules, which must have the adequate energy to favour the capture of the carrier. In addition, electrons can also be provided by localized states of trap centres of the semiconductors, such as Ti^{3+} ions in the case of TiO_2 . In any case, the reduction

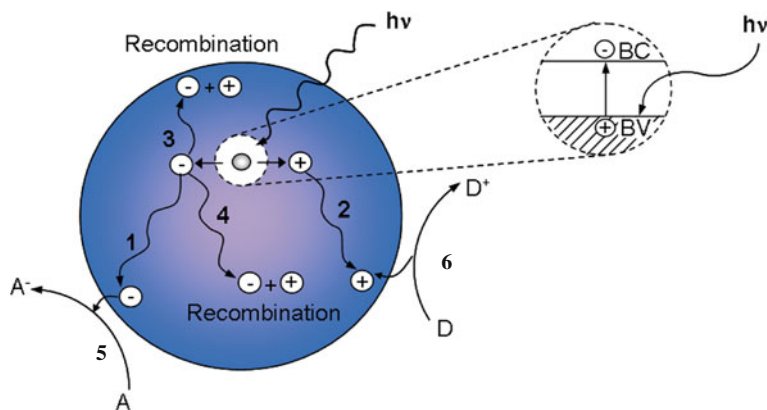
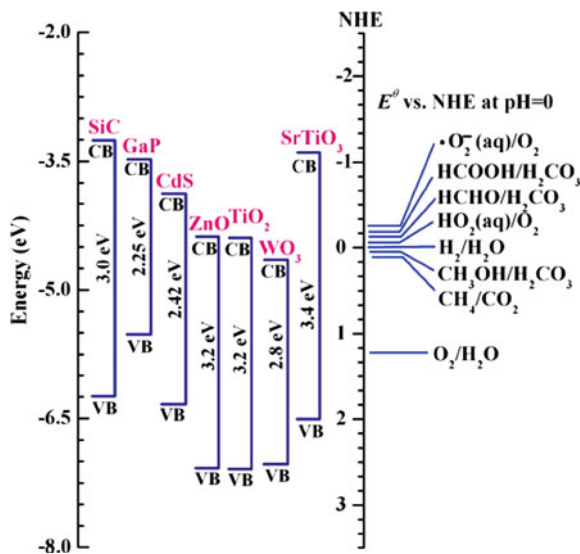


Fig. 2.10 Schematic diagram showing the charge carrier dynamic upon irradiation of a semiconductor: 1 electron transport to the surface, 2 hole transport to the surface, 3 surface recombination, 4 bulk recombination, 5 electron transference to an acceptor molecule and 6 hole trapping by a donor molecule. Adapted from Linsebigler et al. (1995)

potential of VB holes must be higher than that of the donor species, while the CB electrons must possess a lower reduction potential than the acceptor species. The equivalence between the scales of reduction potential and absolute energy can be seen in Fig. 2.11. Two reference energy levels acquire a particular relevance with respect to most photocatalytic processes and are usually taken as reference: the reduction of protons ($E_{\text{NHE}}(\text{H}^+/\text{H}_2) = 0.0 \text{ eV}$) and the oxidation of water ($E_{\text{NHE}}(\text{O}_2/\text{H}_2\text{O}) = 1.23 \text{ eV}$). Figure 2.11 displays the energies of valence and conduction band edges for a series of semiconductor materials. In general, metal oxide semiconductors have valence band with a main contribution from oxygen 2p orbitals, which is at 1–3 eV below the $\text{O}_2/\text{H}_2\text{O}$ redox couple. Conduction bands of transition metal oxides are generally constituted by d orbitals of the metal, and the position of their s is close to, or lower than, the H_2O reduction potential (Xu and Schoonen 2000). Accordingly, these materials are effective photooxidation catalysts, but they present a much more limited reducing power. In contrast, most transition metal sulphides are characterized by bands of complex structure and small gaps (<1 eV). Band edges of metal sulphides are usually situated within or close to both H_2O reduction and oxidation potentials. Hence, both the oxidizing power of the valence band holes and the reducing power of the conduction band electrons are lower than those of non-transition metals. Finally, other semiconductors such as Si present a conduction band edge well above the water reduction and oxidation potential, and consequently, they can be effective for water reduction but not for oxidation.

On the other hand, in aqueous solutions, the photoelectrochemical stability of a semiconductor is determined by the standard potential for anodic decomposition relative to the oxidation potential of water. Most metal oxide semiconductors are kinetically stable against this phenomenon, which is known as photocorrosion,

Fig. 2.11 Band-edge positions of some semiconductor photocatalysts in absolute and NHE scale relative to the energy levels of various redox couples in water. Reproduced with permission from Tong et al. (2012). Copyright Wiley-VCH



while most sulphide semiconductors are unstable and require sacrificial reagents to stabilize their activity, as it will be described in detail in the following chapters.

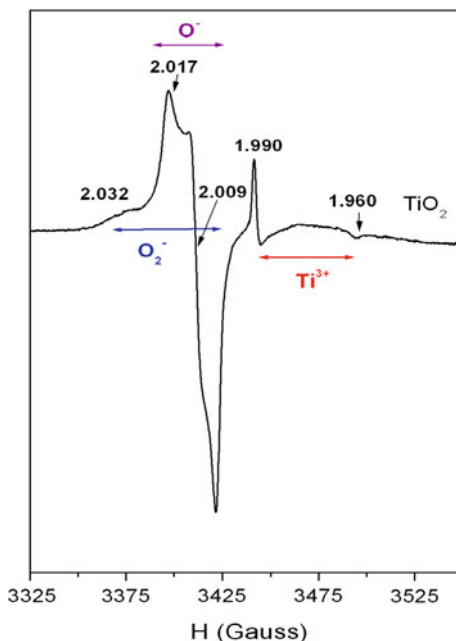
2.3.1 Donor and Acceptor Molecules

Although other chemicals such as ozone or hydrogen peroxide have been occasionally used as oxidant, the oxygen molecule is the most commonly used electron acceptor. This is due to the fact that this compound is readily available and has a high electron affinity (-0.13 eV) and it is easily adsorbed on the surface of many semiconductor oxides. In aqueous solution, although the relatively low oxygen solubility (about 8 mg/L at 25 °C) decreases the concentration at the surface, this molecule is still the usual oxidant. When an electron is trapped by an oxygen molecule, a superoxide species is formed according to the reaction:

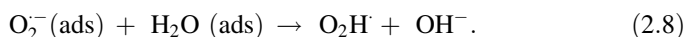
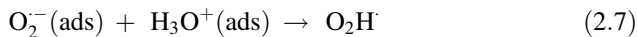


This charged molecule has an unpaired electron, and consequently, it is a radical species. Accordingly, the superoxide radical anion is paramagnetic and it can be detected, usually at liquid nitrogen temperature (77 K), by means of electron paramagnetic resonance (EPR) spectroscopy. In addition, this technique reveals the formation of Ti^{3+} by capture of photoelectrons. An example of the EPR spectrum obtained upon irradiation of TiO_2 in the presence of oxygen is displayed in Fig. 2.12. There is an extensive literature on this subject (Coronado et al. 2001), which accounts for the photoinduced formation of these radicals in TiO_2 , but also in other semiconductor oxides such as CeO_2 , ZrO_2 and ZnO . In addition, as it will

Fig. 2.12 EPR spectrum of a TiO₂ anatase sample prepared from sol to gel upon irradiation at 77 K in the presence of adsorbed oxygen showing different paramagnetic species formed by electron (O₂^{•-}, Ti³⁺) and hole (O⁻) trapping



discussed below, O⁻ radicals are simultaneously produced by hole trapping. Proton transference to the superoxide molecules either from water molecules or from hydronium ions (protons) yields the neutral hydroperoxyl radical O₂H[•], according to



Ultimately, hydrogen peroxide, H₂O₂, is produced by successive trapping of electrons, as experimentally found during photodegradation of low molecular weight chemicals over TiO₂ (Hoffmann et al. 1995). Eventually, this molecule can decompose into water and oxygen, resuming the cycle. Therefore, generally, oxygen is not incorporated into the product molecules by the cathodic route, but by interaction with the intermediates produced from hole trapping (see discussion below). Nevertheless, as it is experimentally observed by photocurrent experiments in semiconductors such as ZnO (Bao et al. 2011), photoelectrons are very efficiently scavenged by oxygen molecules, and accordingly, this process increases the availability of holes for oxidation reactions.

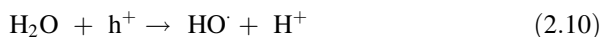
Other oxidant species such as O₃, H₂O₂ and peroxodisulphate (S₂O₈²⁻) have been occasionally used as electron acceptors in order to promote photocatalytic processes, although the enhancement of the efficiency achieved with these alternative reagents does not frequently pay off their higher cost (Malato et al. 2009).

Hydronium ions can also act as an electron acceptor in anaerobic conditions such as those of water splitting reactions, as indicated in following chemical reaction:



Eventually, this reaction results in the formation of H_2 , usually with the participation of a co-catalyst. Similarly, CO_2 can also act as an electron acceptor as it will be discussed in Sect. 4.3. However, these last two processes, in contrast to the case of the capture of photoelectron by oxygen molecules, are much less favourable due to the highly negative reduction potential of water (-0.83 V) and CO_2 (-1.90 V).

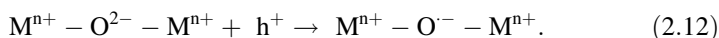
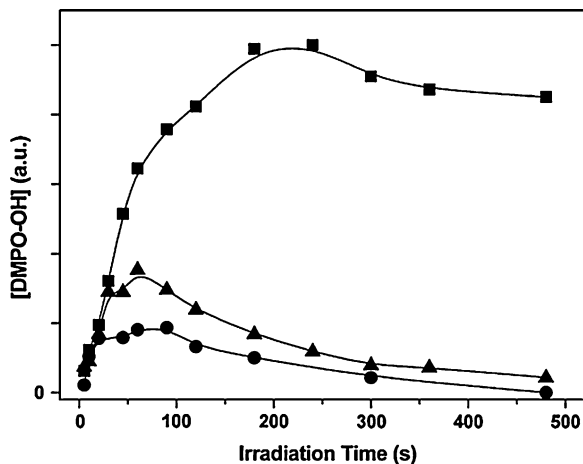
One of the major mechanistic debates in photocatalytic reactions on metal oxide semiconductors such as TiO_2 and ZnO is the relative roles of VB holes for direct oxidation versus hydroxyl radicals (OH^\cdot) for so-called indirect oxidation (Hoffmann et al. 1995; Henderson 2011). In this respect, it has been reported that in photocatalytic oxidation reactions, water is necessary only to replace the terminal oxygen atoms, which actually trap the holes, and that the photooxidation of hydroxyl groups from adsorbed water with holes is hindered both thermodynamically and kinetically (Salvador 2007). This discussion is often focused on how OH^\cdot radicals are formed, for example, via direct whole oxidation of adsorbed H_2O and/or OH^- according to



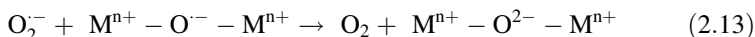
The involvement of OH^\cdot radicals in photocatalytic oxidation is proposed considering the formation of certain hydroxylated intermediates (i.e. catechol during photodegradation of phenol) and the detection by ESR of adducts of that radical with spin trapping molecules such as DMPO (5,5-dimethyl-1-pyrroline-N-oxide). This molecule forms paramagnetic adducts with the HO^\cdot radicals that can be readily monitored by ESR spectroscopy. An example of this is displayed in Fig. 2.13, which shows the evolution of the DMPO- OH^\cdot concentration with irradiation time for three nanostructured samples of CeO_2 with different crystallite size (Hernández-Alonso et al. 2004). In theory, hydroxyl radicals can act at distance as they can detach from the surface and interact with molecules in the bulk of the solution, whereas direct capture of holes requires adsorption of the donor species. Nevertheless, under many circumstances, the identification of the specific pathway is difficult, especially because the direct (hole injection) and indirect (OH^\cdot mediated) routes can take place simultaneously depending on the reaction conditions (Henderson 2011). In this respect, it seems that the direct interaction of the donor molecules with the semiconductor is favoured if their concentration is high or if the solid surface is not highly hydroxylated.

On the other hand, trapping of holes by oxide or sulphide anions has been frequently detected by EPR, as it can be appreciated in Fig. 2.12 for the case of TiO_2 . Radical species are formed according to

Fig. 2.13 Evolution of the signal intensity of the DMPO-OH· adduct as a function of the irradiation time of with UV lamps for nanostructured CeO₂ samples with an average crystallite size of 7.3 nm (*Black circle*), 5.7 nm (*Black Triangle*) and 5 nm (*Black square*). Reproduced with permission from Hernández-Alonso et al. (2004). Copyright Elsevier



Participation of these species in oxidation reactions provides an alternative path for the transference of holes from the semiconductor to the donor molecules (Coronado et al. 2001). Similarly, in the case of sulphide semiconductors, formation of $\text{S}^{\cdot-}$ has been reported to take place by hole capture at sulphide ions (Nakaoka and Nosaka 1997). ESR studies show that different $\text{O}^{\cdot-}$ species can be formed at variable concentrations depending on the morphology of the semiconductor. In any case, secondary reactions of these radicals with organic molecules can generate additional radical species by deprotonation (e.g. R-CH_2^{\cdot}) and subsequent oxygen incorporation (e.g. peroxide radicals of the type $\text{R-CH}_2\text{OO}^{\cdot}$) (Coronado and Soria 2007). On the other hand, interaction between these surface species may also contribute to recombination, especially if electron- and hole-derived species react together as in the following process:

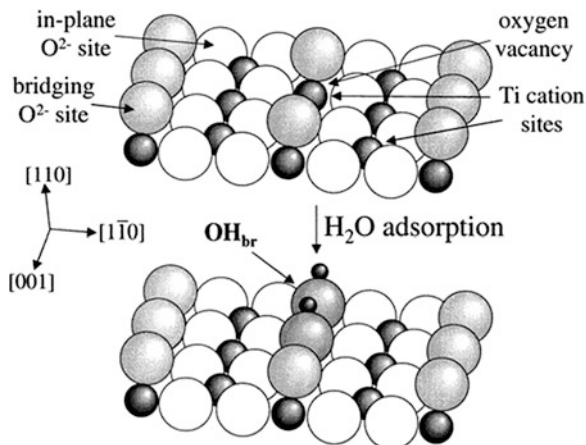


where the charge transference is reverted. Nevertheless, the complexity and the inherent difficulties of studying these short-living radicals under realistic conditions clearly warrant further studies in order to gain a more comprehensive understanding of the initial stages of photocatalytic processes.

2.4 Surface Chemistry and Adsorption

The physicochemical characteristics of the surface are crucial to define the reactivity of a catalyst, because it is there where the interactions between reactive molecules and the solid occur. Accordingly, adsorption depends not only on the density of sites,

Fig. 2.14 Scheme of the water adsorption process on the [110] surface of TiO₂ rutile. Adapted from Henderson et al. (2003). Copyright American Chemical Society



but also on their chemical nature, which determines the strength of the bonding with reagents and products. This relevance of surface properties in photocatalysis constitutes an important additional factor to define the efficiency of the process which is basically absent in the case of other semiconductor applications such as photovoltaics.

Surface chemical composition frequently differs from that of the bulk material because the discontinuity of the crystal imposes an energetic burden, which can be limited by structural rearrangement and/or adsorption of available molecules. In this regard, it is essential noting that numerous studies have revealed that water molecules dissociate on the surface of metallic oxides and sulphides. This process yields to the formation of hydroxyl groups in the case of oxides, while $>SH$ and $>M-OH$ moieties are generated on sulphide surfaces (Henderson et al. 2003; Rönngren et al. 1994). These surface groups complete the coordination of metallic ions, whereas protons bind to the bridging oxygen or sulphur atoms. An example of this process can be observed in Fig. 2.14, which shows a scheme of water adsorption on TiO₂. This process reduces the excess of energy caused by the abrupt discontinuity of the solid structure at the edge of the crystal, and it is so energetically favourable that occurs even in air with low relative humidity. Consequently, adsorption of reactive molecules is determined, to a great extent, by the density and specific characteristics of hydroxyl groups at the semiconductor surface. Many organic substances like aromatic compounds are attached to the TiO₂ surface by hydrogen bonding (Nagao and Suda 1989), but stronger interactions with formation of new bonds can be observed for other molecules. In this way, alcohols such as ethanol can lead to the formation of surface alkoxides of the type $>M-O-CH_2CH_3$ in the gas phase, while molecules with acid character such as HCOOH frequently adsorb as carboxylates such as HCOO⁻ (Henderson 2011). These surface complexes can adopt different topologies (bidentate, bringing...) which can also affect their reactivity.

Table 2.2 PZC of some semiconductors metal oxides and sulphides with relevance in photocatalysis (Xu and Schoonen 2000)

Material	TiO ₂	KTaO ₃	ZnO	SrTiO ₃	Ga ₂ O ₃	WO ₃	KNbO ₃	ZnS	CdS
PZC	5.80	8.55	8.80	8.60	8.47	0.43	8.62	1.70	2.00

In aqueous solution, it is necessary to consider the amphoteric character of the $>M-OH$ species, because the surface charge depends on the pH. Thus, at low pH values, semiconductor surface is positively charged, while in alkaline conditions, it is negatively charged. The pH value, at which the concentration of negative and positive centres is the same, constitutes the so-called point of zero charge (PZC), which varies with the crystalline phase and chemical composition, but also with surface characteristics. Table 2.2 shows the PZC on some representative semiconductors frequently used as photocatalysts, which varies in a wide range. For most oxides, it is around 8.5, whereas for sulphides, it is close to 2. In the case of reactions with ionic species, this parameter is crucial, because it defines the pH interval at which adsorption is facilitated or hindered by electrostatic interactions.

As for any heterogeneous catalyst, specific area is an important parameter to establish the photoactivity of a semiconductor. Although materials with larger surface area (usually estimated by the Brunauer, Emmett and Teller model as S_{BET}) tend to have better performance, a straightforward correlation between the available surface and the efficiency of photocatalysts is rarely found. In fact, paradoxical results can be obtained because under certain circumstances, photocatalysts with high surface area can present poorer photoactivity. This is due to the fact that electronic properties, such as light absorption or the degree of charge recombination, rather than surface properties are the rate limiting steps. In particular, materials with larger specific area often display higher defect concentration, and they show a significant recombination at surface centres. Therefore, an optimal synthesis procedure for photocatalyst must pursue a balance between the number of active sites and their specific activity.

Adsorption of reagents on semiconductors is usually described by the Langmuir isotherm (Hoffmann et al. 1995; Malato et al. 2009), which responds to the following equation:

$$\theta = \frac{KC}{1 + KC} \quad (2.14)$$

where θ corresponds to the coverage of a specific chemical, C is the concentration of such species, and K is the adsorption constant that accounts for the strength of the interaction. This equation can be deduced assuming that there is only one type of adsorption centre, that full coverage corresponds to one monolayer and that the strength of the interaction of the surface with the adsorbate does not vary with coverage. Obviously, these conditions are very restrictive, and in real situations, Langmuir isotherms only hold for low concentration ranges, or they require modifications. In this respect, two different adsorption sites, or competition of two different adsorbates (e.g. water and organic vapour), are frequently considered

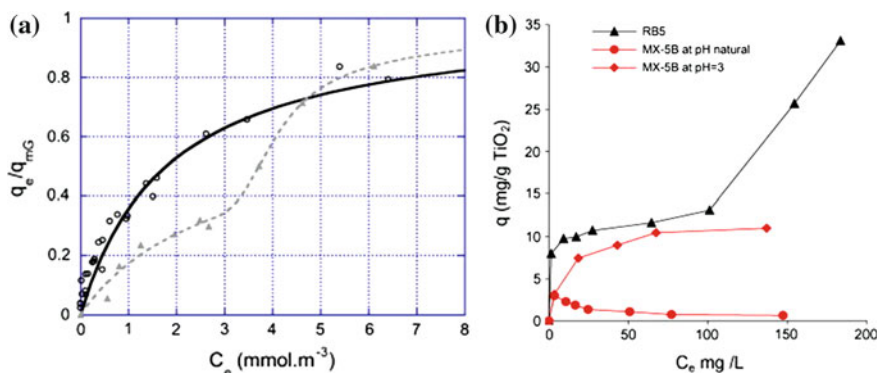


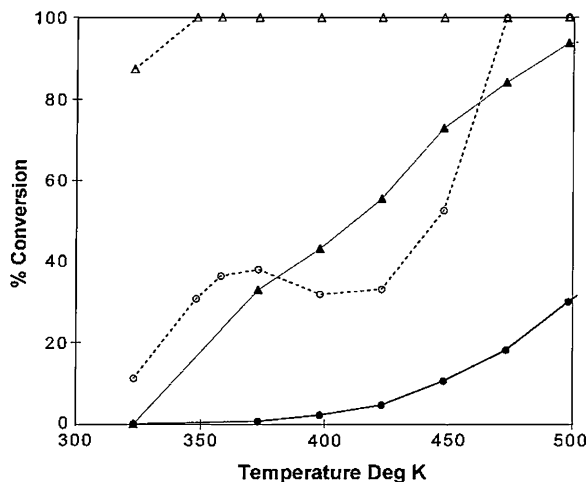
Fig. 2.15 Adsorption isotherms of: **a** toluene over a TiO_2 photocatalyst supported on quartz fibres in dry (circles) and in humid air (triangles). Reproduced from Maudhuit et al. (2011). **b** The dyes Remazol Black 5 (RB5, triangles) and Procion Red (MX-5B, diamonds and circles) over TiO_2 Degussa P25 in aqueous solution at natural pH or pH = 3 (circles). Solid line in A represents the best fitting to the Langmuir adsorption isotherm. Reproduced with permission from Sahel et al. (2007). Copyright Elsevier

situations for more representative models of adsorption. Figure 2.15 shows two illustrative examples of adsorption isotherms experimentally obtained with TiO_2 -based photocatalysts in very different conditions. These results show that the adsorption of vapours of hydrocarbons such as toluene in dry air, or of cationic dyes in aqueous solutions at low concentrations, can be adequately described by Eq. 2.14. However, in humid air, the competitive adsorption of water, which quickly forms a surface layer, completely modifies the interaction, and accordingly, the shape of the isotherms no longer responds to the Langmuir model (Maudhuit et al. 2011). Similarly, in the case of high concentration of dyes, multilayer adsorption occurs as it is reflected by the rise in the concentration of adsorbed molecules (see Fig. 2.15b). On the other hand, the results obtained with dyes also illustrate the strong influence of pH on the adsorption of ionic species. Thus, results of Fig. 2.15b indicate that for a pH lower than the PZC, the surface of TiO_2 is negatively charged and, consequently, retains a limited amount of the cationic dye Procion Red (Sahel et al. 2007).

2.5 Photocatalysis versus Thermal Catalysis

The term “catalysis” was coined by the Swedish chemist Jöns Jacob Berzelius in 1835, and it is currently a central concept in chemistry, which has also pervaded the popular language. According to a conventional textbook definition, a catalyst is “a substance that accelerates a reaction but undergoes no net chemical change” (Atkins 1998). This action is possible because the reaction takes a different path due to the interaction of the reagents with the catalyst, which leads to lowering of

Fig. 2.16 Comparison between the thermal (*filled triangles and circles*) and photothermal (*open triangles and circles*) activities of 0.2 % Pt/TiO₂ for the elimination of ethanol vapours in air. The plot shows total conversion (*triangles*) and mineralization to CO₂ (*circles*). Reproduced with permission from Kennedy et al. (1998). Copyright Elsevier



the activation energy. As a consequence, the reaction rate can be boosted by several orders of magnitude. Following this process, the catalysts are recovered in its initial state, ready for a new cycle of transformation.³ Although homogeneous substances (e.g. acids) and enzymes are important types of catalysts, only heterogeneous catalysts, which comprise solids used in reactions with liquids or gases, are relevant in the scope of the present book.

Most heterogeneous catalysts, such as zeolites, Ni Raney and any other, are thermally activated, and this is an obvious difference with photocatalysts. However, conventional catalysis and photocatalysis are not mutually exclusive, and a good example of this can be the Pt/TiO₂ catalysts, which is very efficient for volatile organic chemical (VOC) removal at moderate temperature, but it can also be activated by light. The graph of Fig. 2.16 shows that thermal and photonic activation can work cooperatively to yield a higher conversion (Kennedy et al. 1998). In the same way, more recently, it has been reported that the purely photocatalytic oxidation of ethylene is favoured at temperatures in the 100–200 °C range (Westrich et al. 2011). Nevertheless, the increment of temperature promotes thermal catalysis according to the expectation of the Arrhenius term of the kinetic equation, while photocatalytic activity usually goes through a maximum at moderate temperatures which is compatible with the reported apparent activation energy of a few kilojoules per mol (Malato et al. 2009). This behaviour is due to the fact that some steps of the process, such as desorption of the products, are thermally activated. However, as temperature rises, photonic efficiency drops because thermal agitation promotes recombination, and in parallel, the coverage of

³ Obviously, real heterogeneous catalysts frequently suffer deactivation, but such phenomenon occurs following several cycles (frequently more than ten hundreds), and consequently, recovery of the initial state (even if imperfect) is still a crucial aspect in catalysis.

reagent decreases. As a consequence, after the initial promotion, further increase in temperature is detrimental for photoactivity.

As mentioned above, catalysis modifies the kinetics of the processes but not the thermodynamics, and consequently, it can only promote spontaneous reactions or, in other words, those with negative Gibbs energy (ΔG) (Ohtani 2010). However, photocatalysts have the ability to convert light into chemical energy, and this fact challenges the conventional definition of catalysis because some non-spontaneous reaction (i.e. those with $\Delta G > 0$) can be promoted. This feature affords photocatalysis the potential to be utilized for storing sunlight energy in the form of chemicals. In fact, this is the goal of the so-called artificial photosynthesis processes like water splitting and CO_2 photoreduction. In contrast, oxidation reactions, such as those of detoxification treatments, are downhill processes ($\Delta G < 0$) and do not accumulate energy, although they must overcome the activation barrier for the rupture of strong bonds like C–C.

In most applications, it is advantageous to keep the substrate-to-catalyst ratio as high as possible to reach the efficiency required by the economy of the process. In this way, even in the relatively unfavourable case of the production of fine chemicals with expensive noble metal catalysts such Rh and Ir complexes, the proportion between substrate and catalyst is typically higher than 1,000. This is in strong contrast to the case of photocatalysts, in which, in a usual assay for the removal of aqueous pollutants, the molar ratio between the organic molecule and TiO_2 is as low as 0.1. This fact gives an indication of the relatively low efficiency of photocatalysis. These considerations remark the importance of reusing photocatalysts many times without a significant lack of efficiency in order to have a viable technological solution for energy and environmental applications.

2.6 Combining Light and Potential: From Photoelectrocatalysis to Dye Cells

Since the early developments of photocatalysis (Fujishima et al. 2000), the application of an electrical bias has been proposed to reduce electron–hole recombination and, consequently, increase the efficiency of the process. This implies, as it can be appreciated in the scheme of Fig. 2.17a, that the semiconductor is disposed as an electrode, which is connected to another counter-electrode and both are placed in an electrolyte solution. Obviously, the photoelectrode should be irradiated, and for that purpose, the cell is provided with an adequate window. In a solar photovoltaic cell, photogenerated charges are driven efficiently in opposite directions by an electric field at the semiconductor/metal junctions. In a photoelectrochemical cell, a space-charge layer is generated within a thin surface region of the semiconductor ($1\text{--}10^3$ nm) at the interface with the solution, in which the electronic energy bands are bent upwards or downwards in n- and p-type semiconductors, respectively. When this electrode is photoexcited, electron–hole

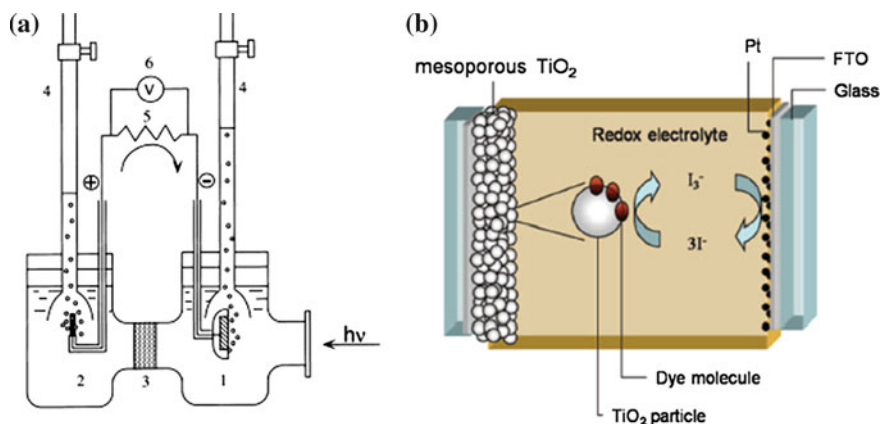


Fig. 2.17 **a** Schematic diagram of a photoelectrochemical cell: 1 TiO_2 electrode, 2 platinum black counter-electrode, 3 ionic exchange membrane for separation, 4 gas burette, 5 load resistance and 6 voltmeter. Reproduced with permission from Fujishima et al. (2000). Copyright Elsevier. **b** Pictorial representation of a dye-sensitized solar cell. Reproduced from Hagfeldt et al. (2010). Copyright American Chemical Society

pairs are created and separated in the space-charge layer. This type of device has been usually utilized for hydrogen production from water splitting because photogenerated electrons can flow to the counter-electrode and reduce protons, generating hydrogen. This is the case of a TiO_2 cell, in which the direction of the current reveals that the oxidation reaction (oxygen evolution) occurs on the semiconductor and the reduction reaction (hydrogen evolution) at the Pt electrode.

Hydrogen evolution can occur without an external bias if the conduction band position of the semiconductor electrode is at least as negative as -0.4 V (SHE) in acid solution or -1.2 V (SHE) in alkaline solution. This is the case among many other materials of SrTiO_3 , CaTiO_3 and TiO_2 in acidic conditions. However, one of the fundamental advantage of photoelectrocatalysis is that by applying an adequate potential, reactions such as water dissociation can take place over semiconductors with insufficient conduction band energy (Fujishima et al. 2000), although at expenses of a higher energy consumption. Similarly to the case of photocatalysis, photon energy cannot be fully utilized in a single-band-gap device, because vibrational relaxation causes a loss of energy as heat. In addition, polarization losses also occur, and accordingly, an increment of the bias over the theoretical values is normally required. An alternative approach to increase the efficiency of the energy transformation is the use of tandem cells by combining different semiconductors. In this respect, using electrodes with layers of GaAs and GaInP_2 , an energy yield of as high as 34 % can be achieved (Fujishima et al. 2000).

Another different kinds of photoelectrochemical devices based on semiconductors are dye-sensitized cells (DSCs), proposed for first time in the seminal paper by O'Regan and Grätzel in 1991 (O'Regan and Grätzel 1991). Although conceived for electricity production and, therefore, far apart from chemical

applications, DSCs share some same basic features with photoelectrocatalytic cells and some type of photocatalysts (see [Chap. 16](#)), as it can be appreciated in the schematic of [Fig. 2.17b](#). Accordingly, although these devices are out of the scope of this book, an elementary description of their molecular mechanism can be of interest to gain a deeper understanding of the interaction of light with semiconductors.

Typically, these cells consist of a mesoporous layer of TiO_2 nanoparticles that have been sintered to establish electronic conduction ([Hagfeldt et al. 2010](#)). The semiconductor film has a thickness of about $10\ \mu\text{m}$ and porosity in 50–60 % range. This photoactive oxide is deposited on a transparent conducting oxide such as fluorine-doped SnO_2 , on a glass substrate. In addition, a monolayer of a charge-transfer dye, generally a ruthenium complex with pyridine-derived ligands, is adsorbed on the surface of the nanocrystalline film. Illumination of this layer results in the injection of an electron into the conduction band of the oxide, leaving the dye in its oxidized state. Then, the dye can recover its ground state by electron transfer from the electrolyte, usually an organic solvent containing the I^-/I_3^- redox couple. The regeneration of the sensitizer impedes the recapture of the conduction band electron by the oxidized dye. The I_3^- ions diffuse a distance $<50\ \mu\text{m}$ through the electrolyte to the cathode. In this component, the cycle is completed by reduction of I_3^- species to I^- by electron transfer with the assistance of a thin layer of a platinum catalyst ([Hagfeldt et al. 2010](#)). These cells are more adaptable and flexible than those based on Si, but in general, they present lower efficiency with record values about 12 %. In addition, stability is another important concern for commercial development of these devices, but steady performance after 1,000 h of operation has been recently achieved.

2.7 Measuring Efficiency

As in any process, determining the efficiency of photocatalysis is crucial to establish comparisons between different photoactive systems. However, this is not a trivial task as it will extensively commented through this book, because the use of different illumination source with dissimilar power and spectral distribution (e.g. Xe or Hg lamps, sunlight...), along with the different reactor configurations (e.g. annular, slurry, flat...), complicates enormously the task of ranking photocatalyst materials. In this context, several parameters can be of interest to infer the performance of photocatalytic reactions. At a very basic level, it is useful to normalize the reaction rate to the amount of catalyst to provide activity values as $\mu\text{mol h}^{-1} \text{g}^{-1}$. Some normalization with surface area has been also used, but these values are more prone to be misleading as photocatalysis also depends significantly on the bulk properties of the semiconductor and therefore should be used carefully. More relevant is the concept of quantum yield (QY), as applied to homogeneous photochemical systems ([Ohtani 2010](#); [Herrmann 2010](#)), which is given by the expression:

$$\text{Quantum Yield} = \frac{\text{product rate} \times \text{number of electrons implied}}{\text{Flux of absorbed photons}} \times 100. \quad (2.15)$$

As monitoring of photocatalytic reactions is carried out by chemical analysis, determining the number of electrons implied requires defining the stoichiometry of the reaction. On the other hand, because measuring photon absorption is usually complex, this parameter is very often substituted by the apparent quantum yield or photonic efficiency, which can be calculated by using the following equation:

$$\text{Photonic Efficiency} = \frac{\text{product rate} \times \text{number of electrons implied}}{\text{Flux of incident photons}} \times 100. \quad (2.16)$$

The apparent quantum yield is smaller than the total quantum yield because the number of absorbed photons is usually smaller than that of incident ones. However, it is necessary to keep in mind that this parameter does not provide an absolute value, because the efficiency in the use of available photons will depend in certain extend on how the photocatalysts are illuminated in the reactor. In addition, solar energy conversion is another useful parameter for assessing those photocatalytic processes used to accumulate solar energy, such as CO₂ reduction or water splitting. This can be estimated according to

$$\text{Energy Conversion} = \frac{\text{Energy in the products}}{\text{Energy of the incident light}} \times 100. \quad (2.17)$$

Finally, it is worth mentioning that in order to overcome the problem derived from comparing tests performed in different conditions, further development of standardization procedures will be warranted in the near future. In this respect, several normalized assays based on diverse photocatalytic reactions carried out in thoroughly controlled conditions have been recently proposed (Mills et al. 2012).

References

- Asahi R, Taga Y, Mannstadt W, Freeman AJ (2000) Electronic and optical properties of anatase TiO₂. *Phys Rev B* 61(11):7459–7465
- Atkins PW (1998) *Physical Chemistry*, 6th edn. Oxford University Press, Oxford
- Bao J, Shalish I, Su Z, Gurwitz R, Capasso F, Wang X, Ren Z (2011) Photoinduced oxygen release and persistent photoconductivity in ZnO nanowires. *Nanoscale Res Lett* 6:404
- Campoccia A, Dusonchet L, Telaretti E, Zizzo G (2009) Comparative analysis of different supporting measures for the production of electrical energy by solar PV and Wind systems: Four representative European cases. *Sol Energy* 83(3):287–297
- Coronado JM, Maira AJ, Conesa JC, Yeung KL, Augugliaro V, Soria J (2001) EPR study of the surface characteristics of nanostructured TiO₂ under UV irradiation. *Langmuir* 17(17):5368–5374
- Coronado JM, Soria J (2007) ESR study of the initial stages of the photocatalytic oxidation of toluene over TiO₂ powders. *Catal Today* 123(1–4):37–41

- Duffy JA (1990) Bonding energy levels & bands, inorganic solids. Longman, Essex
- Fernandez-Garcia M, Martinez-Arias A, Hanson JC, Rodriguez JA (2004) Nanostructured oxides in chemistry: characterization and properties. *Chem Rev* 104:4063–4104
- Fujishima A, Rao TN, Tryk DA (2000) Titanium dioxide photocatalysis. *J Photochem Photobio C* 1:1–21
- Georgia State University, Department of Physics and Astronomy (2011) In Hyperphysics, Semiconductors. <http://hyperphysics.phy-astr.gsu.edu/hbase/hframe.html>
- Guo H, Lin Z, Feng Z, Lin L, Zhou J (2009) White-light-emitting diode based on ZnO nanotubes. *J Phys Chem C* 113:12546–12550
- Hagfeldt A, Boschloo G, Sun L, Kloo L, Pettersson H (2010) Dye-sensitized solar cells. *Chem Rev* 110(11):6595–6663
- Henderson MA (2011) A surface science perspective on TiO₂ photocatalysis. *Surf Sci Reports* 66(6–7):185–297
- Henderson MA, Epling WS, Peden CHF, Perkins CL (2003) Insights into photoexcited electron scavenging processes on TiO₂ obtained from studies of the reaction of O₂ with OH groups adsorbed at electronic defects on TiO₂ (110). *J Phys Chem B* 107(2):534–545
- Hoffmann R (1989) Solid and surfaces: a Chemist's view of bonding in extended structures. VCH, New York
- Hoffmann M, Martin ST, Choi W, Bahnemann DW (1995) Environmental applications of semiconductor photocatalysis. *Chem Rev* 95:69–96
- Hernández-Alonso MD, Hungría AB, Martínez-Arias A, Fernández-García M, Coronado JM, Conesa JC, Soria J (2004) EPR study of the photoassisted formation of radicals on CeO₂ nanoparticles employed for toluene photooxidation. *Appl Catal B* 50:167–175
- Herrmann JM (2010) Photocatalysis fundamentals revisited to avoid several misconceptions. *Appl Catal B* 99(3–4):461–468
- Kennedy JC, Datye AK, Catal J (1998) Photothermal heterogeneous oxidation of ethanol over Pt/TiO₂. *J Catal* 179:375–389
- Linsebigler AL, Lu G, Yates JT (1995) Photocatalysis on TiO₂ surfaces: principles, mechanisms, and selected results. *Chem Rev* 95:735–758
- Nagao M, Suda Y (1989) Adsorption of benzene, toluene, and chlorobenzene on titanium dioxide. *Langmuir* 5:42
- Nakaoka Y, Nosaka Y (1997) Electron spin resonance study of radicals produced by photoirradiation on quantized and bulk ZnS particles. *Langmuir* 13:708–713
- Nelson J (2003) The physics of solar cells. Imperial College Press, London
- Maudhuit A, Raillard C, Héquet V, Le Coq L, Sablayrolles J, Molins L (2011) Adsorption phenomena in photocatalytic reactions: the case of toluene, acetone and heptane. *Chem Eng J* 170(2–3):464–470
- Migas DB, Shaposhnikov VL, Borisenko VE, Arnaud D'Avitaya F (2010) Effects of morphology on stability, electronic, and optical properties of Rutile TiO₂ nanowires. *J Phys Chem C* 114(49):21013–21019
- Mills A, Hill C, Robertson PKJ (2012) Overview of the current ISO tests for photocatalytic materials. *J Photochem Photobio A* 237:7–23
- Miller DAB (2007) Germanium quantum wells for high-performance modulators in silicon photonics. *Photonic Spectra*. September issue. <http://www.photonics.com/Article.aspx?AID=30705>
- Malato S, Fernández-Ibáñez P, Maldonado MI, Blanco J, Gernjak W (2009) Decontamination and disinfection of water by solar photocatalysis: recent overview and trends. *Catal Today* 147:1–59
- Ohtani B (2010) Photocatalysis A to Z—What we know and what we do not know in a scientific sense. *J Photochem Photobio C: Photochem Rev* 11:157–178
- O'Regan B, Grätzel M (1991) A low-cost, high-efficiency solar cell based on dye-sensitized colloidal TiO₂ films. *Nature* 353(6346):737–740

- Rönngren L, Sjöberg S, Sun ZX, Forsling W (1994) Surface reactions in Aqueous metal sulfide systems: 5. The complexation of sulfide ions at the ZnS-H₂O and PbS-H₂O Interfaces. *J Colloid Interface Sci* 162(1):227–235
- Salvador P (2007) On the nature of photogenerated radical species active in the oxidative degradation of dissolved pollutants with TiO₂ aqueous suspensions: A revision in the light of the electronic structure of adsorbed water. *J Phys Chem C* 111(45):17038–17043
- Sahel K, Perol N, Chermette H, Bordesc C, Derriche Z, Guillard C (2007) Photocatalytic decolorization of Remazol Black 5 (RB5) and Procion Red MX-5B—Isotherm of adsorption, kinetic of decolorization and mineralization. *Appl Catal B* 77(1–2):100–109
- Shockley W, Read WT Jr (1952) Statistics of the recombinations of holes and electrons. *Phys Rev* 87:835–842
- Tong H, Ouyang S, Bi Y, Umezawa N, Oshikiri M, Ye J (2012) Nano-photocatalytic materials: possibilities and challenges. *Adv Mater* 24(2):229–251
- Thompson TL, Yates JT Jr (2006) Surface science studies of the Photoactivation of TiO₂ new photochemical processes. *Chem Rev* 106(10):4428–4453
- Westrich TA, Dahlberg KA, Kaviani M, Schwank JW (2011) High-temperature photocatalytic ethylene oxidation over TiO₂. *J Phys Chem C* 115:16537–16543
- Xu Y, Schoonen MAA (2000) The absolute energy positions of conduction and valence bands of selected semiconducting minerals. *Am Mineral* 85:543–556

Chapter 3

Environmental Applications of Photocatalysis

Raquel Portela and María Dolores Hernández-Alonso

The advantages of the photocatalytic processes (operation under ambient temperature and pressure, high stability and low cost of the catalyst, complete mineralization without selectivity restrictions and possibility of using solar light as energy source) open a wide range of environmentally friendly applications that are either under investigation or already in the market. Both the technological and economic relevance of photocatalysis has increased considerably over the past decade.

The applications of semiconductor photochemistry are usually based on photooxidation, photoreduction, photosterilization and photoinduced superhydrophilicity or a combination thereof. The mechanism for all these phenomena has been extensively reviewed (Fox and Dulay 1993; Hoffmann et al. 1995; Fujishima et al. 2000), and the fundamentals have been overviewed in Chap. 2. Figure 3.1 schematically shows all the relevant intermediate species which play a role in the environmental processes discussed in this chapter. The oxidation of surface OH^- to hydroxyl radicals takes place in the photogenerated holes; on the other hand, the photogenerated electrons reduce adsorbed oxygen to superoxide radical anion (O^{2-}), which can be further reduced to hydroperoxyl radical (OOH), to hydrogen peroxide (H_2O_2) and finally to water (H_2O) or hydroxyl radicals (OH^\cdot).

In the presence of organic compounds adsorbed on the photocatalyst surface, these and any subsequent intermediates may be oxidized in several steps until mineralization to carbon dioxide, water and inorganic acids by the highly oxidizing species generated or by direct reaction with the holes. As it was mentioned in Chap. 2, there is some debate concerning the mechanism of holes trapping, but it has been generally accepted that water species adsorbed on terminal Ti atoms trap the holes to form hydroxyl radicals. On the other hand, it seems that some

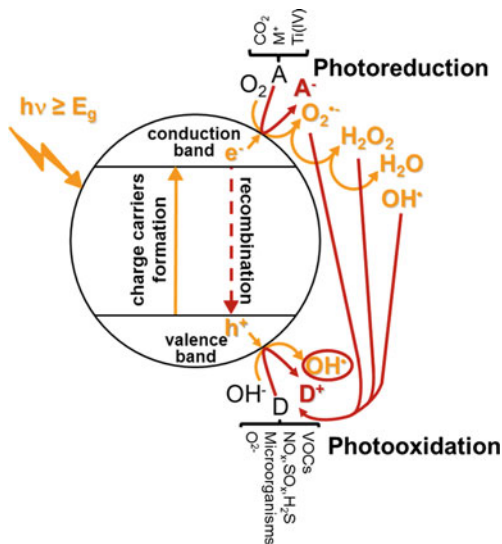
R. Portela (✉)

Institute of Catalysis and Petrochemistry, CSIC, Calle Marie Curie 2 E-28049 Madrid, Spain
e-mail: raquel.portela@csic.es

M. D. Hernández-Alonso

Renewable Energy Division, CIEMAT, Madrid, Spain
e-mail: lolihza@gmail.com

Fig. 3.1 Diagram showing the origin of the photooxidation, photoreduction, photosterilization and photoinduced superhydrophilicity phenomena on irradiated TiO₂. D = e⁻ donor other than hydroxyl, A = e⁻ acceptor other than oxygen



adsorbed compounds may act as electron donors for the oxidation reaction with holes while others not, reacting only with the generated oxidizing species (Benoit-Marquie et al. 2000; Villarreal et al. 2004).

The reactive species are also able to oxidize adsorbed inorganic compounds (NO_x to nitrate, SO_x and H₂S to sulphate, etc.) and to damage the cell wall of microorganisms, leading to their inactivation and the mineralization of the organic matter contained therein. Thus, the photocatalytic oxidation technology may be applied to the complete purification of air and water. The activity will depend on the catalyst properties (composition, surface area, crystallinity, loading, etc.), the type and concentration of contaminants and their relative adsorption properties, the photoreactor configuration, the radiation source (wavelength and irradiance) and the operational parameters: temperature, dissolved oxygen, pH or humidity (Chong et al. 2010; Zhao and Yang 2003).

The photoreduction of oxidized compounds by the electrons is also possible, although most compounds susceptible of reduction cannot compete with oxygen because of the fast reaction kinetics of the latter. Examples of applications of the photoreduction ability are CO₂ capture and transformation into hydrocarbons, which will be commented in Sect. 4.3, or noble metal recovery. At this respect, the reactivity of metals has been observed to follow the order Ag > Pd > Au > Pt ≫ Rh ≫ Ir ≫ Cu = Ni = Fe = 0 (Herrmann et al. 1993).

In the absence of competing adsorbed species, the surface sites available for reaction with electrons are surface Ti(IV) that are reduced to generate hydrophilic Ti(III), while surface O²⁻ are oxidized by the holes giving place to oxygen vacancies that are filled by hydroxyl ions subsequently absorbed. As a result, under exposure to suitable radiation, the hydrophilicity of the surface increases up to contact angles <5° (superhydrophilicity); in the dark, in the presence of oxygen,

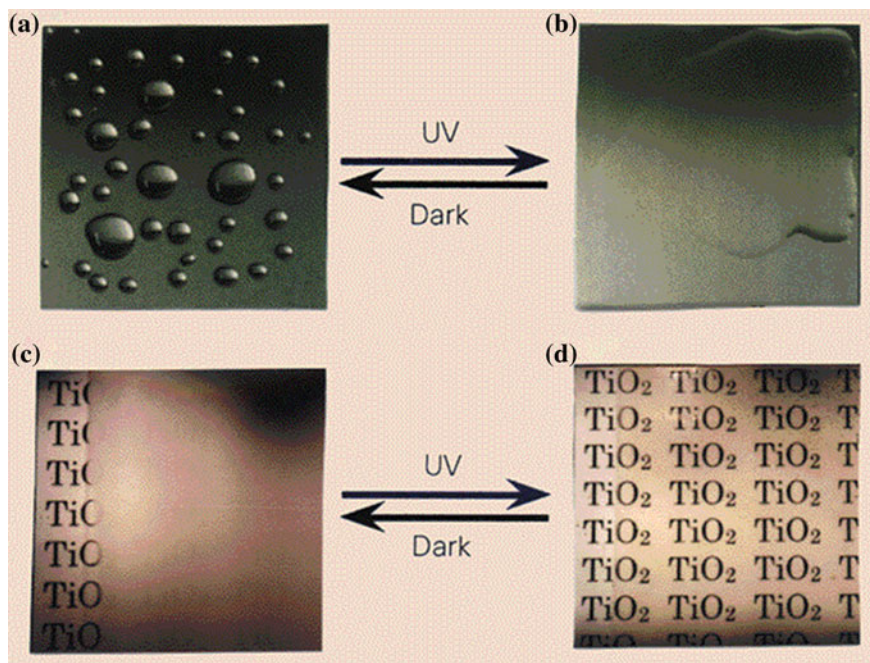


Fig. 3.2 Photoinduced hydrophilicity in a TiO_2 -coated glass. On the left, the non-irradiated surface is exposed to (a) water droplets (water contact angle of 72°) and (c) water vapour. On the right, the irradiated surface is shown, where the (b) increased wettability (contact angle close to 0°) and (d) anti-fogging properties are observed. Reproduced with permission from (Wang et al. 1997). Copyright Nature Publishing Group

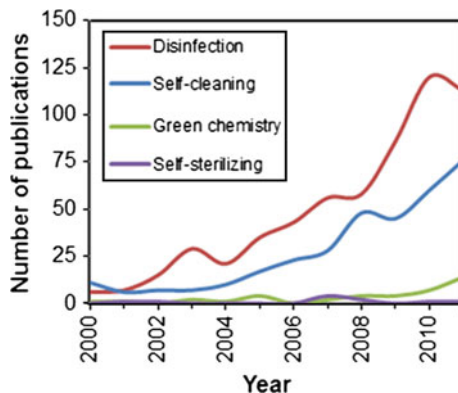
the hydrophilicity decreases to the initial contact angle value as the Ti(III) sites are oxidized back to Ti(IV) , and the vacancies are filled by the generated O^{2-} ions. The photocatalytic superhydrophilicity of TiO_2 -coated surfaces, shown in Fig. 3.2, has a wide range of applications related to the anti-fogging effect and the self-cleaning properties.

In the twenty-first century, and according to the present environmental challenges and the renewed energy crisis, the research on new photocatalysts for solar energy production, together with the photoreduction of CO_2 , is increasing again (see Chaps. 4 and 14). Additionally, there is a growing interest in other applications, as shown in Fig. 3.3. The photocatalytic disinfection has gained the attention of scientists and the industry, and most of the photocatalytic products successfully commercialized are related to the self-cleaning and anti-fogging properties of photocatalytically active surfaces.

Therefore, the main applications of the photocatalytic phenomena are related with the following processes that will be commented in this and subsequent chapters:

- Air treatment: chemical and biological purification of indoor and outdoor air and off-gas emissions, elimination of odours, ethylene elimination during the storage

Fig. 3.3 Number of original research articles and reviews published in this century concerning environmental applications of photocatalysis other than energy production or chemical pollution elimination from water and air. *Data source* Scopus. Search: photocatal* and disinfection/bactericidal/inactivation (*red*) or self-cleaning (*blue*) or green chemistry (*green*) or self-sterilizing (*violet*)



of fruits and vegetables, soil remediation by air stripping and subsequent photocatalytic treatment, etc.

- Water treatment: wastewater detoxification for biological treatment, discoloration, rendering water suitable for human consumption or for agricultural or industrial use, etc.
- Active surfaces: self-cleaning, self-sterilizing, self-degrading or anti-fogging materials (metals, ceramics and tiles, paints, paper, concrete and cements, glass, textiles, plastics, etc.).
- Green chemistry: photocatalysed reactions for cleaner and cheaper synthetic routes for the production of chemicals.
- Energy conversion: H₂ generation from water splitting and photoreduction of CO₂ (See [Chap. 4](#)).

3.1 Air and Water Treatment

Photocatalytic reactions are characterized by the need of irradiation of the catalyst to activate the process. As a consequence, an appropriate radiation source, either artificial or the sun, is required in photocatalytic reactors. Artificial sources can be arc lamps, incandescent lamps, fluorescent lamps, lasers or light-emitting diodes (LEDs); the radiation can be concentrated or redirected with the help of reflectors or fibre optics. Alternatively, solar radiation can be directly collected by the reactor or with the help of reflectors of different shapes, materials and concentration ratios (Malato et al. 2004).

In the scientific literature and patents, many photoreactor configurations for water and air treatment have been proposed, which can be classified according to the radiation characteristics (solar or artificial, concentrated or not), to the distribution of the catalyst (suspended or immobilized in different kind of substrates), to the reactor geometry (tubular, annular, multi-annular, flat plate, parallel plate, U-shaped, fountain, etc.), to the operation mode (batch or continuous), etc.

Once the photocatalyst and radiation source are selected, the design equation of the photoreactor can be obtained by an experimental approach or by theoretical analysis using the kinetic equation, mass transfer equations and the radiative transfer equation (RTE), which leads to simplified or rigorous mathematical models (Alfano et al. 2000).

The photodegradation rate (r) of chemical pollutants in water and gas phases has been traditionally reported to be proportional to the fraction of covered surface, following the Langmuir–Hinshelwood (L–H) kinetic equation (Eq. 3.1):

$$r = -\frac{dC}{dt} = \frac{kKC}{1 + KC} \quad (3.1)$$

where k is the reaction rate constant, K the pollutant adsorption constant, and C the concentration of pollutant. However, it is generally agreed that the rate constants and orders obtained with this kinetic model are only apparent. Alternative kinetic approaches have been developed in the last years, for example, the direct–indirect (D–I) model (Monllor-Satoca et al. 2007), where the kinetic constants have a physical meaning explained by a sequence of primary reactions occurring during the photocatalytic process.

The efficiency and selectivity of a system will depend on the type and concentration of pollutants, the flow rate, the characteristics of the treated air (humidity) or water (turbidity, pH, ionic strength, dissolved oxygen), the catalyst properties (crystallinity, porosity, doping, loading, etc.), the radiation intensity and wavelength distribution, and the reactor design. The effect of temperature should be insignificant because of the photonic activation of the process, but it may affect the lamp performance, and high temperatures may favour the recombination of charge carriers and disfavour the adsorption of pollutants. Therefore, each application must be studied first at laboratory scale, as comparison and scaling-up are difficult tasks.

3.1.1 Water Applications

There is a high demand, fostered by the growing world population and the more restrictive legislation, for the implementation of effective, economic and environmentally benign water treatment technologies. The heterogeneous photocatalysis, alone or combined with other processes, is a clear candidate to improve the current technological options.

The microbial population is the major pollutant to be removed in drinking water purification facilities, and therefore disinfection, which will be treated in [Sect. 3.4](#), is the main photocatalytic process of interest for this application. Meanwhile, the contamination in wastewater includes organic matter and different trace contaminants from pharmaceuticals, pesticides and personal care products. Industrial wastewater may additionally contain heavy loads of metals or organic compounds. Most pollutants, including chlorinated solvents (chloroform, carbon tetrachloride, trichloroethylene, chlorobenzene, etc.), non-chlorinated solvents (acetone, acetonitrile, benzene, cyclohexane, formaldehyde, phenol, methylbenzene, etc.), insecticides (aldrin, dichlorvos, lindane, parathion, monocrotophos, etc.), pesticides (atrazine, monuron), dyes (acid orange 7, malachite green), surfactants (triton X-100) or other emerging contaminants from personal care or pharmaceuticals (ibuprofen, ofloxacin, progesterone, etc.), can be mineralized by photocatalysis.

The degradation mechanism has been elucidated for some of them (Carp et al. 2004), but contradictory conclusions are often drawn by different researchers due to the many factors conditioning the photocatalytic processes and the lack of standardized procedures.

For aqueous phase photocatalytic reactions, TiO_2 suspensions in continuous-flow tubular reactors equipped with non-concentrating solar compound parabolic collectors (CPC) (Ajona and Vidal 2000) are the most widely employed. Figure 3.4 shows an example.

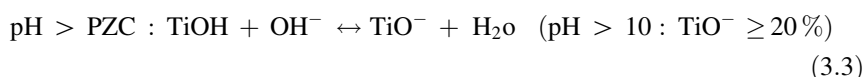
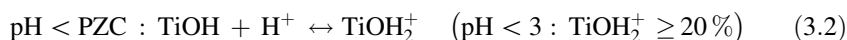
Despite the fact that most research works in water treatment are performed with dispersions of powdered TiO_2 , the need for recovering the catalyst (e.g. sedimentation, filtration) is one important barrier for commercialization (Fernández-Ibáñez



Fig. 3.4 Solar water detoxification demonstration plant installed at Hidrocen factory (Madrid, Spain). *Left* TiO_2 separation system. *Right* CPC photoreactor field (Malato et al. 2009). Copyright Elsevier. Reproduced with permission

et al. 2003). Therefore, a big deal of effort is devoted to the use of immobilized titania in different kinds of supports, including adsorbent substrates, and the design of reactors that maintain a good efficiency despite the reduction in the catalyst surface area and the mass transfer limitations in immobilized systems. Promising alternatives are hybrid membrane photocatalytic reactors (Chong et al. 2010) or recoverable magnetic photocatalytic particles (Makovec et al. 2011).

Many books and reviews have already analysed the effect of the different operational parameters (Chong et al. 2010; Carp et al. 2004). The water pH is one of the main parameters affecting the performance of aqueous photocatalytic systems, especially taking into account the low adsorption of pollutants due to water saturation. At the point of zero charge (PZC) of TiO_2 (pH range of 4.5–7.0), the surface charge of the oxide is neutral and, thus, its interaction with polar compounds minimal. The following water–TiOH equilibrium reactions give place to polar interactions at different pH values:



Other operating parameters that govern the kinetics and costs, and thus, the applicability of this technology for water treatment, are the low solubility of oxygen (and the consequent need for aeration), the radiation absorption in turbid waters, or the presence of water natural components that act as scavengers of the reactive species, for example, carbonates or other inorganic anions (Vidal et al. 1999).

An important drawback of TiO_2 photocatalysis, like for other advanced oxidation technologies (AOTs), is the relatively high operating costs compared to conventional biological treatments, and particularly the slow kinetics compared to the homogeneous photo-Fenton reaction, which makes the latter more interesting for the scientific community despite the consumption of chemicals involved. Consequently, the applicability of heterogeneous photocatalytic water purification systems is currently focused on the treatment of non-biodegradable wastewater and the use of solar radiation, especially in remote areas and developing countries, or in its coupling with other physical or chemical operations to obtain a synergistic effect. In this last case, when combined with ultrasonic irradiation, photo-Fenton reaction, ozonation or electrochemical treatment, the efficiency of the photocatalytic process is enhanced by changes in the mechanism, whereas the coupling with biological treatments, membrane reactors or physical adsorption does not affect the photocatalytic mechanism but improves the efficiency of the overall process (Hernández-Alonso et al. 2002; Augugliaro et al. 2006). The use of photocatalysis as a pre-treatment step prior to biological water treatment is currently attracting the attention of researchers due to its reactivity towards non-biodegradable water-soluble pollutants.

3.1.2 Air Applications

Atmospheric emissions derived from human activities are causing many environmental problems including global warming, climate change, stratospheric ozone depletion and air quality degradation. Photocatalytic processes may help reducing their impact, competing in many applications with conventional air treatment technologies such as adsorption, filtering or combustion, particularly for low-flow and low-concentration emissions. Although the number of scientific publications related to photocatalytic air treatment is significantly lower than to water treatment, the situation of the number of patents is reversed (Paz 2010), indicating that the implementation of photocatalytic systems for air treatment is nowadays more attractive for the industry.

Laboratory results demonstrate that photocatalysis is suitable for the abatement of most air pollutants, including organic compounds, such as alkanes (methane, ethane, propane or hexane), alkenes (ethylene, propylene), alkynes (acetylene, methylacetylene), aromatics (benzene, toluene), alcohols (methanol, ethanol, 2-propanol, butanol or tert-butyl-alcohol), aldehydes (formaldehyde, acetaldehyde), ethers (diethylether, methyl-butyl-ether) or ketones (acetone, methyl-ethyl-ketone), organic halogenated compounds (trichloroethylene, tetrachloroethylene, dichloroacetic acid or trichloromethane), and organic and inorganic molecules containing other type of atoms, such as sulphur (hydrogen sulphide, SO_x, diethyl and dimethyl sulphide or dimethyl disulphide), nitrogen (NO_x, diethylamine, propylamine or pyridine) or silicon (siloxanes). As it was mentioned before, each application must be studied first at laboratory scale because the efficiency of the process depends on many parameters and the degradation mechanism depends on the type of pollutant. For instance, in hydrocarbon oxidation, the carbon atom with the highest electron density and the least steric obstruction is preferentially attacked; low molecular weight favours total mineralization over the formation of partial oxidation products, which are mainly alcohols, ketones and aldehydes. In the case of alcohols, the main intermediates, for instance, in the photocatalytic degradation of ethanol, follow this scheme (Nimlos et al. 1996):



The aromaticity of hydrocarbons has also proved to influence the performance and stability of the photocatalysts (Hernández-Alonso et al. 2011). Nitrogen-, sulphur- and silicon-containing organic compounds can be mineralized to water and CO₂, but lead to catalyst deactivation by accumulation of nitrate, sulphate and silicates, which can be removed by washing with water or alkaline solutions (Sun et al. 2003; Portela et al. 2010). On the other hand, there is still debate concerning the mechanism of chlorinated compounds (Demeestere et al. 2007). Both hydroxyl and oxygen radicals have been proposed to initiate the hydrogen abstraction in saturated compounds or the addition to the double bond in the unsaturated ones as preferential initial steps, although the direct reaction with the holes has been

proposed as well. The formation of highly oxidant chlorine radicals in chlorinated ethenes photodegradation may explain their high reactivity and can be used to favour the reactivity of a second-adsorbed reactant via hydrogen abstraction.

The application of photocatalysis to remove gaseous pollutants may be limited under certain conditions, such as excess or defect of humidity or extremely low or high reactant concentrations. Formation of undesired products or deactivation of the photocatalyst can be observed as well. In these situations, the synergy between photocatalysis and adsorption might be of interest. The coupling of both technologies can be performed in a tandem arrangement, either installing an adsorption unit as pre-concentration step or using the adsorption as backup system, where the adsorbent retains unreacted compounds or by-products. Alternatively, the coupling may be obtained in one single step by utilization of hybrid materials, such as TiO₂-coated or TiO₂-incorporated adsorbents, where the adsorption capacity enhances the photocatalytic activity and, simultaneously, a photocatalytic regeneration of the adsorbent may take place (Suárez et al. 2008; Portela et al. 2012).

Photocatalyst deactivation phenomena are more predominant in gas phase than in aqueous phase, because in the latter the water molecules restore the surface hydroxylation and assist in the removal of the adsorbed species from the photocatalyst surface. In gas phase reactions, intermediate species with slower kinetics and higher adsorption affinity than the target pollutant cause a deactivation that may sometimes be reversed by favouring their desorption or their photocatalytic degradation (Lewandowski and Ollis 2003). Meanwhile, non-volatile final products, such as sulphate, cause irreversible deactivation, and other methods are necessary to remove them, such as washing or thermal treatment (Portela 2009).

On the contrary, compared to aqueous reactions, gas phase processes have the advantage of having quantum efficiencies usually 10-fold higher, with negligible radiation absorption by the gas phase and favoured diffusion of both reagents and products. Moreover, oxygen is rarely the limiting reactant, and there are no hydroxyl radical scavengers. However, the humidity of the gas phase is a key factor; its effect on the conversion and selectivity depends on the target compound. The presence of a certain amount of water molecules seems necessary to replenish the surface hydroxyl groups but, on the other hand, water may compete for the adsorption sites, especially at indoor air pollutant concentration levels. In the literature, an optimum value of water vapour concentration is usually obtained for the treatment of air currents (Obee and Brown 1995; Portela et al. 2010).

3.1.2.1 Waste Gas Treatment

Given that industrial emissions are frequently high-flow or high-pollutant concentration air currents, adsorption or incineration usually result more competitive than photochemical processes. Nonetheless, photocatalytic reduction of CO₂ emissions from industrial flue gas streams with simultaneous generation of added-value chemicals such as methane, methanol and ethanol is being widely explored (Usubharatana et al. 2006), as it will be reviewed in Chap. 4. Besides, there are some

examples of field trials for the treatment of industrial air emissions. A large-scale study for the abatement of volatile organic compounds (VOCs) and nitroglycerine from solvent multi-base propellant production, performed at the Radford Army Ammunition Plant (Virginia, USA) selected UV photocatalytic oxidation over other technologies according to economic, safety and efficiency reasons (Kemme et al. 1999). Another example is the pilot-scale reactor for treatment of off-gases from a soil vapour extraction well at a chlorinated solvent spill site at the Savannah River Site (SC, USA). The dilution of the waste stream with ambient air to below 1,000 ppmv avoided the formation of undesirable by-products (phosgene, chloroform, carbon tetrachloride and pentachloroethane), yielding a conversion >99.5 % with the formation of only <10 ppmv hexachloroethane during an 8-day uninterrupted operation (Read et al. 1996). The continuous elimination of malodorous, toxic and corrosive hydrogen sulphide from the air of a wastewater treatment plant in Madrid (Spain) was achieved in the original solar tubular reactor provided with a complementary artificial radiation source shown in Fig. 3.5. During one month operation, 100 % removal efficiency was attained without release of SO₂ due to the unique properties of the TiO₂-SiMgO_x hybrid material; the photocatalyst was distributed inside the reactor with the help of star-shaped structures that facilitate the air flow and the irradiation of the opaque flat plates (Sánchez et al. 2009; Portela et al. 2012). The elimination of methanol from high-flow low-concentration gases emitted in pulp and paper mills is another promising application (Stokke et al. 2006).

Fig. 3.5 Solar/lamp photocatalytic reactor for gaseous H₂S elimination field test at a wastewater treatment plant in Madrid (Spain). Design and photography by Benigno Sánchez (Ciemat). Reproduced with permission



3.1.2.2 Outdoor Air Treatment

Despite the high concentration of pollutants derived from anthropogenic emissions, the concentration in the outdoor air is usually in the range of parts per billion, due to the dilution effect of the atmosphere. Large-area outdoor photocatalytic construction materials, for example, walls, roofs or roads, may act not only as self-cleaning surfaces, as indicated in the next section, but also as air passive decontamination surfaces that aim to deplete the concentration of typical urban pollutants: VOCs and, in particular, NO_x and SO_x .

The promising results obtained in different studies have motivated the investigation of these materials in real conditions. Thus, several streets have been paved with photocatalytic concrete. NO_x concentration has been monitored over different periods, confirming the photocatalytic removal of NO_x at ambient conditions and at large scale (Chen and Chu 2011). It is worth mentioning the laboratory and macro-scale tests performed within the framework of the project Photocatalytic Innovative Covering Applications for Depollution Assessment (PICADA Project 2006).

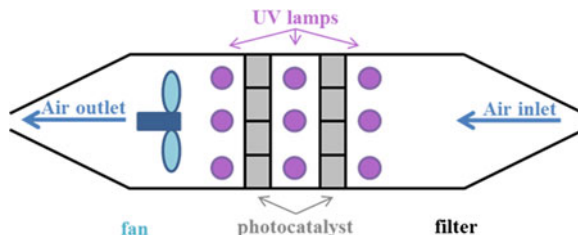
NO_x photooxidation process can be described as a two-stage reaction where NO_2 is the first oxidation product and the key precursor for the further oxidation to nitrate ions. As the active sites of the photocatalyst are blocked by adsorbed nitrates, the NO_x conversion gradually decreases. However, in outdoor applications, the nitrate species are expected to be washed away by rain as weak nitric acid and incorporated to the nitrogen cycle by plants and microorganisms (Chen and Poon 2009; Hüsken et al. 2009; Skalska et al. 2010). The incorporation of substances with high O_2 and NO_3^- adsorption capacity, such as alkaline additives, can retard the deactivation and extend the catalyst lifetime (Ichiura et al. 2003). Some authors have expressed their concerns about the possible negative effects that the application of this technology to building materials may cause. For instance, the formation of gaseous nitrous acid (Langridge et al. 2009) or the potential toxicity derived from nanoparticles inhalation (Lee et al. 2010).

3.1.2.3 Indoor Air Treatment

The concentration of pollutants indoors is usually slightly higher than outdoors, but not comparable to the levels of industrial and automotive exhausts. Additionally, indoor air may be recirculated until satisfactory degradation efficiencies are reached, which is not possible outdoors and usually not acceptable in high-flow industrial emissions. Consequently, the interest in the photocatalytic treatment of indoor air, which includes homes, offices, vehicles or clean-room facilities, among others, is by far larger than that of outdoor air and has increased very fast over the last decade (Mo et al. 2009; Wang et al. 2007).

Despite the fact that photocatalytically active indoor surfaces may contribute to the air purification, indoor air treatment is usually performed in heating, ventilation and air conditioning (HVAC) or filtering systems, where an artificial radiation source (UVA, UVB or UVC) and a photocatalyst may be easily incorporated aiming

Fig. 3.6 Schematic diagram of a typical photocatalytic air purifier



at simultaneous photocatalytic disinfection, deodorization and decomposition of volatile organic compounds. The photocatalyst is usually TiO_2 immobilized on opaque substrates, preferably with large exposed geometric area and causing low pressure drop, such as aluminium honeycomb monoliths or porous filters. The irradiation, the pollutant adsorption and the fluid dynamics strongly condition the photoreactor design and its performance and, thus, modular configurations with groups of lamps located between the photocatalytic units are typically preferred (Raupp et al. 2001), as shown in Fig. 3.6. However, similarly to what happens in water treatment, the patents and scientific literature describe other multiple reactor configurations for air treatment, such as fluidized bed or annular photoreactors (Zaleska et al. 2010).

The long-term performance of commercial photocatalytic air purifiers in real conditions must be further evaluated, because laboratory tests are usually performed for short periods of time, with a single pollutant in parts per million concentration ranges, and at flow rates $<0.1 \text{ m}^3/\text{h}$. On the one hand, in the degradation of multi-component mixtures, which is the case of real air, competitive and synergistic effects must be considered, and the long-term performance can be affected by unexpected deactivation processes, for example, due to siloxanes (Hay et al. 2010). On the other hand, the working flow rate of air purifiers will determine the mass transfer: at too low flow rates, the external mass diffusion in the gas bulk is the rate-limiting step, while at too high flow rates, the mass transfer in the gas-solid interface is limiting; at medium flow rates, the intrinsic kinetics control the reaction rate, which is not affected by changes in the flow rate. Other additional aspects must be well addressed, such as the contribution of photocatalysis versus photolysis, ozone emission when high-energy UV lamps are used, or the formation of undesired by-products released to the outlet air stream or accumulated on the photocatalyst. Standard tests for the evaluation of the photocatalytic performance are still under development, as indicated in the Sect. 3.5 of the chapter.

3.2 Self-Cleaning Materials

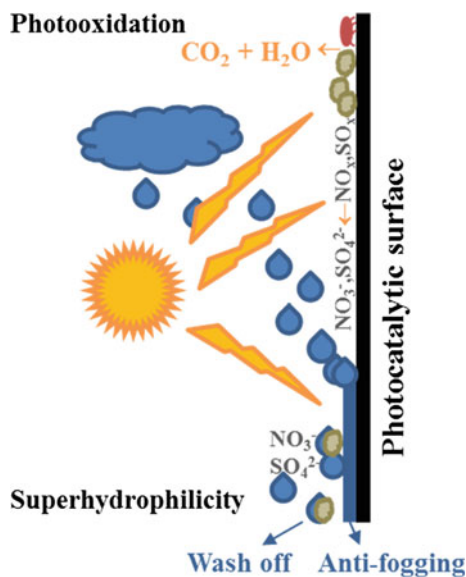
TiO_2 -containing materials may possess air-cleaning, self-cleaning, self-sterilizing and anti-fogging properties and, thus, have attracted increasing attention from the scientific community, but particularly from the construction and automotive

industries. However, these materials are usually optimized according to their main function. While self-cleaning materials present smooth surfaces, like a thin-film on a window glass, for air treatment applications, a rough surface with higher adsorption ability is preferred.

The self-cleaning effect of TiO_2 surfaces is the combination of several phenomena. Firstly, the photocatalytic elimination of organic deposits, which themselves act as adsorption sites for particles of soot and grime, and the simultaneous inactivation and mineralization of surface microorganisms (self-sterilizing properties). Secondly, the photoinduced superhydrophilicity, by which water is prevented from forming surface droplets; instead, under irradiation, a homogeneous thin water layer covers the surface below the dirt, so that dirt can be easily washed off. Moreover, as a consequence of the superhydrophilicity, the surface does not fog (fogging happens at water contact angles $>20^\circ$) and dries faster, because water tends to run off. A scheme of these phenomena is shown in Fig. 3.7.

In addition to the aforementioned properties, TiO_2 coatings may protect metals from corrosion by injection of electrons into the metal, or improve the heat transfer and reduce the water consumption in processes associated with liquid–vapour phase transformations, since the heat transfer rate increases for the thinner water films formed in superhydrophilic surfaces. This latter effect has applications in falling film evaporators or passive cooling of buildings by the latent heat of water evaporation (Fujishima et al. 2008). In nano-functionalized thin films on glasses, the compatibility of anti-reflective and photocatalytic properties, obtained with low refractive index nano-porous silica and high refractive index titania, respectively, has been recently observed in SiO_2 – TiO_2 coatings prepared by sol–gel (Helsch and Deubener 2012).

Fig. 3.7 Scheme of the photoinduced phenomena in photocatalytic surfaces



In outdoor applications, the surfaces are usually cleaned by rainfall and, additionally, contribute to VOCs, NO_x and SO_x abatement, for instance in materials for roads, buildings or vehicles. On the other hand, indoor applications of photocatalytic materials are more related to the cleaning ease, for instance in furnishing, electronic devices or different consumer products. The anti-fogging properties are useful in mirrors, windows and optical lenses.

The photocatalyst may be incorporated during the material manufacturing process, either as an additive, which is the case of most construction materials, or as a coating on the already conformed surface, which is more complicated but results in lower TiO₂ consumption (Martinez et al. 2011). Another option is the use of commercial photocatalytically active TiO₂-containing paints that can be coated on existing surfaces, although the quality can be poor. TiO₂ coatings should be thick enough to assure the radiation absorbance, but also exhibit mechanical resistance and preserve the aesthetic and functional properties of the substrate.

The optimal amount of photocatalyst and binder, their impact on the properties of the materials and their long-term performance should be further investigated. For instance, it has been reported that the addition of commercial TiO₂ pigments to white Portland cement results in photocatalytic properties and improved mechanical properties, although the carbonation of the cement leads to deactivation in several months (Lackhoff et al. 2003). On the other hand, the photooxidative reaction may degrade the binder or the TiO₂ coverage by the binder may reduce the photoactivity (Martinez et al. 2011).

The possible release of TiO₂ nanoparticles to the surroundings should be assessed as well. The risk that TiO₂ nanoparticles pose for the environment and human health has not been totally clarified yet (Wang et al. 2008), but several organizations and national institutes for occupational safety and health have already exposure limit recommendations. This issue will be further commented in Sect. 5.3.

While photocatalytically active glass, metals or ceramics are widely established, conventional high temperature processing is often not suitable for organic polymers (Portela et al. 2007) or textiles (Kiwi and Pulgarin 2010). An intermediate layer between the photocatalyst and the organic material may facilitate the deposition of a TiO₂ coating and help preventing the photodegradation of the organic substrate, although the manufacturing difficulty and cost is increased.

3.3 Disinfection

Solar disinfection of water (www.sodis.ch) has been carried out since the Egyptian times, but it was first reported in scientific literature in the late 1870s and studied as a water disinfection technology only one century thereafter (Acra et al. 1980). The solar water disinfection efficiency can be enhanced through semiconductor photocatalysis, which produces highly reactive species that may inactivate more resistant microorganisms and treat higher volumes. Furthermore, the photocatalytic disinfection effect has been observed not only in aqueous phase, but also in air and on

TiO₂-coated surfaces, in the so-called self-sterilizing materials, and has potential for widespread applications: indoor air disinfection in homes, aircrafts, laboratories and hospitals; wastewater treatment and drinking water disinfection; combating bioterrorism (Anthrax elimination); medical applications (medical implants, sterile tools, anti-tumoral activity); pharmaceutical and food industry, where the use of chemical cleaning agents or biocides is ineffective or is restricted by regulations; etc (Gamage and Zhang 2010). Therefore, the photocatalytic inactivation of a wide range of harmful microorganisms is being examined as a viable alternative to traditional water and air disinfection methods, such as chlorination or UVC irradiation, which are expensive and can produce harmful by-products.

Since the pioneer work on the photocatalytic killing of microbial cells published in 1985 (Matsunaga et al. 1985), the heterogeneous photocatalytic inactivation of many bacteria, virus, fungi, algae, protozoa and even cancer cells has been studied. Most of the scientific research has been conducted at laboratory scale, with single and pure cultures of *Escherichia coli*, used as the model target microorganism. However, there are some recent laboratory works on the successful disinfection of water taken from real sources such as rivers, lakes and wells (Rodrigues et al. 2007; Rincon and Pulgarin 2007).

The titanium dioxide antibacterial activity has been examined on a wide spectrum of microorganisms (Markowska-Szczupak et al. 2011), as shown in Table 3.1, including many gram-negative and gram-positive bacteria, bacterial endospores, many viruses, infectious agents such as prions (Paspaltsis et al. 2006), or fungal species.

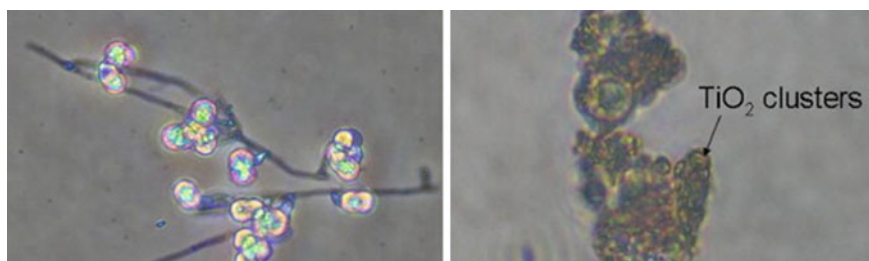
Microorganisms are several orders of magnitude larger than molecules and even larger than TiO₂ particles. Therefore, instead of being adsorbed on the titania surface, they are surrounded by titania particles attached to their external membrane, as observed in Fig. 3.8. When supported photocatalysts are used this difference becomes critical, because the contact is restricted to the external TiO₂ surface. Key parameters in the adsorption and eventual penetration of oxide particles through the cellular wall are the surface electric charge (negative in the case of the cellular membrane, while the TiO₂ surface is charged as a function of pH) and the relative location and size of particle and microorganism. If the titanium dioxide particles are sufficiently small to penetrate the cell membrane, the photocatalytic reactions might take place inside the cell (Blake et al. 1999).

The hydroxyl radical is suggested to be the primary species responsible for the bacteria photocatalytic inactivation and killing, like in the case of chemicals photocatalytic oxidation. However, the active role of H₂O₂ and O₂⁻ cannot be discarded. The mechanism remains under debate (Dalrymple et al. 2010; Markowska-Szczupak et al. 2011), although there exists a rising consensus on the damage that the reactive species formed in the photocatalytic reaction cause to the cell membrane by peroxidation of the polyunsaturated phospholipids, with the subsequent loss of activities that rely on an intact membrane, like transport, semipermeability, respiration and oxidative phosphorylation (Maness et al. 1999).

Due to the complex mechanism of the disinfection processes, the kinetic analysis of the photocatalytic bacterial inactivation has been usually carried out using

Table 3.1 Microorganisms studied in photocatalytic disinfection research works

Gram-negative bacteria	Gram-positive bacteria	Viruses	Fungal species
Coliforms	<i>Lactobacillus</i>	Bacteriophage	<i>Candida albicans</i>
<i>Pseudomonas aeruginosa</i>	<i>acidophilus</i>	T4	<i>S. cerevisiae</i>
<i>Pseudomonas stutzeri</i>	<i>Deinococcus radiophilus</i>	Herpes simplex	<i>Penicillium expansum</i>
<i>Pseudomonas putida</i>	<i>Streptococcus faecalis</i>	Hepatitis B	<i>Daporthe actinidiae</i>
<i>Klebsiella pneumoniae</i>	<i>S. mutans</i>	Poliovirus	<i>Aspergillus niger</i>
<i>Shigella flexneri</i>	<i>S. aureus</i>	MS2 phage	<i>Fusarium solani</i>
<i>S. dysenteriae</i>	<i>S. pyogenes</i>	Rotavirus	<i>F. anthophilum</i>
<i>Acinetobacter baumannii</i>	<i>Enterococcus faecalis</i>	Astrovirus	<i>F. equiseti</i>
<i>A. calcoaceticus</i>	<i>E. hirae</i>	Feline calicivirus	<i>F. oxysporum</i>
<i>Salmonella typhimurium</i>	<i>E. faecium</i>	Influenza virus	<i>F. verticillioides</i>
<i>S. choleraesuis</i>	<i>Listeria monocytogenes</i>		<i>Penicillium chrysogenum</i>
<i>S. enterica</i>	<i>Lactobacillus helveticus</i>		
<i>Vibrio parahaemolyticus</i>	<i>Bacillus anthracis</i>		
<i>V. cholerae</i>	<i>B. subtilis</i>		
<i>Enterobacter cloacae</i>	<i>B. cereus</i>		
<i>Serratia marcescens</i>	<i>B. pumilus</i>		
<i>Bacteroides fragilis</i>	<i>Micrococcus luteus</i>		
<i>Legionella pneumophila</i>	<i>Micrococcus lylae</i>		
	<i>Clostridium perfringens</i>		

**Fig. 3.8** Chlamydospores of *Fusarium solani* before (left) and after 6 h (right) of photocatalytic treatment (Malato et al. 2009). Reprinted with permission. Copyright Elsevier

empirical equations like the Chick–Watson equation (Eq. 3.1) and modifications thereof (Marugán et al. 2008):

$$\log\left(\frac{N}{N_0}\right) = -k[C]^n t \quad (3.5)$$

where N/N_0 is the reduction in the bacterial concentration, k is the disinfection kinetic constant, C is the concentration of the disinfecting agent at time t and n the reaction order.

The photocatalytic inactivation rate obeys a first-order kinetics in a range of initial bacterial concentration that strongly depends on the microorganism. Moreover, the adsorption rate is reported to be correlated with the bactericidal effect.

The photocatalytic sensitivity of fungi is considerably weaker than that of bacteria and depends on the fungal group. Moreover, the sensibility is different for fungal spores and filaments. This variability has been attributed to the different composition, structure and thickness of the cell walls. Only few studies have achieved fungal photocatalytic inactivation, and in those cases long irradiation times were required (Malato et al. 2009).

Cancer cells are eukaryotic. Thus, their structure is complex, and these cells might be more difficult to degrade than microorganisms by photocatalytic reactions, which induce the apoptosis of cancer cells thorough a mechanism still not understood. However, promising results are being obtained. For instance, in a recent research, TiO_2 -mediated destruction of brain cancer cells without damaging nearby healthy cells has been reported (Rozhkova et al. 2009).

In comparison with bacteria (1 μm), viruses are much smaller in size (from 0.01 to 0.3 μm). The viral deactivation rate could be the fastest, even higher than for bacteria; however, the mechanism of virus destruction by photocatalysis is poorly understood (Markowska-Szczupak et al. 2011).

Apparently, the microorganism deactivation rate depends on the complexity and density of the cell wall, following the sequence: viruses > *E. coli* > other gram-negative bacteria > other coliforms > *Enterococcus* species > gram-positive bacteria > endospores > yeasts > filamentous fungi. However, a genetic resistance of some bacteria to the reactive oxygen species has been recently reported (Gogniat and Dukan 2007).

TiO_2 water disinfection research focuses nowadays on resistant microorganisms, like *E. cloacae* (Ibanez et al. 2003), re-growth (Rincon and Pulgarin 2004), and the first trials with real applications. The elimination of total coliforms and *Streptococcus faecalis* from urban wastewater was achieved with an UVC lamp and sunlight, finding very little difference between photocatalysis and solar or UVC photolysis at natural pH (7.8), while at pH 5 or after long dark periods, the presence of TiO_2 notably increased the inactivation rate (Herrera Melián et al. 2000). The organic and inorganic content of real water leads to a reduction in the disinfection rate in comparison with that observed in distilled water.

Air photocatalytic disinfection applications have been less investigated than water applications or self-sterilizing surfaces, partly because the experimental setup is more complicated and partly because there is still a lack of regulation on acceptable concentration levels for microorganisms in air and on standard methods for estimation of this concentration (Sánchez-Muñoz et al. 2012). Several studies have evaluated the effect of the type of photocatalyst and the operating conditions, but very few applied the technology in realistic conditions. The reduction in

bacterial concentration in real air with UVA-irradiated TiO₂ was observed to compete with the conventional photolytic treatment with UVC lamps, more expensive and hazardous. Simultaneously to disinfection, the concentration of VOCs was greatly reduced (Sánchez et al. 2012).

3.4 Photocatalysis for Green Chemistry

Although research studies on photocatalysis generally deal with pollutant abatement, this technology can also be employed as a synthetic route for the production of chemicals. Actually, the first articles where the word “photocatalysis” was used, dated at the beginning of the twentieth century, dealt with the catalysed photochemical synthesis of hydrocarbons and nitrogen compounds. In 1913, Moore and Webster proved that the photosynthesis of formaldehyde under UV light was catalysed in the presence of certain inorganic substances (Moore and Webster 1913). Later, in 1921, Baly et al. showed that some coloured compounds, like colloidal uranium and ferric hydroxides, could catalyse the photosynthesis of formaldehyde from CO₂ and water under visible light (Baly et al. 1921). But it was not until the 1970s, with the works of Formenti et al. and Fujishima and Honda on TiO₂, when the interest in the photocatalytic phenomenon in a broad sense and, in the photocatalytic synthesis of organic compounds in particular, started to exponentially grow (Formenti et al. 1971; Fujishima and Honda 1972).

Photocatalysis have been applied in selective oxidation and reduction processes, isomerization reactions, as well as in reactions implying C–C or C–N bonds (Carp et al. 2004; Palmisano 2007; Fagnoni et al. 2007). However, most studies have been focused on the oxidation of hydrocarbons. Photocatalytic reduction reactions are less frequently considered, partially due to the lower reducing power of an electron in the conduction band compared to the oxidizing power of a hole in the valence band (Fox and Dulay 1993). The specific case of CO₂ photoreduction will be described in Chap. 4.

Oxofunctionalization of gas and liquid hydrocarbons (i.e. alkanes, alkenes, cycloalkanes, aromatics) into higher-value products is a matter of great interest. To the best of our knowledge, photocatalysis is the only way these transformations can proceed at ambient conditions and it has been demonstrated that high selectivities can be obtained, although sometimes with very low quantum yields (Suresh et al. 2000; Maldotti et al. 2002). Traditional methods lead sometimes to environmentally hazardous pollution in expensive and high-energy-consuming processes. In this respect, photocatalysis could represent a good alternative both for environmental and economical reasons, especially if solar light is used as the irradiation source.

Partial photooxidation of light alkanes and alkenes is of great practical importance, being methane and propylene among the most interesting candidates in view of the valuable products that can be potentially obtained from their functionalization. Methanol can be used as building block for different chemicals

or as fuel source for fuel cells. However, low methane-to-methanol conversions have been usually achieved at room temperature (Gondal et al. 2004). Starting from the hypothesis that conversion of methane is limited by its solubility in water, the use of methane hydrates has been explored. These clathrates, naturally formed in the ocean depths as methane–water ice-like crystalline materials, allowed to obtain improved methanol yields at low temperature (Taylor 2005). An efficient direct epoxidation of alkenes by heterogeneous photocatalysis is commercially desirable too, particularly the selective oxidation of propylene to yield propylene oxide, since this product is used in the production of different chemical compounds (e.g. polyurethane plastics) (Pichat et al. 1979). Photooxidation of alcohols to their corresponding ketones or aldehydes, that can prevent the use of strong oxidants in the industry, is subject of research as well. In particular, C₁–C₄ primary alcohols can be easily and selectively transformed into their corresponding carbonyl compounds by means of photocatalysis (Carp et al. 2004; Herrmann et al. 2007).

Generally, the oxidation of cycloalkanes, with or without methyl substituents, leads to ketones as major products (Carp et al. 2004). For instance, cyclohexanone, an important commercial product used to obtain caprolactam for Nylon-6 production, is currently obtained by liquid phase selective oxidation of cyclohexane at elevated temperatures and pressures, which yields a conversion of 3–8 % and a selectivity of 70–80 % (Almeida 2010). An attractive alternative to this industrial process could be the photocatalytic oxidation at room temperature and pressure. Over TiO₂-based photocatalysts, a very high selective transformation of cyclohexane into cyclohexanone can be achieved (Mu et al. 1989; Hernández-Alonso et al. 2009a).

The hydroxylation of aromatic hydrocarbons (e.g. the conversion of benzene to phenol) attracts also a great deal of attention (Palmisano et al. 2007). The conversion of toluene to benzaldehyde, used to synthesize pharmaceutical products and to aromatize perfumes, is an example of the selective photocatalytic oxidation of aromatic compounds. Both liquid–solid and gas–solid reactions have been investigated. Benzaldehyde has been reported to be the only product obtained from pure liquid toluene, although traces of other products, such as benzyl alcohol or benzoic acid, could be strongly adsorbed on the photocatalyst surface. From gaseous toluene, benzaldehyde has also been detected as the main oxidation product, together with CO₂ and small amounts of benzyl alcohol, benzoic acid and benzene, among others (Mao and Bakac 1996; Augugliaro et al. 1999; Hernández-Alonso et al. 2011). Figure 3.9 represents the proposed mechanism for the photocatalytic oxidation of toluene on titania.

For a specific catalytic reaction, selectivity to mild oxidation products usually tends to increase as conversion decreases (Pichat et al. 1979). Selectivity also depends on the nature of the photocatalysts and, thus, controlling the high oxidation capacity of titania or using the appropriate semiconductor to photocatalyse a specific selective reaction is essential to obtain high yields of the desired products. In this regard, the location of the valence and conduction bands plays a key role. For instance, it was observed that the synthesis of ammonia from water and nitrogen was favoured on semiconductors with more negative conduction band

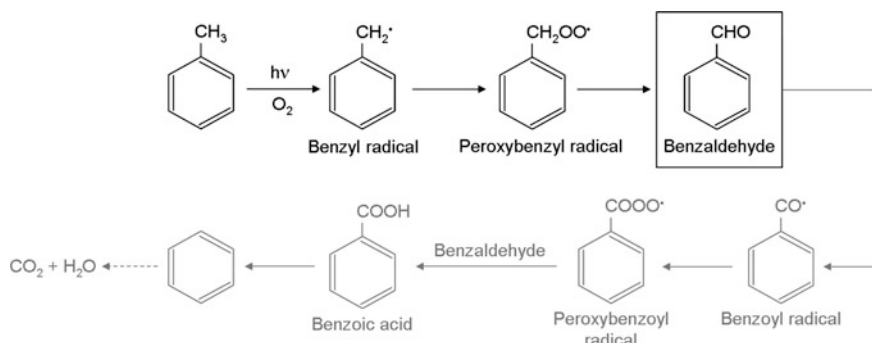


Fig. 3.9 Simplified mechanism for the photooxidation of toluene to benzaldehyde, and products derived from further oxidation of the aldehyde (Augugliaro et al. 1999; Coronado and Soria 2007)

energies, for example, GaP or CdS, with respect to TiO₂ or ZnO (Miyama et al. 1980). CdS has also been employed as photocatalyst for the synthesis of thioorganic compounds, the selective cyclization of amino acids or the formation of bromo-derivatives from phenol (Hernández-Alonso et al. 2009b). In the photooxidation of light alkanes and alkenes into oxygen-containing derivatives, ZnO and MoO₃- or V₂O₅-loaded ZnO greatly improved the selectivity to oxygenated organics, while TiO₂ yielded mainly carbon dioxide (Wada et al. 1996). In a study dealing with the synthesis of pentanal from 1-pentanol, the highest selectivity (97 %) was afforded with Nb₂O₅, despite the higher conversion achieved with titania (Ohuchi et al. 2007). The product distribution of the selective oxidation of α -hydroxycarboxylic acids has also been proved to be dependent on the semiconductor used (Harada et al. 1985).

Photocatalysts for selective oxidation must have, besides an appropriate location of the valence and conduction bands, a good absorption of photons, a long lifetime of the photoactivated species, a good adsorption of reactants and a relatively easy desorption of products. In this sense, structure, particle size and surface characteristics have been found to influence not only the activity, but also the selectivity of photocatalysed synthetic reactions. In the case of the selective photooxidation of cyclohexane, for instance, anatase TiO₂ exhibits higher selectivity to cyclohexanone than rutile. Particle size affects the acid–base properties of the catalyst surface and, consequently, the adsorption properties (Martra 2000). Furthermore, size may affect the kind of oxygen species that act as traps for electrons and holes (Maira et al. 2001). Modification of the photocatalysts surface has been studied as a strategy to improve their performance in selective oxidations (Maldotti et al. 2002). An illustration thereof can be the surface silylation of TiO₂, employed to decrease the hydrophilicity and, thus, enhance the cyclohexanone desorption rate during the selective photooxidation of cyclohexane. However, in this case, the silylated groups were unstable under irradiation (Almeida et al. 2010).

The presence of water in the reaction medium is determinant in these reactions. Usually, when water is present, mineralization turns out to be favoured against selective oxidation. This behaviour has been ascribed to the photogeneration of the strong oxidant OH[•] radicals formed from the hydroxyls groups on the photocatalyst surface, which in the presence of water or water vapour can be continuously renewed. In dry conditions, the high selectivity to partially oxidized products obtained would be ascribed to the formation of different active agents, like the neutral dissociated oxygen species denoted as O^{*} (Herrmann 2001):



However, in some cases, like in the previously mentioned photooxidation of gaseous toluene to benzaldehyde, the presence of water vapour has been proved to be essential in the process. In dry conditions, the conversion of toluene is reduced, accompanied by a progressive and irreversible deactivation of the photocatalyst that has been ascribed to the dehydroxylation of the surface (Augugliaro et al. 1999; Martra et al. 1999).

Oxygen concentration or type of solvent in liquid phase reactions have been proved to affect not only the conversion, but also the selectivity of the photocatalytic process. For instance, in the case of cyclohexane, the selectivity to ketones depends markedly on the solvent, being cyclohexanone the main partial oxidation product when non-polar solvents are used. This effect is related to the relative adsorption strength of reactant, solvent and products on the photocatalytic sites. Thus, the ideal solvent will not compete with the reactant and oxygen for the adsorption sites and, at the same time, will minimize the strength of adsorption of the desired product (Almquist and Biswas 2001). The role of O₂ and the solvent in the products distribution has also been studied in naphthalene photooxidation on TiO₂ (Soana et al. 2000), or in the photocatalytic epoxidation of linear olefins (Ohno et al. 1998). Other aspects, such as photon flux and wavelength distribution of the radiation source, the type of reactor or the residence time, have also demonstrated to play a role on the selectivity of photocatalytic reactions (Amano et al. 2004).

Supported photocatalysts are frequently proposed for the synthesis of chemicals. Besides making the photocatalyst more easily handled and recycled, the support provides an environment that may influence the properties of the catalytic centres, as can be the radiation absorption or the adsorption–desorption equilibria and, thus, the reaction mechanisms (Malato et al. 2009).

Polyoxometalates have been supported to be used as heterogeneous photocatalysts in different selective oxidation reactions, making them easier to be recovered than from solution. Polytungstanates have proved to promote the formation of cyclohexyl hydroperoxide during the oxidation of cyclohexane, favouring cyclohexanone production. In the photooxidation of diols to ketones and aldehydes, selectivities above 90 % have been reported for decatungstates supported on silica. High selectivities and yields have also been obtained with supported polytungstates in the production of carbonylic compounds from benzylic alcohols (Hernández-Alonso et al. 2009b).

Metal oxides supported on alumina or silica have been found to be highly selective in mild oxidation processes. For instance, direct epoxidation of propene is difficult to obtain over semiconductors such as TiO_2 , ZnO or SnO_2 , since complete mineralization is the predominant reaction (Pichat et al. 1979). On the other hand, the presence of isolated, highly dispersed metal oxide species supported on silica (V_2O_5 , Nb_2O_5 , MgO , ZnO , CrO_x) has proved to yield high selectivities to the epoxide under UV irradiation (Yoshida et al. 2000; Amano and Tanaka 2006). V_2O_5 on SiO_2 has also shown to be highly selective in the photooxidation of cyclohexane to cyclohexanone. In the particular case of Cr– SiO_2 systems, they have shown to be effective under visible light irradiation (Murata 2001; Shiraishi et al. 2005). Different mesoporous silicas have been used as support, like the so-called FSM-16, SBA-15, or TUD1 (Zama et al. 2000; Lopez and Martinez 2002; Hamdy et al. 2006). As an example, record selectivities in the epoxidation of olefins have been reported on titanium-containing mesoporous silica with a hexagonal MCM-41 structure (Shiraishi et al. 2005). Frequently, the behaviour of these highly dispersed semiconductors is significantly different than that of the corresponding bulk oxides. These particular systems, denominated single-site photocatalysts, will be further discussed in Chap. 9.

The application of zeolites in photocatalytic reactions has also been extensively studied since Frei and co-workers demonstrated that small hydrocarbons could be selectively photooxidized by cation-exchange zeolites. From the photooxidation of propane and ethane, total selectivity to acetone and acetaldehyde, respectively, could be achieved on zeolites BaY and CaY under visible irradiation (Frei and Blatter 1994; Sun et al. 1997). The internal voids of the zeolite pores can act as host for a photoactive guest, which can be a photosensitizer or a semiconductor. Furthermore, the zeolite cavities can act as microreactors, offering shape selectivity (Myli et al. 1997; Clennan et al. 2002). Another approach involves the incorporation of heteroatoms in the otherwise photochemically inactive zeolite framework, in order to turn the whole structure into a photocatalyst (Corma and Garcia 2004; Hu et al. 2007). The high surface area and adsorption capacity of porous materials can exert a positive influence on their photocatalytic performance. Besides, the high selectivity exhibited by these porous structures in the selective photooxidation of small hydrocarbons has been attributed to the stabilization of the hydrocarbon– O_2 charge transfer complex by electrostatic interaction with the zeolite framework, which can significantly lower the energy required to activate both O_2 and hydrocarbon molecules. This charge transfer reaction path seems to favour the formation of stable products against further oxidation (Myli et al. 1997; Blatter et al. 1998). The proposed reaction mechanism for the specific case of the partial photooxidation of cyclohexane on a zeolite is shown in Fig. 3.10.

Similarly, partial photooxidation of other hydrocarbons, such as propylene or toluene (Myli et al. 1997; Blatter et al. 1998), and photocatalytic transformation of sulphides into the corresponding sulphones and sulfoxides (Clennan et al. 2002) have been conducted in zeolites. However, despite the promising results obtained

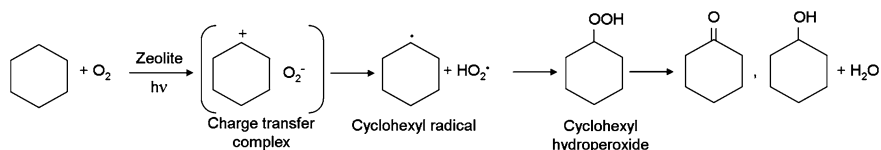


Fig. 3.10 Proposed mechanism for the photooxidation of cyclohexane to cyclohexanone and cyclohexanol on a zeolite (Larsen et al. 2001)

with these materials, the increase in the products desorption rates from the zeolite cages is still a challenge that needs to be addressed (Frei 2006).

In general, it can be concluded that photocatalysis has the ability to selectively produce partial oxidation products, allowing the synthetic procedures to be conducted under mild conditions. Nevertheless, further research is still required in order to increase the efficiency of the processes to make them economically viable.

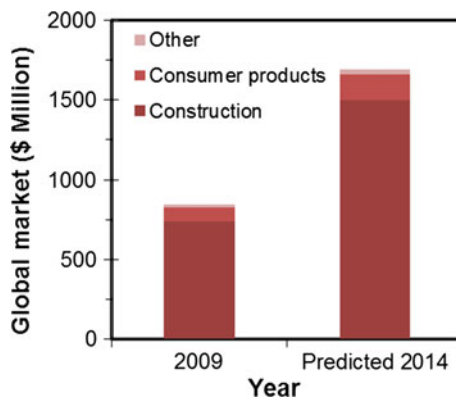
3.5 Commercial Developments

The commercial potential of photocatalysis is impressive, including hygiene and sanitation, architecture and construction, automotive, food and textile industries, and environmental protection (Mills and Lee 2002). The technological and economic importance of photocatalysis has increased considerably in this century.

The commercialization of photocatalysis-based products began in Japan in the mid-1990s and later in the American and European markets. In 2009, the global market for photocatalytic products was \$848 million and it is expected to double in a 5-year period (Fig. 3.11), especially for photocatalytic materials and coatings with self-cleaning, anti-fogging and decontamination and disinfection properties for the construction industry.

The photocatalytic technology readiness level varies depending on the field of application, as shown in the chart of Fig. 3.12.

Fig. 3.11 Sales volume of photocatalytic applications.
Data source Margareth Gagliardi, M.; "Photocatalysts: Technologies and Global Market" BCC Research Report (AVM069A), March 2010



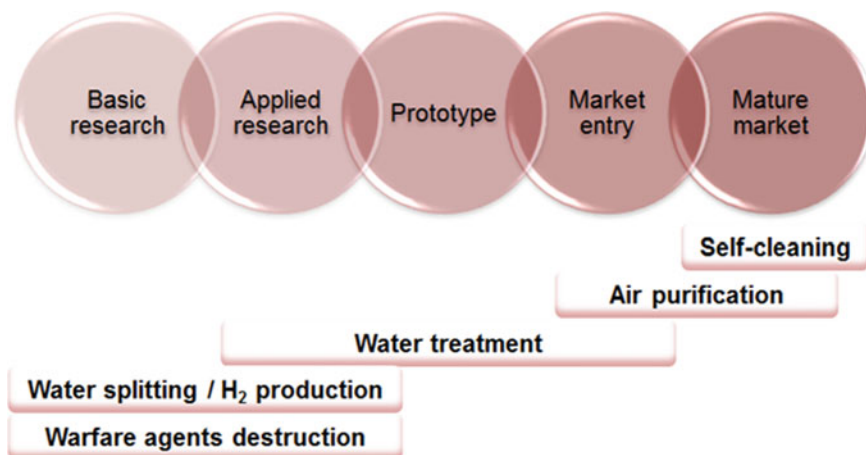
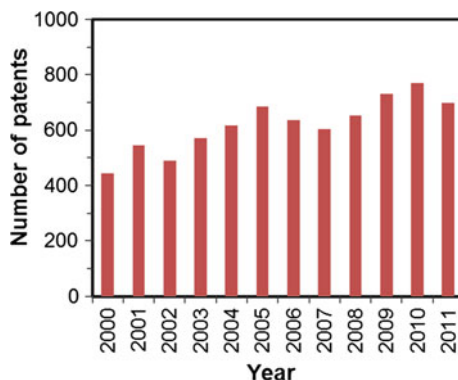


Fig. 3.12 Photocatalytic technology readiness level. *Data source* “Applications of Photocatalysis”; ObservatoryNANO, Briefing No. 10, February 2011

Extensive research continues to optimize and widen the spectrum of potential applications (for instance anti-stick or anti-fingerprint coatings). Accordingly, the annual number of patents on photocatalysis, that seemed to have reached its maximum by the middle of the last decade, has reached a new maximum in 2010 (Fig. 3.13).

Nowadays, there are 1,000 of companies that sell different kinds of products. An example of product especially designed for antibacterial, antiviral or antifungal properties is the anti-flu suit from Haruyama Trading Co. Some architectural materials with self-cleaning properties are the Pilkington Activ[®] self-cleaning glass, TX Active self-cleaning and pollution-mitigating cement from Italcementi Group or the photocatalytic coating material Folium[®] from Kawasaki Heavy Industries Limited. The AiroCide PPT air purifying system from KES Science and Technology has been installed in a variety of industries to reduce mould and bacteria concentration and also to minimize ethylene levels to avoid vegetables and fruits ripening. Purifics Environmental Technologies Inc., with its Photo-Cat[®] system consisting of titanium dioxide slurry and low pressure mercury lamps, is a large supplier of industrial water and air photocatalytic treatment systems and has found markets in the USA, Canada and Korea to treat contaminated ground water and, to a lesser extent, industrial wastewater, lagoons and air. A list of the main companies that commercialize photocatalysis-related products and information thereof can be found in a web-based review, with their classification according to the country of origin and type of product: systems for water purification, for air purification, for sterilization/disinfection and for superhydrophilicity, or the photocatalytically active materials for these systems (Mills and Lee 2002). The Photocatalysis Industry Association of Japan (PIAJ) has more than 100 members, and more than 50 companies are part of the European Photocatalysis Federation (EPF).

Fig. 3.13 Number of patents concerning photocatalysis published worldwide in this century. *Data source* Espacenet. Search: photocatal* in title



Although not currently widespread, solar photocatalytic water purification systems are particularly adaptable to be implemented in developing countries and remote and rural areas. Photocatalytic water treatment systems with artificial UV radiation have been in the market for several years, like the UBE Photocatalytic Fiber Module, and there are solar plants at a demonstration phase, like the Ray-WOx system from KACO.

The growth of the photocatalytic product marketing has taken place without a standardized procedure for assessment of their activity. With the aim of ensuring the photocatalytic properties of the products offered by manufacturers and sellers and that potential customers understand and rely on the photocatalytic properties of materials and equipment, the standardization of a set of procedures related to photocatalysis is underway (Fujishima and Zhang 2006). The Japanese Industrial Standards Committee (JISC) were pioneers, starting in 2002, and nowadays several standards are developed by the JISC, the International Organization for Standardization (ISO) and other national organizations. The task is complex due to the multitude of parameters that influence the photocatalytic processes. It is necessary to make a standardization work for almost every application. For example, the Working Group 37 of the Technical Committee of Fine Ceramics of the ISO (TC 206), devoted to test methods for photocatalytic materials, has developed or is developing the standards summarized in Table 3.2. Additionally, ISO 10677:2011 refers to the ultraviolet light source to be used for testing photocatalytic materials, and ISO 14605, under elaboration, will refer to the light source to be used indoors. In a recent article of Mills and collaborators, most of the existing and forthcoming ISO tests are reviewed, suggesting some improvements and future developments (Mills et al. 2012).

Table 3.2 ISO standards for photocatalysis

Property	ISO number	Year	Test compound
Air purification	ISO 22197-1	2007	Nitric oxide
	ISO 22197-2	2011	Acetaldehyde
	ISO 22197-3	2011	Toluene
	ISO 22197-4	Under elaboration	Formaldehyde
	ISO 22197-5	Under elaboration	Methyl-mercaptan
Water purification	ISO 18560-1	Under elaboration	Formaldehyde (indoors)
	ISO 10676	2010	Dimethyl sulphoxide
Self-cleaning	ISO 10678	2010	Methylene blue (surfaces)
	ISO 27448	2009	Oleic acid/Water contact angle
Disinfection	ISO 27447	2009	Bacteria
	ISO 17094	Under elaboration	Bacteria (indoors)
	ISO 13125	Under elaboration	Fungi
	ISO 18061	Under elaboration	Virus (bacteriophage Q-beta)

References

- Acra A, Karahagopian Y, Raffoul Z, Dajani R (1980) Disinfection of oral rehydration solutions by sunlight. *Lancet* 316(8206):1257–1258
- Ajona JI, Vidal A (2000) The use of CPC collectors for detoxification of contaminated water: design, construction and preliminary results. *Sol Energy* 68(1):109–120
- Alfano OM, Bahnemann D, Cassano AE, Dillert RHG, Goslich R (2000) Photocatalysis in water environments using artificial and solar light. *Catal Today* 58:199–230
- Almeida AR (2010) Cyclohexane photo-catalytic oxidation on TiO₂. Doctoral thesis. Delft University of Technology, The Netherlands
- Almeida AR, Carneiro JT, Moulijn JA, Mul G (2010) Improved performance of TiO₂ in the selective photo-catalytic oxidation of cyclohexane by increasing the rate of desorption through surface silylation. *J Catal* 273:116–124
- Almquist CB, Biswas P (2001) The photo-oxidation of cyclohexane on titanium dioxide: an investigation of competitive adsorption and its effects on product formation and selectivity. *Appl Catal A-Gen* 214:259–271
- Amano F, Tanaka T (2006) Propylene oxide synthesis and selective oxidation over supported metal oxide photocatalysts with molecular oxygen. *Chem Lett* 35:468–473
- Amano F, Tanaka T, Funabiki T (2004) Steady-state photocatalytic epoxidation of propene by O₂ over V₂O₅/SiO₂ photocatalysts. *Langmuir* 20:4236–4240
- Augugliaro V, Coluccia S, Loddo V, Marchese L, Martra G, Palmisano P, Schiavello M (1999) Photocatalytic oxidation of gaseous toluene on anatase TiO₂ catalyst: mechanistic aspects and FT-IR investigation. *Appl Catal B: Environ* 20:15–27
- Augugliaro V, Litter M, Palmisano L, Soria J (2006) The combination of heterogeneous photocatalysis with chemical and physical operations: a tool for improving the photoprocess performance. *J Photochem Photobiol, C* 7(4):127–144
- Baly ECC, Heilbron IM, Barker WF (1921) Photocatalysis. Part I. The synthesis of formaldehyde and carbohydrates from carbon dioxide and water. *J Chem Soc* 119:1025–1035
- Benoit-Marquie F, Wilkenhoner U, Simon V, Braun AM, Oliveros E, Maurette M-T (2000) VOC photodegradation at the gas-solid interface of a TiO₂ photocatalyst: part I: 1-butanol and 1-butylamine. *J Photochem Photobiol, A* 132(3):225–232
- Blake DM, Maness PC, Huang Z, Wolfrum EJ, Huang J, Jacoby WA (1999) Application of the photocatalytic chemistry of titanium dioxide to disinfection and the killing of cancer cells. *Sep Purif Methods* 28(1):1–50

- Blatter F, Sun H, Vasenkov S, Frei H (1998) Photocatalyzed oxidation in zeolite cages. *Catal Today* 41:297–309
- Carp O, Huisman CL, Reller A (2004) Photoinduced reactivity of titanium dioxide. *Prog Solid State Chem* 32(1–2):33–177
- Chen J, Poon C-S (2009) Photocatalytic construction and building materials: from fundamentals to applications. *Build Environ* 44:1899–1906
- Chen M, Chu J-W (2011) NO_x photocatalytic degradation on active concrete road surface—from experiment to real-scale application. *J Clean Prod* 19:1266–1272
- Chong MN, Jin B, Chow CWK, Saint C (2010) Recent developments in photocatalytic water treatment technology: a review. *Water Res* 44(10):2997–3027
- Clennan EL, Zhou W, Chan J (2002) Mechanistic organic chemistry in a microreactor. Zeolite-controlled photooxidations of organic sulfides. *J Org Chem* 67:9368–9378
- Corma A, Garcia H (2004) Zeolite-based photocatalysts. *Chem Commun* 40:1443–1459
- Coronado JM, Soria J (2007) ESR study of the initial stages of the photocatalytic oxidation of toluene over TiO₂ powders. *Catal Today* 123:37–41
- Dalrymple OK, Stefanakos E, Trotz MA, Goswami DY (2010) A review of the mechanisms and modeling of photocatalytic disinfection. *Appl Catal B* 98(1–2):27–38
- Demeestere K, Dewulf J, Van Langenhove H (2007) Heterogeneous photocatalysis as an advanced oxidation process for the abatement of chlorinated, monocyclic aromatic and sulfurous volatile organic compounds in air: state of the art. *Crit Rev Environ Sci Technol* 37(6):489–538
- Fagnoni M, Dondi D, Ravelli D, Albin A (2007) Photocatalysis for the formation of the C–C bond. *Chem Rev* 107:2725–2756
- Fernández-Ibáñez P, Blanco J, Malato S, Nieves FJ (2003) Application of the colloidal stability of TiO₂ particles for recovery and reuse in solar photocatalysis. *Water Res* 37(13):3180–3188
- Formenti M, Juillet F, Meriaudeau P, Teichner SJ (1971) Heterogeneous photocatalysis for partial oxidation of paraffins. *Chem Technol* 1:680
- Fox MA, Dulay MT (1993) Heterogeneous photocatalysis. *Chem Rev* 93(1):341–357
- Frei H (2006) Selective hydrocarbon oxidation in zeolites. *Science* 313:309–310
- Frei H, Blatter F (1994) Selective photooxidation of small alkenes by O₂ with red light in zeolite Y. *J Am Chem Soc* 116:1812–1820
- Fujishima A, Honda K (1972) Electrochemical photolysis of water at a semiconductor electrode. *Nature* 238:37–38
- Fujishima A, Zhang X (2006) Titanium dioxide photocatalysis: present situation and future approaches. *C R Chim* 9(5–6):750–760
- Fujishima A, Rao TN, Tryk DA (2000) Titanium dioxide photocatalysis. *J Photochem Photobiol, C* 1(1):1–21
- Fujishima A, Zhang X, Tryk DA (2008) TiO₂ photocatalysis and related surface phenomena. *Surf Sci Rep* 63(12):515–582
- Gamage J, Zhang Z (2010) Applications of photocatalytic disinfection. *Int J Photoenergy* 2010:1–11
- Gogniat G, Dukan S (2007) TiO₂ photocatalysis causes DNA damage via Fenton reaction-generated hydroxyl radicals during the recovery period. *Appl Environ Microbiol* 73(23):7740–7743
- Gondal MA, Hameed A, Yamani ZH, Arfaj A (2004) Photocatalytic transformation of methane into methanol under UV laser irradiation over WO₃, TiO₂ and NiO catalysts. *Chem Phys Lett* 392:372–377
- Hamdy MS, Berg O, Jansen JC, Maschmeyer T, Moulijn JA, Mul G (2006) TiO₂ nanoparticles in mesoporous TUD-1: synthesis, characterization and photocatalytic performance in propane oxidation. *Chem-Eur J* 12:620–628
- Harada H, Sakata T, Ueda T (1985) Effect of semiconductor on photocatalytic decomposition of lactic acid. *J Am Chem Soc* 107:1773–1774

- Hay SO, Obee TN, Thibaud-Erkey C (2010) The deactivation of photocatalytic based air purifiers by ambient siloxane. *Appl Catal B-Environ* 99(3–4):435–441
- Helsch G, Deubener J (2012) Compatibility of antireflective coatings on glass for solar applications with photocatalytic properties. *Sol Energy* 86(3):831–836
- Hernández-Alonso MD, Almeida AR, Moulijn JA, Mul G (2009a) Identification of the role of surface acidity in the deactivation of TiO₂ in the selective photo-oxidation of cyclohexane. *Catal Today* 143:326–333
- Hernández-Alonso MD, Coronado JM, Maira AJ, Soria J, Loddo V, Augugliaro V (2002) Ozone enhanced activity of aqueous titanium dioxide suspensions for photocatalytic oxidation of free cyanide ions. *Appl Catal B* 39:257–267
- Hernández-Alonso MD, Fresno F, Suárez S, Coronado JM (2009b) Development of alternative photocatalysts to TiO₂: challenges and opportunities. *Energ Environ Sci* 2:1231–1257
- Hernández-Alonso MD, Tejedor-Tejedor I, Coronado JM, Anderdreson MA (2011) Operando FTIR study of the photocatalytic oxidation of methylcyclohexane and toluene in air over TiO₂-ZrO₂ thin films: influence of the aromaticity of the target molecule on deactivation. *Appl Catal B-Environ* 101:283–293
- Herrera Melián JA, Doña Rodríguez JM, Viera Suárez A, Tello Rendón E, Valdés do Campo C, Arana J, Pérez Peña J (2000) The photocatalytic disinfection of urban waste waters. *Chemosphere* 41(3):323–327
- Herrmann J-M (2001) Active agents in heterogeneous photocatalysis: atomic oxygen species vs. OH. radicals: related quantum yields. *Helv Chim Acta* 84:2731–2750
- Herrmann J-M, Duchamp C, Karkmaz M, Hoai BT, Lachheb H, Puzenat E, Guillard C (2007) Environmental green chemistry as defined by photocatalysis. *J Hazard Mater* 146:624–629
- Herrmann J-M, Guillard C, Pichat P (1993) Heterogeneous photocatalysis: an emerging technology for water treatment. *Catal Today* 17(1–2):7–20
- Hoffmann MR, Martin ST, Choi WY, Bahnemann DW (1995) Environmental applications of semiconductor photocatalysis. *Chem Rev* 95(1):69–96
- Hu Y, Wada N, Tsujimaru K, Anpo M (2007) Photo-assisted synthesis of V and Ti-containing MCM-41 under UV light irradiation and their reactivity for the photooxidation of propane. *Catal Today* 120:139–144
- Hüsken G, Hunger M, Brouwers HJH (2009) Experimental study of photocatalytic concrete products for air purification. *Build Environ* 44:2463–2474
- Ibanez JA, Litter MI, Pizarro RA (2003) Photocatalytic bactericidal effect of TiO₂ on *Enterobacter cloacae*. Comparative study with other Gram (–) bacteria. *J Photochem Photobiol A-Chem* 157 (1):81–85
- Ichiura H, Kitaoka T, Tanaka H (2003) Photocatalytic oxidation of NO_x using composite sheets containing TiO₂ and a metal compound. *Chemosphere* 51:855–860
- Kemme MR, Lateulere M, Maloney SW (1999) Reducing air pollutant emissions from solvent multi-base propellant production: CERL (US Army) Technical report
- Kiwi J, Pulgarin C (2010) Innovative self-cleaning and bactericide textiles. *Catal Today* 151(1–2):2–7
- Lackhoff M, Prieto X, Nestle N, Dehn F, Niessner R (2003) Photocatalytic activity of semiconductor-modified cement—influence of semiconductor type and cement ageing. *Appl Catal B* 43(3):205–216
- Langridge JM, Gustafsson RJ, Griffiths PT, Cox RA, Lambert RM, Jones RL (2009) Solar driven nitrous acid formation on building material surfaces containing titanium dioxide: a concern for air quality in urban areas. *Atmos Environ* 43:5128–5131
- Larsen RG, Saladino AC, Hunt TA, Mann JE, Xu M, Grassian VH, Larsen SC (2001) A kinetic study of the thermal and photochemical partial oxidation of cyclohexane with molecular oxygen in zeolite Y. *J Catal* 204:440–449
- Lee J, Mahendra S, Alvarez PJJ (2010) Nanomaterials in the construction industry: a review of their applications and environmental health and safety considerations. *ACS Nano* 4:3580–3590

- Lewandowski M, Ollis DF (2003) A Two-Site kinetic model simulating apparent deactivation during photocatalytic oxidation of aromatics on titanium dioxide (TiO₂). *Appl Catal B* 43(4):309–327
- Lopez HH, Martinez A (2002) Selective photo-assisted oxidation of methane into formaldehyde on mesoporous VOx/SBA-15 catalysts. *Catal Lett* 83:37–41
- Maira AJ, Yeung KL, Soria J, Coronado JM, Belver C, Lee CY, Augugliari V (2001) Gas-phase photo-oxidation of toluene using nanometer-size TiO₂ catalysts. *Appl Catal B-Environ* 29:327–336
- Makovec D, Sajko M, Selisnik A, Drogenik M (2011) Magnetically recoverable photocatalytic nanocomposite particles for water treatment. *Mater Chem Phys* 129(1–2):83–89
- Malato S, Blanco J, Maldonado MI, Fernandez P, Alarcon D, Collares M, Farinha J, Correia J (2004) Engineering of solar photocatalytic collectors. *Sol Energy* 77(5):513–524
- Malato S, Fernández-Ibáñez P, Maldonado MI, Blanco J, Gernjak W (2009) Decontamination and disinfection of water by solar photocatalysis: recent overview and trends. *Catal Today* 147(1):1–59
- Maldotti A, Mollinari A, Amadelli R (2002) Photocatalysis with organized systems for the oxofunctionalization of hydrocarbons by O₂. *Chem Rev* 102:3811–3836
- Maness PC, Smolinski S, Blake DM, Huang Z, Wolfrum EJ, Jacoby WA (1999) Bactericidal activity of photocatalytic TiO₂ reaction: toward an understanding of its killing mechanism. *Appl Environ Microbiol* 65(9):4094–4098
- Mao Y, Bakac A (1996) Photocatalytic oxidation of toluene to benzaldehyde by molecular oxygen. *J Phys Chem* 100:4219–4223
- Markowska-Szczupak A, Ulfing K, Morawski AW (2011) The application of titanium dioxide for deactivation of bioparticulates: an overview. *Catal Today* 169(1):249–257
- Martinez T, Bertron A, Ringot E, Escadeillas G (2011) Degradation of NO using photocatalytic coatings applied to different substrates. *Build Environ* 46(9):1808–1816
- Martra G (2000) Lewis acid and base sites at the surface of microcrystalline TiO₂ anatase: relationships between surface morphology and chemical behaviour. *Appl Catal A-Gen* 200:275–285
- Martra G, Coluccia S, Marchese L, Augugliari V, Loddo V, Palmisano L, Schiavello M (1999) The role of H₂O in the photocatalytic oxidation of toluene in vapour phase on anatase TiO₂ catalyst: a FTIR study. *Catal Today* 53:695–702
- Marugán J, van Grieken R, Sordo C, Cruz C (2008) Kinetics of the photocatalytic disinfection of *Escherichia coli* suspensions. *Appl Catal B* 82(1–2):27–36
- Matsunaga T, Tomoda R, Nakajima T, Wake H (1985) Photoelectrochemical sterilization of microbial cells by semiconductor powders. *FEMS Microbiol Lett* 29(1–2):211–214
- Mills A, Lee S-K (2002) A web-based overview of semiconductor photochemistry-based current commercial applications. *J Photochem Photobiol, A* 152(1–3):233–247
- Mills A, Hill C, Robertson PKJ (2012) Overview of the current ISO tests for photocatalytic materials. *J Photochem Photobiol, A* 237:7–23
- Miyama H, Fujii N, Nagae Y (1980) Heterogeneous photocatalytic synthesis of ammonia from water and nitrogen. *Chem Phys Lett* 74:523–524
- Mo J, Zhang Y, Xu Q, Lamson JJ, Zhao R (2009) Photocatalytic purification of volatile organic compounds in indoor air: a literature review. *Atmos Environ* 43(14):2229–2246
- Monllor-Satoca D, Gómez R, González-Hidalgo M, Salvador P (2007) The “direct-indirect” model: an alternative kinetic approach in heterogeneous photocatalysis based on the degree of interaction of dissolved pollutant species with the semiconductor surface. *Catal Today* 129 (1–2 SPEC. ISS.):247–255
- Moore B, Webster T (1913) Synthesis by sunlight in relationship to the origin of life. Synthesis of formaldehyde from carbon dioxide and water by inorganic colloids acting as transformers of light energy. *Proc R Soc B* 87:163–176
- Moussiopoulos N, Barmpas P, Ossanlis I, Bartzis J (2008) Comparison of numerical and experimental results for the evaluation of the depollution effectiveness of photocatalytic coverings in street canyons. *Environ Model Assess* 13:357–368

- Mu W, Herrmann JM, Pichat P (1989) Room temperature photocatalytic oxidation of liquid cyclohexane into cyclohexanone over neat and modified TiO₂. *Catal Lett* 3:73–84
- Murata C, Yoshida H, Hattori T (2001) Visible light-induced photoepoxidation of propene by molecular oxygen over chromia–silica catalysts. *Chem Commun* 2412–2413
- Myli KB, Larsen SC, Grassian VH (1997) Selective photooxidation reactions in zeolites X, Y and ZSM-5. *Catal Lett* 48:199–202
- Nimlos MR, Wolfrum EJ, Brewer ML, Fennell JA, Bintner G (1996) Gas-phase heterogeneous photocatalytic oxidation of ethanol: pathways and kinetic modeling. *Environ Sci Technol* 30:3102–3110
- Obee TN, Brown RT (1995) TiO₂ Photocatalysis for indoor air applications: effects of humidity and trace contaminant levels on the oxidations rates of formaldehyde, toluene, and 1,3-butadiene. *Environ Sci Technol* 29:1223–1231
- Ohno T, Nakabeya K, Mutsumura M (1998) Epoxidation of olefins on photoirradiated titanium dioxide powder using molecular oxygen as an oxidant. *J Catal* 176:76–81
- Ohuchi T, Miyatake T, Hitomi Y, Tanaka T (2007) Liquid phase photooxidation of alcohol over niobium oxide without solvents. *Catal Today* 120:233–239
- Palmisano G, Augugliaro V, Pagliaro M, Palmisano L (2007) Photocatalysis: a promising route for 21st century organic chemistry. *Chem Commun* 3425–3437
- Paspaltis I, Kotta K, Lagoudaki R, Grigoriadis N, Poullos I, Sklaviadis T (2006) Titanium dioxide photocatalytic inactivation of prions. *J Gen Virol* 87(10):3125–3130
- Paz Y (2010) Application of TiO₂ photocatalysis for air treatment: patents' overview. *Appl Catal B* 99(3–4):448–460
- PICADA Project (2006) <http://picada-project.com>
- Pichat P, Herrmann J-M, Disdler J, Mozzanega M-N (1979) Photocatalytic oxidation of propene over various oxides at 320 K. Selectivity. *J Phys Chem* 83:3122–3126
- Portela R (2009) Eliminación fotocatalítica de H₂S en aire mediante TiO₂ soportado sobre sustratos transparentes en el UV-A. Documentos técnicos, Madrid
- Portela R, Sanchez B, Coronado JM, Candal R, Suarez S (2007) Selection of TiO₂-support: UV-transparent alternatives and long-term use limitations for H₂S removal. *Catal Today* 129(1–2):223–230
- Portela R, Suárez S, Rasmussen SB, Arconada N, Castro Y, Durán A, Ávila P, Coronado JM, Sánchez B (2010) Photocatalytic-based strategies for H₂S elimination. *Catal Today* 151(1–2):64–70
- Portela R, Tessinari RF, Suarez S, Rasmussen SB, Hernandez-Alonso MD, Canela MC, Avila P, Sanchez B (2012) Photocatalysis for continuous air purification in wastewater treatment plants: from lab to reality. *Environ Sci Technol* 46(9):5040–5048
- Raupp GB, Alexiadis A, Hossain MM, Changrani R (2001) First-principles modeling, scaling laws and design of structured photocatalytic oxidation reactors for air purification. *Catal Today* 69(1–4):41–49
- Read HW, Fu X, Clark LA, Anderson MA, Jarosch T (1996) Field trials of a TiO₂ pellet-based photocatalytic reactor for off-gas treatment at a soil vapor extraction well. *Soil Sediment Contam* 5(2):187–202
- Rincon AG, Pulgarin C (2004) Bactericidal action of illuminated TiO₂ on pure *Escherichia coli* and natural bacterial consortia: Post-irradiation events in the dark and assessment of the effective disinfection time. *Appl Catal B* 49(2):112
- Rincon AG, Pulgarin C (2007) Solar photolytic and photocatalytic disinfection of water at laboratory and field scale. effect of the chemical composition of water and study of the postirradiation events. *J Sol Energy Eng* 129(1):100–110
- Rodrigues CP, Zioli RL, Guimarães JR (2007) Inactivation of *Escherichia coli* in water by TiO₂-assisted disinfection using solar light. *J Braz Chem Soc* 18(1):126–134
- Rozhkova EA, Ulasov I, Lai B, Dimitrijevic NM, Lesniak MS, Rajh T (2009) A high-performance nanobio photocatalyst for targeted brain cancer therapy. *Nano Lett* 9(9):3337–3342

- Sánchez B, Portela R, Suárez S, Coronado JM (2009) Fotorreactor tubular para fotocatalizadores soportados (Tubular photoreactor for supported photocatalysts). PCT/ES2010/070799, Spain
- Sánchez B, Sánchez-Muñoz M, Muñoz-Vicente M, Cobas G, Portela R, Suárez S, González AE, Rodríguez N, Amils R (2012) Photocatalytic elimination of indoor air biological and chemical pollution in realistic conditions. *Chemosphere* 87(6):625–630
- Sánchez-Muñoz M, Muñoz-Vicente M, Cobas G, Portela R, Amils R, Sánchez B (2012) Comparison of three high-flow single-stage impaction-based air samplers for bacteria quantification: DUO SAS SUPER 360, SAMPL’AIR and SPIN AIR. *Anal Methods* 4(2)
- Shiraishi Y, Teshima Y, Hirai T (2005) Visible light-induced selective oxidation of cyclohexane to cyclohexanone on Cr–Si binary oxide with molecular oxygen. *Chem Commun* 4569–4571
- Skalska K, Miller JS, Ledakowicz S (2010) Trends in NO_x abatement: a review. *Sci Total Environ* 408:3976–3989
- Soana F, Sturini M, Cermenati L, Albini A (2000) Titanium dioxide photocatalyzed oxygenation of naphthalene and some of its derivatives. *J Chem Soc, Perkin Trans 2*:699–704
- Stokke JM, Mazyck DW, Wu CY, Sheahan R (2006) Photocatalytic oxidation of methanol using silica-titania composites in a packed-bed reactor. *Environ Prog* 25(4):312–318
- Suárez S, Coronado JM, Portela R, Martín JC, Yates M, Ávila P, Sánchez B (2008) On the preparation of TiO₂-sepiolite hybrid materials for the photocatalytic degradation of TCE: influence of TiO₂ distribution in the mineralization. *Environ Sci Technol* 42(16):5892–5896
- Sun H, Blatter F, Frei H (1997) Oxidation of propane to acetone and of ethane to acetaldehyde by O₂ in zeolites with complete selectivity. *Catal Lett* 44:247–253
- Sun R-D, Nakajima A, Watanabe T, Hashimoto K (2003) Decomposition of gas-phase octamethyltrisiloxane on TiO₂ thin film photocatalysts—catalytic activity, deactivation, and regeneration. *J Photochem Photobiol, A* 154(2–3):203–209
- Suresh AK, Sharma MM, Sridhar T (2000) Engineering Aspects of Industrial Liquid-Phase Air Oxidation of Hydrocarbons. *Ind Eng Chem Res* 39:3958–3997
- Taylor CE (2005) Photocatalytic conversion of methane contained in methane hydrates. *Top Catal* 32:179–184
- Usubharatana P, McMartin D, Veawab A, Tontiwachwuthikul P (2006) Photocatalytic process for CO₂ emission reduction from industrial flue gas streams. *Ind Eng Chem Res* 45(8):2558–2568
- Vidal A, Díaz AI, El Hraiki A, Romero M, Muguza I, Senhaji F, González J (1999) Solar photocatalysis for detoxification and disinfection of contaminated water: pilot plant studies. *Catal Today* 54(2–3):283–290
- Villarreal TL, Gómez R, González M, Salvador P (2004) A kinetic model for distinguishing between direct and indirect interfacial hole transfer in the heterogeneous photooxidation of dissolved organics on TiO₂ nanoparticle suspensions. *J Phys Chem B* 108(52):20278–20290
- Wada K, Yoshida K, Watanabe Y, Mitsudo T (1996) Photo-oxidation of light alkenes using solid metal oxide semiconductor-based catalysts: effects of reaction temperature and metal oxide additives. *J Chem Soc, Faraday Trans 92*:685–691
- Wang J, Liu Y, Jiao F, Lao F, Li W, Gu Y, Li Y et al (2008) Time-dependent translocation and potential impairment on central nervous system by intranasally instilled TiO₂ nanoparticles. *Toxicology* 254(1–2):82–90
- Wang S, Ang HM, Tade MO (2007) Volatile organic compounds in indoor environment and photocatalytic oxidation: state of the art. *Environ Int* 33(5):694–705
- Wang R, Hashimoto K, Fujishima A, Chikuni M, Kojima E, Kitamura A, Shimohigoshi M, Watanabe T (1997) Light-induced amphiphilic surfaces. *Nature* 388(6641):431–432
- Yamashita H, Mori K (2007) Applications of single-site photocatalysts implanted within the silica matrices of zeolite and mesoporous silica. *Chem Lett* 36:348–353
- Yoshida H, Murata C, Hattori T (2000) Screening study of silica-supported catalysts for photoepoxidation of propene by molecular oxygen. *J Catal* 194:364–372
- Zaleska A, Hänel A, Nischk M (2010) Photocatalytic air purification. *Recent Pat Eng* 4(3):200–216

- Zama K, Fukuoka A, Sasaki Y, Fukushima Y, Ichikawa M (2000) Selective hydroxylation of benzene to phenol by photocatalysis of molybdenum complexes grafted on mesoporous FSM-16. *Catal Lett* 66:251–253
- Zhao J, Yang X (2003) Photocatalytic oxidation for indoor air purification: a literature review. *Build Environ* 38(5):645–654

Chapter 4

Turning Sunlight into Fuels: Photocatalysis for Energy

**María Dolores Hernández-Alonso, Raquel Portela
and Juan Manuel Coronado**

Environmental and socioeconomic considerations are forcing us to change our energy scheme. The search for primary energy sources alternative to fossil fuels and nuclear power, suitable to maintain the sustainability of the planet and the whole economic system, is therefore of prime interest for scientists and governments. In this context, renewable energy technologies (solar radiation, wind, rain, tides, biomass, geothermal heat, etc.) are called to play a key role in the close future. The strong economic and political global effort in research, development, and implementation of renewable energies has been continuously reducing the existing gap in efficiency and cost optimization compared to conventional technologies.

4.1 The Sun as Energy Source

Sunlight is by far the most abundant energy source on the Earth. The sun, basic element for the existence of life in our planet, is like a nuclear fusion reactor that generates a continuous power of $3.8 \times 1,023$ kW as a result of the permanent conversion into energy of part of its mass. The major part of this energy arrives to the Earth by radiation. When the radiation reaches the atmosphere, a part is reflected to the outer space again, but the 70 % is absorbed and used to maintain

M. D. Hernández-Alonso (✉)
Renewable Energy Division, CIEMAT, Madrid, Spain
e-mail: lolihza@gmail.com

R. Portela
Institute of Catalysis and Petroleochemistry, CSIC, Calle Marie Curie 2 E-28049
Madrid, Spain
e-mail: raquel.portela@csic.es

J. M. Coronado
Institute IMDEA Energía, Avenida de Ramón de la Sagra, 3 E-28935 Móstoles,
Madrid, Spain
e-mail: juanmanuel.coronado@imdea.org

the ambient temperature, to evaporate water in the hydrological cycle, for photosynthesis, or dissipated in wind and ocean currents. Therefore, the sun is responsible for the Earth's climate, and most renewable energies are directly or indirectly powered by the sun.

4.1.1 Components of the Solar Radiation

Before reaching the ground, the solar radiation is modified by absorption and scattering due to the interaction with the gas mixture and small suspended particles that constitute the atmosphere. The Global (G) solar radiation reaching the Earth surface has three components:

$$G = I + D + R \quad (4.1)$$

- Direct radiation (I), which arrives without any alteration of direction.
- Diffuse radiation (D), which arrives from all directions after being scattered in the atmosphere. Its proportion varies from 10 % in a clear day to 100 % in a very cloudy day.
- Reflected radiation (R) or albedo, which arrives as a consequence of reflections on the ground or on vertical surfaces. It can be up to 40 % of the global radiation in the case of white surfaces.

4.1.2 The Solar Spectrum

The energy of the solar radiation (E) is inversely proportional to its wavelength (λ), according to Planck's equation for electromagnetic radiation:

$$E = hc/\lambda \quad (4.2)$$

where c is the speed of light ($c = 299,792,458 \text{ m s}^{-1}$), and h is the Planck's constant ($h = 6.626 \times 10^{-34} \text{ J s}$).

The solar radiation spectrum (Fig. 4.1) can be divided into three main wavelength regions:

- Ultraviolet (UV) radiation, at $\lambda < 400 \text{ nm}$, accounts for only a 2–3 % of the radiation reaching the Earth's surface on clear days and 8–10 % in cloudy days (Escobedo et al. 2009). This region is compressed by three subregions:
 - UVA, or near ultraviolet (320–400 nm), the less energetic. Most of UV radiation reaching the Earth's surface is in this range.
 - UVB or far ultraviolet (290–320 nm). It has enough energy to damage the cellular DNA, yet not enough to be completely absorbed by the atmosphere.

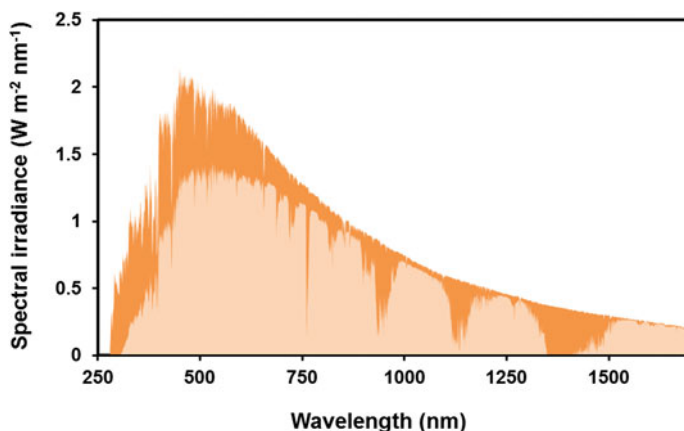


Fig. 4.1 Solar radiation spectrum showing the absorption bands of the atmosphere. *Curves based on the American Society for Testing and Materials (ASTM) terrestrial reference spectra*

- UVC or extreme ultraviolet (220–290 nm). Completely absorbed by stratospheric ozone before reaching the surface.
- Visible radiation, approximately with $\lambda = 400\text{--}750$ nm, the wavelengths to which the human eye is sensitive.
- Infrared (IR) radiation, with $\lambda > 750$ nm. This region is commonly subdivided into:
 - Near infrared (NIR), between 750 and 1,400 nm.
 - Short-wavelength infrared (1,400–3,000 nm).
 - Mid-wavelength or intermediate infrared (3,000–8,000 nm).
 - Long-wavelength infrared (8,000–15,000 nm).
 - Far infrared (15,000– 10^6 nm).

Oxygen and nitrogen absorb very short-wavelength radiation, effectively blocking it below 190 nm. Molecular oxygen photodissociation by UVC absorption leads to the production of the atmospheric ozone layer, which absorbs most UVB and some visible radiation. Water vapor, carbon dioxide and, to a lesser extent, oxygen, selectively absorb in the near infrared. Wavelength-dependent Rayleigh scattering and scattering from aerosols and other particulates, including water droplets, change the spectrum as well and are responsible for the blue color of the sky.

4.1.3 Uses of Solar Energy

The solar constant, $1,353 \pm 21 \text{ W m}^{-2}$, is the radiant power received per unit area on top of the Earth's atmosphere (ASTM E 490-73a). However, the irradiance on the Earth's surface varies widely, depending on latitude, time (month, day, and

Yearly sum of Global Horizontal Irradiation (GHI)

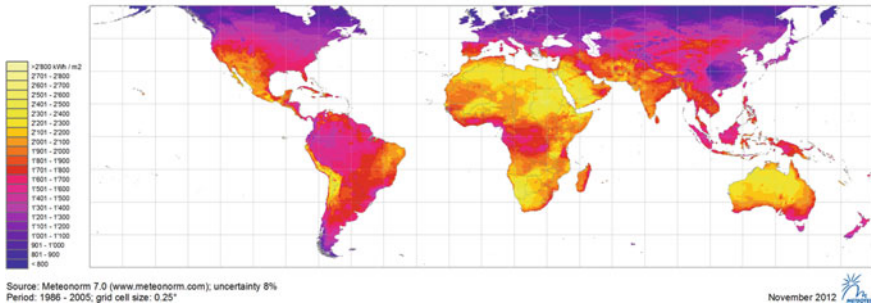


Fig. 4.2 World map of the annual solar irradiation, showing the extensive areas of high insolation in Africa, Australia, the Arabia peninsula and some areas of America. Reproduced from <http://meteonorm.com/download/maps/>

hour) and atmospheric effects (reflection, absorption, and scattering). The world map of yearly solar irradiation is shown in Fig. 4.2. The solar radiation that reaches the Earth surface can be collected, and even concentrated, by means of absorbers, reflectors, lenses or semiconductors, and employed in different, more or less complicated, technological processes. The main applications of solar energy include passive solar technologies, which reduce the energy demand, (for example bioclimatic designs and greenhouses), and active solar technologies, which supply energy, and are expanding nowadays. But the history of solar energy applications is not as recent as one might believe. According to the U.S. Department of Energy, already in the seventh century B.C. magnifying glasses were used to make fire (The history of solar, http://www1.eere.energy.gov/solar/pdfs/solar_timeline.pdf), and it is well known that in the first centuries A.D. the Romans took advantage of the solar heat by means of south facing windows in the bathhouses. In 1515, Leonardo da Vinci showed how solar energy could be industrially used to heat water by employing concave mirrors, and during the 1830s, Sir John Herschel used a solar cooker in his expedition to South Africa (Butti and Perlin 1980). The photovoltaic effect, that allows the direct conversion of radiation into electricity, was discovered by Edmund Becquerel in 1839 (Williams 1960), although no application was developed until one century later. In the 1860s, Augustin Mouchot started the development of the first solar motor, using heat from a solar collector to power a steam engine (Mouchot 1869). Later, Mouchot connected the steam engine to a refrigerator to make ice and continued making solar cookers, solar water pumps, and even water distillation.

After those pioneers, many researchers have explored these and other applications, including solar disinfection and photochemical and photoelectrochemical processes. Today, even though the technology is continuously being optimized, the conversion of solar radiation into electric and thermal energy is a reality. Meanwhile, CO₂ photocatalytic reduction and the production of solar fuels remain the big challenges for researchers, especially in the field of materials science, for the

forthcoming years. The three basic routes for production of storable and transportable fuels from solar energy are the following:

- **Electrochemical:** Solar electricity obtained either directly—from photovoltaic cells—or indirectly—with concentrating solar thermal systems followed by turbines—is used in an electrolytic process. Considering typical yields of commercial PV modules (about 18 %), the variations in incident solar light, the electrical losses and the electrolyzers efficiency (ca. 80 %), an overall efficiency of 10–11 % in water splitting can be achieved (Blankenship 2011). This is probably the most mature way to storage solar power in the form of the chemical vector hydrogen, but the overall yield of these transformations is still too low for being economically competitive. Nevertheless, the rising efficiency of new PV modules can modify completely this situation in the near future.
- **Photochemical/photobiological:** The energy of the solar photons can be directly used for powered photochemical and photobiological processes. This is the case of the photocatalytic route discussed below, but also of the biomass growth in photosynthetic organisms by using chlorophyll, carotenoids, and other pigment molecules. In terrestrial plants, maximum efficiencies of about 4.3 % are achieved with species of C4 metabolism, whereas microalgae in controlled laboratory conditions can achieve up to 7 % efficiency (Blankenship 2011). Surprisingly enough, although photosynthesis sustains life on the Earth, it is not a very efficient process in terms of energy. This fact casts significant doubts about the feasibility of biofuels, which in last instance come from photobiological transformations, to provide a long solution for energy supply in transportation.
- **Thermochemical:** Concentrated solar radiation provides heat at very high temperatures ($>1,100$ °C) for endothermic chemical process, which can be applied to fuel production. In this respect, the use of thermochemical cycles such as those based on reducible oxides, for instance ZnO or CeO₂, can produce solar fuels with elevated theoretical efficiencies (>30 %) (Romero and Steinfeld 2012). This turns concentrating solar power into a very promising approach for sun power storage. However, due to the technical difficulties (materials stability, large thermal losses, etc.) associated with the elevated operation temperatures of these processes, this route for solar fuels production will require further development before becoming a reality.

4.2 Water Splitting

4.2.1 Hydrogen as Energy Vector

Hydrogen is by far the most common element in the Universe, but on Earth it does not occur to a significant extent in its free molecular form, H₂. However, it constitutes a major component of water, biomass, and hydrocarbons such as oil and

natural gas. Leaving apart its importance for the chemical industry, in the last decades, hydrogen has gathered a great deal of interest because it can be used as a sort of “energy currency” or, in more conventional terms, as a suitable energy vector. The reason for that lies on this apparently simple transformation:



which shows that hydrogen oxidation releases an important amount of energy without production of any chemical but water (Navarro et al. 2009). The energy stored in H–H bonds can be utilized by combustion in specially designed engines, but is more frequently connected to electricity production in fuel cells. These electrochemical devices are provided with an anode made of Pt on conductive carbon. H_2 dissociates in the anode to yield H^+ and electrons, which are conducted to the cathode through an external circuit, where they reduce O_2 . At the same time, the protons are driven through a thin H^+ exchange membrane (generally made of Nafion, a perfluorinated polymer with sulfonic groups) to the cathode, where they combine with the reduced oxygen species to form water. These devices can have high efficiency (>30 %) in the transformation of chemical to electrical energy. Therefore, the use of hydrogen in combination with fuel cells has the potential to provide flexibility to the regulation of the energy flow from generation sites to consumers. This fact is particularly relevant in an electricity production scheme that, at a global level, is progressively incorporating a rising number of renewable energy plants (wind, photovoltaics, thermosolar, etc.). Since these energy sources are intrinsically intermittent, they require some type of storage to buffer the mismatch between generation and demand, and in this context, the flexibility of hydrogen as energy vector may play a significant role in the near future. Nevertheless, relevant technological and economic barriers, such as the prize of the Pt used in the electrodes or the need for a hydrogen distribution infrastructure, are slowing down the deployment of the so-called hydrogen economy (Armor 2005).

Hydrogen can be produced from a variety of primary sources, such as natural gas, naphtha, heavy oil, methanol, biomass, wastes, and coal, generally via a reforming process, which for the case of methane is given by:



This equation accounts for the overall process that also implies the water gas shift for increasing the hydrogen ratio. In fact, natural gas reforming is currently the main industrial route for hydrogen production. This process operates at high temperature (700–1,100 °C) using Ni-based catalysts, generating a stream that typically contains 75–78 % H_2 , 30 % CO_2 , traces of CH_4 and 10–20 ppm CO (Heinzel et al. 2002). This gas composition highlights the two main challenges of hydrogen production for a sustainable energy system: the need to reduce CO_2 emissions, in order not to aggravate the greenhouse effect in the atmosphere, and the requirement of an additional purification process for removing CO impurities. This last constraint is imposed by the fact that the Pt component of fuel cell electrodes is deactivated by CO adsorption. The reformed gas can be upgraded by

CO preferential oxidation (CO-PROX) using catalysts typically based on CuO/CeO₂ (Caputo et al. 2008).

In this framework, the development of alternative routes for CO_x-free H₂ production is crucial for both environmental and practical reasons, and the use of solar energy, either directly or indirectly, can play a remarkable role in the activation of the water molecule. In this regard, the photocatalytic dissociation of water constitutes one of the most promising routes for the generation of solar hydrogen.

4.2.2 Photocatalytic Production of Hydrogen

The water molecule is very stable and its thermal dissociation, according to the inverse process to that described in Eq. 4.3, is highly endothermic. As a consequence, a temperature of 2,500 K is required to obtain about 5 % dissociation at atmospheric pressure. In contrast, considering only the thermodynamics of the process, photochemical decomposition of water is potentially feasible by applying photons with a wavelength shorter than 1,100 nm (equivalent to approximately 1.3 eV). However, this photochemical reaction has to overpass a very high activation energy. Therefore dissociation is only significant for irradiation with wavelengths lower than 190 nm, and consequently (and fortunately!), it does not take place under sunlight (Hernández-Alonso et al. 2009).

The use of photocatalysts reduces appreciably the energy barrier and turns the process viable with photons of the solar spectrum. At this point, it is important to recall that, as it was stated in Sect. 2.5, water splitting, as well as CO₂ photoreduction, is not spontaneous, but an uphill process ($\Delta G > 0$), and thus accumulates energy in the bonds of the generated chemicals. Considering only the photons with the required energy for water molecule photodissociation, about 2.8 mmol s⁻¹ m⁻² H₂ (equivalent to 800 W m⁻²) could be potentially produced using solar radiation. Obviously, this value represents an unattainable limit, because activation losses throughout the process will reduce the efficiency. Figure 4.3 illustrates the capacity of storing solar energy as hydrogen at different quantum yield levels. In addition, this plot emphasizes the crucial influence of the wavelength on the efficiency, because shifting the absorption edge of the photoactive component from 400 to 600 nm improves the harvesting of solar power in one order of magnitude. Accordingly, the utilization of efficient visible light-responsive materials is a key aspect of any application of photocatalysis, but especially of those related to the production of fuels.

The classical work by Fujishima and Honda (1972) established that photoelectrochemical decomposition of water was possible over TiO₂ electrodes. Subsequent investigations evidenced that no external potential was required to split the water molecule, and that the photoactivity could be boosted if a noble metal (e.g., Pt) was incorporated (Nozik 1977). However, in contrast to the photoelectrochemical process, which yields oxygen and hydrogen separately, photocatalytic water splitting produces a mixture of both gases, which should be subsequently

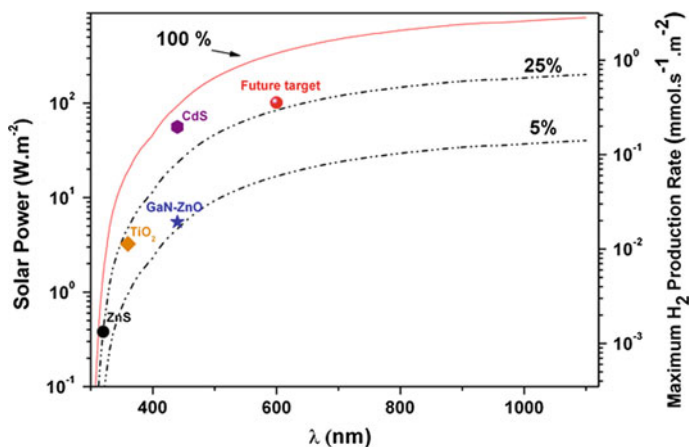


Fig. 4.3 Incident solar power and maximum hydrogen production rate as a function of the photons wavelength as obtained from the integration of the 1.5 AM solar spectrum. *Dashed lines* represent the solar power accumulated at each wavelength considering photonic efficiencies of 5 and 25 %. *The different symbols mark* some of the current or future achievements of photocatalysis for H₂ production using TiO₂, ZnS, CdS, or (Ga_{0.88}Zn_{0.12})(N_{0.88}O_{0.12}) as photocatalyst. It should be noted that these values are upper limits and, consequently, H₂ production rates would be appreciably lower in practice. Reproduced with permission from Hernández-Alonso et al. (2009). Copyright Royal Society of Chemistry

separated. After this groundbreaking works, the interest in photocatalytic water splitting has not decreased. Furthermore, in the last few years, it has revitalized due to the growing concern about global warming and the development of novel photocatalysts with enhanced performance, which holds the promise of the future implementation of solar hydrogen plants. These recent advances have been brought about by a continuous quest for more efficient photoactive materials. The fact that more than 150 different semiconductors, many of them described in this book, have been tested for water splitting reflects the magnitude of the research effort undertaken by the scientific community (Osterloh 2008).

Interestingly, according to their redox potentials, some materials, such as WO₃ or BiVO₄, are only efficient for O₂ evolution, while others, like TiO₂, are more active for H₂ production. This fact opens up a new opportunity to dissociate water combining photoactive materials using what is called a Z-scheme. The basic mechanism of this two-step approach is schematically depicted in Fig. 4.4. The existence of a redox mediator, in order to connect both components by shuttling the photogenerated electrons, is crucial for the functioning of the Z-scheme (Sayama et al. 2001). In water solution, this can be achieved by the IO₃⁻/I⁻ redox couple. The advantage of using two semiconductors for the water splitting system is that the energy of the photons required to power each photocatalyst can be reduced when compared to the one-step water splitting system. In addition, the evolution of H₂ and O₂ takes place separately, and this hampers the reverse reaction to form water. Unfortunately, the redox mediator can also participate in

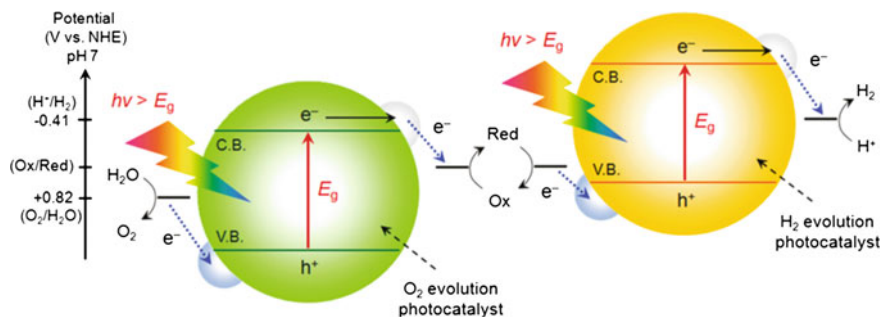


Fig. 4.4 Schematic energy diagrams of photocatalytic water splitting by using a Z-scheme with two separated photocatalytic systems. Reproduced with permission from Maeda and Domen (2010). Copyright American Chemical Society

backward reactions, decreasing the photoactivity. A successful example of a Z-scheme is the combination of Pt/ZrO₂/TaON and Pt/WO₃ systems, which attain a quantum yield of 6.3 % under irradiation at 420 nm (Maeda and Domen 2010).

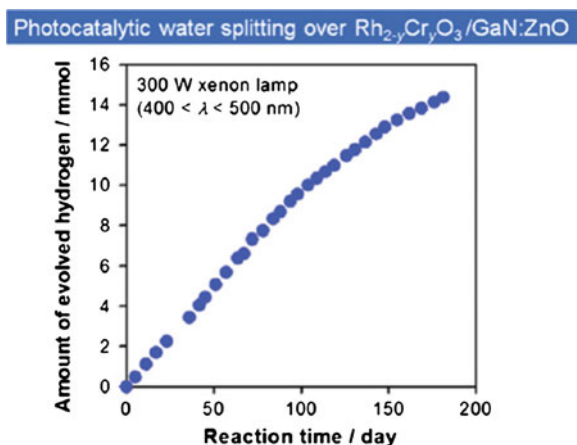
Incorporation of a second component, usually referred to as co-catalyst, to the photoactive semiconductor is normally required to generate H₂ at a significant rate. It is believed that co-catalysts, based on metals oxides such as NiO_x and RuO₂ or noble metals like Pt or Rh, contribute to stabilize photogenerated charge carriers and provide additional reaction sites that further catalyze O₂ and H₂ evolution (Maeda and Domen 2010). The incorporation of these active components must be thoroughly controlled to maximize the dispersion and facilitate the electronic transference from the semiconductor. However, it is important to mention that, despite their significant promotion of water splitting, some of them, for instance noble metals, can also catalyze the reaction of O₂ and H₂ to yield water again. The role of these components will be discussed in detail in Chap. 10, but it can be mentioned here that a fine engineering of Rh_{2-x}Cr_xO₃ co-catalyst has allowed to achieve the record quantum yield of 5.9 % for water splitting using (Ga_{0.88}Zn_{0.12})(N_{0.88}O_{0.12}) under visible light illumination (at 600 nm) (Maeda and Domen 2010; Ohno 2012).

Although a very large photonic efficiency can be achieved with some photocatalysts such as NiO/NaTaO₃:La (QY = 56 % at 270 nm), one of the difficulties of hydrogen photocatalytic production is that the process with pure water is in general inefficient (Kato 2003). This is related to the fact that water oxidation is a multistep reaction, which involves four electrons and requires the reaction of two hydroxyl intermediates to form one hydrogen peroxide molecule, according to:



The use of electron donors as sacrificial agents may enhance H₂ production, since holes are scavenged by this molecules and recombination is greatly reduced. Furthermore, as O₂ is not produced, gas purification is simplified and the back reaction is suppressed. Simple alcohols, like CH₃OH, or NaS/Na₂SO₃ mixtures are

Fig. 4.5 Accumulated H_2 evolution from photocatalytic water splitting as a function of visible light illumination time. Reproduced with permission from Ohno (2012). Copyright American Chemical Society



incorporated to the aqueous solution with this purpose (Hernández-Alonso et al. 2009). However, these additives generate waste products, which have to be disposed, and consequently, their use reduces the sustainability of the process. A more ecological alternative is the use of wastewater pollutants as sacrificial agents, because this very promising approach combines in a single-step water purification and hydrogen production (Patsoura et al. 2007). On the other hand, it is important to keep in mind that a future implementation of photocatalytic hydrogen production will require not only efficient, but also durable photocatalysts. Although this aspect has received still relatively low attention, some long terms studies, as those carried out with GaN:ZnO, have revealed that the photoactivity does not change significantly for the first 3 months, but is almost halved after 6 months operation. This can be appreciated in the plot of Fig. 4.5. The main reason for the deactivation is the loss of the co-catalyst and the hydrolysis of the nitride (Ohno et al. 2012).

Although the use of this technology is not foreseen in short term, it is interesting to theoretically explore its potential to fulfill the energetic needs of the society. In this way, a preliminary estimation indicates that approximately 10,000 solar plants of 25 km^2 of extension working with an efficiency of 10 % would be necessary to provide the projected global energy demand in 2050 (Maeda and Domen 2010). Under these conditions, 570 t H_2 would be produced per day, assuming the standard incident solar energy (AM1.5¹). Although the extension of land required for these solar hydrogen factories is huge, it corresponds to 1 % of the Earth's desert area and, therefore, it can be achievable through a multinational initiative. In this context, the utilization of simple, cost effective reactors, such as shallow pools with plastic components, will be clearly advantageous for reducing the investment. Anyhow, as shown in the picture of Fig. 4.6, after its separation

¹ AM refers to Air Mass, and AM1.5 considers a longer atmospheric path length with a zenith angle of 48°

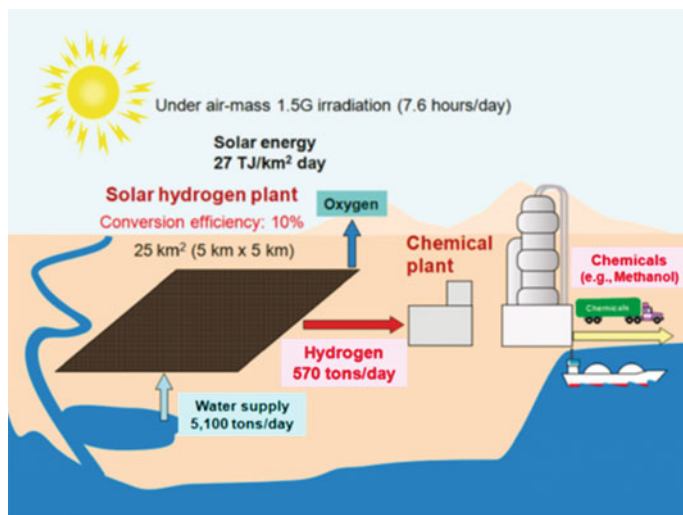


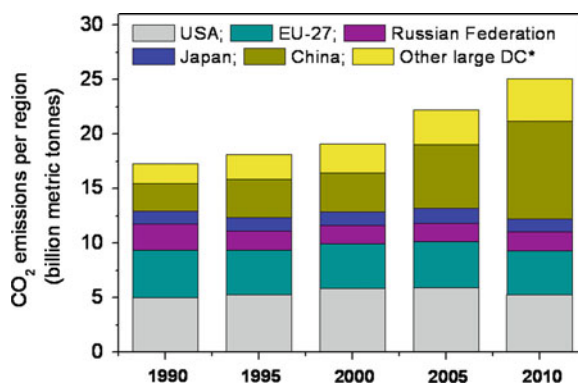
Fig. 4.6 Pictorial diagram for large-scale H₂ production via solar water splitting. Reproduced with permission from Maeda and Domen (2010). Copyright American Chemical Society

from oxygen, the produced hydrogen could be used in fuel cells to produce electricity, or transformed into liquid chemicals like methanol for transportation.

4.3 The Photosynthesis Challenge: Photocatalytic Reduction of CO₂

As the concentration of CO₂ in the atmosphere continuously increases due to anthropogenic causes (Fig. 4.7), mainly derived from deforestation and the use of fossil fuels, the possibility of converting the thermodynamically stable CO₂

Fig. 4.7 Trend in the CO₂ emissions of different countries/regions for the 1995–2010 period. Data extracted from the 2011 report “Long-Term Trend in Global CO₂ Emissions” of the JRC European Commission. (* DC: Developing Countries)



molecule into useful hydrocarbon products is becoming a challenging goal and a research priority in environmental catalysis. The interest in CO₂ reduction lies in the ecological problems derived from this gas, since it is one of the major contributors to the greenhouse effect. By means of photocatalysis, this process can proceed under mild conditions, mimicking the photosynthesis in green plants, although producing partially reduced compounds, such as methanol, instead of sugars.

However, CO₂ reduction into hydrocarbon compounds is not spontaneous, but an endergonic reaction which needs energy input. In a photocatalytic process, it would be provided by irradiation and, ideally, solar irradiation. In this respect, semiconductors have proved to be effective as photocatalysts for CO₂ transformation into useful chemical compounds, in both aqueous and gas phases (Inoue et al. 1979; Indrakanti et al. 2009). In a simplified manner, the photosynthetic production of hydrocarbons requires radiation as energy source, a material that can be oxidized to act as source of electrons (e.g., water), and a compound that can be reduced by those electrons (e.g., CO₂) to yield the desired chemical compound. The principles and mechanisms of the natural photosynthetic process can be used as basis for a rational design of solar energy conversion systems.

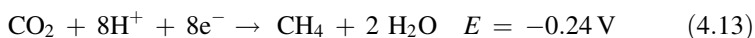
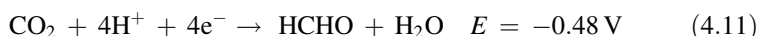
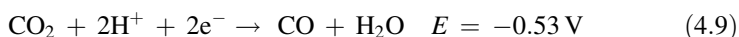
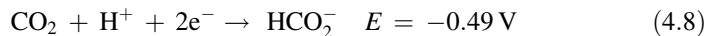
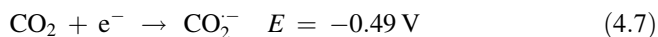
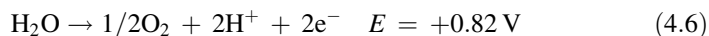
The challenge of artificial photosynthesis represents a direct pathway to produce fuels from solar energy, being at the same time an attractive method for solar energy storage. An effective recycling of CO₂ into a hydrocarbon fuel using sunlight as energy source would be of great interest, since the product would use the current energy infrastructure. In this respect, methanol constitutes the most valuable product since it can be directly employed as a replacement of fossil fuels both in internal combustion engines (ICEs) and in the so-called direct methanol fuel cells (DMFCs). In these electrochemical cells, methanol is directly oxidized with air to produce electricity. Besides, it is used on a large scale as a source of hydrocarbons for the chemical industry (e.g., formaldehyde or acetic acid). Despite the investment that would represent nowadays the transition to a “hydrogen economy”, H₂ is still considered by many as the ideal fuel for the future, due to its clean energetic transformation and its high energy content. However, the extensive safety precautions required for its handling, storage, and distribution could turn “methanol economy,” as proposed by Nobel Prize Olah (2005), into a more feasible alternative. Nevertheless, although artificial systems have been reported to produce fuels using sunlight as energy source at laboratory scale, the low quantum yields achieved in these multielectron processes mean a drawback to implement the photocatalyzed reduction of carbon dioxide. So far, alternative routes to produce solar C-containing fuels, consisting in water splitting for H₂ evolution and its subsequent reaction with CO₂, have demonstrated to yield considerably higher production rates than the direct photoreduction of carbon dioxide (Indrakanti et al. 2009).

Additionally to solar fuels production, as H₂ or methanol, photoreduction of CO₂ could constitute an ecologic alternative for the chemical industry for obtaining added-value hydrocarbons, such as formaldehyde, formic acid, or methane, and therefore converting solar into chemical energy. The utilization of CO₂ as a one-carbon building block would represent a benefit from a safety point of view, compared to other raw materials used in the industry, such as carbon

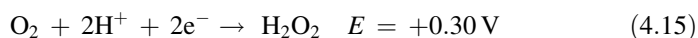
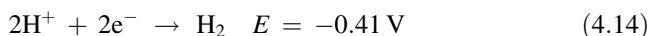
monoxide (CO) or phosgene (COCl₂). For instance, formic acid is industrially produced at high pressures from methanol and carbon monoxide in the presence of a strong base or certain amines. The photoreduction of CO₂ could represent an interesting replacement (Leitner 1995).

In nature, photosynthesis is carried out by different energetically coupled systems through several steps (Gust et al. 2009). In artificial photosynthesis, the photocatalytic system is expected to carry out the whole process in a more direct way, absorbing light, generating electron–hole pairs, and allowing the separation and migration of the generated charges to redox sites for water oxidation and CO₂ reduction. Any inhibition of electron–hole recombination would increase the CO₂ photoreduction rate, since it has to be taken into account that electron–hole recombination is several orders of magnitude faster than any other electron transfer process (Zhou et al. 2011). As described by Indrakanti et al. (2009), the energetic position of the valence and conduction bands, along with the local structure at the photocatalyst surface, determines the feasibility of these processes. Surface area, CO₂:H₂O ratio, and light intensity are some of the factors that can also influence the reactivity.

The equilibrium reduction potentials of CO₂ reduction and H₂O oxidation reactions, at pH 7 and 25 °C, are presented below (Indrakanti et al. 2009):

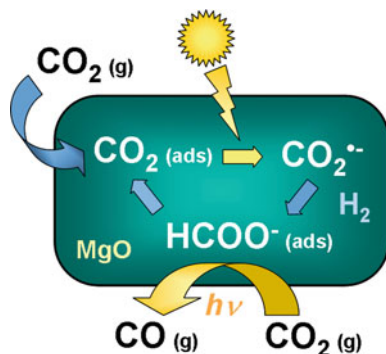


It has to be taken into account that the photoreduction of CO₂ competes with that of protons to H₂ or H₂O₂:



H₂, H₂S, and CH₄, as well as solvents such as propanol, ethanol, or methanol, among others, have been used as reductants. Replacing water by other reductant induces changes in the mechanism of the reaction, modifying the yields and selectivities that can be obtained (Usubharatana et al. 2006). Thus, it has been observed that using H₂ as reductant leads to the formation of CO as the main

Fig. 4.8 Pictorial scheme showing the proposed mechanism of CO_2 photoreduction over MgO or ZrO_2 , using H_2 as reductant



product. As schematically represented in Fig. 4.8, in the particular case of the photoreduction of gaseous CO_2 to CO over MgO in the presence of H_2 , it has been proposed that CO molecules are produced from the surface formate species generated in a previous step, after the photoactivation of adsorbed CO_2 (Kohno et al. 2001; Hernández-Alonso et al. 2009).

On TiO_2 -based photocatalysts, the proposed activation mechanism involves the interaction of the stable CO_2 molecule with a photogenerated electron to form $\text{CO}_2^{\bullet-}$ species adsorbed on the catalyst surface, which utterly undergo further reactions to yield different CH_xO_y products. This one-electron activation of CO_2 is highly endergonic. To ensure this electron transfer, an electronic interaction between CO_2 and the photocatalyst surface is necessary. When acting as an electron acceptor, CO_2 can be adsorbed on the surface as carbonate and bicarbonate species through electrophilic interaction between the C atom and the surface oxygen atoms. Doping with alkali and noble metals may promote CO_2 activation, by means of favoring the formation of $\text{CO}_2^{\bullet-}$ species. Besides, the modification of the photocatalyst with noble metals can hinder electron-hole recombination by acting as charge carriers trap (Brause and Kempter 2001; Indrakanti et al. 2009). In the literature, the presence of Pd, Rh, Pt, Au, Cu, or Ru has been reported to improve the performance of the photoreduction process, increasing the selectivity to products that consume more electrons, such as formaldehyde, methanol, and methane (Usubharatana et al. 2006). For instance, Cu/TiO_2 photocatalysts have been observed to yield methanol as the major product (Tseng et al. 2004). Recently, a relatively high CO_2 conversion rate has been achieved on nitrogen-doped TiO_2 nanotube arrays, co-catalyzed with Cu and/or Pt nanoparticles under solar irradiation. The addition of a co-catalyst enhanced the hydrocarbon production rates and allowed modifying the product selectivity (Varguese et al. 2009). The role of the co-catalyst is to promote the charge carrier transfer between the semiconductor and CO_2 . Dye sensitization of TiO_2 is another approach for decreasing recombination rates while shifting the absorption coverage into the visible range of the solar spectrum, by acting as a photon antenna and injecting electrons into the conduction band of the semiconductor (Nguyen et al. 2008; Wu 2009). As it will be described in detail in Sect. 13.2, doping with

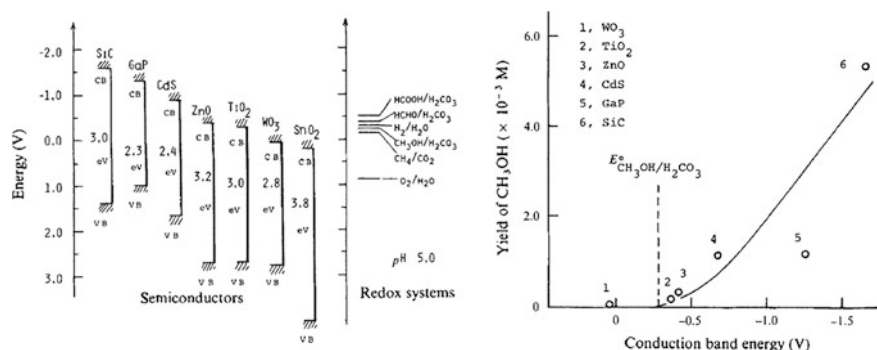


Fig. 4.9 *Left* Schematic representation of the energy correlation between semiconductors and redox couples in water; *Right* correlation between the yield of methanol and the conduction band energy of different semiconductors. Redox potentials are expressed against NHE (Inoue et al. 1979). Reproduced with permission. Copyright Nature Publishing Group (Division of Macmillan Publishers Limited)

transition metals can also lead to a shift of the absorption spectrum to lower energies.

Although most of the research works deal with the use of TiO₂-based photocatalysts, other materials have proved to be able to catalyze CO₂ photoreduction, as is the case of metal complexes. Admitting that the yields obtained with photocatalysts based on metal complexes are higher, besides being expensive and usually unstable under UV light, the consumption of a sacrificial electron donor is usually required (e.g., trimethylamine). On the other hand, the use of semiconductors such as TiO₂ allows the oxidation of inexpensive reductants, as is the case of water (Usubharatana et al. 2006).

In 1979, Inoue et al. (1979) first probed the photocatalytic reduction of carbon dioxide into formic acid, formaldehyde, methanol, and methane, in the presence of a suspension of different semiconductors in water. They observed that the methanol yield increased as the conduction band became more negative with respect to the redox potential of H₂CO₃/CH₃OH. Consequently, a higher yield was obtained on semiconductors such as SiC than on TiO₂ (Fig. 4.9).

As it will be discussed in following chapters, the efficiency of different semiconductors for the photoreduction of CO₂, such as ZnO, ZnS, NiO, and Ga₂O₃, has been subject of later studies (Hernández-Alonso et al. 2009). In large band gap semiconductors, the energy position of the valence and conduction bands makes them more suitable for acting as acceptors and donors of electrons in the photocatalytic reduction of CO₂. However, the larger the band gap, the higher the energy input that will be required in the process. Under visible light, NiO-InTaO₄- and K₂Ti₆O₁₃-based photocatalysts have proved their ability to reduce CO₂. Theoretically, CuO and Cu₂O band positions make these oxides suitable for, in combination with TiO₂, achieving direct photocatalytic CO₂ conversion (Roy et al. 2010). In the case of supported systems, a screening of different metal oxides on

supports of acid/basic nature led to the conclusion that basic supports are more suitable for the selective conversion of CO₂ into hydrocarbon compounds (Surbrahmanyam et al. 1999).

CO₂ photoreduction can be performed in gas–solid systems, avoiding the inconvenience of the low solubility of CO₂ in water. In these cases, the use of nanoparticles and highly dispersed TiO₂ has shown to give rise to higher efficiencies than the use of bulk TiO₂. The application of isolated Ti species on microporous and mesoporous materials, the so-called *single-site* photocatalysts which are the focus of Chap. 9, has been extensively studied. In this case, as it will be commented, the reaction rates also depend on factors such as the dispersion and coordination of the Ti species and the hydrophilic–hydrophobic properties of the porous support (Anpo et al. 1997; Yamashita et al. 1998; Ulagappan and Frei 2000; Ikeue et al. 2001). High selectivities to methanol are obtained in the presence of highly dispersed tetrahedrally coordinated titanium oxide species in zeolites, in contrast to the selectivity to methane exhibited by bulk TiO₂, constituted by octahedral species (Anpo et al. 1997; Yamashita et al. 1998). Besides a high dispersion of the titanium oxide species, the use of zeolites, with a large pore size and a three-dimensional channelled structure, has proved to benefit the activity of these materials in the CO₂ photoreduction reaction (Anpo et al. 1998). The affinity for water of the zeolite has also shown to influence the reactivity and selectivity (Ikeue et al. 2001). High methane and methanol production rates have been obtained over Ti-porous materials such as Ti-ZSM-5, Ti-SBA-15, and Ti-MCM-48, just to mention some of them (Yamashita et al. 1995; Anpo et al. 1998; Hwang et al. 2005). For CO₂ activation under visible light, the use of two different metals (e.g., Ti⁴⁺–Sn²⁺ or Ti⁴⁺–Fe⁴⁺) grafted in the porous material has been explored (Indrakanti et al. 2009).

Today, the implantation of this technology for carbon dioxide recycling is still a long-term perspective. In order to improve the low yields (in the order of μmol g⁻¹ h⁻¹) and selectivities obtained so far, significant advances on the fundamental research on carbon dioxide photoreduction processes are extremely desired. Besides the design and selection of the appropriate photocatalysts and reductants, optimization of the reactor design and operating conditions (e.g., temperature, pressure, light intensity) can lead to improved yields and higher selectivities to the desired products (Usubharatana et al. 2006).

References

- Anpo M, Yamashita H, Ichihashi Y, Fujii Y, Honda M (1997) Photocatalytic reduction of CO₂ with H₂O on titanium oxides anchored within micropores of zeolites: effects of the structure of the active sites and the addition of Pt. *J Phys Chem B* 101:2632–2636
- Anpo M, Yamashita H, Ikeue K, Fujii Y, Zhang SG, Ichihashi Y, Park DR, Suzuki Y, Koyano K, Tatsumi T (1998) Photocatalytic reduction of CO₂ with H₂O on Ti-MCM-41 and Ti-MCM-48 mesoporous zeolite catalysts. *Catal Today* 44:327–332
- Armor JN (2005) Catalysis and the hydrogen economy. *Catal Lett* 101(3–4):131–135

- Blankenship RE, Tiede DM, Barber J, Brudvig GW, Fleming G, Ghirardi M, Gunner MR, Junge W, Kramer DM, Melis A, Moore TA, Moser CC, Nocera DG, Nozik AJ, Ort DR, Parson WW, Prince RC, Sayre RT (2011) Comparing photosynthetic and photovoltaic efficiencies and recognizing the potential for improvement. *Science* 332:805–809
- Brause M, Kempter V (2001) CO₂ chemisorption on alkali-doped TiO₂ (1 0 0)-(1 × 3) studied with MIES and UPS (HeI). *Surf Sci* 476:78–84
- Butti K, Perlin J (1980) A golden thread: 2,500 years of solar architecture and technology. Chesvile Books, New York
- Caputo T, Lisi L, Pirone R, Russo G (2008) On the role of redox properties of CuO/CeO₂ catalysts in the preferential oxidation of CO in H₂-rich gases. *Appl Catal A* 348(1):42–53
- Escobedo JF, Gomes EN, Oliveira AP, Soares J (2009) Modeling hourly and daily fractions of UV, PAR and NIR to global solar radiation under various sky conditions at Botucatu, Brazil. *Appl Energ* 86(3):299–309
- Fujishima A, Honda K (1972) Electrochemical photolysis of water at a semiconductor electrode. *Nature* 238:37–38
- Gust D, Moore TA, Moore AL (2009) Solar fuels via artificial photosynthesis. *Acc Chem Res* 42:1890–1898
- Heinzel A, Vogel B, Hübner P (2002) Reforming of natural gas—hydrogen generation for small scale stationary fuel cell systems. *J Power Sources* 105:202–207
- Hernández-Alonso MD, Fresno F, Suárez S, Coronado JM (2009) Development of alternative photocatalysts to TiO₂: challenges and opportunities. *Energ Environ Sci* 2:1231–1257
- Hwang JS, Chang JS, Park SE, Ikeue K, Anpo M (2005) Photoreduction of carbon dioxide on surface functionalized nanoporous catalysts. *Topics Catal* 35:311–319
- Ikeue K, Yamashita H, Anpo M (2001) Photocatalytic reduction of CO₂ with H₂O on Ti-β Zeolite photocatalysts: effect of the hydrophobic and hydrophilic properties. *J Phys Chem B* 105:8350–8355
- Indrakanti VP, Kubicki JD, Schobert HH (2009) Photoinduced activation of CO₂ on Ti-based heterogeneous catalysts: current state, chemical physics-based insights and outlook. *Energ Environ Sci* 2:745–758
- Inoue T, Fujishima A, Konishi S, Honda Kenichi (1979) Photoelectrocatalytic reduction of carbon dioxide in aqueous suspensions of semiconductor powders. *Nature* 277:637–638
- Kato H, Asakura K, Kudo A (2003) Highly efficient water splitting into H₂ and O₂ over lanthanum-doped NaTaO₃ photocatalysts with high crystallinity and surface nanostructure. *J Am Chem Soc* 125(10):3082
- Kohno Y, Ishikawa H, Tanaka T, Funabiki T, Yoshida S (2001) Photoreduction of carbon dioxide by hydrogen over magnesium oxide. *Phys Chem Chem Phys* 3:1108–1113
- Leitner W (1995) Carbon dioxide as a raw material: the synthesis of formic acid and its derivatives from CO₂. *Angew Chem Int Ed* 34:2207–2221
- Maeda K, Domen K (2010) Photocatalytic water splitting: recent progress and future challenges. *J Phys Chem Lett* 1:2655–2661
- Mouchot A (1869) *La chaleur solaire et ses applications industrielles*. Imprimerie Ernest Mazereau, Tours (France)
- Navarro RM, Sánchez-Sánchez MC, Alvarez-Galvan MC, del Valle F, Fierro JLG (2009) Hydrogen production from renewable sources: biomass and photocatalytic opportunities. *Energ Environ Sci* 2:35–54
- Nguyen TV, Wu JCS, Chiou CH (2008) Photoreduction of CO₂ over Ruthenium dye-sensitized TiO₂-based catalysts under concentrated natural sunlight. *Catal Commun* 9:2073–2076
- Nozik A (1977) Photochemical diodes. *J Appl Phys Lett* 30(11):567–570
- Ohno T, Bai L, Hisatomi T, Maeda K, Domen K (2012) Photocatalytic water splitting using modified GaN: ZnO solid solution under visible light: long-time operation and regeneration of activity. *J Am Chem Soc* 134:8254–8259
- Olah GA (2005) Beyond oil and gas: the methanol economy. *Angew Chem Int Ed* 44:2636–2639
- Osterloh FE (2008) Inorganic materials as catalysts for photochemical splitting of water. *Chem Mater* 20(1):35–54

- Patsoura A, Kondarides DI, Verykios XE (2007) Photocatalytic degradation of organic pollutants with simultaneous production of hydrogen. *Catal Today* 124(3–4):94–102
- Romero M, Steinfeld A (2012) Concentrating solar thermal power and thermochemical fuels. *Energy Environ Sci* 5:9234–9245
- Roy SC, Varghese OK, Paulose M, Grimes CA (2010) Toward solar fuels: photocatalytic conversion of carbon dioxide to hydrocarbons. *ACS Nano* 4:1259–1278
- Sayama K, Mukasa K, Abe R, Abe Y, Arakawa H (2001) Stoichiometric water splitting into H₂ and O₂ using a mixture of two different photocatalysts and an IO₃⁻/I⁻ shuttle redox mediator under visible light irradiation. *Chem Commun Roy Soc Chem* 23:2416–2417
- Subrahmanyam M, Kaneco S, Alonso-Vante N (1999) A screening for the photo reduction of carbon dioxide supported on metal oxide catalysts for C1–C3 selectivity. *Appl Catal B-Environ* 23:169–174
- Tseng IH, Wu JCS, Chou HY (2004) Effects of sol-gel procedures on the photocatalysis of Cu/TiO₂ in CO₂ photoreduction. *J Catal* 221:432–440
- Ulagappan N, Frei H (2000) Mechanistic study of CO₂ photoreduction in Ti silicalite molecular sieve by FT-IR spectroscopy. *J Phys Chem A* 104:7834–7839
- Usubharatana P, MacMartin D, Veawab A, Tontiwachwuthikul P (2006) Photocatalytic process for CO₂ emission reduction from industrial flue gas streams. *Ind Eng Chem Res* 45:2558–2568
- Varghese OK, Paulose M, LaTempa TJ, Grimes CA (2009) High-rate solar photocatalytic conversion of CO₂ and water vapor to hydrocarbon fuels. *Nano Lett* 9:731–737
- Williams R (1960) Becquerel photovoltaic effect in binary compounds. *J Chem Phys* 32(5):1505
- Wu JCS (2009) Photocatalytic reduction of greenhouse gas CO₂ to fuel. *Catal Surv Asia* 13:30–40
- Yamashita H, Shiga A, Kawasaki S, Ichihashi Y, Ehara S, Anpo M (1995) Photocatalytic synthesis of CH₄ and CH₃OH from CO₂ and H₂O on highly dispersed active titanium oxide catalysts. *Energy Convers Manage* 36:617–620
- Yamashita H, Fujii Y, Ichihashi Y, Zhang SG, Ikeue K, Park DR, Koyano K, Tatsumi T, Anpo M (1998) Selective formation of CH₃OH in the photocatalytic reduction of CO₂ with H₂O on titanium oxides highly dispersed within zeolites and mesoporous molecular sieves. *Catal Today* 45:221–227
- Zhou H, Fan T, Zhang D (2011) An insight into artificial leaves for sustainable energy inspired by natural photosynthesis. *ChemCatChem* 3:513–528

Chapter 5

The Keys of Success: TiO₂ as a Benchmark Photocatalyst

Juan M. Coronado and María Dolores Hernández-Alonso

Titanium dioxide is a material with a huge technological relevance because of its numerous applications (e.g. pigments, sensors, catalyst). However, since the seminal work by Fujishima and Honda (1972), this solid is attracting the interest of the scientific community mainly because of its capacity to be photoactivated by solar light. This property is not only exploited in heterogeneous photocatalysis or in self-cleaning coatings, but it can also be applied directly to the production of electrical energy. In this regard, great expectations are deposited in the development of more efficient dye-sensitized solar cells (DSSC) or Grätzel cells, which are typically formed by TiO₂ layers modified with ruthenium complexes (Hagfeldt 2010). Accordingly, despite the continuous quest for novel, more efficient photoactive materials, and despite the recent successful developments described in the following chapters, TiO₂ remains as the most widely used photocatalyst. In fact, this oxide has been considered as a synonym of photocatalyst, because more than 67 % of the articles about photocatalysis are still based on the use of TiO₂.¹ Figure 5.1 plots the number of citations per year in SCI journals regarding TiO₂ preparation, along with those devoted to TiO₂ synthesis for photocatalytic applications..

The reasons for this prominent position of TiO₂ as a photoactive material rely mainly on its particular physicochemical characteristics, although other aspects, like its biocompatibility and its availability at a relatively low cost, have also facilitated the extensive use of this semiconductor. In this chapter, the main properties of this material are described in detail in connection with its photocatalytic behaviour.

¹ Estimation from a simple survey in the period 2008–2012 in the ISI Web of Knowledge.

J. M. Coronado (✉)

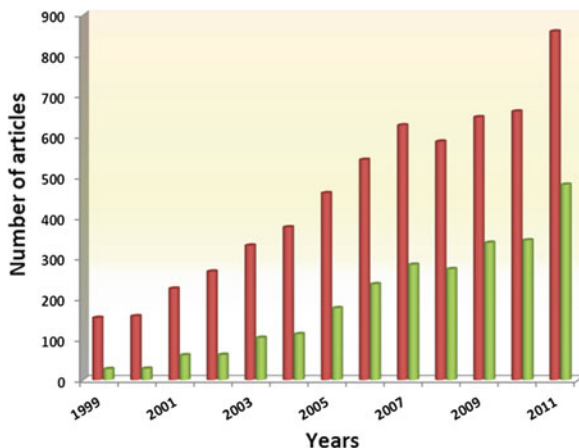
Institute IMDEA Energía, Avenida de Ramón de la Sagra, 3 28935 Móstoles, Madrid, Spain
e-mail: juanmanuel.coronado@imdea.org

M. D. Hernández-Alonso

CIEMAT, Madrid, Spain

e-mail: lolihza@gmail.com

Fig. 5.1 Annual evolution of the number of Scientific Citation Index (SCI) publications devoted to photocatalysis (*red bars*) and photocatalysis with TiO₂ (*green bars*). (Data obtained from ISI Web of Knowledge)



5.1 Structural and Surface Properties of TiO₂

5.1.1 Crystalline Structure of TiO₂

Apart from some high-pressure phases without significant technological relevance (Latroche et al. 1989), there are four TiO₂ polymorphs that can be prepared without using special synthesis conditions: anatase (tetragonal, $I4_1/amd$), rutile (tetragonal, $P4_2/mnm$), brookite (orthorhombic, $Pbca$), and metastable TiO₂ (B) (monoclinic, $C2/m$). All TiO₂ phases can be described as an arrangement of slightly deformed TiO₆ octahedra connected by vertices or edges, while oxygen shows a threefold coordination. The distortion of the octahedra is larger for anatase, but in all cases the two Ti-O apical distances (ca. 1.980 Å for both anatase and rutile) are longer than the four equatorial bonds (1.934 Å for anatase and 1.948 Å for rutile) (Chen and Mao 2007). In the case of rutile, the structure is based on octahedra that share two edges with other to form chains along the c-axis, whereas in anatase the octahedra are linked by the vertices in the (001) plane and connected by edges along other planes. As a result of these different arrangements rutile is denser (4.250 cm³ g⁻¹) than anatase (3.894 cm³ g⁻¹). These two crystal structures are represented in Fig. 5.2. On the other hand, brookite lattice consists of chains of edge-sharing octahedra connected to each other by vertices. Finally, the structure of TiO₂ (B) is closely related to that of anatase, but it presents a different array of octahedral chains which results in less dense crystals.

According to thermodynamic data, the rutile phase is the most stable polymorph at all temperatures and pressures lower than 60 kPa. However, the differences in the Gibbs free energy between rutile and anatase or brookite are small (4–20 kJ mol⁻¹), and consequently, the other polymorphs can be obtained as metastable phases (Zhang and Banfield 2000; Chen and Mao 2007). In this respect, anatase to rutile transformation does not occur at a measurable rate at low temperature, but it takes place by surface nucleation and growth mechanism at

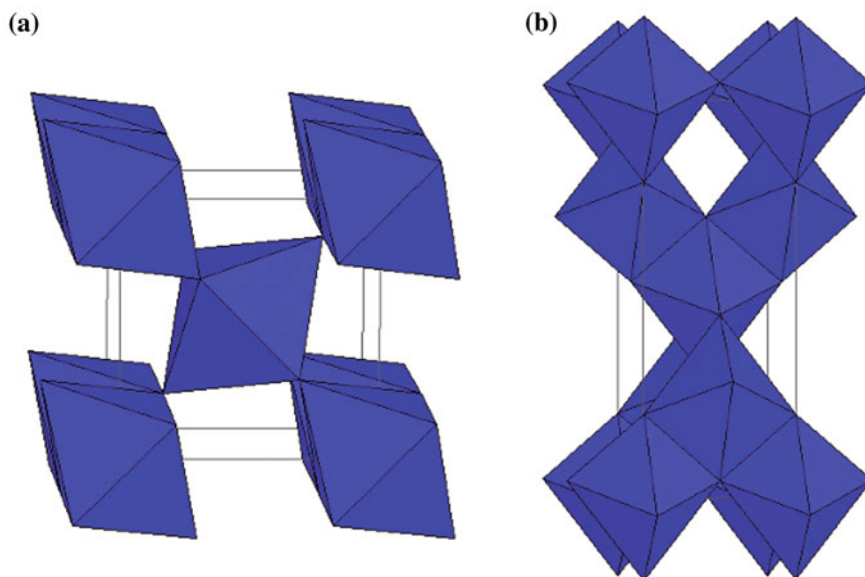


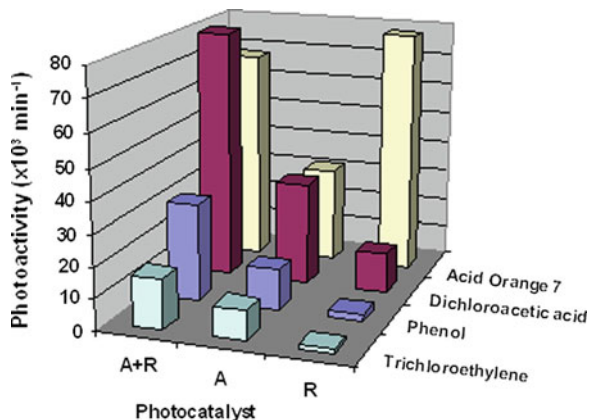
Fig. 5.2 The two most common structures of TiO₂: **a** rutile and **b** anatase

temperatures of about 600 °C in pure TiO₂ (Carp 2004). Therefore, usually anatase or anatase–brookite mixtures are obtained after low-temperature treatments, although in these conditions poorly crystallized or amorphous TiO₂ can constitute a significant proportion of the samples. Usually, rutile appears following calcination at moderate temperatures (300–500 °C), and it becomes the predominant phase after high-temperature (> 600 °C) treatments. More recently, hydrogenation of anatase at high pressure (20 bars) and, moderate temperatures (200 °C) for an extended period has proposed as a way to improve the visible response of TiO₂. This treatment results in the formation of black anatase constituted by a crystalline core with an amorphous shell, which presents an enhanced photoactivity (Chen et al. 2011).

Nevertheless, the presence of impurities or the variations in the surface energy induced by decreasing crystal size can remarkably affect the temperature of these transformations. These facts provide an opportunity to control the phase distribution during preparation, by changing parameters like the type of reagents, the pH, the concentration of additives or the treatment temperature (Carp 2004; Chen and Mao 2007).

Values of the apparent quantum yield obtained with TiO₂ as photocatalyst vary broadly with the process considered, but they are typically lower than 1 % in aqueous suspensions and they can reach up to 25 % for some gas phase reactions (Romero 1999). Although some discrepancies can be found in the literature, anatase is usually considered the most photoactive phase of TiO₂ (Carp 2004; Chen and Mao 2007; Henderson 2011). In this regard, an extensive study by Choi et al. on the photocatalytic degradation of a wide selection of pollutants in aqueous

Fig. 5.3 Photoactivity expressed as the initial rate for the decomposition of four different pollutants in aqueous solution using different TiO₂ commercial photocatalysts with anatase structure (A, Millenium), rutile (R), or a mixture of rutile and anatase (A + R, Evonik-Degussa P25). Reproduced from Hernández-Alonso (2009). Copyright Royal Society of Chemistry



solution indicated that pure rutile is more active than anatase exclusively for some specific substrates, such as the dye orange 7 (Ryu and Choi 2008). Some selected results of this investigation are displayed in Fig. 5.3, where the photoactivity of three different TiO₂ samples for degradation of four pollutants in aqueous solution is represented. Several reasons have been proposed to explain differences in the photoactivity between anatase and rutile, including variations in electronic (e.g. Fermi-level position, electron mobility) or surface (e.g. hydroxyl concentration) structure. In addition, rutile generally presents lower surface area than anatase, due to the larger crystalline size imposed by thermodynamic constrains, and this fact may also contribute to the lower photoactivity of this phase. In this respect, it is worth noting that rutile photocatalysts with high activity are usually constituted by nanostructured, high surface area materials (Henderson 2011) prepared by specific methods such as chloride addition for the surface stabilization of the rutile nuclei. On the other hand, it is also worth mentioning that some reports indicate that brookite can present superior photoactivity than other TiO₂ phases, although these results can be significantly influenced by the morphological characteristics of the samples assayed (Li and Gray 2007). Finally, it is important to highlight that the degree of crystallinity of TiO₂, defined as the ordering of the structure, is a very important factor to determine the photoactivity of this semiconductor, because structural defects can act as recombination centres as it has mentioned in Chap. 2. In fact, several reports indicate that the photoactivity of amorphous TiO₂ is significantly lower than that of its crystalline polymorphs (Henderson 2011).

On the other hand, numerous studies have also shown that elevated rates for organic pollutants degradation and other photoprocesses are achieved with anatase–rutile mixtures, particularly for the case of the benchmark photocatalyst Degussa Evonik P25, hereafter referred to as simply P25. This commercially available powdered TiO₂ is obtained by hydrolysis at high temperature of TiCl₄. Structurally, this widely used photocatalyst is constituted by anatase and rutile nanocrystallites in an approximately 15:80 ratio, along with a minor amount (<5 %) of amorphous phase. Figure 5.3 also provides some examples of the

superior performance of the biphasic TiO₂, which in many reports shows an unbeatable activity, particularly in aqueous solutions. A widely held justification of this behaviour is the formation of a heterojunction between the two TiO₂ polymorphs when they are put in close contact (Li and Gray 2007; Henderson 2011). Due to the differences in the band gap width, the existence of an interface between different TiO₂ phases can facilitate charge separation and, accordingly, reduce the recombination rate. The enhancement of the photocatalytic activity on the heterojunctions will be extensively reviewed in Chap. 15. However, it is worth mentioning here that the study of powdered mixtures of anatase and rutile, with otherwise similar characteristics, has shown an enhancement of the photoactivity with increasing the degree of interaction between both phases (Wu 2004). In a similar way, the increment of the activity of some anatase–brookite mixtures has been attributed to the same electronic phenomenon (Ozawa 2005). Besides, specifically designed TiO₂ thin films have proved that photoactivity can be boosted by establishing contacts between anatase and rutile (Kawahara 2002). In this work, silver photodeposition was used to visualize the photoreduction sites and to track the electron transfer between phases. As it is shown in Fig. 5.4, in these structures, anatase seems to act as the main electron acceptor, but at the interface, the opposite is observed and silver particles are deposited on the rutile side. Therefore, although the heterojunction model can still hold, these observations reveal a more complex dynamic of the photogenerated carriers. Likewise, some authors have proposed the existence of rutile nanoclusters on the anatase surface or specific reaction hot spots (Hurum 2003; Li and Gray 2007). However, other researchers even challenge the role of heterostructures as the main cause for accounting for the remarkable photocatalytic performance of P25 (Ohtani 2010). Therefore, if this debate is to settle, further studies at the nanoscale of these biphasic TiO₂ materials are required.

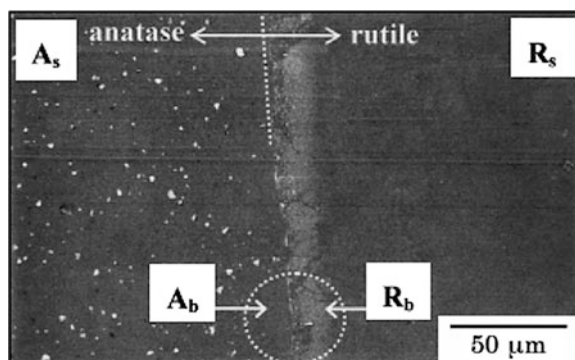


Fig. 5.4 An electron micrograph of a patterned anatase/rutile junction after photodeposition of silver, which labels the reduction sites according to the reaction $2\text{H}_2\text{O} + 4\text{Ag}^+ \rightarrow 4\text{Ag} + \text{O}_2 + 4\text{H}^+$. Reproduced from Kawahara (2002). Copyright Wiley-VCH

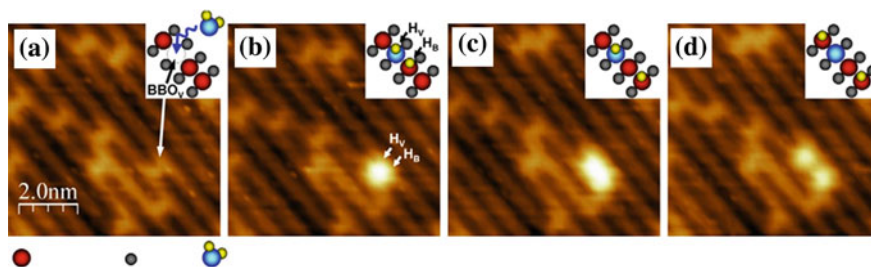
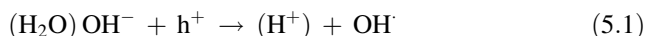


Fig. 5.5 STM images of the same area on rutile exposing the face (110) during dissociative adsorption of water at 357 K: **a** clean surface with several oxygen vacancy sites (labelled “BBOv”); **b** after dissociation of a water molecule at the vacancy generating a geminate hydroxyl pair; **c** after a single hop of the HB hydrogen; and **d** after subsequent hops of the HV hydrogen. Insets show the ball models of the corresponding processes. Reproduced from Li (2008). Copyright of the American Chemical Society

5.1.2 Surface Characteristics of TiO_2

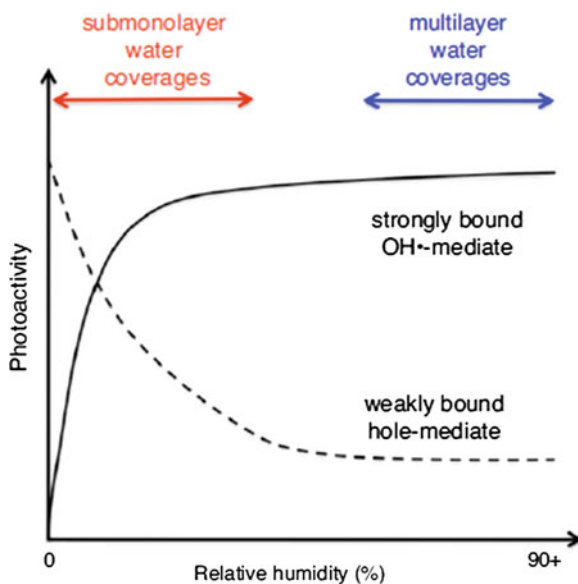
As mentioned in Sect. 2.4, water molecules dissociate on the surface of TiO_2 to yield hydroxyl groups, which saturate the coordination sphere of Ti^{4+} centres, and protons, which bind to the bridging oxygens, as it is shown in the STM images of Fig. 5.5. This process reduces the excess of energy caused by the abrupt discontinuity of the solid structure at the edge of the crystal. Hydration of TiO_2 surface is thermodynamically favoured, and it occurs rapidly even with air moisture. In this respect, a theoretical study has concluded that anatase and rutile polymorphs showed that the lowest values of surface free energy are obtained for water saturated surfaces (Barnard 2005). Consequently, adsorption of reagent molecules is determined, to a great extent, by the density and specific characteristics of hydroxyl groups. Many organic substances like aromatic compounds are attached to the TiO_2 surface by hydrogen bonding as in the case of molecules such as toluene or methylcyclohexane (Hernández-Alonso 2011). These kinds of interactions are relatively weak, and they preserve the molecular structure of the adsorbate. In contrast, partially dehydroxylated TiO_2 can be more reactive as it has observed, for example, in the transformation of acetone into mesityl oxide as monitored by FTIR (El-Maazawi 2000). On the other hand, certain molecules such as alcohols or acids react even with fully hydroxylated surfaces to yield alkoxides or carboxylate surface complexes. This fact is important because photocatalysis shows structure sensitivity with regard to adsorption, and several works have indicated that the conformation of surface complexes affects significantly to the reactivity. An example of that is the observation that formic acid was about 53 times more photoactive than formate on P25 (Liao 2001). In extreme cases, some of these species are so strongly adsorbed that may lead to the deactivation of TiO_2 by blocking the surface sites, as in the case of benzoates or sulphates (Hernández-Alonso 2011; Portela 2010).

Due to the high affinity of water for the TiO₂ surfaces, these molecules play a very relevant role on photoactivity via two main effects: as competitors for surface sites and as the source for OH[•] production. In this respect, although direct oxidation by holes has been proposed in some processes, many studies assume an indirect degradation by hydroxyl radicals produced through the following photochemical reactions:



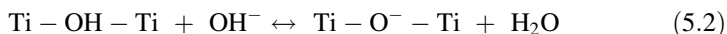
as it is mentioned in [Chap. 3](#). On the other hand, multilayer water forms a network stabilized by hydrogen bonding on TiO₂ surfaces that can limit the access to reactants such as O₂ (Henderson et al. 2003). These opposite effects result in a variation of the efficiency of a particular reaction as a function of relative humidity (RH). Therefore, both inhibition and promotion are possible depending on factors such as the specific mechanism of the process, the ratio between water and organic concentration and strength of the adsorption, and the specific mechanism by which the organic is photooxidized (e.g. OH[•] vs. direct hole attack). Accordingly, different situations can occur as exemplified in [Fig. 5.6](#) for two idealized unspecific processes. Thus, molecules with weak interaction with TiO₂ surface and preferentially oxidized by holes should show a clear decline of the rate with increasing RH. In contrast, strongly adsorbed molecules activated by hydroxyls are eliminated more efficiently at high humidity. Experimentally, numerous studies of the degradation of organic molecules on the gas phase have approached the influence of water, and although some of these photocatalytic processes are basically insensitive to water concentration, most of them have shown a change of regime

Fig. 5.6 Variation of photooxidation activity with relative humidity under two different situations: a weakly bound organic directly attacked by holes (*dashed line*) and a strongly adsorbed organic oxidized by hydroxyl radicals (*solid line*). Reproduced from Henderson (2011). Copyright Elsevier



(from inhibition to promotion, or viceversa) with varying humidity (Henderson 2011).

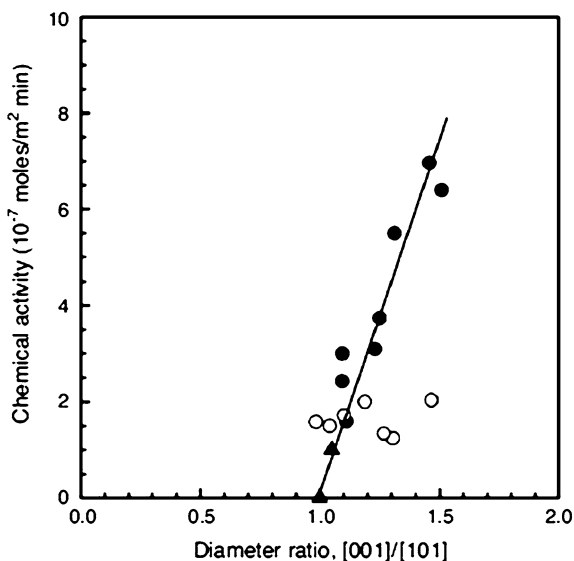
On the other hand, in aqueous solutions, it is necessary to consider the amphoteric character of the Ti-OH species, because the surface charge depends on pH. This is due to the equilibrium between acidic bridging hydroxyls (Eq. 5.2) and more basic terminal hydroxyl (Eq. 5.3):



Thus, at low pH values, the TiO₂ surface is positively charged, while in alkaline conditions it turns negative. The pH value at which the concentration of negative and positive centres is the same constitutes the so-called of point of zero charge (PZC), which varies slightly with the crystalline phase or the preparation method. For example, a PZC value of 6.4 is reported for Degussa P25. In the case of photocatalytic reactions with ionic species, this parameter is crucial, because it defines the pH interval at which adsorption is either facilitated or hindered by electrostatic interactions (Lu 1996).

Although these aspects will be discussed in more detail in Chap. 11, it is important to mention here that recent studies have revealed that photocatalytic activity depends on the type of surfaces exposed (Barnard 2005). The origin of this behaviour lies in the small energetic differences between crystal faces, which can be sufficient to facilitate the preferential separation of electrons and holes in different surfaces. Thus, although the most thermodynamically stable facets are {110} for rutile and {101} for anatase, Ohno and collaborators have reported that rutile {011} and anatase {001} faces provide the sites for oxidation, while the

Fig. 5.7 Chloroform degradation rate on anatase samples as a function of the ratio between {001} and {101} facets. Reproduced from Cho et al. (2005). Copyright Elsevier

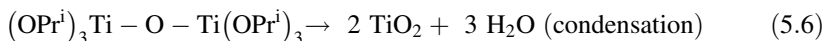
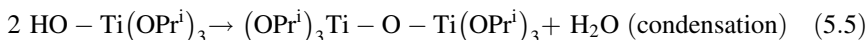
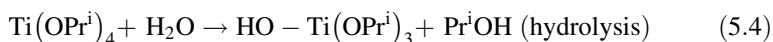


rutile {110} and anatase {101} faces offer the sites for reduction (Murakami et al. 2011). An example of these differences in reactivity is displayed in Fig. 5.7, which shows that the photodegradation of chloroform proceeds at a higher rate in anatase with larger proportion of {001} faces (Cho et al. 2005).

5.1.3 Synthesis of TiO₂

A considerable research effort has been devoted to gain a fine control, not only of the phase composition, but also of the nanoarchitecture of TiO₂ due to the relevance of these physicochemical properties on its photocatalytic performance. Although this topic will be more extensively reviewed in Chap. 11 in connection with nanostructures, some general concepts of TiO₂ are discussed in this section. In a simple way, all the preparation routes can be classified in gas phase or solution methods. Among the gas phase procedures, flame pyrolysis is quite effective because it allows preparing crystalline and homogeneous TiO₂ particles, with relatively large surface area (Johannessen 2001). This method implies the burning of an aerosol containing the titanium precursor and, as mentioned above, is the method used for producing P25.

Solution methods are dominated by sol–gel technique, which provides a very flexible and controllable route for synthesizing TiO₂ in the form of powders, monoliths or thin films. This methodology is based on the utilization of titanium alkoxides, usually Ti(OPrⁱ)₄ (TTIP) but also Ti(OBu)₄ or Ti(OEt)₄, which in the presence of water react according to the following equations:



Progressively, these reactions lead to the formation of TiO₂ nuclei with a high organic content. Ageing of the sol, especially at elevated temperature, results in the coarsening of the particles. The hydrolysis step is usually catalysed by adding acids, either inorganic, such HNO₃ and HCl, or carboxylic, like acetic acid, because reaction (5.4) is promoted by the electrophilic attack of H⁺. Nevertheless, synthesis routes incorporating bases, such as tetramethylammonium hydroxide, have also been described. In any case, preparation at low pH usually results in more crystalline powders, while if the pH of the media is high, condensation is promoted and the resulting solid is less ordered (Carp 2004). The relative rates of nucleation and particle growth can be controlled by adjusting the water-to-alkoxide ratio. Increasing this ratio will favour nucleation while particle growth is favoured by a low content of water and/or excess of titanium alkoxide in the reaction medium (Chen and Mao 2007). On the other hand, reactivity of the alkoxides can be modulated by incorporating other complexing agents like

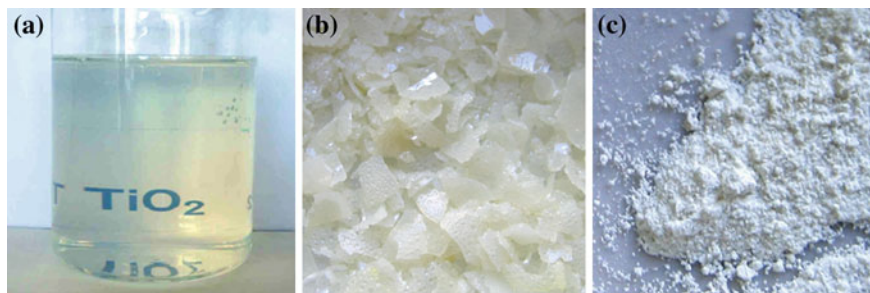


Fig. 5.8 Photographs showing different configurations of a TiO₂ photocatalyst synthesized by a sol–gel method: **a** translucent TiO₂ sol; **b** TiO₂ xerogel; **c** TiO₂ powders. (Pictures by M.D. Hernández-Alonso)

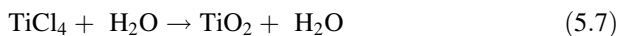
carboxylates or diketones (e.g. acetylacetonate), and this modification promotes polymerization (Carp 2004).

The presence of the acid during the hydrolysis stage induces the peptization of the precipitated oxides, breaking up the aggregates into particles of colloidal dimensions. Particle charging by proton adsorption stabilizes the suspension by electrostatic repulsion. The peptization stage, which completion can take several days, makes it possible to obtain stable colloidal suspensions, which after solvent removal are converted into a solid material known as xerogel (Fig. 5.8). On the other hand, the stable colloidal suspensions can be directly employed to prepare photocatalyst as thin films (Kim and Anderson 1996) on different substrates by application of different coating techniques such as dip-coating, spin-coating or impregnation, as it will further commented in Chap. 12.

Several strategies (e.g. dialysis membranes) can be used to purify the sols, but, in general, preparation of TiO₂ requires a thermal or solvothermal treatment to increase the crystallinity and to remove completely the organic residues (Chen and Mao 2007). Therefore, a calcination stage at moderate temperature (350–450 °C) is a frequent stage in the processing of these materials. In general, the resulting powders present high surface area (>100 m² g⁻¹) and small particle diameter (<10 nm). The phase composition of sol–gel TiO₂ depends on the specific synthesis conditions (temperature of treatment, pH, presence of additives), but anatase is typically the preponderant polymorph in these types of samples.

Multiple variations of the basic scheme of sol–gel synthesis can be adopted to modify the morphology of TiO₂ as it will be detailed in Chap. 11. Some examples of these modifications are the changes in reaction media such in the case of microemulsion synthesis or the use of template molecules such as triblock polymers for the preparation of ordered mesostructures as those displayed in Fig. 5.9 (Nilsson 2011).

Alternatively to the use of titanium alkoxides, TiCl₄ is also widely employed as titanium source. This metal halide is readily hydrolysed according to the reaction:



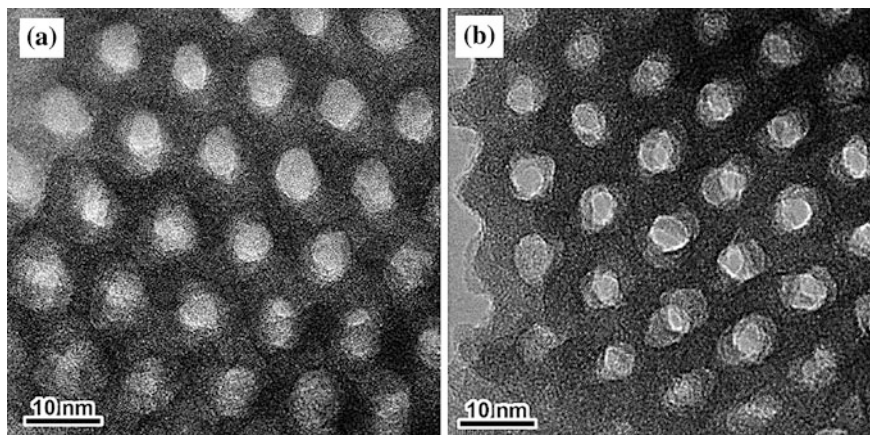
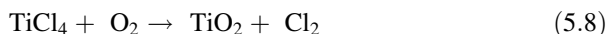


Fig. 5.9 High-resolution TEM images of mesoporous TiO₂ prepared at low temperature using a structure-directing agent and after **a** 3 h or **b** 6 h of ageing. Reproduced from Nilsson (2011). Copyright American Chemical Society

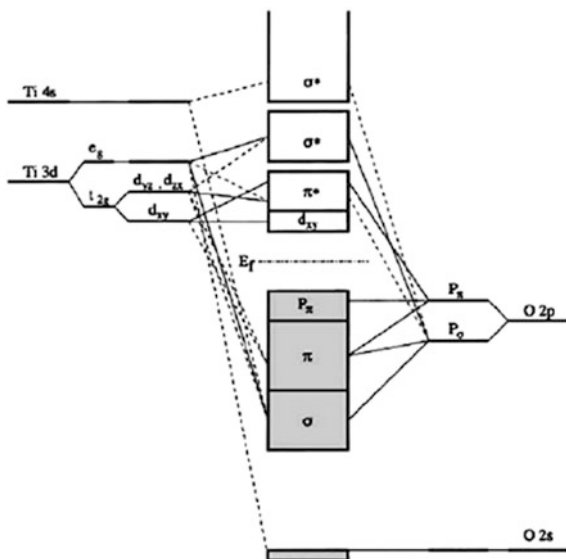
Hydrolysis of this chloride is very rapid, and sometimes is performed at low temperature (e.g. in an ice bath) to gain better control of the synthesis. Besides, reactivity can be better controlled by using other oxygen donor molecules, such as alcohols or even alkoxides, instead of water (Chen and Mao 2007). Less frequently, other titanium reagents such as TiF₄ or TiOSO₄ are used for the synthesis of TiO₂ photocatalyst.

The above-mentioned synthetic routes, mainly based on the use of alkoxides, are performed at bench scale for research or technological applications. However, bulk production of TiO₂ requires less complex and more economically feasible methods. Therefore, this material is industrially produced from the mineral ilmenite (FeTiO₃) using either the sulphate or the chlorine process. The first of these routes consists in the digestion of the ilmenite ore with sulphuric acid to yield TiOSO₄, which subsequently is hydrolysed to obtain TiO₂. The main problem associated with this process is the high amount of Fe(SO₄) formed as by-product, which is a serious environmental burden. For that reason, and also due to economic considerations, most modern plants use the chlorine route developed by DuPont in 1951. This process requires ores containing at least 70 % TiO₂, and it entails first the reduction of the mineral with carbon, and then the oxidation with chlorine to yield titanium tetrachloride. Subsequently, TiCl₄ is distilled and re-oxidized with oxygen to yield pure titanium dioxide according to the reaction:



In this process scheme, the chlorine is recycled and accordingly the emission of pollutants is limited.

Fig. 5.10 Simplified scheme of molecular-orbital bonding structure for anatase (Reproduced with permission from Asahi (2000). Copyright American Physical Society)



5.2 Electronic Structure and Optical Properties of TiO_2

Because of the presence of a small amount of oxygen vacancies, which are compensated by the presence of Ti^{3+} centres, TiO_2 is considered an n-type semiconductor. As displayed in Fig. 5.10, the valence band of anatase can be considered as formed by the overlapping of the oxygen $2p$ orbitals, and it can be divided into three main contributions: the strong σ bonding in the lower energy region, the weaker π bonding in the middle energy region and the nonbonding states at the top of the valence band. On the other hand, the lower part of the conduction band is mainly constituted by the $3d$ orbitals of Ti^{4+} cations with t_{2g} (<5 eV) and e_g (>5 eV) symmetries (Asahi 2000). The d_{xy} states are mainly located at the bottom of the conduction bands, and they provide certain anisotropy to the electronic properties. The rest of the t_{2g} bands, corresponding to the d_{yz} and d_{zx} states, are antibonding with p states of oxygen. A significant feature of the electronic structure of anatase is the existence of nonbonding states near the band gap: the oxygen p orbital at the top of the valence band and the nonbonding d_{xy} orbitals at the bottom of the conduction band. This feature is less pronounced in rutile, because the denser structure of this polymorph favours a more effective overlapping of the electronic states (Chen and Mao 2007).

The band gaps of anatase and rutile are 3.2 and 3.0 eV, respectively, whereas an optical band gap of 3.11 eV has been reported for brookite nanoplates (Chen and Mao 2007; Li et al. 2007). Interband transitions are generally taken as direct (i.e. purely electronic without interactions with lattice phonons) for rutile, whereas anatase and brookite are considered to have indirect band gaps. The threshold for the direct band gap transition in anatase is reported to be at ~ 3.8 – 4.0 eV. However,

other factors like the crystalline size or the presence of dopants can modify the type of transition and somewhat conflicting reports are found in the literature (Henderson 2011). In any case, this is a relevant property for a photocatalyst because indirect semiconductors present lower photon absorption, and consequently, larger mass of solid will be required to achieve the same reaction yield.

As discussed in Chap. 2, the position of the energy levels of a semiconductor determine the chemical potentials of photogenerated charge carriers, and accordingly, these states establish the thermodynamic limits of the processes that can be photocatalysed. In these regards, one of the advantages of TiO₂ over other semiconductors is that its electronic structure is such that it allows simultaneously the oxidation of hydrogen and the reduction of oxygen (Chen and Mao 2007). This is possible because the bottom of the conduction band is more negative than the reduction potential of H⁺/H₂ ($E_{\text{NHE}} = 0.00 \text{ V}$), while the top level of the valence band is more positive than the oxidation potential of O₂/H₂O ($E_{\text{NHE}} = 1.23 \text{ V}$). In this respect, the electrochemical properties of TiO₂ are rather well balanced, in sharp contrast to other semiconductors, which are efficient for either water reduction, like Si, or for water oxidation, like SnO₂. These reference potentials are relevant for water splitting but also for oxidation reactions which require the reduction of molecular oxygen. In addition, surface OH⁻ groups can act as donor species, reacting with valence band holes to yield hydroxyl radicals, OH[•]. These species present a very high oxidation potential [$E_{\text{NHE}}(\text{OH}/\text{H}_2\text{O}) = 2.27 \text{ V}$] and, as mentioned above, are usually considered the key intermediate in the photooxidation reactions with TiO₂. On the other hand, the electrochemical characteristics can also affect the structural integrity of the semiconductor. Corrosion of solids can be intensified under irradiation due to the attack of photogenerated charge carriers to the semiconductor constituents. However, TiO₂ does not suffer anionic photocorrosion because water oxidation ($\text{H}_2\text{O} + 2\text{h}^+ \rightarrow 2\text{H}^+ + 1/2 \text{O}_2$) is thermodynamically more favoured than the formation of molecular oxygen from oxide anions. Accordingly, TiO₂ shows high stability in aqueous suspensions, even at extreme values of pH, and this fact plays a relevant role in its status as reference photocatalyst.

Nevertheless, considering exclusively the photoactivation process, TiO₂ shows a relatively limited performance compared to other semiconductors. Thus, the incident photon-to-current efficiency (IPCE) for TiO₂ is about 45 % at 400 nm, whereas for silicon this parameter approaches 100 % under illumination at 600 nm (Hernández-Alonso 2009; Chen and Mao 2007). However, the major hurdle for the development of solar technologies based on TiO₂ is the wide band gap of all the polymorphs of this material, because only less than 5 % of the sunlight energy ($\lambda < 390 \text{ nm}$) reaching the earth surface can be used for the excitation of this semiconductor (Ohtani 2010). This fact has prompted the search of novel photocatalyst with absorption in the visible range, as it is widely discussed in the following chapters on this book.

5.3 Availability and Safety of TiO₂

Titanium dioxide is a material of great practical significance which commercial production was initiated in 1912. In 2010, the total production as white pigment incorporated in products as diverse as paints (representing a share of about 59 %), polymers (26 %) and paper (9 %) was more than 5.66 million tons, which represents an expansion of about 3.3 % with respect to the previous year. Although the huge scale of the pigment industry dwarfs the importance of other technological applications, in addition, TiO₂ is increasingly incorporated in sensors, catalysts, photochromic devices, photovoltaic cells, etc. In spite of this high consumption, a shortage of TiO₂ is not foreseen in the near future. This is due to the fact than titanium is the ninth most abundant element and constitutes about 0.63 % in weight of the Earth's crust. Several minerals are exploited for titanium extraction but ilmenite, FeTiO₃, accounts for about 91 % of the world's consumption of titanium mineral. Leucoxene (constituted by a complex mixture of rutile, anatase and different iron-containing minerals) is another of the main ores of this element. These minerals are found in relatively large deposits (see Fig. 5.11) in Australia, China, Brazil, India, Norway and many other countries (U.S. Geological Survey 2010). The price of the titanium metal stock has decreased in the last years, and it was of \$11.4 per kilogram in 2010.

Toxicity of TiO₂ is low, and accordingly, it has been approved as a food colouring (identified by the code E-171) by EU legislation. In fact, a number of everyday use products, such as toothpaste, sunscreens, pill coatings or chewing gum, contain TiO₂ (Weir et al. 2012). Nevertheless, although bulk TiO₂ is regarded as biocompatible material, new concerns have arisen as a consequence of the extensive research on nanostructured solids. In the case of TiO₂, oral administration of a high dose of nanoparticles (5 g kg⁻¹ of body mass) does not cause acute toxicity, although evidences of hepatic damage were found. In vitro studies with human intestinal Caco-2 cells showed that their metabolic rate decreased linearly with increasing the surface area of TiO₂ (Gerloff 2012). However, the main risks of nanomaterials are associated with their intake by inhalation, which is

Fig. 5.11 Ilmenite mine in Kälviä area in Finland (reproduced from the webpage of Endomines: <http://www.endomines.fi/index.php>)



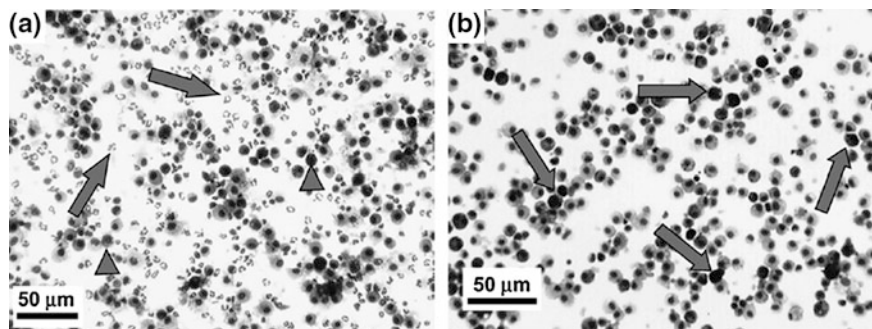


Fig. 5.12 Cytocentrifuge preparation of lavaged cells recovered from a rat's lung exposed to nano-TiO₂ for **a** 24 h and **b** 1 week. In the short term, TiO₂ particles induce an inflammatory response as indicated by the presence of neutrophils (marked with *arrows* in **a**). Some macrophages containing phagocytized TiO₂ nanoparticles can be also observed (marked with *arrow heads* in **a** and *arrows* in **b**). Reproduced with permission from Warheit (2006). Copyright Oxford journals

greatly facilitated by their small size. Thus, severe effects have been reported in the case of exposure to a high concentration of TiO₂ nanoparticles suspended in air, which caused short-term inflammatory response in rat's lungs, as deduced from the histological study shown in Fig. 5.12 (Warheit 2006). Nevertheless, the effect of TiO₂ particles was less intense and less prolonged than that associated with micrometric quartz particles. On the cell level, the formation of reactive oxygen species (ROS), which could induce oxidative stress, has been considered as the underlying molecular mechanism implicated in the cytotoxic, inflammatory and DNA-damaging effects of TiO₂ nanoparticles. In general, low cytotoxicity has been found by using an anatase–rutile containing TiO₂ particles, in the absence of light exposure. On the other hand, some negative environmental impacts on microbial soil communities in terms of biodiversity and biomass have also been reported for relatively large concentrations of TiO₂ nanoparticles.

In any case, nanotoxicity is still a relatively novel research field, with several open debates which will require further exhaustive studies before they settle down. Meanwhile, the precautionary principle should guide any application of TiO₂, especially in large-scale commercial developments.

References

- Asahi R, Taga Y, Mannstadt W, Freeman AJ (2000) Electronic and optical properties of anatase TiO₂. *Phys Rev B* 61(11):7459–7465
- Barnard AS, Zapol P, Curtiss LA (2005) Anatase and rutile surfaces with adsorbates representative of acidic and basic conditions. *Surf Sci* 582:173–188
- Carp O, Huisman CL, Reller A (2004) Photoinduced reactivity of titanium dioxide. *Prog Solid State Chem* 32:33–177

- Chen X, Mao SS (2007) Titanium dioxide nanomaterials: synthesis, properties, modifications, and applications. *Chem Rev* 2007(107):2891–2959
- Chen X, Liu L, Yu PY, Mao SS (2011) Increasing solar absorption for photocatalysis with black hydrogenated titanium dioxide nanocrystals. *Science* 331:746–750
- Cho CH, Han MH, Kim DH, Kim DK (2005) Morphology evolution of anatase TiO₂ nanocrystals under a hydrothermal condition (pH = 9.5) and their ultra-high photo-catalytic activity. *Mater Chem Phys* 92:104–111
- El-Maazawi M, Finken AN, Nair AB, Grassian VH (2000) Adsorption and photocatalytic oxidation of acetone on TiO₂: an in situ transmission FT-IR study. *J Catal* 191:138–146
- Fujishima A, Honda K (1972) Electrochemical photolysis of water at a semiconductor electrode. *Nature* 238:37–38
- Gerloff K, Fenoglio I, Carella E, Kolling J, Albrecht C, Boots AW, Förster I, Schins RPF (2012) Distinctive toxicity of TiO₂ rutile/anatase mixed phase nanoparticles on Caco-2 cells. *Chem Res Toxicol* 25:646–655
- Hagfeldt A, Boschloo G, Sun L, Kloo L, Pettersson H (2010) Dye-sensitized solar cells. *Chem Rev* 110:6595–6663
- Henderson MA (2011) A surface science perspective on TiO₂ photocatalysis. *Surf Sci Reports* 66(6–7):185–297
- Henderson MA, Epling WS, Peden CHF, Perkins CL (2003) Photochemical charge transfer and trapping at the interface between an organic adlayer and an oxide semiconductor. *J Phys Chem B* 107:534
- Hernández-Alonso MD, Fresno F, Suárez S, Coronado JM (2009) Development of alternative photocatalysts to TiO₂: challenges and opportunities. *Energ Environ Sci* 2:1231–1257
- Hernández-Alonso MD, Tejedor-Tejedor I, Coronado JM, Anderson MA (2011) Operando FTIR study of the photocatalytic oxidation of methylcyclohexane and toluene in air over TiO₂-ZrO₂ thin films: influence of the aromaticity of the target molecule on deactivation. *Appl Catal B Environ* 101:283–293
- Hurum DC, Agrios AG, Gray KA, Rajh T, Thurnauer MC (2003) Explaining the enhanced photocatalytic activity of Degussa P25 mixed-phase TiO₂ using EPR. *J Phys Chem B* 107:4545–4549
- Johannessen T, Pratsinis SE, Livbjerg H (2001) Computational analysis of coagulation and coalescence in the flame synthesis of Titania particles. *Powder Technol* 118:242–252
- Kawahara T, Konishi Y, Tada H, Tohge N, Nishii J, Ito S (2002) A patterned TiO₂(anatase)/TiO₂(rutile) bilayer-type photocatalyst: effect of the anatase/rutile junction on the photocatalytic activity. *Angew Chem Int Ed* 41:2811–2813
- Kim DH, Anderson MA (1996) Solution factors affecting the photocatalytic and photoelectrocatalytic degradation of formic acid using supported TiO₂ thin films. *J Photoch Photobio A* 94(2–3):221–229
- Latroche M, Brohan L, Marchand R, Tournoux M (1989) New hollandite oxides: TiO₂(H) and K_{0.06}O₂. *J Solid State Chem* 79:78
- Li G, Gray KA (2007) The solid–solid interface: explaining the high and unique photocatalytic reactivity of TiO₂-based nanocomposite materials. *Chem Phys* 339:173–187
- Li JG, Ishigaki T, Sun X (2007) Anatase, brookite, and rutile nanocrystals via redox reactions under mild hydrothermal conditions: phase-selective synthesis and physicochemical properties. *J Phys Chem C* 111(13):4969–4976L
- Li S-C, Zhang Z, Sheppard D, Kay BD, White JM, Du Y, Lyubinetsky I, Henkelman G, Dohnálek Z (2008) Intrinsic diffusion of hydrogen on rutile TiO₂(110) *J Amer Chem Soc* 130:9080–9088
- Liao F, Wu WC, Chen CY, Lin JL (2001) Photooxidation of formic acid vs formate and ethanol vs ethoxy on TiO₂ and effect of adsorbed water on the rates of formate and formic acid photooxidation. *J Phys Chem B* 105:7678–7685
- Lu MC, Roam WD, Chen JN, Huan CP (1996) Adsorption characteristics of dichlorvos onto hydrous titanium dioxide surface. *Water Res* 30(7):1670–1676

- Murakami N, Katayama S, Nakamura M, Tsubota T, Ohno T (2011) Dependence of photocatalytic activity on aspect ratio of shape-controlled rutile Titanium (IV) oxide nanorods. *J Phys Chem C* 115:419–424
- Nilsson E, Sakamoto Y, Palmqvist AEC (2011) Low-temperature synthesis and HRTEM analysis of ordered mesoporous anatase with tunable crystallite size and pore shape. *Chem Mater* 23:2781–2785
- Ohtani B (2010) Photocatalysis A to Z—what we know and what we do not know in a scientific sense. *J Photochem Photobio C: Photochem Rev* 11:157–178
- Ozawa T, Iwasaki M, Tada H, Akita T, Tanaka K, Ito S (2005) Low-temperature synthesis of anatase–brookite composite nanocrystals: the junction effect on photocatalytic activity. *J Colloid Interface Sci* 281:510–513
- Portela R, Suarez S, Rasmussen SB, Arconada N, Castro Y, Durán A, Avila P, Coronado JM, Sanchez B (2010) Photocatalytic-based strategies for H₂S elimination. *Catal Today* 151(1–2):64–70
- Romero M, Blanco J, Sanchez B, Vidal A, Malato S, Cardona AI, Garcia E (1999) Solar photocatalytic degradation of water and air pollutants: challenges and perspectives. *Sol Energy* 66(2):169–182
- Ryu J, Choi W (2008) Substrate-specific photocatalytic activities of TiO₂ and multiactivity test for water treatment application. *Environ Sci Technol* 42(1):294–300
- US Geological Survey (2011) Mineral commodities summaries. Reston, Virginia. <http://minerals.usgs.gov/minerals/pubs/mcs/2011/mcs2011.pdf>
- Warheit DB, Webb TR, Sayes CM, Colvin VL, Reed KL (2006) Pulmonary instillation studies with nanoscale TiO₂ rods and dots in rats: toxicity is not dependent upon particle size and surface area. *Toxicological Sci* 91(1):227–236
- Weir A, Westerhoff P, Fabricius L, Hristovski K, von Goetz N (2012) Titanium dioxide nanoparticles in food and personal care products. *Environ Sci Technol* 46:2242–2250
- Wu C, Yue Y, Deng X, Hua W, Gao Z (2004) Investigation on the synergetic effect between anatase and rutile nanoparticles in gas-phase photocatalytic oxidations. *Catal Today* 93–95:863
- Zhang HZ, Banfield JF (2000) Understanding polymorphic phase transformation behavior during growth of nanocrystalline aggregates: insights from TiO₂. *J Phys Chem B* 104:3481–3487

Chapter 6

Alternative Metal Oxide Photocatalysts

Sergio García-Rodríguez

6.1 ZnO

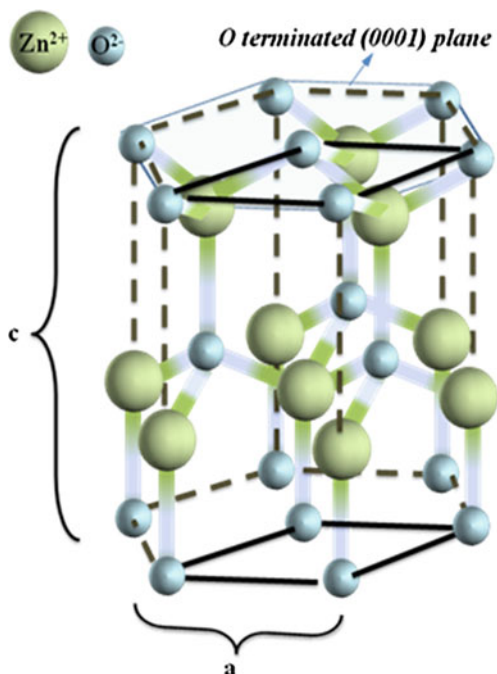
ZnO is a piezoelectric semiconductor which has several interesting properties. This unique material presents good transparency, high electron mobility, strong room temperature luminescence and good optoelectronic (Henglein 1989), catalytic and photocatalytic properties (Aithal et al. 1993; Fox and Dulay 1993; Pichat 1994; Hoffmann et al. 1995; Miyauchi et al. 2002; Burda et al. 2005; Di Paola 2012), along with its low cost (Di Paola 2012). Other emerging applications for ZnO are nanoresonators, cantilevers, transparent electrodes in liquid crystal displays, energy-saving or heat-protecting windows, solar cells, and electronics (Ozgur et al. 2005; Wang 2009).

Zinc oxide is a wide band gap n-type semiconductor ($E_g = 3.2$ eV). The absorption spectrum of ZnO consists of a single, broad intense absorption band from ca. 370 nm to lower wavelengths, ascribed to charge-transfer processes from the valence band to the conduction band (Hoffmann et al. 1995). Since Zn(II) atoms have lost the outer electrons, the electronic configuration is d^{10} , that is, it is a non-transition metal oxide ($[\text{Ar}]3d^{10}4s^0$).

The bottom of the conduction band and the top of the valence band are primarily formed by the Zn s orbitals and the oxygen $2p$ orbitals, respectively (Xu and Schoonen 2000). ZnO crystallizes in three possible polymorphs: hexagonal wurtzite ($P6_3mc$), cubic zinc blende ($F\bar{4}3m$), and cubic rock salt ($Fm\bar{3}m$) (Ozgur et al. 2005). The cubic structures are rarely reported. The cubic zinc blende structure is stabilized only by growth on cubic substrates (Lee et al. 2002), and the rocksalt structure is only obtained at relatively high pressures (Ozgur et al. 2005). The wurtzite structure is the predominant and stable structure at ambient conditions. Each of the two individual atoms, Zn and O, in the hexagonal wurtzite

S. García-Rodríguez (✉)
Sustainable Energy and Chemistry—Institute of Catalysis and Petroleochemistry,
Spanish Council of Research (CSIC), c/Marie Curie 2 E-28049 Madrid, Spain
e-mail: s.garcia@icp.csic.es

Fig. 6.1 Crystal structure of wurtzitic ZnO. Due to *polar bonds*, O- and Zn-terminated (0001) planes present *negative* and *positive* charges, respectively



structure forms two HCP-type sublattices. Cell parameters of wurtzitic ZnO are $a = 3.2498 \text{ \AA}$ and $c = 5.2066 \text{ \AA}$ (ICDD file #36-1451). The absence of inversion symmetry results in the piezoelectric and pyroelectric properties of ZnO (Baruah and Dutta 2009). Alternatively, the wurtzite structure of ZnO can be described as a number of alternating planes composed of tetrahedrally coordinated O²⁻ and Zn²⁺ stacked along the c-axis. The Zn–O bonds are largely ionic due to the contrast between the high electronegativity of oxygen and the low electronegativity of Zn. O- and Zn-terminated (0001) facets have negative and positive charges, respectively (see Fig. 6.1).

Very highly reducing electrons and oxidizing holes are photogenerated on ZnO under UV light irradiation. Besides holes, h^+ , the main oxidizing species in water are hydroxyl radicals, OH. Other oxidizing species such as singlet oxygen, hydroperoxyl radicals and superoxide ions play a minor role in photocatalytic transformations in liquid–solid reactions. In gas–solid reactions, the oxidizing species are predominantly superoxide ions (Doerffler and Hauffe 1964a).

The photocatalytic performance of ZnO is structure sensitive. Lee reported that the band gap of cubic zinc blende ZnO is 0.1 eV lower than that of the wurtzitic ZnO (Lee et al. 2002). Reports on the photoactivity of polymorphs other than wurtzitic ZnO are scarce. Besides the typical blue shift of the band gap of nanostructured ZnO compared to bulk ZnO due to surface and quantum size effects, several studies have established a relationship between ZnO nanoarchitecture and photocatalytic

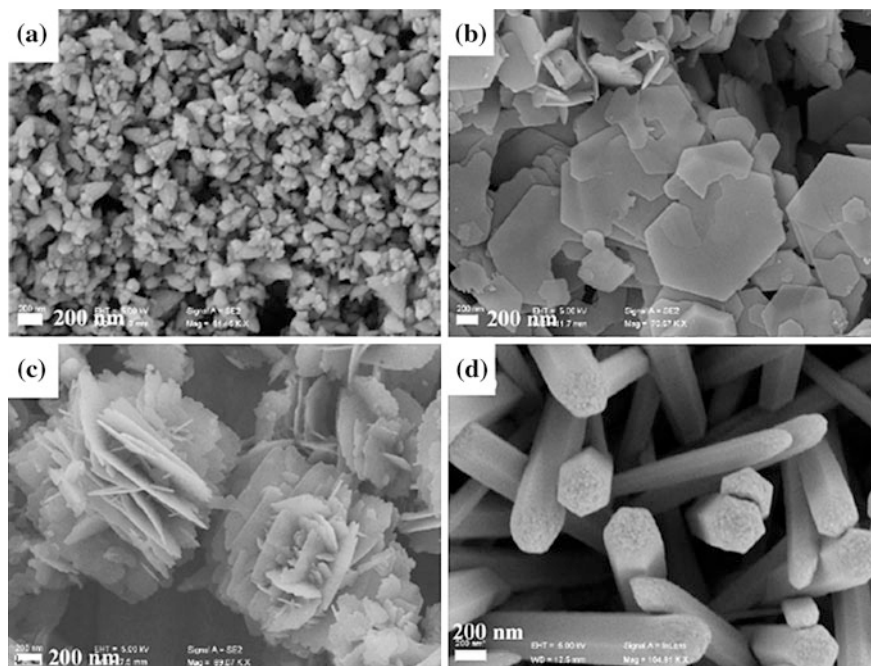
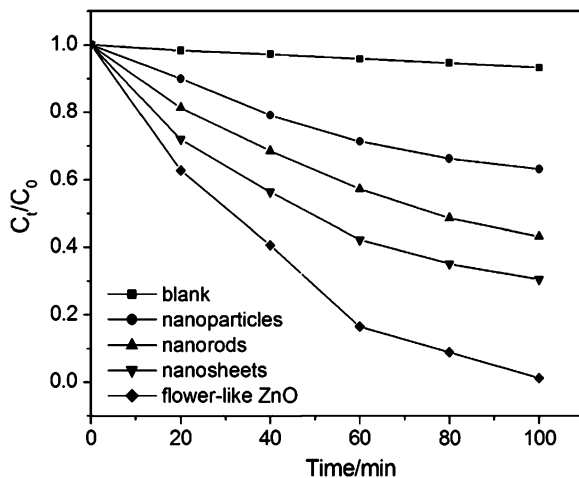


Fig. 6.2 Different ZnO nanoarchitectures: nanoparticles (a), nanosheets (b), nanoflowers (c), and nanorods (d) [adapted and reproduced with permission from (Li and Wang 2010) Copyright American Chemical Society]

activity. A vast number of ZnO nanoarchitectures have been obtained under controlled synthesis conditions. Some examples are shown in Fig. 6.2.

Gupta et al. (2011) reported a red shift of the band edge of rod-shaped ZnO compared to spherical ZnO nanoparticles. The activity experiments demonstrated that the photodegradation rate of methylene blue in aqueous solution was higher for the spherical particles compared to rod-shaped ZnO. Jing et al. (2002) attributed the improvement of the photocatalytic activities in the nanosized system to the increasing formation of surface defects such as oxygen deficiencies and hydroxyl groups. Kislov et al. (2009) reported that the photodecomposition of methyl orange on ZnO was structure sensitive and the lowest photocatalytic activity was that of the O-terminated (0001) basal planes. Li and Wang (2010) controlled the nanostructure of ZnO through a facile hydrothermal synthesis and measured the photodegradation activity of rhodamine B (RhB) in water (Fig. 6.3). Hierarchical flower-like structures built by many interlaced uniform nanosheets with dominant $(2\bar{1}\bar{1}0)$ surfaces displayed an enhanced photocatalytic activity due to the more efficient facets compared to those exposed by nanoparticles, nanorods, or nanosheets. Ma et al. (2011) also observed enhanced photodegradation of RhB by hierarchical nanoporous ZnO spheres compared to rod-shaped ZnO. Wang et al. (2011) reported that flower-like architecture was the most active one in the photodegradation of methylene blue.

Fig. 6.3 RhB concentration changes as a function of UV–vis irradiation time over photocatalyst-free solution, ZnO nanoparticles, ZnO nanosheets, ZnO nanorods scraped off from a Zn foil and flower-like ZnO nanostructures [reproduced with permission from (Li and Wang 2010) Copyright American Chemical Society]



ZnO is sometimes preferred over TiO₂ for degradation of organic pollutants due to its high quantum efficiency (Rehman et al. 2009), especially for the production of peroxides (Kormann et al. 1988; Hoffman et al. 1994). ZnO was also used for photoremediation of industrial waters containing Hg(II) (Domenech and Andres 1987), Cr(VI) (Domenech and Munoz 1987), and cyanides (Domenech and Peral 1988). Bactericidal properties of UV/ZnO were superior to UV/TiO₂ for Gram-negative *Escherichia coli* and Gram-positive *Lactobacillus helveticus* bacteria (Liu and Yang 2003). Compared to TiO₂, ZnO has been used in the photodegradation of contaminants which are difficult to mineralize, like amides (Tang et al. 1982; Roger et al. 1986) or nitrobenzene (Minero et al. 1994), showing the same or lower activity. Besides, different product distribution was found between both semiconductors. For instance, the phototransformation of amides with TiO₂ gave mainly acidic derivatives, while with ZnO both amino and acidic derivatives were obtained (Tang et al. 1982; Roger et al. 1986; Minero et al. 1994).

The pH at the point of zero charge (pH_{PZC}) of colloidal TiO₂ and ZnO suspensions have been determined to be 6.25 (Hoffmann et al. 1995) and 9.3 (Bahnemann et al. 1987), respectively. The lower pH_{PZC} (see Chap. 5) has been used to explain the better performance of ZnO compared to TiO₂ for the degradation of certain organic pollutants such as Acid Brown 14 (Sakthivel et al. 2003) and phenol (Xu et al. 2007). However, the use of ZnO in aqueous solutions is limited by its instability and photocorrosion. The Pourbaix diagram of the Zn–H₂O system (Beverskog and Puigdomenech 1997) shows a narrow pH range for the stability of ZnO in water. At 25 °C and 1 M concentration of dissolved Zn(II) species, ZnO is only stable at pH between 4 and 14 (Goux et al. 2005). The dissolution of ZnO is decreased at low temperatures, high concentration of dissolved Zn(II) species and the presence of certain ionic species in the media (Domenech and Prieto 1986). In the absence of dissolved Zn(II) species, the pH stability range is narrower, between 6.5 and 10, even in the dark. Under UV illumination and stable pH conditions, ZnO suffers

photocorrosion (Khodja et al. 2001). On the contrary, Pardeshi and Patil (2008), Kansal et al. (2010) and Akyol and Bayramoglu (2010) reported reusability of ZnO with negligible lost of activity for the photodegradation of organic pollutants in a wider pH range, between 5 and 10. Many studies have been devoted to avoid ZnO photocorrosion. Comparelli reported that the presence of passivating molecules on the ZnO surface preserved the oxide from photocorrosion and pH-dependent dissolution (Comparelli et al. 2005). Kislov et al. (2009) reported that ZnO photocorrosion was strongly orientation dependent, with only O-terminated (0001) facets exhibiting strong photocorrosion, while Zn-terminated (0001) facets and non-polar surfaces suffered only localized dissolution, most likely at defect sites. Surface hybridization of ZnO with graphite-like carbon layers (Zhang et al. 2009b) and with a monolayer polyaniline (Peralta-Zamora et al. 1996; Zhang et al. 2009a; Ameen et al. 2011) suppressed the photocorrosion of the ZnO nanoparticles and enhanced the photocatalytic activity of ZnO.

Although reports on photoactivity of ZnO in gas phase are lately scarce, the early studies on the photoactivity of ZnO were focused mainly on gas phase (Fujita and Kwan 1958; Gray and Amigues 1969). During the 1950s and 1960s decades, different studies were reported on the photocatalytic oxidation of CO (Doerffler and Hauffe 1964a, b; Steinbac 1967), isopropanol (Filimonov 1964; Muller and Steinbac 1970), and formic acid (Morrison 1967) in gas phase. After TiO₂ was prompted as benchmark photocatalyst, renewed attention on ZnO grew due predominantly to the higher product selectivity of ZnO compared to TiO₂ in the photocatalytic partial oxidation of propene (Pichat et al. 1979) and other olefins (Kodama et al. 1982, 1985; Lacoste et al. 1982, 1984, 1987, 1988; Penot et al. 1983). It was found that ZnO was more active than commercial and home-prepared TiO₂ for the photodecomposition of acetic acid in gas phase (Sclafani et al. 1988). Wada et al. (1993) reported that ZnO showed a superior selectivity toward aldehydes in the partial oxidation of light alkanes, compared to the almost total mineralization showed by TiO₂ and CeO₂ or the low conversion of other semiconductor oxides. ZnO showed higher activity for the photodegradation of chlorofluorocarbon (Tanaka and Hisanaga 1994) and trichloroethylene (Driessen et al. 1998) compared to other metal oxides except TiO₂. Pd deposition on the surface of ZnO nanoparticles using a photoreduction method can improve the gas phase photocatalytic oxidation of n-heptane. This promotion has been related to the increase of adsorbed oxygen measured by surface photovoltage spectroscopy (Jing et al. 2004). Studies on the effect of ZnO nanoarchitecture in gas phase reaction are scarce. Long et al. (2009a, b) found the following increasing activity on the deNO_x photoactivity: plate-like < rod-like < spindle-like < hierarchical spindle flower-like < screw-like < TiO₂ P25. Photocorrosion in gas phase has not been reported (Mitchnick et al. 1999).

ZnO light absorption is restricted to the UV region by its wide band gap (E_g , ZnO = 3.2–3.37 eV). Similar to TiO₂, several strategies have been undertaken to improve the visible light absorption. Qiu et al. (2008) demonstrated that surface-modified ZnO with copolymer poly(fluorine-co-thiophene) resulted in light absorption up to 500 nm wavelength. Lin et al. (2005) obtained N-doped ZnO with

different morphologies exhibiting a noticeable displacement of the absorption edge toward visible wavelengths with a thermal plasma method. Doping of ZnO by substitution Zn^{2+} ions with Co, Mn, or Ni narrows the band gap by $sp-d$ exchange interactions between conduction band electrons and d electrons of these transition metals (Rehman et al. 2009). Maeda reported an absorption band at 520 nm for a solid solution of ZnO and GaN used for water splitting (Maeda and Domen 2010). The coupling of ZnO with other semiconductor has also been attempted in order to improve its photocatalytic properties. Thus, ZnO/SnO₂ and ZnO/ZnO₂ coupled oxides and deposition of Fe₂O₃, WO₃, and CdS onto ZnO substrates have been evaluated for the photocatalytic degradation of aqueous organic pollutants solutions which resulted in faster degradation kinetics with respect to ZnO itself. The increase in activity in these coupled systems is ascribed to charge separation at the interface (Hernández-Alonso et al. 2009). Yoshida also reported that in the oxidation of propene in gas–solid regime, the coupled system ZnO/SiO₂ presented higher selectivity toward propene oxide (Yoshida 1999, 2000).

ZnO is also considered a runner up to TiO₂ for dye-sensitized solar cells (DSC) (Hagfeldt et al. 2010), but although ZnO presents higher electron mobility than TiO₂, which should favor electron transport, its chemical stability is poor, giving rise to filter effect, that is, a layer of inactive dye–Zn²⁺ insoluble complexes.

6.2 WO₃

Tungsten trioxide, WO₃, is a small band gap ($E_g = 2.7$ eV) n-type semiconductor that exhibits interesting optical, electrical, and photocatalytic properties. Some typical applications of WO₃ materials are electrochromic devices, dye-sensitized solar cells, sensors, field-emission, high-temperature superconductors, and photocatalysis. The synthesis, properties, and applications of nanostructured WO₃ have been recently reviewed (Zheng et al. 2011). A number of phase transitions have been reported for bulk WO₃ with increasing temperature (Locherer et al. 1999; Howard et al. 2002). The crystal structure is monoclinic in space group Pc or ϵ -WO₃ at temperature below -43 °C. At this temperature, the structure changes to triclinic in space group P1 or δ -WO₃. At 17 °C, a second monoclinic structure in space group P21/n or γ -WO₃ is observed. Four phase transitions have been reported during annealing of δ -WO₃ at 330, 740, 800, and 900 °C, assigned to orthorhombic in space group Pbcn or β -WO₃, monoclinic in space group P21/c, tetragonal in space group P4/ncc and another tetragonal structure in group space P4/nmm. All these polymorphs are three-dimensional networks of corner-linked WO₆ octahedra, which are considered to adopt different deviations from the ideal ReO₃ cubic structure. At room temperature, it is generally recognized that the most stable structure is monoclinic γ -WO₃. However, it has been reported that the transition temperature between triclinic δ -WO₃ and monoclinic γ -WO₃ could be higher than 17 °C and thus explain that monoclinic γ -WO₃ changes slowly with time to δ -WO₃ at room temperature (Woodward et al. 1995). Furthermore, another

stable form is hexagonal structure *h*-WO₃ originated during the slow dehydration of WO₃·H₂O (Khyzhun et al. 2001). Besides, there exist several hydrated oxides and stable substoichiometric oxides that may play an important role in the photocatalytic performance of this material as explained below.

The methods for the preparation of WO₃ materials can be classified in vapor and liquid phases (Zheng et al. 2011). Vapor phase methods are best used for preparing films. Some examples are sputtering, thermal evaporation deposition and other physical vapor deposition methods. Liquid phase methods render a better control of the morphology when powder WO₃ is required. These methods are mainly sol–gel processes, templates, hydrothermal, and solvothermal. WO₃ photoanodes are typically prepared by anodization of W substrates in a variety of corrosive media and at controlled range of voltage.

WO₃ is a visible light–responsive photocatalyst that absorbs light up to ca. 480 nm. Its band gap depends mainly on the crystallinity of the sample and lies in a range between 2.36 and 3.2 eV, respectively, for highly crystalline and amorphous samples (Kim et al. 2010; Zhang et al. 2011). The electron configuration of W(VI) is [Xe]4f¹⁴ 5d⁰ 6s⁰. The bottom of the conduction band is formed by W 5d orbitals, and the top of the valence band is formed by O 2p orbitals. The upper edge position of the valence band on the vacuum energy scale lies 1.74 eV below the H₂O/O₂ oxidation potential at standard conditions, indicating favorable energetics for the water oxidation reaction. The position of the lower edge of the conduction band is estimated to lie between 0.31 eV above and 0.08 eV below the H⁺/H₂ reduction potential (Weinhardt et al. 2008). This implies that WO₃ will present strong oxidizing holes but weak reducing electrons under irradiation.

WO₃ was first used in 1976 for the photoelectrolysis of water (Butler et al. 1976; Hodes et al. 1976; Butler 1977). Oxygen evolution on WO₃ electrodes occurs at 2 V versus NHE in the dark, and under visible light illumination, the reaction takes place with a bias of just 1 V versus NHE (Wang et al. 2000). Water photoelectrolysis yields between 70 and 90 % in 1 M H₂SO₄ under potential bias of 1.2 V versus NHE have been reported (Cristino et al. 2011). Nanostructured WO₃ photoanodes have also been used for the degradation of a variety of organic effluents with a 0.8–1 V bias (Santato et al. 2001a).

Photocatalytic water splitting in the presence of WO₃ powder have also been reported, although it requires a redox couple such as Fe³⁺/Fe²⁺ to assist on the hydrogen evolution (Sayama et al. 1997; Bamwenda et al. 1999). Best results are obtained with WO₃ with monoclinic structure annealed at high temperatures (>500 °C) (Bamwenda and Arakawa 2001).

The position of the conduction band of WO₃ is too positive to allow oxygen reduction, which renders the photocatalytic degradation of organic pollutants difficult without an external bias. Nevertheless, it absorbs a higher fraction of light than TiO₂, and it is stable at moderate and highly acidic media. Pelizzetti et al. (1988) studied the photocatalytic degradation of polychlorinated dioxins and polychlorinated biphenyls in aqueous suspensions under Xe lamp irradiation and found the following activity order: TiO₂ > WO₃ ≫ ZnO. During the photocatalytic reduction of nitrobenzene in the presence of cyclohexene, WO₃ showed a

different product distribution, maximizing $C_6H_5N(O) = NC_6H_5$, in contrast to TiO_2 and CdS which maximized $C_6H_5N = NC_6H_5$ and $C_6H_5NH_2$, respectively (Maldotti et al. 2000). Hepel studied the photoelectrochemical mineralization of diazo compounds using nanocrystalline WO_3 electrodes (Hepel and Luo 2001).

The photocatalytic reduction of aqueous $Cr(VI)$ was conducted by Khalil et al. (1998) over TiO_2 , ZnO , and WO_3 . The obtained order of activity in the same experimental conditions was TiO_2 (Degussa P25) > ZnO > WO_3 . WO_3 has been used for simultaneous photocatalytic reduction of $Cr(VI)$ and oxidation of the methylene blue dye in aqueous solutions (Watcharenwong et al. 2008).

Differences in crystalline structure and morphology may cause a great change in the photocatalytic reactivity of WO_3 films. Santato et al. (2001b) demonstrated that nanostructured films presented much higher incident photon-to-current conversion efficiencies (IPCE) during methanol photoelectrooxidation compared to bulk WO_3 due to an improvement of the charge separation in nanocrystalline WO_3 electrodes. Furthermore, the photocurrent efficiency for those wavelengths close to the band edge can be increased simply by adapting the thickness of the semiconductor film. IPCE is higher for porous materials compared to dense electrodes. Furthermore, annealing at 500 °C enhances the activity and changes the band gap from 3.2 eV (amorphous) to 2.6 eV (monoclinic) (Berger et al. 2006). Kominami et al. (2001), (2003) studied the preparation of WO_3 by solvothermal methods and found that 300 °C and short treatment times rendered WO_3 active powders for water splitting assisted by the Ag^+/Ag couple. Lower temperatures gave inactive orthorhombic $WO_3 \cdot 0.33 H_2O$, while higher temperatures or times resulted in coagulation of particles which resulted in higher electron-hole recombination and efficiency lost. Wang et al. (1998), (2002) studied the photodegradation of RhB over WO_3 films prepared by radio frequency magnetron sputtering at temperatures between 0 and 150 °C, exhibiting amorphous and polycrystalline monoclinic structures, respectively. The films deposited at higher temperatures were found to present a better efficiency, as a consequence of improved crystallinity and a decreased number of oxygen vacancies. Guo reported that porous WO_3 electrodes prepared by a certain electrochemical procedure exhibiting (002) planes preferentially showed much higher activity than film WO_3 or even TiO_2 nanotube arrays in the pentachlorophenol degradation in aqueous solution under Xe lamp illumination (Guo et al. 2007). Baeck prepared lamellar WO_3 films by electrodeposition using sodium dodecyl sulfate as templating agent, which showed higher photocatalytic activity compared to non-porous WO_3 (Baeck et al. 2003).

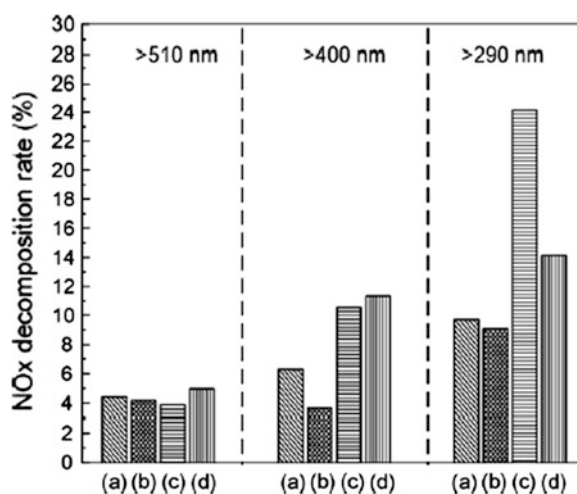
Hierarchical structures result in improved activities and efficiencies. Chen and Ye (2008) prepared several hollow WO_3 shells through a template method and reported a higher activity for RhB and 2-propanol degradation under Xe lamp illumination compared to powder WO_3 . Yu and Qi (2009) reported a relevant increase in RhB degradation activity under UV light by flower-like structures prepared by a hydrothermal method and explained the results by the combination of high specific surface area, bimodal macro/mesoporous structures and the simultaneous presence of h- WO_3 and orthorhombic $WO_3 \cdot 0.33 H_2O$ crystal phases. Li et al. (2010) reported an enhanced activity for the degradation of methylene

Table 6.1 Morphology, crystal phase, specific surface area, and band gap of the products synthesized by the solvothermal reactions at 200 °C with different solvents [reproduced with permission from (Liu et al. 2011a) Copyright Elsevier]

Solvent	Morphology	Crystal phase	Specific surface area (m ² /g)	Band gap (eV)
Ethanol	Urchin like nanowire spheres	Amorphous with slight tendency of crystallization	128.75	2.76
1-Propanol	Spindle shapes nanowire bundles	Amorphous with slight tendency of crystallization	81.42	2.95
42.9 vol % water-ethanol	Composite morphology with micrometer-sized plates and rods	Composite crystals with WO ₃ (H ₂ O) _{0.333} and WO ₃	3.13	2.43
85.7 vol % water-ethanol	Accumulation of microrods	WO ₃	5.72	2.43

blue under visible light irradiation of well-ordered mesoporous WO₃ architecture prepared by a sol-gel process in the presence of a structure-directing agent compared to reference powder particles. The results of Liu et al. (2011a) are in accordance with that conclusion. Liu et al. prepared WO₃ with different morphologies and crystal phases by solvothermal reaction, adjusting the solvent composition and treatment time (Table 6.1). The activity for the NO photooxidation was studied under irradiation of these materials with different wavelengths (Fig. 6.4). Although all samples were less active than TiO₂ P25, the highest activity among W-based materials was observed for plate-like particles with preferential (002) facets and the same monoclinic WO₃ and orthorhombic

Fig. 6.4 NO destruction activity of WO₃ synthesized by solvothermal reaction at 200 °C for 12 h with **a** ethanol, **b** 1-propanol, **c** 42.9 vol. % water-ethanol mixed solution, and **d** 85.7 vol. % water-ethanol mixed solution [reproduced with permission from (Liu et al. 2011a) Copyright Elsevier]



WO₃·0.33 H₂O heterojunction. Substoichiometric oxides, WO_{3-x}, containing up to 5 % oxygen vacancies are stable phases at most photocatalytic reaction conditions. Nevertheless, oxygen vacancies are detrimental for photocatalysis (Cross et al. 2003).

Corrosion of WO₃ in aqueous solutions has been reported in the whole range of pH. The Pourbaix diagram of W shows that the thermodynamic stability region of WO₃ lies at pH < 4 (Lillard et al. 1998; Anik and Cansizoglu 2006). Powder WO₃ and hydrated WO₃·xH₂O present pH_{PZC} values close to 1.5 and 2.5. No reports on corrosion or photocorrosion have been published for WO₃ materials used as photocatalysts in aqueous solutions. On the other hand, when WO₃ is used as photoanode, it has been reported to produce accumulation of peroxy species, leading to a gradual dissolution and structural disintegration (Seabold and Choi 2011). Some solutions proposed to increase the long-term stability of WO₃ photoanodes are heterojunctions with an oxygen evolution catalyst (Seabold and Choi 2011), adding an oxo-bridged Mn₂ catalyst (Liu et al. 2011b) or substoichiometric WO_{3-x} (Wang et al. 2012).

Under visible light irradiation WO₃ has higher activity compared to TiO₂ on the photoelectrochemical degradation of azo dye pollutants, such as Remazol Black B, due to the lower valence band edge energy compared (Hepel and Hazelton 2005). Sayama reported a higher activity of WO₃ for the photodegradation of hexane and other VOCs (Sayama et al. 2010a) and antibacterial improved activity (Sayama et al. 2010b) compared to nitrogen-doped TiO₂ under visible light irradiation. Under UV light irradiation, the activity of WO₃ is typically lower than TiO₂ photocatalysts. Ivankovic (Ivankovic et al. 2003) used WO₃ for carcinoma cells photokilling with good results although activity was much less than that of Fe-doped TiO₂. This low photoactivity in the degradation of pollutants under UV light showed generally by WO₃ has been attributed to the high recombination rate of the photoproduced electron/hole pairs and/or to the low rate of electron transfer to O₂. Charge separation in WO₃ is enhanced with Pt loading (Sclafani et al. 1998; Ho et al. 2012) or in heterojunctions with BiVO₄ (Su et al. 2011). Pt/WO₃ exhibits better photocatalytic performance than TiO₂ and N-TiO₂ under UV and visible light irradiation, respectively (Abe et al. 2008; Zhao and Miyauchi 2008). Another problem of WO₃ is the limited rate of electron transfer, which hinders its degradation photoactivity. Since the position of the conduction band is so close to the reduction potential of H⁺/H₂, electrons are accumulated and the reaction is stopped. Adding an electrochemical couple in the aqueous media improves the capacity of releasing electrons and, thus, improves the photoactivity. Catalytic activity of WO₃ exceeding that of N-TiO₂ has been reported adding CuCl₂ (Arai et al. 2008a) or Fe₂(SO₄)₃ (Arai et al. 2008b) under visible light. Another approach for reducing the electronic accumulation on the surface of WO₃ particles is doping with multi-walled carbon nanotubes to improve electronic transfer and enhance WO₃ photocatalytic performance (Wang et al. 2008; Tian et al. 2012).

Recent applications exploit the storage ability of WO₃ as an electron pool for metal protection and bactericidal activity in the dark. Tatsuma et al. (2001) recently designed a TiO₂-WO₃ photoelectrochemical anticorrosion system with

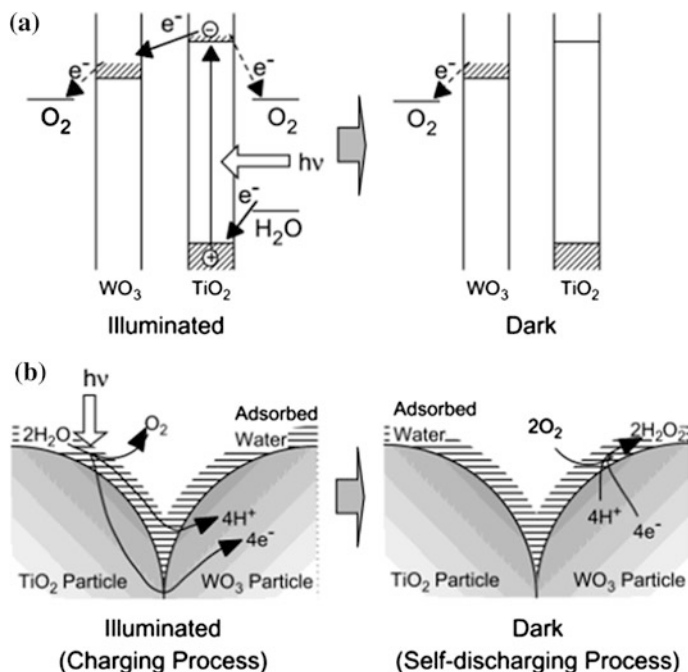


Fig. 6.5 **a** Mechanism of reductive energy storage of TiO_2 - WO_3 combined system. **b** Proposed models of electron and ion transfer in the charging and self-discharging processes of the TiO_2 - WO_3 composite film in humid air [reproduced with permission from (Tatsuma et al. 2002) Copyright American Chemical Society]

energy storage ability on the basis of the reductive energy generated by TiO_2 under UV irradiation and using the WO_3 as an electron pool. This concept was extended to photocatalysis in gas phase (Tatsuma et al. 2002). Figure 6.5 illustrates the mechanism of reductive energy storage and the proposed models of electron and ion transfer. In the dark, the reduced WO_3 is slowly oxidized by oxygen, which leads to the generation of H_2O_2 , expecting some bactericidal effect. When the system is combined with $\text{Ni}(\text{OH})_2$, it also exhibits oxidative energy storage abilities. It is claimed that a $5 \times 5 \times 3$ m room with ceiling and walls fully covered by a $\text{Pt-WO}_3/\text{Ni}(\text{OH})_2$ bilayer film could remove up to 5.7×10^2 μmol , that is, 0.18 ppm of formaldehyde in the dark, after 10 h of fluorescent light irradiation (Yang et al. 2011).

6.3 Other Photocatalytically Active Oxides

The research on the photocatalytic properties of metal oxide semiconductors is based on the band gap/irradiation wavelengths, adsorption of species and, especially in aqueous media, stability and pH_{PZC} . Table 6.2 contains the energy levels

Table 6.2 Band gaps and energy levels of calculated conduction band (E_{CB}) and valence band (E_{VB}) with respect to absolute vacuum scale and measured or estimated pH_{PZC} for semiconducting metal oxides and electron configuration of the metals in its fundamental state [adapted with permission of (Xu and Schoonen 2000) Copyright Mineralogical Society of America]

Metal oxide	E_g (eV)	E_{CB} (eV)	E_{VB} (eV)	pH_{PZC}	Electron configuration of M^0
ZrO ₂	5.00	-3.41	-8.41	6.70	[Kr]4d ² 5s ²
Ga ₂ O ₃	4.80	-2.95	-7.75	8.47	[Ar]3d ¹⁰ 4s ² 4p ¹
Ta ₂ O ₅	4.00	-4.33	-8.33	2.90	[Xe]4f ¹⁴ 5d ¹⁰ 6s ² 6p ¹
NiO	3.50	-4.00	-7.50	10.30	[Ar]3d ⁸ 4s ²
SnO ₂	3.50	-4.50	-8.00	4.30	[Kr]4d ¹⁰ 5s ² 5p ²
Nb ₂ O ₅	3.40	-3.40	-6.80	6.06	[Kr]4d ⁴ 5s ¹
TiO ₂	3.20	-4.21	-7.41	5.80	[Ar]3d ² 4s ²
ZnO	3.20	-4.19	-7.39	8.80	[Ar]3d ¹⁰ 4s ²
CeO ₂	2.94	-5.9	-8.7	6.80	[Xe]4f ¹ 5d ¹ 6s ²
In ₂ O ₃	2.80	-3.88	-6.68	8.64	[Kr]4d ¹⁰ 5s ² 5p ¹
WO ₃	2.70	-5.24	-7.94	0.43	[Xe]4f ¹⁴ 5d ⁴ 6 s ²
FeO	2.40	-4.33	-6.73	8.00	[Ar]3d ⁶ 4s ²
Fe ₂ O ₃	2.20	-4.78	-6.98	8.60	[Ar]3d ⁶ 4s ²
Cu ₂ O	2.20	-4.22	-6.42	8.53	[Ar]3d ¹⁰ 4s ¹
CuO	1.70	-4.96	-6.66	9.50	[Ar]3d ¹⁰ 4s ¹
Fe ₃ O ₄	0.10	-5.73	-5.83	6.50	[Ar]3d ⁶ 4s ²

of the E_{VB} and the E_{CB} , the point of zero charge pH_{PZC} , and the electron configuration of the metal in its fundamental state of the metal oxides which present certain photocatalytic activity ordered by its band gap. Xu and Schoonen (2000) reviewed the schematics of the absolute energy positions of conduction and valence bands of metal oxides classifying them into three groups according to the degree of electronic occupation of the metal d orbital in the oxide.

In low d electron occupancy metal oxides, such as TiO₂, ZrO₂, and WO₃, the top of the valence band is formed by oxygen $2p$ orbitals, and the conduction band edge is generally formed by metal d orbitals. The energy level of the conduction band edge is typically close to the reduction potential of water (-4.5 eV, H^+/H_2), while valence band edges are situated at energy levels much lower than the oxidation potential of water (-6.5 eV, O_2/H_2O couple). Hence, electrons in the conduction band and holes in the valence band of low d electron occupancy transition metal oxides are highly reducing and oxidizing agents, respectively. Usually, these metal oxides present large band gaps, that is, absorbing in the UV region. High d electron occupancy transition metal oxides (Fe₂O₃, MnO₂) present the metal d states forming part of both valence and conduction band edges, and the valence band consists of hybridizations of d metal orbitals with O $2p$ orbital (Hu et al. 2010). As a result, the band structures become complicated. The hybridization results in an increase in the valence band level, smaller band gap energy sufficient to absorb visible light, ca. 2.5 eV, and less oxidant holes. In non-transition metal oxides, such as ZnO, PbO, CdO, or SnO₂, the conduction band is primarily formed by metal s and p orbitals, whereas the top of the valence band is derived primarily from oxygen $2p$ orbitals.

Regarding photocatalytic activity, only a few works have dealt with the screening of several metal oxides. An early work of Pichat et al. (1979) dealt with the photocatalytic activity of different metal oxides in the oxidation of propylene at 50 °C under UV irradiation. Total oxidation to CO₂ and water predominated for CeO₂ and TiO₂ and, to a lesser extent, for ZrO₂ and ZnO. Partial oxidation products, that is, ethanal, acrolein, acetone, propene oxide, and traces of propanal, were obtained with SnO₂, WO₃ and a Sn–O–Sb mixed oxide, and almost solely over Sb₂O₄. Only V₂O₅ was found photoinactive. This study suggested that some of these metal oxides which do not lead to full mineralization might be interesting in the field of photocatalytic synthesis, but not for decontamination. Pichat (1994) also studied the photocatalytic activities of metal oxides in aqueous media under UV irradiation for the oxidation of alcohols, aromatic compounds, sulfides, amines, saturated and unsaturated alicyclic hydrocarbons, and alkanes under UV irradiation. Only ZnO, SnO₂, ZrO₂, MoO₃, WO₃, and TiO₂ were found active (anatase the highest). On the contrary, Fe₂O₃ and V₂O₅ were found unsuitable for photocatalysis in aqueous media due to photocorrosion. Miyauchi et al. (2002) studied the activities of thin films of several oxides for the degradation of MB adsorbed on their surface from aqueous solutions. TiO₂, SnO₂, ZnO, WO₃, V₂O₅, CeO₂, CuO, MoO₃, Fe₂O₃, Cr₂O₃, and In₂O₃ were used for this purpose. Among them, TiO₂ and ZnO exhibited a high activity for the oxidation of MB under UV illumination, while SnO₂ showed relatively low activity and the rest of oxides were not active for decomposing the dye molecules. The redox potentials of the electrons and holes photogenerated in the different materials were invoked to explain the obtained results. Both the band gap and the position of the valence and conduction bands showed to be relevant.

Metal oxides may be classified in three groups according to its band gap and type of irradiation needed. Photocatalytic reactions over oxides with a band gap of ca. 3 eV, similar to that of TiO₂, require UV light irradiation. Under this type of light, anatase presents usually the highest activities. However, other oxides can result more suitable for particular applications for reasons other than activity. For example, Prado et al. (2008) found that although Nb₂O₅ was less efficient than TiO₂ and ZnO for the degradation of the indigo carmine dye in aqueous solution, its reusability was much higher. Separation of TiO₂ and ZnO by centrifugation was difficult due to the formation of stable hydrocolloids in the reaction conditions, so that their reuse was not effective.

Many metal oxides with band gaps below that of anatase present better photocatalytic activities under visible light or sun light irradiation, due to the higher absorption fraction in the visible light region of the spectra. This is especially so for WO₃ ($E_g = 2.70$ eV) (see Sect. 6.2) and Bi₂O₃ ($E_g = 2.80$ eV). Nanocrystallite Bi₂O₃ synthesized by a simple sonochemical route showed a photoactivity for methyl orange degradation in water greatly superior to that of microsized Bi₂O₃ and P25 (Zhang et al. 2006). Another example is CeO₂, an n-type semiconductor with a band gap of 2.94 eV. The better performance of CeO₂ for the degradation of acid orange 7 under visible light irradiation compared to Degussa P25 is explained by the narrower band gap of CeO₂, which enables a greater

fraction of light absorption, along with the superior adsorption capacity of this contaminant on CeO₂ (Ji et al. 2009). The performance of CeO₂ in the photodegradation of toluene in gas phase is preferred compared to that of P25 for its selectivity toward more desired oxidation products under UV light (Coronado et al. 2002). TiO₂ produced CO₂ and a measurable quantity of benzaldehyde, which is an undesirable by-product. Although the photooxidation rate of CeO₂ was an order of magnitude lower than that observed in the presence of TiO₂, toluene was completely mineralized, only CO₂ and traces of benzene were detected, without significant catalyst deactivation (Hernández-Alonso et al. 2004).

Finally, metal oxides with a band gap greater than that of TiO₂ absorb the major part of far UV. ZrO₂ ($E_g = 5.0$ eV) nanoparticles prepared through a high current electrical arc discharge of Zr electrodes in water showed a photocatalytic activity for the degradation of RhB in aqueous solution under UV irradiation (254 nm) near two times higher than that of P25 (Ashkarran et al. 2010). NiO ($E_g = 3.7$ eV) nanoparticles synthesized by a sol-gel method (Hayat et al. 2011) demonstrated better photocatalytic efficiency than TiO₂ for the degradation of phenol in water solution at 266 nm. The degradation rate was increased significantly by increasing the initial pH of the solution. Ga₂O₃ ($E_g = 4.8$ eV) is a wide band gap semiconductor that can be photoexcited only by UVC irradiation ($\lambda < 260$ nm). The position of its conduction band is much higher than that of TiO₂, so that Ga₂O₃ has been reported to act as a photocatalyst for some reductive reactions. Three polymorphs of Ga₂O₃ were evaluated for the decomposition of benzene, toluene, and ethylbenzene in dry air stream under UV illumination (Hou et al. 2007). The Ga₂O₃ catalysts showed much higher photocatalytic activity than commercial TiO₂. The efficiency of the polymorphs followed the sequence β -Ga₂O₃ > α -Ga₂O₃ > γ -Ga₂O₃. The superior performance of β -Ga₂O₃ was attributed to its good crystallinity and distorted geometric structure.

References

- Abe R, Takami H, Murakami N, Ohtani B (2008) Pristine simple oxides as visible light driven photocatalysts: highly efficient decomposition of organic compounds over platinum-loaded tungsten oxide. *JACS* 130:7780–7781
- Aithal US, Aminabhavi TM, Shukla SS (1993) Photomicroelectrochemical detoxification of hazardous materials. *J Hazard Mater* 33:369–400
- Akyol A, Bayramoglu M (2010) Performance comparison of ZnO photocatalyst in various reactor systems. *J Chem Technol Biotechnol* 85:1455–1462
- Ameen S, Akhtar MS, Kim YS, Yang OB, Shin HS (2011) An effective nanocomposite of polyaniline and ZnO: preparation, characterizations, and its photocatalytic activity. *Colloid Polym Sci* 289:415–421
- Anik M, Cansizoglu T (2006) Dissolution kinetics of WO₃ in acidic solutions. *J Appl Electrochem* 36:603–608
- Arai T, Yanagida M, Konishi Y, Ikura A, Iwasaki Y, Sugihara H, Sayama K (2008a) The enhancement of WO₃-catalyzed photodegradation of organic substances utilizing the redox cycle of copper ions. *Appl Catal B* 84:42–47

- Arai T, Yanagida M, Konishi Y, Sugihara H, Sayama K (2008b) Utilization of $\text{Fe}^{3+}/\text{Fe}^{2+}$ redox for the photodegradation of organic substances over WO_3 photocatalyst and for H_2 production from the electrolysis of water. *Electrochemistry* 76:128–131
- Ashkarran AA, Afshar SAA, Aghigh SM, Kaviani-pour M (2010) Photocatalytic activity of ZrO_2 nanoparticles prepared by electrical arc discharge method in water. *Polyhedron* 29:1370–1374
- Baeck SH, Choi KS, Jaramillo TF, Stucky GD, McFarland EW (2003) Enhancement of photocatalytic and electrochromic properties of electrochemically fabricated mesoporous WO_3 thin films. *Adv Mater* 15:1269–1270
- Bahnemann DW, Kormann C, Hoffmann MR (1987) Preparation and characterization of quantum size zinc-oxide: a detailed spectroscopic study. *J Phys Chem* 91:3789–3798
- Bamwenda GR, Arakawa H (2001) The photoinduced evolution of O_2 and H_2 from a WO_3 aqueous suspension in the presence of $\text{Ce}^{4+}/\text{Ce}^{3+}$. *Sol Energy Mater Sol Cells* 70:1–14
- Bamwenda GR, Sayama K, Arakawa H (1999) The effect of selected reaction parameters on the photoproduction of oxygen and hydrogen from a $\text{WO}_3\text{-Fe}^{2+}\text{-Fe}^{3+}$ aqueous suspension. *J Photochem Photobiol, A* 122:175–183
- Baruah S, Dutta J (2009) Hydrothermal growth of ZnO nanostructures. *Sci Technol Adv Mater* 10:013001
- Berger S, Tsuchiya H, Ghicov A, Schmuki P (2006) High photocurrent conversion efficiency in self-organized porous WO_3 . *Appl Phys Lett* 88:203119
- Beverkog B, Puigdomenech I (1997) Revised Pourbaix diagrams for Zinc at 25–300°C. *Corros Sci* 39:107–114
- Burda C, Chen XB, Narayanan R, El-Sayed MA (2005) Chemistry and properties of nanocrystals of different shapes. *Chem Rev* 105:1025–1102
- Butler MA (1977) Photoelectrolysis and physical properties of semiconducting electrode WO_3 . *J Appl Phys* 48:1914–1920
- Butler MA, Nasby RD, Quinn RK (1976) Tungsten trioxide as an electrode for photoelectrolysis of water. *Solid State Commun* 19:1011–1014
- Chen D, Ye JH (2008) Hierarchical WO_3 hollow shells: Dendrite, sphere, dumbbell, and their photocatalytic properties. *Adv Funct Mater* 18:1922–1928
- Comparelli R, Fanizza E, Curri ML, Cozzoli PD, Mascolo G, Agostiano A (2005) UV-induced photocatalytic degradation of azo dyes by organic-capped ZnO nanocrystals immobilized onto substrates. *Appl Catal B* 60:1–11
- Coronado JM, Maira AJ, Martinez-Arias A, Conesa JC, Soria J (2002) EPR study of the radicals formed upon UV irradiation of ceria-based photocatalysts. *J Photochem Photobiol, A* 150:213–221
- Cristino V, Caramori S, Argazzi R, Meda L, Marra GL, Bignozzi CA (2011) Efficient photoelectrochemical water splitting by anodically grown WO_3 electrodes. *Langmuir* 27:7276–7284
- Cross WB, Parkin IP, O'Neill SA, Williams PA, Mahon MF, Molloy KC (2003) Tungsten oxide coatings from the aerosol-assisted chemical vapor deposition of $\text{W}(\text{OAr})_6$ ($\text{Ar}=\text{C}_6\text{H}_5$, $\text{C}_6\text{H}_4\text{F}$ -4, $\text{C}_6\text{H}_3\text{F}_2$ -3,4); photocatalytically active gamma- WO_3 films. *Chem Mater* 15:2786–2796
- Di Paola A, García-López E, Marci G, Palmisano L (2012) A survey of photocatalytic materials for environmental remediation. *J Hazard Mater* 211–212:3–29
- Doerfler W, Hauffe K (1964a) Heterogeneous photocatalysis. 1 The influence of oxidizing and reducing gases on the electrical conductivity of dark and illuminated zinc oxide surfaces. *J Catal* 3:156–170
- Doerfler W, Hauffe K (1964b) Heterogeneous photocatalysis. 2 The mechanism of the carbon monoxide oxidation at dark and illuminated zinc oxide surfaces. *J Catal* 3:171–178
- Domenech J, Andres M (1987) Elimination of $\text{Hg}(\text{II})$ ions from aqueous-solutions by photocatalytic reduction over ZnO powder. *New J Chem* 11:443–447
- Domenech J, Munoz J (1987) Photocatalytical reduction of $\text{Cr}(\text{VI})$ over ZnO powder. *Electrochim Acta* 32:1383–1386
- Domenech J, Peral J (1988) Removal of toxic cyanide from water by heterogeneous photocatalytic oxidation over ZnO . *Sol Energy* 41:55–59

- Domenech J, Prieto A (1986) Stability of ZnO particles in aqueous suspensions under IV illumination. *J Phys Chem* 90:1123–1126
- Driessen MD, Goodman AL, Miller TM, Zaharias GA, Grassian VH (1998) Gas-phase photooxidation of trichloroethylene on TiO₂ and ZnO: influence of trichloroethylene pressure, oxygen pressure, and the photocatalyst surface on the product distribution. *J Phys Chem B* 102:549–556
- Filimonov VN (1964) Photocatalytic oxidation of gaseous isopropanol on ZnO+TiO₂. *Dokl Akad Nauk SSSR* 154:922–923
- Fox MA, Dulay MT (1993) Heterogeneous photocatalysis. *Chem Rev* 93:341–357
- Fujita Y, Kwan T (1958) Photodesorption and photoadsorption of oxygen on zinc oxide. *Bull Chem Soc Jpn* 31:379–380
- Goux A, Pauporte T, Chivot J, Lincot D (2005) Temperature effects on ZnO electrodeposition. *Electrochim Acta* 50:2239–2248
- Gray TJ, Amigues P (1969) Photocatalysis and electronic structure of zinc oxide. *Surf Sci* 13:209–210
- Guo Y, Quan X, Lu N, Zhao H, Chen S (2007) High photocatalytic capability of self-assembled nanoporous WO₃ with preferential orientation of (002) planes. *Environ Sci Technol* 41:4422–4427
- Gupta J, Barick KC, Bahadur D (2011) Defect mediated photocatalytic activity in shape-controlled ZnO nanostructures. *J Alloy Compd* 509:6725–6730
- Hagfeldt A, Boschloo G, Sun L, Kloo L, Pettersson H (2010) Dye-sensitized solar cells. *Chem Rev* 110:6595–6663
- Hayat K, Gondal MA, Khaled MM, Ahmed S (2011) Effect of operational key parameters on photocatalytic degradation of phenol using nano nickel oxide synthesized by sol-gel method. *J Mol Catal A* 336:64–71
- Henglein A (1989) Small-particle research: physicochemical properties of extremely small colloidal metal and semiconductor particles. *Chem Rev* 89:1861–1873
- Hepel M, Hazelton S (2005) Photoelectrocatalytic degradation of diazo dyes on nanostructured WO₃ electrodes. *Electrochim Acta* 50:5278–5291
- Hepel M, Luo J (2001) Photoelectrochemical mineralization of textile diazo dye pollutants using nanocrystalline WO₃ electrodes. *Electrochim Acta* 47:729–740
- Hernández-Alonso MD, Hungría AB, Martínez-Arias A, Fernández-García M, Coronado JM, Conesa JC, Soria J (2004) EPR study of the photoassisted formation of radicals on CeO₂ nanoparticles employed for toluene photooxidation. *Appl Catal B* 50:167–175
- Hernández-Alonso MD, Fresno F, Suárez S, Coronado JM (2009) Development of alternative photocatalysts to TiO₂: challenges and opportunities. *Energy Environ Sci* 2:1231–1257
- Ho GW, Chua KJ, Siow DR (2012) Metal loaded WO₃ particles for comparative studies of photocatalysis and electrolysis solar hydrogen production. *Chem Eng J* 181:661–666
- Hodes G, Cahen D, Manassen J (1976) Tungsten trioxide as a photoanode for a photoelectrochemical cell (PEC). *Nature* 260:312–313
- Hoffman AJ, Carraway ER, Hoffmann MR (1994) Photocatalytic production of H₂O₂ and organic peroxides on quantum-sized semiconductor colloids. *Environ Sci Technol* 28:776–785
- Hoffmann MR, Martin ST, Choi W, Bahnemann DW (1995) Environmental applications of semiconductor photocatalysis. *Chem Rev* 95:69–96
- Hou Y, Wu L, Wang X, Ding Z, Li Z, Fu X (2007) Photocatalytic performance of α -, β -, and γ -Ga₂O₃ for the destruction of volatile aromatic pollutants in air. *J Catal* 250:12–18
- Howard CJ, Luca V, Knight KS (2002) High-temperature phase transitions in tungsten trioxide—the last word? *J Phys: Condens Matter* 14:377–387
- Hu X, Li G, Yu JC (2010) Design, fabrication, and modification of nanostructured semiconductor materials for environmental and energy applications. *Langmuir* 26:3031–3039
- Ivankovic S, Gotic M, Jurin M, Music S (2003) Photokilling squamous carcinoma cells SCCVII with ultrafine particles of selected metal oxides. *J Sol-Gel Sci Technol* 27:225–233
- Ji P, Zhang J, Chen F, Anpo M (2009) Study of adsorption and degradation of acid orange 7 on the surface of CeO₂ under visible light irradiation. *Appl Catal B* 85:148–154

- Jing LQ, Xu ZL, Shang J, Sun XJ, Cai WM, Guo HC (2002) The preparation and characterization of ZnO ultrafine particles. *Mater Sci Eng A, Struct Mater, Prop Microstruct Process* 332:356–361
- Jing LQ, Wang BQ, Xin BF, Li SD, Shi KY, Cai WM, Fu HG (2004) Investigations on the surface modification of ZnO nanoparticle photocatalyst by depositing Pd. *J Solid State Chem* 177:4221–4227
- Kansal SK, Ali AH, Kapoor S (2010) Photocatalytic decolorization of bieberich scarlet dye in aqueous phase using different nanophotocatalysts. *Desalination* 259:147–155
- Khalil LB, Mourad WE, Rophael MW (1998) Photocatalytic reduction of environmental pollutant Cr(VI) over some semiconductors under UV/visible light illumination. *Appl Catal B* 17:267–273
- Khodja AA, Sehili T, Pilichowski JF, Boule P (2001) Photocatalytic degradation of 2-phenylphenol on TiO₂ and ZnO in aqueous suspensions. *J Photochem and Photobiol A* 141:231–239
- Khyzhun OY, Solonin YM, Dobrovolsky VD (2001) Electronic structure of hexagonal tungsten trioxide: XPS, XES, and XAS studies 320:1–6
- Kim H, Senthil K, Yong K (2010) Photoelectrochemical and photocatalytic properties of tungsten oxide nanorods grown by thermal evaporation. *Mater Chem Phys* 120:452–455
- Kislov N, Lahiri J, Verma H, Goswami DY, Stefanakos E, Batzill M (2009) Photocatalytic degradation of methyl orange over single crystalline ZnO: orientation dependence of photoactivity and photostability of ZnO. *Langmuir* 25:3310–3315
- Kodama S, Yabuta M, Kubokawa Y (1982) Photocatalytic isomerization of butenes over TiO₂ and ZnO. *Chem Lett* 11:1671–1674
- Kodama S, Yabuta M, Anpo M, Kubokawa Y (1985) Photocatalytic isomerization of butenes over ZnO and SnO₂. *Bull Chem Soc Jpn* 58:2307–2310
- Kominami H, Yabutani K, Yamamoto T, Kara Y, Ohtani B (2001) Synthesis of highly active tungsten (VI) oxide photocatalysts for oxygen evolution by hydrothermal treatment of aqueous tungstic acid solutions. *J Mater Chem* 11:3222–3227
- Kominami H, Kato J, Murakami S, Ishii Y, Kohno M, Yabutani K, Yamamoto T, Kera Y, Inoue M, Inui T, Ohtani B (2003) Solvothermal syntheses of semiconductor photocatalysts of ultra-high activities. *Catal Today* 84:181–189
- Kormann C, Bahnemann DW, Hoffmann MR (1988) Photocatalytic production of H₂O₂ and organic peroxides in aqueous suspensions of TiO₂, ZnO, and desert sand. *Environ Sci Technol* 22:798–806
- Lacoste J, Arnaud R, Lemaire J (1982) Modelization of the photocatalyzed oxidation of polyolefins. 1. ZnO and TiO₂ photocatalyzed oxidation of normal-heptane. *CR Acad Sci, Ser IIc: Chim* 295:1087–1088
- Lacoste J, Arnaud R, Lemaire J (1984) Modelization of photocatalyzed oxidation of polyolefins. 2. ZnO and TiO₂ photocatalyzed decomposition of tert-butyl hydroperoxide and atactic polypropylene hydroperoxides. *J Polym Sci, Part A: Polym Chem* 22:3885–3893
- Lacoste J, Singh RP, Boussand J, Arnaud R (1987) TiO₂-photocatalyzed, ZnO-photocatalyzed, and CdS-photocatalyzed oxidation of ethylene-propylene thermoplastic elastomers. *J Polym Sci, Part A: Polym Chem* 25:2799–2812
- Lacoste J, Arnaud R, Singh RP, Lemaire J (1988) Modelization of photocatalyzed oxidation of polyolefins. 3. Oxidation of model hydrocarbons with ZnO. *Macromol Chem Phys* 189:651–661
- Lee GH, Kawazoe T, Ohtsu M (2002) Difference in optical band gap between zinc-blende and wurtzite ZnO structure formed on sapphire (0001) substrate. *Solid State Commun* 124:163–165
- Li BX, Wang YF (2010) Facile synthesis and enhanced photocatalytic performance of flower-like ZnO hierarchical microstructures. *J Phys Chem C* 114:890–896
- Li L, Krissanasaeeranee M, Pattinson SW, Stefik M, Wiesner U, Steiner U, Eder D (2010) Enhanced photocatalytic properties in well-ordered mesoporous WO₃. *Chem Commun* 46:7620–7622

- Lillard RS, Kanner GS, Butt DP (1998) The nature of oxide films on tungsten in acidic and alkaline solutions. *J Electrochem Soc* 145:2718–2725
- Lin HF, Liao SC, Hung SW (2005) The DC thermal plasma synthesis of ZnO nanoparticles for visible-light photocatalyst. *J Photochem Photobiol A* 174:82–87
- Liu HL, Yang TCK (2003) Photocatalytic inactivation of *Escherichia coli* and *Lactobacillus helveticus* by ZnO and TiO₂ activated with ultraviolet light. *Process Biochem* 39:475–481
- Liu J-X, Dong X-L, Liu X-W, Shi F, Yin S, Sato T (2011a) Solvothermal synthesis and characterization of tungsten oxides with controllable morphology and crystal phase. *J Alloys Compd* 509:1482–1488
- Liu R, Lin Y, Chou L-Y, Sheehan SW, He W, Zhang F, Hou HJM, Wang D (2011b) Water splitting by tungsten oxide prepared by atomic layer deposition and decorated with an oxygen-evolving catalyst. *Angew Chem Int Ed* 50:499–502
- Locherer KR, Swainson IP, Salje EKH (1999) Phase transitions in tungsten trioxide at high temperatures—a new look. *J Phys: Condens Matter* 11:6737–6756
- Long TF, Takabatake K, Yin S, Sato T (2009a) Mild solvothermal synthesis and characterization of ZnO crystals with various morphologies on borosilicate glass substrate. *J Cryst Growth* 311:576–579
- Long TF, Yin S, Takabatake K, Zhnag P, Sato T (2009b) Synthesis and characterization of ZnO nanorods and nanodisks from zinc chloride aqueous solution. *Nanoscale Res Lett* 4:247–253
- Ma PY, Wu Y, Fu ZY, Wang WM (2011) Shape-controlled synthesis and photocatalytic properties of three-dimensional and porous zinc oxide. *J Alloys Compd* 509:3576–3581
- Maeda K, Domen K (2010) Solid Solution of GaN and ZnO as a Stable Photocatalyst for Overall Water Splitting under Visible Light. *Chem Mater* 22:612–623
- Maldotti A, Andreotti L, Molinari A, Tollari S, Penoni A, CENINI S (2000) Photochemical and photocatalytic reduction of nitrobenzene in the presence of cyclohexene. *J Photochem Photobiol A* 133:129–133
- Minero C, Pelizzetti E, Piccinini P, Vincenti M (1994) Photocatalyzed transformation of nitrobenzene on TiO₂ and ZnO. *Chemosphere* 28:1229–1244
- Mitchnick MA, Fairhurst D, Pinnell SR (1999) Microfine zinc oxide (Z-Cote) as a photostable UVA/UVB sunblock agent. *J Am Acad Dermatol* 40:85–90
- Miyachi M, Nakajima A, Watanabe T, Hashimoto K (2002) Photocatalysis and photoinduced hydrophilicity of various metal oxide thin films. *Chem Mater* 14:2812–2816
- Morrison SR, Freund T (1967) Chemical role of holes and electrons in ZnO photocatalysis. *J Chem Phys* 47:1543–1551
- Muller HD, Steinbac F (1970) Decomposition of isopropyl alcohol photosensitized by zinc oxide. *Nature* 225:728–729
- Ozgur U, Alivov YI, Liu C, Teke A, Reshchikov MA, Dogan S, Avrutin V, Cho SJ, Morkoc H (2005) A comprehensive review of ZnO materials and devices. *J Appl Phys* 98:041301
- Pardeshi SK, Patil AB (2008) A simple route for photocatalytic degradation of phenol in aqueous zinc oxide suspension using solar energy. *Sol Energy* 82:700–705
- Pelizzetti E, Borgarello M, Minero C, Pramauro E, Borgarello E, Serpone N (1988) Photocatalytic degradation of polychlorinated dioxins and polychlorinated-biphenyls in aqueous suspensions of semiconductors irradiation with simulated solar light. *Chemosphere* 17:499–510
- Penot G, Arnaud R, Lemaire J (1983) ZnO-photocatalyzed oxidation of isotactic polypropylene. *Angew Makromol Chem* 117:71–84
- Peralta-Zamora P, Gomes de Moraes S, Reyes J, Durán N (1996) Heterogeneous photocatalysis treatment of Kraft and textile effluents using metallic and polymeric semiconductors (ZnO and polyaniline) *Polym Bull* 37:531–537
- Pichat P (1994) Partial or complete heterogeneous photocatalytic oxidation of organic-compounds in liquid organic or aqueous phases. *Catal Today* 19:313–333
- Pichat P, Herrmann JM, Disdier J, Mozzanega MN (1979) Photocatalytic oxidation of propene over various oxides at 320 K: Selectivity. *J Phys Chem* 83:3122–3126

- Prado AGS, Bolzon LB, Pedroso CP, Moura AO, Costa LL (2008) Nb₂O₅ as efficient and recyclable photocatalyst for indigo carmine degradation. *Appl Catal B* 82:219–224
- Qiu RL, Zhang DD, Mo YQ, Song L, Brewer E, Huang XF, Xiong Y (2008) Photocatalytic activity of polymer-modified ZnO under visible light irradiation. *J Hazard Mater* 156:80–85
- Rehman S, Ullah R, Butt AM, Gohar ND (2009) Strategies of making TiO₂ and ZnO visible light active. *J Hazard Mater* 170:560–569
- Roger A, Sallet D, Lacoste J, Lemaire J (1986) Photochemistry of aliphatic polyamides. 5. Oxidation of polydodecanamide (PA12) photocatalyzed by TiO₂ and ZnO. *Makromol Chem-Macromol Chem Phys* 187:1819–1832
- Sakthivel S, Neppolian B, Shankar MV, Arabindoo B, Palanichamy M, Murugesan V (2003) Solar photocatalytic degradation of azo dye: comparison of photocatalytic efficiency of ZnO and TiO₂. *Sol Energy Mater Sol Cells* 77:65–82
- Santato C, Ulmann M, Augustynski J (2001a) Photoelectrochemical properties of nanostructured tungsten trioxide films. *J Phys Chem B* 105:936–940
- Santato C, Ulmann M, Augustynski J (2001b) Enhanced visible light conversion efficiency using nanocrystalline WO₃ films. *Adv Mater* 13:511–512
- Sayama K, Yoshida R, Kusama H, Okabe K, Abe Y, Arakawa H (1997) Photocatalytic decomposition of water into H₂ and O₂ by a two-step photoexcitation reaction using a WO₃ suspension catalyst and an Fe³⁺/Fe²⁺ redox system. *Chem Phys Lett* 277:387–391
- Sayama K, Hayashi H, Arai T, Yanagida M, Gunji T, Sugihara H (2010a) Highly active WO₃ semiconductor photocatalyst prepared from amorphous peroxy-tungstic acid for the degradation of various organic compounds. *Appl Catal B* 94:150–157
- Sayama K, Hayashi H, Konishi Y, Gunji T, Sugihara H (2010b) Photocatalytic and antibacterial activities over WO₃ on glass filters. *Chem Lett* 39:884–885
- Scalafani A, Palmisano L, Schiavello M, Augugliaro V, Coluccia S, Marchese L (1988) The photodecomposition of ethanoic acid adsorbed over semiconductor and insulator oxides. 1. Pure oxides. *New J Chem* 12:129–135
- Scalafani A, Palmisano L, Marci G, Venezia AM (1998) Influence of platinum on catalytic activity of polycrystalline WO₃ employed for phenol photodegradation in aqueous suspension. *Sol Energy Mater Sol Cells* 51:203–219
- Seabold JA, Choi K-S (2011) Effect of a cobalt-based oxygen evolution catalyst on the stability and the selectivity of photo-oxidation reactions of a WO₃ photoanode. *Chem Mater* 23:1105–1112
- Steinbac F (1967) Photocatalysis by semiconductors on metal supports. Photosensitized oxidation of CO with Co₃O₄, NiO and ZnO on silver supports. *Angew Chem Int Ed* 6:999–1000
- Su J, Guo L, Bao N, Grimes CA (2011) Nanostructured WO₃/BiVO₄ heterojunction films for efficient photoelectrochemical water splitting. *Nano Lett* 11:1928–1933
- Tanaka K, Hisanaga T (1994) Photodegradation of chlorofluorocarbon alternatives on metal-oxide. *Sol Energy* 52:447–450
- Tang L, Sallet D, Lemaire J (1982) Photochemistry of polyundecanamides. 2. TiO₂-photocatalyzed and ZnO-photocatalyzed oxidation. *Macromolecules* 15:1437–1441
- Tatsuma T, Saitoh S, Ohko Y, Fujishima A (2001) TiO₂-WO₃ photoelectrochemical anticorrosion system with an energy storage ability. *Chem Mater* 13:2838–2842
- Tatsuma T, Saitoh S, Ngaotranakawit P, Ohko Y, Fujishima A (2002) Energy storage of TiO₂-WO₃ photocatalysis systems in the gas phase. *Langmuir* 18:7777–7779
- Tian L, Ye L, Liu J, Zan L (2012) Solvothermal synthesis of CNTs-WO₃ hybrid nanostructures with high photocatalytic activity under visible light. *Catal Commun* 17:99–103
- Wada K, Yoshida K, Takatani T, Watanabe Y (1993) Selective photooxidation of light alkanes using solid metal-oxide semiconductors. *Appl Catal A* 99:21–36
- Wang ZL (2009) Ten years' venturing in ZnO nanostructures: from discovery to scientific understanding and to technology applications. *Chin Sci Bull* 54:4021–4034
- Wang TM, Wang HY, Xu P, Zhao XC, Liu YL, Chao S (1998) The effect of properties of semiconductor oxide thin films on photocatalytic decomposition of dyeing waste water. *Thin Solid Films* 334:103–108

- Wang HL, Lindgren T, He JJ, Hagfeldt A, Lindquist SE (2000) Photoelectrochemistry of nanostructured WO_3 thin film electrodes for water oxidation: Mechanism of electron transport. *J Phys Chem B* 104:5686–5696
- Wang HY, Xu P, Wang TM (2002) The preparation and properties study of photocatalytic nanocrystalline/nanoporous WO_3 thin films. *Mater Des* 23:331–336
- Wang S, Shi X, Shao G, Duan X, Yang H, Wang T (2008) Preparation, characterization and photocatalytic activity of multi-walled carbon nanotube-supported tungsten trioxide composites. *J Phys Chem Solids* 69:2396–2400
- Wang XJ, Zhang QL, Wan QA, Dai GZ, Zhou CJ, Zou BS (2011) Controllable ZnO Architectures by Ethanolamine-Assisted Hydrothermal Reaction for Enhanced Photocatalytic Activity. *J Phys Chem C* 115:2769–2775
- Wang G, Ling Y, Wang H, Yang X, Wang C, Zhang JZ, Li Y (2012) Hydrogen-treated WO_3 nanoflakes show enhanced photostability. *Energy Environ Sci* 5:6180–6187
- Watcharenwong A, Chanmanee W, de Tacconi NR, Chenthamarakshan CR, Kajitvichyanukul P, Rajeshwar K (2008) Anodic growth of nanoporous WO_3 films: Morphology, photoelectrochemical response and photocatalytic activity for methylene blue and hexavalent chrome conversion. *J Electroanal Chem* 612:112–120
- Weinhardt L, Blum M, Baer M, Heske C, Cole B, Marsen B, Miller EL (2008) Electronic surface level positions of WO_3 thin films for photoelectrochemical hydrogen production. *J Phys Chem C* 112:3078–3082
- Woodward PM, Sleight AW, Vogt T (1995) Structure refinement of triclinic tungsten trioxide. *J Phys Chem Solids* 56:1305–1315
- Xu Y, Schoonen MAA (2000) The absolute energy positions of conduction and valence bands of selected semiconducting minerals. *Am Mineral* 85:543–556
- Xu F, Zhang P, Navrotsky A, Yuan ZY, Ren TZ, Halasa M, Su BL (2007) Hierarchically assembled porous ZnO nanoparticles: Synthesis, surface energy, and photocatalytic activity. *Chem Mater* 19:5680–5686
- Yang F, Takahashi Y, Sakai N, Tatsuma T (2011) Visible light driven photocatalysts with oxidative energy storage abilities. *J Mater Chem* 21:2288–2293
- Yoshida H, Murata C, Hattori T (1999) Photooxidation of propene to propene oxide by molecular oxygen over zinc oxide dispersed on silica. *Chem Lett* 9:901–902
- Yoshida H, Murata C, Hattori T (2000) Screening study of silica-supported catalysts for photoepoxidation of propene by molecular oxygen. *J Catal* 194:364–372
- Yu J, Qi L (2009) Template-free fabrication of hierarchically flower-like tungsten trioxide assemblies with enhanced visible-light-driven photocatalytic activity. *J Hazard Mater* 169:221–227
- Zhang LS, Wang WZ, Yang JO, Chen ZG, Zhang WQ, Zhou L, Liu SW (2006) Sonochemical synthesis of nanocrystallite Bi_2O_3 as a visible-light-driven photocatalyst. *Appl Catal A* 308:105–110
- Zhang H, Zong RL, Zhu YF (2009a) Photocorrosion inhibition and photoactivity enhancement for zinc oxide via hybridization with monolayer polyaniline. *J Phys Chem C* 113:4605–4611
- Zhang LW, Cheng HY, Zong RL, Zhu YF (2009b) Photocorrosion suppression of ZnO nanoparticles via hybridization with graphite-like carbon and enhanced photocatalytic activity. *J Phys Chem C* 113:2368–2374
- Zhang X, Lu X, Shen Y, Han J, Yuan L, Gong L, Xu Z, Bai X, Wei M, Tong Y, Gao Y, Chen J, Zhou J, Wang ZL (2011) Three-dimensional WO_3 nanostructures on carbon paper: photoelectrochemical property and visible light driven photocatalysis. *Chem Commun* 47:5804–5806
- Zhao Z-G, Miyauchi M (2008) Nanoporous-walled tungsten oxide nanotubes as highly active visible-light-driven photocatalysts. *Angew Chem Int Ed* 47:7051–7055
- Zheng H, Ou JZ, Strano MS, Kaner RB, Mitchell A, Kalantar-zadeh K (2011) Nanostructured tungsten oxide—properties, synthesis, and applications. *Adv Func Mater* 21:2175–2196

Chapter 7

The New Promising Semiconductors: Metallates and Other Mixed Compounds

Fernando Fresno

7.1 UV and Visible Light Absorbing Metallates

A general classification of the elements composing photocatalysts based on their contribution to the characteristics of the material was made by Kudo and Miseki (2009): (1) elements which contribute to the formation of both the crystal and the electronic structures; (2) those contributing only to the crystal structure; (3) elements used as dopants; and (4) those that can be employed as co-catalysts for certain applications (Fig. 7.1). Simple oxides frequently used as photocatalysts, such as TiO_2 , ZnO and others, described in Chaps. 5 and 6, contain d^0 and d^{10} cations (e.g. Ti^{4+} and Zn^{2+} , respectively), and their valence and conduction bands are essentially formed by oxygen 2p and metal d or sp orbitals, respectively. These electronic structures lead to band gaps matching in most cases the UV region, which inherently limits the use of solar light as excitation source for photocatalytic processes.

Many strategies have been followed in order to obtain novel visible light–active photocatalysts by chemical modification of the classical ones, and many of which are reviewed in this book (doping in Chaps. 13 and 14, sensitisation in Chaps. 15 and 16). Another approach that immediately arises is to explore new materials that absorb in the visible region and present adequate photocatalytic activities. Visible light absorption should be higher in these materials than in doped semiconductors, due to the inherently low density of the states that induce the absorption of the latter in this range.

Binary oxides of transition metals with d^n configuration absorb visible light, for example, Fe_2O_3 ($E_g \sim 2.0$ eV) and Co_3O_4 ($E_g \sim 1.3$ eV). However, photogenerated charge transport is limited because of the small polaron-dominated conductivity. Oxides of post-transition metals with occupied s states also present low band gap energies, for example, PbO (2.1 eV), SnO (2.4 eV) and Bi_2O_3 (2.5 eV), the main problem arising from unfavourable indirect band gaps. Therefore, to overcome

F. Fresno (✉)

Laboratory for Environmental Research, University of Nova Gorica, Nova Gorica, Slovenia
e-mail: fernando.fresno@ung.si






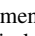





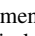





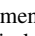
1	2	3	4	5	6	7	8	9	10	11	12	13	14	15	16	17	18																						
H																	He																						
Li	Be											B	C	N	O	F	Ne																						
Na	Mg											Al	Si	P	S	Cl	Ar																						
K	Ca	Sc	Ti	V	Cr	Mn	Fe	Co	Ni	Cu	Zn	Ga	Ge	As	Se	Br	Kr																						
Rb	Sr	Y	Zr	Nb	Mo	Tc	Ru	Rh	Pd	Ag	Cd	In	Sn	Sb	Te	I	Xe																						
Cs	Ba	La	Hf	Ta	W	Re	Os	Ir	Pt	Au	Hg	Tl	Pb	Bi	Po	At	Rn																						
<table border="1"> <tr><td>Ce</td><td>Pr</td><td>Nd</td><td>Pm</td><td>Sm</td><td>Eu</td><td>Gd</td><td>Tb</td><td>Dy</td><td>Ho</td><td>Er</td><td>Tm</td><td>Yb</td><td>Lu</td></tr> </table>																		Ce	Pr	Nd	Pm	Sm	Eu	Gd	Tb	Dy	Ho	Er	Tm	Yb	Lu								
Ce	Pr	Nd	Pm	Sm	Eu	Gd	Tb	Dy	Ho	Er	Tm	Yb	Lu																										
<table border="0"> <tr><td>i)</td><td></td><td>: d⁰ ion</td><td rowspan="3">} to construct crystal structure and energy structure</td></tr> <tr><td></td><td></td><td>: d¹⁰ ion</td></tr> <tr><td></td><td></td><td>: Non-metal</td></tr> <tr><td>ii)</td><td></td><td></td><td>to construct crystal structure but not energy structure</td></tr> <tr><td>iii)</td><td></td><td></td><td>to form impurity levels as dopants</td></tr> <tr><td>iv)</td><td></td><td></td><td>to be used for cocatalysts</td></tr> </table>																		i)		: d ⁰ ion	} to construct crystal structure and energy structure			: d ¹⁰ ion			: Non-metal	ii)			to construct crystal structure but not energy structure	iii)			to form impurity levels as dopants	iv)			to be used for cocatalysts
i)		: d ⁰ ion	} to construct crystal structure and energy structure																																				
		: d ¹⁰ ion																																					
		: Non-metal																																					
ii)			to construct crystal structure but not energy structure																																				
iii)			to form impurity levels as dopants																																				
iv)			to be used for cocatalysts																																				

Fig. 7.1 Elements constructing heterogeneous photocatalysts. Reproduced with permission from Kudo and Miseki (2009). Copyright Royal Society of Chemistry

the intrinsic limitations of binary metal oxides for visible light photocatalytic applications with pristine (non-doped) materials, it is becoming increasingly clear that it is necessary to combine multiple cations (Walsh et al. 2009).

If one looks at the positions of the valence and conduction bands in typical oxide semiconductors (see Chap. 2), it appears that the energy of the conduction band minimum is a little higher (the reduction potential is a little more negative) than those required for both pollutant degradation and water splitting, while the top of the valence band is generally well below in energy (more positive reduction potential) the required positions for the oxidation processes. Therefore, in order to obtain a narrower band gap while maintaining favourable chemical potentials of the photogenerated charge carriers, it is thermodynamically more convenient to increase the valence band energy rather than to decrease that of the conduction band. The formation of mixed oxides (metallates) with those cations classified above as group (1), such as alkali and alkaline earth metals or some lanthanides, generally results in a material with a band gap similar to that of the parent oxide (e.g. TiO_2 vs. SrTiO_3 or Ta_2O_5 vs. KTaO_3), also lying in the UV region. On the other hand, cations with filled or partially filled orbitals in their outer shell, such as 6s in Pb^{2+} and Bi^{3+} , 5s in Sn^{2+} or 4d in Ag^+ , may form valence bands above the level of O 2p orbitals by hybridisation with them, giving rise to narrower band gaps. This kind of visible light-active metallates is receiving much attention nowadays, especially for the water splitting reaction but also for environmental applications. Regarding the latter, many tests are currently carried out under visible light using dyes as probe molecules (Herrmann 2010). It is worth mentioning here that, when working under visible light, and depending on the employed dye and the irradiation wavelength, a photosensitised (see Chap. 16) rather than a

photocatalytic process may be occurring, as demonstrated by Fu and co-workers in their work with Bi_2WO_6 (Fu et al. 2005). Therefore, it is generally advisable to use non-visible light-absorbing target molecules to evaluate photocatalysts under visible light irradiation in order to ensure that a photocatalytic reaction is taking place. Considering only water splitting studies, more than 110 (and growing) different structures have been tested up to now (Kudo and Miseki 2009; Osterloh 2008). In this chapter, specific examples of both UV- and visible light-absorbing metallates and their photocatalytic activities for different reactions will be described, not trying to be exhaustive though, but remarking only the most relevant photocatalysts to the best of the authors' knowledge. At the end of the chapter, a mention to a new type of photocatalysts, bismuth oxyhalides, that is currently attracting a good deal of attention, is included.

7.2 Titanates

Among the large number of titanium-based metallates that have been explored as photocatalysts, SrTiO_3 was the first one in time and is probably the most widely known and studied. Actually, it is considered as one of the "classical" photocatalysts. SrTiO_3 crystallises in the simple perovskite structure (space group $\text{Pm}\bar{3}\text{m}$), with the cubic unit cell formed by a titanium atom in the centre of the cube and oxygen and strontium in the centre of the faces and in the vertices, respectively, with $Z = 1$. It has an indirect band gap of 3.25 eV, as determined experimentally by spectroscopic ellipsometry, and therefore, it is a UV-active photocatalyst. Similarly to what is found in TiO_2 , the top of the valence band is formed by O 2p orbitals, while Ti 3d orbitals give the main contribution to the bottom of the conduction band. Sr 5s orbitals contribute to the conduction band at much higher energies. Theoretical calculations reveal Mulliken net charges for Ti and O quite different from the formal ionic charges B^{4+} and O^{2-} in ABO_3 perovskites, illustrating the marked covalent character of the Ti–O bonds. In contrast, there is practically no bonding of O with Sr, which charge remains close to the formal +2 (Piskunov et al. 2004). It has been reported that the surface of SrTiO_3 is composed of titanium and oxygen, with no Sr^{2+} ions exposed (Miyachi et al. 2000).

Strontium titanate has been historically explored as a photocatalyst mostly for the water decomposition reaction, with or without sacrificial reagents. Soon after the publication of the celebrated paper by Fujishima and Honda (1972), the activity of SrTiO_3 was first reported by Wrighton et al. who showed that a $\text{SrTiO}_3/\text{Pt}/\text{H}_2\text{O}$ photoelectrolytic cell worked with no bias and with a 25 % efficiency with respect to UV photons (Wrighton et al. 1976), unlike Fujishima's rutile-based photoelectrochemical cell, which required an electrical or chemical bias. The reason for this success is that in SrTiO_3 , unlike rutile (but similarly to anatase), the positions of the valence and conduction bands exceed the necessary potentials for oxygen and hydrogen evolution, respectively. Indeed, SrTiO_3 splits water vapour stoichiometrically under UV irradiation when loaded with NiO as co-catalyst, with

no detection of the reverse reaction that occurs with Pt (Domen et al. 1980). This catalytic system is usually pre-treated in hydrogen then in oxygen to form a NiO/Ni double layer that is invoked to be convenient for electron migration from the photocatalyst to the co-catalyst (Kudo and Miseki 2009). The efficiency of other co-catalysts that have been explored for stoichiometric splitting of pure liquid water follows the order $\text{Rh} > \text{Ru} > \text{Re} > \text{Pt} > \text{Ir} > \text{Pd} > \text{Os} > \text{Co}$ (Osterloh 2008). In the liquid phase, the activity of NiO/SrTiO₃ for water splitting can be considerably increased if the reaction is performed using a concentrated NaOH solution. Some dopants have also been reported to increase the activity of strontium titanate, being the effect of La, Ga and Na remarkable (Chen et al. 2010), or to extend its light absorption into the visible range, being worth mentioning the results attained with chromium and antimony co-doping, with Pt as co-catalyst, for sacrificial H₂ evolution under visible light. Structural and electronic characterisation of the co-doped photocatalyst reveals, as depicted in Fig. 7.2, that Cr doping creates a discrete level in the band gap that under visible irradiation is able to oxidise sacrificial molecules, but not water (Kato and Kudo 2002). As a consequence, this system is not able to evolve O₂, and therefore, it cannot be used to produce H₂ without a sacrificial reagent. However, it can be used to split water under visible light in a Z-scheme system (see Chap. 4), as it has been demonstrated with the similar Cr–Ta co-doped SrTiO₃ using Pt/WO₃ and Pt/(Cr–Ta)SrTiO₃ as oxidation and reduction photocatalysts, respectively, and I[−]/IO₃[−] as a redox mediator couple (Sayama et al. 2001). The role of the co-dopant in these materials is to keep the charge balance.

The activity of SrTiO₃ for water splitting is rather low if compared to other more recently tested titanates, especially those with a structure formed by “titania” layers and different interlayers. Layered titanates belonging to different composition series have been studied for the water decomposition reaction, obtaining good results under UV radiation with NiO as co-catalyst (Osterloh 2008). La₂Ti₂O₇ is a $m = 4$ member of the (110) layered perovskite series A_mB_mX_{3m+2}. It is formed by four TiO₆-unit-thick slabs separated by layers of La³⁺ ions and shows a band gap of 3.8 eV. Under UV irradiation, the material splits water stoichiometrically with a quantum efficiency of 12 %. This value can be increased up to 50 % by doping with BaO and using a NaOH solution instead of pure water. In the same series with $m = 5$, La₄CaTi₅O₁₇, with the same band gap, reaches a 20 % quantum efficiency. The Dion–Jacobson (100) layered perovskite La₂Ti₃O₉ splits water at significantly lower rates. Sr₃Ti₂O₇ is a (110) layered perovskite in the Ruddlesden–Popper series also absorbing in the UV region ($E_g = 3.2$ eV). On its own, it is only able to reduce water to form H₂, but when loaded with NiO, it splits H₂O stoichiometrically.

Another class of titanate structure studied for water splitting is constituted of TiO₆ units forming tunnels occupied by alkali or alkaline earth cations. In the barium titanate series BaTi₄O₉, Ba₄Ti₁₃O₃₀, Ba₂Ti₉O₂₀, Ba₆Ti₁₇O₄₀, only the first one is able to produce H₂ and O₂ from water under UV, after modification with RuO₂. With the same co-catalyst, all the alkaline titanates M₂Ti₆O₁₃, with M: Na, K, Rb, are able to stoichiometrically split water under UV irradiation, with the

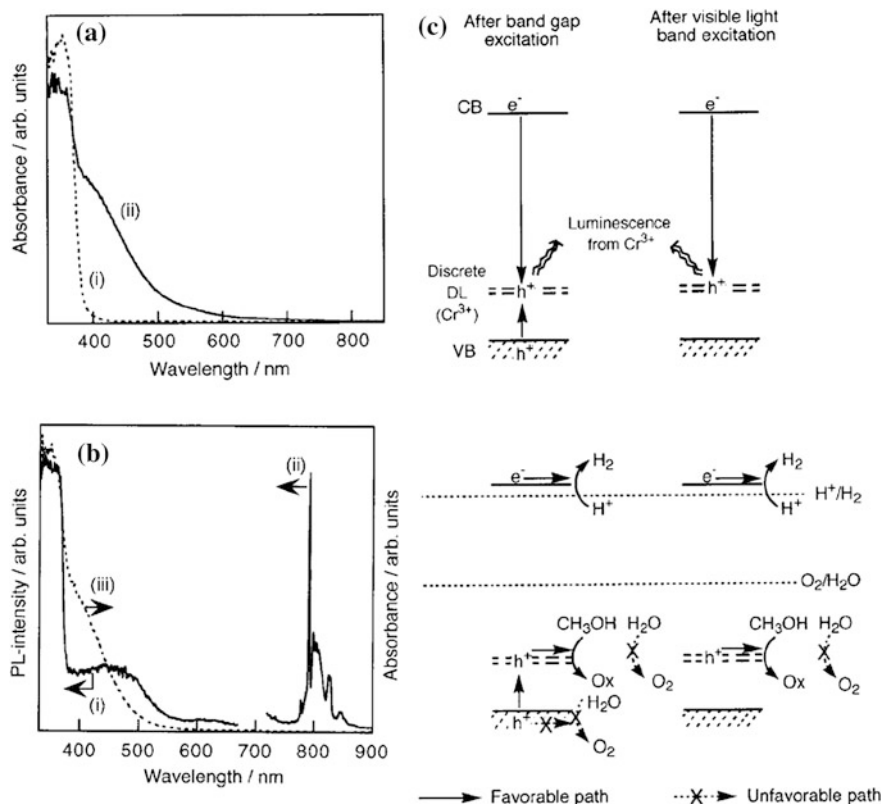


Fig. 7.2 **a** Diffuse reflectance UV-vis spectra of (i) undoped SrTiO₃ and (ii) SrTiO₃ co-doped with Sb(2.5 %)/Cr(2 %). **b** Photoluminescence spectra of SrTiO₃:Sb(5 %)/Cr(2 %): (i) excitation spectrum monitored at 790 nm and (ii) emission spectrum excited at 350 nm at 77 K, and (iii) diffuse reflectance spectrum at 300 K. **c** Schemes of photoluminescence and photocatalytic reactions on SrTiO₃:Sb/Cr. Reproduced with permission from Kato and Kudo (2002). Copyright American Chemical Society

activity increasing with decreasing cation sizes. The photocatalytic activity of this type of structures is believed to be related to the distortion of the TiO₆ octahedra, which causes dipole moments that help charge separation (Inoue 2009). Indeed, the trend in activity correlates with the calculated magnitude of the dipole moment. This theory will be described more in detail in Sect. 7.2.

Attempts to shift the absorption spectrum of these structures into the visible region have been carried out using different strategies (Osterloh 2008). Doping Cr or Fe into La₂Ti₂O₇ does not increase its H₂ production activity under UV irradiation, but allows H₂ evolution from aqueous methanol under visible light. As introduced in the previous section about the construction of photocatalyst materials, substitution of Pb²⁺ for the alkaline earth cations produces a red shift in the band gap, from 3.2 eV in SrTiO₃ or Sr₃Ti₂O₇ to 2.98 eV in PbTiO₃ and from 3.36 eV

$\text{CaBi}_4\text{Ti}_4\text{O}_{15}$ to 3.02 in $\text{PbBi}_4\text{Ti}_4\text{O}_{15}$. However, still wide band gaps, narrowly matching the visible region, are obtained, and thus small activities are found under visible light irradiation. In another approach, sulphur doping of $\text{Sm}_2\text{Ti}_2\text{O}_7$ produces $\text{Sm}_2\text{Ti}_2\text{S}_2\text{O}_5$, which belongs to the Ruddlesden–Popper layered perovskites and has a band gap of 2.0 eV. Under visible light, the sulphur-containing material, loaded with Pt or IrO_2 , is able to produce H_2 or O_2 , respectively, using sacrificial reagents, but not to split pure water.

The application of titanates to other photocatalytic reactions than water splitting is scarcer, but not negligible. The activity of SrTiO_3 for the photocatalytic degradation of organic compounds is similar to that of TiO_2 , as it could be expected from their similar electronic structures and quantum efficiencies for water splitting. As illustrative examples, nanocrystalline SrTiO_3 powders decompose phenol in water in the presence of strong oxidising agents (H_2O_2 or NaOCl) at similar or higher rates than TiO_2 P25, depending on their characteristics (Ahuja 1996). The higher the annealing temperature, the higher the oxidation rate is, which may be related to a lower concentration of defects acting as trapping centres, in spite of a lower surface area. Similarly, SrTiO_3 thin films degrade adsorbed methylene blue under UV irradiation in air at a slightly higher rate than anatase TiO_2 films (Miyachi et al. 2000). However, photoinduced superhydrophilicity and XPS measurements reveal different surface reactivities in TiO_2 and SrTiO_3 (Miyachi et al. 2000). Together with electron paramagnetic resonance (EPR) experiments carried out after the usage of SrTiO_3 samples, the results suggest different reaction mechanisms governing photocatalytic oxidation (PCO) reactions in these closely related oxides (Ahuja 1996). Despite the mentioned similar activities, SrTiO_3 apparently represents no efficient alternative to TiO_2 for environmental applications, considering that it is more expensive and shows the same main disadvantage than titania, namely being a UV-absorbing semiconductor. In this respect, attempts to displace the absorbance of this titanate towards the visible region aimed at pollutant degradation can be added to those already mentioned for the water splitting process. Thus, anion-doped SrTiO_3 has been tested for the oxidation of organic and inorganic pollutants under visible light. Introduction of fluorine or nitrogen in SrTiO_3 results in a red shift of the absorption spectrum, although it is not clear if the visible light absorption is due to an actual change in the valence band energy or it is related to the presence of discrete states or defects. Indeed, the wide absorption tails observed in some cases suggest the effect of this kind of phenomena. Nevertheless, both F- and N-doped samples have shown a higher photocatalytic activity than pristine SrTiO_3 for NO oxidation (Wang et al. 2003, 2004). Sulphur–carbon co-doping has also led to a red shift in both the absorption spectrum and the photocatalytic response of SrTiO_3 , as tested for the isopropanol-to-acetone oxidation reaction (Ohno et al. 2005).

Due to its higher conduction band-edge position with respect to the redox potential of $\text{H}_2\text{CO}_3/\text{CH}_3\text{OH}$, strontium titanate can effectively reduce carbon dioxide dissolved in an aqueous electrolyte (see Chap. 4). Indeed, the illumination by sunlight of SrTiO_3 powder, suspended in an aqueous solution through which CO_2 is bubbled, produces formic acid, formaldehyde and methanol (Roy et al.

2010). Other reduction reactions have been reported as well, such as the formation of NH_3 from N_2 and water with the concomitant production of oxygen, although with a very low yield, and the reduction of nitrate ions using water as electron donor (Kudo and Miseki 2009; Hernández-Alonso et al. 2009).

Little has been reported for pollutant degradation reactions with other titanates than SrTiO_3 . In this respect, bismuth titanates can be regarded as the most illustrative example. The layered perovskite $\text{Bi}_4\text{Ti}_3\text{O}_{12}$, with a structure formed by alternating triple layers of TiO_6 octahedra and single Bi_2O_2 layers stacked along the c axis, can photocatalyse the oxidation of methyl orange under UV irradiation (Yao et al. 2003), although a high catalyst concentration (6.5 g/L) is needed to attain the maximum degradation rate. In any case, its activity is rather low if compared to that of TiO_2 . The photocatalytic activity of the sillenite-type $\text{Bi}_{12}\text{TiO}_{20}$ for the same reaction can be increased by obtaining single-crystalline one-dimensional structures in hydrothermal conditions similar to those employed to prepare titania nanotubes (see Chap. 11), which lead to a remarkably higher methyl orange degradation rate than the bulk material (Hou et al. 2009). Regarding visible light-active materials, a mesoporous bismuth titanate with unclear phase composition, but mainly formed by the metastable phase $\text{Bi}_{20}\text{TiO}_{32}$, has been observed to absorb visible light up to ca. 600 nm (Kong et al. 2008). However, its activity under visible irradiation is not well assessed, although it appears to slightly degrade 2,4-dichlorophenol in water.

7.3 Layered Niobates

Although Nb_2O_5 itself ($E_g = 3.4$ eV) was shown some time ago to be inactive for photocatalytic water splitting under UV irradiation, some modifications of it have been reported to possess improved photocatalytic properties. Thus, when loaded with a Pt photocatalyst, it can efficiently produce hydrogen from aqueous solutions with methanol as electron donor. In turn, if synthesised with a mesoporous structure, its activity for the same reaction can be increased by a factor of 20 (Chen et al. 2010). For PCO applications, although it is somewhat active, its activity is considerably lower than those of TiO_2 or ZnO (Prado et al. 2008). When highly dispersed on a silica support, it can be a selective photocatalyst for propylene oxide production, as already mentioned in Chap. 3. In general, the higher the dispersion of niobium oxide, the higher the selectivity to propylene oxide, since this product is considered to form preferentially on isolated NbO_4 tetrahedra rather than on oligomeric NbO_x clusters. Indeed, lowly dispersed $\text{Nb}_2\text{O}_5/\text{SiO}_2$ leads mostly to carbonyl products in propylene oxidation (Tanaka et al. 1993). More information about single-site photocatalysts will be given in Chap. 9. In addition, bulk Nb_2O_5 has been proposed as a photocatalyst for partial and selective oxidation of organic molecules like alcohols and amines, although, according to the proposed mechanism, the process appears to be a photosensitised reaction, in which the substrate absorbs a photon and transfers an electron to the solid, rather

than a photocatalytic reaction (Furukawa et al. 2011). Indeed, the reaction takes place even under visible light, in spite of the absence of absorption in this spectral region by Nb_2O_5 .

A number of niobates show photocatalytic activity, especially for the water splitting reaction, for which some of them are among the best catalysts to date. Many of these niobates possess layered structures analogous to those described in the previous section about titanates, and most of them are white coloured as a consequence of absorbing only in the UV part of the spectrum. The first niobate to be reported as an active material for photocatalytic water splitting was $\text{K}_4\text{Nb}_6\text{O}_{17}$, by Domen's group (Domen et al. 1986). This layered structure is composed of Nb_6O_{17} sheets formed by edge- and corner-sharing NbO_6 octahedra. The sheets are held together by two different kinds of alternating interlayer spaces, where K^+ ions are located. The first interlayer space has a capacity to take up water molecules, but the second layer is not hydrated under ambient conditions. Its band gap is 3.3 eV. Without any co-catalyst, $\text{K}_4\text{Nb}_6\text{O}_{17}$ gives rise to a stable H_2 evolution from methanol aqueous solutions under UV irradiation at a low rate. The exchange of interlayer potassium ions with H^+ , Cr^{3+} or Fe^{3+} enhances the photocatalytic activity, with particularly good results in the case of the H^+ -exchanged catalyst, which achieves 50 % quantum efficiency at 330 nm (Chen et al. 2010). In distilled water, $\text{K}_4\text{Nb}_6\text{O}_{17}$ itself exhibits activity for simultaneous generation of H_2 and O_2 , although the amount of evolved O_2 is ca. 20 % of the stoichiometric ratio. With the addition of NiO_x as co-catalyst, stoichiometric H_2 and O_2 amounts are obtained. When an alkaline hydroxide is added to the $\text{Ni}(\text{NO}_3)_2$ solution used for impregnation, and the product is subsequently reduced and calcined, larger NiO clusters are formed and the overall water splitting yield is enhanced, with a quantum efficiency of 5.3 % at 330 nm. In this catalytic system, it has been suggested that H_2 evolution occurs in one of the mentioned interlayers, while O_2 evolution proceeds in the other one, as concluded from XRD, XPS, TEM and EXAFS data. Thus, in $\text{NiO}_x/\text{K}_4\text{Nb}_6\text{O}_{17}$, H_2 and O_2 evolution sites would be separated by the photoactive niobate sheet, as depicted in Fig. 7.3 (Kudo and Miseki 2009).

With the same layered structure as $\text{K}_4\text{Nb}_6\text{O}_{17}$ and equal band gap, $\text{Rb}_4\text{Nb}_6\text{O}_{17}$ also shows a high activity for pure water splitting when loaded with NiO as co-catalyst, although the evolution rates are less stable over time. At the initial stage

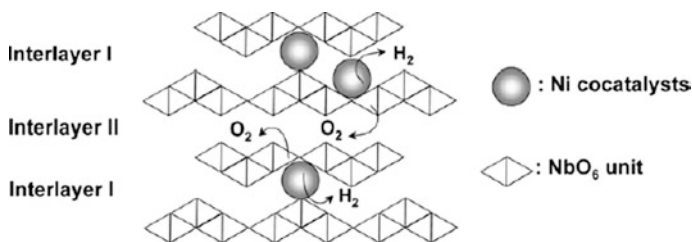


Fig. 7.3 Schematic structure of the $\text{NiO}_x(0.1\text{wt } \%)$ - $\text{K}_4\text{Nb}_6\text{O}_{17}$ photocatalyst and the reaction mechanism of H_2O decomposition into H_2 and O_2 . Reproduced with permission from Kudo et al. (1988). Copyright Elsevier

of the reaction, it gives a quantum efficiency of 10 % at 330 nm, (Chen et al. 2010). Since water splitting is found to occur in the interlayer, the higher activity of the rubidium than the potassium compound is attributed to the larger interlayer spaces in the former, considering the higher radius of Rb^+ . On the other hand, since the oxidation of the ultrafine nickel particles formed in the reduction stage after impregnation is invoked to explain the gradual loss of activity, the larger interlayer may also lead to the faster observed deactivation. Some other alkaline metal niobates, such as ANbO_3 (A: Li, Na, K) and $\text{Cs}_2\text{Nb}_4\text{O}_{11}$, also catalyse overall water decomposition under UV irradiation after the addition of Pt, RuO_2 or NiO as co-catalysts (Chen et al. 2010).

Alkaline earth niobates with Ca, Sr and Ba have also been studied for the water splitting reaction. Among them, several strontium derivatives, like SrNb_2O_6 , $\text{Sr}_2\text{Nb}_2\text{O}_7$ and $\text{Sr}_5\text{Nb}_4\text{O}_{15}$, have been reported to possess activity for pure water decomposition (Chen et al. 2010), being $\text{Sr}_2\text{Nb}_2\text{O}_7$ ($E_g = 3.9$ eV) particularly interesting. It belongs to the Ruddlesen–Popper layered perovskite series and, with NiO as co-catalyst, gives a quantum efficiency of 23 % at 300 nm in the overall water splitting reaction, while only H_2 is produced in the absence of co-catalyst. This efficiency has been increased up to 32 % using a hydrothermal synthetic method that results in one-dimensional nanostructures with high surface area (see Chap. 11). In turn, $\text{Ca}_2\text{Nb}_2\text{O}_7$ ($E_g = 4.3$ eV) gives a photonic efficiency of 7 % at $\lambda < 288$ nm after NiO loading.

Some mixed metal niobates in the Dion–Jacobson layered perovskite series, with general formula $\text{AB}_{n-1}\text{Nb}_n\text{O}_{3n+1}$ (A: K, Rb, Cs; B: Ca, Sr, Na, Pb; n: 2–4) have shown a remarkable activity for H_2 production using methanol as a sacrificial molecule (Hernández-Alonso et al. 2009). These materials comprise perovskite layers of NbO_6 corner-sharing octahedra, with B cations placed in the centre of the cube delimited by 8 of these niobium polyhedra. Cations A are sandwiched between these slabs to compensate the charge and are rather mobile. Indeed, interchange of the alkaline cations in the A positions by protons has been used to boost H_2 generation under UV irradiation. For instance, $\text{HCA}_2\text{Nb}_3\text{O}_{10}$ modified with Pt produces as much as $19 \text{ mmol h}^{-1} \text{ g}^{-1}$ (which is more than 40 times larger than the rate obtained with Pt/TiO_2), while the alkaline derivatives give only small amounts of H_2 . Enhancement of photoactivity upon protonation of these layered perovskites has been related to the widening of the interlayer gap, which favours the interaction with methanol. Longer-chain alcohols like ethanol and propanol, however, cannot enter this space, and consequently, hydrogen production diminishes. Further enlargement of the space between slabs of $\text{Pt/HCA}_2\text{Nb}_3\text{O}_{10}$ can be achieved using SiO_2 pillars, and accordingly, a remarkable increment in the H_2 production rate can be obtained, even with larger alcohol molecules than methanol. On the other hand, the photoactivity of $\text{KCA}_2\text{Nb}_3\text{O}_{10}$ can be significantly improved (up to 10 times) if the surface area is increased by alternating acid and alkaline treatments, which results in a restacking of perovskite sheets. In these catalysts, the co-catalyst can be intercalated in the interlayer spaces, which enhances the activity with respect to the system with a surface-loaded co-catalyst (Osterloh 2008). Other niobates able to produce H_2 and/or O_2 from water under

UV light include Zn and Bi derivatives. For example, NiO-loaded ZnNb_2O_6 , with the columbite layered structure and a 4.0 eV band gap, produces both gases from pure water, although with lower rates than other previously mentioned layered niobates. The niobates MBi_2NbO_7 (M: Al, Ga, In), with pyrochlore structure, produce H_2 or O_2 in the presence of sacrificial molecules. In contrast, the isostructural M_2BiNbO_7 (M: Ga, In) are able to stoichiometrically split pure water under UV irradiation. The layered perovskites $\text{MBi}_2\text{Nb}_2\text{O}_9$ (M: Ca, Sr, Ba) yield hydrogen or oxygen from sacrificial solutions at rates depending on the M cation, in the order $\text{Sr} > \text{Ba} > \text{Ca}$ (Chen et al. 2010).

Regarding water splitting under visible light, much fewer niobate photocatalysts with considerable activity have been reported. Connecting with the already mentioned materials, doping of the Dion–Jacobson layered perovskite $\text{K}_{0.5}\text{La}_{0.5}\text{Ca}_{1.5}\text{Nb}_3\text{O}_{10}$ ($E_g = 3.44$ eV) with $\text{PbO}/\text{Bi}_2\text{O}_3$ forms the phase $\text{K}_{0.5}\text{La}_{0.25}\text{Bi}_{0.25}\text{Ca}_{0.75}\text{Pb}_{0.75}\text{Nb}_3\text{O}_{10}$, with a reduced band gap of 3.06 eV. After loading with Pt nanoparticles, this material gives only traces of H_2 from aqueous methanol under visible light irradiation, but medium rates of O_2 from AgNO_3 solutions. The isostructural undoped $\text{RbPb}_2\text{Nb}_3\text{O}_{10}$ ($E_g = 2.5$ eV) produces, with Pt as co-catalyst, only traces of H_2 from CH_3OH solutions under irradiation with $\lambda < 500$ nm. However, protonation and internal platinisation enable good H_2 rates. In contrast, the Aurivillius-type layered perovskite $\text{PbBi}_2\text{Nb}_2\text{O}_9$, with a band gap of 2.88 eV, produces small rates of H_2 evolution (PE = 0.95) from aqueous methanol, but large rates of O_2 formation from aqueous AgNO_3 under visible light after Pt loading (Osterloh 2008). With a feordite structure and a narrow band gap of 2.3 eV, SnNb_2O_6 shows activity for both H_2 and O_2 evolution in sacrificial systems when suitable co-catalysts are employed. For instance, $\text{IrO}_2/\text{SnNb}_2\text{O}_6$ shows relatively high activity for O_2 evolution from aqueous AgNO_3 . However, the stoichiometric water splitting over this photocatalyst has not been successful yet (Kudo and Miseki 2009). InNbO_4 ($E_g = 2.5$ eV), one of the first visible light-active water splitting photocatalysts reported in the literature, is active under both for H_2 evolution from aqueous CH_3OH and for O_2 evolution from aqueous AgNO_3 . The spectral response of this material in the water reduction reaction is in good agreement with its absorption spectrum, and the same can be stated for the corresponding V and Ta derivatives, as depicted in Fig. 7.4 (Zou and Arakawa 2003). The band gap of AgNbO_3 , with a perovskite structure, is 2.8 eV, 0.6 eV smaller than that of NaNbO_3 . This difference results from the contribution of Ag-filled 4d orbitals to the formation of the valence band by hybridisation with O 2p orbitals, as demonstrated by DFT calculations. Consequently, Ag is able to evolve H_2 or O_2 from water in the presence of sacrificial reagents (Kato et al. 2002).

Photocatalytic degradation of organic pollutants in water and air over niobate catalysts has been studied to a much lesser extent than the water splitting application, with only a few reports in the literature. Most of them use dyes as model pollutants, both under UV and visible light, and do not obtain remarkable results in terms of photocatalytic activity, especially if compared to that of TiO_2 (Roof et al. 2008). In the classical model reaction of gas phase isopropanol-to-acetone photocatalytic oxidation, lead niobates show interesting activities under visible light

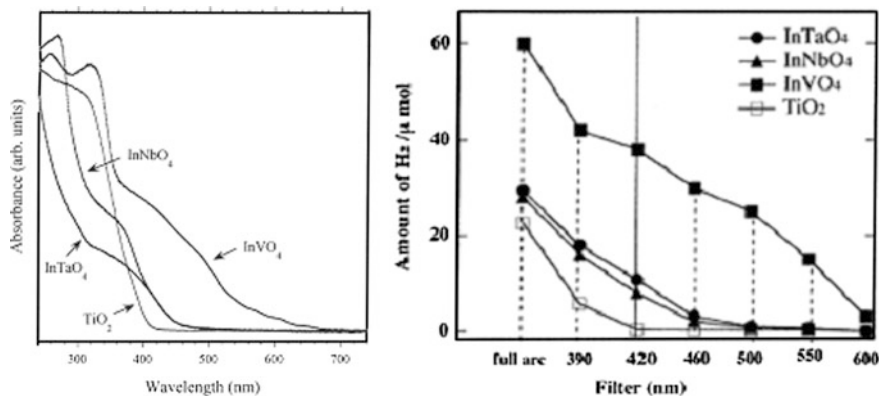


Fig. 7.4 *Left* UV–visible diffuse reflectance spectra of InVO_4 , InNbO_4 , InTaO_4 and TiO_2 . *Right* Spectral response of the platinised materials for H_2 evolution from $\text{CH}_3\text{OH}/\text{H}_2\text{O}$ solutions. Reproduced with permission from Zou and Arakawa (2003). Copyright Elsevier

irradiation. This niobates show decreasing band gaps with increasing Pb/Nb molar ratio, suggesting a higher valence band position due to a higher contribution of Pb 6s orbitals in the hybridisation with O 2p. Thus, E_g values decrease in the series: Nb_2O_5 (3.25 eV) > $\text{Pb}_3\text{Nb}_4\text{O}_{13}$ (2.95) > $\text{Pb}_3\text{Nb}_2\text{O}_{13}$ (2.72) > PbO (2.65) (Li et al. 2007). The highest acetone evolution under irradiation with $400 < \lambda < 520$ is achieved with $\text{Pb}_3\text{Nb}_4\text{O}_{13}$, with good agreement between photocatalytic response and absorption spectrum. This activity can be further increased if the catalyst is obtained via co-precipitation, followed by calcination at a temperature leading to the best crystallinity—surface area compromise. In turn, the so-obtained photocatalyst leads to a much higher isopropanol mineralisation degree than a sample obtained by the ceramic method. The well-known ferroelectric niobate PMN ($\text{Pb}_3\text{MgNb}_2\text{O}_9$), as well as the related non-stoichiometric compound $\text{Pb}_{1.83}\text{Mg}_{0.29}\text{Nb}_{1.71}\text{O}_{6.39}$, also show photocatalytic activity for the gas phase oxidation of isopropanol-to-acetone under visible light (Kako and Ye 2007). Of these two catalysts, the latter shows the highest acetone evolution and isopropanol mineralisation, although slightly lower than those obtained with $\text{Pb}_3\text{Nb}_4\text{O}_{13}$.

7.4 Ta_2O_5 and Tantalates

Under UV irradiation, tantalum oxide itself ($E_g = 4.0$ eV) produces only traces of H_2 from pure water, with no O_2 evolution. However, when loaded with NiO , Pt or RuO_2 as co-catalyst, its activity becomes considerable for stoichiometric water splitting (Osterloh 2008). This activity can be further increased if Ta_2O_5 is synthesised in a mesoporous structure with crystalline walls using silicone scaffolding (Noda et al. 2008). In this form, and loaded with nickel oxide, Ta_2O_5 shows one of the highest activities reported so far in photocatalytic water splitting. This high

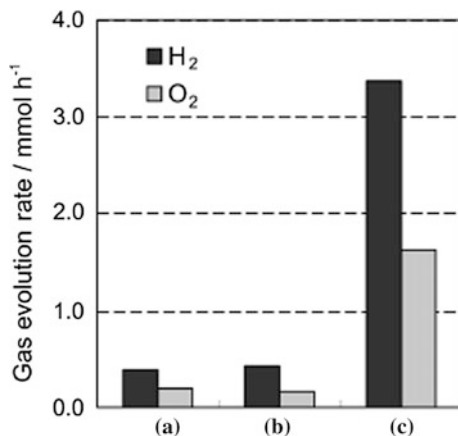


Fig. 7.5 Photocatalytic activities of different Ta₂O₅ samples loaded with NiO for overall water splitting under UV irradiation ($\lambda > 200$ nm). (a) Crystallised non-porous Ta₂O₅ loaded with NiO_x (1 wt % as NiO). (b) Amorphous mesoporous Ta₂O₅ (3 wt % as NiO), and (c) crystallised mesoporous Ta₂O₅ (3 wt % as NiO). Reproduced with permission from Noda et al. (2008). Copyright American Chemical Society

activity is attributed to the efficient transfer of the excited electrons and holes from the bulk to the surface of the catalyst through the thin-walled crystalline phase (Fig. 7.5).

Tantalates are, in general, rather efficient photocatalysts for water dissociation. Alkali tantalates ATaO₃ (A: Li, Na, K) form perovskite-like structures with corner-sharing TaO₆ octahedra, as depicted in Fig. 7.6. Their energy structure and UV photocatalytic activity, high in any case, depend largely on the nature of the A cation. As the interoctahedral Ta–O–Ta angle gets closer to 180°, the delocalisation of the energy bands (and thus of the excited e⁻-h⁺ pairs) increases and the band gap decreases (Wiegel et al. 1994). A higher charge carrier delocalisation is expected to lead to lower recombination and, thus, higher availability of electron-hole pairs in

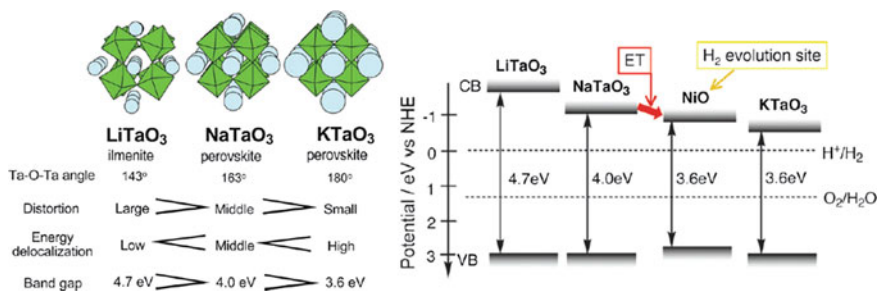


Fig. 7.6 *Left* Structure and energy characteristics of alkali tantalates. *Right* Band positions of alkali tantalate photocatalysts and NiO co-catalyst. Adapted with permission from Kato and Kudo (2001). Copyright American Chemical Society

the surface for photocatalytic reactions. On the other hand, the relative position of the photocatalyst and co-catalyst conduction bands, shown in Fig. 7.6, is essential for electron transference from the former to the latter to occur (see Chap. 10). Therefore, the higher photocatalytic activity for water splitting observed in NiO/NbTaO₃ compared to the Li and K derivatives (Kudo and Miseki 2009) can be ascribed to a compromise situation between suitable band position and increased e⁻-h⁺ delocalisation. Indeed, NbTaO₃ is a remarkable water splitting photocatalyst, with 28 % PE at 270 nm when loaded with NiO (Chen et al. 2010). This efficiency can be increased up to 56 % by 2 % La doping, which is the highest PE reported to date for a photocatalyst in pure water. The high activity is ascribed to the La dopant reducing the particle size of the catalyst and causing the formation of nanosteps on its surface. According to the authors, the grooves in the nanosteps serve as O₂ formation sites, while H₂ evolution occurs on the ultrafine NiO particles at the step edges (Kato et al. 2003).

The reason why tantalates are generally more active than their niobate counterparts lies on the positions of their respective conduction bands, mainly formed by Ta 5d orbitals in the former, with higher energy than Nb 4d. A good example of this is given by the comparison of the Ruddlesen–Popper layered perovskite Sr₂Ta₂O₇ to the structurally related Sr₂Nb₂O₇ (they differ slightly in the M–O–M angles connecting the octahedra) described in the previous section. The higher conduction band of the tantalates further enables the electron transference to the NiO co-catalyst, and thus, the NiO/Sr₂Ta₂O₇ system shows a higher activity for water decomposition than the niobate compound in the same working conditions (Kudo and Miseki 2009). Meanwhile, Ca₂Ta₂O₇, crystallising in a pyrochlore structure with a three-dimensional TaO₆ octahedra network, gives rise to a higher H₂ production than the isostructural Ca₂Nb₂O₇.

In the same line as alkaline earth tantalates, both Sr₂TaO₆ and Ba₂TaO₆ are active for photocatalytic water splitting, the former with a 7 % PE. Among the three crystalline modifications of the latter (hexagonal with E_g = 4.0 eV, tetragonal with 3.8 eV and orthorhombic with 4.1 eV), the orthorhombic one shows the highest photocatalytic activity because of its larger band gap. Other structures like the cubic perovskite Sr₄Ta₂O₉ and the (111) layered perovskites M₅Ta₄O₁₅ (M: Sr, Ba) catalyse H₂ and O₂ evolution from pure water when modified with NiO, with Ba₅Ta₄O₁₅ displaying the highest activity. Regarding the importance of the crystalline structure, chains of corner-sharing TaO₆ octahedra seem to be more efficient than three-dimensional networks, as suggested by the difference in activities found for La₃TaO₇ when crystallised in both forms. Thus, weberite-type (chained) La₃TaO₇ shows much higher activity than the (3D) pyrochlore modification in spite of both having the same band gap. Other tantalates of the same stoichiometry lacking TaO₆ chains, like Y₃TaO₇, Yb₃TaO₇ and Gd₃TaO₇, give only traces of H₂ under the same working conditions (Osterloh 2008).

Mixed metal tantalates A₂A'Ta₂O₇ (A: H, K; A': Sr, La_{2/3}) with a hydrated perovskite structure have proved to be efficient for overall water splitting even without a co-catalyst. These catalysts are more active than the anhydrous tantalate perovskites Li₂SrTa₂O₇, La_{1/3}TaO₃ and KTaO₃. This has been attributed to their

hydrated layered structure, where the photogenerated charge carriers can be effectively transferred to the interlayer water. In the presence of a co-catalyst like NiO, these structures are remarkably active because of the intercalation of small nickel oxide clusters into the layers via an ion exchange reaction. The effect of a hydrated layered structure has also been observed in $H_{1.81}Sr_{0.81}Bi_{0.19}Ta_2O_7$. Ion exchange reactions have also been used to prepare $M Ln Ta_2 O_7$ photocatalysts (M: Cs, Rb, Na, H; Ln: La, Pr, Nd, Sm) from lanthanide tantalates. Their activity depends on the nature not only of the lanthanide element, but also of the interlayer cation, with the highest activity obtained with Ln = Nd and M = Rb. In the pure lanthanide tantalates $Ln Ta O_4$ (Ln: La, Ce, Pr, Nd, Sm), however, the one with Ln = La shows the highest water splitting activity (Chen et al. 2010).

As for previously commented metallates, studies on tantalum oxide and tantalates for other applications of photocatalysis, such as pollutant degradation, have been much scarcer. However, considering their band energies, UV-active tantalates are fully applicable to PCO reactions. For example, the already mentioned $Na Ta O_3$ is able to degrade aqueous dyes and gaseous formaldehyde. When prepared in a size-controlled, high surface area modification via soft chemical synthesis, it can be more active than $Ti O_2$ P25 in both gaseous and liquid media (Li and Zang 2009). As in the case of water splitting, its activity for PCO can be further increased if doped with lanthanum (Li and Zang 2011). $Ba_5 Ta_4 O_{15}$ is also an active photocatalyst for organics oxidation both in water and in air, in certain conditions comparable to $Ti O_2$ P25 too (Xu et al. 2006).

Due to the high energy of the Ta 5d orbitals forming their conduction bands, only a few visible light-active tantalate photocatalysts have been developed. Photocatalytic splitting of pure water under visible light was achieved by Arakawa et al. with $In_{1-x}Ni_x Ta O_4$ obtained from the parent oxides by solid-state synthesis (Zou et al. 2001). $In Ta O_4$ forms a wolframite-type structure consisting of zigzag chains of edge-sharing $Ta O_6$ octahedra. The Ni^{2+} ions replace In^{3+} on its sites, leading to a contraction of the lattice and a band gap reduction from 2.6 eV in the undoped tantalate to 2.3 in a doped sample with $x = 0.1$. The band gap change in Ni-doped compounds can be attributed to internal transitions in a partly filled Ni d shell, which is supported by the appearance of an absorption band at 420–520 nm, corresponding to an energy range of about 2.9–2.3 eV. The best one among the doped catalysts, $Ni O / In_{0.9} Ni_{0.1} Ta O_4$, produces H_2 and O_2 from water stoichiometrically with PE = 0.66 % at $\lambda = 402$ nm with no deactivation. In turn, undoped $Ni O / In Ta O_4$ is 5 times less active. In a similar way, $Ni Ta_2 O_6$ leads to the evolution of small amounts of hydrogen from pure water without any co-catalyst. The valence band of $Ni Ta_2 O_6$ is assumed to be formed by O 2p orbitals from two kinds of octahedra, $Ni O_6$ and $Ta O_6$, and to have an energy level above that of O 2p levels in simple oxides. The resulting absorption onset is 2.3 eV, and it is believed that the Ni d–d transition between the 3d t_{2g} and e_g levels also plays an important role in the visible light photoexcitation and photocatalytic activity of this tantalate (Ye et al. 2003). $Ni O / In Ta O_4$ has also been used for photocatalytic CO_2 reduction under visible light with selective production of methanol (Hernández-Alonso et al. 2009). Regarding PCO applications, bismuth tantalates have been explored as

visible light–active photocatalysts. For example, BiTaO_4 , with an experimental band gap of 2.75 eV (2.3 by DFT), degrades methylene blue in water under visible light ($\lambda > 420$ nm) with a rate comparable to that obtained with a nitrogen-doped titania and with ca. 50 % mineralisation. The wavelength dependence of the reaction rate fairly matches the absorption spectrum of the photocatalyst (Shi et al. 2010). A more complex mixed tantalate, $\text{Ba}(\text{In}_{1/3}\text{Pb}_{1/3}\text{Ta}_{1/3})\text{O}_3$, has been reported to photocatalyse the degradation of 4-chlorophenol in water under irradiation with $\lambda > 420$ nm (Hur et al. 2005). The activity under visible light in this case is largely related to the presence of lead.

7.5 BiVO_4 and Other Vanadates

BiVO_4 exists in four polymorphs: orthorhombic pucherite, tetragonal dreyerite and monoclinic clinobisvanite, plus a tetragonal scheelite-like phase, reversibly formed from the latter at 528 K. It occurs naturally as the first one (Bierlein 1975), but is generally obtained in the laboratory as the next two, being the thermodynamically stable clinobisvanite phase the one with the best photoelectrochemical behaviour. This structure (space group C_{2h}) presents unique crystallographic positions for Bi and V, and two for oxygen. A primitive cell with two formula units can be constructed. Bi–O–V layers stack parallel to the *c* axis, with the Bi atoms sixfold coordinated in a distorted octahedron and V atoms at the centre of a distorted oxygen tetrahedron. The lone-pair distortion typically found in structures with ns^2 cations (Bi^{3+} : $[\text{Xe}]4f^{14}5d^{10}6s^2$) is related to the asymmetry of the bismuth and vanadium polyhedra in this crystalline phase (Sleight et al. 1979). The band gap of clinobisvanite BiVO_4 is direct, with the valence and conduction bands extrema away from the centre of the Brillouin zone, where the hybridisation within the Bi–V–O layers is increased. The calculated (PBE-DFT) value of 2.16 eV underestimates the experimental results (2.4–2.5 eV) only slightly, in contrast to other oxides in which the underestimation is larger (Walsh et al. 2009). The top of the valence band is mainly formed by O 2p orbitals with some contribution of Bi 6s. Similarly to Bi_2O_3 , calculations suggest the interaction of Bi 6s and O 2p to be antibonding near the top of the valence band. While an isolated O 2p valence band is resilient to oxidation, the presence of antibonding anion–cation states is beneficial for hole formation and mobility. In addition, this hybridisation raises the valence band maximum by 0.4 eV with respect to pure O 2p levels, giving rise to visible light absorption. The conduction band is dominated by V 3d states, with significant contributions from O 2p and Bi 6p. Effective masses of about 0.3 m_e are predicted for both electrons and holes, much lighter than the typical values in metal oxides. This should facilitate efficient photoexcited charge carrier separation and extraction. Indeed, high photon-to-current efficiencies are obtained under visible light with BiVO_4 electrodes (Walsh et al. 2009).

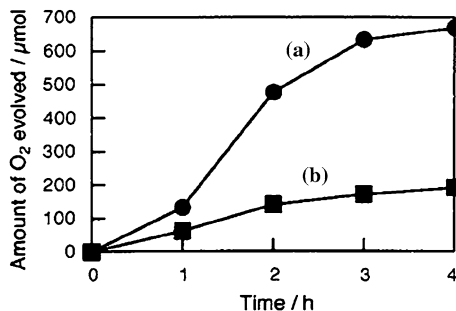
The tetragonal dreyerite phase of BiVO_4 exhibits a zircon-like structure (space group $I4_1/amd$) and is most frequently obtained in low-temperature syntheses, while

high-temperature ones lead to the monoclinic phase. It has a calculated band gap of 2.8 eV (Stoltzfus et al. 2007) versus experimental 2.9 (Kudo et al. 1999), higher than that of the monoclinic phase as a result of quite different electronic structures. On the one hand, the conduction band minimum is higher in energy in dreyerite. On the other hand, the valence band maximum in the monoclinic form is slightly higher, with a larger contribution of Bi 6s orbitals. This can be related to a stronger Bi 6s–O 2p interaction in a structure with a distorted Bi^{3+} environment due to a lone-pair distortion not existing in the tetragonal form (Stoltzfus et al. 2007). This higher orbital overlap should also lead to more delocalised photogenerated holes and, thus, to better charge separation and photocatalytic activity. Indeed, the order of photocatalytic activities for O_2 evolution of different clinobisvanite samples correlates well with the degree of lone-pair distortion indicated by their Raman spectra (Yu and Kudo 2006). Accordingly, the activity obtained with the tetragonal phase is much lower for the same reaction (Kudo et al. 1999) and in the degradation of aqueous methylene blue under visible light (Zhang et al. 2007a).

The synthesis conditions, including not only the temperature, strongly influence the crystalline phase of the obtained vanadate. In this respect, either the tetragonal or the monoclinic phase can be selectively obtained by simple co-precipitation–hydrothermal processes, starting from aqueous Bi^{3+} and vanadate salts, by adjusting the reaction temperature (Zhang et al. 2007a). In cation exchange syntheses from alkali vanadates, not only post-synthetic calcination temperature (or absence of treatment), but also the starting material and the V:Bi ratio, exert a strong influence on the final crystalline form. The monoclinic form can also be obtained by solid-state synthesis from Bi_2O_3 and V_2O_5 , but a much lower activity is observed (Kudo et al. 1999). Therefore, it is important to carefully control the synthesis conditions if one wishes to obtain the more active clinobisvanite phase with the adequate characteristics for photocatalytic applications.

As indicated above, monoclinic BiVO_4 is active for O_2 evolution from AgNO_3 aqueous solutions (Fig. 7.7). In fact, its activity is remarkable if compared to other photocatalysts (Kudo and Miseki 2009). However, it does not show activity for H_2 evolution due to a low conduction band energy. It is active though for the oxidation of organic molecules, and therefore, it has been tested for the degradation of several aqueous pollutants such as dyes, surfactants and aromatic hydrocarbons (Hernández-Alonso et al. 2009). However, its activity for organics degradation

Fig. 7.7 Photocatalytic O_2 evolution from aqueous AgNO_3 solutions (0.05, 300 mL) under visible light irradiation ($\lambda > 420$ nm) on (a) BiVO_4 synthesised from $\text{K}_3\text{V}_5\text{O}_{14}$ and (b) WO_3 (reproduced with permission from Kudo and Hiji 1999. Copyright American Chemical Society)



under simulated sunlight has been found to be similar to that of TiO_2 unless oxygen is bubbled in the reaction medium. Under purely visible light, monoclinic BiVO_4 is considerably more active than TiO_2 , which is not surprising taking into account their respective absorption spectra. However, the activity of BiVO_4 for pollutant photocatalytic degradation must be taken cautiously, since most of the published works use dyes as target molecules, and, when other organics have been employed, little mineralisation has been obtained (e.g. 0.3 % in 4-nonylphenol degradation, Hernández-Alonso et al. 2009). In this sense, chemical modifications of this vanadate have been tested in order to improve its photocatalytic properties. Ag-loading seems to increase the mineralisation degree with respect to bare BiVO_4 , but still to a low value (1.3 % in the degradation of 4-nonylphenol), and improved initial rates have been reported with Pd, Pt and Cu oxide loading in the oxidation of some dyes, but with no mention to mineralisation (Hernández-Alonso et al. 2009). Regarding mechanistic aspects, chemiluminescence experiments using terephthalic acid as a OH radical scavenger (to yield the highly fluorescent 2-hydroxyterephthalic acid) have shown that a little amount of OH radicals is generated upon irradiation of BiVO_4 in the presence of water, compared to that formed with TiO_2 (Kohtani et al. 2008). This could just come from a low charge mobility, but the fact that BiVO_4 shows a relatively high activity for the water oxidation reaction with sacrificial reagents suggests that different mechanisms are involved in photocatalytic reactions over this material (and other ones described later in this chapter), rather than the usually accepted ones intermediated by OH radicals. Specifically, for oxygen evolution, a mechanism involving the 4-electron oxidation of the water molecule initiated by direct reaction with photogenerated holes has been proposed (Kohtani et al. 2008).

Ag^+ 4d orbitals can also contribute to the formation of the valence band together with O 2p in mixed oxides, raising the top of the band with respect to O 2p levels and giving visible light-absorbing solids. Thus, silver vanadates have been explored as possible photocatalysts (Konta et al. 2003). Among different stoichiometries and crystalline forms, Ag_3VO_4 has been found the most active for O_2 evolution from AgNO_3 aqueous solutions. This activity has been related to the higher dispersion of the valence band. It is not active though for H_2O reduction to H_2 , due to a low conduction band level, but it shows remarkable activity for the gas phase photocatalytic oxidation of isopropanol and benzene. The activity of different silver vanadates (Ag_3VO_4 and $\text{Ag}_4\text{V}_2\text{O}_7$ with different morphological characteristics) seems to correlate with the amount of surface hydroxyl groups (Huang et al. 2009). The problem of this silver compounds may arise from photocorrosion due to the reduction of the lattice Ag^+ ions by conduction band electrons.

Although much less information has been published about it, BiCu_2VO_6 , with a monoclinic unit cell, has been reported to show better activity for O_2 evolution than BiVO_4 under visible light, both using Ag^+ and Fe^{3+} as electron scavengers (Liu et al. 2005). However, its activity is worse than that of low-temperature-synthesised bismuth vanadate, and no reports about other preparation of BiCu_2VO_6 than solid-state reaction have been published, so that comparison of the activities of both materials is rather difficult. It presents a narrow band gap of 2.1 eV.

Current–potential curves suggest the conduction band of the bismuth–copper vanadate to be 0.2 eV higher in energy than that of BiVO_4 , although it is still too low for H_2 production. Indeed, no H_2 evolution is observed with NiO-loaded BiCu_2VO_6 with methanol as hole scavenger. The introduction of Zn instead of Cu increases the band gap by 0.3 eV and leads to a lower apparent quantum yield for O_2 evolution from Fe^{3+} aqueous solutions (Liu et al. 2006). Regarding other complex vanadates, Bi_2GaVO_7 and Bi_2YVO_8 , with tetragonal structures, initiate both H_2 and O_2 evolution from pure water only under UV irradiation, in spite of the fact that both show intense absorption in the visible region (Chen et al. 2010).

7.6 $d^{10}s^2d^0$ Tungstates and Molybdates

Bi_2WO_6 is known for its electrical properties, such as ferroelectric piezoelectricity, pyroelectricity and nonlinear dielectric susceptibility, and its catalytic activity for the oxidation and ammoxidation of olefins and for CO oxidation. More recently, it has been proposed as a native visible light–active photocatalyst, being firstly reported by Kudo and co-worker to be active for the evolution of O_2 from AgNO_3 solutions (Kudo and Hijii 1999). Later, it was also found active for the mineralisation of CHCl_3 and CH_3CHO under visible light irradiation (Tang et al. 2004a). In the recent years, it has been subject of many studies as a promising visible light–driven photocatalyst.

Bi_2WO_6 is a member of the family of Aurivillius phases, $\text{Bi}_2\text{O}_2\cdot\text{A}_{n-1}\text{B}_n\text{O}_{3n-1}$. It occurs naturally as the rare mineral Russellite, first discovered in tungsten concentrates in 1934 and described as a new species in 1938 (Hey and Bannister 1938). Russellite crystallises in the orthorhombic system ($\text{Pca}2_1$), and its structure can be described as alternating layers of perovskite-like WO_4^{2-} and fluorite-like $\text{Bi}_2\text{O}_2^{2+}$ lying perpendicular to the c axis (Fig. 7.8). The tungsten atoms exhibit a moderately regular octahedral environment, with the W atom displaced from the centre of the octahedron by 0.278 Å, where neighbouring octahedra share corners. There are two crystallographically independent positions for bismuth, in both of which it is bonded to six oxygen atoms. Bond valence calculations give results in very good accordance with the expected formal oxidation of +6 and +3 for tungsten and bismuth, respectively. The lone pairs in Bi^{3+} cations are found to be non-centrosymmetrically related between the two Bi layers surrounding W. This lone-pair asymmetry has been suggested to be related to the tilting of the tungsten octahedra (Mohn and Stølen 2011).

The band structure of Bi_2WO_6 , calculated by DFT (GGA) (Fu et al. 2005), essentially consists of a valence band formed by hybrid O 2p + Bi 6s orbitals and a conduction band formed by W 5d, with a small contribution of Bi 6p orbitals to both bands (Fig. 7.8). The lone-pair electrons are located at the valence band edge and constitute a mixture of 10 % Bi 6s, 5 % Bi 6p and 85 % O 2p characters, according to recent DFT (GGA) calculations (Mohn and Stølen 2011). The

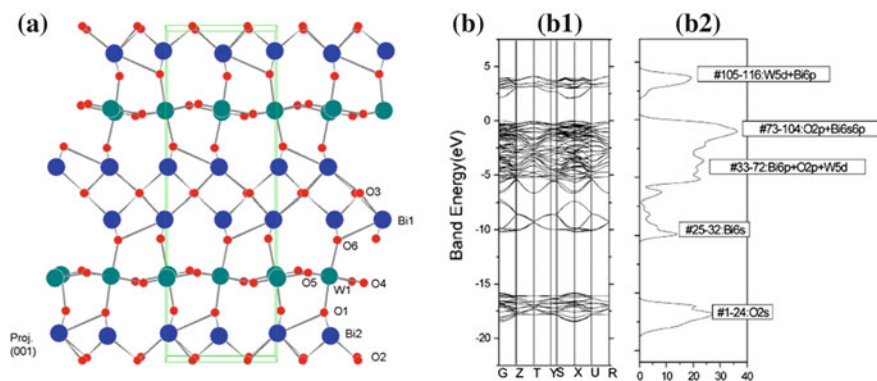


Fig. 7.8 a: Crystal structure of Bi_2WO_6 . b: band energy diagram (b1) and density of states (b2) for Bi_2WO_6 calculated by DFT. The zero energy is located at the Fermi level (part b reproduced with permission from Fu et al. 2005. Copyright American Chemical Society)

theoretical band gap (2.13 eV) underestimates the experimental value of ~ 2.7 eV (yellow-coloured), as is common in DFT calculations at the GGA theory level.

Bi_2WO_6 shows a relatively low activity for O_2 evolution under visible light using AgNO_3 as electron-trapping sacrificial reagent (Kudo and Hiji 1999); on the other hand, it is rather inactive for H_2 evolution due to its low conduction band level. In spite of being a natively visible light-absorbing semiconductor, its absorption spectrum still matches the UV region to a higher extent than the visible one, and thus, under UV illumination, its activity for the O_2 evolution reaction is raised by a factor of 10.

Bi_2WO_6 has been most frequently tested for pollutant elimination, for what it does exhibit the appropriate band energies. A suspension of Bi_2WO_6 degrades dilute aqueous solutions of chloroform under visible light illumination (Tang et al. 2004a), although with a low conversion degree (ca. 1 % CO_2 yield after 200 h) and slow kinetics (CO_2 formation rate of $7.2 \mu\text{mol l}^{-1} \text{h}^{-1}$). In contrast, ca. 50 % CO_2 yield is achieved after a 7-h reaction when a low concentration of acetaldehyde in synthetic air is flowed over powdered Bi_2WO_6 ($\lambda \geq 420$ nm, Tang et al. 2004a). The wavelength dependence of the reaction yield fairly matches the absorption spectrum of the photocatalyst. In the degradation of the commonly used rhodamine B dye in aqueous solution, nanocrystalline modifications of Bi_2WO_6 have shown remarkably higher activity under visible light irradiation than TiO_2 P25 (Fu et al. 2005; Wu et al. 2007; Zhang et al. 2007b). Under UV light, Bi_2WO_6 can show photocatalytic activities comparable to those of anatase TiO_2 for the degradation of organic pollutants both in aqueous suspensions and in the gas phase, depending on its morphological and surface characteristics (Amano et al. 2008). However, Bi_2WO_6 presents a drawback related to its decomposition into H_2WO_4 and Bi_2O_3 at low pH values, with a dramatic loss of activity that hinders its application to the degradation of aqueous pollutants (Fu et al. 2005). Regarding the mechanisms of organics oxidation by photoactivated Bi_2WO_6 , spin-trapping

EPR together with photocatalytic experiments in the presence of a hydroxyl radical scavenger have suggested that OH species are not involved in the first oxidation step, but rather a direct electron transfer from organic adsorbates to the valence band of the photocatalyst (i.e. direct oxidation by holes) may occur (Fu et al. 2005). From a theoretical point of view, this possibility may be plausible, since an estimation of the redox potential of photogenerated holes in Bi_2WO_6 gives a value that lies below (less positive) the standard redox potential of OH/OH^- , the holes in the CB of Bi_2WO_6 being in this case not able to produce OH radicals from surface hydroxyl groups.

Other tungstates have been explored as photocatalysts, but to a lesser extent. $\text{Bi}_2\text{W}_2\text{O}_9$ is a defect Aurivillius structure in which A sites are empty. It presents a larger band gap (3.0 eV) than Bi_2WO_6 . Under UV light irradiation, and similarly to Bi_2WO_6 , it shows a remarkable activity for O_2 evolution from AgNO_3 solutions, but its activity for H_2 generation with sacrificial reagents using Pt as co-catalyst is rather low compared to other photocatalysts (Kudo and Hiji 1999; Kudo and Miseki 2009). RuO_2 -loaded PbWO_4 , with a scheelite structure and a band gap of 3.9 eV, is able to produce hydrogen and oxygen at moderate rates from pure water under UV light (Kudo and Miseki 2009). Compared to CaWO_4 , a counterpart compound with a cation from the previously mentioned group (2), PbWO_4 shows a larger dispersion of the valence and conduction bands, due to the contribution of Pb 6s and 6p atomic orbitals, respectively, reinforcing the idea of the convenience of the $d^{10}s^2d^0$ configuration for photocatalytic systems (Kadowaki 2007). On the other hand, when employed for rhodamine B degradation, PbWO_4 gives rise to low degradation rates, whatever the irradiation wavelength. Neither ZnWO_4 nor CdWO_4 are more active than Bi_2WO_6 for the photocatalytic oxidation of organic molecules.

In its low-temperature (LT) form, Bi_2MoO_6 is isostructural with Bi_2WO_6 and presents a band gap of 2.70 eV, being therefore activated by visible light (Shimodaira et al. 2006). In contrast, when obtained at high temperatures, it forms a different structure (HT) with isolated WO_4 tetrahedra and a larger band gap. The comparison with other bismuth molybdates leads to a correlation between structure and gap width. HT- Bi_2MoO_6 and $\text{Bi}_2\text{Mo}_2\text{O}_9$, both formed by MoO_4 tetrahedra, show band gaps of 3.02 and 3.10 eV, respectively, in contrast to the value obtained for LT- Bi_2MoO_6 containing corner-sharing MoO_6 octahedra. $\text{Bi}_2\text{Mo}_3\text{O}_{12}$, which possesses both MoO_4 and MoO_6 units, presents an intermediate value of 2.88 eV. However, in contrast to Bi_2WO_6 , no contribution of Bi 6s orbitals has been obtained in DFT calculations for Aurivillius-type Bi_2MoO_6 , being visible light-absorption ascribed to the width of the conduction band provoked by the octahedral coordination around Mo ions. The larger dispersion of the band structure in octahedra-forming molybdates would also lead to a higher charge mobility and a higher photocatalytic activity. Indeed, “octahedral” molybdates show higher activity for O_2 evolution from aqueous AgNO_3 solutions than those with tetrahedral units. These results contribute to the idea of the convenience of layered structures for photocatalytic applications. However, in common with bismuth tungstates, no bismuth molybdate is active for H_2 production from sacrificial solutions, owing to the position of their conduction bands. Differently, PbMoO_4 ,

with a scheelite-type structure and a band gap of 3.31 eV, is able to produce H_2 from methanol solutions when loaded with Pt, and O_2 from aqueous $AgNO_3$. From pure water, only O_2 is formed, however. Cr doping extends the response of $PbMoO_4$ to the visible range, but the ability to form hydrogen is lost (Osterloh 2008). Photocatalytic activity for the degradation of organic pollutants under visible light has also been reported for Bi_2MoO_6 (Kudo and Miseki 2009).

Although solid-state synthesis has been conventionally employed to prepare these tungstate and molybdate materials, this method implies the disadvantage, from the viewpoint of heterogeneous catalysis, of low specific surface areas and little control on crystal sizes and shapes. Thus, other milder synthetic methods have been developed in order to overcome the mentioned limitations. When suitable reaction conditions (reagents mole ratios, pH, temperature and time) are chosen, single-phase Bi_2WO_6 or Bi_2MoO_6 with good crystallinity can be obtained from simple precursors in sealed autoclaves under autogenous pressure (Shi et al. 2000). Recently, different authors have reported the preparation of bismuth–tungsten and bismuth–molybdenum oxides with Aurivillius structure and optimum photocatalytic properties through more complex “soft” synthetic procedures, such as complex organic precursors, microwave-assisted synthesis or the citrate precursor (Pechini) technique (Belver et al. 2009). Different nanoshapes and superstructures (see Chap. 11) have also been obtained via soft chemical syntheses with or without structure-directing agents, with good results from the point of view of photocatalytic activity (Hernández-Alonso et al. 2009).

7.7 Other Mixed Oxides

In recent works, it has been demonstrated that some main group metal mixed oxides with d^{10} configuration are effective as photocatalysts for water splitting and for the oxidation of organic molecules. Among them, indates are probably the most studied ones, but also others based of antimony, tin, germanium, gallium and bismuth are worth of mention (Chen et al. 2010; Kudo and Miseki 2009; Osterloh 2008).

Alkali, alkaline earth and lanthanide metal indates can be obtained by solid-state reactions between In_2O_3 and the corresponding metal oxides or carbonates, or by high-temperature calcination of a precipitate obtained from a mixed solution of the respective nitrates (Sato et al. 2003a; Tang et al. 2004a). Their crystal structures considerably differ depending on the cation. Alkaline earth metal indates of formula MIn_2O_4 with $M = Ca$ or Sr present the calcium ferrite structure (orthorhombic), built up of double blocks of edge-sharing InO_6 distorted octahedra, extending infinitely in the b axis direction. Each double string is joined by octahedral corners to other double strings to form pentagonal-prism-like tunnels large enough to accommodate the alkaline earth ions (Reid 1967). However, $BaIn_2O_4$ crystallises in a monoclinic structure, in which InO_6 octahedra are more closely packed and no such tunnel structure exists (ICSD card # 202986). $NaInO_2$ has a tetragonal layered structure that is reflected in its macroscopic morphology, with

Na^+ ions sandwiched between two slabs of edge-sharing InO_6 octahedra (ICSD card #31932), while LiInO_2 is a closely packed tetragonal three-dimensional structure (ICSD card # 33954). As for the orthorhombic LaInO_3 , its structure resembles those of the calcium and strontium indates, with corner-sharing InO_6 units forming tunnels along the *b* direction in which La atoms are located (ICSD card # 281549). The electronic structures of these indates are essentially described by a valence band predominantly formed by O 2p orbitals and the bottom of the conduction band composed of hybridised In 5s and 5p orbitals with a higher contribution of the former (Sato et al. 2003b, c), similarly to what is found in In_2O_3 (Sun et al. 2010). However, their band gaps are 3.9, 3.6 and 3.2 eV for CaIn_2O_4 , SrIn_2O_4 and BaIn_2O_4 , respectively (Esther Dali et al. 1998), and 3.9 and 4.1 eV for NaInO_2 and LaInO_3 , respectively (Kudo and Miseki 2009), in most cases larger than that of In_2O_3 (3.0–3.5 eV). As indicated in Fig. 7.1, the, say, electropositive cations do not contribute to the states involved in photocatalytic reactions, but indirectly exert an influence in the electronic and optical properties of these materials by determining their crystal structure and, hence, the orbital overlapping.

RuO_2 -loaded CaIn_2O_4 is active for the photocatalytic evolution of hydrogen and oxygen from pure water and is stable in reaction conditions after several runs, reaching an apparent quantum yield of ca. 5 %. (Sato et al. 2003a) The activity of the indate obtained from a nitrates solution is higher than that obtained with the solid-state-prepared catalyst by a factor of 13. Nevertheless, a compromise between crystallinity and surface area or particle size must be attained, and thus, the activity of CaIn_2O_4 for overall water splitting increases with calcination temperature up to ca. 1500 K and sharply decreases at higher temperatures. When strontium is substituted for calcium, the amounts of evolved gases diminish, and at the terminus composition of SrIn_2O_4 , they are decreased by a factor of 2. Introduction of Ba^{2+} in SrIn_2O_4 , but still maintaining the orthorhombic structure, has the same effect (see Table 7.1). LaInO_3 is less active than the previously cited indates, while no gases evolution is observed with NdInO_3 , LiInO_2 and NaInO_2 .

$\text{Ba}_2\text{In}_2\text{O}_5$, a barium indate containing alternating layers of corner-sharing InO_4 tetrahedra and InO_6 octahedra with Ba^{2+} ions in between, has also been proposed as a water splitting photocatalyst. It releases H_2 from an aqueous methanol solution with Pt deposited as co-catalyst, and O_2 from aqueous AgNO_3 with no co-catalyst needed (Wang et al. 2005). When loaded with NiO and dispersed in pure water, however, only hydrogen is evolved, which makes it unclear if a sacrificial reaction is not taking place. Its activity is reduced by Cr doping, but if the Cr-doped material is mixed with Cr– In_2O_3 , the activity for both sacrificial H_2 and O_2 evolution is increased. Moreover, a composite NiO/Cr– $\text{Ba}_2\text{In}_2\text{O}_5$ /Cr– In_2O_3 catalyst does give rise to hydrogen and oxygen evolution from pure water with stoichiometric ratio (Wang et al. 2005).

A detailed analysis of the crystalline and electronic characteristics of these indates and their correlation with photocatalytic activities reveals that indates with highly distorted InO_6 octahedra (alkaline earth) show high photocatalytic activity, while this activity is negligible in those containing nearly regular octahedra (alkali) (Sato et al. 2003b). Moreover, as it was pointed out in the titanates section,

Table 7.1 Photocatalytic activity of some d^{10} metallates for overall water splitting

Photocatalyst	Irradiation conditions	H ₂ (mol h ⁻¹ g ⁻¹)	O ₂ (μmol h ⁻¹ g ⁻¹)	Molar H ₂ /O ₂
CaIn ₂ O ₄	400 W Xe lamp	60	25.6	2.3
SrIn ₂ O ₄	400 W Xe lamp	30	12.4	2.4
Sr _{0.93} Ba _{0.07} In ₂ O ₄	400 W Xe lamp	25.3	12	2.1
LaInO ₃	200 W Hg–Xe lamp	5	2	2.5
NdInO ₃	200 W Hg–Xe lamp	0	0	–
LiInO ₂	400 W Xe lamp	0	0	–
NaInO ₂	400 W Xe lamp	0	0	–
NaSbO ₃	200 W Hg–Xe lamp	6.8	3.2	2.1
CaSb ₂ O ₆	200 W Hg–Xe lamp	5.6	1.0	5.6
Ca ₂ Sb ₂ O ₇	200 W Hg–Xe lamp	11.2	4.0	2.8
Sr ₂ Sb ₂ O ₇	200 W Hg–Xe lamp	30.8	11.6	2.7
MgGa ₂ O ₄	200 W Hg–Xe lamp	3.6	0	–
SrGa ₂ O ₄	200 W Hg–Xe lamp	28.0	12.0	2.3
BaGa ₂ O ₄	200 W Hg–Xe lamp	12.0	7.2	1.7
ZnGa ₂ O ₄	200 W Hg–Xe lamp	40.4	14.0	2.9
Ca ₂ SnO ₄	450 W Hg lamp	1.1	0.3	3.7
Sr ₂ SnO ₄	450 W Hg lamp	1.0	0.5	2.0
Ba ₂ SnO ₄	450 W Hg lamp	0	0.05	–

In all cases, 1 % RuO₂ is loaded as co-catalyst. Data taken from Sato et al. (2003a, b, c); (Ikarashi et al. 2002)

there is a correlation between calculated dipole moments and photocatalytic activity for overall water splitting in alkali and alkaline earth indates. This association between photocatalytic activity and the distortion of the InO_x structural units has been proposed also for other d^{10} metallates (Sato et al. 2003b). For instance, alkaline earth and sodium antimonates, with distorted SbO₆ octahedra, are active for water decomposition when loaded with RuO₂. Their activities are summarised in Table 7.1. NaSbO₃ (band gap 4.4 eV) produces both H₂ and O₂ from pure water under UV irradiation. The initial reaction rate is considerably higher for hydrogen than for oxygen evolution, the latter showing an induction period. After several photocatalytic runs, both gases are evolved at constant rates with nearly stoichiometric ratios. This behaviour is also observed in Ca₂Sb₂O₇ and Sr₂Sb₂O₇, with weberite-type structure and respective band gaps of 3.3 and 3.5 eV, both of which show a higher activity than NaSbO₃, with the Sr compound displaying the highest one (in contrast to the case of indates). In the steady state, however, the hydrogen-to-oxygen molar ratios attained with the weberite-like photocatalysts are higher than the stoichiometric value. CaSb₂O₆ shows the weakest activity of these four antimonates and gives an excessively high H₂/O₂ value (Sato et al. 2003c).

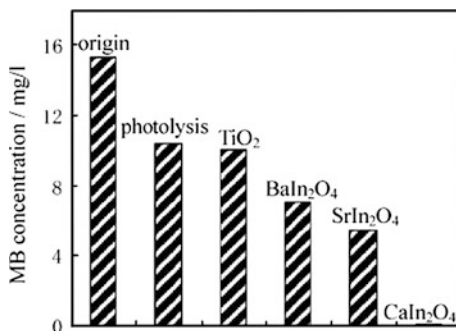
RuO₂-loaded alkaline earth gallates MGa₂O₄ (M: Mg, Sr, Ba) showed a dependence of photocatalytic activity on the nature of the M ion. The activity is negligible for M: Mg, with a structure formed by distortion-free GaO₆ octahedra, but significant for M: Sr and Ba, both possessing distorted GaO₄ tetrahedra with

dipole moments (Sato et al. 2003b). This trend is also observed in alkaline earth stannates, among which Ca_2SnO_4 and Sr_2SnO_4 , with angle-distorted and z-compressed octahedral SnO_6 units, respectively, show a remarkably higher activity (although relatively low, see Table 7.1) than Ba_2SnO_4 , which exhibits a regular octahedral coordination for tin atoms (Inoue 2009). Distorted polyhedra are also present in the photocatalytically active ZnGe_2O_6 and LiInGeO_4 (Chen et al. 2010).

These results suggest an important effect of distorted octahedral and tetrahedral coordination on the photocatalytic activity of d^{10} metallates. Several explanations can be given for this role. The mostly invoked possibility is the contribution of local internal fields due to the dipole moments inside the distorted units: these fields are considered useful for the separation of photogenerated electron–hole pairs (Inoue 2009). ZnGa_2O_4 , however, deviates from this trend, given that it possesses regular GaO_6 but shows a relatively high activity for overall water splitting. This leads to the effect of the electronic characteristics of these materials on their photocatalytic activity. In metallates with d^{10} configuration, large conduction band dispersions are generally calculated, which should favour photocatalytic activity by increasing the photoelectrons mobility. Indeed, in the case of the previously mentioned indates, the calculated conduction band dispersions in alkaline earth–containing materials are higher than those in the alkali and lanthanide ones, in agreement with the observed differences in photocatalytic activity. The extreme case in this respect is found in ZnGa_2O_4 , with Zn^{2+} ions extensively contributing to the electronic structure (see Fig. 7.1), in which strong Zn–O and Zn–Ga interactions lead to a large dispersion of the conduction band (Ikarashi et al. 2002).

The activity of alkaline earth indates for the degradation of organic molecules has been only tested, to the best of the authors' knowledge, for the decolouration of aqueous dyes under visible light ($\lambda > 420$ nm). MIn_2O_4 (M: Ca, Sr, Ba) photocatalysts obtained by solid-state reaction between MCO_3 and In_2O_3 have been reported to show photocatalytic activities in the order $\text{CaIn}_2\text{O}_4 > \text{SrIn}_2\text{O}_4 > \text{BaIn}_2\text{O}_4 > \text{TiO}_2$ (P25) (Fig. 7.9) (Tang et al. 2004b). In spite of their large band gaps, the absorption tail observed above 400 nm might be responsible for this activity. Nevertheless, the dye sensitisation mechanism, as in many other cases, cannot be ruled out. DFT calculations showed that the smaller the radius of M^{2+} in MIn_2O_4 , the higher the oxidising power of the conduction band, which

Fig. 7.9 Photocatalytic degradation of methylene blue under visible light over metal indates and P25 TiO_2 after 120 min. Reproduced with permission from Tang et al. (2004b). Copyright Elsevier



agrees with the order of photocatalytic activities. In addition, the previously mentioned theory based on dipole moments has also been invoked for this photocatalytic reaction, and this should be plausible considering that this effect involves only the very initial steps of the photocatalytic reaction and should not be influenced by the substrate.

$\text{Ca}_2\text{Sb}_2\text{O}_7$ with weberite structure decolourates aqueous methyl orange solutions under UV irradiation, with the apparent reaction rate increasing with improved crystallinity. Thus, $\text{Ca}_2\text{Sb}_2\text{O}_7$ obtained by self-combustion of a solution of the involved cations in aqueous citric acid and calcined at 1573 K achieves total decolouration of a 10 mg l^{-1} dye solution in 60 min, while only 35 % decolouration is obtained after 120 min with the same material treated at 873 K. The activity of this photocatalyst, however, is lower than that of TiO_2 P25 for the same reaction and under the same conditions (Monteiro et al. 2010). On the contrary, a related large surface area oxyhydroxide, $\text{CaSb}_2\text{O}_5(\text{OH})_2$, was found to be more active than TiO_2 (P25) for the UV photocatalytic decolouration of aqueous dyes, with good mineralisation efficiencies of 72.5 % for rhodamine B and 65.2 % for methyl orange (Sun et al. 2009).

AgSbO_3 can be obtained by ion exchange at 300 °C between AgNO_3 and NaSbO_3 . After 2-h reaction, total ion exchange is observed, resulting in a pure ilmenite phase of AgSbO_3 (Singh and Uma 2009). In this layered structure, the same of the starting sodium antimonate, SbO_6 and AgO_6 octahedra is alternately stacked along the *c* axis. It is a metastable polymorph of the thermodynamically stable pyrochlore AgSbO_3 , which is actually obtained by heating the ilmenite phase. As a difference to the previously mentioned antimonates, AgSbO_3 absorbs visible light in both crystalline forms, due to the orbital interactions Ag 4d–O 2p and Ag 5s–Sb 5s in the formation of the valence and conduction bands, respectively. In the decolouration of methylene blue and rhodamine B solutions under UV light, ilmenite AgSbO_3 displays efficiencies similar to those of TiO_2 P25. Negligible degradation is observed, however, with pyrochlore-type AgSbO_3 . Similar results are obtained under visible light irradiation. The same order of activities is found in the photocatalytic degradation of aqueous 4-chlorophenol under visible light, which rules out the contribution of only a dye sensitisation mechanism (Singh and Uma 2009).

Other bismuth-containing oxides than those already exposed in the preceding sections can be mentioned. CaBi_2O_4 has been found active for the photocatalytic oxidative decomposition of organic pollutants. For instance, 65 % of gaseous acetaldehyde is photocatalytically oxidised to CO_2 after 20 min irradiation with visible light, and a stable value of 80 % CO_2 yield is reached within 2 h. In aqueous phase, nearly total decolouration of a methylene blue solution is obtained over this material under visible light within 120 min (Tang et al. 2004c). In addition, SrBi_2O_4 is also able to oxidise acetaldehyde in the gas phase, with the oxidation rate significantly improved by the addition of 1 % NiO as co-catalyst. In this system, spin-trapping EPR experiments indicate that O_2^- and OH radicals are produced on the surface and constitute the active species in the photocatalytic

reaction, in contrast to what was mentioned in the preceding sections about BiVO_4 and Bi_2WO_6 (Hernández-Alonso et al. 2009).

7.8 Bismuth Oxyhalides

Bismuth oxyhalides of the type BiOX (X: F, Cl, Br, I) are nowadays attracting an increasingly good deal of attention due to their photocatalytic properties under UV or visible light irradiation, depending on the halogen element. All of them crystallise in a tetragonal structure analogous to that of the mineral matlockite (PbClF) (space group $P4/nmn$) and formed by fluorite-like Bi_2O_2 slabs interleaved by double layers of halide ions, as depicted in Fig. 7.10. The Bi atom is coordinated to four O and four X atoms. The cell dimensions are obviously larger with increasing size of the X ions, being the elongation along the c axis, that is, perpendicular to the Bi–O and X layers, remarkably higher than that in the two other directions.

In parallel to their crystal lattices, the electronic structures of the four oxyhalides are similar, although with some differences in the case of BiOF (Huang 2009). The valence band in these structures is mainly constructed by the bonding hybridisation O 2p and X np orbitals, with a small contribution of Bi 6s at the top of the band. The conduction band consists principally of the antibonding hybridisation of Bi 6p and O 2p, with negligible contribution of X np, and is largely dominated by the former. With higher X atomic number the width of the valence band increases, while that of the conduction band decreases. This is due to the variation of the bond lengths and angles and, hence, of the extent of the orbital overlapping. The band gap is indirect in all cases except for BiOF and decreases with increasing X atomic number. The experimental values reported in the literature vary to some extent (see Hernández-Alonso et al. 2009, and references

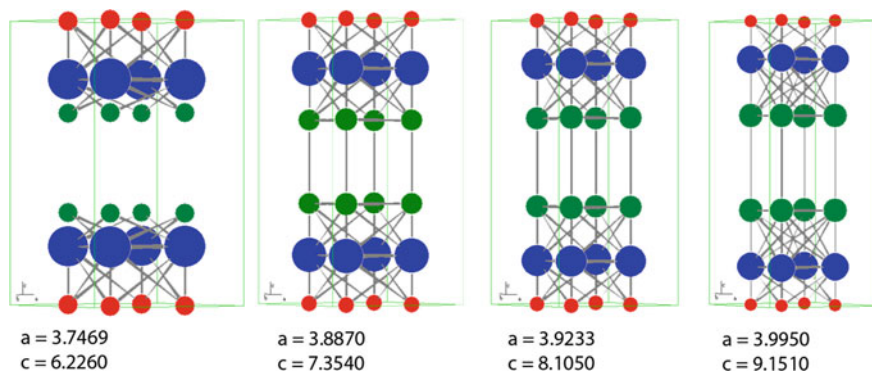


Fig. 7.10 Tetragonal unit cells of bismuth oxyhalides BiOX . From *left to right*, X: F, Cl, Br and I. *Blue* Bi, *red* O, *green* X

therein) and are about 3.64, 3.22, 2.64 and 1.77 eV for BiOF, BiOCl, BiOBr and BiOI, respectively (Su et al. 2010; Zhang et al. 2008b). Therefore, BiOBr and BiOI appear as visible light-driven photocatalysts, while BiOF and BiOCl are activated by ultraviolet light. In this respect, BiOI gives an illustrative example of the quantum size effect (QSE, see Chap. 11), with its band gap ranging from 1.94 (carmine red) up to 2.96 (pale yellow) eV when obtained with decreasing crystal size (Henle et al. 2007).

Bismuth oxyhalides can be easily obtained via standard soft chemical procedures. Precipitation of solutions containing Bi^{3+} (BiO^+) and the corresponding halide leads to the desired BiOX compound, with or without a crystallisation treatment depending on the specific case. For example, well-crystallised, single-phase BiOCl is obtained by the addition of ammonia to a HCl solution of Bi_2O_3 without any further treatment (Zhang et al. 2006), while calcination at 400 °C is needed to obtain a single BiOF phase from the precipitate obtained by addition of NH_4F to a solution of $\text{Bi}(\text{NO}_3)_3$ in ethylene glycol followed by neutralisation with ammonia. Large plate-like crystals of BiOX (X: Cl, Br, I) are obtained after hydrothermal treatment of a solution containing Bi^{3+} and the stoichiometric amount of the appropriate halide salt (KCl, NaBr, KI). When a solvothermal method with ethylene glycol is employed, these plate-shaped crystals tend to arrange in sphere-like secondary particles (Zhang et al. 2008a, b). A fine control of the crystal size with a narrow distribution is achieved from the same precursors by using water-in-oil microemulsions with different micelle sizes, without any further treatment (Henle et al. 2007).

The four BiOX oxyhalides have been tested for photocatalytic oxidation of organic molecules, in both gas and aqueous phases, although in the case of the fluoride only one report has been published to date, to the best of the authors' knowledge (Su et al. 2010). Therefore, this activity must be taken cautiously, although it will be interesting to compare it to those of the rest of BiOX. In the photocatalytic degradation of aqueous phenol under UV irradiation, BiOF gives rise to a remarkable substrate disappearance rate, comparable to that obtained with TiO_2 P25, although no mineralisation data are available. After several cycles, a slight deactivation is observed. In the gas phase oxidation of benzene, a little pseudo-steady-state conversion is obtained (5.5 %) with a slight deactivation, but with a noteworthy mineralisation degree (67 %). In this case, it has to be pointed out that the studied BiOF sample presents a rather low surface area of $3.2 \text{ m}^2 \text{ g}^{-1}$. For the sake of comparison, 93 % selectivity to CO_2 has been obtained with P25 in benzene PCO (Einaga et al. 1999), independently of conversion.

The rest of oxyhalides has been investigated to a higher extent, mainly for the photocatalytic degradation of organic compounds. Under illumination from a high-pressure mercury lamp, which emits mainly in the ultraviolet region, BiOCl leads to a higher methyl orange disappearance than P25 and is apparently stable against photocorrosion, with no decrease in activity after 3 photocatalytic runs (Zhang et al. 2006). A similar comparison is obtained when both catalysts (BiOCl and P25) are irradiated with an unfiltered Xe arc lamp, what some authors call “UV-vis irradiation” (Zhang et al. 2008a). In this case, however, a photosensitisation

mechanism cannot be ruled out. Actually, this mechanism has been proposed as the one leading to rhodamine B degradation under visible light, given that BiOCl leads to the decolouration of the dye aqueous solution under illumination from a Xe lamp cut-off filtered under 420 nm, even though it absorbs light only below ca. 390 nm (An et al. 2007). The TOC analysis may support this proposal, since the TOC value is constant after total decolouration of the solution. However, BiOCl also leads to the oxidation, and even stoichiometric mineralisation, of gaseous isopropanol under visible light irradiation (400–520 nm), which indicates that this material is somehow active under visible light in spite of its wide band gap. Actually, it turns grey when illuminated with a high-power Xe lamp and its UV–vis spectrum after this irradiation reveals a raise in the absorption baseline, in accordance with the grey colour, but no change in the band gap. EPR experiments have suggested the creation of oxygen vacancies, which introduce electronic states within the band gap, as responsible for this absorption and for the visible light activity. Some authors have also observed visible light activity in BiOCl for the degradation of other organic molecules that do not absorb in this region, but with no change in the catalyst colour (Shenawi-Khalil et al. 2011), while other ones report a negligible activity under similar irradiation conditions (Chai et al. 2009; Li et al. 2011a). Therefore, and considering that no plausible explanation has been given for it, the visible light activity observed in some cases for BiOCl may come from uncontrolled parameters, or it could just come from dye sensitisation. This is an illustrative example of the uncertainty that still exists around this new type of photocatalysts that, nevertheless, appear as promising materials for photocatalytic applications if further research, which is indeed taking place at an increasing rate, permits the assessment of their actual capability.

Differently to BiOF and BiOCl, the bromide and the iodide are inherently active under visible light irradiation due to their lower band gap. Under unfiltered Xe-light (UV–vis) irradiation, the bromide shows higher activity than BiOCl for O₂ evolution from aqueous AgNO₃ solutions, while no oxygen is evolved using BiOI (An et al. 2007). Due to their electronic characteristics, no BiOX compound is active for hydrogen evolution from water, though (An et al. 2007). Under visible light (low powered), BiOBr also achieves faster decolouration of RhB solutions than BiOCl, but the mineralisation degree is lower. However, it is apparently less active than the mentioned white–grey oxychloride for the oxidation of gaseous isopropanol (An et al. 2007). Methyl orange decolouration is also observed with BiOBr under visible or UV–vis irradiation (Zhang et al. 2008a, b), with the sphere-like secondary particles mentioned above leading to a faster reaction than bare nanocrystals (Zhang et al. 2008b). Regarding other reactions than dye decolouration, the same microspheres have also been found active for the oxidation of NO to nitrite and nitrate in a continuous air flow under UV–visible and visible light irradiation (45 and 30 % NO removal, respectively), with a slight deactivation after several cycles due to the adsorption of the reaction products on the catalyst surface (Ai et al. 2009). Again, the solvothermally prepared nanospheres show higher activity than hydrothermal nanocrystals. In addition, BiOBr is also capable of oxidising iodide ions to yield I₃[−] in aqueous solution (Shenawi-Khalil et al. 2011). Therefore, although the

degradation of coloured molecules like dyes may come from a photosensitisation mechanism, these other experiments with non-coloured substrates demonstrate that the oxybromide is photocatalytically active itself.

BiOI has the lowest band gap of the BiOX group of materials, and therefore, it is potentially the one capable of harvesting the highest portion of solar light for photocatalytic reactions. It is generally found active for the degradation of methyl orange under visible light irradiation, and its activity appears to be greater than that of BiOBr under identical reaction conditions (Zhang et al. 2008a; Wang et al. 2007; Cao et al. 2011). However, An and co-workers (An et al. 2007) found that only de-ethylation occurred in the degradation of rhodamine B over BiOI (resulting in a yellow solution), in contrast to the total decolouration achieved with BiOBr and BiOCl. In addition, no O₂ evolved from AgNO₃ solutions under UV, as mentioned above, and no degradation of gaseous isopropanol was observed over BiOI under visible light irradiation. Other authors, however, report a considerable activity for the degradation of non-coloured phenols under light with $\lambda > 400$ nm (Li et al. 2011b; Xiao and Zhang 2010), which confirms the inherent photocatalytic activity of this material. As it was mentioned for BiOBr, BiOI sphere-like secondary particles obtained via a solvothermal procedure give rise to a faster photocatalytic degradation reaction than randomly distributed flat nanocrystals (Xiao and Zhang 2010).

Apart from pure BiOX phases, mixed BiOX_x¹X_{x-1}² compounds have been applied to photocatalytic reactions, the intermediate compositions being more active than the parent compounds (Shenawi-Khalil et al. 2011; Wang et al. 2007). In addition, BiOX¹/BiOX² composite photocatalysts, with improved activity based on charge separation in heterojunctions (see Chap. 15), have been reported (Li et al. 2011a; Cao et al. 2011).

The most generally invoked reason for the photocatalytic activity of BiOX materials is based on their layered structure. The internal electric fields between the [Bi₂O₂]²⁺ and [X₂]²⁻ layers are proposed to induce efficient separation of photogenerated electrons and holes by the polarisation of the involved orbitals (Su et al. 2010; Zhang et al. 2006; Wang et al. 2007), similar to what was mentioned about indates and related compounds. According to this, BiOX with a more polarisable halogen atom (that is, higher atomic number) would be more efficient in charge separation. On the other hand, as described above, the interlayer distance is higher with increasing X atomic number, which would produce the opposite effect. The higher activity of BiOI than BiOBr described by some authors would reflect the domination of the first factor. Some others, in contrast, have published activities under UV light in the order BiOBr > BiOCl > BiOI, which would be the result of a competition between contrary factors (An et al. 2007). Competing factors are also found regarding the widths of the valence and conduction bands, the former increasing (positive for photoactivity) and the latter decreasing (negative) with higher X atomic number (Huang 2009). However, direct comparison of the activities of the four materials is not obvious since, on the one hand, no report has been given for the whole X range in the same reaction conditions and, on the

other hand, no quantum yields (or apparent quantum yields), probably the most universal figure of merit for photocatalyst comparison, have been reported. Regarding mechanistic aspects, as it has been mentioned about other materials in this chapter, OH radicals do not appear as the main oxidising agents, suggesting direct reaction of adsorbed organic molecules with holes.

In order to mention other related compounds, oxyfluorides with general formula MO_2F , which crystallise in the ABO_3 perovskite structure with the A site vacant, have been tested for air photocatalytic detoxification (Hernández-Alonso et al. 2009). For example, NbO_2F , more stable than TiOF_2 , only absorbs UV light, but the incorporation of Ag^+ to the vacant A site has been proposed to shift of the photoresponse due to the $\text{Ag } 4d + \text{O } 2p$ hybridisation in the valence band. Consequently, $\text{Ag}^+/\text{NbO}_2\text{F}$ can decompose gaseous 2-propanol to CO_2 with acetone as intermediate product under 400–530 nm light irradiation.

References

- Ahuja S, Kuttly TRN (1996) Nanoparticles of SrTiO_3 prepared by gel to crystallite conversion and their photocatalytic activity in the mineralization of phenol. *J Photochem Photobiol A Chem* 97:99–107
- Ai Z, Ho W, Lee S, Zhang L (2009) Efficient photocatalytic removal of NO in indoor air with hierarchical bismuth oxybromide nanoplate microspheres under visible light. *Environ Sci Technol* 43:4143–4150
- Amano F, Nogami K, Abe R, Ohtani B (2008) Preparation and characterization of bismuth tungstate polycrystalline flake-ball particles for photocatalytic reactions. *J Phys Chem C* 112:9320–9326
- An H, Du Y, Wang T, Wang C, Hao W, Zhang J (2007) Photocatalytic properties of BiOX ($X = \text{Cl, Br, and I}$). *Rare Met* 27:243–250
- Belver C, Adán C, Fernández-García M (2009) Photocatalytic behaviour of Bi_2MO_6 polymetallates for rhodamine B degradation. *Catal Today* 143:274–281
- Bierlein JD, Sleight AW (1975) Ferroelasticity in BiVO_4 . *Solid State Commun* 16:69–10
- Cao J, Xu B, Luo B, Lin H, Chen S (2011) Novel BiOI/BiOBr heterojunction photocatalysts with enhanced visible light photocatalytic properties. *Catal Commun* 13:63–68
- Chai SY, Kim YJ, Jung MH, Chakraborty AK, Jung D, Lee WI (2009) Heterojunctioned $\text{BiOCl}/\text{Bi}_2\text{O}_3$, a new visible light photocatalyst. *J Catal* 262:144–149
- Chen X, Shen S, Guo L, Mao SS (2010) Semiconductor-based photocatalytic hydrogen generation. *Chem Rev* 110:6503–6570
- Domen K, Naito S, Soma M, Onishi T, Tamaru K (1980) Photocatalytic decomposition of water vapour on an NiO-SrTiO_3 catalyst. *J Chem Soc Chem Commun*: 543–544
- Domen K, Kudo A, Shibata M, Tanaka A, Maruya KI, Onishi T (1986) Novel photocatalysts, ion-exchanged $\text{K}_4\text{Nb}_6\text{O}_{17}$, with a layer structure. *J Chem Soc Chem Commun*: 1706–1707
- Einaga H, Futamura S, Ibusuki T (1999) Photocatalytic decomposition of benzene over TiO_2 in a humidified airstream. *Phys Chem Chem Phys* 1:4903–4908
- Esther Dali S, Sai Sundar VVSS, Jayachandran M, Chockalingam MJ (1998) Synthesis and characterization of AlIn_2O_4 indates, $A = \text{Mg, Ca, Sr, Ba}$. *J Mater Sci Lett* 17:619–623
- Fu H, Pan C, Yao W, Zhu Y (2005) Visible-light-induced degradation of rhodamine B by nanosized Bi_2WO_6 . *J Phys Chem B* 109:22432–22439
- Fujishima A, Honda K (1972) Electrochemical photolysis of water at a semiconductor electrode. *Nature (London)* 238:37–38

- Furukawa S, Ohno Y, Shishido T, Teramura K, Tanaka T (2011) Selective Amine Oxidation Using Nb_2O_5 Photocatalyst and O_2 . *ACS Catal* 1:1150–1153
- Henle J, Simon P, Frenzel A, Scholz S, Kaskel S (2007) Nanosized BiOX (X = Cl, Br, I) particles synthesized in reverse microemulsions. *Chem Mater* 19:366–373
- Hernández-Alonso MD, Fresno F, Suárez S, Coronado JM (2009) Development of alternative photocatalysts to TiO_2 : challenges and opportunities. *Energy Environ Sci* 2:1231–1257
- Herrmann JM (2010) Photocatalysis revisited to avoid several misconceptions. *Appl Catal B Environ* 99:461–468
- Hey MH, Bannister FA (1938) Russellite, a new British mineral. *Mineral Mag* 25:41–55
- Hou J, Qu Y, Krsmanovic D, Ducati C, Eder D, Kumar RV (2009) Solution-phase synthesis of single-crystalline $\text{Bi}_{12}\text{TiO}_{20}$ nanowires with photocatalytic properties. *Chem Commun*: 3937–3939
- Huang WL (2009) Electronic structures and optical properties of BiOX (X = F, Cl, Br, I) via DFT calculations. *J Comput Chem* 30:1882–1891
- Huang CM, Pan GT, Li YCM, Li MH, Yang TCK (2009) a. Crystalline phases and photocatalytic activities of hydrothermal synthesis Ag_3VO_4 and $\text{Ag}_4\text{V}_2\text{O}_7$ under visible light irradiation. *Appl Catal A Gen* 358:164–172
- Hur SG, Kim TW, Hwang SJ, Park H, Choi W, Kim SJ, Choy JH (2005) Synthesis of new visible light active photocatalysts of $\text{Ba}(\text{In}_{1/3}\text{Pb}_{1/3}\text{M}'_{1/3})\text{O}_3$ ($\text{M}' = \text{Nb, Ta}$): a band gap engineering strategy based on electronegativity of a metal component. *J Phys Chem B* 109:15001–15007
- Ikarashi K, Sato J, Kobayashi H, Saito N, Nishiyama H, Inoue Y (2002) Photocatalysis for water decomposition by RuO_2 -Dispersed ZnGa_2O_4 with d^{10} configuration. *J Phys Chem B* 106:9048–9053
- Inoue Y (2009) Photocatalytic water splitting by RuO_2 -loaded metal oxides and nitrides with d^0 —and d^{10} —related electronic configurations. *Energy Environ Sci* 2:364–386
- Kadowaki HJ (2007) Overall splitting of water by RuO_2 loaded PbWO_4 photocatalyst with $d^{10}s^2 d^0$ configuration. *J Phys Chem C* 111: 439–444
- Kako T, Ye J (2007) Comparison of photocatalytic activities of two kinds of lead magnesium niobate for decomposition of organic compounds under visible-light irradiation. *J Mater Res* 22:2590–2597
- Kato H, Kudo A (2001) Water splitting into H_2 and O_2 on alkali tantalate photocatalysts ATaO_3 (A = Li, Na, and K). *J Phys Chem B* 105:4285–4292
- Kato H, Kudo A (2002) Visible-light-response and photocatalytic activities of TiO_2 and SrTiO_3 photocatalysts codoped with antimony and chromium. *J Phys Chem B* 106:5029–5034
- Kato H, Kobayashi H, Kudo A (2002) Role of Ag^+ in the band structures and photocatalytic properties of AgMO_3 (M: Ta and Nb) with the perovskite structure. *J Phys Chem B* 106:12441–12447
- Kato H, Asakura K, Kudo A (2003) Highly efficient water splitting into H_2 and O_2 over Lanthanum-Doped NaTaO_3 photocatalysts with high crystallinity and surface nanostructure. *J Am Chem Soc* 125:3082–3089
- Kohtani S, Kazuhiro Y, Maekawa T, Iwase A, Kudo A, Miyabe H, Nakagaki R (2008) Loading effects of silver oxides upon generation of reactive oxygen species in semiconductor photocatalysis. *Phys Chem Chem Phys* 10:2986–2992
- Kong L, Chen H, Hua W, Zhang S, Chen J (2008) Mesoporous bismuth titanate with visible-light photocatalytic activity. *Chem Commun* 4977–4979
- Konta R, Kato H, Kobayashib H, Kudo A (2003) Photophysical properties and photocatalytic activities under visible light irradiation of silver vanadates. *Phys Chem Chem Phys* 5:3061–3065
- Kudo A, Hijii S (1999) H_2 or O_2 evolution from aqueous solutions on layered oxide photocatalysts consisting of Bi^{3+} with $6s^2$ configuration and d^0 transition metal ions. *Chem Lett* 1999:1103–1104
- Kudo A, Miseki Y (2009) Heterogeneous photocatalyst materials for water splitting. *Chem Soc Rev* 38:253–278

- Kudo A, Tanaka A, Domen K, Maruya K, Aika K, Onishi T (1988) Photocatalytic decomposition of water over NiO/K₄Nb₆O₁₇ catalyst. *J Catal* 111:67–76
- Kudo A, Omori K, Kato H (1999) A novel aqueous process for preparation of crystal form-controlled and highly crystalline BiVO₄ powder from layered vanadates at room temperature and its photocatalytic and photophysical properties. *J Am Chem Soc* 121:11459–11467
- Li X, Zang J (2009) Facile Hydrothermal Synthesis of Sodium Tantalate (NaTaO₃) Nanocubes and High Photocatalytic Properties. *J Phys Chem B* 113:19411–19418
- Li X, Zang J (2011) Hydrothermal synthesis and characterization of Lanthanum-doped NaTaO₃ with high photocatalytic activity. *Catal Commun* 12:1380–1383
- Li X, Kako T, Ye J (2007) 2-Propanol photodegradation over lead niobates under visible light irradiation. *Appl Catal A Gen* 326:1–7
- Li TB, Chen G, Zhou C, Shen ZY, Jin RC, Sun JX (2011a) New photocatalyst BiOCl/BiOI composites with highly enhanced visible light photocatalytic performances. *Dalton Trans* 40:6751–6758
- Li Y, Wang J, Yao H, Dang L, Li Z (2011b) Chemical etching preparation of BiOI/Bi₂O₃ heterostructures with enhanced photocatalytic activities. *Catal Commun* 12:660–664
- Liu H, Nakamura R, Nakato Y (2005) Bismuth–copper vanadate BiCu₂VO₆ as a novel photocatalyst for efficient visible-light-driven oxygen evolution. *ChemPhysChem* 6:2499–2502
- Liu H, Nakamura R, Nakato Y (2006) A visible-light responsive photocatalyst, BiZn₂VO₆, for efficient oxygen photoevolution from aqueous particulate suspensions. *Electrochem Solid State Lett* 9:G187–G190
- Miyauchi M, Nakajima A, Fujishima A, Hashimoto K, Watanabe T (2000) Photoinduced surface reaction on TiO₂ and SrTiO₃ films: photocatalytic oxidation and photoinduced hydrophilicity. *Chem Mater* 12:3–5
- Mohn CE, Stølen S (2011) Influence of the stereochemically active bismuth lone pair structure on ferroelectricity and photocatalytic activity of Aurivillius phase Bi₂WO₆. *Phys Rev B* 83:014103
- Monteiro OC, Marques R, Carvalho MD (2010) Photocatalytic studies of antimonate compounds prepared by a self-combustion route. *Mater Chem Phys* 119:418–423
- Noda Y, Lee B, Domen K, Kondo JN (2008) Synthesis of crystallized mesoporous tantalum oxide and its photocatalytic activity for overall water splitting under ultraviolet light irradiation. *Chem Mater* 20:5361–5367
- Ohno T, Tsubota T, Nakamura Y, Sayama K (2005) Preparation of S, C cation-codoped SrTiO₃ and its photocatalytic activity under visible light. *Appl Catal A Gen* 288:74–79
- Osterloh FE (2008) Inorganic materials for photochemical splitting of water. *Chem Mater* 20:35–54
- Piskunov S, Heifets E, Eglitis RI, Borstel G (2004) Bulk properties and electronic structure of SrTiO₃, BaTiO₃, PbTiO₃ perovskites: an ab initio HF/DFT study. *Comput Mater Sci* 29:165–178
- Prado AGS, Bolzon LB, Pedroso CP, Moura AO, Costa LL (2008) Nb₂O₅ as efficient and recyclable photocatalyst for indigo carmine degradation. *Appl Catal B Environ*. 82:219–224
- Reid AF (1967) Calcium Indate, an isotope of calcium ferrite and sodium scandium titanate. *Inorg Chem* 6:631–633
- Roof IP, Park S, Vogt T, Rassolov V, Smith MD, Omar S, Nino J, Zur Loye HC (2008) Crystal growth of two new niobates, La₂KNbO₆ and Nd₂KNbO₆: Structural, dielectric, photophysical, and photocatalytic properties. *Chem Mater* 20:3327–3335
- Roy SC, Varghese OK, Paulose M, Grimes CA (2010) Toward solar fuels: photocatalytic conversion of carbon dioxide to hydrocarbons. *ACS Nano* 4:1259–1278
- Sato J, Saito N, Nishiyama H, Inoue Y (2003a) Photocatalytic activity for water decomposition of indates with octahedrally coordinated d¹⁰ configuration. I. Influences of preparation conditions on activity. *J Phys Chem B* 107:7965–7969

- Sato J, Kobayashi H, Inoue Y (2003b) Photocatalytic activity for water decomposition of indates with octahedrally coordinated d10 configuration. II. Roles of geometric and electronic structures. *J Phys Chem B* 107:7970–7975
- Sato J, Kobayashi H, Saito N, Nishiyama H, Inoue Y (2003c) Photocatalytic activities for water decomposition of RuO₂-loaded AlInO₂ (A = Li, Na) with d¹⁰ configuration. *J Photochem Photobiol A: Chem* 158:139–144
- Sayama K, Mukasa K, Abe R, Abe Y, Arakawa H (2001) Stoichiometric water splitting into H₂ and O₂ using a mixture of two different photocatalysts and an IO₃⁻/I⁻ shuttle redox mediator under visible light irradiation. *Chem Commun*: 2416–2417
- Shenawi-Khalil S, Uvarov V, Kritsman Y, Menes E, Popov I, Sasson Y (2011) *Catal Commun* 12:1136–1141
- Shi Y, Feng S, Cao C (2000) Hydrothermal synthesis and characterization of Bi₂MoO₆ and Bi₂WO₆. *Mater Lett* 44:215–218
- Shi R, Lin J, Xu J, Zhu Y (2010) Visible-light photocatalytic degradation of BiTaO₄ photocatalyst and mechanism of photocorrosion suppression. *J Phys Chem C* 114:6472–6477
- Shimodaira Y, Kato H, Kobayashi H, Kudo A (2006) Photophysical properties and photocatalytic activities of bismuth molybdates under visible light irradiation. *J Phys Chem B* 110:17790–17797
- Singh J, Uma S (2009) Efficient photocatalytic degradation of organic compounds by ilmenite AgSbO₃ under visible and UV light irradiation. *J Phys Chem C* 113:12483–12488
- Sleight AW, Chen HY, Ferretti A, Cox DE (1979) *Mater Res Bull* 14:1571–1581
- Stoltzfus MW, Woodward PM, Seshadri R, Klepeis JH, Bursten B (2007) Structure and bonding in SnWO₄, PbWO₄, and BiVO₄: lone pairs vs inert pairs. *Inorg Chem* 46:3839–3850
- Su W, Wang J, Huang Y, Wang W, Wu L, Wang X, Liu P (2010) Synthesis and catalytic performances of a novel photocatalyst BiOF. *Script Mater* 62:345–348
- Sun M, Li D, Chen Y, Chen W, Li W, He Y, Fu X (2009) Synthesis and photocatalytic activity of calcium antimony oxide hydroxide for the degradation of dyes in water. *J Phys Chem C* 113:13825–13831
- Sun H, Fan W, Li Y, Cheng X, Li P, Zhao X (2010) Origin of the visible photocatalytic activity of n-doped In₂O₃: a quantum mechanical study. *J Phys Chem C* 114:3028–3036
- Tanaka T, Nojima H, Yoshida H, Nakagawa H, Funabiki T, Yoshida S (1993) Preparation of highly dispersed niobium oxide on silica by equilibrium adsorption method. *Catal Today* 16:297–307
- Tang J, Zou Z, Ye J (2004a) Photocatalytic decomposition of organic contaminants by Bi₂WO₆ under visible light irradiation. *Catal Lett* 92:53–56
- Tang J, Zou Z, Katagiri M, Kako T, Ye J (2004b) Photocatalytic degradation of MB on MIn₂O₄ (M = alkali earth metal) under visible light: effects of crystal and electronic structure on the photocatalytic activity. *Catal Today* 93:885–889
- Tang J, Zou Z, Ye J (2004c) Efficient photocatalytic decomposition of organic contaminants over CaBi₂O₄ under visible-light irradiation. *Angew Chem Int Ed* 43:4463–4466
- Walsh A, Yanfa Y, Huda MN, Al-Jassim MM, Wei SH (2009) Band Edge electronic structure of BiVO₄ elucidating the role of the Bi s and V d orbitals. *Chem Mater* 21:547–551
- Wang J, Yin S, Zhang Q, Saito F, Sato T (2003) Mechanochemical synthesis of SrTiO_{3-x}F_x with high visible light photocatalytic activities for nitrogen monoxide destruction. *J Mater Chem* 13:2348–2352
- Wang J, Yin S, Komatsu M, Zhang Q, Saito F, Sato T (2004) Photo-oxidation properties of nitrogen doped SrTiO₃ made by mechanical activation. *Appl Catal B Environ* 52:11–21
- Wang D, Zou Z, Ye J (2005) Photocatalytic water splitting with the Cr-Doped Ba₂In₂O₅/In₂O₃ composite oxide semiconductors. *Chem Mater* 17:3255–3261
- Wang W, Huang F, Lin X (2007) xBiOI-(1-x)BiOCl as efficient visible-light-driven photocatalysts. *Script Mater* 56:669–672
- Wiegel M, Edmond MHJ, Stobbe ER, Blasse G (1994) Luminescence of alkali niobates and tantalates. *J Phys Chem Solids* 55:773–778

- Wrighton MS, Ellis AB, Wolczanski PT, Morse DL, Abrahamson HB, Ginley DS (1976) Strontium titanate photoelectrodes. Efficient photoassisted electrolysis of water at zero applied potential. *J Am Chem Soc* 98:2774–2779
- Wu J, Duan F, Zheng Y, Xie Y (2007) Synthesis of Bi_2WO_6 nanoplate-built hierarchical nest-like structures with visible-light-induced photocatalytic activity. *J Phys Chem C* 111:12866–12871
- Xiao X, Zhang WD (2010) Facile synthesis of nanostructured BiOI microspheres with high visible light-induced photocatalytic activity. *J Mater Chem* 20:5866–5870
- Xu TG, Zhang C, Shao X, Wu K, Zhu YF (2006) Monomolecular-layer $\text{Ba}_5\text{Ta}_4\text{O}_{15}$ nanosheets: synthesis and investigation of photocatalytic properties. *Adv Funct Mater* 16:1599–1607
- Yao WF, Wang H, Xu XH, Shang SX, Hou Y, Zhang Y, Wang M (2003) Synthesis and photocatalytic property of bismuth titanate $\text{Bi}_4\text{Ti}_3\text{O}_{12}$. *Mater Lett* 57:1899–1902
- Ye J, Zou Z, Matsushita A (2003) A novel series of water splitting photocatalysts NiM_2O_6 ($M = \text{Nb}; \text{Ta}$) active under visible light. *Int J Hydrogen Energy* 28:651–655
- Yu J, Kudo A (2006) Effects of structural variation on the photocatalytic performance of hydrothermally synthesized BiVO_4 . *Adv Funct Mater* 16:2163–2169
- Zhang KL, Liu CM, Huang FQ, Zheng C, Wang WD (2006) Study of the electronic structure and photocatalytic activity of the BiOCl photocatalyst. *Appl Catal B: Environ* 68:125–129
- Zhang X, Ai Z, Jia F, Zhang L, Fan X, Zou Z (2007a) Selective synthesis and visible-light photocatalytic activities of BiVO_4 with different crystalline phases. *Mater Chem Phys* 103:162–167
- Zhang LH, Wang W, Chen ZG, Zhou L, Xu HL, Zhu W (2007b) Fabrication of flower-like Bi_2WO_6 superstructures as high performance visible-light driven photocatalysts. *J Mater Chem* 17:2526–2532
- Zhang X, Ai Z, Jia F, Zhang L (2008a) Generalized one-pot synthesis, characterisation and photocatalytic activity of hierarchical BiOX ($X = \text{Cl}, \text{Br}, \text{I}$) nanoplate microspheres. *J Phys Chem C* 112:747–753
- Zhang J, Shi F, Lin J, Chen D, Gao J, Huang Z, Ding X, Tang C (2008b) Self-assembled 3-D architectures of BiOBr as a visible light-driven photocatalyst. *Chem Mater* 20:2937–2941
- Zou Z, Arakawa H (2003) Direct water splitting into H_2 and O_2 under visible light irradiation with a new series of mixed oxide semiconductor photocatalysts. *J Photochem Photobiol A Chem* 158:145–162
- Zou Z, Ye J, Sayama K, Arakawa H (2001) Direct splitting of water under visible light irradiation with an oxide semiconductor photocatalyst. *Nature* 414:625–627

Chapter 8

Chalcogenides and Other Non-oxidic Semiconductors

Fernando Fresno

Although, as seen so far in this book oxidic materials constitute the main group of semiconductors employed for photocatalytic applications, some non-oxide compounds have been used for these purposes too. After oxides, sulphides are the most widely used photocatalysts, with special importance in water splitting applications. CdS and ZnS are two of the “classical” photocatalysts, which have been used since the early beginning of the research in this field. In particular, CdS presents the advantage of absorbing visible light ($E_g = 2.4$ eV), and it has become somewhat a “standard” photocatalyst for reactions undertaken under visible irradiation. More recently, some other sulphides, like ternary sulphides and solid solutions, have shown interesting photocatalytic properties. However, sulphides present the drawback of suffering anodic photocorrosion unless prevented with certain reaction conditions or with special modifications, which limits their applications as we will see below. At the end of the chapter, selenides and other non-oxidic semiconductors will be overviewed.

8.1 CdS, ZnS and Other Simple Sulphides

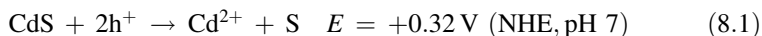
CdS can be considered as the most studied sulphide photocatalyst. It crystallises in three main phases. The hexagonal wurtzite-type structure is formed at normal conditions of temperature and pressure, although the cubic zinc blende type is also known in stable form in those conditions. In addition, CdS transforms into a rock salt structure at high pressure. Of the two former crystal forms, the wurtzite type is generally considered as the most photocatalytically active one, and it is indeed the most widely used and studied phase, because of its higher stability and ease of production. While the hexagonal phase has been observed in both bulk and

F. Fresno (✉)

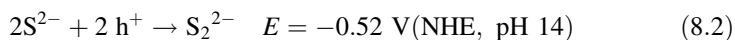
Laboratory for Environmental Research, University of Nova Gorica, Nova Gorica, Slovenia
e-mail: fernando.fresno@ung.si

nanocrystalline CdS, the cubic phase is only observed in the nanocrystalline material. As the size of CdS nanoparticles increases, the equilibrium crystal structure tends to change from the cubic type to the hexagonal one, being the critical size at which the cubic-to-hexagonal transformation occurs lower than 4 nm. Therefore, the hexagonal phase is obtained in most of the synthetic procedures, although a pure cubic phase can be attained if the synthesis conditions are carefully controlled. Nevertheless, as mentioned above, comparison of the two phases results in a higher photocatalytic activity of the wurtzite-type one (Bao et al. 2008).

The unit cell of wurtzite CdS is a hexagonal prism belonging to the space group P63mc (No. 186) and contains four atoms. As calculated by DFT (Nishidate et al. 2006), the valence band, of 4.3 eV width, arises from S 3p states and the conduction band mainly from Cd 5s states. The calculated band gap is 1.20 eV, showing the common underestimation of DFT calculations with respect to the experimental value of 2.42 eV at room temperature. Nevertheless, cadmium sulphide is a good example of a semiconductor experiencing quantum size effects: Its absorption onset can be tuned up to 4.5 eV as the size is varied from a macroscopic crystal down to the molecular regime; moreover, this quantum size effect can be maintained during the assembly of CdS films from quantum-sized particles (Zhang et al. 2009). With these electronic characteristics, CdS absorbs visible light with wavelengths lower than 510 nm, and the positions of its valence and conduction bands correspond to potentials of 1.7 and -0.66 V versus NHE at pH = 7, respectively. Accordingly, the photogenerated charge carriers are oxidative and reducing enough to oxidise water and organic molecules (or OH groups) and to reduce both molecular oxygen and water. Therefore, this semiconductor fulfils the thermodynamic requirements to be employed for water splitting and pollutant degradation reactions. However, a self-oxidation reaction under irradiation (anodic photocorrosion) occurs in CdS, and in sulphides, in general, according to the half-reaction:



which results in the dissolution of the catalyst. This reaction is much more favoured than water oxidation, so that sulphide photocatalysts can be hardly employed for stoichiometric water splitting on their own. In the presence of a suitable sacrificial electron donor, however, this phenomenon can be avoided. The use of a sulphide solution gives rise to hydrogen formation with simultaneous oxidation of sulphide to disulphide ions according to the anodic half-reaction:

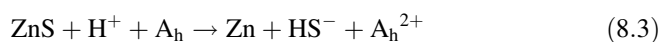


Further addition of a strongly reducing agent, such as sulphite or hypophosphite, is required to avoid the accumulation of disulphide ions, which, on the one hand, are reduced in competition with protons and, on the other hand, act as an optical filter reducing the light absorption of the photocatalyst. The activity of CdS in this sacrificial system is optimised at basic pH. In these conditions, and under irradiation with wavelengths larger than 300 nm, platinised CdS gave quantum yields up to 25 % for sacrificial hydrogen production in the first studies performed

in the early 1980s (Bubler et al. 1984). Without Pt as co-catalyst, the photocatalytic activity decreased by a factor of 10. By the same dates, Gratzel and co-workers (Kalyanasundaram et al. 1981) reported the suppression of photocorrosion in colloidal CdS particles co-loaded with RuO₂ and Pt that were able to stoichiometrically decompose water under irradiation with wavelengths larger than 400 nm. In this system, water oxidation occurs at the expense of photocorrosion. Other attempts that have been used in order to avoid photocorrosion of CdS include stabilisation in micelles, coupling with other semiconductors (see Chap. 15), and doping (Osterloh 2008). In any case, the current record of sacrificial hydrogen production in the visible range corresponds to nanostructured CdS (in the form of nanosheets or hollow nanorods) loaded with nanocrystalline Pt as co-catalyst, which achieves a quantum yield of 60 % at 440 nm (Bao et al. 2008).

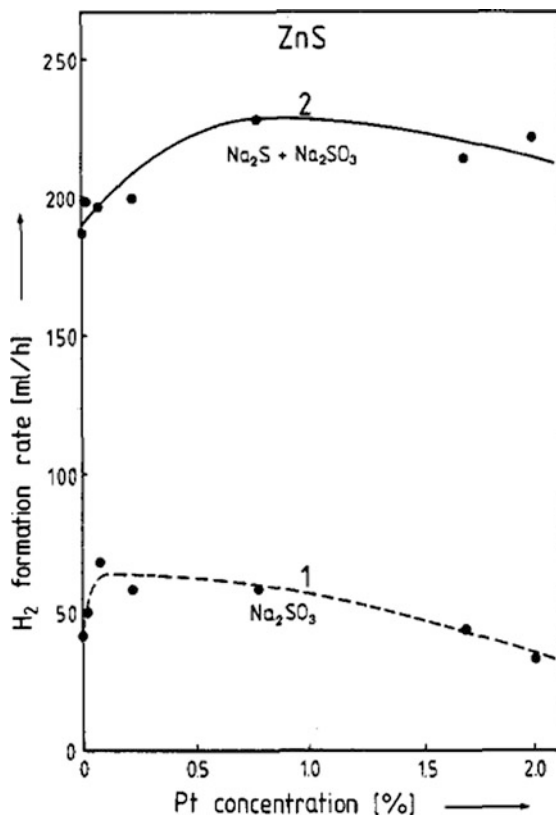
Zinc sulphide is the other major metallic sulphide investigated for photocatalytic applications. ZnS exists in two main polymorphs. In zinc blende, or sphalerite (cubic), the anions form a cubic close-packed structure and the Zn²⁺ ions are placed in tetrahedral positions. In the high-temperature hexagonal wurtzite structure, the cations exist in the tetrahedral positions of the hexagonal close packing of the anions (Rao and Pisharody 1975). Apparently, both crystalline forms have very similar photocatalytic activity (Reber and Meier 1984). Most of the bands in the electronic structure of zinc sulphide consist of hybridised orbitals due to the high covalent bonding character. Thus, the valence band maximum mainly consists of slightly hybridised S 3p orbitals and Zn 4s4p orbitals. On the other hand, the conduction band minimum consists of hybrid Zn 4s4p orbitals with a certain contribution of S 3p (Tsuji et al. 2004). The optical properties of ZnS have been extensively investigated because of its luminescent behaviour. The band gap is 3.6 eV, and therefore, it is photocatalytically active only under UV irradiation. Similarly to CdS, it suffers from anodic photocorrosion, decomposing in the absence of a sacrificial electron donor. However, in the presence of a suitable sacrificial reagent, it is highly active for photocatalytic water reduction to hydrogen even in the absence of a metallic co-catalyst. Nevertheless, using Pt as a co-catalyst and under irradiation with UV light (313 nm), ZnS has led to a quantum yield as high as 90 % for photocatalytic hydrogen evolution from an aqueous solution containing sulphide and sulphite (Reber and Meier 1984). Anyway, as observed in Fig. 8.1, the differences in the hydrogen formation rates with or without the presence of Pt are rather small, in contrast to what is observed with CdS.

The high activity of unplatinated ZnS has been ascribed to the formation of metallic Zn nuclei on the surface, which would act as electron transference catalysts, resulting from a cathodic photodecomposition according to the following reaction, where A(sub)h denotes a hole scavenger:



As with TiO₂, attempts to shift the photocatalytic response of ZnS towards visible wavelengths have been carried out. Doping with different metal cations

Fig. 8.1 Influence of Pt concentration (wt %) on the hydrogen formation rate obtained with ZnS. Reproduced with permission from Reber and Meier (1984). Copyright American Chemical Society



leads to absorption tails in the visible region and gives rise to activity for sacrificial hydrogen production with QY of, for example, 1.3 and 3.7 % at 420 nm for Ni- and Cu-doped ZnS, respectively (Kudo and Miseki 2009; Osterloh 2008).

Solid solutions of CdS and ZnS have also been explored as water splitting photocatalysts. Both sulphides form a solid solution with wurtzite structure in the whole composition range $Zn_{1-x}Cd_xS$ with $0 \leq x \leq 1$. The absorption edge of the resulting material gradually shifts towards longer wavelengths with increasing Cd content, adding visible light absorption to the interesting photocatalytic properties of ZnS. Thus, hydrogen is evolved under visible light irradiation when Cd is introduced in the ZnS lattice, reaching a maximum at a value of $x = 0.3$ (Navarro et al. 2009). This maximum should correspond to a compromise of different factors influenced by the solid solution composition, such as light absorption, conduction band position and crystal size. The activity can be further increased by a high-temperature treatment leading to improved crystallinity.

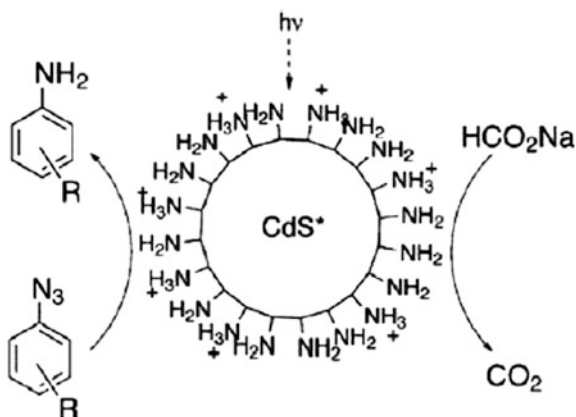
Other simple sulphides are worth to be mentioned regarding photocatalytic hydrogen production. Thus, WS₂, formed by layers of trigonal-prismatic WS₆ units, and with a 1.7 eV direct band gap, produces hydrogen from EDTA solutions when loaded onto SiO₂ and sensitised by fluorescein. Bi₂S₃ (1.3 eV) on its own

produces hydrogen from a sulphide aqueous solution at intermediate rates that decline after 100 min. These rates can be improved by 25 % using Pt as co-catalyst (Osterloh 2008).

Regarding environmental photocatalysis, the corrosion-related drawbacks explain why photocatalytic detoxification is not a main application of sulphide photocatalysts. Not only the catalyst is unstable under the reaction conditions (generally low pollutant concentrations that do not inhibit sulphide oxidation by acting as sacrificial electron donors), but also, with catalyst dissolution, metallic ions, especially toxic if CdS is used, may be liberated to the environment, either directly, in the case of water remediation, or by means of leaching processes when dealing with immobilised catalysts for air purification. Nevertheless, a number of works have been devoted to their application to pollutant degradation (Hernández-Alonso et al. 2009). Obviously, the (un)stability under the photocatalytic reaction conditions depends on the nature of the catalyst, and, for instance, the visible-light-absorbing sulphides In_2S_3 and SnS_2 have been revealed to be more stable than CdS in the degradation of aqueous formic acid (Lucena et al. 2012a, b), being active in all the range of absorbed wavelengths.

Cadmium sulphide has also been employed in photocatalytic selective transformations of organic molecules, discussed in Chap. 3. Due to its relatively high conduction band energy, it is especially interesting for reduction reactions (Palmisano et al. 2007). For example, in nitrobenzene reduction in the presence of cyclohexene, the use of a semiconductor drastically modifies the final products, with CdS leading to the highest yield of reduced compounds if compared to TiO_2 and WO_3 . The photocatalytic reduction of aryl azides to amines in water over CdS nanoparticles takes place with comparatively high quantum yields (near to 0.5 %) and with almost complete selectivity towards amines, at room temperature and pressure and at neutral pH. A schematic mechanism of this reaction is depicted in Fig. 8.2. Other examples of the use of CdS for photocatalytic organic synthesis are the production of thio-compounds, the selective cyclisation of amino acids and the formation of bromo-derivatives from phenol (Hernández-Alonso et al. 2009).

Fig. 8.2 Photoreduction of azides to amines by using CdS or CdSe as catalysts and sodium formate as a sacrificial electron donor. Reproduced with permission from Palmisano et al. (2007). Copyright American Chemical Society



Even if both CdS and ZnS exhibit adequate band energies for the photocatalytic CO₂ reduction reaction, they have been much less used than TiO₂ for this purpose (see Chap. 4). The formation of carboxylic acids with up to 2 carbon atoms (glyoxylic, formic and acetic acids) as the main products has been reported using colloidal CdS particles, although with very low quantum efficiencies. Meanwhile, the use of ZnS has led to formic acid and methanol as the final products with efficiencies up to 5.9 % (Roy et al. 2010). In the case of ZnS, sulphur vacancies have been postulated as the active sites for CO₂ reduction.

8.2 Complex Sulphides

Some sulphides containing more than one type of metal atoms have also been tested as photocatalytic materials. For instance, several indium-containing sulphides have shown interesting activities for sacrificial hydrogen evolution. NaInS₂, with a structure consisting of layers of edge-sharing InS₆ octahedra and sodium cations in the interlayer spaces, absorbs light with wavelength below 550 nm, corresponding to a band gap of 2.3 eV. Under visible light irradiation (440 nm), the Pt-loaded photocatalyst gives rise to hydrogen evolution from aqueous SO₃²⁻ solutions with a quantum yield of 6 % (Kudo and Miseki 2009). Pt-loaded AgIn₅S₈ ($E_g = 1.8$ eV) shows a good performance too, with QY = 5.3 % at 411 nm using K₂SO₃ and Na₂S as sacrificial reagents. A similar amount of hydrogen is evolved using ZnIn₂S₄ ($E_g = 2.3$ eV) in the same conditions. On the contrary, CuInS₂, with zinc blende structure, and CuIn₅S₈, with spinel-type structure, produce very low amounts of hydrogen in the presence of sulphite under irradiation with wavelengths larger than 300 nm, leading to QY of 0.02 % at 460 nm in the case of the latter and 6 times lower in that of the former.

Chalcopyrite-structured AgGaS₂ has a band gap energy of 2.6 eV, with the valence band consisting of hybridised S 3p and Ag 4d orbitals and the conduction band formed mainly by the contribution of S 3p and Ga 4s4p. Under visible light irradiation, it is active for water reduction in the presence of sacrificial reagents, with the onset of the action spectrum in good accordance with that of the diffuse reflectance UV-vis spectrum. This activity is dramatically increased by noble metal deposition. In particular, Rh(1 %wt)-AgGaS₂ gives a quantum yield of 25 % for hydrogen evolution at 440 nm from an aqueous Na₂S and K₂SO₃ solution (Kudo and Miseki 2009).

Other interesting sulphide-based photocatalysts are those formed by zeolite-like, open-framework structures containing supertetrahedral clusters as depicted in Fig. 8.3 (Zheng et al. 2005a). In addition to the improved catalytic properties expected from the high surface area of a porous material, the electron-hole recombination rate is likely to be reduced, because, unlike in a dense solid, the charge carriers do not need to travel all the way to the external surface of the particle for a reaction to occur. Moreover, it is possible to tune the band structure of these materials by controlling the framework architecture and composition.

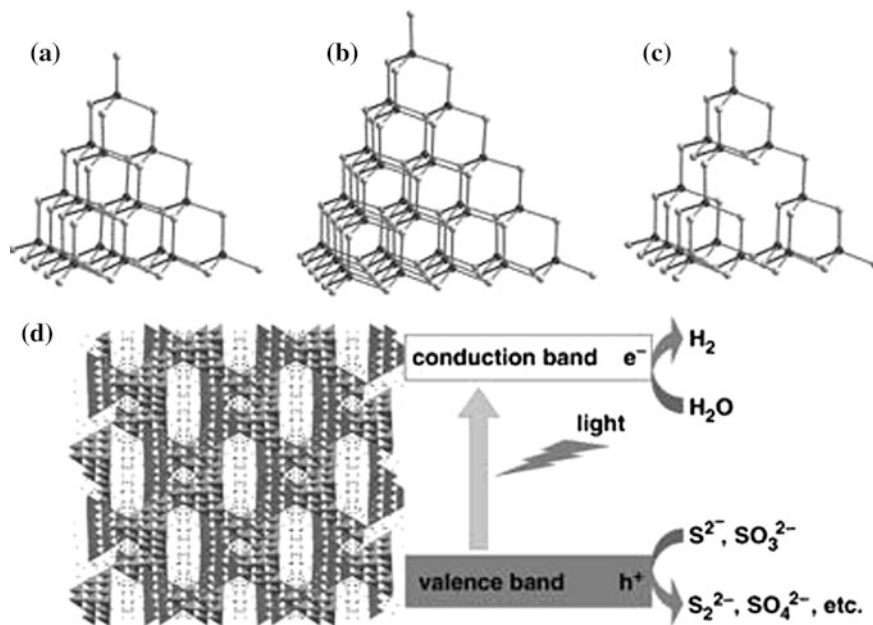


Fig. 8.3 Diagrams of representative supertetrahedral clusters, chalcogenide frameworks and their photocatalytic activity: **a** T4 cluster; **b** T5 cluster; **c** coreless T4 cluster; **d** the 3D diamond-type superlattice in $\text{Na}_{14}\text{In}_{17}\text{Cu}_2\text{S}_{35} \cdot x\text{H}_2\text{O}$: Unconnected spheres are water molecules and Na^+ sites. Reproduced with permission from Zheng et al. (2005a). Copyright Wiley-VCH

Both the band gap and the conduction band minimum are expected to increase when porosity is crated in a crystalline semiconductor, which provides a higher reductive power for hydrogen generation from water under UV light. As an example, let us compare the band gap of the above-mentioned NaInS_2 (2.3 eV) to that of the open-framework structure $\text{LiInS}_2 \cdot x\text{H}_2\text{O}$ (3.3 eV). On the contrary, the incorporation of different transition metals is a convenient means to reduce the band gap by raising the valence band maximum in order to obtain visible light absorption while keeping the activity for water reduction. For instance, the introduction of Cu^+ ions into a In–S framework reduces the band gap to 2.0 eV in $\text{Na}_{14}\text{In}_{17}\text{Cu}_2\text{S}_{35} \cdot x\text{H}_2\text{O}$. Under visible light irradiation, hydrogen is produced over this sulphide from an aqueous Na_2S solution with a quantum yield of about 3.7 % at 420 nm in the absence of any co-catalyst. This yield is much higher than those obtained with the already mentioned, and compositionally related, non-porous CuInS_2 and CuIn_5S_8 . Other photocatalysts of this type that have been successfully tested in similar conditions for hydrogen evolution are $\text{Na}_{16}\text{Mn}_{13}\text{In}_{22}\text{S}_{54} \cdot x\text{H}_2\text{O}$ and $\text{Na}_{10}\text{Cd}_4\text{In}_{16}\text{S}_{33} \cdot x\text{H}_2\text{O}$. A special case in this type of materials is $\text{Na}_5\text{In}_7\text{S}_{13} \cdot 6\text{H}_2\text{O}$. Unusual Sn_4 tetrahedra were reported for the first time in this open-framework sulphide. It has a band gap of 3.2 eV and shows photocatalytic activity under UV light for hydrogen generation from an aqueous solution containing Na_2SO_3 as a sacrificial agent even in the absence of any co-catalyst (Zheng et al. 2005b).

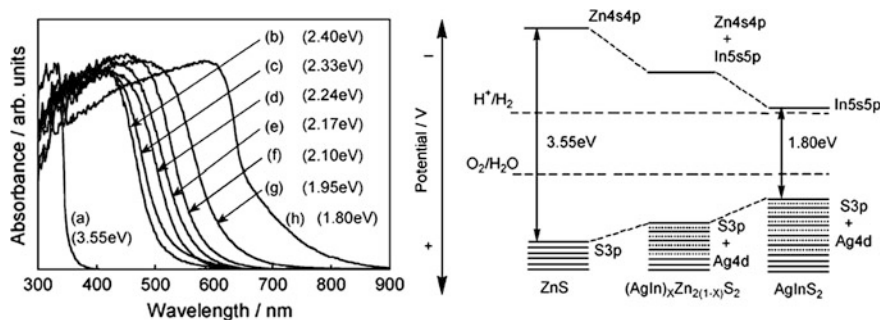


Fig. 8.4 On the *left*, diffuse reflectance spectra of $(\text{AgIn})_x\text{Zn}_{2(1-x)}\text{S}_2$ solid solutions; the values of x are (a) 0, (b) 0.17, (c) 0.22, (d) 0.29, (e) 0.33, (f) 0.40, (g) 0.5 and (h) 1. On the *right*, band structures of $(\text{AgIn})_x\text{Zn}_{2(1-x)}\text{S}_2$ solid solutions, ZnS and AgInS_2 . Reproduced with permission from Tsuji et al. (2004). Copyright American Chemical Society

As mentioned in the previous section regarding CdS and ZnS, solid solutions of more complex sulphides have also been tested for photocatalytic water splitting. The utilisation of these solid solutions may permit a fine tuning of the band gap of the final material. For example, the absorption onset in the diffuse reflectance spectra of solid solutions in the system $\text{AgInS}_2\text{-ZnS}$, with wurtzite-type structure, shifts monotonically with composition variation, as shown in Fig. 8.4 (left). DFT calculations indicate that both the conduction band minimum and the valence band maximum are shifted to intermediate energies with respect to the two extreme compositions, as schematically depicted in Fig. 8.4 (right).

These solid solutions give rise to hydrogen evolution from aqueous sulphite, being the best results obtained with Pt-loaded $(\text{AgIn})_x\text{Zn}_{2(1-x)}\text{S}_2$ in which $x = 0.22 - 0.29$. The activity maximum observed in this composition range is ascribed to the facts that, with lower x values, In and Ag orbitals are not forming bands but discrete levels and that, with higher AgInS_2 contents, the conduction band position is too low. In optimised reaction conditions, the Pt-loaded $(\text{AgIn})_{0.22}\text{Zn}_{1.56}\text{S}_2$ photocatalyst gives a quantum yield of 20 % at 420 nm. On the other hand, substituting Cu for Ag in $\text{Pt/Cu}_{0.09}\text{In}_{0.09}\text{Zn}_{1.82}\text{S}_2$ results in a lower quantum yield at the same wavelength, with Cu 3d orbitals contributing to the valence band formation (Kudo and Miseki 2009). Similar results in terms of crystal and band structure are obtained with the three-component system $\text{CuInS}_2\text{-AgInS}_2\text{-ZnS}$, which, after Ru deposition, gives rise to a remarkable QY of 7.4 % at 520 nm. This solid solution can use visible light with wavelength up to 700 nm. It should be emphasised, however, that these materials are only active in the presence of suitable sacrificial reagents (which nevertheless will be interesting if sulphur-containing by-products of chemical industries are used as electron donors), while in pure water only hydrogen but not oxygen is produced, the oxidation reaction corresponding in this case to photocorrosion (Tsuji et al. 2004).

8.3 Selenides and Other Non-oxidic Semiconductors

A few semiconductors other than oxides and sulphides have been tested as photocatalysts, including some selenides (mainly CdSe and ZnSe), silicon-derived solids and nitrides. We shall not consider the latter here, however, since they will be covered in [Chap. 14](#).

Some selenides, mainly CdSe, have been proposed for photocatalytic processes. As in the case of sulphides, their stabilities (both relative to photocorrosion and to contact with water) are lower compared to oxides but, in any case, their visible light absorption and their extensive use in photovoltaic devices make them potentially interesting photocatalysts. CdSe with wurtzite structure is a narrow band gap semiconductor (indirect, 1.74 eV in the bulk material) mainly used in photovoltaic devices (Trindade et al. 2001). Similarly to CdS, its band gap energy is quite sensitive to size effects, and E_g values of 1.90 and 2.1 eV have been reported for CdSe nanocrystals (Ho and Yu 2006; Zhu et al. 2000). In photocatalysis, it is more often used in coupled systems as a visible light sensitiser for wider band gap materials like TiO₂, rather than on its own (see [Chap. 15](#)). By itself, CdSe shows a modest photocatalytic activity under visible light that may be due to a fast electron–hole recombination because of its narrow band gap. Nevertheless, it induces hydrogen evolution under visible light irradiation in the presence of sacrificial reagents. This process was first demonstrated by Uchihara and co-workers (1990) with Pt–CdSe powders suspended in an aqueous solution consisting of sodium sulphite and EDTA, the former acting as hole scavenger and the latter displacing the flatband potential of CdSe towards more negative values. The hydrogen yields obtained with CdSe are much lower than those achieved with CdS, though. As an example of the application of CdSe to the photocatalytic oxidation of organic pollutants, ca. 10 % degradation of aqueous 4-chlorophenol is achieved after irradiation at wavelengths larger than 400 nm for 8 h (Ho and Yu 2006). The positive point is that the whole of the degraded pollutant is converted into CO₂ according to TOC measurements. Charge separation, and hence photocatalytic activity, of CdSe can apparently be enhanced by the addition of gold as a co-catalyst, as shown by methylene blue reduction under irradiation at 473 nm using methanol as a hole scavenger (Costi et al. 2008). A considerably higher conversion is obtained with Au-capped CdSe nanorods ([Fig. 8.5](#)) compared to the bare selenide structures, although the quantum yield is still very low. In comparison with CdS, a different mechanism in the reduction of methyl viologen, related to their different conduction band positions, has been proposed (Stroyuk et al. 2010).

ZnSe, with wurtzite structure and a band gap of 2.70 eV, is another important II–VI selenide semiconductor that has been tested as a possible photocatalyst. The apparently promising results obtained under UV light, nevertheless, need to be assessed (Xiong et al. 2007). As a final example, β -Ag₂Se nanostructures have been found to degrade (decolourise) RhB solutions under UV irradiation, although the mineralisation degrees were not reported (Cao et al. 2010).

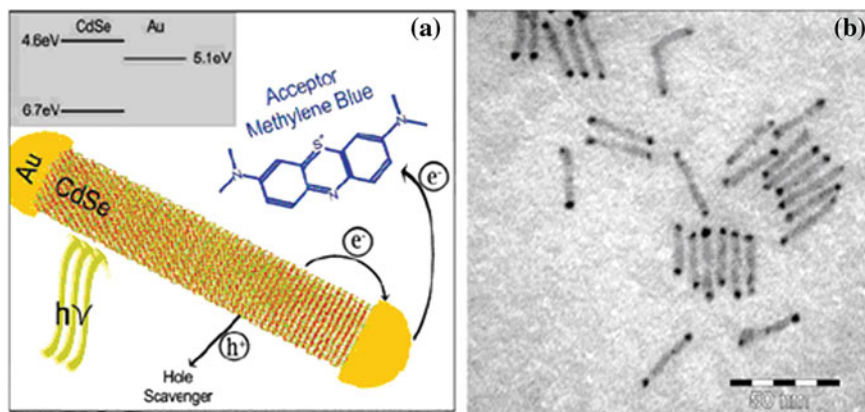


Fig. 8.5 **a** Scheme of a light-induced charge separation mechanism in Au-capped CdSe nanorods. **b** TEM image of Au-capped CdSe nanorods. Reproduced with permission from Costi et al. (2008). Copyright American Chemical Society

Titanium disilicide (TiSi_2) is an excellent electronic material, essential in the ultra-large-scale integration semiconductor industry. It absorbs nearly the entire visible spectrum, from ca. 360 to 800 nm (grey in colour). TiSi_2 was recently reported as a promising photocatalyst for solar water splitting (Ritterskamp et al. 2007). According to the authors, catalytic centres are formed in situ by an initial TiSi_2 photooxidation process that, at the same time, prevents further photocorrosion of the semiconductor. XPS analyses, together with powder X-ray diffraction, suggest that a layer of TiO_2 and SiO_2 , either amorphous or too thin to be detected by XRD, is formed at this first stage, with concomitant non-photocatalytic hydrogen production. Afterwards, hydrogen and oxygen are formed under visible light irradiation, although only the former is evolved through a photocatalytic reaction. Oxygen is desorbed in the dark at 100 °C, revealing a high O_2 storage ability of TiSi_2 ; thereafter, the material is capable of repeating the process. The catalytic nature of the reaction is demonstrated by (1) hydrogen production exceeds the stoichiometric value of a hypothetical total oxidation of TiSi_2 by water; (2) in the overall process, H_2 and O_2 are produced in 2:1 molar ratio, as corresponds to water splitting; and (3) ^{18}O -labelled dioxygen is found in the gas phase during reactions with ^{18}O -enriched water.

Pt-loaded indium phosphide (InP), with zinc blende structure and a band gap of 1.25 eV, has been reported to lead to hydrogen evolution under visible light from a variety of sacrificial solutions, among which sulphide ions led to the highest amount of evolved hydrogen (Ohmori et al. 2000). The catalytic nature of this reaction, however, has been doubted in a recent review (Osterloh 2008).

Ag_3PO_4 is a body-centred cubic structure with an indirect band gap of 2.36 eV. The bottom of the conduction band is mainly composed of hybridised Ag 5s5p with a small contribution of P 3s orbitals, whereas the top of the valence band is composed of hybridised Ag 4d and O 2p orbitals. According to the relative

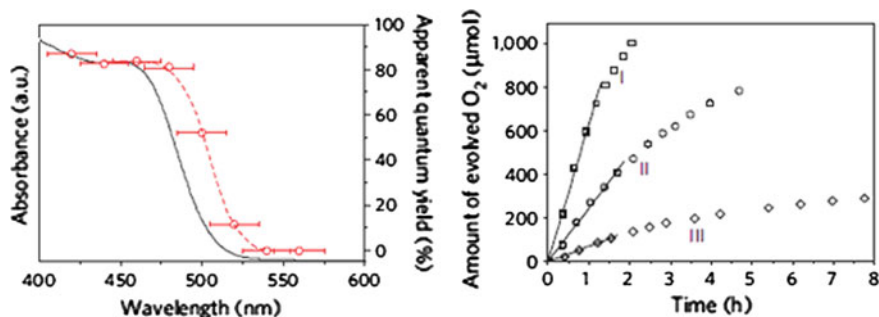


Fig. 8.6 *Left* Ultraviolet–visible diffuse reflectance spectrum (*continuous line*) and apparent quantum yields (*symbols*) of the Ag_3PO_4 semiconductor plotted as a function of wavelength of the incident light. *Right* O_2 evolution from aqueous AgNO_3 solutions under visible illumination ($\lambda > 400 \text{ nm}$) over (I) Ag_3PO_4 , (II) BiVO_4 and (III) WO_3 . Reproduced with permission from Yi et al. (2010). Copyright Nature Publishing Group

positions of its valence and conduction bands, silver orthophosphate is able to oxidise water to oxygen but not to reduce protons, so it has been tested for the evolution of O_2 under visible light irradiation in the presence of AgNO_3 as an electron scavenger (Yi et al. 2010). In this reaction, a maximum apparent quantum yield of ca. 80 % at 480 nm is obtained. The quantum yield dependence on irradiation wavelength closely fits the absorption spectrum of the catalyst (Fig. 8.6), which, together with experiments with isotope-labelled water, confirms the photocatalytic nature of oxygen evolution. However, in the absence of a sacrificial electron acceptor, and in accordance with the higher (more positive) reduction potential of the pair $\text{Ag}_3\text{PO}_4/\text{Ag}$ with respect to H^+/H_2 , silver orthophosphate decomposes in water upon irradiation. This semiconductor also decolourises aqueous solutions of organic dyes in the presence of AgNO_3 , although, according to TOC measurements, mineralisation only occurs to some extent, if any (Yi et al. 2010). A more complex phosphate-like $\text{Li}_9\text{Fe}_3(\text{P}_2\text{O}_7)_3(\text{PO}_4)_2$ exhibits photocatalytic activity under visible light irradiation ($\lambda > 400 \text{ nm}$) for the degradation of methylene blue and phenol solutions. In addition, it is capable of reducing water to hydrogen in the presence of I^- as electron donor (Ji 2010).

As already mentioned in Chap. 4, SiC was one of the first semiconductors tested for photocatalytic CO_2 reduction (Inoue et al. 1979). As a result of its high conduction band energy, the yield of reduced compounds such as formic acid and methanol was higher than with other semiconductors like TiO_2 , ZnO or CdS . Silicon carbide is diverse in band gap energies because it exists in over 200 crystalline forms, among which the most common types are the cubic 3C and the hexagonal 6H and 4H, which have band gaps of 2.2, 3.02 and 3.20 eV, respectively (Fan and Chu 2010). Under visible light and without any co-catalyst, a green mixture of the polytypes 6H and 3C leads to hydrogen evolution from different aqueous sacrificial solutions, being those containing sulphide ions the most efficient hole scavengers. At basic pH, the amount of evolved hydrogen is

significantly increased. In pure water, however, SiC apparently suffers anodic photocorrosion, with only hydrogen and no oxygen evolution (Gao et al. 2007). In the form of nanowires, the cubic zinc-blende-structured 3H polytype has been reported to oxidise gaseous acetaldehyde under UV irradiation. Apparently, the formation of a passivation layer of SiO₂ on the SiC surface is positive for the photocatalytic activity (Zhou et al. 2006).

References

- Bao N, Shen L, Takata T, Domen K (2008) Self-templated synthesis of nanoporous CdS nanostructures for highly efficient photocatalytic hydrogen production under visible light. *Chem Mater* 20:110–117
- Bubler N, Meier K, Reber JF (1984) Photochemical hydrogen production with cadmium sulfide suspensions. *J Phys Chem* 88:3261–3268
- Cao H, Xiao Y, Lu Y, Yin J, Li B, Wu S, Wu X (2010) Ag₂Se complex nanostructures with photocatalytic activity and superhydrophobicity. *Nano Res* 3:863–873
- Costi R, Saunders AE, Elmaleh E, Salant A, Banin U (2008) Visible light-induced charge retention and photocatalysis with hybrid CdSe-Au nanodumbbells. *Nano Lett* 8:637–641
- Fan J, Chu PK (2010) Group IV nanoparticles: synthesis, properties, and biological applications. *Small* 6:2080–2098
- Gao Y, Wang Y, Wang Y (2007) Photocatalytic hydrogen evolution from water on SiC under visible light irradiation. *Reac Kinet Catal Lett* 91:13–19
- Hernández-Alonso MD, Fresno F, Suárez S, Coronado JM (2009) Development of alternative photocatalysts to TiO₂: challenges and opportunities. *Energy Environ Sci* 2:1231–1257
- Ho W, Yu JC (2006) Sonochemical synthesis and visible light photocatalytic behavior of CdSe and CdSe/TiO₂ nanoparticles. *J Mol Catal A: Chem* 247:268–274
- Inoue T, Fujishima A, Konishi S, Honda K (1979) Photocatalytic reduction of carbon dioxide in aqueous suspensions of semiconductor powders. *Nature* 277:637–638
- Ji F, Li C, Zhang J (2010) Hydrothermal synthesis of Li₉Fe₃(P₂O₇)₃(PO₄)₂ nanoparticles and their photocatalytic properties under visible-light illumination. *ACS Appl Mater Interfaces* 2:1674–1678
- Kalyanasundaram K, Borgarello E, Duonghong D, Gratzel M (1981) Cleavage of water by visible-light irradiation of colloidal CdS solutions; inhibition of photocorrosion by RuO₂. *Angew Chem Int Ed Engl* 20:987–988
- Kudo A, Miseki Y (2009) Heterogeneous photocatalyst materials for water splitting. *Chem Soc Rev* 38:253–278
- Lucena R, Fresno F, Conesa JC (2012a) Hydrothermally synthesized nanocrystalline tin disulphide as visible light-active photocatalyst: Spectral response and stability. *Appl Catal A Gen* 415–416:111–117
- Lucena R, Fresno F, Conesa JC (2012b) Spectral response and stability of In₂S₃ as visible light-active photocatalyst. *Catal Commun* 20:1–5
- Navarro RM, Sánchez-Sánchez MC, Alvarez-Galvan MC, del Valle F, Fierro JLG (2009) Hydrogen production from renewable sources: biomass and photocatalytic opportunities. *Energy Environ Sci* 2:35–54
- Nishidate K, Sato T, Matsukura Y, Baba M, Hasegawa M (2006) Density-functional electronic structure calculations for native defects and Cu impurities in CdS. *Phys Rev B* 74:035210
- Ohmori T, Mametsuka H, Suzuki E (2000) Photocatalytic hydrogen evolution on InP suspension with inorganic sacrificial reducing agent. *Int J Hydrogen Energy* 25:953–955

- Osterloh FE (2008) Inorganic materials for photochemical splitting of water. *Chem Mater* 20:35–54
- Palmisano G, Augugliaro V, Pagliaro M, Palmisano L (2007) Photocatalysis: a promising route for 21st century organic chemistry. *Chem Commun* 3425–3437
- Rao CNR, Pisharody KPR (1975) Transition metal sulphides. *Progr Solid State Chem* 10:207–270
- Ritterskamp P, Kuklya A, Wüstkamp MA, Kerpen K, Weidenthaler C, Demuth M (2007) A titanium disilicide derived semiconducting catalyst for water splitting under solar radiation—reversible storage of oxygen and hydrogen. *Angew Chem Int Ed* 46:7770–7774
- Reber JF, Meier K (1984) Photochemical production of hydrogen with zinc sulfide suspensions. *J Phys Chem* 88:5903–5913
- Roy SC, Varghese OK, Paulose M, Grimes CA (2010) Toward solar fuels: photocatalytic conversion of carbon dioxide to hydrocarbons. *ACS Nano* 4:1259–1278
- Stroyuk OL, Rayevska OY, Kozytzkiy AV, Kuchmiy SY (2010) Electron energy factors in photocatalytic methylviologen reduction in the presence of semiconductor nanocrystals. *J Photochem Photobiol A Chem* 210:209–214
- Trindade T, O'Brien P, Pickett NL (2001) Nanocrystalline semiconductors: synthesis. Properties Perspectives *Chem Mater* 13:3843–3858
- Tsuji I, Kato H, Kobayashi H, Kudo A (2004) Photocatalytic H₂ evolution reaction from aqueous solutions over band structure-controlled (AgIn)_xZn₂(1 – x)S₂ solid solution photocatalysts with visible-light response and their surface nanostructures. *J Am Chem Soc* 126:13406–13413
- Uchihara T, Matsumura M, Ono J, Tsubomura H (1990) Effect of Ethylenediaminetetraacetic Acid on the Photocatalytic Activities and Flat-Band Potentials of Cadmium Sulfide and Cadmium Selenide. *J Phys Chem* 94:415–418
- Xiong S, Xi B, Wang C, Xi G, Liu X, Qian Y (2007) Solution-phase synthesis and high photocatalytic activity of wurtzite ZnSe ultrathin nanobelts: a general route to 1D semiconductor nanostructured materials. *Chem Eur J* 13:7926–7932
- Yi Z, Ye J, Kikugawa N, Kako T, Ouyang S, Stuart-Williams H, Yang H, Cao J, Luo W, Li Z, Liu Y, Withers RL (2010) An orthophosphate semiconductor with photooxidation properties under visible-light irradiation. *Nature Mater* 9:559–564
- Zhang H, Chen G, Bahnemann DW (2009) Photoelectrocatalytic materials for environmental applications. *J Mater Chem* 19:5089–5121
- Zheng N, Bu X, Vu H, Feng P (2005a) Open-framework chalcogenides as visible-light photocatalysts for hydrogen generation from water. *Angew Chem Int Ed* 44:5299–5303
- Zheng N, Bu X, Feng P (2005b) Na₅(In₄S)(InS₄)₃·6H₂O, a Zeolite-like structure with unusual SIn₄ tetrahedra. *J Am Chem Soc* 127:5286–5287
- Zhou W, Yan L, Wang Y, Zhang Y (2006) SiC nanowires: a photocatalytic nanomaterial. *Appl Phys Lett* 89:013105
- Zhu J, Palchik O, Chen S, Gedanken A (2000) Microwave assisted preparation of CdSe, PbSe, and Cu_{2–x}Se nanoparticles. *J Phys Chem B* 104:7344–7347

Chapter 9

Single-Site Photocatalysts: Photoactive Species Dispersed on Porous Matrixes

Silvia Suárez

The unique band-gap structure of semiconductor-based photocatalysts allows the mobility of charge carriers towards the surface, where they can react with adsorbed molecules. However, photocatalytic processes can also take place at isolated photoactive centres dispersed on materials with no significant absorption of radiation in the UVA–Vis range (Hernandez-Alonso et al. 2009). This special configuration is generally referred to as *single-site* photocatalyst, and because of its special properties, it should be differentiated from conventional photocatalysts based upon semiconductor materials (Anpo and Thomas 2006; Anpo et al. 2009). A sketch to illustrate the processes that take place on semiconductor-based and single-site photocatalysts is shown in Fig. 9.1. The electronic levels of a single-site photocatalyst are discrete and not continuous like in a semiconductor, and consequently, the photocatalytic process occurs without transportation of charge carriers. The active sites are constituted by transition metal cations, whose d orbitals are involved in charge transfer transitions. The distance between the electron–hole pairs generated upon irradiation is very short as compared to conventional semiconductor-based photocatalysts, providing the system with unique properties. In order for the photocatalytic process to occur, the active sites must be located at the surface of the catalyst so that the interaction between the reagent molecules is possible. Thus, substrates with high specific surface area are desired because the dispersion of cationic species plays a pivotal role in the photocatalytic performance.

Single-site photocatalysts can be used in applications such as pollutants elimination, CO₂ photoreduction, production of chemicals with added value and superhydrophilic surfaces. As the active sites are spatially isolated, they modulate the product selectivity. This feature permits to characterize and identify at atomic scale the active sites and to ascertain the interactions between the reactants by means of techniques such as XANES, EXAFS, FTIR, UV–Vis and EPR. Furthermore, it

S. Suárez (✉)

División de Energías Renovables, Avda, Grupo de Tratamiento Fotocatalítico de Contaminantes en Aire, Complutense 40, 28040 Madrid, Spain
e-mail: silvia.suarez@ciemat.es

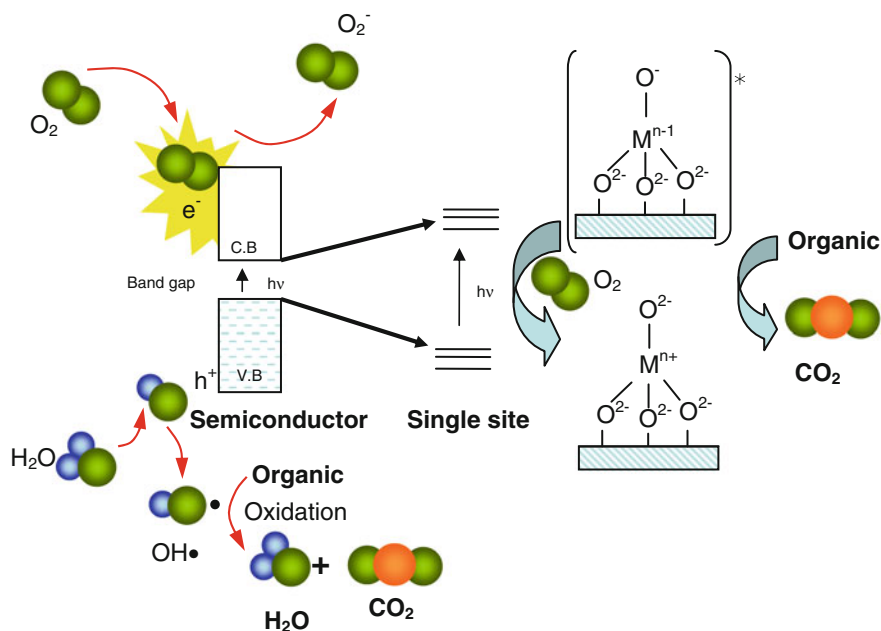


Fig. 9.1 Comparison between the photooxidation processes taking place on a semiconductor-based photocatalyst (*left*) and on a single-site photocatalyst (*right*). M transition metal

opens up the possibility to study the evolution of the single-site photocatalyst surface under realistic in situ conditions, analysing the effect of different operation parameters such as temperature, pressure and component concentration (Anpo and Thomas 2006).

Zeolites and mesoporous materials are the perfect hosts to prepare single-site photocatalysts due to their ordered and open structure. Tetrahedrally coordinated metal oxide centres, such as TiO_2 , V_2O_5 , Cr_2O_3 and Mo_2O_3 moieties, can be implanted and isolated from the silica matrix.

This chapter is divided in two sections, the first one dealing with zeolite-based materials and the second with the use of mesoporous structures. In both cases, the main characteristics, the synthetic routes and the catalytic properties of these single-site photocatalysts will be detailed, and the benefits of their use in different applications will be discussed.

9.1 Metal-Substituted Zeolites

Zeolites are crystalline aluminosilicates based on silica or alumina tetrahedral units linked through an oxygen atom to form a three-dimensional framework, which has well-defined micropore and channel structures and great capacity for ion

exchange. There are excellent books, reviews and scientific articles dealing with the most relevant characteristics and properties of this type of materials. The reader is referred to the following examples: (Breck 1974; Barrer 1978; Kalyanasundaram 1987; Dyer 1988; Ramamurphy 1991; van Bekkum et al. 1991; Auerbach et al. 2003). Although many naturally occurring zeolites are known, since early 1950s, they are usually synthesized in order to modify some of their properties. The main advantages of the zeolite structure as solid matrix are their large surface area, ranging between 350 and 700 m² g⁻¹, and their internal pore volume of around 0.1 cm³ g⁻¹, with a defined pore size in the range of 1 nm. The channels often contain cations (frequently Na⁺), which compensate the negative framework charge, and zeolitic water. The micropore structure, in the range of nm, significantly improves the internal mass transfer of reactants to the active sites. Furthermore, the synthetic zeolite structure can be tuned to improve the selectivity to desired products (Corma and Garcia 2004).

Besides, zeolites present additional distinctive properties for photocatalytic applications. The most important features are listed below:

- Photochemical stability, high thermal resistance and high chemical inertness.
- High adsorption capacity, combining together adsorption and photocatalytic properties in the so-called hybrid materials (Suárez et al. 2008; Hewer et al. 2009).
- Shape selectivity associated with their channelled porous structure.
- Quantum confinement effect due to the influence of the cavity dimensions on the electronic structure of some guest organic molecules.
- The zeolite framework can participate in the electron transfer process, either as electron acceptor or as donor (García and Roth 2002).
- The interaction between guest species with the zeolite framework is mainly associated with the electron-donating properties of the zeolite (Hashimoto 2003).
- Transparency to UV–Vis radiation above 240 nm, which makes possible the penetration of light into the opaque solid to reach guest molecules located in intra-particle positions.
- The chemical framework and out-of-the-framework compositions can be easily modified by varying the Si/Al ratio or by the presence of certain types of cations, such as Na⁺ or K⁺.
- Presence of Brønsted and Lewis acid sites, being the former responsible for the zeolites ion-exchange ability (Weitkamp 2000).

Although there are a large number of materials with the zeolite structure, only few of them have found application in the field of photocatalysis. Among those, the most used photocatalytic applications are zeolites X and Y, and ZSM-5. The structure and the representative porous system of these two types of aluminosilicates are illustrated in Fig. 9.2. Twenty-four linked tetrahedra lead to a cuboctahedron sodalite unit, which is the base of the faujasite structure (sodalite units connected via hexagonal faces). Both zeolites X and Y have the faujasite structure, being their main difference the $n_{\text{Si}}/n_{\text{Al}}$ ratio, $1 \leq n_{\text{Si}}/n_{\text{Al}} \leq 1.5$ and $n_{\text{Si}}/n_{\text{Al}} \geq 1.5$,

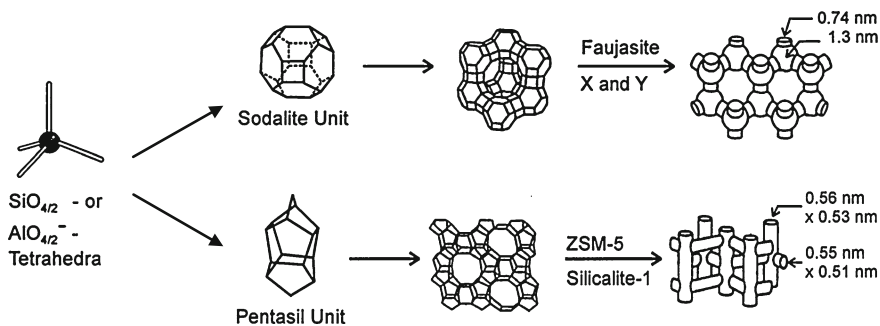


Fig. 9.2 Structure of the most used zeolites for photocatalytic applications showing the pore system and dimensions [adapted with permission from (Weitkamp 2000). Copyright Elsevier]

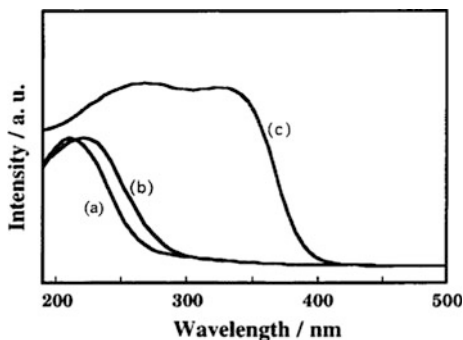
respectively. Faujasite possesses three-dimensionally connected microchannels consisting of supercages with a diameter of 1.30 nm and bridging tunnels with a smaller diameter of 0.74 nm. Their high adsorption capacity and excellent mass transfer properties make these materials ideal candidates for industrial applications. ZSM-5 present MFI structure, which consists of pentasil units containing intersecting systems of ten-membered rings pores, one straight and one sinusoidal.

9.1.1 Characterization Techniques

In general, the available literature related to single sites on zeolites focuses mainly on the incorporation of titania into the zeolitic structure. For the sake of simplicity, TiO_2 has been selected to show the most used characterization techniques to determine whether a synthesized material is in a single-site structure or not. Nevertheless, the field of single sites is not only limited to titanium oxide, and other transition metals, such as vanadium, chromium and molybdenum, to name but the most representative ones, have been incorporated as single sites.

In general, zeolite-based photocatalysts consist of highly dispersed titanium oxide species in tetrahedral coordination anchored to the aluminosilicate matrix. As a consequence, a shift of the absorption band onset towards a lower wavelength (blue shift) with respect to that of bulk anatase is produced. This can be attributed to a direct transition in oxide clusters although modifications in the band-gap energy due to a size quantization effect have been also suggested as a possible cause of these changes in the optical properties (Serpone et al. 1995; Corrent et al. 2001), as commented in [Chaps. 2](#) and [11](#). It is generally assumed that single-site photocatalyst activity arises from the ligand-to-metal charge transfer (LMCT) at the excited state, that is, photoinduced single-electron transfer from O^{2-} species, which are considered as ligand, to the Ti^{4+} atom. The observation of

Fig. 9.3 Diffuse reflectance UV–Vis absorption spectra of Ti/ZSM-5 catalysts prepared by different methods: (a) ion exchange, (b) impregnation and (c) P25 (reference) [reproduced with permission from (Zhang et al. 2001). Copyright American Chemical Society]



photoluminescence can be considered as indicative of the presence of nanoscopic TiO_2 moieties, since bulk anatase and rutile are non-luminescent materials. UV–Vis spectroscopy, along with XANES and EXAFS techniques, is essential to determine the presence of isolate atoms in the structure. Besides, it is worth mentioning that the detection of crystalline TiO_2 by XRD analysis discards the single-site configuration type.

In Fig. 9.3, an example of the absorption edge blue shift of Ti/ZSM-5 prepared by ion exchange compared to TiO_2 P25 is shown. The band with a maximum at around 230 nm is associated with Ti single sites in tetrahedral coordination. The decrease in the edge energy of the LMCT transitions obtained by changing the preparation method from impregnation to ion exchange may be associated with the increase in the number of nearest Ti atoms, which suggests a modification in the degree of polymerization of surface Ti atoms. The zeolite crystalline structure and the metal loading define the size of the encapsulated TiO_2 clusters and, therefore, the band gap and the onset of the optical adsorption.

The edge region in the X-ray absorption spectra can provide information on the environment, geometry and electronic structure of the absorbing atom. Figure 9.4 shows the X-ray absorption near-edge structure (XANES) and Fourier transform extended X-ray absorption fine structure (FT-EXAFS) spectra for Ti–O in tetrahedral coordination (black line) and Ti–O–Ti in octahedral coordination (dot line).

The lack of inversion symmetry in the tetrahedral environment results in a single intense pre-edge peak located at around 4965 eV, which was assigned to the normally symmetry-forbidden $1s$ – $3d$ transition. When octahedral Ti is present as extra-framework anatase, or in systems with significant disorder in the Ti–O distances and Ti–O–Si angles, the pre-edge peak becomes less intense and broader and shifts to higher energy values. These two different environments are represented in the FT-EXAFS spectrum by a strong peak at around 1.6 Å, characteristic of isolated four-coordinated titanium ions, and 2.7 Å, assigned to octahedral titanium oxide species.

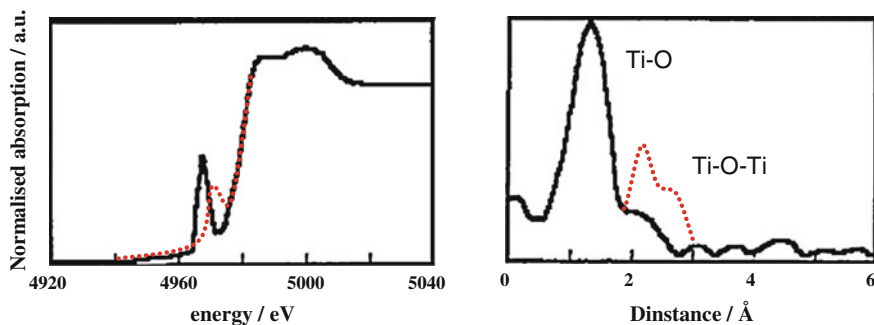


Fig. 9.4 XANES (*left*) and FT-EXAFS (*right*) spectra of Ti-ZSM-5 [adapted with permission from (Zhang et al. 2001) Copyright American Chemical Society]

9.1.2 Synthesis Methods

Hydrothermal methods are the usual way to prepare zeolites. This process requires a source of silicon, the most typical ones being fumed silica (Cab-O-Sil), sodium silicate or $\text{Si}(\text{OEt})_4$, a source of aluminium, such as aluminium oxyhydroxide, $\text{Al}(\text{OEt})_3$, sodium aluminate and other Al^{3+} salts and a templating ion, generally an organic cation or a hydrated metal ion. The reaction is conducted at high pH by adding alkali metal hydroxide or quaternary ammonium hydroxide.

Different heteroatoms (other than aluminium or silicon) can be inserted into the zeolite structure as T-atoms (tetrahedral metals), including titanium, vanadium, iron and other transition metals. The easiness of the process is determined by the density of negative framework charge, cation-exchange capacity, density and strength of Brønsted acid sites, thermal stability, unit cell dimensions and hydrophobic/hydrophilic characters of the surface.

Transition metal ions, frequently titanium, can be introduced into the zeolite framework either by the hydrothermal synthesis or by post-synthesis methods. Ti-containing β -zeolite has been synthesized by means of hydrothermal methods. Anpo et al. have achieved a precise control of their hydrophobic and hydrophilic characters (Ikeue et al. 2001). Ti- β zeolites synthesized with hydroxide ions (e.g. N, N'-dibenzyl-4,4'-trimethylene bis(N-methylpiperidinium) dihydroxide) exhibit hydrophilic properties, whereas those synthesized with fluoride ions, such as tetraethylammonium fluoride, have hydrophobic properties. Titanosilicalite (TS-1) presents a mordenite-inverted MFI structure, and it has been synthesized by a sol-gel method with silicon and titanium alkoxides as precursors and tetrapropylammonium hydroxide (TPAOH) as structure-directing agent (Taramasso et al. 1983). Yamamoto and co-workers have developed a novel alkoxide-free synthesis method involving a mechanochemical process (Yamamoto et al. 2006). In this method, silica and titania nanoparticles, used as silicon and titanium sources instead of the corresponding alkoxides, are milled under dry conditions. The milling treatment causes a mechanochemical reaction between the silica and

tania, resulting in the formation of an amorphous silica–titania composite powder, precursor of TS-1. Micrometre-sized TS-1 with good catalytic activity has been successfully obtained through crystallization via hydrothermal treatments. The incorporation of vanadium or chromium leads to similar structures (Hari Prasad Rao et al. 1992; Anpo et al. 1999, 2003).

Among post-synthesis methods, ion exchange has been extensively used. The negative charge porous framework and the small and mobile cations sitting on the pores endow zeolites with very high ion-exchange ability. In this simple synthetic approach, the zeolite is suspended in an aqueous solution of a salt containing the desired cation to be exchanged by Na^+ , in conditions which favour the mass transfer phenomena, such as high temperatures and strong stirring. The synthesis of titania clusters (Liu et al. 1993) can be accomplished by using mixed oxalate salts, such as $(\text{NH}_4)_2(\text{TiNO})(\text{C}_2\text{O}_4)_2$. Another alternative is the absorption of titanium tetraisopropoxide within the zeolite in isopropyl alcohol with citric acid, followed by addition of ethylene glycol (Park et al. 2003). In contrast, impregnation method, which has also been used to prepare Ti/ZSM-5 photocatalysts using aqueous solutions of titanium ammonium oxalate, does not allow a proper control of the metal dispersion, and it generally leads to the formation of aggregates (Zhang et al. 2001). Other transition metals have also been incorporated into zeolites by ion exchange. For example, Cu^{2+} -ZSM-5 has been prepared using an aqueous $\text{Cu}(\text{NH}_3)_4^{2+}$ solution (Matsuoka and Anpo 2003a). Evacuation of the original Cu^{2+} -ZSM-5 at high temperature allows the reduction of Cu^{2+} , obtaining Cu^+ -ZSM-5, active in the photodecomposition of nitric oxide (Anpo et al. 1994). In the same line, Ag^+ /ZSM-5 can be prepared in aqueous $\text{Ag}(\text{NH}_3)_2^+$ solution (Matsuoka and Anpo 2003b). The ion-exchange technique has some limitations: in some cases, the hydrated cations become too bulky to enter inside zeolite pores; in others, the precursor salt containing the cation in the desired valence state is unstable or insoluble in water. In these situations, solid-state ion exchange emerges as a suitable alternative. The zeolite, usually in its H^+ form, and a precursor containing the in-going cation, for example V_2O_5 , are intimately mixed and heated under an inert atmosphere (Higashimoto et al. 2000; Kerc et al. 2003).

A great deal of attention has been devoted as well to incorporate metals such as Pd, Pt, Ag and Au, into the zeolite matrix through the proper synthesis method in order to control the particle size, which will define the photocatalytic properties of these materials. The metal can be introduced into the zeolite pores by ion exchange with the ammonia-complexed cationic form, for example $[\text{Pd}(\text{NH}_3)_4]^{2+}$ or $[\text{Pt}(\text{NH}_3)_4]^{2+}$, followed by thermal removal of the ammine ligands and the creation of Brønsted acid sites by the metal reduction.

The photoassisted deposition (PAD) method is frequently used for the incorporation of metals into zeolitic structures with controlled size (Yamashita et al. 2007). The process is based on UV–Vis irradiation of the zeolitic material in an aqueous solution containing the metal precursor. Hexachloroplatinic acid is habitually used for the incorporation of Pt into the silica matrix, but other salts or mixtures of salts can be employed as precursors. For example, nanosized Pd–Au

alloy particles have been prepared with aqueous solutions of PdCl_2 and HAuCl_4 under UV–Vis irradiation at 25 °C.

9.1.3 Applications of Single-Site Zeolites

The high dispersion of the metal moieties in the zeolite structure generally leads to higher photocatalytic activity and selectivity as compared to conventional photocatalysts. Although the photocatalytic properties of single site in zeolites have been less explored than those of mesoporous materials, some remarkable results have been obtained for pollution remediation, in particular for the decomposition of NO into N_2 and O_2 , and for the removal of organic compounds in air or water phase. Promising results have been also obtained for CO_2 photoreduction with H_2O to produce methanol or methane, and the synthesis of high added value organic products.

An important aspect in the field of pollutants degradation is that the development of zeolites with hydrophobic properties will certainly improve their adsorption ability towards organic compounds such as alcohols and organic halides, both diluted in water or in gas phase, and consequently, higher quantum yields can be expected. In this way, TS-1 has been successfully applied, for instance, to the decomposition of 4-nitrophenol (Lee et al. 2003) and monoethanolamine (Ban et al. 1999) from aqueous solutions. Concerning the abatement of pollutants in gas phase, highly dispersed tetrahedral titanium species in a zeolite matrix are amongst the most promising photocatalysts reported to promote direct NO reduction to N_2 under UV irradiation (Takeuchi et al. 2009), with higher reaction rate and selectivity to N_2 than to pure TiO_2 . A well-accepted reaction path for this photocatalytic process, depicted in Fig. 9.5, is based on the weak adsorption of two NO molecules on Ti^{4+} species. Once excited at a precise wavelength, an electron transfer takes place with the subsequent formation of Ti^{3+} and O^- , which can react with the two NO molecules, resulting in the formation of N_2 and O_2 .

Fig. 9.5 Proposed mechanism for the photocatalytic decomposition reaction of NO into N_2 and O_2 adapted from (Takeuchi et al. 2009)

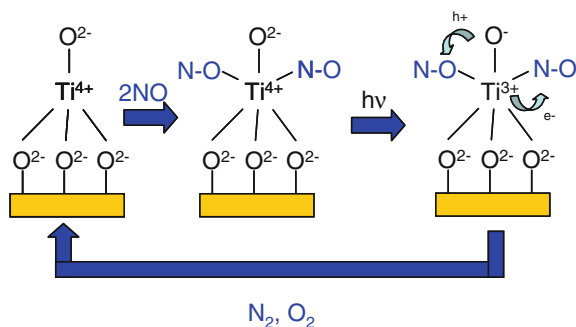
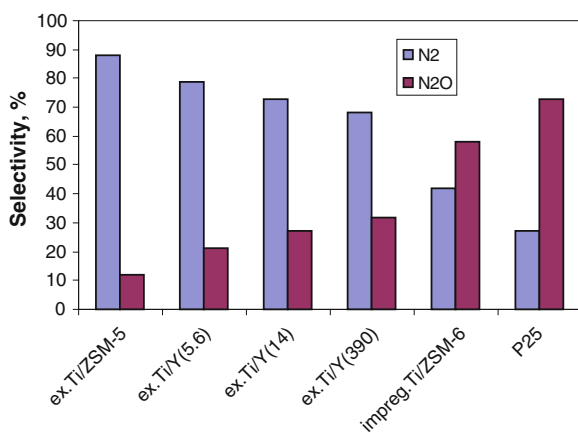


Figure 9.6 shows the selectivity to N_2 and N_2O obtained with different photocatalysts based on zeolites in comparison with TiO_2 P25. It can be observed that N_2 selectivity of zeolites is higher than on P25, but especially on the ion-exchanged ones, and increasing at lower Si/Al ratios (figuring in brackets). This photocatalytic performance can be associated with the different coordination geometry and polymerization degree of surface titanium oxide species. In the case of aggregated particles of octahedrally coordinated titanium dioxide, the photo-generated electrons and holes react with NO molecules at different sites, and the N and O formed in the primary NO decomposition process immediately react with close NO molecules, forming NO_2 and N_2O . Thus, the photocatalytic reaction mechanism on the highly dispersed isolated tetrahedrally coordinated TiO_4 species is completely different from the mechanism operating on titanium oxide semiconductor particles (Anpo et al. 1985). Polymerization of titanium oxide species, usually observed when titanium oxide is incorporated by impregnation methods, results in a lower fraction of Ti–O–Si bonds. As a consequence, the photocatalytic performance significantly decreases.

This behaviour has also been reported for Cu^+ /zeolite photocatalysts, which exhibit superior photocatalytic performances when copper species are incorporated into ZSM-5 rather than into Y-zeolite. This observation has been rationalized by taking into account the narrower pores of ZSM-5 that could enhance the electrostatic field on the Cu^+ sites (Anpo and Thomas 2006). This family of catalysts has been proved to be very efficient in the NO decomposition reaction at temperatures as low as 2 °C (Anpo et al. 1994). The performance of V-oxide species highly dispersed within zeolite frameworks has also been investigated in this reaction both in the absence and in the presence of reducing agents. (Higashimoto et al. 2000). The reaction rate increases in the presence of propane, leading to the formation of propylene-, ethylene- and oxygen-containing compounds, such as CH_3CHO and CO_2 , in addition to N_2 . The abstraction of a hydrogen atom from the hydrocarbon by a charge-transfer excited state ($V^{4+}-O^-$)* plays a significant role in the promotion of the reaction, propane being more active than more stable

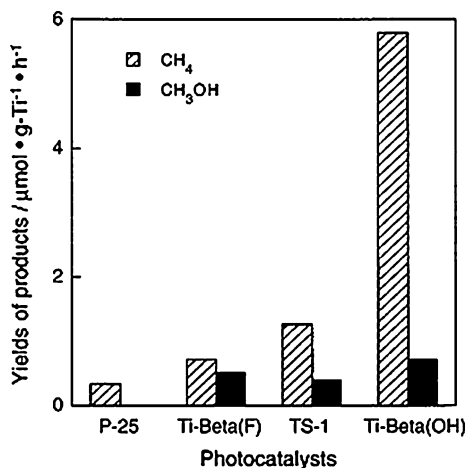
Fig. 9.6 Influence of the nature of the photocatalyst on the formation of N_2 and N_2O during the NO decomposition reaction. Preparation method: ex. = ion exchange, impreg. = impregnation; figures in brackets: Si/Al ratio. Adapted from (Zhang et al. 2001)



molecules such as methane or ethane. $\text{Ag}^+/\text{ZSM-5}$ also presents high photoactivity in the decomposition of NO, although N_2O and NO_2 are also detected. The electron transfer from the excited Ag^+ ion to the Π antibonding molecular orbital of the NO molecule plays a significant role in the photocatalytic decomposition of NO. The higher performance of $\text{Ag}^+/\text{ZSM-5}$ (Matsuoka et al. 1996) compared to $\text{Cu}^+/\text{ZSM-5}$ (Anpo et al. 1994) has been assigned to the high chemical stability of the Ag^+ ion and to its efficient interaction with the NO molecule.

As commented in Chap. 4, the generation of valuable chemicals via CO_2 photoreduction in the presence of H_2O and the photocatalytic decomposition of H_2O into H_2 and O_2 have been successfully performed with this type of materials (Takeuchi et al. 2009). During the hydrogenation of CO_2 with single-site photocatalysts, Ikeue et al. (2001) have detected the formation of CH_3OH and CH_4 as main reaction products, as well as CO , O_2 , C_2H_4 and C_2H_6 in minor proportion. As shown in Fig. 9.7, the photocatalytic activity of hydrophilic Ti- β (OH) is slightly higher than that of P25, almost non-active in this case; however, a remarkable photocatalytic performance is observed on the hydrophobic Ti- β (F). On the other hand, CdS/zeolite catalysts have been reported active for water splitting, generating H_2 in the presence of suitable sacrificial agents (Tel'biz et al. 1994). In general, it can be concluded that the zeolite nature affects the photocatalytic activity and selectivity of photocatalytic reactions. The generation of a high concentration of $(\text{Ti}^{3+}-\text{O}^-)^*$ is directly related to the reactivity, and more selective materials are obtained with tetrahedrally coordinated Ti. In any case, it is worth noting that due to the optical characteristic of these materials, photoactivation requires, in general, UV-C irradiation and this fact excludes the use of sunlight.

Fig. 9.7 Methane and methanol formations during the photocatalytic reduction of CO_2 with H_2O [reproduced with permission from (Ikeue et al. 2001). Copyright American Chemical Society]



9.2 Metal-Loaded Mesostructured Silica

Ordered mesoporous materials, discovered by Mobil Oil scientists in 1992, opened up new possibilities for modulating the selectivity of catalytic reactions. Mobil crystalline material number 41 (MCM-41) is one of the most commonly employed, mainly due to its large surface area and to its structural arrangement, consisting of hexagonally ordered pores with diameters ranging from 2 to 10 nm. Along with the MCM-41 hexagonal phase, cubic MCM-48 and laminar MCM-50 arrange the so-called M41S family. Six years later, silica materials with much larger pores, between 4.6 and 30 nm, were produced at the University of California, Santa Barbara (Zhao et al. 1998). The material was named Santa Barbara Amorphous-type material or SBA-15. This solid has also a hexagonal array of pores, with some microporous contribution. In addition, other mesoporous silicas, like FSM-16 (Zama et al. 2000) or TUD-1 (Hamdy et al. 2006; Mul et al. 2008), have been used as matrixes for obtaining different single-site photocatalysts.

The main difference between mesoporous materials and zeolites is that the former present larger pore size, lying within the mesopore range, but constituted by non-crystalline pure silica walls (Vartuli et al. 1998). Owing to the lack of active sites in the pure siliceous mesoporous solid, much effort has been devoted to increase their activity by chemical modification (Kerc et al. 2003).

In this section, the main relevant details concerning the synthesis and applications of metal-loaded mesoporous structures will be discussed, in particular for MCM-41, one of the most representative mesoporous molecular sieves.

9.2.1 Characterization Techniques

The preservation of the mesoporous structure and the successful implantation of a semiconductor in a single-site configuration can be determined by N₂ adsorption–desorption isotherms, XRD, TEM, UV–Vis, XANES and EXAFS spectroscopies (Rey et al. 1996). An example of the results obtained by these techniques is shown in Fig. 9.8 for M-oxide moieties (M = V-, Cr-, Mo-, W-). The typical type IV N₂ adsorption–desorption isotherm of a mesoporous material, indicating the presence of mesopores with an average pore diameter of around 3 nm, is shown in Fig. 9.8A. The XRD pattern shows a sharp peak between 2 and 4°, depending on the metal selected, ascribed to the (100) reflection of the hexagonally packed mesoporous structure. It is important to notice that diffraction lines of bulk metal oxides are not observed in the X-ray diffraction pattern, indicating that the metal oxide moieties are present as highly dispersed phases within mesoporous silica matrixes (Fig. 9.8B).

The UV–Vis spectrum of the Ti-mesoporous silica thin film (MSTF) shows an absorption band in the UV region below 280 nm, with a peak at 215 nm attributed to the LMCT (ligand-to-metal charge transfer) transition from O²⁻ to Ti⁴⁺, as also

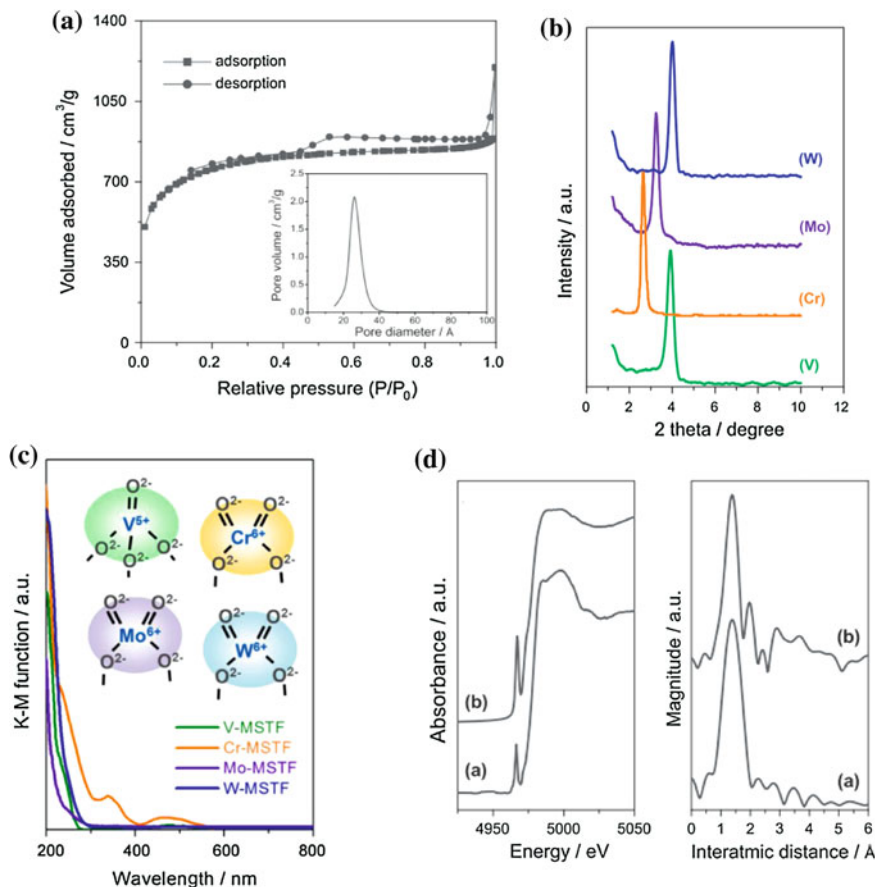


Fig. 9.8 **A** N₂ adsorption–desorption isotherms (Ti-), **B** XRD, **C** UV–Vis spectra (V-, Cr-, Mo- and W-) and **D** XANES, EXAFS curves (Ti-); **(a)** Ti-containing ordered mesoporous thin films (MSTF) and **(b)** tetrapropyl orthotitanate, obtained for M-substituted mesoporous materials [reproduced with permission from (Horiuchi and Yamashita 2011). Copyright Elsevier]

described for zeolites in Sect. 9.1.1. An example of the typical UV–Vis spectra obtained with other metal-substituted mesoporous materials is shown in Fig. 9.8C. Clearly, transition metal oxide moieties in the M-MSTF (M = V, Cr, Mo and W) exist in isolated and tetrahedrally coordinated states within mesoporous silica matrixes. The XANES and EXAFS spectra of Ti-MSTF and tetrapropyl orthotitanate (TPOT), which is a reference sample for tetrahedrally coordinated TiO₄ species, are also shown in Fig. 9.8D. Both samples record XANES spectra with a sharp pre-edge peak at 4967 eV, attributed to the 1s–3d transition in the regular tetrahedron structure (Blasco et al. 1995). In addition, the FT-EXAFS spectrum shows only one peak at 1.4 Å, corresponding to the neighbouring oxygen atom (Ti–O bond). These results confirm that Ti-oxide moieties incorporated into the

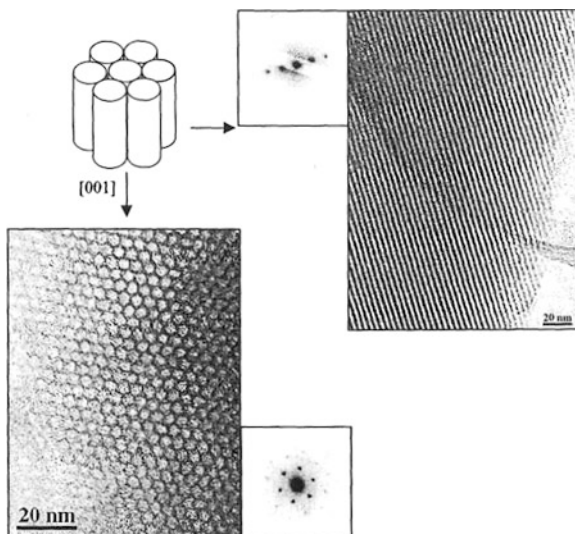
silica matrix exist as isolated and tetrahedrally coordinated species (Horiuchi and Yamashita 2011).

9.2.2 Synthesis

The preparation of mesostructured materials can be accomplished by different approaches, such as the hydrothermal and sol-gel methods. (Davis and Lobo 1992; Casci 1994; Zhao et al. 1996). The process involves a silica precursor and a surfactant, typically an organic amine, in aqueous media. The physical properties of the final material depend on the synthesis conditions (temperature, pH, reaction time, type of surfactant and surfactant-to-silica molar ratio). Thus, the surface area of the final material may range from 400 to 1700 m² g⁻¹, the pore size between 1.5 and 10 nm and pore volumes of up to 1.1 cm³ g⁻¹ can be obtained (Kresge 1992). The typical mesoporous structure of MCM-41 is shown in Fig. 9.9. The hexagonal pore structure, constituted by ordered parallel channels, can be clearly appreciated in the TEM micrographs.

MCM-41 silica can be prepared by one of two possible electrostatic assembly pathways. The S⁺I⁻ pathway involves electrostatic interactions and charge matching between positively charged assemblies of rod-like micelles of quaternary ammonium surfactants (S⁺) and anionic silicate species (I⁻). The second pathway, the so-called counter-ion-mediated S⁺X⁻I⁺ pathway, makes use of the same surfactant cations under strongly acidic conditions in order to assemble positively charged silica precursors (I⁺). As in the case of zeolites, a great body of work has been accomplished by different research groups in order to incorporate titanium

Fig. 9.9 TEM micrographs of two possible orientations, parallel and perpendicular to (001) plane, for the MCM-41 structure (Díaz 2001)



moieties into the structure of mesoporous molecular sieves, generally using titanium alkoxide as a precursor (Blasco et al. 1995; Alba et al. 1996). Ti-containing MCM-41 has been synthesized in acidic systems by using either ionic surfactants or primary amine as template (Tanev et al. 1994; Blasco et al. 1995; Yamashita et al. 1998). The Ti/Si ratio is the key parameter for maintaining the silica structure. Mesoporous materials prepared with $\text{Ti/Si} = 0.1$ lead to the collapse of the silica framework due to the excess of Ti in the final solid.

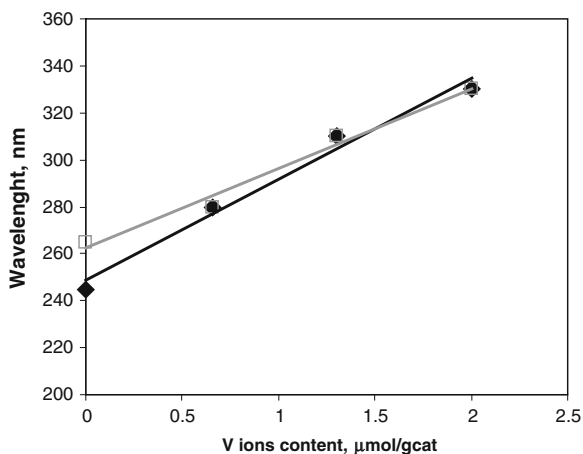
Ti substitution via ambient temperature electrostatic assembly S^+I^- and $\text{S}^{\circ}\text{I}^{\circ}$ allows an almost complete incorporation of titanium into the mesoporous framework, whereas $\text{S}^+\text{X}^-\text{I}^+$ impedes the titanium incorporation (Zhang et al. 1996, 2000). On the other hand, the temperature-controlled microwave-assisted synthesis method shortens the crystallization time as compared to conventional hydrothermal conditions (Wu and Bein 1996). A further approach to prepare these modified MCM-41 materials under softer conditions and shorter synthesis reaction times is through a photoassisted procedure. Ti- and V-mesoporous materials have been prepared by this process using tetraisopropyl orthotitanate and vanadium precursors. The XRD results indicate that this preparation route shortens the crystallization time and preserves the formation of the single-site configuration (Hu et al. 2004, 2007; Araújo 2007). Grafting methods have also been employed for the insertion of heteroatoms such as Ti and Mo into silica-based materials. In the case of titanium, titanocene dichloride precursor has been used (Maschmeyer et al. 1995; Danon et al. 2011). Mo species can be introduced in a highly disperse state by reaction of MoCl_5 with the surface OH groups (Louis et al. 1993).

The incorporation of other semiconductors into the synthesized MCM-41 and HSM structures, with or without Ti, opens the possibility of designing visible-light-active materials (Rey et al. 1996; Anpo and Takeuchi 2003). With this purpose, V, Cr, Mo, W and precious metals, such as Pt, Pd and Ag, are some of the most studied metals. Large transition metal cations such as those of Mo and W, scarcely used with zeolite structures, can be easily incorporated into the MCM-41 framework because of its more flexible structure. The displacement of the absorption band for both Ti-MCM-41 and Ti-HSM samples at different vanadium loadings is represented in Fig. 9.10. As can be observed, the incorporation of vanadium results in a progressive red shift of the absorption band located between 240 and 260 nm.

The PAD method has also shown excellent results for the incorporation of metal atoms such as Cr, Pd and Pt into Ti-oxide moieties. As in the case of zeolites, the incorporation of Pt is generally accomplished by this method, with particle sizes in the range 4–5 nm. On the contrary, conventional impregnation leads to a broad distribution of particle sizes in the range 2–20 nm (Yamashita 1998; Shironita et al. 2008, 2009). The photoassisted process has been applied to prepare visible-light-sensitive Cr/Ti binary oxide photocatalysts through a direct interaction between the Cr-oxide and Ti-oxide moieties (Yamashita et al. 2005, 2008b).

Mesoporous TiO_2 thin films are very attractive photocatalyst conformations, since they combine a highly ordered mesoporous structure along with a very high transmittance, provided that transparent substrates such as glass and organic

Fig. 9.10 Effect of the incorporation of vanadium into the Ti-MCM-41 (◆) and Ti-HSM (□) structures on the 50 % absorption values (based on data from (Anpo and Takeuchi 2003))



polymers are employed. Structure-directing agents such as Brij 30, F127 and polyethylene glycol can be used in the sol-gel preparation technique. Thereafter, a thin film can be created by dip-coating or any other suitable deposition method. The samples are subsequently treated at high temperature to promote the decomposition of the structure-directing agent, but avoiding cation migration processes, frequently observed for glass materials.

Recently, a great deal of interest is shown in the insertion of metals with high redox potentials, typically V, Cr, Ti, Fe or Ni, into the MCM-41 structure (Blasco et al. 1995; Ulagappan and Frei 2000). These metals produce isomorphous substitutions which increase the catalytic activity in photooxidation processes involving organic molecules of commercial interest such as phenols and bulky aromatics (Araújo et al. 2007).

9.2.3 Photocatalytic Applications

Mesoporous silicas incorporating metals in single-site configuration have been investigated in many reactions, including the elimination of pollutants, such as NO, benzene, propane, acetaldehyde and trichloroethylene, in gas phase and water solutions; the development of superhydrophilic materials; organic synthesis reactions; the photocatalytic reduction of CO₂ with water; or the photooxidation of carbon monoxide.

Ti-HSM and Ti-MCM-41 have been extensively studied in the direct decomposition of nitric oxide (Zhang et al. 2000; Hu et al. 2006). These single-site photocatalysts record very high activity and N₂ selectivity as compared to pure TiO₂ anatase, like in the case of zeolitic supports (see Sect. 9.1.3). For photocatalysts containing up to 0.6 wt % Ti, isolated tetrahedrally coordinated species predominate. For higher Ti contents, adjacent species with Ti⁴⁺ in octahedral

coordination are also detected. A direct relationship between the yield of charge transfer excited states of the isolated species and the N_2 formation is observed. The implantation of V ions results in the formation of Ti–O–V ensembles, yielding photocatalysts able to work even under visible light irradiation ($\lambda > 420$ nm) with high photocatalytic efficiency (Anpo and Takeuchi 2003). Anpo et al. have also analysed the photocatalytic activity of Ti-, V- and Mo-MCM-41 for NO decomposition (Anpo et al. 2009).

The effect of the incorporation of a reducing agent has also been investigated with Mo- and Cr-mesoporous molecular sieves (Matsuoka and Anpo 2003a; Anpo et al. 2009). Based on photoluminescence results, obtained in the presence of NO or propane and their mixtures, a mechanism was proposed, where hydrocarbon radicals are formed by H abstraction of the photoexcited Mo oxide from propane. These intermediate species react with NO to produce N_2 along with oxygen-containing compounds. The photocatalytic decomposition of NO is promoted by the presence of carbon monoxide, leading to the formation of N_2 and CO_2 . The formation of N_2 is higher with photocatalysts containing 1 wt % Mo concentration, which generates the highest amount of Mo^{4+} species through the photoreduction of Mo^{6+} with CO. Moreover, Cr-based materials show good activity under visible light irradiation with N_2 selectivity of around 97 %, whereas it decreases to 45 % under UV conditions.

Another photocatalytic application of Ti–Cr-MCM-41 is the decomposition of hydrogen sulphide under visible light, mainly related to the presence of Cr^{6+} species (Wang et al. 2012). Deactivation is observed as a consequence of sulphate accumulation and reduction of Cr^{6+} , as previously observed for TiO_2 -impregnated Cr-MCM-41 (Portela et al. 2008).

Due to the rather good performance of bulk photocatalysts for the elimination of organic compounds, more costly single-site photocatalysts have been less explored in this field. Nevertheless, the interest in single-site photocatalysts has been triggered because of their higher activity and selectivity for some particular photocatalytic applications. The most active and interesting research field relates to the development of active photocatalysts in the visible region. V-, Fe- or Cr-substituted titania-containing MCM-41 has been tested in the degradation of organic pollutants in water (Davydov et al. 2001). The chromium-substituted MCM-41 was identified as the best support for titania incorporation. This configuration yielded the highest degradation rates for HCOOH, 2,4,6-trichlorophenol and 4-chlorophenol. Si–O–Cr and Ti–O–Cr arrangements create an opportunity for a two-step excitation in the visible range. Moreover, Co- and Cr–Al-MCM-41 have been used in the photocatalytic degradation of acetaldehyde (Rodrigues et al. 2004) and trichloroethylene (Rodrigues et al. 2005) in the gas phase using UV and visible light. Although the rate constant of TiO_2 P25 is higher than that of M-Al-MCM-41 under UV irradiation, the latter presents reasonable photoactivity under visible irradiation. The increasing acidity and ion-exchange ability of Al-substituted MCM-41, with surface areas over $1000 \text{ m}^2 \text{ g}^{-1}$, account for the choice of Al-MCM-41 as a support for the incorporation of well-dispersed photoactive sites.

On the other hand, Ti-MCM-41 molecular sieves have been studied in the UV-assisted sonophotocatalytic removal of salicylic acid (Reddy et al. 2003). In this process, the use of ultrasounds allows the creation of microbubbles, which promotes the production of active radicals such as H^\bullet and OH^\bullet . Clearly, the combination of solid particles and ultrasounds in this case produces a synergetic effect, and the formation of toxic by-products is decreased. Ti-HSM photocatalysts have also been tested for the degradation of benzene. Its unique properties, which relate to the high dispersion of Ti-oxide species, explain their enhanced photoactivity and stability as compared to TiO_2 P25 (Zhuang et al. 2010).

The design of mesoporous thin films with controlled hydrophobic–hydrophilic properties is a promising field of application. Single-site Ti, V, Cr, Mo or W cations contained in mesoporous silica thin films induce *superhydrophilicity*, an essential property, even in the dark, for the self-cleaning and antifogging properties commented in Chap. 3. The water contact angle of these materials is kept below 10° , decreases upon UV irradiation, and, in some cases, is even further reduced upon visible light irradiation (Yamashita et al. 2006; Yamashita and Mori 2007; Yamashita et al. 2008a). This behaviour has been explained considering that the introduction of tetrahedrally coordinated M-oxide moieties into the mesoporous silica matrix leads to the formation of new adsorption sites for water molecules. The charge transfer excited state of the metal oxide moieties (Ti, Mo, W, Cr) formed under UV–Vis irradiation plays an active role in the process. In addition, the mesoporous structure enhances their hydrophilicity by increasing the number of silanol groups exposed on the inner surface of the mesopores and inducing capillary phenomena.

The surface of metal oxide mesoporous materials can be transformed from hydrophilic to hydrophobic by a polymerization process. Ethylene polymerization over mesostructured silica incorporating Ti- and Cr-oxide moieties has been performed under UV irradiation. The resulting inorganic–organic materials can maintain their transparency after the deposition of the organic phase, with a significant increase in the water contact angle (Wang et al. 2006; Yamashita et al. 2008a, b).

Organic synthesis is another important field where single-site photocatalysis can be successfully applied. The production of chemicals with these photocatalysts has been mainly related to the photooxidation of hydrocarbons in the presence of oxygen, for example, the oxidation of benzene to phenol (Zama et al. 2000), the photooxidation of methane to produce formaldehyde (López and Martínez 2002) or the photooxidation of propane to acetone (Hamdy et al. 2006). The photocatalytic epoxidation of olefins with Ti-containing mesoporous silica in the presence of acetonitrile has also been investigated, obtaining a higher selectivity than with bulk TiO_2 (Shiraishi et al. 2005; Morishita et al. 2006). Moreover, Cr- and Cr/Ti-containing mesoporous silicas prepared by the photoassisted method show higher reactivity and selectivity in the propane-to-propene photooxidation under visible light than the same catalysts prepared by the impregnation method (Yamashita et al. 2008b). Cr-HSM shows good photocatalytic activity in the partial oxidation of propane for the production of oxygen-containing hydrocarbons, such as acetone and acrolein, both under UV light and visible light (Yamashita et al. 2001), and V-

and Ti-containing MCM-41 for obtaining acetone (Hu et al. 2007). VO_x/SBA-15 has been tested in the selective photoassisted oxidation of methane to produce formaldehyde (López and Martínez 2002). Ti-TUD-1 and V-TUD-1 have been tested for the selective photooxidation of propane to acetone under UV and visible irradiation (Hamdy et al. 2006; Mul et al. 2008). Photocatalytic oxidation of cyclohexane with molecular oxygen to cyclohexanol and cyclohexanone, an important intermediate in the ϵ -caprolactam synthesis, can be carried out using hydrophobically modified Cr-containing mesoporous silica under visible light (Shiraishi et al. 2008). Photoactivation of tetrahedrally coordinated chromate species (Cr⁶⁺) led to the formation of electrophilic excited state Cr^{4+*} species, able to strongly attract cyclohexane protons, hence promoting their efficient oxidation.

The photooxidation of CO by O₂ is essential in the fuel cell technology to remove CO impurities from H₂, hence avoiding electrode poisoning. Mo-MCM-41 has been used in this reaction, showing good quantum yields of around 12 %, which are still far from the efficiencies of conventional heterogeneous catalytic processes with precious metal-based catalysts (Anpo et al. 2009). The proposed reaction mechanism starts with the formation of a charge transfer triplet excited state. Then, Mo⁵⁺-O⁻ excited species are reduced by CO to Mo⁴⁺, and finally, the initial oxidation state is recovered by oxidation with O₂.

The development of single-site photocatalysts has allowed as well a better characterization and control of the active sites for the photocatalytic reduction of CO₂ with H₂O, as commented in Chap. 4 (Thomas et al. 2005; Indrakanti et al. 2009). Frei and co-workers studied the reaction mechanism under UV light using methanol as the electron donor for TS-1. HCO₂H, CO and HCO₂CH₃ were the detected products, and formic acid was detected as the primary 2-electron reduction product of CO₂ at the LMCT-excited Ti centres (Ulagappan and Frei 2000). They also proposed a mechanism for the CO₂ photoreduction on a bimetallic ZrCu(I)-MCM-41 silicate sieve, in which CO₂ splits into CO and O₂ at the excited metal-to-metal charge transfer sites (Lin et al. 2004; Lin and Frei 2005). Hwang et al. (2005) reported that CH₃OH is the main reaction product for the PCR of CO₂ with water, with the highest production for Ti-SBA-15 in the series Ti-SBA-15, Ti-MCM-41, Ti-MCM-48 and TS-1. This observation was correlated with the higher dispersion of Ti active sites on SBA-15 due to the acidic medium used for the synthesis. Yamashita et al. (1998) studied the effect of pore size on the reaction. The MCM-48 structure, with large pores >20 Å and three-dimensional channels, shows better results than the one-dimensional MCM-41, and the lower pore size of TS-1 seems to be the reason for the lower photoactivity of this material. Moreover, the incorporation of a low quantity of Pt into the Ti-MCM-41 structure significantly promotes methane formation, with the subsequent decrease in the methanol yield. XAFS and photoluminescence analyses revealed a certain electron transfer from the photoexcited Ti-oxide species to the neighbouring Pt metal, resulting in the better charge separation. Lin et al. (2004) reported that the primary product for the photoreduction of CO₂ with water over Ti-MCM-41 was CO, and no methane and methanol formations were detected.

9.3 Stability and Other General Aspects of Single-Site Photocatalysts

Although it is well known that the presence of water vapour provokes zeolite dealumination at high temperatures, which leads to the collapse of the zeolitic structure, not much information is available about the stability of these materials at lower temperatures. However, this fact should be considered in long-term photocatalytic applications. Other aspect to be taken into account is the likely leaching of the photoactive component during the reaction; this phenomenon can be very acute in water-phase reactions. This is one of the problems of metal-based zeolite photocatalysts, reflected not only in the decrease in the active-phase content but also in the competition between the homogeneous (e.g. photo-Fenton) and heterogeneous processes. These facts, in which extension depends strongly on the pH of the medium, limit the applicability of zeolitic materials for aqueous solutions processes.

Another feature to be considered is pore blocking by deposition of non-desired compounds. Aramendía et al. (2007) have studied the photooxidation of 2-propanol in gas phase with several zeolites, reporting a photoactivity reduction of around 30 % with respect to the initial values. Deactivation and regeneration are demanding issues that require a detailed study in each case. In this line, it is reported in the literature that the treatment of CN^- -containing wastewaters leads to catalyst deactivation after an initial photocatalytic activity of 90 % (Domenech and Peral 1989; Corma and Garcia 2004). The photocatalyst efficiency can be restored by flushing with distilled water, distilled water plus irradiation or treatment with acid or bases.

The price of the final photocatalyst is determined by the price of the raw materials used for the synthesis (e.g. precursors, templates). The cost of metal-based photocatalysts, however, is dominated by the price of the metal component. Synthetic zeolites have been used for many years in the oil industry, but natural zeolites, less expensive, are becoming very attractive alternatives.

Concerning mesoporous structures, the stability of the pore walls against chemical agents, reaction products or water are some aspects to be considered for long-term applications. In this respect, thicker silica walls as those of SBA-15 confer additional resistance to these materials. As in zeolites, other aspects to be taken into account for mesoporous structures are metal leaching and deactivation. Metal leaching is one of the problems of photocatalysts based on M oxide (e.g. V, Cr, Mo) dispersed on mesoporous silicas, as they tend to undergo ion leaching after prolonged contact of the solid with liquids. Furthermore, under reaction conditions, Cr^{+6} species are transformed into Cr^{+3} , leading to catalyst deactivation in both H_2S (Wang et al. 2012) and formic acid degradation (Davydov et al. 2001). It seems clear that $\text{Cr}^{+6}=\text{O}^{2-} \rightarrow \text{Cr}^{+5}-\text{O}^{1-}$ transitions are responsible for the photoactivity under visible light, and the accumulation of electrons on the surface of the catalyst leads to the depletion of the six-valence chromium and subsequent deactivation of the catalyst. This is a very serious limitation to the practical use of these types of photoactive materials. In fact, no real catalytic cycle would take

place if this process occurs extensively, and the materials would rather behave as a consumable reagent. Further studies would be required to better understand this aspect and to establish viable strategies of regeneration.

References

- Alba MD, Luan Z, Klinowski J (1996) Titanosilicate mesoporous molecular sieve MCM-41: synthesis and characterization. *J Phys Chem* 100(6):2178–2182
- Anpo M, Aikawa N, Kubokawa Y, Che M, Louis C, Giamello E (1985) Photoluminescence and photocatalytic activity of highly dispersed titanium oxide anchored onto porous Vycor glass. *J Phys Chem* 89(23):5017–5021
- Anpo M, Higashimoto S, Matsuoka M, Zhanpeisov N, Shioya Y, Dzwigaj S, Che M (2003) The effect of the framework structure on the chemical properties of the vanadium oxide species incorporated within zeolites. *Catal Today* 78(1–4 SPEC.):211–217
- Anpo M, Kim TH, Matsuoka M (2009) The design of Ti-, V-, Cr-oxide single-site catalysts within zeolite frameworks and their photocatalytic reactivity for the decomposition of undesirable molecules-The role of their excited states and reaction mechanisms. *Catal Today* 142(3–4):114–124
- Anpo M, Shioya Y, Yamashita H, Giamello E, Morterra C, Che M, Patterson HH, Webber S, Ouellette S (1994) Preparation and characterization of the Cu +/ZSM-5 catalyst and its reaction with NO under UV irradiation at 275 K. In situ photoluminescence, EPR, and FT-IR investigations. *J Phys Chem* 98(22):5744–5750
- Anpo M, Takeuchi M (2003) The design and development of highly reactive titanium oxide photocatalysts operating under visible light irradiation. *J Catal* 216(1–2):505–516
- Anpo M, Thomas JM (2006) Single-site photocatalytic solids for the decomposition of undesirable molecules. *Chem Commun* 31:3273–3278
- Anpo M, Zhang SG, Higashimoto S, Matsuoka M, Yamashita H, Ichihashi Y, Matsumura Y, Souma Y (1999) Characterization of the local structure of the vanadium silicalite (VS-2) catalyst and its photocatalytic reactivity for the decomposition of NO into N₂ and O₂. *J Phys Chem B* 103(43):9295–9301
- Aramendía MA, Colmenares JC, López-Fernández S, Marinas A, Marinas JM, Urbano FJ (2007) Screening of different zeolite-based catalysts for gas-phase selective photooxidation of propan-2-ol. *Catal Today* 129(1–2 SPEC. ISS.):102–109
- Araújo RS, Costa FS, Maia DAS, Sant’Ana HB, Cavalcante CL (2007) Synthesis and characterization of Al- and Ti-MCM-41 materials: application to oxidation of anthracene. *Braz J Chem Eng* 24:135–141
- Auerbach SM, Carrado KA, Dutta PK (2003) *Handbook of zeolite science and technology*. Marcel Dekker, Inc., New York
- Ban T, Kondoh S, Ohya Y, Takahashi Y (1999) Degradation reaction of monoethanolamine using TS-1 zeolite as a photocatalyst. *Phys Chem Phys* 1(24):5745–5752
- Barrer RM (1978) *Zeolites and clay minerals as sorbents and molecular sieves*. Academic Press (Orig. pub), London
- Blasco T, Corma A, Navarro MT, Pariente JP (1995) Synthesis, characterization, and catalytic activity of Ti-MCM-41 structures. *J Catal* 156(1):65–74
- Breck DW (1974) *Zeolite molecular sieves: structure, chemistry and use*. Wiley, New York
- Casci JL (1994) The preparation and potential applications of ultra-large pore molecular sieves: a review. *Stud Surf Sci Catal* 85:329–356
- Corma A, Garcia H (2004) Zeolite-based photocatalysts. *Chem Commun* 10(13):1443–1459

- Corrent S, Cosa G, Scaiano JC, Galletero MS, Alvaro M, Garcia H (2001) Intrazeolite photochemistry. 26. Photophysical properties of nanosized TiO_2 clusters included in zeolites Y, F^2 , and mordenite. *Chem Mater* 13(3):715–722
- Danon A, Stair PC, Weitz E (2011) Mechanistic and adsorption studies of relevance to photocatalysts on titanium grafted mesoporous silicalites. *Catal Lett* 141(8):1057–1066
- Davis ME, Lobo RF (1992) Zeolite and molecular sieve synthesis. *Chem Mater* 4(4):756–768
- Davydov L, Reddy EP, France P, Smirniotis PG (2001) Transition-metal-substituted titania-loaded MCM-41 as photocatalysts for the degradation of aqueous organics in visible light. *J Catal* 203(1):157–167
- Díaz I (2001) Síntesis, caracterización y propiedades catalíticas de materiales mesoporosos ordenados funcionalizados con grupos ácidos. PhD thesis. Universidad Autónoma de Madrid, Instituto de Catálisis y Petroleoquímica (CSIC), Madrid
- Domenech X, Peral J (1989) Cyanide photo-oxidation using a TiO_2 -coated zeolite. *Chem Ind* 606
- Dyer A (1988) An introduction to zeolite molecular sieves. Wiley, Bath
- García H, Roth HD (2002) Generation and reactions of organic radical cations in zeolites. *Chem Rev* 102(11):3947–4007
- Hamdy MS, Berg O, Jansen JC, Maschmeyer T, Arafat A, Moulijn JA, Mul G (2006) Chromium-incorporated TUD-1 as a new visible light-sensitive photo-catalyst for selective oxidation of propane. *Catal Today* 117(1–3):337–342
- Hari Prasad Rao PR, Ramaswamy AV, Ratnasamy P (1992) Synthesis and catalytic properties of crystalline, microporous vanadium silicates with MEL structure. *J Catal* 137(1):225–231
- Hashimoto S (2003) Zeolite photochemistry: impact of zeolites on photochemistry and feedback from photochemistry to zeolite science. *J Photochem Photobiol C* 4(1):19–49
- Hernandez-Alonso MD, Fresno F, Suarez S, Coronado JM (2009) Development of alternative photocatalysts to TiO_2 : challenges and opportunities. *Energy & Environmental Science* 2(12):1231–1257
- Hewer TLR, Suárez S, Coronado JM, Portela R, Avila P, Sanchez B (2009) Hybrid photocatalysts for the degradation of trichloroethylene in air. *Catal Today* 13(3–4):302–308
- Higashimoto S, Matsuoka M, Yamashita H, Anpo M, Kitao O, Hidaka H, Che M, Giamello E (2000) Effect of the Si/Al ratio on the local structure of V Oxide/ZSM-5 catalysts prepared by solid-state reaction and their photocatalytic reactivity for the decomposition of NO in the absence and presence of propane. *J Phys Chem B* 104(44):10288–10292
- Horiuchi Y, Yamashita H (2011) Design of mesoporous silica thin films containing single-site photocatalysts and their applications to superhydrophilic materials. *Appl Catal A* 400(1–2):1–8
- Hu Y, Martra G, Zhang J, Higashimoto S, Coluccia S, Anpo M (2006) Characterization of the local structures of Ti-MCM-41 and their photocatalytic reactivity for the decomposition of NO into N_2 and O_2 . *J Phys Chem B* 110(4):1680–1685
- Hu Y, Wada N, Matsuoka M, Anpo M (2004) Photo-assisted synthesis of V-MCM-41 under UV light irradiation. *Catal Lett* 97(1–2):49–52
- Hu Y, Wada N, Tsujimaru K, Anpo M (2007) Photo-assisted synthesis of V and Ti-containing MCM-41 under UV light irradiation and their reactivity for the photooxidation of propane. *Catal Today* 120(2):139–144
- Hwang JS, Chang JS, Park SE, Ikeue K, Anpo M (2005) Photoreduction of carbon dioxide on surface functionalized nanoporous catalysts. *Top Catal* 35(3–4):311–319
- Ikeue K, Yamashita H, Anpo M, Takewaki T (2001) Photocatalytic reduction of CO_2 with H_2O on Ti^{IV} zeolite photocatalysts: Effect of the hydrophobic and hydrophilic properties. *J Phys Chem B* 105(35):8350–8355
- Indrakanti VP, Kubicki JD, Schobert HH (2009) Photoinduced activation of CO_2 on Ti-based heterogeneous catalysts: current state, chemical physics-based insights and outlook. *Energy Environ Sci* 2(7):745–758
- Kalyanasundaram K (1987) Photochemistry in microheterogeneous systems. Academic Press, New York

- Kerc A, Bekbolet M, Saatci AM (2003) Sequential oxidation of humic acids by ozonation and photocatalysis. *Ozone: Sci Eng* 25(6):497–504
- Kresge CT, Leonowicz ME, Roth WJ, Vartuli JC, Beck JS (1992) Ordered mesoporous molecular sieves synthesized by a liquid-crystal template mechanism. *Nature* 359(6397):710–712
- Lee GD, Jung SK, Jeong YJ, Park JH, Lim KT, Ahn BH, Hong SS (2003) Photocatalytic decomposition of 4-nitrophenol over titanium silicalite (TS-1) catalysts. *Appl Catal A* 239(1–2):197–208
- Lin W, Frei H (2005) Photochemical CO₂ splitting by metal-to-metal charge-transfer excitation in mesoporous ZrCu(1)-MCM-41 silicate sieve. *J Am Chem Soc* 127(6):1610–1611
- Lin W, Han H, Frei H (2004) CO₂ splitting by H₂O to CO and O₂ under UV light in TiMCM-41 silicate sieve. *J Phys Chem B* 108(47):18269–18273
- Liu X, Iu K, Thomas JK (1993) Preparation, characterization and photoreactivity of titanium(IV) oxide encapsulated in zeolites. *J Chem Soc Faraday Trans* 89(11):1861–1865
- López HH, Martínez A (2002) Selective photo-assisted oxidation of methane into formaldehyde on mesoporous VOx/SBA-15 catalysts. *Catal Lett* 83(1–2):37–41
- Louis C, Che M, Anpo M (1993) Characterization and modelling of the Mo species in grafted Mo/SiO₂ catalysts after redox thermal treatments. *J Catal* 141(2):453–464
- Maschmeyer T, Rey F, Sankar G, Thomas JM (1995) Heterogeneous catalysts obtained by grafting metallocene complexes onto mesoporous silica. *Nature* 378(6553):159–162
- Matsuoka M, Anpo M (2003a) Local structures, excited states, and photocatalytic reactivities of highly dispersed catalysts constructed within zeolites. *J Photochem Photobiol C* 3(3):225–252
- Matsuoka M, Anpo M (2003b) Photoluminescence properties and photocatalytic reactivities of Cu+/zeolite and Ag+/zeolite catalysts prepared by the ion-exchange method. *Curr Opin Solid State Mater Sci* 7(6):451–459
- Matsuoka M, Matsuda E, Tsuji K, Yamashita H, Anpo M (1996) The photocatalytic decomposition of nitric oxide on Ag+/ZSM-5 catalyst prepared by ion-exchange. *J Mol Catal A: Chem* 107(1–3):399–403
- Morishita M, Shiraishi Y, Hirai T (2006) Ti-containing mesoporous organosilica as a photocatalyst for selective olefin epoxidation. *J Phys Chem B* 110(36):17898–17905
- Mul G, Wasylenko W, Hamdy MS, Frei H (2008) Cyclohexene photo-oxidation over vanadia catalyst analyzed by time resolved ATR-FT-IR spectroscopy. *Phys Chem Chem Phys* 10(21):3131–3137
- Park SE, Hwang JS, Chang JS, Kim JM, S., K, Chai HS (2003) Titania photocatalyst and its preparing method US 6566300B2
- Portela R, Canela MC, Sanchez B, Marques FC, Stumbo AM, Tessinari RF, Coronado JM, Suarez S (2008) H₂S photodegradation by TiO₂/M-MCM-41 (M = Cr or Ce): deactivation and by-product generation under UV-A and visible light. *Appl Catal B* 84(3–4):643–650
- Ramamurphy V (1991) Photochemistry in organized and constrained media. VCH, New York
- Reddy EP, Davydov L, Smirniotis P (2003) TiO₂-loaded zeolites and mesoporous materials in the sonophotocatalytic decomposition of aqueous organic pollutants: The role of the support. *Appl Catal B* 42(1):1–11
- Rey F, Sankar G, Maschmeyer T, Thomas JM, Bell RG, Neville Greaves G (1996) Synthesis and characterisation by x-ray absorption spectroscopy of a suite of seven mesoporous catalysts containing metal ions in framework sites. *Top Catal* 3(1–2):121–134
- Rodrigues S, Ranjit KT, Uma S, Martyanov IN, Klabunde KJ (2005) Visible-light photooxidation of trichloroethylene by Cr-Al-MCM-41. *J Catal* 230(1):158–165
- Rodrigues S, Uma S, Martyanov IN, Klabunde KJ (2004) Visible light induced photocatalytic activity for degradation of acetaldehyde using transition metal incorporated Al-MCM-41 (aluminum doped silica zeolitic material). *J Photochem Photobiol A* 165(1–3):51–58
- Serpone N, Lawless D, Khairutdinov R (1995) Size effects on the photophysical properties of colloidal anatase TiO₂ particles: Size quantization or direct transitions in this indirect semiconductor? *J Phys Chem* 99(45):16646–16654

- Shiraishi Y, Morishita M, Hirai T (2005) Acetonitrile-assisted highly selective photocatalytic epoxidation of olefins on Ti-containing silica with molecular oxygen. *Chem Commun* 48:5977–5979
- Shiraishi Y, Ohara H, Hirai T (2008) Visible light-induced partial oxidation of cyclohexane on hydrophobically modified chromium-containing mesoporous silica with molecular oxygen. *J Catal* 254(2):365–373
- Shironita S, Mori K, Ohmichi T, Eiji T, Hirota M, Yamashita H (2009) Synthesis of highly dispersed platinum nanoparticles on Ti-containing mesoporous silica using photo-assisted deposition. *J Nanosci Nanotechnol* 9(1):557–561
- Shironita S, Mori K, Shimizu T, Ohmichi T, Mimura N, Yamashita H (2008) Preparation of nano-sized platinum metal catalyst using photo-assisted deposition method on mesoporous silica including single-site photocatalyst. *Appl Surf Sci* 254(23):7604–7607
- Suárez S, Coronado JM, Portela R, Martín JC, Yates M, Ávila P, Sánchez B (2008) On the preparation of TiO₂-sepiolite hybrid materials for the photocatalytic degradation of TCE: influence of TiO₂ distribution in the mineralization. *Environ Sci Technol* 42(16):5892–5896
- Takeuchi M, Sakai S, Ebrahimi A, Matsuoka M, Anpo M (2009) Application of highly functional Ti-oxide-based photocatalysts in clean technologies. *Top Catal* 52(12):1651–1659
- Tanev PT, Chibwe M, Pinnavaia TJ (1994) Titanium-containing mesoporous molecular sieves for catalytic oxidation of aromatic compounds. *Nature* 368(6469):321–323
- Taramasso M, Perego G, Notari B (1983) Preparation of porous crystalline synthetic materials composed of silicon and titanium oxides. US 4410501
- Tel'biz G, Shwets A, Gun'ko V, Stoch J, Tamulajtis G, Kukhtarev N, J Weitkamp, H.G.K.H.P.a.W.H.I. 1994. Preparation and Properties Quantized Semiconductor Particles in Zeolites. In *Stud Surf Sci Catal* 84:1099–1106 (Elsevier)
- Thomas JM, Raja R, Lewis DW (2005) Single-site heterogeneous catalysts. *Angew Chemie Int Ed* 44(40):6456–6482
- Ulagappan N, Frei H (2000) Mechanistic study of CO₂ photoreduction in Ti silicalite molecular sieve by FT-IR spectroscopy. *J Phys Chem A* 104(33):7834–7839
- van Bekkum H, Flanigen EM, Jansen JC (1991) Introduction to zeolite science and practice. Elsevier, Amsterdam
- Vartuli JC, Roth WJ, Beck JS, McCullen SB, Kresge CT (1998) Molecular sieves—science and technology. Springer, Berlin, p 97
- Wang J, Leeman H, Schoonheydt RA (2006) SiO₂/Cr monolayers and formation of polyethylene films. *J Colloid Interface Sci* 299(2):713–718
- Wang Z, Ci X, Dai H, Yin L, Shi H (2012) One-step synthesis of highly active Ti-containing Cr-modified MCM-48 mesoporous material and the photocatalytic performance for decomposition of H₂S under visible light. *Appl Surf Sci* 258(20):8258–8263
- Weitkamp J (2000) Zeolites and catalysis. *Solid State Ionics* 131(1–2):175–188
- Wu C-G, Bein T (1996) Microwave synthesis of molecular sieve MCM-41. *Chem Commun* 8:925–926
- Yamamoto K, Garcia SEB, Saito F, Muramatsu A (2006) Synthesis of titanasilicate zeolite from bulk titania via mechanochemical route. *Chem Lett* 35(6):570–571
- Yamashita H, Chiyoda O, Masui Y, Ohshiro S, Kida K, Anpo M (2005) Design of visible light sensitive (Cr,Ti)-containing mesoporous silica photocatalyst using a photo-assisted deposition (PAD) method. In *Stud Surf Sci Catal* 158:43–50
- Yamashita H, Fujii Y, Ichihashi Y, Zhang SG, Ikeue K, Park DR, Koyano K, Tatsumi T, Anpo M (1998) Selective formation of CH₃OH in the photocatalytic reduction of CO₂ with H₂O on titanium oxides highly dispersed within zeolites and mesoporous molecular sieves. *Catal Today* 45(1–4):221–227
- Yamashita H, Horiuchi Y, Imaoka S, Nishio S, Nishiyama N, Mori K (2008a) Surface hydrophilic-hydrophobic property on transparent mesoporous silica thin films containing chromium oxide single-site photocatalyst. *Catal Today* 132(1–4):146–152

- Yamashita H, Miura Y, Mori K, Ohmichi T, Sakata M, Mori H (2007) Synthesis of nano-sized Pd metal catalyst on Ti-containing zeolite using a photo-assisted deposition (PAD) method. *Catal Lett* 114(1–2):75–78
- Yamashita H, Mori K (2007) Applications of single-site photocatalysts implanted within the silica matrixes of zeolite and mesoporous silica. *Chem Lett* 36(3):348–353
- Yamashita H, Mori K, Shironita S, Horiuchi Y (2008b) Applications of single-site photocatalysts to the design of unique surface functional materials. *Catal Surv Asia* 12(2):88–100
- Yamashita H, Nishio S, Katayama I, Nishiyama N, Fujii H (2006) Photo-induced superhydrophilic property and photocatalysis on transparent Ti-containing mesoporous silica thin films. *Catal Today* 111(3–4):254–258
- Yamashita H, Yoshizawa K, Ariyuki M, Higashimoto S, Anpo M, Che M (2001) Photocatalytic reactions on chromium containing mesoporous silica molecular sieves (Cr-HMS) under visible light irradiation: decomposition of NO and partial oxidation of propane. *Chem Commun* 5:435–436
- Zama K, Fukuoka A, Sasaki Y, Inagaki S, Fukushima Y, Ichikawa M (2000) Selective hydroxylation of benzene to phenol by photocatalysis of molybdenum complexes grafted on mesoporous FSM-16. *Catal Lett* 66(4):251–253
- Zhang J, Hu Y, Matsuoka M, Yamashita H, Minagawa M, Hidaka H, Anpo M (2001) Relationship between the local structures of titanium oxide photocatalysts and their reactivities in the decomposition of NO. *J Phys Chem B* 105(35):8395–8398
- Zhang J, Minagawa M, Matsuoka M, Yamashita H, Anpo M (2000) Photocatalytic decomposition of NO on Ti-HMS mesoporous zeolite catalysts. *Catal Lett* 66(4):241–243
- Zhang W, Frába M, Wang J, Tanev PT, Wong J, Pinnavaia TJ (1996) Mesoporous titanasilicate molecular sieves prepared at ambient temperature by electrostatic (S^+I^- , $S^+X^-I^+$) and neutral (S^0I^0) assembly pathways: a comparison of physical properties and catalytic activity for peroxide oxidations. *J Am Chem Soc* 118(38):9164–9171
- Zhao D, Feng J, Huo Q, Melosh N, Fredrickson GH, Chmelka BF, Stucky GD (1998) Triblock copolymer syntheses of mesoporous silica with periodic 50–300 angstrom pores. *Science* 279(5350):548–552
- Zhao XS, Lu GQ, Millar GJ (1996) Advances in mesoporous molecular sieve MCM-41. *Ind Eng Chem Res* 35(7):2075–2090
- Zhuang Y, Song HY, Li G, Xu YJ (2010) Ti-HMS as a single-site photocatalyst for the gas-phase degradation of benzene. *Mater Lett* 64(22):2491–2493

Chapter 10

The Role of Co-catalysts: Interaction and Synergies with Semiconductors

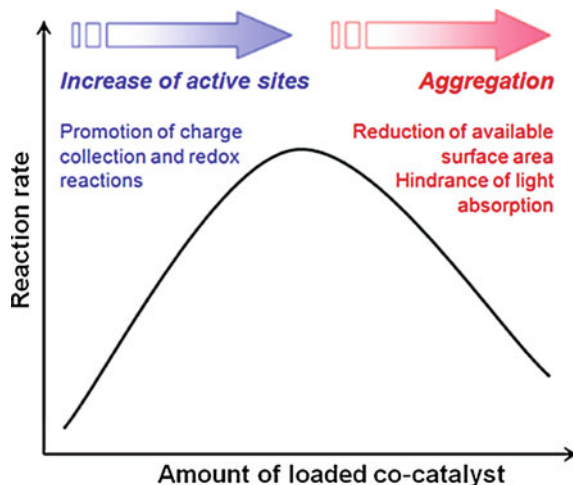
Víctor A. de la Peña O'Shea

It is well known that the selection of an appropriate semiconductor is the key to obtain the desired results in a photocatalytic reaction. In the previous chapters, it has been shown which are the requirements for several photocatalytic processes, including pollutant removal, water detoxification or solar fuel production (from water splitting or CO₂ photoreduction), and how semiconductor engineering can help to improve the intrinsic physico-chemical and catalytic properties of a single-phase photocatalyst attending to solve the main drawbacks in photocatalytic reactions. However, in some cases, the modification of the photocatalyst with an appropriate co-catalyst leads to an improvement in the photoactivity. The use of co-catalysts leads to (1) a better charge separation and a decrease in the recombination rate, because these co-catalysts act as electron attractors; (2) an enhancement in the activity or a selectivity control in the redox reactions, because of their performance as specific catalytic active sites for reaction evolution; and, in some cases, (3) a broadening in the light operating conditions from UV to visible wavelengths.

The effect of the co-catalyst is mainly related to its ability to extract and manage the photogenerated electrons. These processes are governed by various factors such as band-edge potential and work function of the photocatalyst (Kudo et al. 2000; Kato et al. 2003) and the loaded species (Nosaka et al. 1984). Regarding the last point, the photocatalytic activity of a given material (co-catalyst/semiconductor) is, in general, highly dependent on the optimal distribution of the co-catalyst. An increase in the metal loading and a good dispersion lead to faster reaction rates. However, undue amounts provoke a decrease in the activity because the co-catalyst sites can act as recombination centres or impede light absorption. This behaviour is explained by a volcano-type trend between the co-catalyst amount and the photoactivity (Maeda 2011), as shown in Fig. 10.1.

V. A. de la Peña O'Shea (✉)
Institute IMDEA Energy, Avenida de Ramón de la Sagra, 3 28935 MOSTOLES,
(MADRID), Spain
e-mail: victor.delapenya@imdea.org

Fig. 10.1 Trade-off between co-catalyst loading and activity. Reprinted with permission from Maeda (2011). Copyright Elsevier



Therefore, the loading method is a key factor to control the photocatalytic reactivity. Several procedures have been used in photocatalysis to deposit the co-catalyst over the semiconductor:

Incipient wetness impregnation (IWI), also called dry impregnation or capillary impregnation, where the semiconductor is soaked with a volume of the metallic precursor solution (in water or in an organic solvent), equal to the pore volume of the support. The maximum charge of metal phase is determined by the solubility of the precursor salt. When the solution is added in excess of solvent, the method is called *wet impregnation (WI)*. Thereafter, the catalysts can be dried and calcined in air or inert atmosphere, to complete the precursor decomposition.

Precipitation deposition, where the co-catalyst is deposited by slow addition of a precipitating agent to a metallic solution. The precipitating agent is selected taking into account the nature of the precursor, the solvent and the characteristics of the support. This procedure is more adequate for non-porous supports.

In-situ photochemical deposition method (PD), developed by Kraeutler and Bard (1978), which has been extensively used during the last years (Nakamatsu et al. 1986; Einaga and Harada 2005). In this procedure, the semiconductor is dispersed in a solution of the metal precursor. The suspension is then irradiated leading to the reduction in the metal cations to their metallic state. An electron donor can be included to favour the photodeposition.

If several active components are to be introduced, they can be deposited by *co-impregnation*, when all co-catalysts are deposited at the same time, or *successive impregnation*, if the components are sequentially introduced. In this case, drying and calcination take place between impregnations and as final step.

10.1 Co-catalyst/Semiconductor Interaction

As it has been previously described, the use of a co-catalyst influences the optoelectronic properties of the semiconductor photocatalysts. This effect leads to changes in the light absorption and in the recombination processes. Depending on the co-catalyst nature, different kinds of behaviours have been observed.

The charge separation effect that takes place in metal (M) or metal oxide (MO) co-catalysts deposited over a semiconductor surface can be explained, from the electrochemical point of view, as a set of homogeneously distributed “short circuits”, where each nanoparticle acts as cathode or anode, thus improving the catalytic redox behaviour of the bare semiconductor (Wang et al. 1992).

In the case of using metals as co-catalysts, metal nanoparticles (NPs) act as electron scavengers, delaying the recombination processes. The efficiency of this electron transfer depends on the metal ability to compete for the photogenerated electrons with other acceptor molecules at the semiconductor interface. Besides, depending on the metal, different behaviours are observed; thus, Pt and Pd provide an ohmic contact, while other metals such as Ag and Au exhibit capacitive properties.

In the general case of a metal/semiconductor system, it is known that UV light leads to a decrease in the metal Fermi level (more negative potential), which approaches the conduction band due to the electron storage. This change is due to an electronic transfer from the semiconductor to the metallic NPs, leading to an excess of negative charge in the metal and a positive charge in the semiconductor. As a result, a Schottky barrier is formed between the semiconductor conduction band and the metal Fermi level. Some studies have shown that the shift in the Fermi level could be as high as 0.1 V per stored electron in a nanoparticle (Chen et al. 1998a, b; Chen and Murray 1999; Takai and Kamat 2011; Templeton et al. 2000). This shift allows the photogenerated electrons in the semiconductor to be trapped on the metal nanoparticles, improving the charge separation (Fujishima et al. 2008; Tada et al. 2009; Zhang and Yates 2012). Smaller size particles were found to induce a maximum shift in the Fermi level of the metal/semiconductor catalyst. Radiative recombination occurs in the range of picoseconds for bare semiconductors, while in the case of trapped photoelectrons, it happens at the nanosecond to microsecond scale, depending on the size of metal and support. A decrease in the semiconductor particle size increases the trapped electrons recombination rate. Regarding metal particles, a decrease in the size leads to a higher modification in the Fermi level towards more negative potentials, provoking an increase in the photogenerated electrons lifetime.

Taking into account that sunlight possesses a high quantity of visible light photons, as it can be observed in Fig. 4.1 (Chap. 4), it is very important to know the response of metal/semiconductor systems to this kind of irradiation. In the visible wavelength range, the expected charge transfer is from the metal nanoparticles to the semiconductor. Some studies have shown that under visible light, electron transfer from the metal nanoparticles produces the formation of radical

species on the semiconductor surface. In this case, the co-catalyst acts as electron donor or even acceptor, depending on the relative position of the Fermi level with respect to the CB (Gao et al. 2011; Ismael et al. 2009).

One of the main important challenges in the last years has been the use of metal nanoparticles with surface plasmon resonance (SPR) in photocatalytic applications. This effect is due to the collective electron oscillation in metallic nanoparticles, which at specific wavelengths can be driven resonantly, generating an electric field. These materials can thereby, and also because of their high scattering ability, concentrate and trap the light in the semiconductor and therefore enhance the photocatalytic activity. These materials can be designed to absorb light from the ultraviolet to the near-infrared region through a choice of their particle size, shape and dielectric environment (Shuller et al. 2010). This fact enables the synthesis of photocatalysts with a broadband enhancement across the wide solar spectrum. Two of the mainly used co-catalysts with SPR effect are Au and Ag NPs, which possess intense optical absorption and scattering properties, often with 10^5 times higher extinction coefficients than individual organic dye molecules (see Chap. 16).

Under UV light, the electron transfer from the semiconductor to SPR nanoparticles (such as Ag or Au) is easily distinguished by the changes observed in the plasmon frequency. The addition of photogenerated electrons to the NPs leads to a blue shift in the absorption spectrum (Hirakawa and Kamat 2005; Novo and Mulvaney 2007) that makes it possible to calculate the number of stored electrons. Takai et al. show that by UV irradiation of TiO_2 nanoparticles and Ag^+ ions, silver is reduced and deposited over the titania surface (Takai and Kamat 2011). These Ag^0 nanoparticles depict an absorption band at 430 nm due to SPR effect, which is shifted to 415 nm when the irradiation time is increased. This behaviour is due to an excess of electrons kept in the Ag NPs. Under illumination, the discharge has a lower rate than the charge process and a fraction of these electrons keeps in trap. However, in the dark, the plasmon band slowly returns to its previous value. Therefore, the electron storage is reversible and dependent on the amount of Ag deposited on TiO_2 (Fig. 10.2).

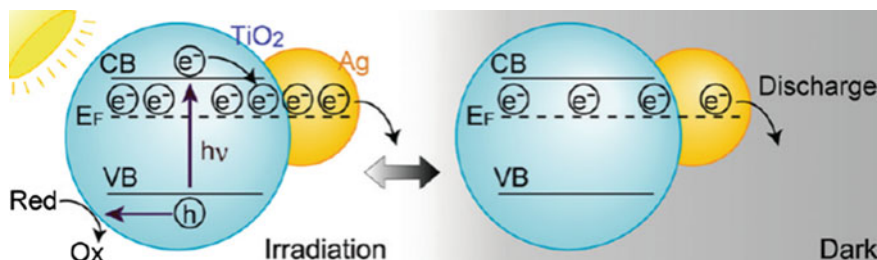


Fig. 10.2 Charge equilibration scenarios between TiO_2 and Ag nanoparticles during continuous UV irradiation and in the dark. Reproduced with permission from Takai and Kamat (2011). Copyright American Chemical Society

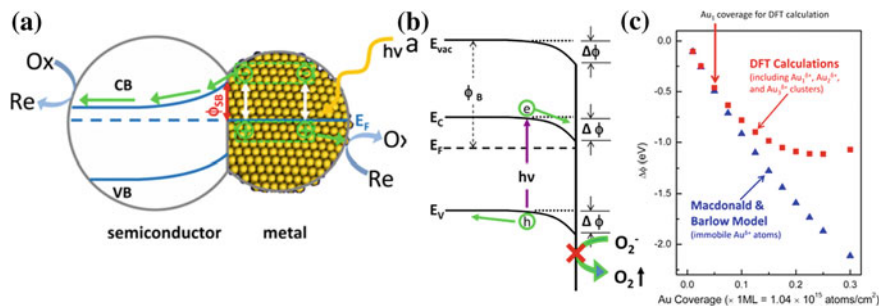


Fig. 10.3 **a** Schematic diagram of plasmon-induced charge separation and associated photochemistry at the metal/semiconductor photocatalyst. **b** Schematic diagram of downward band bending by Au and its effect on hole transport, causing decreasing $^{18}\text{O}_2$ PSD yield. **c** Plots of the work function change, calculated by DFT and the Macdonald and Barlow model versus Au coverage on $^{18}\text{O}_2/\text{TiO}_2(110)$ surface. Reproduced with permission from Zhang and Yates (2012). Copyright American Chemical Society

In the case of visible light irradiation, light absorption by SPR/semiconductor catalysts also occurs, but through the metal SPR. The electron transfer from the SPR nanoparticles to the semiconductor is observed in the range of picoseconds, with yields between 10 and 50 % (Kubacka et al. 2012). As depicted in Fig. 10.3, recent theoretical calculations have pointed out that the photocatalytic activity of these materials under visible light is due to the SPR–semiconductor interaction, involving surface-localized gap states of semiconductor (Zhang et al. 2011; Zhang and Yates 2012). This theory is in divergence with the proposed charge transfer phenomenon.

The use of other elements in the form of oxides, such as Cu, Cr and Fe, among others, which have a more ionic character, leads to a different behaviour in the photocatalytic activity. These oxides supported over semiconductors are used under UV, visible or even sunlight. The charge transfer depends on the light wavelength and the type of metal oxide.

The case of Cu oxides (with the presence of $\text{Cu}_2\text{O}/\text{CuO}$ phases) on anatase is a clear example of size effect on the charge transfer at different wavelengths (Borghain et al. 2002; Rafea and Roushdy 2009; Xu and Schoonen 2000; Yin et al. 2005; Lalitha et al. 2010). Catalysts with Cu-oxide NPs larger than 15 nm lead to an increase in the charge separation only under UV irradiation. The decrease in the particle size to 10 nm produces a modification in the Fermi-level position, and an increase in the band gap allows charge transfer from the copper oxide to the semiconductor in the visible region. For lower particle sizes, the band gap reaches a 3.0 eV value, and under UV irradiation, the charge transfer is possible in both directions.

On the other hand, the opto-electronic characteristics of iron oxide ($\alpha\text{-Fe}_2\text{O}_3$) allow the charge transfer even under visible light irradiation. When the particle size of this co-catalyst is between 10 and 3 nm, visible photon-excited electrons can be transferred to the anatase phase with the adequate distribution of the density of states (Libera et al. 2010; Tada et al. 2011).

10.2 Photocatalytic Behaviour

Although many unmodified wide-band-gap semiconductors are active for overall water splitting, their activities are drastically improved by loading with co-catalysts. Noble metals, such as Pt, Pd, Rh, Au and Ag, and oxides, such as CuO, NiO and, in minor proportion, RuO₂ and IrO₂, have been reported to be effective co-catalysts, as it has been observed in many examples cited throughout this book. Thus, the development of new co-catalysts has brought about numerous breakthroughs in different photocatalytic reactions.

10.2.1 Noble Metals

As it is mentioned above, noble metals like Pt, Pd, Rh, Au and Ag are well known as excellent co-catalysts, playing a crucial role in different redox reactions such as water detoxification, H₂ generation by water splitting or fuels and fine chemicals production by CO₂ photoreduction.

The main role of these metals is to prevent the recombination reaction (Bamwenda et al. 1995; Chong et al. 2010; Maeda and Domen 2007; Ni et al. 2007; Osterloh 2008). Furthermore, their particularity is that their Fermi levels have energy that is usually located below the CB of a great number of semiconductor materials. This characteristic allows the transference of photogenerated electrons from the VB to the metal nanoparticles, while holes remain in the semiconductor (Hernandez-Alonso et al. 2009; Subramanian et al. 2001, 2003, 2004; Jakob et al. 2003; Kamat et al. 2002; Liu et al. 2004).

10.2.1.1 Platinum

One of the mainly used elements in photocatalysts is platinum. Since the early studies in environmental applications, this metal has been used in different investigations on water purification (Sobczynski and Dobosz 2001). Izumi et al. showed the role of Pt over TiO₂ in the photooxidation of benzene (Izumi et al. 1980). This study pointed out that Pt NPs facilitate hydrocarbon oxidation by lowering the oxygen reduction potential and demonstrated the important effect of OH radicals on this kind of reactions. Crittenden et al. studied the influence of surface admixtures of Pt on the photocatalytic activity of TiO₂ in the abatement of chlorinated hydrocarbons, such as trichloroethylene and 1,4-dichlorobenzene, observing an improvement in the photoactivity compared to that of bare TiO₂ (Crittenden et al. 1997). On the other hand, Matsunaga et al. reported the first heterogeneous photocatalyst based on Pt/TiO₂ applied in disinfection. This group carried out their studies using photochemical and photoelectrochemical processes (Matsunaga et al. 1985).

Pt is one of the most used co-catalysts for water splitting. The transfer of photogenerated electrons from TiO_2 to Pt islands was investigated by Anpo and Takeuchi (2003), employing electron spin resonance (ESR). This work revealed an increase in the Ti 3p signals that is higher for longer irradiation times and is reduced for larger Pt loadings. This behaviour was attributed to an accumulation of electrons in Pt NPs that brings the Pt Fermi level closer to the CB of TiO_2 . Furthermore, smaller metal particles deposited on TiO_2 surface exhibit a more negative Fermi-level shift (Subramanian et al. 2003). However, a rapid back reaction between H_2 and O_2 may diminish the activity of Pt/ TiO_2 photocatalyst for water splitting (Maeda 2011). In order to minimize this drawback, some additives have been used in aqueous solution reactions, NaOH being the first of them (Fujishima 2000). In addition, the use of carbonate salts leads to an increase in the H_2/O_2 ratio close to the stoichiometric value, as reported by Sayama et al. IR studies showed the formation of several carbonate species, such as HCO_3^- , CO_3^{2-} , HCO_3^- and $\text{C}_2\text{O}_6^{2-}$, over Pt, by consumption of photogenerated holes (Sayama and Arakawa 1992). Further experiments using different additives and Pt/semiconductor catalysts were performed, showing an increase in the H_2 production (Sayama et al. 1998; Arakawa and Sayama 2000). On the other hand, the addition of other anions as I^- favours the suppression of the backward reaction (Abe et al. 2003). The use of high amounts of carbonate or iodide anions leads to poisoning by the coverage of the catalyst surface, producing a decrease in the light absorption (Sayama and Arakawa 1996).

Until the early 1990s, only a few visible-light-active catalysts had been developed. One of these systems was Pt/CdS, which appeared to be suitable for water splitting due to the appropriate position of conduction and valence bands (Mau et al. 1984; Reber and Rusek 1986). Nevertheless, these catalysts are unstable in water and highly toxic, as explained in Chap. 8 (Williams 1960). With other semiconductors such as SrTiO_3 , Pt has shown a low activity in overall water splitting under UV light (Kudo 2003). However, co-doped with Sb or Ta and Cr, H_2 production was higher even under visible light irradiation, with $\lambda > 420$ nm (Zou et al. 2001). In the case of Pt/TaNO, the activity for H_2 evolution upon visible irradiation in aqueous methanol solutions is one order of magnitude less than for O_2 evolution (Hitoki et al. 2002). Other interesting case under visible light is the Pt/AgInZn $_7$ S $_9$ that shows a H_2 evolution rate of 944 $\mu\text{mol/h}$ (Kudo et al. 2002). Platinum has also been used with niobates such as $\text{HCa}_2\text{Nb}_3\text{O}_{10}$, observing an increase in H_2 production of 40 times higher than that for a Pt/ TiO_2 sample (Yamaguti and Sato 1985).

Pt has been also used as co-catalyst in CO_2 photoreduction over different TiO_2 forms. Zhang et al. found that an optimal amount of Pt leads to a higher CH_4 production over TiO_2 nanotubes than over TiO_2 NPs (Zhang et al. 2009). These studies shown an increase in the methane formation with higher $\text{H}_2\text{O}/\text{CO}_2$ ratio for TiO_2 NT, which is not observed on TiO_2 NPs. This behaviour has been reported as well for Pt/ TiO_2 nanorods. A possible explanation is the preferential exposure of (0 1 0) TiO_2 faces in the nanorods (Pan et al. 2011).

10.2.1.2 Palladium

The role of palladium NPs as co-catalyst for photooxidation processes was studied by Wang et al. The Pd islands formed in this catalyst eliminate the excess of negative charge accumulated on the semiconductor surface, increasing the quantum yield of 2,2-dichloropropionate photooxidation up to 7 times in comparison with bare titania (Wang et al. 1992). Other studies performed by Papp et al. showed the influence of surface Pd additives on the activity of TiO₂ in 1,4-dichlorobenzene photodegradation and in salicylic acid photooxidation (Papp et al. 1993). A 30 % increase was observed with an optimized metal loading on titania (0.15 or 0.2 at %). Chen et al. compared the photodegradation of methanol, ethanol, trichloromethane, trichloroethylene and dichloropropionic acid in water suspensions of TiO₂, Pt/TiO₂ and Pd/TiO₂ (Chen et al. 1999a, b, c). In the case of dichloropropionic acid, the Pt NPs did not lead to an important increase in the photoactivity of TiO₂; however, Pd/TiO₂ catalyst strongly retarded the photodecarboxylation reaction. These studies show that oxygen reduction by photogenerated electrons occurs on metal islands in the pores, whereas oxidation by holes takes place on an illuminated part of the surface. In addition, Pd/TiO₂ has been used in CO₂ photoreduction. Yui et al. studied the effect of Pd (1 % wt) NPs supported on TiO₂ by the photodeposition method (Yui et al. 2011). The main obtained product was CH₄, and small amounts of CO and C₂H₆ were also detected. The drawback of this catalyst is the deactivation by Pd oxidation during the reaction.

Pd has been also deposited over ZnO surfaces using a photodeposition method, leading to an increase in the gas-phase photocatalytic oxidation of n-heptane. This improvement in the catalytic behaviour has been related to the proliferation of adsorbed oxygen measured by surface photovoltage spectroscopy (Liqiang et al. 2004).

10.2.1.3 Rhodium

Rh has been used as co-catalyst in different photocatalytic reactions. In the case of H₂ production by water splitting, the obtained results show that the catalytic activity is highly influenced by the dispersion of Rh NPs, because they tend to aggregate, decreasing the photocatalytic yield. Thus, Hata et al. prepared highly dispersed Rh NPs, stabilized by 3-mercapto-1-propanesulphuric acid, over KCa₂Nb₃O₁₀ and HCa₂Nb₃O₁₀, obtaining an enhancement in the H₂ production (Hata et al. 2008). In this case, Rh(OH)₃ and Rh₂O₃ nanoparticles were anchored to the calcium niobate sheets by covalent interactions. The same group published a work investigating other Rh–O–Nb systems based on K₄Nb₆O₁₇ nanoscrolls to elucidate the effect of expanding the interlayer space on activity. A higher hydrogen generation rate was achieved in this system compared to the previous one.

CO₂ photoreduction using hydrogen as a reductant has also been performed using Rh/semiconductor catalysts illuminated with an Hg lamp. The main product is CO, with rates changing as a function of the used semiconductor (TiO₂, ZrO₂, MgO and Ga₂O₃) (Kohno et al. 1997a, 1999; Teramura et al. 2004, 2008). The higher H₂ production was obtained for Rh/TiO₂. When TiO₂ and ZrO₂ were illuminated with UV light (365 and 254 nm), CH₄ was also produced (Lo 2007).

10.2.1.4 Gold

As in the case of platinum, Au nanoparticles can act as an electron scavenger (Chen et al. 1998c, 1999), but the latter exhibits capacitive properties (Kamat 2012). Electron accumulation of Au/TiO₂ catalyst is produced by a shift from the Au Fermi level (+0.45 vs NHE) to more negative potentials; this change is also observed in Au/ZnO catalysts (Subramanian et al. 2003; Wood et al. 2001). Another evidence is the appearance of the surface plasmon frequency (SPF) effect that shows a blue shift in the absorption spectrum due to the increasing SPF of the electron gas (Novo and Mulvaney 2007; Takai and Kamat 2011; Hirakawa and Kamat 2005).

Dobosz et al. prepared Au/TiO₂ catalyst for phenol photodegradation (Dobosz and Sobczynski 2001). This study shows that gold prevents the deactivation compared to bare TiO₂. Catechol, hydroquinone and p-benzoquinone were found as main intermediates in the photoreaction. Sakthivel et al. investigated the photooxidation of Acid Green 16 using Pt-, Au- and Pd-loaded TiO₂ as photocatalysts (Sakthivel et al. 2004). Loadings of Pt and Au were more effective than Pd because of suitable electron affinity and work function of Pt and Au.

Iwase et al. studied the effect of the photodeposition of gold particles on several niobates and tantalates: K₄Nb₆O₁₇, Sr₂Nb₂O₇, KTaO₃ and NaTaO₃ (Iwase et al. 2006). Overall water splitting was most efficient on Au/NaTaO₃ catalyst. In the first stage of the reaction, H₂ production is five times higher than for Au(1 %)-loaded La-doped NaTaO₃ catalyst (See Chap. 7). The comparison with a Pt catalyst shows a slightly higher H₂ production and negligible back reaction for Au co-catalyst.

As has been commented in the previous section, gold NPs possess surface plasmon effects that, in combination with an appropriate semiconductor, lead to photoactivity under a broad region of the spectrum (from UV to visible). The plasmonic excitation of an Au/TiO₂ system by visible light leads to the selective oxidation of thiol to disulphide, while UV light irradiation leads to the reverse reduction reaction (Naya et al. 2010).

Hou et al. analysed in depth the metal–semiconductor charge transfer processes that take place in an Au/TiO₂ catalyst used in a CO₂ photoreduction reaction carried out under different wavelengths (Hou et al. 2011). Under irradiation with visible light near to the Au plasmon resonance (532 nm), a 24-fold improvement in the photocatalytic activity is observed due to the intense local electromagnetic fields created by the surface plasmons of the Au nanoparticles. These authors

demonstrate that plasmon-excited electrons in the Au NPs cannot be directly transferred to TiO_2 . Thus, the photoactivity under visible light at the plasmon resonance wavelength is explained by the fact that because of the strong electromagnetic fields, electron-hole pairs are locally produced in TiO_2 with a rate several orders of magnitude higher than in the case of irradiation with other wavelengths. Only when the incident light (254 nm) is sufficient to excite the d-band electrons of Au to a conduction band that lies above that of TiO_2 , a direct charge transfer between these two materials is possible. In this case, a different mechanism occurs, resulting in the production of additional reaction products, including C_2H_6 , CH_3OH and HCHO . Under intermediate wavelength illumination (365 nm), Au/TiO_2 also catalyses reactions with a similar CH_4 production than bare TiO_2 (Fig. 10.4). This behaviour means that the electron transfer is not produced, confirming that the plasmonic enhancement in photocatalysis under visible illumination is a result of the strong electric fields created by the SPR of the Au NPs rather than of direct charge transfer.

10.2.1.5 Silver

Silver has mainly been used in photocatalysis as bactericidal agent in hygiene and medicinal applications. Several studies have indicated that Ag/TiO_2 catalyst may enhance the photodestruction, even under visible irradiation, of different azodyes and pathogenic bacteria, such as *E. coli*, *Streptococcus pyogenes*, *Staphylococcus aureus* and *Acinetobacter baumannii* (Hu et al. 2006; Yao et al. 2008; Hu et al. 2007; Matsui et al. 2004).

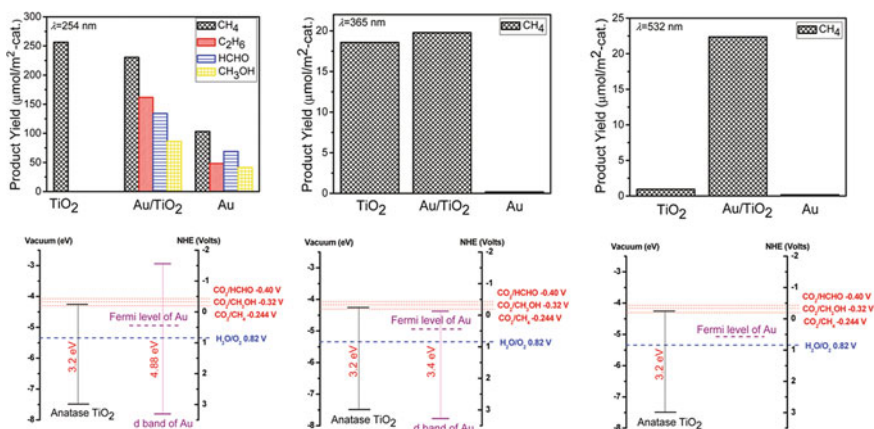
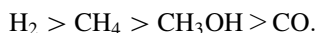


Fig. 10.4 Photocatalytic product yields after 15 h and energy band alignment of anatase TiO_2 , Au and the relevant redox potentials of CO_2 and H_2O products under different illumination wavelengths: 254, 365 and 532 nm. Reproduced with permission from Hou et al. (2011). Copyright American Chemical Society

Silver is also used for water detoxification, where several studies have shown an increase in the activity of 1,4-dichlorobenzene and phenol photooxidation after Ag photodeposition over TiO₂ (Lee et al. 1993; Dobosz and Sobczyński 2003). In the field of water purification, Kohtani et al. have applied Ag/BiVO₄ to the photocatalytic degradation of various aqueous pollutants (Kohtani et al. 2005a, b). This catalyst shows a higher activity than bare BiVO₄ in the photodegradation of 4-n-octyl- and 4-n-nonylphenol. The enhancement in the activity behaviour is connected with the strong adsorption of the pollutant over the surface of the silver co-catalyst.

Koci et al. have studied the role of silver NPs supported on TiO₂ in CO₂ photoreduction under UV and visible irradiation (Koci et al. 2010). The best results were obtained in an Ag(7 %)/TiO₂ photocatalyst that showed the subsequent products in the decrease order:



On the other hand, an AgBr/TiO₂ photocatalyst prepared by the deposition-precipitation method was also tested for CO₂ photoreduction under visible light in aqueous solutions (Asi et al. 2011). The maximum yield of CH₄, CH₃OH, ethanol and CO at pH 8.5 under visible light was achieved using AgBr (23.2 wt%)/TiO₂. Characterization studies showed that this catalyst is stable under reaction conditions, and the leaching of silver is not observed.

As in the case of gold, silver nanoparticles possess surface plasmon effect, and under a determinate wavelength illumination (in the range of the visible light near to the UV region), an excitation of localized plasmon polaritons on the surface of silver NPs leads to an increase in the near-field amplitude. As previously commented, the exact resonance wavelength depends on the shape and the dielectric environment of the NPs. Awazu et al. demonstrated that thanks to the intensification of the localized surface plasmon in an Ag/TiO₂ catalyst coated with SiO₂ (to prevent the metal oxidation), an enhancement by a factor of 7 was obtained in the photodecomposition of methylene blue under near-UV illumination (Awazu 2008).

10.2.2 Transition Metals

Since noble metals are very expensive, more research is needed to identify low-cost metals with acceptable enhancement in photocatalytic activity. Some examples of these photocatalytic systems are explained in this section.

10.2.2.1 Copper

Copper is one of the most used co-catalysts for both photocatalytic oxidation and reduction processes. Several Cu-based supported co-catalysts have been used in the degradation of different organic water pollutants and bacteria. It has been

reported that in Cu/TiO₂ catalysts, metallic copper (Cu⁰) and copper (CuO and Cu₂O) coexist in the same material (Sunada et al. 2003). This concurrence is explained because when Cu/TiO₂ is irradiated, copper oxides can be reduced to Cu⁰, which in turn can be oxidized back by photogenerated electrons and holes, respectively. The antibacterial function of TiO₂ photocatalysts is markedly enhanced, even with weak UV light, when copper is used. In the study performed by Sunada et al., *E. coli* cells survived under dark conditions. However, when the Cu/TiO₂ film was irradiated with very weak UV light, the survival fraction began to decrease (Sunada et al. 2003). Initial illumination had a negligible effect, but after 2 h, a marked decrease in survival was observed. The conclusion of this work is that cell deactivation proceeds as follows: TiO₂ attacks the bacteria membrane, and copper acts against the cytoplasmic membrane. In fact, TiO₂ allow the intrusion of the copper ions into the cell, facilitating the effective kill of *E. Coli* on a Cu/TiO₂ film even under very weak UV light.

Dhanalakshmi et al. investigated dye-sensitized hydrogen production, where Cu/TiO₂ and Pt/TiO₂ were used as photocatalysts (Dhanalakshmi et al. 2001). An enhancement in the H₂ production was observed, and the effect of Cu loading was almost comparable with Pt loading. Differently, Wu and Lee studied a Cu/TiO₂ catalyst for hydrogen production from methanol solution (Wu and Lee 2004). At the optimal Cu loading, hydrogen production rate was enhanced as much as 10 times.

In CO₂ photoreduction studies performed by Tseng et al. using different Cu–TiO₂ systems (doped and supported), all catalysts are more efficient than bare P25, being doped systems twice more efficient in CH₃OH production than the supported ones. However, other products obtained in the supported system, such as CH₄, HCOOH and other hydrocarbons, were not detected in Cu-doped TiO₂ (Tseng et al. 2002, 2004; Tseng and Wu 2004). The higher activity of this catalyst was attributed to the good dispersion of predominant Cu(I) species, with 25 % of total copper loading located on the outermost TiO₂ surface. Later studies using an optical fibre photoreactor showed that methanol formation is a function of Cu oxidation state (Wu and Lin 2005; Wu 2005). The maximum amount of methanol was obtained for CuO–TiO₂ and then with Cu₂O–TiO₂ and Cu–TiO₂ (Slamet et al. 2005). Cu/TiO₂ catalyst has also been used embedded inside the mesoporous channels of SBA-15, obtaining CH₃OH as the main product (Yang et al. 2009). Loading copper on titania somewhat increases the photocatalytic CO₂ reduction efficiency. Thus, inert mesoporous matrices also contribute to improve the CO₂ photoconversion by dispersion of copper over titania particles. A recent study of Cu–TiO₂ supported on a molecular sieve leads to oxalic acid as main product in pure and basic water (Srinivas et al. 2011). Trace amounts of CH₄, CH₃OH and acetic acid were also observed when the reaction was carried out in basic water.

10.2.2.2 Nickel

Other low-cost metals, such as NiO_x (Anpo and Takeuchi 2003), were also found to be effective for photocatalytic activity enhancement. This metal oxide is expected to be a promising material to improve photocatalytic activities for

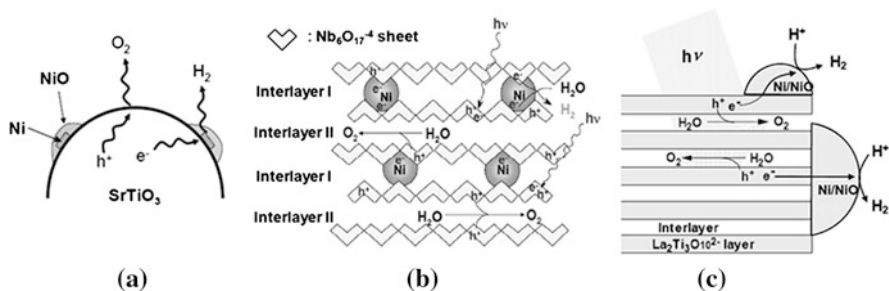


Fig. 10.5 Oxide photocatalysts active for overall water splitting under UV light. (a) NiO/Ni/SrTiO₃, (b) Ni/K₄Nb₆O₁₇ and (c) NiO/Ni/Rb₂La₂Ti₃O₁₀. Reproduced with permission from (Hisatomi and Kazunari 2009). Copyright SPIE Digital Library

practical applications. In this context, several NiO-loaded catalysts have been reported to be effective to stoichiometrically decompose H₂O into H₂ and O₂ (see Fig. 10.5), using different materials such as:

1. SrTiO₃ (Domen et al. 1980, 1982a, b, 1986a, b) and NaTaO₃ (Kato and Kudo 1999, 2001, 2002, 2003; Kato et al. 2003) has been used for photoelectrochemical water splitting with a good performance, but when the bare semiconductors are used, the photoactivity is negligible. However, if this system is modified with NiO, the studies revealed that the Ni/NiO core/shell formed is more effective for H₂ evolution, because the interface between Ni–NiO and SrTiO₃ or NaTaO₃ facilitates electron transfer.
2. K₄Nb₆O₁₇ (Kudo et al. 1989a, b) is a layered material where K⁺ cations can be replaced by Ni²⁺ in alternate layers. Under irradiation, the photoelectrons generated in Ni NPs reduce H⁺ to H₂, while the photoholes formed in the other layers lead to water oxidation to produce O₂.
3. K₂La₂Ti₃O₁₀ (Takata et al. 1997a, b)-layered perovskite was used as support for Ni/NiO core–shell nanoparticles, similarly to SrTiO₃ and NaTaO₃. In this case, thanks to Ni NPs, a separation of the photogenerated electrons and holes, at the external surface and the interlayer spaces, leads to an increase in the H₂ production.

10.2.2.3 Oxides of Other Transition Metals

Ruthenium oxide has been demonstrated by many researchers to be effective as an oxidation site for the evolution of O₂ gas (Borgarello et al. 1981; Duonghong et al. 1981; Kawai and Sakata 1980a, b). RuO₂ NPs over n-type semiconductors act as reduction catalyst (Amouyal et al. 1980; Keller et al. 1982), being an important co-catalyst for promoting overall water splitting. Sakata et al. reported that the rate of H₂ evolution in the presence of ethanol is 30 times higher over RuO₂/TiO₂ than for bare TiO₂ (Sakata et al. 1984). RuO₂ has been used as co-catalyst with barium

titanate semiconductors (Kohno et al. 1996, 1997a, b, c, 1998): BaTi_4O_9 , $\text{Ba}_6\text{Ti}_{17}\text{O}_{40}$, $\text{Ba}_4\text{Ti}_{13}\text{O}_{30}$ and $\text{Ba}_2\text{Ti}_9\text{O}_{20}$. The higher activity was obtained with $\text{RuO}_2/\text{BaTi}_4\text{O}_9$ sample, despite metallic Ru species themselves being poor co-catalysts (Ogura et al. 1998, 2000). These studies show that pentagonal-prism tunnel structure of BaTi_4O_9 prevents the aggregation of the RuO_2 NPs, leading to an increase in the metal oxide dispersion and an enhancement in the overall water-splitting activity. Recently, Sato et al. have discovered that the use of RuO_2 with various p-block metal oxides is also effective for overall water splitting (Sato et al. 2002, 2003, 2005). Finally, $\text{RuO}_2/(\text{Ga}_{1-x}\text{Zn}_x)(\text{N}_{1-x}\text{O}_x)$ has been shown to be an effective photocatalyst for overall water splitting under visible light irradiation (Maeda et al. 2005, Teramura et al. 2005).

As another example, iridium oxide plays an important role as hole transfer mediator under UV irradiation. Spectroscopic studies have enabled to identify trapped holes on TiO_2 suspensions and to monitor their transfer to IrO_2 (Meekins and Kamat 2011). An estimation of three holes per particle has been realized by titration measurements under UV irradiation (7 min) of a TiO_2 suspension in ethanol containing 5 % acetic acid. IrO_2 also catalyses the oxidation of reduced oxygen species by trapped holes to produce molecular oxygen.

10.2.3 Bi-metallic Co-catalysts

Recently, some authors have proposed a combination of different metals and metal oxides that leads to a synergistic effect between them and gives rise to a qualitative improvement in the photocatalytic activity. One of the most recent examples of the use of a metal–metal oxide mixture was developed by Liu et al., who synthesized different photocatalysts based on Zn_2GeO_4 for CO_2 photoreduction (2010). The inclusion of RuO_2 (1 wt%) as co-catalyst led to an increase in methane production from 0.41 to 1.9 $\mu\text{mol/h g}$, while the further addition of Pt as another co-catalyst increased the CH_4 production to 6.5 $\mu\text{mol/h g}$. The use of both additives favours CO_2 reduction and avoids the back reaction between H_2 and O_2 in water splitting.

Other most interesting examples are core–shell structures with a metal oxide covering a metallic core. As previously mentioned, one of the first core/shell structures used for photocatalytic applications was the Ni/NiO system (Kudo and Miseki 2009), but the main advance in these multicomponent co-catalysts has been performed by Maeda et al., who have developed very efficient materials for overall water splitting. As it was commented above, although metal nanoparticles (such as Pt or Rh) improve the photocatalytic activity in H_2 production, the aggregation of these NPs under reaction conditions leads to a decrease in the photocatalytic activity, even when these nanoparticles are highly dispersed (Hata et al. 2008). However, the pioneer study developed by Maeda et al. points out that when a core/shell structure is used in photo-co-catalytic water splitting, like in GaN:ZnO loaded with metal/ Cr_2O_3 core–shell co-catalyst, an enhancement in the H_2 production from pure water is obtained, due to a notable decrease in recombination rates with respect to the case of the uncovered Rh or Pt particles (Maeda et al.

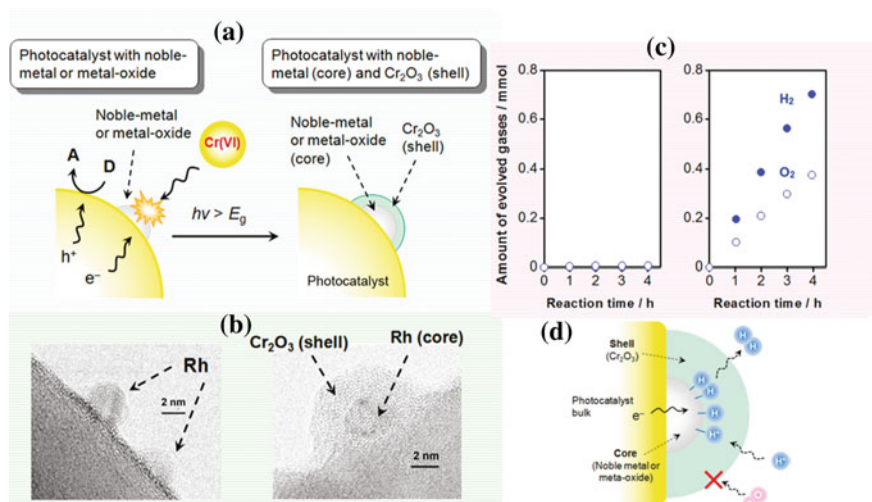


Fig. 10.6 **a** Schematic illustration of Cr_2O_3 deposition through the reduction in $Cr(VI)$ cations (**d** and **a** indicate electron donor and acceptor, respectively). **b** HR-TEM images of GaN:ZnO with photodeposited Rh before (*left*) and after (*right*) photodeposition of a Cr_2O_3 shell. **c** Time course of overall water splitting under visible light ($\lambda > 400$ nm) using GaN:ZnO modified with Rh and (*left*) core/shell-structured Rh/ Cr_2O_3 (*right*). **d** Schematic illustration of H_2 evolution on core/shell-structured nanoparticles (with a noble metal or metal oxide core and a Cr_2O_3 shell) as a co-catalyst for photocatalytic overall water splitting. Reproduced with permission from Maeda and Domen (2010c). Copyright American Chemical Society

2006, 2010a). These core-shell co-catalysts were firstly prepared by photoreduction of $Cr(IV)$ ions over Rh NPs in air-free conditions. Structural studies performed by high-resolution transmission electron microscopy and X-ray photoelectron spectroscopy show that the Rh core is covered by a Cr_2O_3 shell of 2 nm thickness (Fig. 10.6).

The results obtained with these systems suggest that metal/ Cr_2O_3 structures suppress metal deactivation and avoid both the backward reaction to produce water and the O_2 photoreduction reaction that decreases the activity (Maeda et al. 2007). These authors optimized the preparation procedure using stabilized Rh NPs that showed a particle size 4 times lower than those obtained by the photodeposition method. These nanoparticles were covered with a shell of Cr_2O_3 , leading to a three-time photoactivity enhancement compared to the equivalent systems with poorer dispersion (Sakamoto et al. 2009). Later studies performed with spectroscopic and electrochemical techniques indicate that the Cr_2O_3 shell is permeable to protons, but not to O_2 molecules, and that H_2 formation is produced in the metal/ Cr_2O_3 interface (Fig. 10.6d) (Yoshida et al. 2009).

Subsequent studies have shown an increase in the photocatalytic activity under visible light irradiation with Rh/ Cr_2O_3 catalyst mixed with Mn_3O_4 nanoparticles. This new system leads to separate active sites for H_2 (core-shell structure) and O_2 (Mn_3O_4 NPs) evolution in water splitting (Maeda et al. 2010b).

References

- Abe R, Sayama K, Arakawa H (2003) Significant effect of iodide addition on water splitting into H_2 and O_2 over Pt-loaded TiO_2 photocatalyst: suppression of backward reaction. *Chem Phys Lett* 371:360
- Amouyal E, Keller P, Moradpour A (1980) Light-induced hydrogen generation from water catalysed by ruthenium dioxide. *J Chem Soc Chem Commun* 21:1019
- Anpo M, Takeuchi M (2003) The design and development of highly reactive titanium oxide photocatalysts operating under visible light irradiation. *J Catal* 216:505
- Arakawa H, Sayama K (2000) Solar hydrogen production: significant effect of Na_2CO_3 addition on water splitting using simple oxide semiconductor photocatalysts. *Catal Surv Jpn* 4:75
- Asi MS, He C, Su M, Xia D, Lin L, Deng H, Xiong Y, Qiu R, Li X-Z (2011) Photocatalytic reduction of CO_2 to hydrocarbons using AgBr/ TiO_2 nanocomposites under visible light. *Catal Today* 175:256
- Awazu K (2008) A plasmonic photocatalyst consisting of silver nanoparticles embedded in titanium dioxide. *J Am Chem Soc* 130:1676
- Bamwenda GR, Tsubota S, Nakamura T, Haruta M (1995) Photoassisted hydrogen production from a water ethanol solution: a comparison of activities of Au- TiO_2 and Pt- TiO_2 . *J Photochem Photobiol A Chem* 89:177
- Borgarello E, Kiwi J, Pelizzetti E, Visca M, Gratzel M (1981) Photochemical cleavage of water by photocatalysis. *Nature* 289:158
- Borgohain K, Morase N, Mahumani S (2002) Synthesis and properties of Cu_2O quantum particles. *J Appl Phys* 92:129
- Chen J, Ollis DF, Rulkens WH, Bruning H (1999a) Photocatalyzed oxidation of alcohols and organochlorides in the presence of native TiO_2 and metallized TiO_2 suspensions. Part (I): Photocatalytic Activity and pH Influence. *Water Res* 33:661
- Chen J, Ollis DF, Rulkens WH, Bruning H (1999b) Photocatalyzed oxidation of alcohols and organochlorides in the presence of native TiO_2 and metallized TiO_2 suspensions. Part (II): photocatalytic mechanisms. *Water Res* 33:669
- Chen J, Ollis DF, Rulkens WH, Bruning H (1999c) Kinetic processes of photocatalytic mineralization of alcohols on metallized titanium dioxide. *Water Res* 33:1173
- Chen S, Ingram RS, Hostetler MJ, Pietron JJ, Murray RW, Schaaff TG, Khoury JT, Alvarez MM, Whetten RL (1998a) Gold nanoelectrodes of varied size: transition to molecule-like charging. *Science* 280:2098
- Chen S, Murray RW, Feldberg SW (1998b) Quantized capacitance charging of monolayer-protected Au clusters. *J Phys Chem B* 102:9898
- Chen S, Ingram RS, Hostetler MJ, Pietron JJ, Murray RW, Schaaff TG, Khoury JT, Alvarez MM, Whetten RL (1998c) Gold nanoelectrodes of varied size: transition to molecule-like charging. *Science* 280:2098
- Chen S, Murray RW (1999) Electrochemical quantized capacitance charging of surface ensembles of gold nanoparticles. *J Phys Chem B* 103:9996
- Chong M-N, Bo Jin B, Chow CW, Saint K (2010) Recent developments in photocatalytic water treatment technology: a review. *Water Res* 44:2997
- Crittenden JC, Liu J, Hand D, Perram D (1997) Photocatalytic oxidation of chlorinated hydrocarbons in water. *Water Res* 31:429
- Dhanalakshmi KB, Latha S, Anandan S, Maruthamuthu P (2001) Dye sensitized hydrogen evolution from water. *Int J Hydrogen Energy* 26:666
- Dobosz A, Sobczykński A (2001) Water detoxification: photocatalytic decomposition of phenol on Au/ TiO_2 . *Monatshefte für Chemie* 132:1037–1045
- Dobosz A, Sobczykński A (2003) The influence of silver additives on titania photoactivity in the photooxidation of phenol. *Water Res* 37:1489
- Domen K, Naito S, Soma M, Onishi T, Tamaru KJ (1980) Photocatalytic decomposition of water vapour on an NiO- $SrTiO_3$ catalyst. *Chem Soc Chem Commun* 12:543

- Domen K, Naito S, Onishi T, Tamaru K (1982a) Photocatalytic decomposition of liquid water on a NiO-SrTiO₃ catalyst. *Chem Phys Lett* 92:433
- Domen K, Naito S, Onishi T, Tamaru K (1982b) Study of the photocatalytic decomposition of water vapor over a nickel(II) oxide-strontium titanate (SrTiO₃) catalyst. *J Phys Chem* 86:3657
- Domen K, Kudo A, Onishi T, Kosugi N, Kuroda HJ (1986a) Photocatalytic decomposition of water into hydrogen and oxygen over nickel(II) oxide-strontium titanate (SrTiO₃) powder. I structure of the catalysts. *Phys Chem* 90:292
- Domen K, Kudo A, Onishi T (1986b) Mechanism of photocatalytic decomposition of water into H₂ and O₂ over NiO-SrTiO₃. *J Catal* 102:92
- Duonghong D, Borgarello E, Gratzel M (1981) Sustained water cleavage by visible light. *J Am Chem Soc* 103:4685
- Einaga H, Harada M (2005) Photochemical preparation of poly(N-vinyl-2-pyrrolidone)-stabilized platinum colloids and their deposition on titanium dioxide. *Langmuir* 21:2578
- Fujishima A, Zhang X, Tryk AD (2008) TiO₂ photocatalysis and related surface phenomena. *Surf Sci Rep* 63:515
- Gao S, Ueno K, Misawa H (2011) Plasmonic antenna effects on photochemical reactions. *Acc Chem Res* 44:251
- Hata H, Kobayashi Y, Bojan V, Youngblood WJ, Mallouk TE (2008) Direct deposition of trivalent rhodium hydroxide nanoparticles onto a semiconducting layered calcium niobate for photocatalytic hydrogen evolution. *Nano Lett* 8:794
- Hernandez-Alonso MD, Fresno F, Suarez S, Coronado JM (2009) Development of alternative photocatalysts to TiO₂: challenges and opportunities. *Energy Environ Sci* 2:1231
- Hirakawa T, Kamat PV (2004) Electron storage and surface plasmon modulation in Ag@TiO₂ clusters. *Langmuir* 20:5645
- Hirakawa T, Kamat PV (2005) Charge separation and catalytic activity of Ag@TiO₂ core-shell composite clusters under UV irradiation. *J Am Chem Soc* 127:3928
- Hisatomi T, Kazunari Domen K (2009) Recent progress in photocatalysts for overall water splitting under visible light. In: Frank EO (ed) *Proceedings of solar hydrogen and nanotechnology*, Vol 7408, p 740802-1
- Hitoki G, Takata T, Kondo JN, Hara M, Kobayashi H, Domen K (2002) An oxynitride, TaON, as an efficient water oxidation photocatalyst under visible light irradiation ($\lambda \leq 500$ nm). *Chem Commun* 16:1698
- Hou W, Hung WH, Pavaskar P, Goepfert A, Aykol M, Cronin SB (2011) Photocatalytic conversion of CO₂ to hydrocarbon fuels via plasmon-enhanced absorption and metallic interband transitions. *ACS Catal* 1:929
- Hu C, Lan Y, Qu J, Hu X, Wang A (2006) Ag/AgBr/TiO₂ visible light photocatalyst for destruction of azodyes and bacteria. *J Phys Chem B* 110:4066
- Hu C, Guo J, Qu J, Hu X (2007) Photocatalytic degradation of pathogenic bacteria with AgI/TiO₂ under visible light irradiation. *Langmuir* 23:4982
- Ismael AA, Bahnemann DW, Bannat I, Wak MJ (2009) Gold nanoparticles on mesoporous interparticle networks of titanium dioxide nanocrystals for enhanced photonic efficiencies. *Phys Chem C* 113:7429
- Iwase A, Kato H, Kudo A (2006) Nanosized Au particles for photocatalytic overall water splitting. *Catal Lett* 108:7
- Izumi I, Dunn WW, Wilbourn KO, Fun F, Bard AJ (1980) Heterogeneous photocatalytic oxidation of hydrocarbons on platinized TiO₂ Powders. *J Phys Chem* 84:3207
- Jakob M, Levanon H, Kamat PV (2003) Charge distribution between UV-irradiated TiO₂ and gold nanoparticles: determination of shift in the Fermi level. *Nano Lett* 3:353
- Kamat PV, Flumiani M, Dawson A (2002) Metal-metal and metal-semiconductor composite nanoclusters. *Colloids Surf A: Physio Chem Eng Aspects* 202:269
- Kamat PV (2012) Manipulation of charge transfer across semiconductor interface. A criterion that cannot be ignored in photocatalyst design. *J Phys Chem Lett* 3:663
- Kato H, Kudo A (1999) Highly efficient decomposition of pure water into H₂ and O₂ over NaTaO₃ photocatalysts. *Catal Lett* 58:153

- Kato H, Kudo AJ (2001) Water splitting into H₂ and O₂ on alkali tantalate photocatalysts ATaO₃ (A = Li, Na, and K). *Phys Chem B* 105:4285
- Kato H, Kudo A (2002) Photocatalytic reduction of nitrate ions over tantalate photocatalysts. *Phys Chem Chem Phys* 4:2833
- Kato H, Kudo A (2003) Photocatalytic water splitting into H₂ and O₂ over various tantalate photocatalysts. *Catal Today* 78:561
- Kato H, Asakura K, Kudo A (2003) highly efficient water splitting into H₂ and O₂ over lanthanum-doped NaTaO₃ photocatalysts with high crystallinity and surface nanostructure. *J Am Chem Soc* 125:3082
- Kawai T, Sakata T (1980a) Conversion of carbohydrate into hydrogen fuel by a photocatalytic process. *Nature* 286:474
- Kawai T, Sakata T (1980b) Photocatalytic decomposition of gaseous water over TiO₂ and TiO₂—RuO₂ surfaces. *Chem Phys Lett* 72:87
- Keller P, Moradpour A, Amouyal E (1982) Ruthenium dioxide: a redox catalyst for the generation of hydrogen from water. *J Chem Soc Faraday Trans 1* 78:3331
- Kohno M, Ogura S, Inoue Y (1996) Preparation of BaTi₄O₉ by a sol-gel method and its photocatalytic activity for water decomposition. *J Mater Chem* 6:1921
- Kohno M, Ogura S, Sato K, Inoue Y (1997a) Properties of photocatalysts with tunnel structures: formation of a surface lattice O⁻ radical by the UV irradiation of BaTi₄O₉ with a pentagonal-prism tunnel structure. *Chem Phys Lett* 267:72
- Kohno M, Ogura S, Sato K, Inoue Y (1997b) Reduction and oxidation of BaTi₄O₉ with a pentagonal prism tunnel structure—effects on radical formation upon UV irradiation and on the activity of RuO₂/BaTi₄O₉ photocatalyst for water decomposition. *J Chem Soc Faraday Trans* 93:2433
- Kohno M, Kaneko T, Ogura S, Sato K, Inoue Y (1998) Dispersion of ruthenium oxide on barium titanates (Ba₆Ti₁₇O₄₀, Ba₄Ti₁₃O₃₀, BaTi₄O₉ and Ba₂Ti₉O₂₀) and photocatalytic activity for water decomposition. *J Chem Soc Faraday Trans* 94:89
- Kohno Y, Tanaka T, Funabiki T, Yoshida S (1997c) Photoreduction of carbon dioxide with hydrogen over ZrO₂. *Chem Commun* 9:841
- Kohno Y, Hayashi H, Takenaka S, Tanaka T, Funabiki T, Yoshida S (1999) Photo-enhanced reduction of carbon dioxide with hydrogen over Rh/TiO₂. *J Photochem Photobiol A* 126:117
- Koci K, Mateju K, Obalova L, Krejciikova S, Lacny Z, Placha D, Capek L, Hospodkova A, Solcova O (2010) Effect of silver doping on the TiO₂ for photocatalytic reduction of CO₂. *Appl Catal B* 96:239
- Kohtani S, Hiro J, Yamamoto N, Kudo A, Tokumura K, Nakagaki R (2005a) Adsorptive and photocatalytic properties of Ag-loaded BiVO₄ on the degradation of 4-n-alkylphenols under visible light irradiation. *Catal Commun* 6:185
- Kohtani S, Tomohiro M, Tokumura K, Nakagaki R (2005b) Photooxidation reactions of polycyclic aromatic hydrocarbons over pure and Ag-loaded BiVO₄ photocatalysts. *Appl Catal B* 58:265
- Kraeutler B, Bard AJ (1978) Heterogeneous photocatalytic preparation of supported catalysts. Photodeposition of platinum on titanium dioxide powder and other substrates. *J Am Chem Soc* 100:4317
- Kubacka A, Fernandez-García M, Colon G (2012) Advanced nanoarchitectures for solar photocatalytic applications. *Chem Rev* 112:1555
- Kudo A, Tanaka A, Domen K, Maruya K, Aika K, Onishi T (1989a) Photocatalytic decomposition of water over NiO-K₄Nb₆O₁₇ catalyst. *J. Catal* 111:67
- Kudo A, Sayama K, Tanaka A, Asakura K, Domen K, Maruya K, Onishi T (1989b) Nickel-loaded K₄Nb₆O₁₇ photocatalyst in the decomposition of H₂O into H₂ and O₂: structure and reaction mechanism. *J Catal* 120:337
- Kudo A, Kato H, Nakagawa S (2000) Water splitting into H₂ and O₂ on New Sr₂M₂O₇ (M = Nb and Ta) photocatalysts with layered perovskite structures: factors affecting the photocatalytic activity. *J Phys Chem B* 104:571

- Kudo A, Tsuji I, Kato H (2002) AgInZn₇S₉ solid solution photocatalyst for H₂ evolution from aqueous solutions under visible light irradiation. *Chem. Commun* 17:1958
- Kudo A (2003) Photocatalyst materials for water splitting. *Catal Surv Asia* 7:31
- Kudo A, Miseki Y (2009) Heterogeneous photocatalyst materials for water splitting. *Chem Soc Rev* 38:253
- Lalitha K, Sadanandam G, Kumari VD, Subrmanyam M, Sreedar B, Hebalkar NY (2010) Highly stabilized and finely dispersed Cu₂O/TiO₂: a promising visible sensitive photocatalyst for continuous production of hydrogen from glycerol:water mixtures. *J Phys Chem C* 114:22181
- Lee W, Shen H-S, Dwight K, Wold A (1993) Effect of silver on the photocatalytic activity of TiO₂. *J Solid State Chem* 106:288
- Libera JA, Elen JW, Saiter NI, Rajh T, Dimitrijevic ND (2010) Iron(III)-oxo centers on TiO₂ for visible-light photocatalysis. *Chem Mater* 22:409
- Liqiang J, Baiqi W, Baifu X, Shudan L, Keying S, Weimin C, Honggang F (2004) Investigations on the surface modification of ZnO nanoparticle photocatalyst by depositing Pd. *J Solid State Chem* 177:4221
- Liu SX, Qu ZP, Han XW, Sun CL (2004) A mechanism for enhanced photocatalytic activity of silver-loaded titanium dioxide. *Catal Today* 93–95:877
- Liu Q, Zhou Y, Kou J, Chen X, Tian Z, Gao J, Yan S, Zou Z (2010) High-yield synthesis of ultralong and ultrathin Zn₂GeO₄ nanoribbons toward improved photocatalytic reduction of CO₂ into renewable hydrocarbon fuel. *J Am Chem Soc* 130:14385
- Lo, C-Ca, Hung, C-Hb, Yuan C-Sa , Wu J-Fa (2007) Photoreduction of carbon dioxide with H₂ and H₂O over TiO₂ and ZrO₂ in a circulated photocatalytic reactor. *Sol Energy Mat Sol C* 91:1765
- Maeda K, Takata T, Hara M, Saito N, Inoue Y, Kobayashi H, Domen K (2005) GaN: ZnO solid solution as a photocatalyst for visible-light-driven overall water splitting. *J Am Chem Soc* 127:8286
- Maeda K, Teramura K, Lu D, Saito N, Inoue Y, Domen K (2006) Noble-metal/Cr₂O₃ core/shell nanoparticles as a cocatalyst for photocatalytic overall water splitting. *Angew Chem Int Ed* 45:7806
- Maeda K, Domen K (2007) New non-oxide photocatalysts designed for overall water splitting under visible light. *J Phys Chem C* 111:7851
- Maeda K, Teramura K, Lu D, Saito N, Inoue Y, Domen K (2007) Roles of Rh/Cr₂O₃ (core/shell) nanoparticles photodeposited on visible-light-responsive (Ga_{1-x}Zn_x)(N_{1-x}O_x) solid solutions in photocatalytic overall water splitting. *J Phys Chem C* 111:7554
- Maeda K, Sakamoto N, Ikeda T, Ohtsuka H, Xiong A, Lu D, Kanehara M, Teranishi T, Domen K (2010a) Preparation of core/shell-structured nanoparticles (with a noble-metal or metal-oxide core and a chromia shell) and their application in visible-light water splitting. *Chem Eur J* 16:7750
- Maeda K, Xiong A, Yoshinaga T, Ikeda T, Sakamoto N, Hisatomi T, Takashima M, Lu D, Kanehara M, Setoyama Teranishi T, Domen K (2010b) Photocatalytic overall water splitting promoted by two different cocatalysts for hydrogen and oxygen evolution under visible light. *Angew Chem Int Ed* 49:4096
- Maeda K, Domen K (2010) Photocatalytic water splitting: recent progress and future challenges. *J Phys Chem Lett* 1:2655
- Maeda K (2011) Photocatalytic water splitting using semiconductor particles: history and recent developments. *J. Photochem Photobiol C Photochem Rev* 12:237
- Matsui Y, Otomo K, Ishida S, Yanagihara K, Kawanobe Y (2004) Effect of silver-carrying photocatalyst “Hikari-Gintech” on mycobacterial growth in vitro. *Microbiol Immunol* 48:489
- Matsunaga T, Tomoda R, Nakajima T, Wake H (1985) Photoelectrochemical sterilization of microbial cells by semiconductor powders *FEMS Microbiol. Lett.* 29:211
- Mau AW-H, Huang CB, Kakuta N, Bard A J (1984) Hydrogen photoproduction by Nafion/cadmium sulfide/platinum films in water/sulfide ion solutions. *J Am Chem Soc* 106:6537

- Meekins BH, Kamat PV (2011) Role of water oxidation catalyst, IrO₂ in shuttling photogenerated holes across TiO₂ interface. *J Phys Chem Lett* 2:2310
- Nakamatsu H, Kawai T, Koreeda A, Kawai S (1986) Electron-microscopic observation of photodeposited Pt on TiO₂ particles in relation to photocatalytic activity. *J. Chem Soc Faraday Trans 1*:527
- Naya S, Teranishi M, Isobe T, Tada H (2010) Light wavelength-switchable photocatalytic reaction by gold nanoparticle-loaded titanium (IV) dioxide. *Chem Commun* 46:815
- Ni M, Leung MKH, Leung DYC, Sumathy K (2007) A review and recent developments in photocatalytic water-splitting using TiO₂ for hydrogen production. *Renew Sust Energy Rev* 11:401
- Nosaka Y, Norimatsu K, Miyama H (1984) The function of metals in metal-compounded semiconductor photocatalysts. *Chem Phys Lett* 106:12
- Novo C, Mulvaney P (2007) Charge-induced Rayleigh instabilities in small gold rods. *Nano Lett* 7:520
- Ogura S, Kohno M, Sato K, Inoue Y (1998) Effects of RuO₂ on activity for water decomposition of a RuO₂/Na₂Ti₃O₇ photocatalyst with a zigzag layer structure. *J Mater Chem* 8:2335
- Ogura S, Sato K, Inoue Y (2000) Effects of RuO₂ dispersion on photocatalytic activity for water decomposition of BaTi₄O₉ with a pentagonal prism tunnel and K₂Ti₄O₉ with a zigzag layer structure. *Phys Chem Chem Phys* 2:2449
- Osterloh FE (2008) Inorganic materials as catalysts for photochemical splitting of water. *Chem Mater* 20:35
- Pan J, Wu X, Wang L, Liu G, Lu GQ, Cheng HH (2011) Synthesis of anatase TiO₂ rods with dominant reactive {010} facets for the photoreduction of CO₂ to CH₄ and use in dye-sensitized solar. *Chem Commun* 47:8361
- Papp J, Shen HS, Kershaw R, Dwight K, Wold A (1993) Titanium(IV) oxide photocatalysts with palladium. *Chem Mater* 5:284
- Rafea MA, Roushdy NJ (2009) Determination of the optical band gap for amorphous and nanocrystalline copper oxide thin films prepared by SILAR technique. *Appl Phys D* 42:015413
- Reber JF, Rusek M (1986) Photochemical hydrogen production with platinized suspensions of cadmium sulfide and cadmium zinc sulfide modified by silver sulfide. *J Phys Chem* 90:824
- Sakamoto N, Ohtsuka H, Ikeda T, Maeda K, Lu D, Kanehara M, Teramura K, Teranishi T, Domen K (2009) Highly dispersed noble-metal/chromia (core/shell) nanoparticles as efficient hydrogen evolution promoters for photocatalytic overall water splitting under visible light. *Nanoscale* 1:106
- Sakata T, Hashimoto K, Kawai T (1984) Catalytic properties of ruthenium oxide on n-type semiconductors under illumination. *J Phys Chem* 88:5214
- Sakthivel S, Shankar MV, Palanichamy M, Arabindoo B, Bahnemann DW, Murugesan V (2004) Enhancement of photocatalytic activity by metal deposition: characterization and photonic efficiency of Pt, Au and Pd deposited on TiO₂ catalyst. *Water Res* 38:3001
- Sato J, Saito N, Nishiyama H, Inoue Y (2002) Photocatalytic water decomposition by RuO₂-loaded antimonates, M₂Sb₂O₇ (M = Ca, Sr), CaSb₂O₆ and NaSbO₃, with d¹⁰ configuration. *J Photochem Photobiol A Chem* 148:85
- Sato J, Kobayashi H, Saito N, Nishiyama H, Inoue Y (2003) Photocatalytic activities for water decomposition of RuO₂-loaded AlInO₂ (A = Li, Na) with d¹⁰ configuration. *J Photochem Photobiol A Chem* 158:139
- Sato J, Saito N, Yamada Y, Maeda K, Takata T, Kondo JN, Hara M, Kobayashi H, Domen K, Inoue Y (2005) RuO₂-loaded β-Ge₃N₄ as a non-oxide photocatalyst for overall water splitting. *J Am Chem Soc* 127:4150
- Sayama K, Arakawa H (1992) Significant effect of carbonate addition on stoichiometric photodecomposition of liquid water into hydrogen and oxygen from platinum-titanium (IV) oxide suspension. *J Chem Soc Chem Commun* 2:150
- Sayama K, Arakawa H (1996) Effect of carbonate addition on the photocatalytic decomposition of liquid water over a ZrO₂ catalyst. *J Photochem Photobiol A Chem* 94:67

- Sayama K, Yase K, Arakawa H, Asakura K, Tanaka A, Domen K (1998) Photocatalytic activity and reaction mechanism of Pt-intercalated $K_4Nb_6O_{17}$ catalyst on the water-splitting in carbonate salt aqueous solution. *J Photochem Photobiol A Chem* 114:125
- Slamet HWN, Purnama E, Kosela S, Gunlazuardi J (2005) Photocatalytic reduction of CO_2 on copper-doped titania catalysts prepared by improved-impregnation method. *Catal Commun* 6:313
- Sobczyński A, Dobosz A (2001) Water purification by photocatalysis on semiconductors. *Polish J Environ Stud* 10:195
- Srinivas S, Shubhamangala B, Lalitha K, Reddy PAK, Kumari VD, Subrahmanyam M, De Ranjan B (2011) Photocatalytic reduction of CO_2 over Cu-TiO₂/molecular sieve 5A composite. *Photochem Photobiol* 87:995
- Subramanian V, Wolf E, Kamat P (2001) Semiconductor-metal composite nanostructures, to what extent do metal nanoparticles improve the photocatalytic activity of TiO₂ films? *J Phys Chem B* 105:11439
- Subramanian V, Wolf E, Kamat P (2003) Green emission to probe photoinduced charge events in ZnO-Au nanoparticles charge distribution and Fermi-level equilibration. *J Phys Chem B* 107:7479
- Subramanian V, Wolf EE, Kamat P (2004) Catalysis with TiO₂/gold nanocomposites: effect of metal particle size on the fermi level equilibration. *J Am Chem Soc* 126:4943
- Sunada K, Watanabe T, Hashimoto K (2003) Bactericidal activity of copper-deposited TiO₂ thin film under weak UV light illumination. *Environ Sci Technol* 37:4785
- Shuller JA, Barnard ES, Cai W, Jun YC, White JS, Brongersma ML (2010) Plasmonics for extreme light concentration and manipulation. *Nat Mater* 9:193
- Tada H, Kiyonaga T, Naya S-i (2009) Rational design and applications of highly efficient reaction systems photocatalyzed by noble metal nanoparticle-loaded titanium(IV) dioxide. *Chem Soc Rev* 38:1849
- Tada H, Jin Q, Nihijima H, Yamamoto H, Fujishima M, Okuoka S-L, Hattori T, Sumida Y, Kobayashi H (2011) Titanium(IV) dioxide surface-modified with iron oxide as a visible light photocatalyst. *Angew Chem Int Ed* 50:3501
- Takai A, Kamat PV (2011) Capture, store and discharge. Shuttling photogenerated electrons across TiO₂-silver interface. *ACS Nano* 5:7369–7376
- Takata T, Shinohara K, Tanaka A, Hara M, Kondo JN, Domen KV (1997a) A highly active photocatalyst for overall water splitting with a hydrated layered perovskite structure. *J Photochem Photobiol A Chem* 106:45
- Takata T, Furumi Y, Shinohara K, Tanaka A, Hara M, Kondo JN, Domen K (1997b) Photocatalytic decomposition of water on spontaneously hydrated layered perovskites. *Chem Mater* 9:1063
- Templeton AC, Wuelfing WP, Murray RW (2000) Monolayer protected cluster molecules. *Acc Chem Res* 33:27
- Teramura K, Tanaka T, Ishikawa H, Kohno Y, Funabiki Y (2004) Photocatalytic reduction of CO_2 to CO in the presence of H_2 or CH_4 as a reductant over MgO. *J Phys Chem B* 108:346
- Teramura K, Maeda K, Saito T, Takata T, Saito N, Inoue Y, Domen K (2005) Characterization of ruthenium oxide nanocluster as a cocatalyst with $(Ga_{1-x}Zn_x)(N_{1-x}O_x)$ for photocatalytic overall water splitting. *J Phys Chem B* 109:21915
- Teramura K, Tsuneoka H, Shishido T, Tanaka T (2008) Effect of H_2 gas as a reductant on photoreduction of CO_2 over a Ga_2O_3 photocatalyst. *Chem Phys Lett* 467:191
- Tseng I-H, Chang W-C, Wu JCS (2002) Photoreduction of CO_2 using sol-gel derived titania and titania-supported copper catalysts. *Appl Catal B* 37:37
- Tseng I-H, Wu JCS, Chou H-Y (2004) Effects of sol-gel procedures on the photocatalysis of Cu/TiO₂ in CO_2 photoreduction. *J Catal* 221:432
- Tseng I-H, Wu JCS (2004) Chemical states of metal-loaded titania in the photoreduction of CO_2 . *Catal Today* 97:113

- Wang C-M, Heller A, Gerischer H (1992) Palladium catalysis of O₂ reduction by electrons accumulated on TiO₂ particles during photoassisted oxidation -of organic compounds. *J Amer Chem Soc* 114:5230
- Williams R (1960) Becquerel photovoltaic effect in binary compounds. *J Chem Phys* 32:1505
- Wood A, Giersig M, Mulvaney P (2001) Fermi level equilibration in quantum dot-metal nanojunctions. *J Phys Chem B* 105:8810
- Wu JCS, Lin H-M (2005) Photo reduction of CO₂ to methanol via TiO₂ photocatalyst. *Int J Photoenergy* 7:115
- Wu JCS, Lin H-M, Lai C-L (2005) Photoreduction of CO₂ to methanol using optical-fiber photoreactor. *Appl Catal A* 296:194
- Wu NL, Lee MS (2004) Enhanced TiO₂ photocatalysis by Cu in hydrogen production from aqueous methanol solution. *Int J Hydrogen Energy* 29:1601
- Xu Y, Schoonen MAA (2000) The absolute energy position of conduction and valence bands of selected semiconducting minerals. *Am Mineral* 85:543
- Yamaguti K, Sato S (1985) Photolysis of water over metallized powdered titanium dioxide. *J Chem Soc Faraday Trans 1* 81:1237
- Yang H-C, Lin H-Y, Chien Y-S, Wu JCS, Wu H-H (2009) Mesoporous TiO₂/SBA-15, and Cu/TiO₂/SBA-15 composite photocatalysts for photoreduction of CO₂ to methanol. *Catal Lett* 131:381
- Yao Y, Ohko Y, Sekiguchi Y, Fujishima A, Kubota Y (2008) Self-sterilization using silicone catheters coated with Ag and TiO₂ nanocomposite thin film. *J Biomed Mater Res B Appl Biomater* 85:45
- Yin M, Wu CK, Lon YB, Burda C, Koberstein JT, Zhu YM, O'Brien S (2005) Copper oxide nanocrystals. *J Am Chem Soc* 127:950
- Yoshida M, Takanabe K, Maeda K, Ishikawa A, Kubota J, Sakata Y, Ikezawa Y, Domen K (2009) Role and function of noble-metal/Cr-layer core/shell structure cocatalysts for photocatalytic overall water splitting studied by model electrodes. *J Phys Chem C* 113:10151
- Yui T, Kan A, Saitoh C, Koike K, Ibusuki T, Ishitani O (2011) Photochemical reduction of CO₂ using TiO₂: effects of organic adsorbates on TiO₂ and deposition of Pd onto TiO₂ACS. *Appl Mater Interfaces* 3:2594
- Zhang Q-H, Han W-D, Hong Y-J, Yu J-G (2009) Photocatalytic reduction of CO₂ with H₂O on Pt-loaded TiO₂ catalyst. *Catal Today* 148:335
- Zhang Z, Tang WJ, Neurock M, Yates JT Jr (2011) Electric charge of single Au atoms adsorbed on TiO₂ (110) and associated band bending. *J Phys Chem C* 115:23848
- Zhang Z, Yates JT Jr (2012) Band bending in semiconductors: chemical and physical consequences at surfaces and interfaces. *Chem Rev* 112:5520
- Zou Z, Ye J, Sayama K, Arakawa H (2001) Direct splitting of water under visible light irradiation with an oxide semiconductor photocatalyst. *Nature* 414:625

Chapter 11

Shaping Photocatalysts: Morphological Modifications of Semiconductors

María Dolores Hernández-Alonso

11.1 The Relevance of Size and Shape

Tuning the size and shape of semiconductor particles to improve the performance and widen the range of application of these materials has attracted an extraordinary interest in nanotechnology, and it is matter of extensive research. Besides composition and structure, at the nanometre scale, material properties have proved to be very sensitive not only to the size but also to the shape of the particles. Control over nanocrystal architecture has opened the range of applications of semiconductors from light-emitting diodes (LEDs), medical diagnosis and energy storage, to information processing, besides their conventional uses in catalysis (Trindade 2001; Chen 2007).

Particle size is a parameter that strongly influences the characteristics of photocatalysts, especially when the particle decreases to the nanometre scale. Nanostructured materials have been attracting an increasing attention in the last decades due to their unique electronic, optical, magnetic and chemical properties, different from those of the bulk, conferred by the ultrafine crystallite sizes and high surface areas, considering that surface-to-volume ratio increases as the crystal size decreases. The term nanoparticle embraces particles with sizes between 1 and 100 nm, at least in one of their dimensions. The primary particle size of a photocatalyst defines the size of the crystals and determines the available surface area for adsorption and photooxidation. However, it has to be taken into account that aggregation of particles is difficult to avoid, and aggregation can influence the adsorption of molecules, light scattering and light absorptivity, charge carrier dynamics, etc. (Friedmann et al. 2010).

For instance, the optical properties of TiO₂ substantially change by decreasing the particle size and aggregation. As previously commented, titanium dioxide is the most widely used white pigment due to its excellent opacity and brightness and

M. D. Hernández-Alonso (✉)
Renewable Energy Division, CIEMAT, Madrid, Spain
e-mail: lolihza@gmail.com

very high refractive index ($n = 2.7$), which enables an efficient scattering of light. Pigmentary titania is manufactured as particles of around 0.2–0.4 microns, where light scattering ability is maximized. For these sizes, Mie's light scattering theory can be applied, being this approach valid for objects whose size is in the same order of magnitude than the wavelength of the scattered light. However, for photocatalytic purposes, nanocrystalline titania is usually employed. In this case, the optical properties of TiO_2 nanoparticles can be interpreted by the Rayleigh's theory of light scattering, which describes the elastic scattering by particles much smaller than the wavelength of the light. Thus, in contrast to opaque titania, aggregates, solutions and films of isolated nanosized TiO_2 crystals are transparent in the visible range (Allen et al. 2009).

In a semiconductor material, the small size is also translated into a spatial confinement of the wave function of the charge carriers, known as quantum size effect (QSE), especially significant when the size is comparable with or smaller than the so-called exciton Bohr radius, a_B :

$$a_B = \frac{\hbar^2 \varepsilon}{\mu e^2} \quad (11.1)$$

where \hbar is the reduced Planck's constant, ε is the dielectric constant of the semiconductor, μ is the effective mass of the exciton (electron + hole), and e is the elementary charge (Trindade 2001).

These special characteristics turn nanoparticles into very attractive potential catalysts. As commented in Chap. 2, in a bulk semiconductor, the molecular orbitals of the atoms, of similar energy, form a continuum band: the valence band constituted by the lower energy levels and filled with electrons and the conduction band formed by the unoccupied higher energy levels. These two bands are separated by an energy gap (band gap, E_g), typically in the range 0.3–3.8 eV, and characteristic of each semiconductor. Reducing the size of the semiconductor particles decreases the space in which the excitons move, confining their motion (El-Sayed 2004). In the case of nanocrystalline semiconductors, the density of states and energy levels can be considered as an intermediate state between bulk and molecules (Fig. 11.1) and, thus, the band structure as discrete sets of electronic levels near the band edges (Trindade 2001). Due to the QSE phenomenon, semiconductor particles with sizes smaller than their corresponding Bohr radius are also called quantum dots.

For a spherical particle, the original QSE formulation proposed by Louis Brus in 1984 (Brus 1984) predicts, by applying a series of approximations, that as the size decreases, the effective band gap increases and the absorption spectrum shifts to lower wavelengths (higher energy). This means that for a small particle, the energy required to excite an electron to the lowest level of the conduction band is higher than for bigger particles. The modification of the band gap with particle size can be estimated as

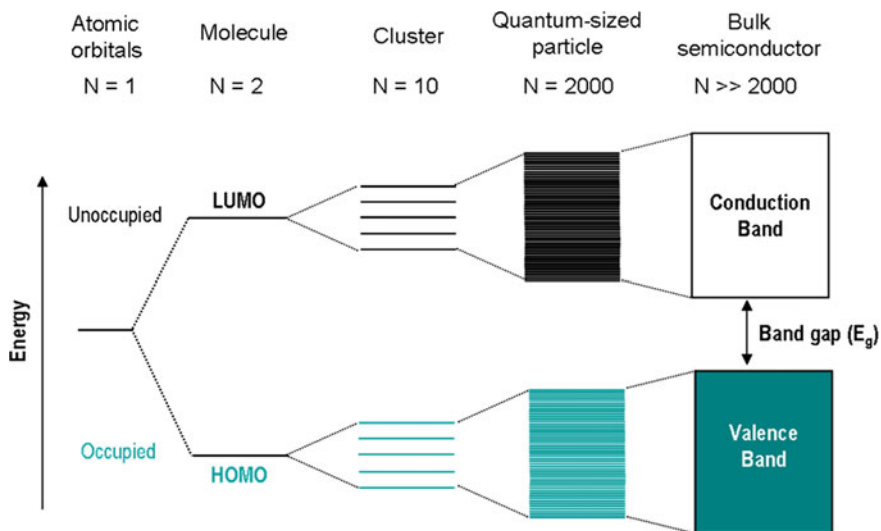


Fig. 11.1 Schematic representation of the energy levels in a molecule, nanostructured semiconductor and a bulk semiconductor (based on Hoffmann et al. 1995)

$$E_g \approx \left(\frac{\pi^2 \hbar^2}{2R^2 \mu} \right) - \frac{1.8e^2}{\epsilon R} \tag{11.2}$$

where R is the particle radius.

Consequently, quantum confinement allows tuning the band gap of a semiconductor particle by selecting the size, and by excitation at high energies, quantum dots could give result to the production of more than one exciton in a single particle from one photon (Klimov 2007).

This blue shift has been experimentally observed by some authors for different semiconductors (e.g. $a_B = 9.6$ nm for CdSe; 2.4 nm for CdS; 7.5 nm for CdTe). As an example, Fig. 11.2 shows the changing colour observed in BiOI

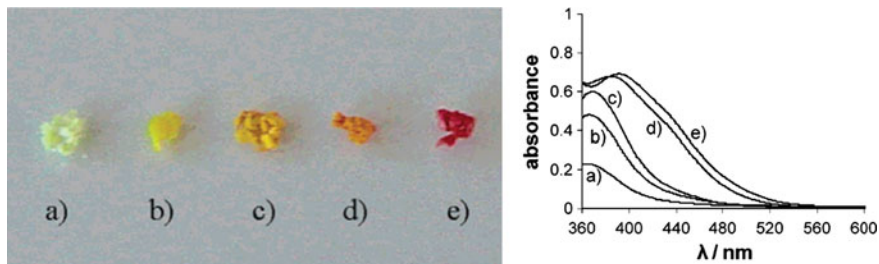


Fig. 11.2 Photograph of BiOI nanoparticles of increasing size from (a) to (e) and their corresponding UV-vis absorption spectra (reproduced with permission from Henle et al. 2007. Copyright American Chemical Society)

nanoparticles of different particle sizes, together with their corresponding UV–vis absorption spectra (Henle et al. 2007).

In the particular case of TiO_2 , it has been also reported both for anatase and for rutile particles (Anpo et al. 1987; Maira et al. 2000). Nevertheless, it is worth saying that the existence of the QSE in nanostructured TiO_2 is controversial and some authors claim that the effect is not perceptible for particle sizes lower than a threshold diameter in the range 0.6–3.8 nm (Serpone et al. 1995; Monticone et al. 2000), although significant effects of the size on the electronic band structure and surface characteristics were observed in those cases. Other considerations attribute the appearance of the blue shift when decreasing the size of titania not to the QSE, but to the presence of an amorphous part of titania (Ohtani 2008) or to allowed direct band transitions in the otherwise indirect band-gap semiconductor (Serpone et al. 1995). Although bulk anatase TiO_2 is an indirect band-gap semiconductor, with direct electron transitions between band centres prohibited by crystal symmetry, nanosized titania may behave as a direct semiconductor. This fact can be advantageous for photonic applications due to the improved optical absorption.

It is also worth mentioning that the stability of the different crystalline phases of a material is also size dependent. From a thermodynamic point of view, the surface free energy becomes an important component of the total Gibbs free energy and, together with stress contributions, influences the overall stability of nanoparticles. As a consequence, phases that have low stability in bulk materials can become stable in the nanostructured form. This phenomenon has been observed in TiO_2 , VO_x , Al_2O_3 or MoO_x . Thus, the anatase phase becomes more stable than rutile at small TiO_2 particle sizes (Grassian 2008).

How are all these size-dependant properties translated in terms of performance of a nanostructured photocatalyst? The correlation between particle size and photocatalytic activity is not simple. On the one hand, due to a weaker electron–phonon interaction with decreasing size, the electron lifetime is expected to increase. Besides, the smaller the crystallite size of a catalyst, the larger the surface area available for adsorption and photocatalytic reaction. However, the spatial confinement of small nanoparticles can also increase the electron/hole recombination rate. The large surface-to-volume ratio in nanoparticles introduces a number of atoms with unsaturated coordination and surface defects, generating a high density of “surface states” that can fall within the band gap of the photocatalyst, which may act as recombination centres (Zhang 1997).

There are numerous works that claim that decreasing the particle size of the semiconductor leads to an increased photocatalytic activity and improved selectivity in the decomposition of pollutants than bulk particles (Anpo et al. 1987; Xu et al. 1999). Nonetheless, other reports show that there is not a continuous increase in the photocatalytic performance when decreasing the particle size (Wang et al. 1997; Rivera et al. 1993). Actually, there seems to be an optimum size, around 7–10 nm for TiO_2 , below which a detrimental effect of size predominates (Fig. 11.3). This lower performance has been attributed to an increased surface e^-/h^+ recombination rate in the very small particles that counteracts their beneficial larger surface area and to the inherent structural and optoelectronic properties of

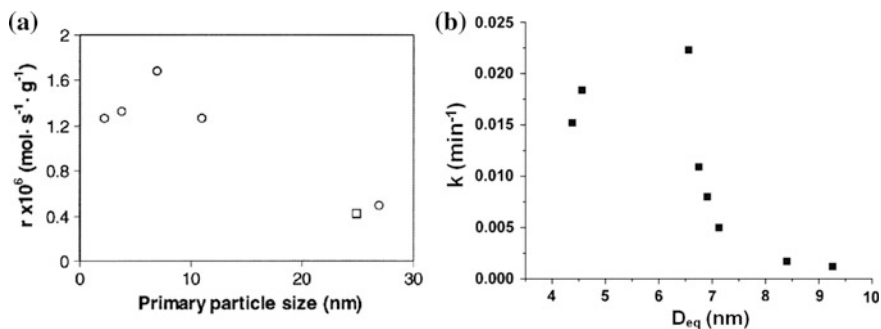


Fig. 11.3 Examples of the influence of TiO₂ particle size on photoactivity: **a** trichloroethylene conversion rate as a function of anatase TiO₂ primary particle size [(○) samples prepared by the sol-gel process; (□) Commercial TiO₂ Degussa P25] (reproduced with permission from Maira et al. 2000. Copyright Elsevier); **b** first-order kinetic constants (min⁻¹) versus average sample size (given as D_{eq} , the diameter of the sphere of equivalent volume) for the photochemical degradation of methylene blue under UV-vis irradiation (adapted with permission from Cernuto et al. 2011. Copyright American Chemical Society)

nanosized particles (Zhang et al. 1998; Maira et al. 2000; Cernuto et al. 2011). In the case of photocatalytic reactions in aqueous phase, the tendency of nanoparticles to form aggregates depending on pH has to be taken into account, since it could affect the surface area available for adsorption and reaction.

Advances in nanotechnology have allowed gaining control also over the shape and surface structure of nanosized materials, by understanding the kinetics of the nucleation and growth stages of the synthetic processes. Thus, nanoparticles with rods, tubes, plates, sheets or flower-like shapes, among others, can be obtained through the selection of the synthesis conditions. For instance, both size and shape of nanoparticles can be modulated by wet chemical techniques, using surfactant molecules or templates, which allow controlling the space in which the crystals grow. Epitaxial growth methods [e.g. chemical vapour deposition (CVD)] can also be successfully applied for shaping semiconductors, although they have the peculiarity of producing nanocrystals attached to a substrate.

As mentioned before, the shape also influences the properties of photocatalysts at the nanoscale range by defining the number of atoms at the surface, and the crystal facets exposed. Thus, the band gap of a semiconductor may be tuned by confining the exciton through modification, not only of the size, but also of the dimensionality of the nanocrystal (Fig. 11.4). While spherical particles are thermodynamically the most stable, they have the smallest number of total surface atoms; one-dimensional or two-dimensional nanostructures have a large fraction of atoms on their surface, making them useful for (photo)catalytic applications (Smith and Nie 2010).

Quantum mechanical modelling methods show that the electronic structure and the expected blue shift in nanosized particles strongly depend on the shape (Auvinen et al. 2011). Theoretical approximations also predict that quantum confinement should be stronger for dots than for rods and, in turn, stronger for rods

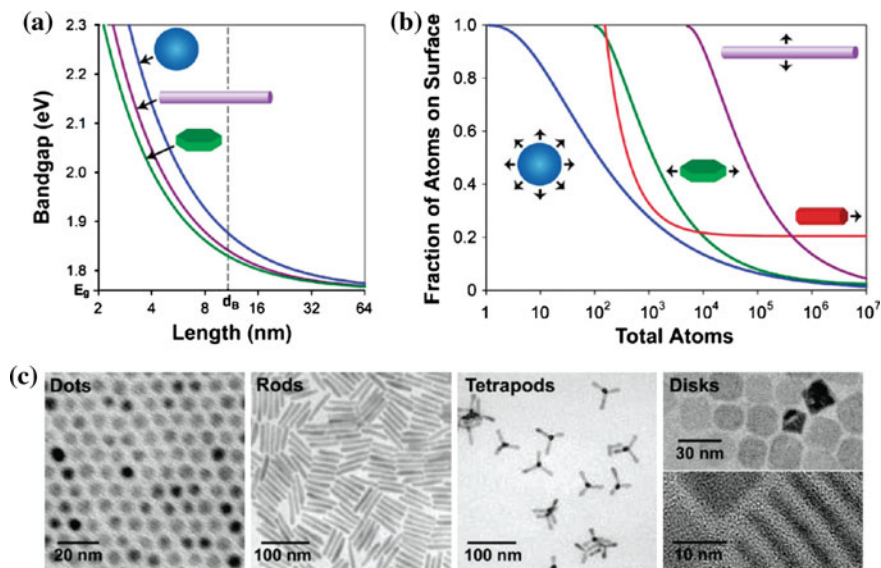


Fig. 11.4 Influence of shape on the electronic and surface properties of semiconductor nanocrystals: **a** band gap of CdSe quantum discs, wires and dots versus the length of the confined dimension. The bulk band gap and exciton diameter are noted on the axes; **b** fractions of atoms on the nanocrystal surface against the total number of atoms; **c** TEM micrographs of CdSe *dots*, *rods*, *tetrapods* and *discs* (reproduced with permission from Smith and Nie 2010. Copyright American Chemical Society)

than for plates. Quantum dots (Sect. 16.3) are confined in the three dimensions, while plates, being two-dimensional nanostructures, are confined only in the third dimension; finally, one-dimensional morphologies such as nanotubes, nanorods and nanowires are confined in two dimensions, with the electronic and optical properties depending on the aspect ratio (length/diameter). This fact has been experimentally observed for CdSe quantum rods, whose band gap was found to decrease as the rod length increases (Li et al. 2001).

Some studies have also concluded that in the case of spheres (aspect ratio = 1), the non-radiative relaxation rate of the excited electrons decreases as the diameter increases, while in the case of nanorods, the relaxation rate decreases as the aspect ratio increases. It means that for the same diameter, the relaxation rate of rods would be lower than that of spheres. The mechanism of relaxation (e.g. electron–hole recombination, trapping of the electron...) can differ from one system to another, depending basically on the quality of the surface and the presence of trapping sites (El-Sayed 2004).

In another example, the photocatalytic activity dependence of BiVO_4 on the morphology was explored, showing that rod-like structures presented higher surface area, surface oxygen vacancy density and lower band gap than BiVO_4 with spherical or sheet-like morphology, which was translated into an enhanced photocatalytic performance under visible light (Jiang et al. 2011).

At present, the synthesis of nanocrystals with tailored exposed surfaces is attracting a great deal of interest as a novel strategy to improve the efficiency of photocatalysts and particularly of TiO_2 (Ohno 2002). On the basis that $\{101\}$ facets are thermodynamically more stable in anatase crystals than the highly reactive, but minority in the equilibrium state, $\{001\}$ surfaces, the synthesis of TiO_2 crystals with a large percentage of reactive facets is being explored aimed at enhancing its photocatalytic efficiency. In this respect, anatase TiO_2 single crystals with a large percentage of $\{001\}$ facets could be recently produced using fluorine-containing species (e.g. hydrofluoric acid) as capping agent under hydrothermal conditions (Fig. 11.5). It was observed that in this fluorinated surfaces, the relative stability of $\{001\}$ and $\{101\}$ was reversed and that no crystal facet control could be achieved in the absence of hydrofluoric acid in the synthesis. It has been reported that the role of hydrofluoric acid is, on the one hand, to retard the hydrolysis of the titanium precursor and, on the other hand, to reduce surface energy, so the isotropic growth along the $[010]$ and $[100]$ direction is promoted (Yang et al. 2008). Theoretical calculations indicate that $\{001\}$ facets of anatase TiO_2 may have improved photocatalytic performance with respect to $\{101\}$ facets, and accordingly, a higher generation of hydroxyl radicals ($\cdot\text{OH}$) has been experimentally observed on $\{001\}$ surfaces. In contrast to the previous results, higher activities in the photocatalytic oxidation of acetone or toluene have been obtained on anatase with dominant $\{101\}$ facets than on reference photocatalyst Degussa P25 (Xiang et al. 2010; Cao et al. 2011). High photocatalytic activity has been also observed in the degradation of acetaldehyde on anatase crystals with dominant $\{101\}$ crystal facets. Therefore, reported results on the photocatalytic performance of these highly faceted materials are sometimes contradictory, and further research and experimental evidences are required (Fang et al. 2011). Recently, the dependence of the photogenerated species on the exposed crystal faces in anatase has been explored by electron spin resonance (ESR). The study observed that the concentration of trapped holes (O^- centres) increased with the increase in the $\{001\}$ surface area, leading to a high photoactivity, while the amount of Ti^{3+}

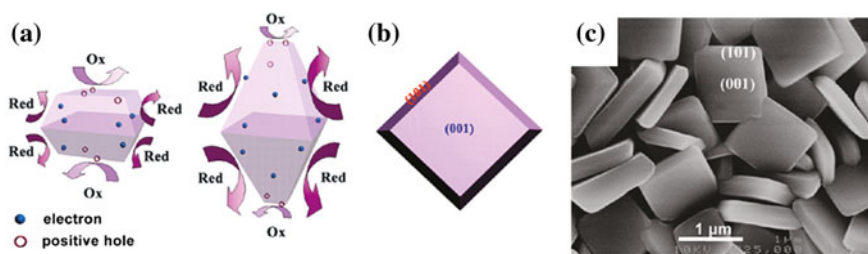


Fig. 11.5 **a** Schematic illustration of the electrons and holes transfer on anatase TiO_2 particles with a specific exposed crystal face; **b** geometric model of an anatase crystal with preferential $\{001\}$ facets; **c** SEM image of TiO_2 single-crystal nanosheets with a large percentage of exposed $\{001\}$ facets (adapted with permission from Fang et al. 2011. Copyright American Chemical Society)

centres increased with the {101} surface area, the latter leading to a worse photocatalytic efficiency. This would indicate that {001} surfaces play the main role in the photocatalytic process by providing oxidation sites, while the {101} ones seem to be only directly involved as reductive site supplier (D'Arienzo et al. 2011).

It is worth saying that as a consequence of the extensive research on particles of nanometric size, new concerns have recently arisen about their potential toxicity. Most of the studies show that the toxicity associated with TiO₂ nanoparticles seems to be relatively mild, as it has been addressed in detail in Chap. 5. However, further studies are necessary to definitively set the limits of safety for nanomaterials (Liao et al. 2009).

11.2 Synthesis of Nanostructured Photocatalysts

In contrast to techniques such as spray pyrolysis or CVD, wet chemical methods allow obtaining nanoparticles with tailored size, shape and crystal structure, at relatively low temperatures. These structural and morphological parameters can be easily tuned by modification of the synthetic conditions.

For obtaining nanoparticulate photocatalysts, different wet chemical procedures can be employed, such as direct oxidation, sol–gel, reverse microemulsions and hydrothermal methods. Some of the most commonly used preparation procedures will be described below. Besides wet chemical methods, aerosol flame-assisted processes and other frequently used synthetic procedures for the preparation of photocatalysts will be briefly defined.

11.2.1 Sol–Gel Methods

Sol–gel methodologies allow obtaining well-crystallized nanoparticles with a high chemical homogeneity at mild temperatures (Li et al. 2004; Hernández-Alonso et al. 2006). The process involves the formation of metal-oxo-polymer networks from metal alkoxides or metal salt precursors, as it was described in detail in Chap. 5. The tendency of alkoxides to rapidly hydrolyse can make the sol–gel synthesis difficult to control, so different products can be obtained by introducing different variations in the preparation routes.

Wet gels are formed when the sols are casted in a mould. Dense ceramics can be obtained by drying and thermal treatment of the wet gels, while highly porous materials can be synthesized if the solvent in a wet gel is removed under supercritical conditions. These high surface area materials, called aerogels, present very interesting properties, as a very low thermal conductivity and a remarkable low density (Fig. 11.6). They are also known as frozen or solid smoke due to their translucent appearance. Anatase TiO₂ aerogels, with a BET surface area above

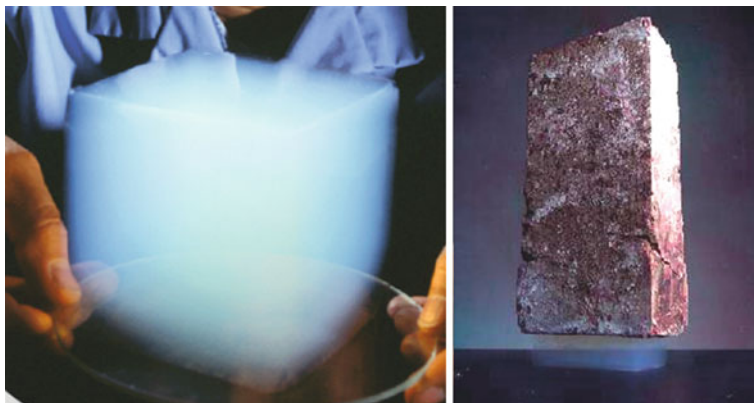


Fig. 11.6 Photographs of aerogels as those used in the NASA's Stardust spacecraft (images reproduced from the NASA Aerogel Factsheet, http://stardust.jpl.nasa.gov/aerogel_factsheet.pdf)

200 m²/g and mesopores in the range 2–10 nm, have been prepared by extracting the solvent from the gel with supercritical CO₂ (Campbell et al. 1992).

In sol–gel processing, products' microstructure and their surface characteristics can be controlled by changing parameters such as pH of the reaction medium, water-to-alkoxide ratio and reaction temperature (Bischoff and Anderson 1995). For instance, the relative rates of nucleation and particle growth can be controlled by adjusting the water-to-alkoxide ratio. Increasing this ratio will favour nucleation versus particle growth. The hydrolysis and condensation rates can be modified by acid or base catalysis. The addition of an acid in the reaction medium will prevent the particle growth and agglomeration, as previously commented (Wang and Ying 1999). The use of surfactants and templates can be used as shape controllers.

Thus, highly crystalline TiO₂ nanoparticles of different sizes and shapes can be produced by sol–gel methods by tuning the synthesis parameters. Some examples of well-defined nanocrystals with controlled shape, obtained through hydrolysis and polycondensation of titanium alkoxide in the presence of tetramethylammonium hydroxide (Me₄NOH), are presented in Fig. 11.7 (Chemseddine and Moritz 1999).

11.2.2 Hydrothermal and Solvothermal Synthesis

A hydrothermal technique is a wet chemical method that involves the synthesis of crystalline powders in aqueous solutions upon heating at temperatures above the boiling point of water, with the consequent generation of vapour pressure.

Hydrothermal synthesis of nanoparticles can be carried out at soft temperatures, usually between 100 and 200 °C, generating crystalline and effective nanostructured photocatalysts. In a typical hydrothermal procedure, a high-pressure

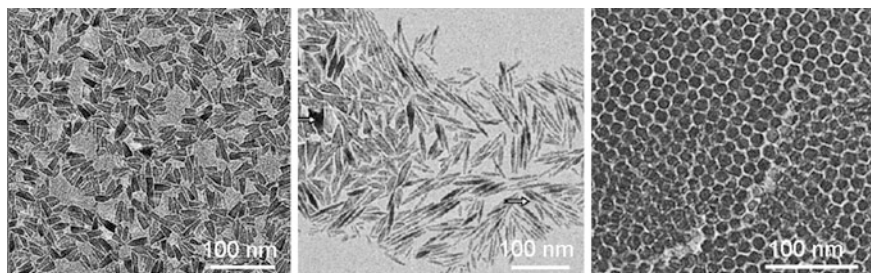


Fig. 11.7 TEM images of TiO₂ nanoparticles of different shape prepared by hydrolysis of Ti(OR)₄ in the presence of tetramethylammonium hydroxide (Me₄NOH) (adapted with permission from Chemseddine and Moritz 1999. Copyright Wiley–VCH)

apparatus, called “autoclave”, provided with a Teflon-lined vessel, is employed in a reaction in aqueous solution under controlled temperature and pressure. Temperature can be risen above the boiling point of water, reaching the pressure of vapour saturation. The temperature and the volume of solution added to the autoclave will determine the internal pressure. Crystalline structure, particle size and morphology or surface characteristics, can be controlled by changing synthetic parameters such as the pH, temperature and length of treatment and reactant concentrations (Wang and Ying 1999). Other processes give rise to amorphous precipitates which require a calcination treatment to induce crystallization. These heat treatments lead to grain growth (with the subsequent decrease in surface area) and may induce phase transformations. However, the hydrothermal synthesis procedure makes it possible to prepare metastable phases, as well as the use of considerable lower synthesis temperatures which lead to crystalline materials with a small particle size.

Anatase TiO₂ nanoparticles, with crystal sizes in the range 2–11 nm, can be easily obtained by means of hydrothermal techniques (Maira et al. 2000). Crystallite size is controlled by the composition of an alcohol–water mixture, while the temperature and length of the treatment are used to ensure the crystallinity of the product and for a fine-tuning of the size. Thus, hydrothermal methods can be an alternative to calcination post-treatments for promoting crystallization under mild temperatures. Besides conventional-shaped TiO₂ nanoparticles, one-dimensional nanostructures such as nanotubes, nanorods and nanowires can also be produced by hydrothermal methods.

The solvothermal technology is analogous to the hydrothermal method, but in this case, a non-aqueous solvent is employed. This feature allows, by selecting the solvent according to its boiling point, to elevate the temperature of the synthesis much higher than in the hydrothermal method. Thus, the shape, size and crystallinity of the products can be more precisely controlled in a solvothermal reaction, being able to provide a wide variety of nanoparticles with narrow size and shape distribution (Chen 2007). Figure 11.8 shows TEM images of TiO₂ nanoparticles and nanorods prepared by this method.

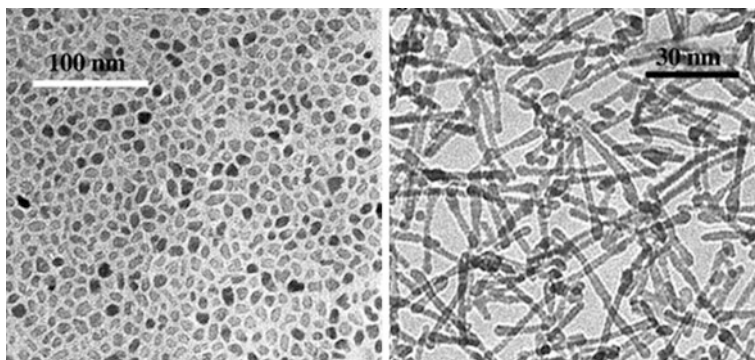


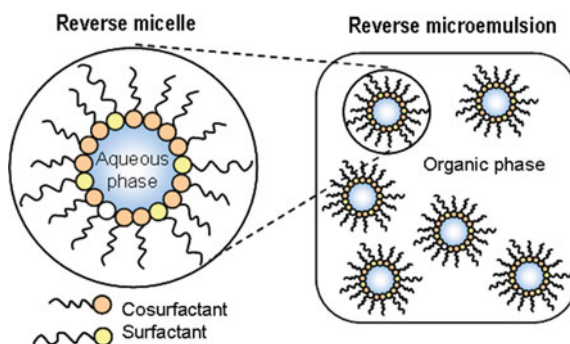
Fig. 11.8 TEM micrographs of TiO_2 nanoparticles and nanorods synthesized by a solvothermal method (adapted with permission from Li et al. 2006a. Copyright Wiley-VCH)

11.2.3 Reverse Microemulsions

The term “microemulsion” was used for the first time by J.H. Schulman, who defined it as a thermodynamically stable mixture of two immiscible components like, for example, oil and water (Schulman and Friend 1949), although it was Boutonnet et al. in 1982 who firstly reported the synthesis of nanoparticles from microemulsions (Boutonnet et al. 1982).

A microemulsion is an isotropic system optically transparent, consisting of an aqueous phase, an organic phase and an amphiphilic substance (surfactant). These mixtures, macroscopically homogeneous, are heterogeneous solutions at molecular level, and their structure is derived from the ratio of the different components of the microemulsion. In the particular case of reverse microemulsions (water-in-oil), the internal structure is constituted by nanosized droplets of aqueous phase surrounded by a monolayer of surfactant molecules (micelles), dispersed in a non-polar organic solvent (Fig. 11.9). A cosurfactant (usually an alcohol) is often added in order to favour obtaining stable and transparent microemulsions, reducing the surfactant concentration and enhancing the interactions with the surfactant

Fig. 11.9 Schematic representation of a reverse micelle and a reverse microemulsion



molecules, which confers an increased flexibility of the interfacial film. The amphiphilic nature of the cosurfactant is also able to modulate the exchange dynamics of water droplets (Curri et al. 2000).

Reverse micelles are used as microreactors to synthesize ultrafine powders with controlled size and a narrow particle size distribution. The synthetic procedure is based on the possibility of dissolving a certain amount of a water-soluble precursor in the inner hydrophilic part of the micelles. The nanoparticle growth is determined by the size of the micelles, which, in turn, is determined by the surfactant and the water/surfactant ratio employed in the reaction. The nuclei are formed inside the droplet, while the surfactant sterically controls the particle growth and thus the final particle size. The size is also influenced by the concentration of the precursor species in the aqueous domains due to its effect on the nucleation rate. For example, it has been reported that smaller particles of CdS can be obtained by increasing the concentration of the reactant due to an increase in the nucleation rate (Lianos and Thomas 1987). However, larger aggregates can be formed after nucleation by agglomeration.

Reverse microemulsions constitute a very suitable technique for the preparation of photocatalysts (Fuerte et al. 2001), with a fine-tuning of the particle size and the composition of multicomponent systems. In a general procedure, one microemulsion containing the precursor and one microemulsion containing a precipitating agent are mixed. However, in the case of TiO₂-based materials, a precipitating agent is not needed and the synthesis can proceed by the hydrolysis of the alkoxide solution into the aqueous phase of the reverse microemulsion system.

An additional advantage of this method is that unlike aqueous-phase chemical reactions that take place very fast and are difficult to control, in a microemulsion, the reactions between micelles containing the different reactants are considerably slower, which allows the reactions to be carried out in multiple steps and to synthesize multicomponent materials.

This synthesis procedure normally requires a post-synthesis calcination step in order to get rid of any organic residue, coming from the surfactant or the cosurfactant, and to transform the usually amorphous precipitate into a crystalline oxide. Annealing in the presence of the micelles can avoid the growth and agglomeration of the nanoparticles (Chen 2007).

New developments of this methodology have allowed obtaining TiO₂ nanoparticles from water-in-CO₂ microemulsions, which avoid the use of organic solvents (Lim et al. 2002).

11.2.4 Aerosol Flame Synthesis

Aerosol technology is also being extensively applied in nanotechnology. In aerosol techniques, the synthesis of nanoparticles can be generated by atomization of a liquid solution, for instance by electrospray or ultrasonic atomization, and subsequent particle formation in a droplet upon evaporation of the solvent. If spray

pyrolysis (e.g. laser spray pyrolysis, flame spray pyrolysis) is employed as atomizer method, the high temperatures provided can also induce chemical reactions inside the droplets, besides fragmentation of the particles that will result in the production of smaller nanoparticles. Aerosol particle formation can also occur in the gas phase. In this case, the volatile precursors are vaporized using energy provided by a furnace, plasma, laser or a flame reactor (Biskos et al. 2008).

Among aerosol techniques, flame-assisted procedures deserve especial mention since reference photocatalyst Degussa P25 is industrially prepared by a flame process, through the hydrolysis of volatile titanium precursor in an oxyhydrogen (H_2/O_2) flame (Inorganic Materials for Catalyst Innovation AEROSIL[®], AER-OXIDE[®] and SIPERNAT[®] Metal Oxides and Silica Based Materials Industry Information). The precursor is transformed into the titanium oxide and starts to form particles by nucleation and growth in the gas phase. Flame-assisted technology makes possible to obtain nanostructures of high purity in a continuous process and allows the large-scale production of nanoparticles since materials are processed without the requirement of any further post-treatment steps, such as filtration and washing. Furthermore, this technique reduces wastes generation. The crystalline structure, size and morphology of the generated particles can be modulated by selecting the precursors or the operating parameters of the flame (Strobel et al. 2006; Biskos et al. 2008). Besides commercial P25, flame-prepared TiO_2 photocatalysts, with nanoparticle size in the range 6–50 nm, have been successfully synthesized and a high efficiency in the photooxidation of different compounds has been reported. Doped- TiO_2 , ZnO or $BiVO_4$ photocatalysts have been also prepared by flame-assisted techniques (Strobel et al. 2006; Castillo et al. 2010).

11.2.5 Other Preparation Methods

Vapour deposition techniques refer to synthesis processes in which the reactants are in vapour state and condense to form a solid-phase material. These methods are particularly useful for the deposition of photocatalysts as films on different substrates. If no chemical reaction takes place, the process is called physical vapour deposition (PVD), while in the so-called CVD, the precursors react or decompose on the substrate surface forming the desired film. The morphology of the nanostructures can be controlled by modifying the reaction conditions. Other physical methods for films deposition are sputtering, thermal deposition, ion implantation, laser vaporization and molecular beam epitaxy. Atomic layer epitaxy, diffusion flame pyrolysis, thermal plasma pyrolysis and spray pyrolysis are comprised among chemical deposition approaches used for preparing nanomaterials. A pyrolysis technique is a combustion method that involves the thermal decomposition of a precursor into the desired product, as powder or thin film, while unwanted wastes evaporate. Although generally pyrolytic methods lead to particles with a wide size distribution, it is possible to obtain nanosized materials with

uniform composition and size by modifying the procedure and reaction conditions (Eslamian and Ashgriz 2006). Coatings consisting of photocatalyst nanoparticles can be also obtained by electrochemical deposition. In this method, the substrate to be coated, acting as cathode, is immersed into a solution that contains the salt of the metal to be deposited. The metallic ions are attracted to the cathode and reduced to the metallic form. Electrodeposition has proved to be a convenient method to prepare TiO₂ films.

Ultrasound (sonochemical method) and microwave radiation (microwave method) are also useful approaches for the preparation of nanostructured photocatalysts. For instance, TiO₂ nanotubes and nanorods can be prepared either by sonication or by microwave heating of TiO₂ particles in strong basic conditions (Chen 2007).

Highly active multicomponent oxide nanosized photocatalysts, with high crystallinity and homogeneity, have been prepared at relatively low temperatures by the so-called polymerized complex technique. The method is based on the polymerization between ethylene glycol and citric acid in the presence of soluble metal–citric acid complexes (Ikeda et al. 1998). Different titanate-based photocatalysts (e.g. SrTiO₃, BaTi₄O₉/RuO₂, NiO/Sr₃Ti₂O₇, K₂La₂Ti₃O₁₀) have been successfully obtained by this route.

11.3 Low-Dimensional Nanostructures: Tubes, Rods, Fibres or Belts

Traditionally, nanostructured photocatalysts have been manufactured as spheroidal particles. Recently, the synthesis, characterization and applications of low-dimensional semiconductor nanostructures have been attracting a great deal of attention due to their dimensional confinement and their structurally dependent physical and chemical properties. Anisotropy in a semiconductor nanoparticle breaks the symmetry of the electronic energy levels along the different directions of the crystal, and thus, in one-dimensional nanostructures such as rods and tubes, the band-gap emission will be mainly defined by the diameter, as it is the “confining” dimension. Their large surface area and their high electron and proton conductivity contribute to the interest in their potential applications in photocatalysis. In particular, titania and titanate-elongated nanostructures, such as nanorods, nanofibres, nanosheets and nanotubes, have been the subject of study of a fair amount of works. In addition to the high specific surface area, low dimensionality has proved to affect charge carrier recombination dynamics, and thus, a longer half-life and a longer diffusion length of the photogenerated charge carriers can be expected (Tachikawa et al. 2007).

In this context, the discovery of a simple synthetic method for the preparation of titanate nanotubes, consisting of the digestion of TiO₂ nanoparticles under strong basic conditions followed by acidic washing, opened a new potential route

for the preparation of nanostructures with a high specific surface area and narrow pore-size distribution in the mesoporous range, without using expensive template molecules (Kasuga et al. 1998). All polymorphs of TiO_2 can be used as precursors in the hydrothermal synthesis of nanotubes. These nanotubular structures combine the properties of conventional titania nanoparticles as a wide-band-gap semiconductor with a considerable higher surface area, which is expected to increase their adsorption capacity and, therefore, favour catalytic and photocatalytic processes.

A fair number of works where Kasuga's hydrothermal method has been applied can be found in the literature, and the effect of changing synthetic parameters on the nanotube structure and photocatalytic activity has been analysed (Hernández-Alonso et al. 2011a, b). Although nanotubes were reported to have TiO_2 anatase structure by Kasuga et al., recent works seem to agree that without calcination, the nanotubes obtained by the hydrothermal method normally have $\text{Na}_{2-x}\text{H}_x\text{Ti}_3\text{O}_7$ stoichiometry. The presence of Na^+ in the titanate structure has proved to have a negative effect on the photocatalytic activity on these materials, and thus, the complete sodium removal by protonation of the titanate nanotubes during the acidic washing is highly desirable. The most general description of the structure of protonated titanate nanotubes, after sodium exchange, is $\text{H}_{2(1-z)}\text{Ti}_n\text{O}_{2n-m+(1-z)}(\text{OH})_{2m}\cdot x\text{H}_2\text{O}$, where x and z refer to crystallographic water and ion-exchangeable OH groups, and n and m account for the type of crystal lattice. These structures can be monoclinic ($\text{H}_2\text{Ti}_3\text{O}_7$, $\text{H}_2\text{TiO}_4\text{O}_9$, $\text{TiO}_2\text{-B}$), orthorhombic (dititanate $\text{H}_2\text{Ti}_2\text{O}_4(\text{OH})_2$ or lepidocrocite-type $\text{H}_4x\text{Ti}_{2-x}\square_x\text{O}_4\cdot n\text{H}_2\text{O}$, \square = oxygen vacancy) or tetragonal (anatase). These protonated titanate nanotubes can formally be considered as hydrated forms of TiO_2 . The nanotubular morphology has been proposed to be adopted in order to reduce the charge imbalance caused by unsaturated or dangling bonds on the edges of the intermediate structures or to an asymmetric chemical environment or mechanical stress that would justify the formation of the nanotubes. It has been suggested that the nanotubes would be formed by helical scrolling of single (010) layer ("snail") or by curving of several conjoined nanosheets ("onion"), as it is schematically represented in Fig. 11.10 (Bavykin et al. 2004). The resultant nanotubes are several hundreds of nanometres in length, with an outer tube diameter of around 10 nm (Fig. 11.11). The high ion-exchange capacity of the titanates can be exploited to functionalize nanotubes. Taking advantage of this property, transition metal titanates has been prepared with the aim of shifting the absorption edge of these materials to the visible range for solar applications (Bavykin and Walsh 2009).

Upon calcination, a progressive transformation of the titanate structure into anatase takes place. Below 350–400 °C, the nanotubular morphology is still predominant, and at 500 °C, titanate nanotubes evolved into elongated anatase particles. Despite the larger surface area of the non-calcined or low-temperature calcined materials, increasing the temperature of the post-synthesis thermal treatment up to 300–400 °C boosted the photocatalytic activity of these materials due to an optimal balance between surface and structural characteristics (Hernández-Alonso et al. 2011b).

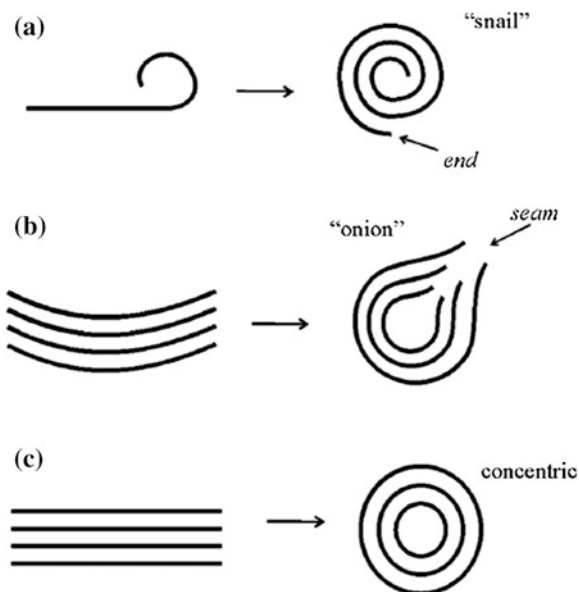


Fig. 11.10 Schematic representation of the possible formation mechanisms of multiwalled nanotubes (reproduced with permission from Bavykin et al. 2004. Copyright Royal Society of Chemistry)

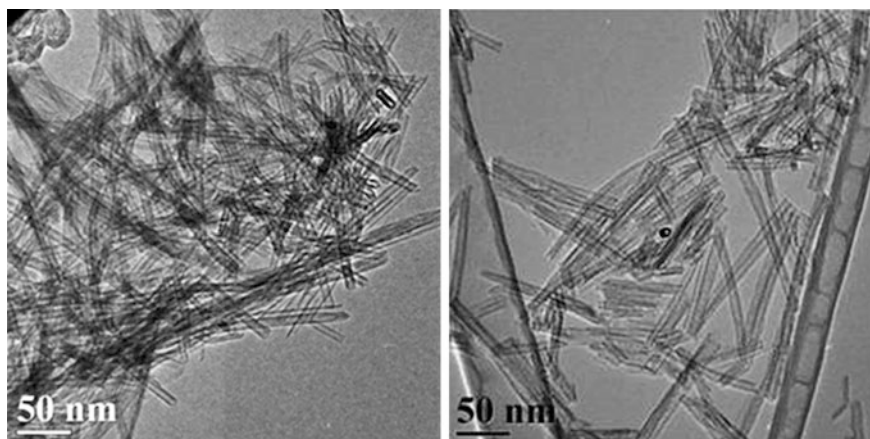


Fig. 11.11 Titanate nanotubes synthesized by hydrothermal treatment of TiO_2 in 10 M NaOH (adapted with permission from Hernández-Alonso et al. 2011a. Copyright The Royal Society of Chemistry)

Although the efficiency exhibited by titanate nanotubes in the degradation of dyes in aqueous solutions has been sometimes reported to be lower than reference TiO_2 photocatalysts, the elongated particles have proved to be more easily

recovered from solutions, which would be a benefit in large-scale applications that could compensate, at least partly, their poorer photoactivity. On the other hand, the results of the performance of these materials for the photocatalytic degradation of pollutants in the gas phase are more promising (Bavykin and Walsh 2009; Hernández-Alonso et al. 2011b).

For practical applications, it has to be considered that titanates are thermodynamically metastable phases and mechanically fragile nanostructures. The use of alkaline or neutral conditions, organic solvents and temperatures below 400 °C will provide a stable environment for titanate nanotubes (Bavykin and Walsh 2009).

Besides nanotubes, other low-dimensional TiO₂-based nanostructures can be developed by hydrothermal methods, such as nanorods, nanofibres, nanosheets and nanobelts (Fig. 11.12), which differ in the shape and aspect ratio. For instance, nanosheets are structures usually less than 10 nm in thickness and more than 100 nm in the other two dimensions, and nanofibres have 10–100 nm width and can be as large as several tens of microns. While titanate nanotubes are obtained by hydrothermal treatment of raw TiO₂ under strong alkaline conditions at temperatures in the range 110–150 °C, the formation of nanofibres and nanobelts takes place at higher temperatures with lower specific surface area and porosity. Nanorod morphologies, with a lower aspect ratio, can be obtained by annealing the protonated nanotubes at temperatures higher than 400 °C, while in the case of sodium-containing titanates, temperatures higher than 600 °C are needed to transform the nanotubular structures into nanorods. Nanorods can also be directly synthesized by hydrothermal methods. The morphology of the hydrothermally obtained nanorods may be tuned by using different surfactants or by changing the

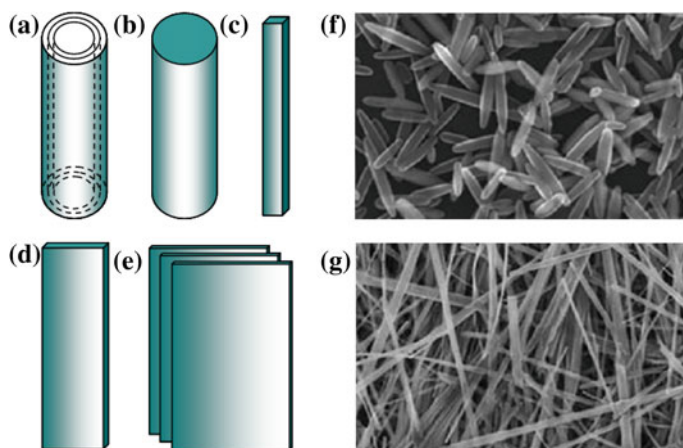


Fig. 11.12 a–e Schematic representation of different low-dimensional morphologies; f SEM image of anatase TiO₂ tetragonal faceted-nanorods (adapted with permission from Li and Xu 2010. Copyright The Royal Society of Chemistry); and g SEM image of H₂Ti₃O₇ nanobelts (reproduced with permission from Zhou et al. 2011. The Royal Society of Chemistry)

solvent composition. In the case of TiO_2 nanosheets, they can be obtained by delamination of layered protonated titanate into layers (Chen 2007).

Elongated TiO_2 -based nanostructures have shown higher surface wettability than conventional titania, which is beneficial for self-cleaning and antifogging applications, due to an increased surface roughness that results in a higher hydrophilicity. For these purposes, it is necessary to immobilize these structures on a substrate. Among other approaches, it is worth emphasizing the fabrication of films by electrochemical methods that, instead of the randomly oriented titanate nanotubes obtained by hydrothermal techniques, fabricate ordered arrays of titania nanotubes (Fig. 11.13). Anodic oxidation of titanium foils in a fluoride-containing electrolyte produces a continuous film of self-organized nanotubes, oriented perpendicular to the substrate, with an inner diameter ranging from 20 to 250 nm, wall thicknesses of 5–35 nm and length of several microns. These parameters can be precisely controlled. One end of the nanotubes is open, while the other one, in contact with the substrate, is always closed (Bavykin and Walsh 2009; Paramasivam et al. 2012). Although a post-anodization calcination stage was usually required to render photocatalytic active crystalline structures, a two-step anodizing process has been successfully developed for the synthesis of crystalline anatase TiO_2 nanotube arrays at low temperature, which allows the process to be applied on temperature-sensitive substrates (e.g. polymers) (Allam et al. 2008). TiO_2 nanotube arrays formed by anodization have shown remarkable performance in gas sensing, photovoltaic and photocatalytic applications. These nanotube arrays have also been widely studied for water photoelectrolysis, photoreduction of CO_2 into chemical fuels or dye-sensitized solar cells, where a significantly lower charge carrier recombination has been demonstrated. Furthermore, the porosity of the self-organized structure favours the diffusion of reactant molecules to the active surface area and allows the incident photons to be more effectively absorbed, with anisotropic optical scattering taking place when the pores periodicity and the light wavelength have comparable values (Allen et al. 2009).

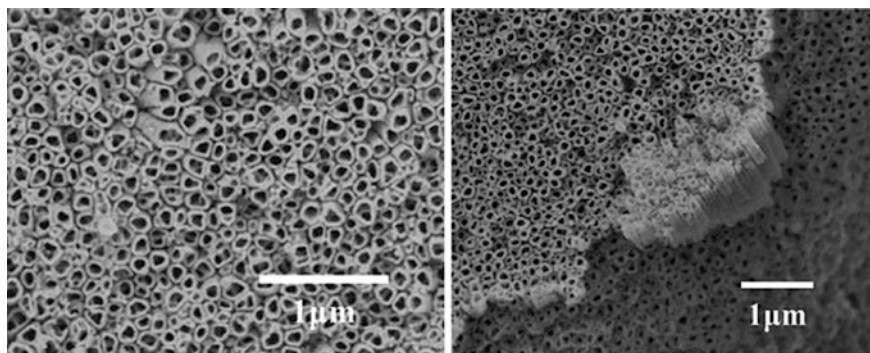


Fig. 11.13 Top view and cross-section of crystalline TiO_2 nanotube arrays obtained by anodization of a Ti foil (reproduced with permission from Allam et al. 2008, Copyright Wiley-VCH; and Shankar et al. 2009, Copyright American Chemical Society)

Attempts to shift the optical response of TiO₂ nanotube arrays from the UV to the visible region have been carried out. With this purpose, the use of external sensitizers or compositional dopants such as nitrogen has been reported (Mor et al. 2006).

11.4 More Complex Morphologies: From Hierarchical Structures and Photonic Crystals to Biomimetic Materials

In addition to the already mentioned nanostructures, different approaches to synthesize photocatalysts with unusual and more complex morphologies are being developed. Besides, new approaches based on the spatial structuring of semiconductors are being adopted with the aim of enhancing the photocatalytic activity. Controlling the physical structure from the subnanometric to the submillimetric scale has opened the window to obtain a new generation of more efficient photocatalysts (Aprile et al. 2008). In this respect, the design of hierarchical three-dimensional (3D) structures is attracting an increasing interest in nanotechnology. Some of these hierarchical architectures, with multimodal or multiscale pores, have been reported to exhibit improved photocatalytic efficiency with respect to other morphologies and to the reference photocatalyst Degussa P25. For instance, flower-shaped TiO₂ with high photocatalytic activities has been obtained by simple hydrothermal methods (Fig. 11.14a). The good performance exhibited by these morphologies has been attributed to their large specific surface area and to their special superstructure, which has proved to enhance light harvesting and favour the diffusion and separation of the photogenerated charge carriers (Nguyen-Phan et al. 2011; Tian et al. 2011). Other flower-like photocatalysts, like BiVO₄, have also showed improved performance with respect to other morphologies (Fan et al. 2011).

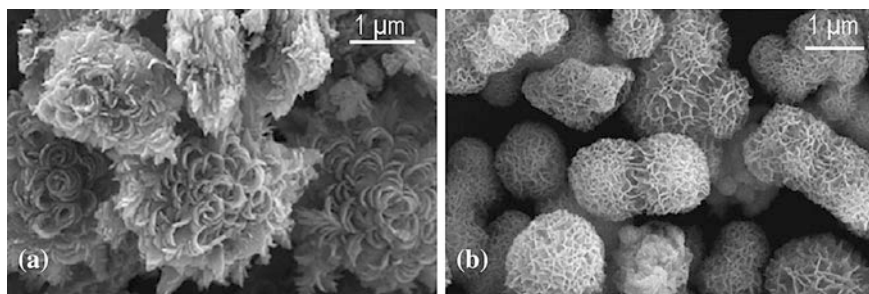


Fig. 11.14 SEM images of: **a** Hierarchical flower-like TiO₂ photocatalyst (reproduced with permission from Nguyen-Phan et al. 2011. Copyright Elsevier); **b** Porous ZnO spheres (reproduced with permission from Ma et al. 2011. Copyright Elsevier)

Porous ZnO spheres have also been successfully synthesized and tested as photocatalysts, showing improved activity when compared to conventional ZnO, ascribed to the higher surface area and to the special assembled structure, which is said to enable the efficient charge carrier separation through interparticle charge transfer (Fig. 11.14b).

A good example of three-dimensional organization at the nanoscale is the incorporation of TiO₂ clusters inside the rigid framework of microporous materials (pore size < 2 nm). Zeolites are the most widely used hosts, as it is described in detail in Chap. 9.

Recently, mesostructured semiconductors have come on scene. The synthesis of mesoporous materials without the use of organic templates has been often attempted (Chen and Mao 2007). Nevertheless, with the assistance of structure-directing agents, such as surfactants, ordered metal oxide mesoporous materials with a pore size ranging from 2 to 50 nm can be obtained. Among them, the synthesis of highly ordered mesoporous TiO₂ is of particular interest, whose large surface area and pore size may result beneficial for photocatalytic purposes. Different approaches to obtaining mesostructured titania have been developed, with the main difficulty of preserving the structural integrity of the material while introducing crystallinity into the porous framework, and uniformly organized and oriented mesoporous titania thin films, constituted by ordered anatase particles, have been grown with 2D or 3D mesostructure (Yang et al. 1998; Crepaldi et al. 2003). This can be obtained by incorporating, during the hydrolysis stage, template molecules such as polyethylene oxide-based triblock polymers (commercially available as Pluronic-127) which act as scaffolds for the assembly of the TiO₂ nuclei (Yu et al. 2004). However, these structures are rather unstable, and they can collapse when the size of the anatase domains in the walls grows (Nilsson et al. 2011). In any case, these simple sol-gel techniques can be employed to build these 3D mesostructured TiO₂, allowing at the same time the integration of other photoactive nanomaterials in order to promote charge separation and electron or

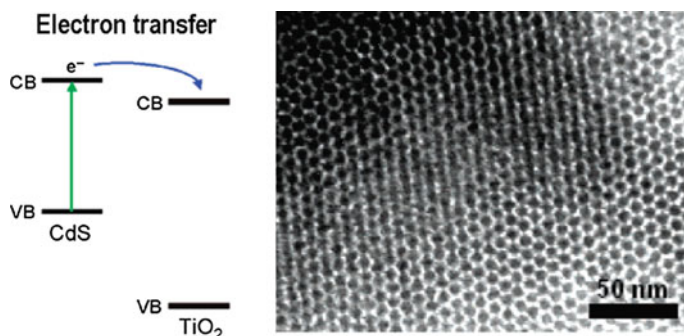


Fig. 11.15 Scheme of the sensitization of titania to visible light through electron transfer from CdS to anatase nanocrystals and TEM image of the mixed nanocrystalline TiO₂/CdS mesoporous film along the [111] axis of the structure (adapted with permission from Bartl et al. 2004. Copyright Wiley-VCH)

energy transfer. Thus, sensitization of titania to visible light has been produced, through electron transfer, by designing mixed TiO_2/CdS mesoporous frameworks, with walls composed of integrated arrays of the wide and narrow band-gap semiconductor nanocrystals (Bartl et al. 2005) (Fig. 11.15). Besides, the channels of mesoporous TiO_2 can act as host for different species, such as metal particles (Ag, Pt, etc.), for the sake of improving the performance of the photocatalyst.

High-ordered macroporous TiO_2 has also been developed. These nanostructures, with lattice periodicity in the range of the wavelength of light, are known as photonic crystals and constitute a novel class of nanomaterials with unique optical properties, such as high refractive index and high photocatalytic efficiencies. The improved photocatalytic performance has been attributed to the enhanced light-harvesting efficiency, affected by the morphology and macroscopic structure of the photocatalyst. The large reflectivity in the visible light range and multiple scattering effects, caused by the ordered macropores, may give rise to a more effective utilization of solar light in photocatalytic applications. In a photonic crystal, the structural periodicity allows the propagation of photons of specific wavelengths through the structure, forming allowed bands, analogous to electron bands in conventional materials. On the other hand, coherent Bragg's diffraction forbids light of certain wavelengths to propagate through the material, and the spectral range of large reflectivity is known as stop-band or photonic band gap. A complete photonic band gap occurs when a range of wavelengths is forbidden for every state of polarization and crystallographic direction. At the frequency edges of the stop-band, photons propagate at a strongly reduced velocity, and consequently, they are called slow photons. If the energy of these slow photons overlaps with the absorbance of the material, an enhancement of the absorption is expected as a consequence of the increase in the effective optical path length (Chen et al. 2006). One-, two- and three-dimensional photonic crystals have been developed, having one-, two and three-dimensional photonic band gaps, respectively. Self-assembly of colloidal crystals is a simple and inexpensive route to synthesize photonic crystals. The result of the crystallization of a colloidal monodispersion of spheres to form a material with a three-dimensional periodic structure is called opal.

The long-range periodic order in the photonic crystal increases the light/photocatalyst contact time and the probability of electronic excitation. 3D-ordered titania can be fabricated as inverse-opal photonic crystals, in which the above-described effects, the presence of a stop-band and multiple scattering, are present. Inverse-opal structures can be synthesized by filling the voids in a colloidal crystal template (opal) with the dielectric material and, then, by removing the original opal template by wet chemical etching or calcination (Fig. 11.16) (Waterhouse and Waterland 2007). The potential of TiO_2 inverse opals in photocatalytic applications has been explored. The studies conclude that the intrinsic properties of the TiO_2 crystals of inverse opals and conventional titania nanoparticles are similar, being the effect of the photonic crystal structure and slow photons responsible for the enhanced photocatalytic performance of the former materials. For a superior photoactivity, the energy of the photonic stop-band must be optimized with respect to the semiconductor electronic band gap, in order to effectively harvest slow

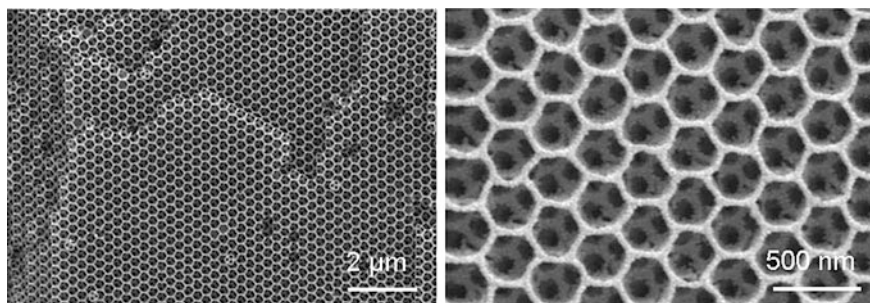


Fig. 11.16 SEM micrographs of TiO₂ inverse opals fabricated from colloidal crystal templates (PMMA) (adapted with permission from Waterhouse 2007. Copyright Elsevier)

photons at the same time that undesirable reflectivity losses are suppressed. It has been also demonstrated the high tolerance to structural disorder of their photocatalytic efficiency, which opens the door for a practical utilization of these photonic crystals (Chen et al. 2006; Chen et al. 2007).

However, some studies consider that other structures are more desirable for certain optical applications since the omnidirectional photonic band gap of inverse opals is narrow and located at high frequency. Thus, alternative colloidal crystal-based structures have been developed. This is the case of three-dimensional photonic crystals of TiO₂ hollow spheres, which can be obtained with different sphere diameters and shell thicknesses by sol-gel processes and template techniques (Li et al. 2006b). These opals do not possess a complete photonic gap since the stop-band position varies with the angle of incidence of incoming photons. Non-close-packed structures of these hollow spheres have proved to present a photonic band gap at visible wavelengths, wider than close-packed systems (Zhu et al. 2007). SEM micrographs of both close-packed and non-close-packed structures are presented in Fig. 11.17.

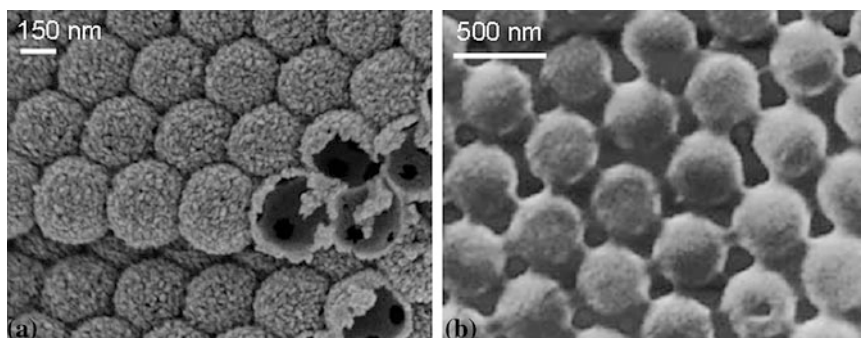


Fig. 11.17 Three-dimensional photonic crystals of TiO₂ hollow spheres: **a** close-packed structure connected through pores (adapted with permission from Li et al. 2006b. Copyright American Chemical Society) and **b** non-close-packed structure (adapted with permission from Zhu et al. 2007. Copyright Elsevier)

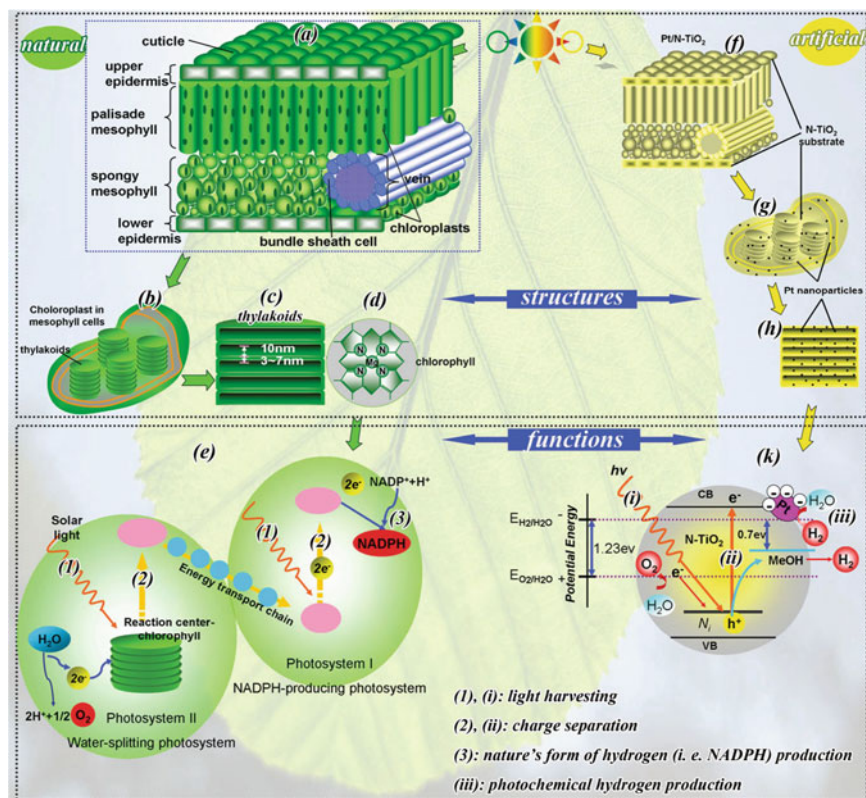


Fig. 11.18 Comparison of the structure and function of natural and artificial leaves (reproduced with permission from Zhou et al. 2010. Copyright Wiley-VCH)

As a variation in inverse opals, the so-called photonic sponges have been recently developed, formed from a random distribution (quasi-fractal) of interconnected spherical air cavities with different micrometric sizes. These systems are said to present the ideal architecture to harvest photons from the whole solar spectrum, with most of the incident photons trapped in the network, in contrast to other photonic structures that diffract light in a narrow range of wavelengths. Comparison of the photocatalytic performance of a photonic sponge film prepared from P25 and the unstructured reference photocatalyst indicated that the use of the photonic sponge increased the photoactivity in one order of magnitude (Carbonell et al. 2008).

All these previously described systems prove that it is possible to increase the photocatalytic efficiency by spatial structuring of the photocatalysts, without the need of introducing modifications in its chemical composition.

It is worth mentioning recent studies that seek to imitate the structure and functionality of biological systems, using them as models or templates for the design and fabrication of photoactive materials. These structures intend to

revolutionize the development of cost-efficient photocatalytic and photoelectrochemical solar devices. For instance, biomimetic structures inspired in the hierarchical structure of leaves are being developed in an effort to replicate, artificially, the natural process of the photosynthesis (Fig. 11.18). In these artificial leaves, natural photosynthetic pigments are replaced by manufactured photocatalysts. These systems are expected to promote the capture of sunlight photons and long-lifetime electron–hole separation, favouring processes such as CO₂ fixation and photochemical hydrogen production, in an artificial photosynthesis pathway (Zhou et al. 2010).

Other example of biomimetic photocatalyst design is the fabrication of a mesoporous TiO₂ by imitation of the bamboo inner membrane structure (Li et al. 2007). However, real progress in terms of significantly increased photoactivity still needs to be proved.

References

- Allam NK, Shankar K, Grimes CA (2008) A general method for the anodic formation of crystalline metal oxide nanotube arrays without the use of thermal annealing. *Adv Mater* 20:3942–3946
- Allen NS, Edge M, Verran J, Caballero L, Abrusci C, Stratton J, Maltby J, Bygott C (2009) Photocatalytic surfaces: environmental benefits of nanotitania. *Open Mater Sci J* 3:6–27
- Anpo M, Shima T, Kodama S, Kubokama Y (1987) Photocatalytic hydrogenation of CH₃CCH with H₂O on small-particle TiO₂: size quantization effects and reaction intermediaries. *J Phys Chem* 91:4305–4310
- Aprile C, Corma A, Garcia H (2008) Enhancement of the photocatalytic activity of TiO₂ through spatial structuring and particle size control: from subnanometric to submillimetric length scale. *Phys Chem Chem Phys* 10:769–783
- Auvinen S, Alatalo M, Haario H, Jalava J-P, Lamminmäki R-J (2011) Size and shape-dependence of the electronic and spectral properties in TiO₂ nanoparticles. *J Phys Chem C* 115(17):8484–8493
- Bartl MH, Boettcher SW, Frindell KL, Stucky GD (2005) 3-D molecular assembly of function in titania-based composite material systems. *Accounts Chem Res* 38(4):263–271
- Bartl MH, Puls SP, Tang J, Lichtenegger HC, Stucky GD (2004) Cubic mesoporous frameworks with a mixed semiconductor nanocrystalline wall structure and enhanced sensitivity to visible light. *Angew Chem Int Ed* 43:3037–3040
- Bavykin DV, Parmon VN, Lapkin AA, Walsh FC (2004) The effect of hydrothermal conditions on the mesoporous structure of TiO₂ nanotubes. *J Mater Chem* 14:3370–3377
- Bavykin DV, Walsh FC (2009) Elongated titanate nanostructures and their applications. *Eur J Inorg Chem* 8:977–997
- Bischoff BL, Anderson MA (1995) Peptization process in the sol-gel preparation of porous anatase (TiO₂). *Chem Mater* 7:1772–1778
- Biskos G, Vons V, Yurteri U, Schmidt-Ott A (2008) Generation and sizing of particles for aerosol-based nanotechnology. *KONA Powder Part J* 23:13–35
- Boutonnet M, Kizling J, Stenius P, Maire G (1982) The preparation of monodisperse colloidal metal particles from microemulsions. *Colloids Surf* 5:209–225
- Brus LE (1984) Electron-electron and electron-hole interactions in small semiconductor crystallites—the size dependence of the lowest excited electronic state. *J Phys Chem* 80:4403–4409

- Campbell LK, Na BK, Ko EI (1992) Synthesis and characterisation of Titania Aerogels. *Chem Mater* 4:1329–1333
- Cao FL, Wang JG, Lv FJ, Zhang DQ, Huo YH, Li GS, Li HX, Zhu J (2011) Photocatalytic oxidation of toluene to benzaldehyde over anatase TiO₂ hollow spheres with exposed 001 facets. *Catal Commun* 12:946–950
- Carbonell E, Ramiro-Manzano F, Rodriguez I, Corma A, Meseguer F, Garcia H (2008) Enhancement of TiO₂ photocatalytic activity by structuring the photocatalyst film as photonic sponge. *Photoch Photobio Sci* 7:931–935
- Castillo NC, Heel A, Graule T, Pulgarin C (2010) Flame-assisted synthesis of nanoscale, amorphous and crystalline, spherical BiVO₄ with visible-light photocatalytic activity. *Appl Catal B-Environ* 95:335–347
- Cernuto G, Masciocchi N, Cervellino A, Colonna GM, Guagliardi A (2011) Size and shape dependence of the photocatalytic activity of TiO₂ nanocrystals: a total scattering debye function study. *J Am Chem Soc* 133:3114–3119
- Chemseddine A, Moritz T (1999) Nanostructuring titania: control over nanocrystal structure, size, shape, and organization. *Eur J Inorg Chem*, pp 235–245
- Chen JIL, von Freymann G, Choi SY, Kitaev V, Ozin GA (2006) Amplified photochemistry with slow photons. *Adv Mat* 18:1915–1919
- Chen JIL, von Freymann G, Choi SY, Kitaev V, Ozin GA (2007) Effect of disorder on the optically amplified photocatalytic efficiency of titania inverse opals. *J Am Chem Soc* 129:1196–1202
- Chen X, Mao SS (2007) Titanium dioxide nanomaterials: synthesis, properties, modifications, and applications. *Chem Rev* 107:2891–2959
- Crepaldi EL, Soler-Illia GJAA, Grosso D, Cagnol F, Ribot F, Sanchez C (2003) Controlled formation of highly organized mesoporous titania thin films: from mesostructured hybrids to mesoporous nanoanatase TiO₂. *J Am Chem Soc* 125:9770–9786
- Curri ML, Agostiano A, Manna L, Della Monica M, Catalano M, Chiavarone L, Spagnolo V, Lugara M (2000) Synthesis and characterization of CdS nanoclusters in a quaternary microemulsion: the role of the cosurfactant. *J Phys Chem B* 104:8391–8397
- D'Arienzo M, Carbajo J, Bahamonde A, Crippa M, Polizzi S, Scotti R, Wahba L, Morazzoni F (2011) Photogenerated defects in shape-controlled TiO₂ anatase nanocrystals: a probe to evaluate the role of crystal facets in photocatalytic processes. *J Am Chem Soc* 133:17652–17661
- El-Sayed MA (2004) Small is different: shape-, size-, and composition-dependent properties of some colloidal semiconductor nanocrystals. *Accounts Chem Res* 37:326–333
- Eslamian M, Ashgriz N (2006) The effect of pressure on the crystallinity and morphology of powders prepared by spray pyrolysis. *Powder Technol* 167:149–159
- Fan HM, Wang DJ, Wang LL, Li HY, Wang P, Jiang TF, Xie TF (2011) Hydrothermal synthesis and photoelectric properties of BiVO₄ with different morphologies: An efficient visible-light photocatalyst. *Appl Surf Sci* 257(17):7758–7762
- Fang WQ, Gong XQ, Yang HG (2011) On the unusual properties of anatase TiO₂ exposed by highly reactive facets. *J Phys Chem Lett* 2:725–734
- Friedmann D, Mendive C, Bahnemann D (2010) TiO₂ for water treatment: parameters affecting the kinetics and mechanisms of photocatalysis. *Appl Catal B-Environ* 99:398–406
- Fuerte A, Hernández-Alonso MD, Maira AJ, Martínez-Arias A, Fernández-García M, Conesa JC, Soria J (2001) Visible light-activated nanosized doped-TiO₂ photocatalysts. *Chem Commun*, pp 2718–2719
- Grassian VH (2008) When size really matters: size-dependent properties and surface chemistry of metal and metal oxide nanoparticles in gas and liquid phase environments. *J Phys Chem C* 112:18303–18313
- Henle J, Simon P, Frenzel A, Scholz S, Kaskel S (2007) Nanosized BiOX (X = Cl, Br, I) particles synthesized in reverse microemulsions. *Chem Mater* 19:366–373

- Hernández-Alonso MD, García-Rodríguez S, Sánchez B, Coronado JM (2011a) Revisiting the hydrothermal synthesis of titanate nanotubes: new insights on the key factors affecting the morphology. *Nanoscale* 3:2233–2240
- Hernández-Alonso MD, García-Rodríguez S, Suárez S, Portela R, Sánchez B, Coronado JM (2011b) Highly selective one-dimensional TiO₂-based nanostructures for air treatment applications. *Appl Catal B-Environ* 110:251–259
- Hernández-Alonso MD, Tejedor-Tejedor I, Coronado JM, Soria J, Anderson MA (2006) Sol-gel preparation of TiO₂-ZrO₂ thin films supported on glass rings: influence of phase composition on photocatalytic activity. *Thin Solid Films* 502:125–131
- Hoffmann MR, Martin ST, Choi W, Bahnemann DW (1995) Environmental applications of semiconductor photocatalysis. *Chem Rev* 95:69–96
- Ikeda S, Hara M, Kondo JN, Domen K, Takahashi H, Okubo T, Kakihana M (1998) Preparation of K₂La₂Ti₃O₁₀ by polymerized complex method and photocatalytic decomposition of water. *Chem Mater* 10:72–77
- Jiang HY, Dai HX, Meng X, Zhang L, Deng JG, Ji KM (2011) Morphology-dependent photocatalytic performance of monoclinic BiVO₄ for methyl orange degradation under visible-light irradiation. *Chinese J Catal* 32(6):939–949
- Kasuga T, Hiramatsu M, Hoson A, Sekino T, Niihara K (1998) Formation of titanium oxide nanotube. *Langmuir* 14:3160–3163
- Klimov VI (2007) Spectral and dynamical properties of multiexcitons in semiconductor nanocrystals. *Annu Rev Phys Chem* 58:635–673
- Li J, Shi X, Wang L, Liu F (2007) Synthesis of biomorphological mesoporous TiO₂ templated by mimicking bamboo membrane in supercritical CO₂. *J Colloid Interf Sci* 315:230–236
- Li J, Xu D (2010) Tetragonal faceted-nanorods of anatase TiO₂ single crystals with a large percentage of active 100 facets. *Chem Commun* 46:2301–2303
- Li L-S, Hu J, Yang W, Alivisatos AP (2001) Band gap variation of size- and shape-controlled colloidal CdSe quantum rods. *Nano Lett* 1:349–351
- Li XL, Peng Q, Yi JX, Wang X, Li YD (2006a) Near monodisperse TiO₂ nanoparticles and nanorods. *Chem-Eur J* 12:2383–2391
- Li Y, Kunitake T, Fujikawa S (2006b) Efficient fabrication and enhanced photocatalytic activities of 3D-ordered films of titania hollow spheres. *J Phys Chem B* 110:13000–13004
- Li Y, White TJ, Lim SH (2004) Low-temperature synthesis and microstructural control of titania nano-particles. *J Solid State Chem* 177:1372–1381
- Lianos P, Thomas JK (1987) Small CdS particles in inverted micelles. *J Colloid Interf Sci* 117:505–512
- Liao C-M, Chiang Y-H, Chio C-P (2009) Assessing the airborne titanium dioxide nanoparticle-related exposure hazard at workplace. *J Hazard Mater* 162(1):57–65
- Lim KT, Hwang HS, Lee MS, Lee GD, Hong S-S, Johnston KP (2002) Formation of TiO₂ nanoparticles in water-in-CO₂ microemulsions. *Chem Commun*, pp 1528–1529
- Ma P, Wu Y, Fu Z, Wang W (2011) Shape-controlled synthesis and photocatalytic properties of three-dimensional and porous zinc oxide. *J Alloy Compd* 509:3576–3581
- Maira AJ, Yeung KL, Lee CY, Yue PL, Chan CK (2000) Size effects in gas-phase photo-oxidation of trichloroethylene using nanometer-sized TiO₂ catalysts. *J Catal* 192:185–196
- Monticone S, Tufeu R, Kanaev AV, Socolan E, Sanchez C (2000) Quantum size effect in TiO₂ nanoparticles: does it exist? *Appl Surf Sci* 162–163:565–570
- Mor KG, Varghese OK, Paulose M, Shankar K, Grimes CA (2006) A review on highly ordered, vertically oriented TiO₂ nanotube arrays: fabrication, material properties, and solar energy applications. *Sol Energy Mater Sol Cells* 90:2011–2075
- Nguyen-Phan T-D, Kim EJ, Hahn SH, Kim W-J, Shin EW (2011) Synthesis of hierarchical rose bridal bouquet- and humming-top-like TiO₂ nanostructures and their shape-dependent degradation efficiency of dye. *J Colloid Interf Sci* 356:138–144

- Nilsson E, Sakamoto Y, Palmqvist AEC (2011) Low-temperature synthesis and HRTEM analysis of ordered mesoporous anatase with tunable crystallite size and pore shape. *Chem Mater* 23:2781–2785
- Ohno T, Sarukawa K, Matsumura M (2002) Crystal faces of rutile and anatase TiO₂ particles and their roles in photocatalytic reactions. *New J Chem* 26(9):1167–1170
- Ohtani B (2008) Preparing articles on photocatalysis—beyond the illusions, misconceptions, and speculation. *Chem Lett* 37(3):217–229
- Paramasivam I, Jha H, Liu N, Schmuki P (2012) A review of photocatalysis using self-organized TiO₂ nanotubes and other ordered oxide nanostructures. *Small* 8:3073–3103
- Rivera P, Tanaka K, Hisanaga T (1993) Photocatalytic degradation of pollutant over TiO₂ in different crystal structures. *Appl Catal B-Environ* 3:37–44
- Schulman JH, Friend JA (1949) Light scattering investigation of the structure of transparent oil-water disperse systems II. *J Colloid Interf Sci* 4:497–501
- Serpone N, Lawless D, Khairutdinov R (1995) Size effects on the photophysical properties of colloidal anatase TiO₂ particles: size quantization or direct transitions in this indirect semiconductor? *J Phys Chem* 99:16646–16654
- Shankar K, Basham JI, Allam NK, Varghese OK, Mor GK, Feng X, Paulose M, Seabold JA, Choi K-S, Grimes CA (2009) Recent advances in the use of TiO₂ nanotube and nanowire arrays for oxidative photoelectrochemistry. *J Phys Chem C* 113:6327–6359
- Smith AM, Nie S (2010) Semiconductor nanocrystals: structure, properties, and band gap engineering. *Acc Chem Res* 43:190–200
- Strobel R, Baiker A, Pratsinis SE (2006) Aerosol flame synthesis of catalysts. *Adv Powder Technol* 17:457–480
- Tachikawa T, Fujitsuka M, Majima T (2007) Mechanistic insight into the TiO₂ photocatalytic reactions: design of new photocatalysts. *J Phys Chem C* 111:5259–5275
- Tian G, Chen Y, Zhou W, Pan K, Tian C, Huang X-R, Fu H (2011) 3D hierarchical flower-like TiO₂ nanostructure: morphology control and its photocatalytic property. *Cryst Eng Comm* 13:2994–3000
- Trindade T (2001) Nanocrystalline semiconductors: synthesis, properties, and perspectives. *Chem Mater* 13:3843–3858
- Wang C-C, Ying JY (1999) Sol-Gel synthesis and hydrothermal processing of anatase and rutile titania nanocrystals. *Chem Mater* 11:3113–3120
- Wang C-C, Zhanag Z, Ying JY (1997) Photocatalytic decomposition of halogenated organics over nanocrystalline titania. *Nanostruct Mater* 9:583–586
- Waterhouse GIN, Waterland MR (2007) Opal and inverse opal photonic crystals: fabrication and characterization. *Polyhedron* 26:356–368
- Xiang Q, Lv K, Yu J (2010) Pivotal role of fluorine in enhanced photocatalytic activity of anatase TiO₂ nanosheets with dominant (0 0 1) facets for the photocatalytic degradation of acetone in air. *Appl Catal B-Environ* 96:557–564
- Xu N, Shi Z, Fan Y, Dong J, Shi J, Hu MZ-C (1999) Effect of TiO₂ particle size on photocatalytic degradation of methylene blue in aqueous suspensions. *Ind Eng Chem Res* 38:373–379
- Yang HG, Sun CH, Qiao SZ, Zou J, Liu G, Smith SC, Cheng HM, Lu GQ (2008) Anatase TiO₂ single crystals with a large percentage of reactive facets. *Nature* 453:638–642
- Yang PD, Zhao DY, Margolese DI, Chmelka BF, Stucky GD (1998) Generalized syntheses of large-pore mesoporous metal oxides with semicrystalline frameworks. *Nature* 396:152–155
- Yu JC, Wang X, Fu X (2004) Pore-wall chemistry and photocatalytic activity of mesoporous titania molecular sieve films. *Chem Mater* 16:1523–1530
- Zhang JZ (1997) Ultrafast studies of electron dynamics in semiconductor and metal colloidal nanoparticles: effects of size and surface. *Accounts Chem Res* 30:423–429
- Zhang Z, Wang C-C, Zakaria R, Ying JY (1998) Role of particle size in nanocrystalline TiO₂-based photocatalysts. *J Phys Chem B* 102:10871–10878

- Zhou H, Li X, Fan T, Osterloh FE, Ding J, Sabio EM, Zhang D, Guo Q (2010) Artificial inorganic leaves for efficient photochemical hydrogen production inspired by natural photosynthesis. *Adv Mater* 22:951–956
- Zhou W, Du G, Hu P, Li G, Wang D, Liu H, Wang J, Boughton RI, Jiang H (2011) Nanoheterostructures on TiO₂ nanobelts achieved by acid hydrothermal method with enhanced photocatalytic and gas sensitive performance. *J Mater Chem* 21:7937–7945
- Zhu Y, Cao Y, Li Z, Ding J, Liu J, Chi Y (2007) Synthesis and photonic band calculations of NCP face-centered cubic photonic crystals of TiO₂ hollow spheres. *J Colloid Interf Sci* 306:133–136

Chapter 12

Immobilised Photocatalysts

Silvia Suárez

Suspensions of photocatalysts, where the photoactive phase is placed in contact with the fluid to be purified, are commonly used in photocatalytic applications for the sake of simplicity. However, working with suspensions is not technologically feasible due to the high cost of the filtration process for the recovery/removal of the photocatalyst. Besides, the proper illumination of all the photocatalytic particles in the fluid is complicated. The penetration of photons into the fluid is hindered by the scattering/absorption of the particles close to the irradiation source, resulting in a deficient utilisation of the photocatalyst.

Some of these drawbacks can be overcome by using semiconductors immobilised on a substrate such as glass, alumina or silica. In contrast to mixed materials, described in [Chap. 15](#), the carrier does not enhance the optoelectronic properties of the photocatalyst but it mainly plays a structural role. The utilisation of supported photocatalysts opens a wide range of possibilities for the treatment of pollutants in either aqueous or air phase and for energetic applications as water splitting. Nowadays, the strategies in this area are focussed on improving the method of fixation of TiO_2 on the support, increasing the illuminated area or the adsorption capacity of the photocatalyst, and analysing the influence of these parameters on the photocatalytic activity and reaction selectivity. The selection of the substrate is also an important issue, where the combination of a good interaction with the semiconductor, an efficient use of photons, the shape, the lightness and the final price of the composite material are some important factors to be taken into account. This chapter will address the most important aspects to be considered for the preparation of immobilised photocatalysts, the techniques available for the immobilisation of the active phase, and the description of some of the most commonly used substrates, paying special attention to a novel family of

S. Suárez (✉)

División de Energías Renovables, CIEMAT-Grupo de Tratamiento Fotocatalítico de Contaminantes en Aire, Avda. Complutense 40, 28040 Madrid, Spain
e-mail: silvia.suarez@ciemat.es

bi-functional materials in which adsorption and photocatalytic properties are combined, the so-called adsorbent–photocatalyst hybrid composites.

12.1 Deposition Methods

In order to obtain an adequate supported photocatalyst, two key aspects must be considered: the nature of the substrate, which should be adequate to allow a good interaction between the support and the photoactive phase (coating) and the incorporation of the photocatalyst into the substrate, which must be accomplished without damaging the photocatalytic performance. The first condition is essential because the substrate must withstand the forces generated during the deposition process of the semiconductor. Moreover, the semiconductor layer must bear erosion processes taking place under the photocatalytic process.

However, the catalytic activity can be affected by the following factors:

1. Changes in the structure of the energy bands of the semiconductor, caused by the interaction with the substrate or by modification of the catalyst particle size.
2. Transformation of the crystal structure as a result of the heat treatment necessary to improve its fixation onto the support.
3. Formation of agglomerates or aggregates with the consequent reduction in surface area.
4. Penetration of the photocatalyst particles into the pores of opaque substrates, hindering illumination.

The immobilisation of a semiconductor on a substrate can be achieved by two general approaches: (a) those in which the photoactive phase, for instance, TiO_2 , is synthesised and then deposited, as such, on the carrier; and (b) those in which the precursor phase is deposited on the substrate by methods such as sol–gel or chemical vapour deposition (CVD), and then, the active phase is generated by chemical or physical methods.

In this section, the most relevant techniques used for the development of thin films on non-porous supports (dip-coating, spin-coating) or porous media (slip-casting), and vapour phase methods (CVD or sputtering) are described. Finally, the last section is devoted to the spray techniques, including spray pyrolysis (SP) and electrospray (ES). Most of the methods described may be applied for both transparent and opaque supports, such as the dip-coating procedure, chemical or physical vapour deposition (PVD), or plasma generation–associated techniques, to mention some examples (Meille 2006). In the last section of the chapter, the most relevant techniques specifically associated with the preparation of ceramic and metal-based substrates will be discussed, in connection with photocatalytic applications.

12.1.1 Dip-Coating

The dip-coating technique is widely used in the industry for the manufacture of materials with high optical quality such as glass plates (Schott), for solar power

control systems (Calorex[®]) and for anti-reflective coatings on windows (Amiran[®]). In this process, the substrate is immersed in a liquid and then lifted under well-controlled speed, temperature, pressure and humidity conditions. As a consequence, a thin layer of the components present in the liquid is deposited on the substrate (Candal et al. 2004). It is important to stress that the preparation should be performed at a constant speed to ensure the uniformity of the layer. A schematic representation of the process is shown in Fig. 12.1.

The thickness of the coating becomes defined by the speed of the extraction and the composition of the liquid phase and can be calculated by the Landau–Levich equation (Eq. 12.1) assuming that the system is in Newtonian regime:

$$h = 0.94 \cdot \frac{(\eta \cdot v)^{2/3}}{\gamma_{LV}^{1/6} (\rho \cdot g)^{1/2}} \quad (12.1)$$

where h is the thickness of the coating, η is the viscosity, v is the velocity, γ_{LV} the surface tension between liquid and vapour, ρ the density, and g gravity. Thus, the thickness of the layer depends directly on the speed of the process.

Experimental results indicate that the dimensions of the layers generated by dip-coating fit well to those calculated from the Eq. (12.1) (Strawbridge and James 1986). Thus, film thicknesses between 20 nm and 1 μm can be obtained by a careful selection of both the viscosity of the liquid phase and the raising rate. In the case of coatings prepared by reactive systems, such as the sol–gel systems where alkoxides or pre-hydrolysed precursors are used, the accurate control of the atmosphere is a key parameter. The ambient conditions determine the evaporation of the solvent and the resulting destabilisation of the sol. As a consequence, the gelation process occurs and the formation of a transparent layer with small particles in the range of nanometres is formed. (Brinker et al. 1988). An outline of the process is shown in Fig. 12.2.

In general, the particles in a sol are stabilised by surface charges, and according to Stern's theory (Stern 1924), the gelation process is based on the approach of charged particles at distances below the potential of repulsion. Thus, the repulsion force becomes an attractive force, and the gelation process is accelerated. Finally, the density of the resulting layer increases during the heat treatment process.

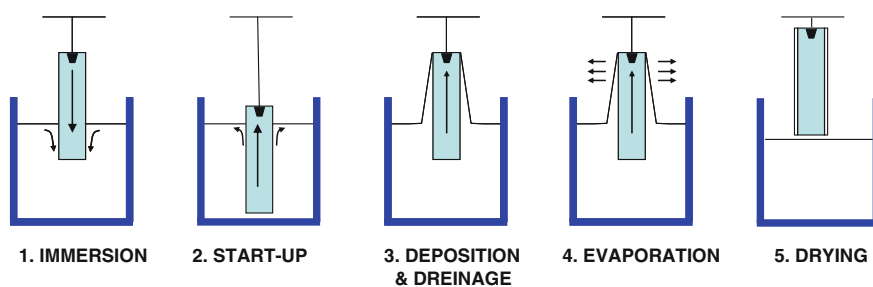


Fig. 12.1 Dip-coating stages. 1 Immersion, 2 start-up, 3 deposition and drainage, 4 evaporation, 5 drying

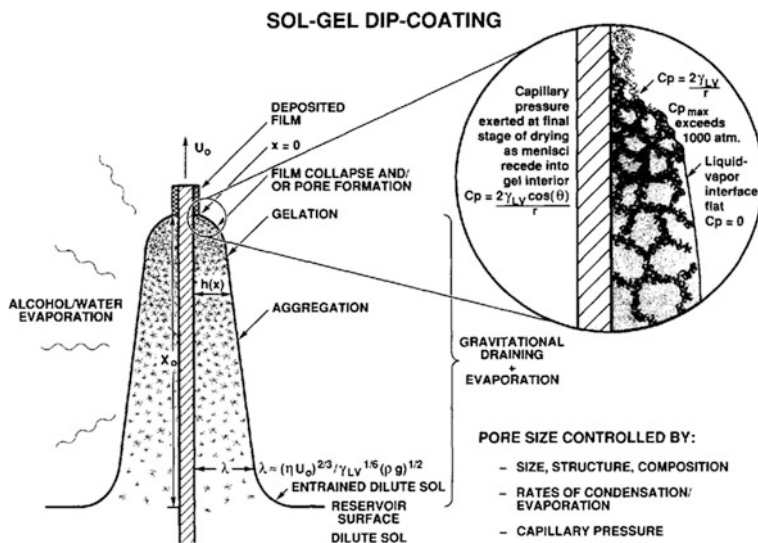


Fig. 12.2 Diagram of the steady state dip-coating process [reproduced with permission from Brinker et al. (1991). Copyright Elsevier]

There are some important parameters determining the final photocatalytic properties of the layer. The composition of the sol has a relevant role by tuning the physicochemical characteristics of the photoactive component. The layer thickness affects directly the photocatalytic activity. For Zr-modified titania layers, Sirisik et al. (1999) reported that an increase in the thickness from 150 to 300 nm significantly improved the activity for the removal of ethylene, but further increment of photocatalyst content had little effect on the efficiency. The difficulty of light to penetrate the entire depth of the photocatalyst layer in the reactor bed is the main reason for this behaviour.

An example of the effect of the sintering time and calcination temperature of thin films in the degradation of trichloroethylene is shown in Fig. 12.3 (Arconada et al. 2009). Prolonged sintering times lead to a reduction in the photocatalytic activity due to the densification of the layer accompanied with a reduction in the surface area and the pore volume. Moreover, increasing the temperature treatment leads to a progressive elimination of the surface organic residues along with further crystallisation of the TiO_2 anatase phase (Deng et al. 2002; Zhu et al. 2007). A compromise between the calcination temperature and the sintering time to ensure the desired crystal phase, maintaining a high porosity of the layer, should be attained. Another alternative strategy is the addition of pore generating agents to create a more open structure reducing the internal mass transfer limitations (Suárez et al. 2011a).

It is worth noting that in the case of using conventional glasses such as soda lime glass as substrate, diffusion of alkaline elements from the support to the photoactive layer can occur during the heat treatment at temperatures above

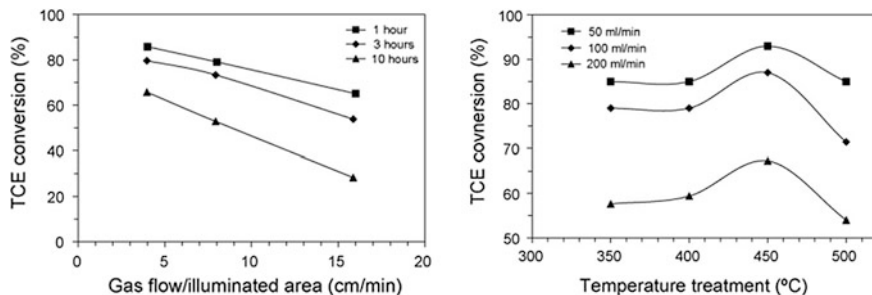


Fig. 12.3 Effect of the sintering time and temperature treatment of TiO_2 thin films on glass prepared by dip-coating on the degradation of trichloroethylene (reproduced with permission of Arconada et al. (2009). Copyright Elsevier)

300 °C, which would lead to a remarkable decrease in the photoactivity (Yu and Zhao 2000). The presence of a protective silica layer avoids the diffusion of alkali ions into the active TiO_2 film (Guglielmi and Zenezini 1990; Herman et al. 2000; Yu and Zhao 2000; Nam et al. 2004).

A modification of the dip-coating method is the so-called angle-dependent dip-coating process (Arfsten et al. 1997). This procedure permits to obtain samples with asymmetric coatings of different thickness depending on the angle between each side of the substrate and the liquid, as shown in Fig. 12.4a.

A particularly suitable technique for designing systems with rotational symmetry is the spin-coating process shown in Fig. 12.4b (Lai 1979; Chen 1983; Pan and Lee 2006). In this method, the precursor of the active phase is placed on the substrate by means of a dispenser and submitted to rotation until uniform distribution of the layer is achieved by centrifugal spreading. This process usually results in the partial evaporation of the solvent, but frequently the material needs an additional thermal treatment to stabilise the layer. The thickness of the films obtained by spin-coating depends on the concentration of the solution and the

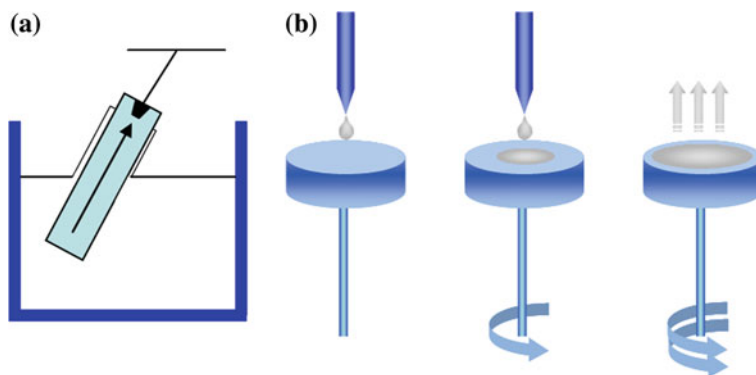


Fig. 12.4 Scheme of **a** angle-dependent dip-coating process and **b** spin-coating process

rotation speed in such a way that the higher the angular speed of spinning, the thinner the film. When porous substrates are used, the process is called *slip-casting* (Candal et al. 2004). The approach is in fact rather similar to the dip-coating one, but in this case the fluid is introduced into the support by capillary action, creating a gel layer on the surface. This technique has been applied for the preparation of membranes (Leenaars et al. 1984; Molinari et al. 2000; Zhang et al. 2006a). The capillary pressure difference between the pores of the support and the liquid—that is proportional to the surface tension—and the contact angle between liquid and solid are the driving force of the deposition of the layer.

12.1.2 Vapour Phase Deposition

The most common vapour phase deposition techniques are CVD (Chemical Vapour Deposition) and PVD (Physical Vapour Deposition) methods such as sputtering. The CVD technique allows the production of high purity thin films on substrates of different nature. The substrate is exposed to one or more volatile precursors, which react or decompose on the solid surface producing the desired deposit (Anpo et al. 1989; Jung and Imaishi 2001; Lee et al. 2001a; O'Neill et al. 2003; Nogier et al. 2009; Shan et al. 2010). In order to facilitate the formation of the solid layer, the substrate is generally maintained at high temperature. Diffusion, adsorption of the reactant into the surface, chemical reaction followed by desorption, and diffusion of the products are the main step in this process (Ding et al. 2001).

There are variations of the technique which depend on the operation pressure: atmospheric pressure CVD, low-pressure CVD and ultrahigh vacuum CVD, presenting the potential advantage of reducing undesired reactions in the gas phase. Most importantly, such methods improve the uniformity of the deposited film. Attending to the physical characteristics of the vapour phase, the methods can be classified as aerosol-assisted CVD and direct liquid injection CVD. Finally, the so-called plasma-enhanced CVD (PECVD) method takes advantage of the use of plasma to increase chemical reaction rates, which allows working at lower temperatures (Wu et al. 2011; Maeda and Watanabe 2005; Nizard et al. 2008; Rico et al. 2009; Hájková et al. 2009). This method is especially interesting in the case of temperature-sensitive substrates such as organic polymers. Another advantage of CVD techniques is that they make it possible to process large surfaces of substrate, regardless the shape, in a short period of time, producing high quality and high purity solid materials (Carp et al. 2004). CVD methods have been extensively used for the deposition of semiconductors on carbon-based materials (Zhang et al. 2006b; Li Puma et al. 2008), silica (Ding et al. 2000; Hirai et al. 2001) or alumina supports (Lei et al. 1999; Jung et al. 2005). With regard to transparent substrates, TiO₂ coatings on glass have been successfully prepared by reaction of TiCl₄ and a co-oxygen source (MeOH, EtOH, iPrOH or H₂O), resulting in excellent uniformity, surface coverage, adherence and optical properties and

giving rise to total degradation of stearic acid (O'Neill et al. 2003). Sarantopoulos et al. (2009) prepared glass microfibres fabrics and glass plates by using a metal-organic precursor for chemical vapour infiltration (MOCVI) and chemical vapour deposition (MOCVD), respectively, using titanium tetraisopropoxide (TTIP). These materials were tested for the degradation of organic pollutants such as imazapyr and malic acid in aqueous solutions, and toluene in air. Parameters such as temperature treatment, thickness of coating and the effect of the substrate were further analysed. Photocatalytic coatings prepared by these techniques have also been applied for isomerisation reactions of 2-butene (Anpo et al. 1989), the elimination of nitrogen and sulphur oxides (Nasonova et al. 2010), or the bactericidal effect for Ag/TiO₂ prepared by PECVD (Hájková et al. 2009), amongst others.

PVD methods are similar to CVD but, in this case, no chemical reaction takes place. These methods can be classified into mechanical ones, such as sputtering, and thermal ones, where the deposition phenomenon is promoted by the evaporation of the target. Cathodic sputtering, electron beam evaporation and pulsed laser deposition, to cite some of them, are included as PVD techniques. Sputtering is one of the most frequently used methods for obtaining thin films because it is a rather simple, versatile and flexible process. In this technique, the source material (e.g. Ti metal) is bombarded with a beam of gas ions such as Ar⁺, and the ejected atoms are subsequently deposited in the substrate. Although inert gases are typically used, in the process known as reactive sputtering, which is applied to the preparation of TiO₂ coatings, reactive gases like oxygen are also utilised. The sputtering approach covers a number of techniques, ranging from direct current (DC) discharge in conductive materials to the more sophisticated sputtering magnetrons operating in radiofrequency (RF), where the target material is an insulator. Much effort has been devoted to the development of photocatalysts active in the visible region by the sputtering technique. Thus, besides TiO₂ thin films studied for the degradation of ethanol (Eufinger et al. 2007), Ta- and N-co-doped TiO₂ (Obata et al. 2007), nitrogen-substituted TiO₂ (N-TiO₂) (Kitano et al. 2006a) and TiO₂-CeO₂ films (Liu et al. 2005) have also been synthesised and tested in the photocatalytic oxidation of oleic acid, 2-propanol and dyes, respectively, whilst Pt-loaded TiO₂ thin films have been tested in water splitting (Kitano et al. 2006b).

12.1.3 *Spraying Methods*

Spraying is the preferred option for the industry to coat large surface areas, since it is a simple and economical method (Takahashi et al. 1989; Byrne et al. 1998). Generally, a suspension containing the precursor, or the previously synthesised semiconductor, is prepared. The selection of the solvent, the addition of stabilisers or additives promoting the adhesion of the layer to the substrate and the physicochemical properties of the substrate are some important points to be considered. The substrate is coated by special devices designed for this purpose, as a spray

gun, or by effect of a gas passing through the liquid containing the photoactive material.

Nanostructured materials with one-dimensional shape can be prepared by the Spray Pyrolysis (SP) technique (Quintana et al. 2002; Chung et al. 2004; Chiarello et al. 2008; Pawinrat et al. 2009).

SP is a versatile and low-cost thin film deposition method, which allows scaling up the material deposition with rod morphology onto large areas. The depositing solution is placed in an ultrasonic device in which a controlled pressure is applied by means of a gas flow. Passing through the nozzle, the cloud formed will reach the substrate that is maintained at a controlled temperature. On the substrate, solvent evaporation occurs and the film starts to grow (Krunks and Mellikov 1995). The deposition of a seed layer, prepared by SP technique, allows the control of the growth of nanorods (Quintana et al. 2002). Changes in the solvent composition allow the modification of the seed layer properties and the ulterior formation of the nanorods. For the growth of the nanorods, the substrate is immersed in a NaOH solution containing the metal oxide precursor at a controlled temperature to facilitate the crystal growth into the substrate for a controlled time. Layers around 600 nm can be prepared by this technique with particles sizes around 30–50 nm (Fig. 12.5). These materials have been successfully used in disinfection (Rodríguez et al. 2010), degradation of dyes (Quintana et al. 2002), acetaldehyde decomposition (Li and Haneda 2003), reforming of methanol (Chiarello et al. 2011) or hydrogen production (Chiarello et al. 2008).

An interesting way to create a film on a conductive support is the Electro spray (ES) technique. This process is based on the generation of a very thin aerosol through electrostatic charges. Thus, microdroplets are generated by means of electricity instead of air. The material to be deposited passes, as a liquid, through a nozzle, where it becomes electrically charged by applying a potential. This charged liquid is very unstable and tends to accumulate more charge until a critical point is reached, where droplets of a size smaller than 10 μm in diameter are stabilised. These drops move towards any surface with opposite charge. In this process, the solvent evaporates from the surface and the distance between electrical charges within the microdroplet decreases, so that if the drop does not reach

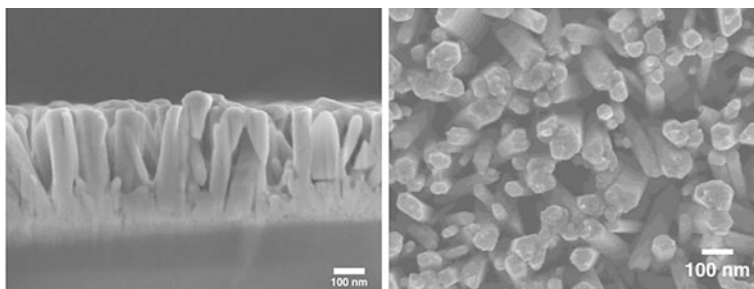


Fig. 12.5 SEM images of ZnO nanorods at pH 4.8 prepared by spray pyrolysis [reproduced with permission of Rodríguez et al. (2010). Copyright Elsevier]

an appropriate surface to dissipate this charge, it reaches a critical point and is expelled (Chen et al. 1998, 1999; Nomura et al. 2003; Fujimoto et al. 2006).

The ES approach is used in the industry for the application of paints and as coating for metals. The use of a transparent conductive oxide (TCO) or metal sheets allows the synthesis of TiO_2 thin films by this technique (Chen et al. 1998, 1999; Fujimoto et al. 2006; Nomura et al. 2003). The ES deposition method makes it possible to prepare photocatalysts in a single step and to create complex designs in both the chemical composition and the geometric arrangement, with significant savings of time and materials. An example of the coral-like morphology obtained by deposition of a TiO_2 precursor on a conductive glass substrate with an indium tin oxide (ITO) coating is shown in Fig. 12.6.

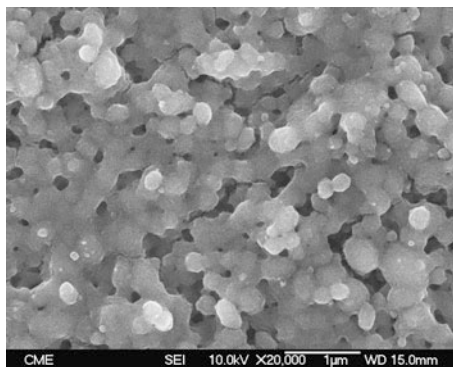
12.2 Substrate Materials

An important issue to be considered for immobilised photocatalysts preparation is the selection of the support. The substrate should meet certain requirements, although it may be difficult for a single support to fulfil all of them:

1. The material must be transparent to the applied radiation.
2. It should promote a strong physical–chemical interaction with the active phase without adversely affecting the chemical properties of the photocatalyst.
3. It should have a high specific surface area and high adsorption capacity of the pollutant to be treated.
4. It should be structured, so that it ensures easy handling and recovery.
5. It should have the proper geometry to facilitate mass transfer processes and irradiation of the photoactive component.

A number of possible substrates are available in the market, such as those based on SiO_2 , quartz optical fibers, glass fibers, cellulose membranes, microporous ceramic membranes, clays, monolithic supports, zeolites, stainless steel or organic polymers. The selection of the appropriate substrate must consider technological, economical and practical aspects.

Fig. 12.6 Coral-type structure for TiO_2 films prepared by Electro spray technique



In this section, firstly, a description of the most commonly transparent substrates reported in the literature is commented, and secondly, the most relevant opaque substrates will be described, in connection with the photocatalytic applications.

12.2.1 Transparent Substrates

From the viewpoint of the optical properties, because of its high transmittance, glass is amongst the most interesting candidates to support photoactive materials. There are numerous studies that report the use of the walls of a reactor made of Pyrex glass to support photocatalysts based on oxides, which has the added advantage of good adhesion between both materials. This favourable interaction between the substrate and the photocatalytic layer can be attributed to the presence of a high concentration of hydroxyl groups on the surface, which can promote the attachment of the active phase. Moreover, this material can withstand high temperature treatments (up to 500°C) allowing the consolidation of the coating process and the elimination of undesirable compounds from the synthesis. Another advantage of glass is that this material is chemically rather inert. Amongst the main disadvantages, the high weight, the difficulty associated with its fragility during manipulation and the diffusion of cations from the support to the active layer at high temperature can be cited. Shaped glass of different geometries such as Raschig rings (Hernández-Alonso et al. 2006), pellets (Al-Ekabi and Serpone 1988), microspheres (Nair et al. 1993) or glass microbeds are some of the most relevant proposals for the treatment of pollutants (Schwitzgebel et al. 1995). In Fig. 12.7, SEM micrographs of the top and the cross-section views of a TiO₂ thin film coated on Pyrex glass are shown. A transparent and uniform thin layer of around 65 nm, made of TiO₂ aggregates of around 40 nm, characterised the coating. Silica has been used in many forms, from common sand to silica gel or quartz particles, including commercial fuse silica glass fibres covered by TiO₂ (Matthews 1987; Hofstadler et al. 1994; Mikula et al. 1995).

Organic polymers such as polydimethylsiloxane (Iketani et al. 2003; Pascualino et al. 2006), polyesters (Sánchez et al. 2006; Portela et al. 2007), polymethylmethacrylate or polycarbonate (Langlet et al. 2002) are very interesting supports because of their high transmittance in the UVA and Vis regions. Additionally, they are light materials, easy to handle and with the possibility of being easily structured in different geometries such as honeycomb structures (Sánchez et al. 2006; Yang et al. 2006; Lunawat et al. 2007). An example is shown in Fig. 12.8, where SEM micrographs of CdS semiconductor with different loadings coated on polyethylene terephthalate fibres are reproduced.

Nevertheless, organic polymers present some disadvantages to be considered. These materials are temperature sensitive and, depending on their nature, can suffer significant degradation under UV light irradiation, especially in the presence of the semiconductor, which would decrease the initial transmittance values (Wiles

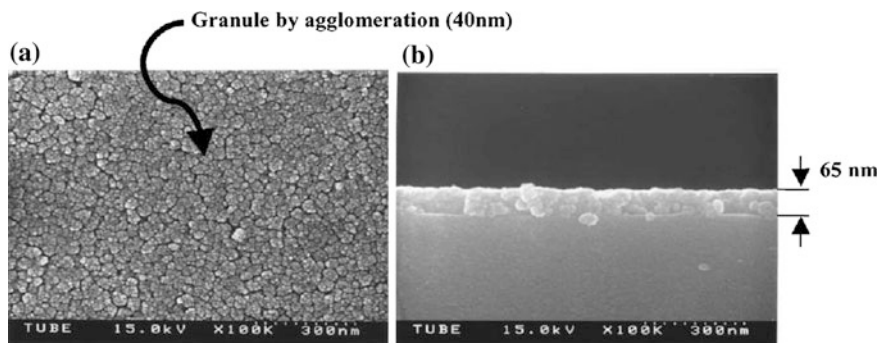


Fig. 12.7 SEM micrographs of top **a** and cross-sectional **b** views of a TiO_2 thin film on a Pyrex glass support [reproduced with permission of Kim and Hong (2002). Copyright Elsevier]

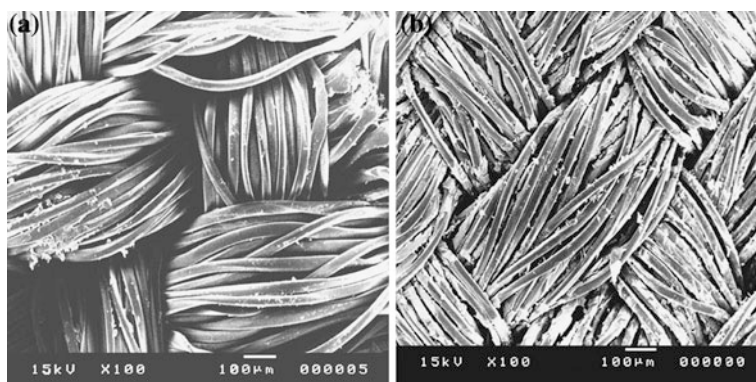
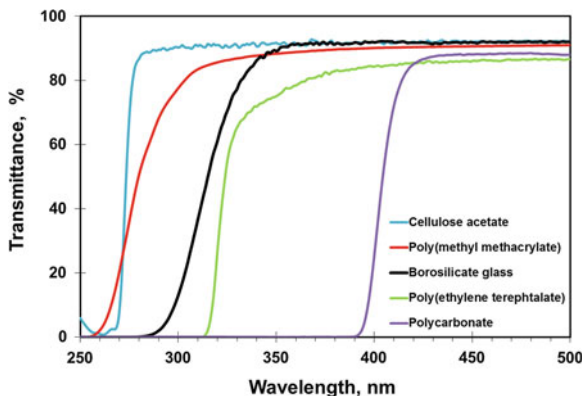


Fig. 12.8 SEM micrographs of CdS-based photocatalysts immobilised on polyethylene terephthalate fibres for two different loadings. **a** 5 wt %. **b** 17 wt % [reproduced with permission of Lunawat et al. (2007). Copyright Elsevier Ltd.]

1973; Nyok-Sai 1977; Gijnsman et al. 1999; Kumar et al. 2009; Yang et al. 2011). Moreover, the hydrophobicity of the surface hinders the interaction with the active phase, usually in an aqueous medium. In this respect, the deposition of a silica protective layer or the incorporation of poly(diallyldimethylammonium) chloride, which provides a positively charged surface for the fixation of the inorganic layers, has been used as a way to prevent the degradation effect and to improve the adhesion of the photoactive coating (Matsuda et al. 2003; Sánchez et al. 2006). Alternatively, the organic polymer surface can be pre-treated with techniques such as low-pressure plasma (LPP) or atmospheric pressure plasma (APP) in a controlled atmosphere, in order to create carbonyl groups, which will act as anchoring sites for the fixation of the semiconductor layer (Hegemann et al. 2003). A comparison of the wavelength dependence of the transmittance of glass and different organic polymers is depicted in Fig. 12.9. This graph clearly shows the high transmittance of the glass base support at 330 nm. Similar transmittance values

Fig. 12.9 Dependence of the transmittance of glass and different organic polymers on wavelength



can be obtained with some polymeric substrates such as cellulose acetate or poly(methyl methacrylate). Regarding polymers, the composition, the preparation route and the type of additives strongly influence their transmittance. Thus, some of these polymeric materials present significant limitations for UV applications, but they can be applied under visible light.

These polymeric substrates have been applied in several photocatalytic reactions, for instance, water splitting to obtain hydrogen using CdS deposited on polyester (Lunawat et al. 2007), or elimination of organic molecules in gas phase, such as trichloroethylene over TiO_2 on poly(ethylene terephthalate) (PET) (Sánchez et al. 2006; Coronado et al. 2008a), or acetaldehyde using TiO_2 on poly(dimethylsiloxane) (Iketani et al. 2003). In addition, TiO_2 coated on orthophthalic polyester and poly(dimethylsiloxane) has also been applied to degradation of salicylic acid and phenol (Paschoalino et al. 2006). Similarly, TiO_2/PET has been used for the removal of inorganic molecules, such as hydrogen sulphide (Portela et al. 2007).

12.2.2 Opaque Supports

Opaque supports have also been used as substrates for photocatalytic applications. Although these substrates present the drawback of the null transmission of light compared to conventional transparent glass supports or organic transparent polymers, the selection of materials with high surface area and pore volume (high adsorption capacity), or materials with improved affinity for the active phase precursor may be of interest for some applications. Besides, non-adsorbent materials, such as non-porous ceramics with high thermal resistance or metal foils, or hybrid composites that combine the adsorption and photocatalytic properties, have been explored and used in several photocatalytic applications (Carp et al. 2004; Shan et al. 2010; Meille 2006).

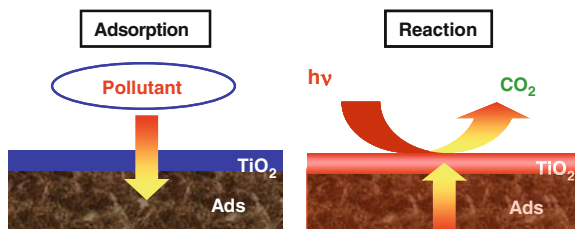
Basically, the incorporation of the photocatalytic material on porous substrates can be accomplished by two different approaches (Cybulsky and Moulijn 1998). The first one deals with the incorporation of the active element homogeneously dispersed on the entire body of the porous substrate, in order to obtain a composite material. The second method relates with the impregnation of the active phase on the substrate, resulting in an uneven layered structure. The preparation of bulk catalysts according to the first approach is generally made by extrusion of a dough that contains all the elements of the catalyst or its precursors. This route of synthesis favours the homogeneous distribution of the active phase along the extrudate. It usually includes additives that become essential part of the catalyst conformation. Amongst them, natural silicates are very interesting since they provide the ceramic paste with optimal rheological properties to be extruded (Blanco et al. 2000; Avila et al. 2005). Plates, cylinders or monolithic structures have been prepared by this technique. In the impregnated catalysts, the photoactive phase is deposited on the previously prepared support by different methods, such as wet impregnation or deposition–precipitation as preferred options. The soaking time and the drying step are essential to determine the distribution and homogeneity of the active phase of the catalyst.

The coating of opaque materials with photocatalysts can be a complex and laborious task. Once the ceramic- or metal-based material with the desired physical and mechanical properties is prepared, it should be coated with a film of thickness $<50\ \mu\text{m}$ of the photoactive component, which usually presents a high surface area (between 50 and $200\ \text{m}^2\ \text{g}^{-1}$); this process is called washcoating. The washcoat particles, displaying diameters of 10 – $20\ \text{nm}$ may be porous themselves, providing the system with the meso-microporosity characteristics.

Amongst the numerous methods for incorporating the washcoat to the support, slip-casting is the most used one. Alternatively, the catalyst can be synthesised in situ from its precursor, for example, by CVD from TiCl_4 . The specific preparation method should be adapted to the specific application in order to achieve major advantages in terms of mechanical stability and photocatalytic activity.

Adsorbent–photocatalyst hybrid materials are very interesting for environmental applications (Yoneyama and Torimoto 2000; Carp et al. 2004). The principle of operation is based on the adsorption of the contaminant molecules on the adsorbent sites and their diffusion towards a vicinal photocatalytic centre (Fig. 12.10), where the photocatalytic process takes place. Ideally, the adsorbent should have high specific surface area and high affinity for the pollutants. The expected benefits from the use of these type of hybrid photocatalysts are (1) increasing the concentration of pollutant molecules in the neighbourhood of the active centres, which can enhance the reaction rate; (2) the complete degradation of the contaminant is favoured, since reaction intermediates can be adsorbed and further oxidised; (3) these materials allow treating pollutants even at very low concentration (in the range of ppb), widening the niche of indoor air treatment; (4) the photocatalyst deactivation by poisoning is delayed, as the mineralisation is generally promoted.

Fig. 12.10 Scheme of the process which takes place on a hybrid photocatalyst based on two steps: adsorption (*left*) and photocatalytic reaction (*right*)



Adsorbents such as alumina (Lee et al. 2001b), molecular sieves (see Chap. 9) (Xu and Langford 1995; Sampath et al. 1994; Takeda et al. 1995), clays (Ilsz et al. 2002) or activated carbon (Herrmann et al. 1999; Nozawa et al. 2001) have been used. Amongst them, activated carbons show the strongest interaction between the adsorbent and the pollutant.

Activated carbon mixed with TiO_2 has been successfully used in the removal of NO_x (Yoneyama and Torimoto 2000) and benzene, toluene, ethylbenzene and xylene (BTEX) in air, or methylene blue in solutions (Ao and Lee 2003). However, the behaviour of these carbon–photocatalyst hybrid materials in the photocatalytic degradation of phenol is comparable to that of commercial TiO_2 . These results reveal the importance of the nature of the contaminant in determining the performance of these mixed photocatalytic systems. In addition, the physico-chemical properties of the carbon component, such as the acidity, seem to play a key role in the photoactivity. The poor control of these factors could explain, at least partially, some of the contradictory results related to the use of activated carbon reported in the literature, which points out the difficulty to assess its real impact as adsorbent materials photocatalytic applications. Due to their inherent high surface area, carbon nanotubes have also been a popular choice for the removal of pollutants. Micrographs of a TiO_2 photocatalyst coated on carbon nanotubes prepared by liquid phase deposition (LPD), and a summary of the obtained photocatalytic results are shown in Fig. 12.11. A considerable higher photocatalytic performance compared to TiO_2 P25 was achieved for the degradation of dichloroacetic acid in water (Herbig and Lobmann 2004).

The studies conducted with high surface area SiO_2 show that addition of this oxide to TiO_2 promotes the photocatalytic activity for the degradation of cyanide, phenol, acetophenone and dyes in water. The interaction of silica and titania centres results in new centres of higher photoactivity. Besides, the presence of silica increases the mechanical strength, thermal stability and surface area of the material (Minero et al. 1992).

Sepiolite is a magnesium silicate with a fibre structure. It is a light and inexpensive material used as an adsorbent due to its high surface area and porosity. TiO_2 /sepiolite bi-functional materials have shown excellent results for the gas phase degradation of both organic compounds, such as trichloroethylene (Suárez et al. 2008; Hewer et al. 2009), and inorganic compounds, such as hydrogen sulphide (Rasmussen et al. 2010), at laboratory scale and under sun irradiation conditions using a compound parabolic collector (Suárez et al. 2011b; Portela et al.

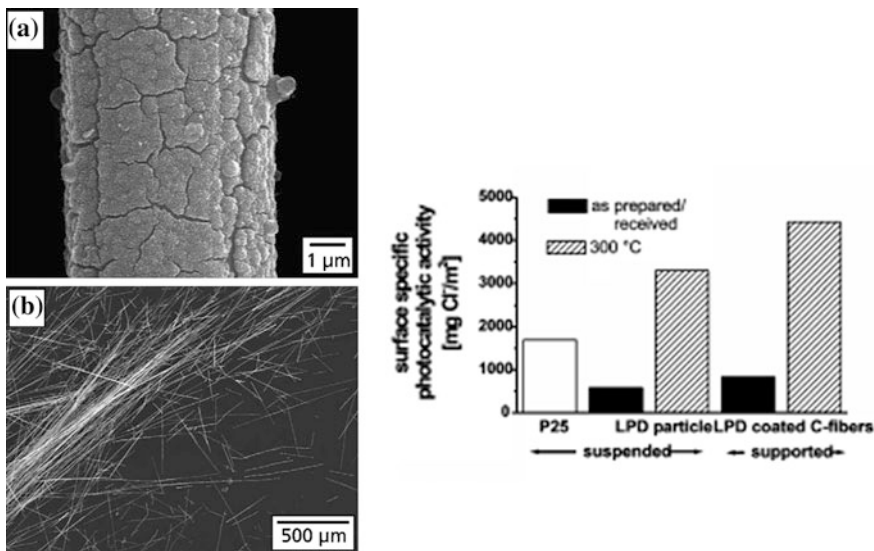


Fig. 12.11 Carbon nanotubes synthesised at different temperatures. **a** 350 °C. **b** 600 °C (left); photocatalytic activity results obtained for carbon nanotubes for degradation of dichloroacetic acid in water [reproduced with permission of Herbig and Lobmann (2004). Copyright Elsevier]

2012). An intimate contact between the sepiolite fibres and the titania oxide particles favoured the mineralisation process, probably due to the contribution of the sepiolite hydroxyl groups to the mineralisation of undesirable by-products such as phosgene (Suárez et al. 2008). Regarding hydrogen sulphide elimination, it has been demonstrated that this hybrid material avoids the SO₂ release to the atmosphere observed for conventional TiO₂-based materials. This effect is shown in Fig. 12.12, where the evolution of H₂S conversion and selectivity to SO₂ for TiO₂ and sepiolite/TiO₂ thin films on glass plates are represented.

Materials such as stainless steel, brass, ferritic alloys (Fecralloy[®], Kanthal[®]), aluminium or titanium can also find application as supports for photocatalysts. Such systems are indeed attractive alternatives because of their low-cost and high

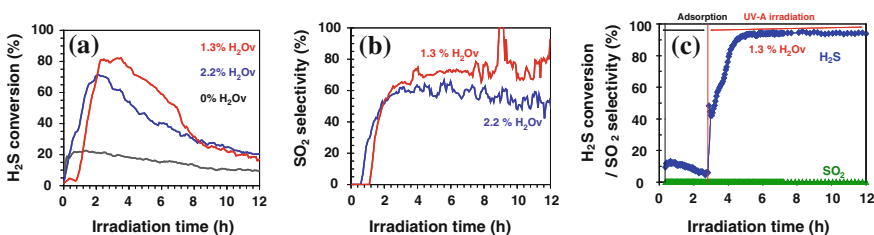


Fig. 12.12 Evolution curves of **a** H₂S conversion, **b** SO₂ selectivity at different water vapour content for TiO₂ thin films and **c** for SiMgOx/TiO₂ hybrid material [adapted from Portela et al. (2010)]

mechanical strength. In addition, they are easy to cast in the desired shape (Fernandez et al. 1995; Byrne et al. 1998; Balasubramanian et al. 2004; Chen and Dionysiou 2006a, b; Giornelli et al. 2006). Notwithstanding these properties, there are relatively few studies dealing with the application of these materials for the treatment of pollutants. Candal et al. (1998) developed a TiO₂/aluminium matrix prepared by sol–gel with good photocatalytic activity; however, due to corrosion issues, the stability of the coating was far from acceptable. The outermost layers of aluminium are prone to be oxidised by means of anodisation processes, resulting in the stabilisation of a very adherent surface layer of alumina, which can improve the subsequent adhesion of TiO₂. Another alternative discussed in the literature is the surface modification by thermal treatment, often applied to FeCrAl substrates (Camra et al. 2005). During treatment at high temperature, an aluminium oxide layer on the top of the surface in the range of 1 µm thickness is produced. Electrophoretic deposition technique (Fernandez et al. 1995) and plasma treatment (Kang et al. 2011) have also been explored for the incorporation of semiconductor layers on these metallic materials. The diffusion of cations from the substrate to the photoactive layer is a factor that must be considered due to its negative effect in the photoactivity. For example, the migration of cations (Cr⁺³, Mn⁺³ or Fe⁺³) from stainless steel substrates treated above 600 °C has been reported (Chen and Dionysiou 2006b). Applications of these materials in the photocatalysis field include the destruction of bacteria and VOC in indoor air (Vohra et al. 2005; Muñoz-Vicente et al. 2011, 2012), the degradation of NO_x (Bianchi et al. 2012) and the removal of organic compounds (Tennakone et al. 1997; Yu et al. 2003; Shang et al. 2003; Balasubramanian et al. 2004).

Immobilised photocatalysts can be conformed in multitude of shapes. Plates (Suárez et al. 2008), rings (Schultes 2003; Twesme et al. 2006; Coronado et al. 2008b; Neti et al. 2010), spheres (Bouazza et al. 2008; Verbruggen et al. 2011), monolithic structures (Sánchez et al. 1999; Avila et al. 2005; Carneiro et al. 2009) or foams (Sanz et al. 2008; Raupp et al. 2001) are some of the most common conformations (Fig. 12.13). Each of them provides particular fluid dynamic conditions resulting in different pressure drop values and mass transfer phenomena.

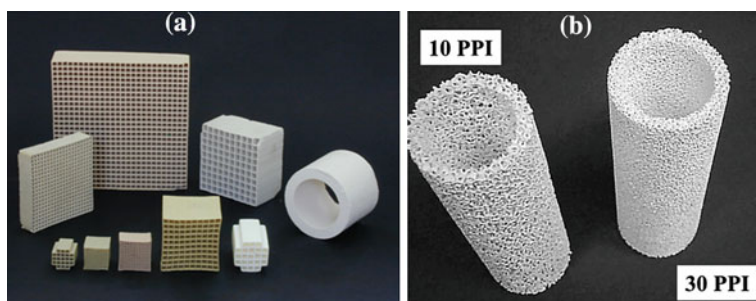


Fig. 12.13 Ceramic materials with different geometries. **a** monolithic supports prepared at the ICP-CSIC (Madrid, Spain) Suárez (2002) and **b** alumina ceramic foams of 10 and 30 pores per inch (PPI) [reproduced with permission from Raupp et al. (2001). Copyright Elsevier]

These properties must be considered in order to select the optimum reactor design for implementation of immobilised photocatalysts at commercial scale.

References

- Al-Ekabi H, Serpone N (1988) Kinetic studies in heterogeneous photocatalysis. 1. Photocatalytic degradation of chlorinated phenols in aerated aqueous solutions over TiO₂ supported on a glass matrix. *J Phys Chem* 92(20):5726–5731
- Anpo M, Sunamoto M, Che M (1989) Preparation of highly dispersed anchored vanadium oxides by photochemical vapor deposition method and their photocatalytic activity for isomerization of trans-2-butene. *J Phys Chem* 93(4):1187–1189
- Ao CH, Lee SC (2003) Enhancement effect of TiO₂ immobilized on activated carbon filter for the photodegradation of pollutants at typical indoor air level. *Appl Catal B* 44(3):191–205
- Arconada N, Durán A, Suárez S, Portela R, Coronado JM, Sánchez B, Castro Y (2009) Synthesis and photocatalytic properties of dense and porous TiO₂-anatase thin films prepared by sol-gel. *Appl Catal B* 86(1–2):1–7
- Arfsten NJ, Eberle A, Otto J, Reich A (1997) Investigations on the angle-dependent dip coating technique (ADDC) for the production of optical filters. *J Sol-Gel Sci Technol* 8(1–3):1099–1104
- Avila P, Montes M, Miró EE (2005) Monolithic reactors for environmental applications: a review on preparation technologies. *Chem Eng J* 109(1):11–36
- Balasubramanian G, Dionysiou DD, Suidan MT, Baudin I, Laine J-M (2004) Evaluating the activities of immobilized TiO₂ powder films for the photocatalytic degradation of organic contaminants in water. *Appl Catal B* 47(2):73–84
- Bianchi CL, Pirola C, Sellì E, Biella S (2012) Photocatalytic NO_x abatement: The role of the material supporting the TiO₂ active layer. *J Hazard Mater* 211–212:203–207
- Blanco J, Avila P, Suarez S, Martin JA, Knapp C (2000) Alumina- and titania-based monolithic catalysts for low temperature selective catalytic reduction of nitrogen oxides. *Appl Catal B* 28(3–4):235–244
- Bouazza N, Lillo-Ródenas MA, Linares-Solano A (2008) Enhancement of the photocatalytic activity of pelletized TiO₂ for the oxidation of propene at low concentration. *Appl Catal B* 77(3–4):284–293
- Brinker CJ, Hurd AJ, Ward KJ (1988) Ultrastructure processing of advanced ceramics. Wiley, New York
- Brinker CJ, Frye GC, Hurd AJ, Ashley CS (1991) Fundamentals of sol-gel dip coating. *Thin Solid Films* 201(1):97–108
- Byrne JA, Eggins BR, Brown NMD, McKinney B, Rouse M (1998) Immobilisation of TiO₂ powder for the treatment of polluted water. *Appl Catal B* 17(1–2):25–36
- Camra J, Bielanska E, Bernasik A, Kowalski K, Zimowska M, Bialas A, Najbar M (2005) Role of Al segregation and high affinity to oxygen in formation of adhesive alumina layers on FeCr alloy support. *Catal Today* 105(3–4):629–633
- Candal RJ, Zeltner WA, Anderson MA (1998) TiO₂-mediated photoelectrocatalytic purification of water. *J Adv Oxid Technol* 3:270–276
- Candal R, Rodríguez J, Colón G, Gelover S, Vigil-Santos E, Jimenez-Gonzalez A, Blesa MA (2004) Materiales para fotocatalisis y electrofotocatalisis. In: Blesa MA, Sánchez B (eds) Eliminación de contaminantes por fotocatalisis heterogénea Madrid
- Carneiro JT, Berger R, Moulijn JA, Mul G (2009) An internally illuminated monolith reactor: pros and cons relative to a slurry reactor. *Catal Today* 147(Supplement 1):S324–S329
- Carp O, Huisman CL, Reller A (2004) Photoinduced reactivity of titanium dioxide. *Prog Solid State Chem* 32(1–2):33–177

- Chen BT (1983) Investigation of the solvent-evaporation effect on spin coating of thin films. *Polym Eng Sci* 23(7):399–403
- Chen Y, Dionysiou DD (2006a) Correlation of structural properties and film thickness to photocatalytic activity of thick TiO₂ films coated on stainless steel. *Appl Catal B* 69(1–2):24–33
- Chen Y, Dionysiou DD (2006b) TiO₂ photocatalytic films on stainless steel: the role of Degussa P-25 in modified sol-gel methods. *Appl Catal B* 62(3–4):255–264
- Chen CH, Kelder EM, Schoonman J (1998) Effects of additives in electrospraying for materials preparation. *J Eur Ceram Soc* 18(10):1439–1443
- Chen CH, Kelder EM, Schoonman J (1999) Electrostatic sol-spray deposition (ESSD) and characterisation of nanostructured TiO₂ thin films. *Thin Solid Films* 342(1–2):35–41
- Chiarello GL, Selli E, Forni L (2008) Photocatalytic hydrogen production over flame spray pyrolysis-synthesised TiO₂ and Au/TiO₂. *Appl Catal B* 84(1–2):332–339
- Chiarello GL, Ferri D, Selli E (2011) Effect of the CH₃OH/H₂O ratio on the mechanism of the gas-phase photocatalytic reforming of methanol on noble metal-modified TiO₂. *J Catal* 280(2):168–177
- Chung YS, Park SB, Kang DW (2004) Magnetically separable titania-coated nickel ferrite photocatalyst. *Mater Chem Phys* 86(2–3):375–381
- Coronado JM, Sánchez B, Fresno F, Suárez S, Portela R (2008a) Influence of catalysts properties and reactor configuration on the photocatalytic degradation of trichloroethylene under sunlight irradiation. *J Solar Energy Eng* 130(4):041012–041015
- Coronado JM, Sánchez B, Portela R, Suárez S (2008b) Solar photocatalysis for the elimination of trichloroethylene in the gas phase. *J Solar Energy Eng* 130(1):011014–011016
- Cybalsky A, Moulijn JA (1998) Structurated catalysts and reactors. CRC Press, USA
- Deng X, Yue Y, Gao Z (2002) Gas-phase photo-oxidation of organic compounds over nanosized TiO₂ photocatalysts by various preparations. *Appl Catal B* 39(2):135–147
- Ding Z, Hu X, Lu GQ, Yue PL, Greenfield PF (2000) Novel silica gel supported TiO₂ photocatalyst synthesized by CVD method. *Langmuir* 16(15):6216–6222
- Ding Z, Hu X, Yue PL, Lu GQ, Greenfield PF (2001) Synthesis of anatase TiO₂ supported on porous solids by chemical vapor deposition. *Catal Today* 68(1–3):173–182
- Eufinger K, Poelman D, Poelman H, De Gryse R, Marin GB (2007) Photocatalytic activity of dc magnetron sputter deposited amorphous TiO₂ thin films. *Appl Surf Sci* 254(1):148–152
- Fernandez A, Lassaletta G, Jimenez VM, Justo A, Gonzalez-Elipse AR, Herrmann J-M, Tahiri H, Ait-Ichou Y (1995) Preparation and characterization of TiO₂ photocatalysts supported on various rigid supports (glass, quartz and stainless steel): comparative studies of photocatalytic activity in water purification. *Appl Catal B* 7(1–2):49–63
- Fujimoto M, Kado T, Takashima W, Kaneto K, Hayase S (2006) Dye-sensitized solar cells fabricated by electrospray coating using TiO₂ nanocrystal dispersion solution. *J Electrochem Soc* 153(5):A826–A829
- Gijsman P, Meijers G, Vitarelli G (1999) Comparison of the UV-degradation chemistry of polypropylene, polyethylene, polyamide 6 and polybutylene terephthalate. *Polym Degrad Stab* 65(3):433–441
- Giornelli T, Lofberg A, Bordes-Richard E (2006) Preparation and characterization of VO_x/TiO₂ catalytic coatings on stainless steel plates for structured catalytic reactors. *Appl Catal A-Gen* 305(2):197–203
- Guglielmi M, Zenezini S (1990) Thickness of sol-gel silica coatings obtained by dipping. *J Non-Cryst Solids* 121(1–3):303–309
- Hájková P, Spatenka P, Krumeich J, Exnar P, Kolouch A, Matousek J, Koci P (2009) Antibacterial effect of silver modified TiO₂/PECVD films. *Eur Phys J D* 54(2):189–193
- Hegemann D, Brunner H, Oehr C (2003) Plasma treatment of polymers for surface and adhesion improvement. *Nucl Instrum Methods Phys Res, Sect B* 208(1–4):281–286
- Herbig B, Lobmann P (2004) TiO₂ photocatalysts deposited on fiber substrates by liquid phase deposition. *J Photochem Photobiol, A* 163(3):359–365

- Herman GS, Gao Y, Tran TT, Osterwalder J (2000) X-ray photoelectron diffraction study of an anatase thin film: TiO₂(001). *Surf Sci* 447(1):201–211
- Hernández-Alonso MD, Tejedor–Tejedor I, Coronado JM, Soria J, Anderson MA (2006) Sol-gel preparation of TiO₂-ZrO₂ thin films supported on glass rings: Influence of phase composition on photocatalytic activity. *Thin Solid Films* 502(1–2):125–131
- Herrmann JM, Matos J, Disdier J, Guillard C, Laine J, Malato S, Blanco J (1999) Solar photocatalytic degradation of 4-chlorophenol using the synergistic effect between titania and activated carbon in aqueous suspension. *Catal Today* 54(2–3):255–265
- Hewer TLR, Suárez S, Coronado JM, Portela R, Avila P, Sanchez B (2009) Hybrid photocatalysts for the degradation of trichloroethylene in air. *Catal Today* 13(3–4):302–308
- Hirai T, Okubo H, Komasa I (2001) Incorporation of CdS nanoparticles formed in reverse micelles into mesoporous silica. *Colloid Interface Sci* 235(2):358–364
- Hofstadler K, Bauer R, Novalic S, Heisler G (1994) New reactor design for photocatalytic wastewater treatment with TiO₂ immobilized on fused-silica glass fibers: Photomineralization of 4-chlorophenol. *Env Scien Tech* 28(4):670–674
- Iketani K, Sun R-D, Toki M, Hirota K, Yamaguchi O (2003) Sol-gel-derived TiO₂/poly(dimethylsiloxane) hybrid films and their photocatalytic activities. *J Phys Chem Solids* 64(3):507–513
- Ilsz I, Dombi A, Mogyorosi K, Farkas A, Dekany I (2002) Removal of 2-chlorophenol from water by adsorption combined with TiO₂ photocatalysis. *Appl Catal B* 39(3):247–256
- Jung SC, Imaishi N (2001) Preparation, crystal structure, and photocatalytic activity of TiO₂ films by chemical vapor deposition. *Korean J Chem Eng* 18(6):867–872
- Jung SC, Kim SJ, Imaishi N, Cho YI (2005) Effect of TiO₂ thin film thickness and specific surface area by low-pressure metal-organic chemical vapor deposition on photocatalytic activities. *Appl Catal B* 55(4):253–257
- Kang H, Lee CS, Kim DY, Kim J, Choi W, Kim H (2011) Photocatalytic effect of thermal atomic layer deposition of TiO₂ on stainless steel. *Appl Catal B* 104(1–2):6–11
- Kim SB, Hong SC (2002) Kinetic study for photocatalytic degradation of volatile organic compounds in air using thin film TiO₂ photocatalyst. *Appl Catal B* 35(4):305–315
- Kitano M, Funatsu K, Matsuoka M, Ueshima M, Anpo M (2006a) Preparation of nitrogen-substituted TiO₂ thin film photocatalysts by the radio frequency magnetron sputtering deposition method and their photocatalytic reactivity under visible light irradiation. *J Phys Chem B* 110(50):25266–25272
- Kitano M, Tsujimaru K, Anpo M (2006b) Decomposition of water in the separate evolution of hydrogen and oxygen using visible light-responsive TiO₂ thin film photocatalysts: Effect of the work function of the substrates on the yield of the reaction. *Appl Catal A* 314(2):179–183
- Krunk M, Mellikov E (1995) Zinc oxide thin films by the spray pyrolysis method. *Thin Solid Films* 270(1–2):33–36
- Kumar AP, Depan D, Singh Tomer N, Singh RP (2009) Nanoscale particles for polymer degradation and stabilization—trends and future perspectives. *Prog Polym Sci* 34(6):479–515
- Lai JH (1979) An investigation of spin coating of electron resists. *Polym Eng Sci* 19(15):1117–1121
- Langlet M, Kim A, Audier M, Herrmann JM (2002) Sol-gel preparation of photocatalytic TiO₂ films on polymer substrates. *J Sol-Gel Sci Technol* 25(3):223–234
- Lee GH, Yamamoto Y, Kourogi M, Ohtsu M (2001a) Blue shift in room temperature photoluminescence from photo-chemical vapor deposited ZnO films. *Thin Solid Films* 386(1):117–120
- Lee SH, Kang M, Cho SM, Han GY, Kim BW, Yoon KJ, Chung CH (2001b) Synthesis of TiO₂ photocatalyst thin film by solvothermal method with a small amount of water and its photocatalytic performance. *J Photochem Photobiol, A* 146(1–2):121–128
- Leenaars AFM, Keizer K, Burggraaf AJ (1984) The preparation and characterization of alumina membranes with ultra-fine pores—part I microstructural investigations on non-supported membranes. *J Mater Sci* 19(4):1077–1088

- Lei L, Chu HP, Hu X, Yue PL (1999) Preparation of heterogeneous photocatalyst (TiO₂/alumina) by metallo-organic chemical vapor deposition. *Ind Eng Chem Res* 38(9):3381–3385
- Li D, Haneda H (2003) Photocatalysis of sprayed nitrogen-containing Fe₂O₃-ZnO and WO₃-ZnO composite powders in gas-phase acetaldehyde decomposition. *J Photochem Photobiol, A* 160(3):203–212
- Li Puma G, Bono A, Collin JG (2008) Preparation of titanium dioxide photocatalyst loaded onto activated carbon support using chemical vapor deposition: a review paper. *J Hazard Mater* 157(2–3):209–219
- Liu B, Zhao X, Zhang N, Zhao Q, He X, Feng J (2005) Photocatalytic mechanism of TiO₂-CeO₂ films prepared by magnetron sputtering under UV and visible light. *Surf Sci* 595(1–3):203–211
- Lunawat PS, Senapati S, Kumar R, Gupta NM (2007) Visible light-induced splitting of water using CdS nanocrystallites immobilized over water-repellant polymeric surface. *Int J Hydrogen Energy* 32(14):2784–2790
- Maeda M, Watanabe T (2005) Evaluation of photocatalytic properties of titanium oxide films prepared by plasma-enhanced chemical vapor deposition. *Thin Solid Films* 489(1–2):320–324
- Matsuda A, Matoda T, Kogure T, Tadanaga K, Minami T, Tatsumisago M (2003) Formation of anatase nanocrystals-precipitated silica coatings on plastic substrates by the sol-gel process with hot water treatment. *J Sol-Gel Sci Technol* 27(1):61–69
- Matthews RW (1987) Solar-electric water purification using photocatalytic oxidation with TiO₂ as a stationary phase. *Sol Energy Mater* 38(6):405–413
- Meille V (2006) Review on methods to deposit catalysts on structured surfaces. *Appl Catal A* 315:1–17
- Mikula M, Brezova V, Ceppan M, Pach L, Karpinsky L (1995) Comparison of photocatalytic activity of sol-gel TiO₂ and P25 TiO₂ particles supported on commercial fibreglass fabric. *J Mater Sci Lett* 14(9):615–616
- Minero C, Catozzo F, Pelizzetti E (1992) Role of adsorption in photocatalyzed reactions of organic molecules in aqueous TiO₂ suspensions. *Langmuir* 8(2):481–486
- Molinari R, Mungari M, Drioli E, Di Paola A, Loddo V, Palmisano L, Schiavello M (2000) Study on a photocatalytic membrane reactor for water purification. *Catal Today* 55(1–2):71–78
- Muñoz-Vicente M, Suárez S, Hernández-Alonso MD, Sánchez B (2011) TiO₂-Al based monolithic photocatalyst for VOCs degradation. *EuropaCat X, Glasgow*
- Muñoz-Vicente M, Hernández-Alonso MD, Suárez S, Sánchez-Muñoz M, Sánchez B (2012) Indoor air bacteria and VOCs elimination using Al/one-dimensional TiO₂ nanostructures as photocatalysts for air conditioning systems. In: 7th European meeting on solar chemistry and photocatalysis: environmental applications (SPEA7). Oporto, Portugal
- Nair M, Luo Z, Heller A (1993) Rates of photocatalytic oxidation of crude oil on salt water on Buoyant, Cenosphere-attached titanium dioxide. *Ind Eng Chem Res* 32:2318–2323
- Nam HJ, Amemiya T, Murabayashi M, Itoh K (2004) Photocatalytic activity of sol-gel TiO₂ thin films on various kinds of glass substrates: the effects of Na⁺ and primary particle size. *J Phys Chem B* 108(24):8254–8259
- Nasonova A, Pham HC, Kim DJ, Kim KS (2010) NO and SO₂ removal in non-thermal plasma reactor packed with glass beads-TiO₂ thin film coated by PCVD process. *Chem Eng J* 156(3):557–561
- Neti NR, Parmar GR, Bakardjieva S, Subrt J (2010) Thick film titania on glass supports for vapour phase photocatalytic degradation of toluene, acetone, and ethanol. *Chem Eng J* 163(3):219–229
- Nizard H, Kosinova ML, Fainer NI, Rummyantsev YM, Ayupov BM, Shubin YV (2008) Deposition of titanium dioxide from TTIP by plasma enhanced and remote plasma enhanced chemical vapor deposition. *Surf Coat Technol* 202(17):4076–4085
- Nogier JP, Millot Y, Man PP, Shishido T, Che M, Dzwigaj S (2009) Probing the incorporation of Ti(IV) into the BEA zeolite framework by XRD, FTIR, NMR, and DR UV-jp810722bis. *J Phys Chem C* 113(12):4885–4889

- Nomura M, Meester B, Schoonman J, Kapteijn F, Moulijn JA (2003) Improvement of thermal stability of porous titania films prepared by electrostatic sol-spray deposition (ESSD). *Chem Mater* 15(6):1283–1288
- Nozawa M, Tanigawa K, Hosomi M, Chikusa T, Kawada E (2001) Removal and decomposition of malodorants by using titanium dioxide photocatalyst supported on fiber activated carbon. *Water Sci Technol*, 127–133
- Nyok-Sai H (1977) Photodegradation of cellulose acetate fibers. *J Polym Sci: Polym Chemistry Edition* 15(3):725–744
- Obata K, Irie H, Hashimoto K (2007) Enhanced photocatalytic activities of Ta, N co-doped TiO₂ thin films under visible light. *Chem Phys* 339(1–3):124–132
- O'Neill SA, Parkin IP, Clark RJH, Mills A, Elliott N (2003) Atmospheric pressure chemical vapour deposition of titanium dioxide coatings on glass. *J Mater Chem* 13(1):56–60
- Pan JH, Lee WI (2006) Preparation of highly ordered cubic mesoporous WO₃/TiO₂ films and their photocatalytic properties. *Chem Mater* 18(3):847–853
- Paschoalino MP, Kiwi J, Jardim WF (2006) Gas-phase photocatalytic decontamination using polymer supported TiO₂. *Appl Catal B* 68(1–2):68–73
- Pawinrat P, Mekasuwandumrong O, Panpranot J (2009) Synthesis of Au-ZnO and Pt-ZnO nanocomposites by one-step flame spray pyrolysis and its application for photocatalytic degradation of dyes. *Catal Commun* 10(10):1380–1385
- Portela R, Sanchez B, Coronado JM, Candal R, Suarez S (2007) Selection of TiO₂-support: UV-transparent alternatives and long-term use limitations for H₂S removal. *Catal Today* 129(1–2):223–230
- Portela R, Suárez S, Rasmussen SB, Arconada N, Castro Y, Durán A, Ávila P, Coronado JM, Sánchez B (2010) Photocatalytic-based strategies for H₂S elimination. *Catal Today* 151(1–2):64–70
- Portela R, Tessinari RF, Suárez S, Rasmussen SB, Hernández-Alonso MD, Canela MC, Ávila P, Sánchez B (2012) Photocatalysis for continuous air purification in wastewater treatment plants: from lab to reality. *Environ Sci Tech* 46(9):5040–5048
- Quintana M, Ricra E, Rodríguez J, Estrada W (2002) Spray pyrolysis deposited zinc oxide films for photo-electrocatalytic degradation of methyl orange: influence of the pH. *Catal Today* 76(2–4):141–148
- Rasmussen SB, Portela R, Suárez S, Coronado JM, Rojas-Cervantes ML, Avila P, Sánchez B (2010) Hybrid TiO₂/SiMgOX composite for combined chemisorption and photocatalytic elimination of gaseous H₂S. *Ind Eng Chem Res* 49(15):6685–6690
- Raupp GB, Alexiadis A, Hossain MM, Changrani R (2001) First-principles modeling, scaling laws and design of structured photocatalytic oxidation reactors for air purification. *Catal Today* 69(1–4):41–49
- Rico V, Romero P, Hueso JL, Espinos JP, Gonzalez-Elipse AR (2009) Wetting angles and photocatalytic activities of illuminated TiO₂ thin films. *Catal Today* 143(3–4):347–354
- Rodríguez J, Paraguay-Delgado F, López A, Alarcón J, Estrada W (2010) Synthesis and characterization of ZnO nanorod films for photocatalytic disinfection of contaminated water. *Thin Solid Films* 519(2):729–735
- Sampath S, Uchida H, Yoneyama H (1994) Photocatalytic degradation of gaseous pyridine over zeolite-supported titanium dioxide. *J Catal* 149(1):189–194
- Sánchez B, Cardona AI, Romero M, Avila P, Bahamonde A (1999) Influence of temperature on gas-phase photo-assisted mineralization of TCE using tubular and monolithic catalysts. *Catal Today* 54:369–377
- Sánchez B, Coronado JM, Candal R, Portela R, Tejedor I, Anderson MA, Tompkins D, Lee T (2006) Preparation of TiO₂ coatings on PET monoliths for the photocatalytic elimination of trichloroethylene in the gas phase. *Appl Catal B* 66(3–4):295–301
- Sanz O, Almeida LC, Zamaro JM, Ulla MA, Miró EE, Montes M (2008) Washcoating of Pt-ZSM5 onto aluminium foams. *Appl Catal B* 78(1–2):166–175

- Sarantopoulos C, Puzenat E, Guillard C, Herrmann JM, Gleizes AN, Maury F (2009) Microfibrillar TiO₂ supported photocatalysts prepared by metal-organic chemical vapor infiltration for indoor air and waste water purification. *Appl Catal B* 91(1–2):225–233
- Schultes M (2003) Raschig super-ring: a new fourth generation packing offers new advantages. *Chem Eng Res Des* 81(1):48–57
- Schwitzgebel J, Ekerdt JG, Gerischer H, Heller A (1995) Role of the oxygen molecule and of the photogenerated electron in TiO₂-photocatalyzed air oxidation reactions. *J Phys Chem* 99:5633–5638
- Shan AY, Ghazi TIM, Rashid SA (2010) Immobilisation of titanium dioxide onto supporting materials in heterogeneous photocatalysis: a review. *Appl Catal A* 389(1–2):1–8
- Shang J, Li W, Zhu Y (2003) Structure and photocatalytic characteristics of TiO₂ film photocatalyst coated on stainless steel webnet. *J Mol Catal A: Chem* 202(1–2):187–195
- Sirisuk A, Hill CG Jr, Anderson MA (1999) Photocatalytic degradation of ethylene over thin films of titania supported on glass rings. *Catal Today* 54(1):159–164
- Stern O (1924) *Z Elektrochem, Angew Phys Chem* 30:508–516
- Strawbridge I, James PF (1986) Thin silica films prepared by dip coating. *J Non-Cryst Solids* 82(1–3):366–372
- Suárez S (2002) Desarrollo de catalizadores SCR altamente selectivos a nitrógeno para plantas de ácido nítrico. Alcalá University, Madrid
- Suárez S, Coronado JM, Portela R, Martín JC, Yates M, Ávila P, Sánchez B (2008) On the preparation of TiO₂-sepiolite hybrid materials for the photocatalytic degradation of TCE: influence of TiO₂ distribution in the mineralization. *Environ Sci Technol* 42(16):5892–5896
- Suárez S, Arconada N, Castro Y, Coronado JM, Portela R, Durán A, Sánchez B (2011a) Photocatalytic degradation of TCE in dry and wet air conditions with TiO₂ porous thin films. *Appl Catal B* 108–109:14–21
- Suárez S, Hwer TLR, Portela R, Hernandez-Alonso MD, Freire RS, Sanchez B (2011b) Behaviour of TiO₂-SiMgOx hybrid composites on the solar photocatalytic degradation of polluted air. *Appl Catal B* 101(3–4):176–182
- Takahashi M, Mita K, Toyuki H, Kume M (1989) Pt-TiO₂ thin films on glass substrates as efficient photocatalysts. *J Mater Sci* 24(1):243–246
- Takeda N, Torimoto T, Sampath S, Kuwabata S, Yoneyama H (1995) Effect of inert supports for titanium dioxide loading on enhancement of photodecomposition rate of gaseous propionaldehyde. *J Phys Chem* 99(24):9986–9991
- Tennakone K, Tilakaratne CTK, Kottegoda IRM (1997) Photomineralization of carbofuran by TiO₂-supported catalyst. *Water Res* 31(8):1909–1912
- Twesme TM, Tompkins DT, Anderson MA, Root TW (2006) Photocatalytic oxidation of low molecular weight alkanes: Observations with ZrO₂-TiO₂ supported thin films. *Appl Catal B* 64(3–4):153–160
- Verbruggen SW, Ribbens S, Tytgat T, Hauchecorne B, Smits M, Meynen V, Cool P, Martens JA, Lenaerts S (2011) The benefit of glass bead supports for efficient gas phase photocatalysis: case study of a commercial and a synthesised photocatalyst. *Chem Eng J* 174(1):318–325
- Vohra A, Goswami DY, Deshpande DA, Block SS (2005) Enhanced photocatalytic inactivation of bacterial spores on surfaces in air. *J Ind Microbiol Biotechnol* 32(8):364–370
- Wiles DM (1973) The effect of light on some commercially important polymers. *Polym Eng Sci* 13(1):74–77
- Wu CY, Chiang BS, Chang S, Liu DS (2011) Determination of photocatalytic activity in amorphous and crystalline titanium oxide films prepared using plasma-enhanced chemical vapor deposition. *Appl Surf Sci* 257(6):1893–1897
- Xu Y, Langford CH (1995) Enhanced photoactivity of a titanium(IV) oxide supported on ZSM5 and zeolite A at low coverage. *J Phys Chem* 99(29):11501–11507
- Yang J-H, Han Y-S, Choy J-H (2006) TiO₂ thin-films on polymer substrates and their photocatalytic activity. *Thin Solid Films* 495(1–2):266–271

- Yang R, Christensen PA, Egerton TA, White JR, Maltby A (2011) Spectroscopic studies of photodegradation of polyethylene films containing TiO₂ nanoparticles. *J Appl Polym Sci* 119(3):1330–1338
- Yoneyama H, Torimoto T (2000) Titanium dioxide/adsorbent hybrid photocatalysis for photodestruction of organic substances of dilute concentrations. *Catal Today* 58:133–140
- Yu J, Zhao X (2000) Effect of substrates on the photocatalytic activity of nanometer TiO₂ thin films. *Mater Res Bull* 35(8):1293–1301
- Yu JC, Ho W, Lin J, Yip H, Wong PK (2003) Photocatalytic activity, antibacterial effect, and photoinduced hydrophilicity of TiO₂ films coated on a stainless steel substrate. *Environ Sci Technol* 37(10):2296–2301
- Zhang H, Quan X, Chen S, Zhao H, Zhao Y (2006a) Fabrication of photocatalytic membrane and evaluation its efficiency in removal of organic pollutants from water. *Sep Purif Technol* 50(2):147–155
- Zhang X, Zhou M, Lei L (2006b) TiO₂ photocatalyst deposition by MOCVD on activated carbon. *Carbon* 44(2):325–333
- Zhu J, Yang J, Bian ZF, Ren J, Liu YM, Cao Y, Li HX, He HY, Fan KN (2007) Nanocrystalline anatase TiO₂ photocatalysts prepared via a facile low temperature nonhydrolytic sol-gel reaction of TiCl₄ and benzyl alcohol. *Appl Catal B* 76(1–2):82–91

Chapter 13

Metal Doping of Semiconductors for Improving Photoactivity

María Dolores Hernández-Alonso

Anatase TiO₂ is, by far, the most studied photocatalyst, due to its particular physicochemical characteristics explained in detail in [Chap. 5](#). Doping the structure of TiO₂ has been extensively used as an approach for improving its photocatalytic properties, and therefore, this and the following chapter are focussed on reviewing the cationic and anionic doping of this semiconductor.

Metal doping has proved to be a successful approach for obtaining photocatalysts with improved photonic efficiencies, generally using less than 10 % of foreign cations for modifying the semiconductor (Carp et al. [2004](#)). With this strategy, it is possible to shift the optical response towards higher wavelengths, increasing the photoactivity under visible irradiation, and to hinder electron–hole recombination. This may allow using sunlight as an inexpensive and renewable energy source in photocatalytic applications. Besides optical absorption, other properties that strongly influence the photocatalytic activity, such as surface area, pore size, density of hydroxyl groups, surface acidity, and adsorption/desorption properties, can also be modulated by incorporating a dopant into the photocatalyst structure. These surface modifications can also lead to a higher selectivity in different processes (Hernández-Alonso et al. [2007](#), [2009](#)).

Impregnation, co-precipitation, ion implantation technique, and sol–gel methods can be employed to incorporate cationic dopants into TiO₂.

13.1 Surface Dispersion Versus Lattice Incorporation

The presence of dopants can, basically, alter the charge transfer properties of TiO₂, modify the adsorption capacity of its surface, or produce a shift of the absorption edge of the photocatalyst to the visible range (Carp et al. [2004](#)). This last

M. D. Hernández-Alonso (✉)
Renewable Energy Division, CIEMAT, Madrid, Spain
e-mail: lolihza@gmail.com

modification is highly desirable for a more efficient use of sunlight. It can be associated with a decrease in the band gap, by interaction of the cation states with the valence or conduction bands of anatase, or with the creation of intra-band-gap states, induced by the incorporation of the dopant ions (Kubacka et al. 2012). Pronounced red shifts can be obtained by means of ion implantation processes, which consist of the acceleration of the dopant ions in an electric field and their impact on the semiconductor (Anpo and Takeuchi 2003).

In 1994, a systematic study of quantum-sized (3–4 nm) doped TiO₂ with 21 cations was conducted by Hoffmann and co-workers (Choi et al. 1994), who reported on the influence of the metal dopants on the photoreactivity by acting as electron and hole traps, and by altering the electron–hole recombination rate as follows:



with the energy level of $M^{n+}/M^{(n-1)+}$ located below the conduction band edge and the energy level of $M^{(n+1)+}/M^{n+}$ above the valence band edge. The presence of these intra-band-gap energy levels would lead to the already mentioned red shift and the photocatalytic response under visible light. They also observed the existence of an optimum dopant concentration, above which the photoactivity decreases. In the case of quantum-sized particles, this behaviour has been attributed to an increasing recombination rate with dopant concentration due to the concomitant decrease in the average distance between trap sites. Nevertheless, similar results have also been obtained for bulk materials (Karakitsou and Verykios 1993).

Thus, it is worth taken into account that the reported results show that an effective absorption of visible light does not always guarantee an enhanced photocatalytic activity under visible irradiation (Choi et al. 2010). A dopant can act as an effective mediator of interfacial charge transfer, inhibiting the electron–hole recombination (Choi et al. 1994; Cao et al. 2004), or it can produce the opposite effect. Despite an extended response in the visible range, metal ions can act as recombination centres, decreasing the photocatalytic activity of the catalyst under UV irradiation (Herrmann et al. 1984; Di Paola et al. 2002). Furthermore, provided that holes with sufficient oxidizing power are generated in the TiO₂-based photocatalyst, a minimum band gap of ca. 2.5 eV will be required to generate electrons that can practically interact with O₂ to form oxygen radicals (e.g. O₂ + e⁻ → O₂⁻), key intermediates for many redox reactions to proceed (Kubacka et al. 2012).

Depending on the dopant, two different situations can be reached, as schematically represented in Fig. 13.1: (1) a p-type doping, by introduction of cations with a lower valence than that of Ti⁴⁺ (M^{n+} , $n \leq 4$), which act as acceptors of electrons; (2) an n-type doping by incorporating electron donors, cations with higher valence than Ti⁴⁺ (M^{n+} , $n \geq 5$).

Metal dopants can occupy substitutional or interstitial sites at the titania lattice or form segregated metal oxide clusters or islands on the surface, depending on the

1 H Hydrogen 1.00797		<div style="display: flex; justify-content: space-around; align-items: center;"> <div style="width: 20px; height: 20px; background-color: #ffffcc; border: 1px solid black; margin-right: 5px;"></div> Low solubility (< 5 atom %)</div> <div style="width: 20px; height: 20px; background-color: #c8e6c9; border: 1px solid black; margin-right: 5px;"></div> Intermediate solubility (ca. 5-12 atom %)															
-------------------------------	--	---	--	--	--	--	--	--	--	--	--	--	--	--	--	--	--

Fig. 13.3 Solubility limit of different doping elements of the periodic table into the anatase structure (based on data from Kubacka et al. 2012)

absorption spectrum is not expected in the case of surface dispersion. In order to keep the charge neutrality in the structure of doped TiO_2 , cation or anion vacancies are created. In these cases, the presence of defects associated with the creation of oxygen vacancies may also contribute to the visible light absorption of the modified TiO_2 (Choi et al. 1994; Rehman et al. 2009).

The solubility of the metal cations in the anatase structure is governed by parameters such as the primary particle size, the M^{n+}/Ti^{4+} radius ratio, and the structural strain, the latter influenced in turn by factors such as the metal oxidation state (Fig. 13.3). A large M^{n+}/Ti^{4+} radius ratio favours the presence of oxygen vacancies, which efficiently release strain in the anatase structure. The solubility of M^{n+} will determine the tendency of the dopant element to form solid solutions, with a homogeneous chemical composition throughout the particle ($\text{Ti}_{1-x}\text{M}_x\text{O}_2$), or to segregate at the surface of TiO_2 . In any case, at concentrations above the solubility limit of each metal ion, an enrichment of the dopant at the surface is expected, finally leading to the formation of pure MO_x phases (Kubacka et al. 2012).

Other characteristics, such as the surface area or the surface acidity, are also strongly affected by the incorporation of a dopant into the photocatalyst structure. The increase in surface acidity observed in chemically mixed binary oxides has been proposed to appear in order to preserve the electrical neutrality. This model, proposed by Tanabe and co-workers (Tanabe et al. 1974), postulates that the coordination number of the guest cation is maintained in the host oxide lattice and that the coordination number of all the oxygen ions in the major component oxide is retained in the binary compound. Thus, to keep electric neutrality, Brønsted

acidity (extra protons) is expected to appear when the charge imbalance is negative, while Lewis acidity will be formed when the charge imbalance is positive. Surface acidity can be linked to other properties, like the population of hydroxyl groups at the surface of the photocatalyst and its adsorption/desorption capacity. A specific example of this will be presented in the next section.

Furthermore, surface or bulk metal doping is able to stabilize the anatase or the rutile phases of titania and modify the temperature of the anatase-to-rutile transformation. This effect has been ascribed to a hindered crystal growth due to the formation of Ti–O–M bonds. It has been suggested that the creation of oxygen vacancies, derived from the incorporation of ions of lower valence than Ti^{4+} and relatively small ionic radius, accelerates the phase transition by reducing the strain energy that must be overcome for the rearrangement of the Ti–O octahedra and the other way around for ions of higher valence and larger ionic radius (Shannon and Pask 1965). Thus, for instance, the presence of Zr^{4+} seems to inhibit this transition, stabilizing the anatase phase at higher temperatures than for bare TiO_2 (Hernández-Alonso et al. 2006). Similarly, doping with Al, Ni, Ga, Nb, Ta, and W has proved to retard the anatase-to-rutile transformation, while Mn, Fe, Cu, or Zn promote, generally, this transition (Fernández-García et al. 2004).

The presence of the corresponding dopant oxide as a segregate phase will affect the physicochemical properties of the photocatalyst and, consequently, its photoactivity. For instance, Fresno et al. reported a significantly different behaviour for Sn- and Zr-doped samples with respect to the coupled $\text{TiO}_2/\text{SnO}_2$ and $\text{TiO}_2/\text{ZrO}_2$ materials in the photocatalytic degradation of toluene vapours under UV irradiation. In this study, TiO_2/MO_2 photocatalysts exhibited a high resistance to deactivation not observed in the corresponding mixed oxides and bare TiO_2 , due to a lower accumulation of adsorbed intermediates during reaction on the coupled photocatalysts (Fresno et al. 2008). On the other hand, the incorporation of these cations into the TiO_2 structure proved to be beneficial in the degradation of methylcyclohexane (Fresno et al. 2005; Hernández-Alonso et al. 2007). In another example, Kubacka and co-workers observed that the appearance of MO_x local environments (MO_x clusters) in Ti–M substitutional mixed oxides implied a decrease in their photoactivity under sunlight excitation, ascribed to the generation of localized electronic states involved directly in charge recombination processes (Kubacka et al. 2008).

Basically, the photocatalytic efficiency of doped TiO_2 will be influenced by the electronic configuration of the dopant, its concentration, and its distribution in titania. However, there are controversial and sometimes contradictory results in the literature regarding the influence that doping exerts on the photoactivity of TiO_2 . The discrepancies are probably ascribed to the different synthetic procedures employed and to the different reactions selected to test the photocatalytic activity. The selection of the target molecule to decompose may lead, as commented above, to diametrically opposed results. These differences make it difficult to compare results among the published reports. Next, we will briefly discuss some relevant examples on doped TiO_2 photocatalysts.

13.2 Transition Metal Doping

Doping TiO₂ with transition metal cations with a partially filled *d* shell creates energy states in the band gap of the titania (intra-band-gap energy states), which may induce absorption of visible light caused by the excitation of an electron from an intra-band-gap energy level to the conduction band of TiO₂ (Carp et al. 2004). These electronic levels may be localized or merged with the anatase bands. The nature and concentration of the doping cation will determine the extent of the absorption edge red shift. In 1999, Anpo and co-workers reported that Cr and V cationic implantation of titanium dioxide gave rise to a significant shift in the absorption spectra towards the visible region, which enabled these photocatalysts to efficiently operate under visible light (Yamashita et al. 1999). However, as previously commented, an improved optical absorption in the visible range is not sufficient to guarantee an enhancement in the photocatalytic performance, and the whole picture of the structural and electronic modifications induced by the incorporation of the dopant needs to be taken into account. Besides their role in charge trapping, dopants should also allow an efficient interfacial transfer of charge carriers. In the study of Choi et al., only a small enhancement in photoactivity was observed for dopants with a closed-shell electronic configuration (Al³⁺, Zn²⁺, Ga³⁺, Zr⁴⁺, Nb⁵⁺, Sn⁴⁺, Sb⁵⁺, and Sn⁵⁺), which was ascribed to a hindered charge carrier trapping caused by their stability. The authors also observed the existence of an optimum dopant concentration, above which the photocatalytic activity decreased as a consequence of a higher recombination rate (Choi et al. 1994).

The *d*-electron configuration of the transition metal, its concentration, and its distribution in the titania structure (i.e. the presence at substitutional or interstitial positions of the lattice and the presence at the surface and/or bulk of the particles), along with other physicochemical factors, play a complex role in the photoactivity of the modified TiO₂ (Choi et al. 1994; Kubacka et al. 2012).

Promising results have been obtained with V-, Cr-, Mn-, Fe-, Co-, and Ni-doped titania photocatalysts under solar irradiation. The incorporation of these 3d transition metal ions into the titania lattice induces the formation of occupied electron levels, with the electrons localized around the dopant, as determined by ab initio calculations (Umebayashi et al. 2002). The localized mid-gap state levels shift to lower energy as the atomic number of the dopant increases. Consequently, a red shift of the absorption edge to the visible range is produced, with an observed effectiveness increasing with the atomic number: V > Cr > Mn > Fe > Ni (Carp et al. 2004; Chen and Mao 2007). In some cases, a higher extent of the shift can be obtained by increasing the concentration of the dopant (Kubacka et al. 2012). V, Nb, Mo, and W also improve the absorption in the visible range, by decreasing the band-gap energy (Fuerte et al. 2001; Kubacka et al. 2008). Fuerte et al. studied the influence of highly substitutionally doped anatase, prepared by the inverse microemulsion procedure, and found a photoactivity enhancement in the case of Mo⁶⁺ and W⁶⁺ in the degradation of gas-phase toluene under simulated sunlight

irradiation. The study indicated that at high dopant concentration, the heavier elements of group VI were the best options for an efficient oxidation of toluene under visible light. In contrast, at low doping levels, group V elements also led to an improved performance. The influence of the dopant concentration on the photocatalytic activity was especially relevant in the case of W. The inverse microemulsion preparation method allowed the incorporation of up to ca. 20 at.% of W in substitutional positions of the anatase network. The photoactivity was found to increase with the W content of the material. The presence of the orthorhombic WO_3 phase was only detected at W contents higher than 20 at.%, and was accompanied by a moderate reduction in the activity. The enhanced photoactivity was ascribed to the presence of W-related charge-trapping centres at the surface, together with the larger power of absorption in the visible region of W-doped TiO_2 , caused by the existence of electronic impurity levels close to the conduction band (Fuerte et al. 2002). Although an enhancement in the visible light absorption could be obtained with the incorporation of V, Nb, Mo, or W, the synthesis of mixed oxides with the minimal disturbance of the TiO_2 anatase structure proved to be an additional requirement to obtain highly active photocatalysts under visible irradiation, which could be achieved only for Ti-V and Ti-W materials. Furthermore, the activity enhancement was limited by the solubility limit of the dopant cations (Kubacka et al. 2008).

Besides the electronic effects, the presence of transition metals also produces modifications in the morphological (size and shape) and textural (porosity) properties of doped TiO_2 . In Ti-M (M = V, Mo, Nb, W) mixed oxides with anatase structure, an increase in the surface area with respect to bare titania, together with a moderate decrease in the particle size, was generally observed when the metal cations were mainly occupying substitutional positions in the lattice. On the other hand, the presence of metal atoms at the surface of the material led to a decreased surface area (Kubacka et al. 2008). The surface acidity can also be altered. For instance, it was observed that the presence of a relatively high content of V, Mo, and W, incorporated by the incipient wet impregnation method, leads to the formation of surface Brønsted sites that increase the overall surface acidity of the material (Di Paola et al. 2004). The higher acidity was ascribed to the enrichment of the surface with the corresponding acidic oxides (MoO_3 , V_2O_5 , and WO_3). Nevertheless, it is worth noticing that in this case, only the sample loaded with W showed an enhanced photocatalytic activity with respect to bare TiO_2 .

The incorporation of Zr into TiO_2 causes significant changes in the surface characteristics of the photocatalyst. At low contents, Zr cations can randomly substitute Ti^{4+} in the anatase lattice, without introducing important structural modifications. No significant changes in the band-gap energy are observed. Nevertheless, higher photoactivities have been obtained with $\text{Ti}_{1-x}\text{Zr}_x\text{O}_2$ materials with respect to anatase TiO_2 . The higher surface area at a given firing temperature, higher surface acidity, higher hydrophilicity, or the creation of active defects on the TiO_2 surface have been proposed as possible reasons for the improved photocatalytic performance of these materials (Fu et al. 1996; Yu et al. 1998; Zorn

et al. 1999; Hernández-Alonso et al. 2007). As previously mentioned, the increase in acidity in binary systems has been proposed to appear in order to preserve the electrical neutrality (Tanabe et al. 1974). The charge imbalance is calculated for each individual bond to the guest cation and multiplied by the number of bonds to that cation. As an example, in the particular case of ZrO_2 shown in Fig. 13.4, each Zr atom is bonded to eight oxygen atoms, and each oxygen is bonded to four Zr atoms. In the anatase structure, each Ti is octahedrally coordinated with six oxygen atoms, which are bonded to three Ti atoms. Taking this into account, when a Zr atom enters the anatase lattice, each of its eight bonds is now attached to an oxygen atom that is bonded to only two other cations instead of three. Therefore, four valence electrons on Zr divided by eight bonds, minus two electrons available on the oxygen atom divided by three bonds gives a charge imbalance value of $-1/6$ per bond (total charge imbalance = $-4/3$). As a result of this negative imbalance, new Brønsted acid sites are created from the association of protons with the nearby oxygen atoms (Hernández-Alonso et al. 2009).

However, an increase in the surface acidity is not necessarily beneficial for the photoactivity. Depending on the target molecule to decompose, an increase in the number and strength of acid sites on the photocatalyst surface can lead to a lower selectivity and a faster deactivation of the catalyst. This effect has been basically attributed to a slower desorption of by-products from the strong adsorption sites created with the formation of Ti-O-M assemblies in the binary oxide (Fresno et al. 2008; Hernández-Alonso et al. 2009).

Among transition metals, Fe-doped TiO_2 has received special attention in the literature. Due to its similar radius, Fe^{3+} is able to occupy substitutional positions in the titania lattice forming solid solutions at low concentrations ($<1\%$), while at higher concentrations, the formation of Fe_2O_3 has been observed. The presence of iron at a low level of doping is said to enhance the efficiency of the photocatalysed redox reactions and to shift the absorption edge from ca. 375 nm of bare titania to the 400–500 nm range. The improved activity is attributed to an effective trapping of electrons and holes by the Fe^{3+} ions (Fig. 13.5). The half-filled electronic configuration of Fe^{3+} (d^5) might promote a rapid electron transfer to molecular oxygen, in order to recover the initial stability, and a more efficient electron-hole separation (Wang et al. 2003; Carp et al. 2004). At high dopant concentrations, iron ions can act as recombination centres, lowering the photoactivity.

Fig. 13.4 Schematic representation of the Ti–O–Zr bonds, according to the model proposed by Tanabe (Tanabe et al. 1974) to explain the increase in surface acidity observed in binary metallic oxides (based on Hernández-Alonso et al. 2009)

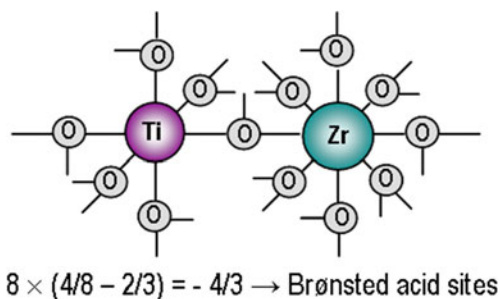
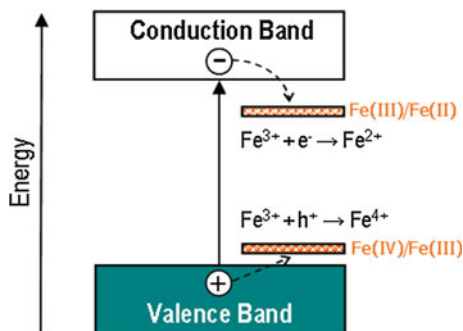


Fig. 13.5 Schematic representation of the possible charge transfer mechanisms in an Fe³⁺-doped TiO₂ photocatalyst (based on Wang et al. 2003)



Furthermore, the incorporation of iron into the titania lattice has shown to inhibit crystal growth (Carp et al. 2004).

Improved efficiencies have been obtained with Fe-doped TiO₂ photocatalysts, both under UV and visible light (Yamashita et al. 2003; Adán et al. 2007). However, controversial results are usually found in the literature about the role of Fe³⁺. It seems plausible that besides the key influence of the dopant content, the synthesis procedure and doping technique are playing a crucial role in controlling the reactivity of doped photocatalysts (Wang et al. 2003). For instance, Piera et al. observed that changes in the preparation method, like variations in the pH and concentration of the Fe³⁺ solution used to dope titania, led to the presence of different iron species at the surface, which seemed to play a role in the photoactivity of the materials (Piera et al. 2003).

13.3 Incorporation of Rare-Earth Elements

The incorporation of rare-earth (RE) elements into the titania structure has also been explored as an attractive strategy to extend its response under solar irradiation (Bingham and Daoud 2011). The sol-gel process is the most frequently reported technique applied to synthesize RE-doped TiO₂. As it will be discussed in this section, the presence of rare-earth cations induces the modification of the photocatalyst properties, leading to an enhanced photocatalytic performance, both under UV and visible irradiation.

Under visible light, the increased activity is caused by the reduction in the band-gap energy of RE-doped TiO₂. The red shift can be attributed to the charge transfer transition between the *f*-electrons of the RE ions, which introduce electronic states into the band gap of TiO₂, and the bands of the semiconductor (Xu et al. 2002). For instance, a narrowing of the band gap of 0.55 eV was found in Nd³⁺-doped TiO₂. In this material the absorption edge is attributed to the O 2p to Nd 4f transition, whose electronic states are located closed to the bottom of the conduction band (Li et al. 2003). It is worth reminding that as previously commented, narrowing the band gap of the semiconductor can be beneficial for

photocatalytic purposes as long as the redox potential of the $\text{H}_2\text{O}/\text{OH}$ couple lies within the band gap. Furthermore, an effective dopant should provide the photocatalyst with an improved interfacial charge transfer rate (Xu et al. 2002).

Despite their larger ionic radii, the incorporation of rare-earth ions (e.g. Sm^{3+} , Gd^{3+}) into the anatase lattice has been reported. When Ti^{4+} is substituted by a 3+ ion, the creation of oxygen vacancies that can act as electron traps may be expected, delaying the recombination of the electron–hole pairs (Shi et al. 2008). However, a dispersion of the corresponding rare-earth oxides on the surface of RE-doped TiO_2 is more usually reported, justified by the much larger ionic radii of these elements in comparison with Ti^{4+} that hampers their incorporation into the anatase lattice (see Fig. 13.2). The synthesis conditions probably influence whether the rare-earth cations are incorporated into the titania matrix or can be found as dispersed oxides on the surface of the semiconductor (Bingham and Daoud 2011). Their presence on the surface may favour a more efficient charge carriers separation that will explain the observed improved performance. Some authors have speculated that at the interface, the smaller Ti^{4+} might substitute rare-earth ions in the lattice of the RE oxides, with the formation of $\text{Ti}-\text{O}-\text{RE}$ bonds. The replacement of a RE^{3+} ion would create a charge imbalance, whose compensation could induce the absorption of more hydroxyl groups (OH^-) that could, subsequently, lead to the formation of more hydroxyl radicals by accepting photogenerated holes (Xu et al. 2002). In heat-treated La-doped TiO_2 , the charge imbalance caused by the incorporation of titanium into the La_2O_3 lattice was reported to reduce Ti^{4+} to Ti^{3+} that, later, may be oxidized by adsorbed O_2 to generate the superoxide anion radical ($\text{O}_2^{\cdot-}$) (Li et al. 2004).

In a benchmark example, doping TiO_2 with La^{3+} , Ce^{3+} , Er^{3+} , Pr^{3+} , Gd^{3+} , Nd^{3+} , and Sm^{3+} proved to produce an absorption red shift, an increase in the interfacial electron transfer rate, and stronger adsorption capacities (Xu et al. 2002). Among the tested rare-earth-doped samples, the Gd^{3+} -doped titania showed the highest photocatalytic activity in the degradation of nitrite in water, attributed to a higher efficiency in the separation and transfer of charge carriers. An optimum amount of dopant around 0.5 wt% was observed in this work, at which the samples showed the highest photoactivity, always higher than that of the undoped titania (Fig. 13.6). As the concentration of RE ions increases, the space-charge region in the *p*-doped semiconductor becomes narrower, theoretically reducing the capacity to separate the charge carriers. The optimum concentration is the one that makes the thickness of the space-charge region sufficiently similar to the light penetration depth into the TiO_2 photocatalyst, making the separation of photogenerated electron–hole pairs more efficient. At higher concentrations of dopant, the penetration depth of light will exceed the space-charge layer, favouring recombination processes (Ranjit et al. 2001; Xu et al. 2002). In terms of photocatalytic performance, other studies situate this optimum value at a slightly higher concentration of the RE dopant (1–1.2 %) (Li et al. 2004; Zhang et al. 2005; Anandan et al. 2012). The high photocatalytic efficiency observed for Gd^{3+} -doped titania has also been reported by other authors and ascribed to its high surface area and pore

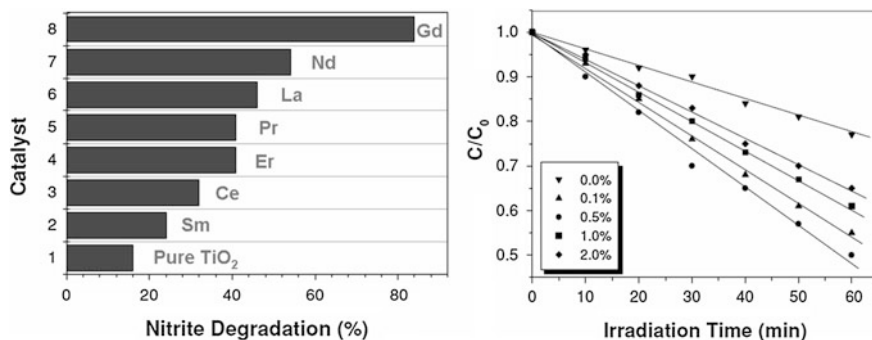


Fig. 13.6 Photocatalytic conversion of nitrite over different 1 wt% rare-earth-doped TiO₂ (left); normalized concentration as a function of the reaction time for nitrite degradation over Sm³⁺-doped TiO₂ photocatalysts with different dopant concentration (right) (adapted with permission from Xu et al. 2002. Copyright Elsevier)

volume, together with its lower band gap compared to bare TiO₂ (El-Bahy et al. 2009). It has also been postulated that the high activity could be related to its half-filled electronic configuration (7 f-electrons), which would favour the transfer of the previously trapped electrons to the oxygen molecules adsorbed on the surface to form superoxide radicals, in order to return to its original stability and, thus, hinder recombination (Xu et al. 2002).

Besides the potential enhancement in the photoelectrochemical properties, lanthanide-doped titania is expected to present improved adsorption capacities due to the ability of lanthanides to form complexes with different organic compounds (e.g. acids, thiols, aldehydes, alcohols, amines) through the interaction of these molecules with the f-orbitals of the lanthanides (Carp et al. 2004). Consequently, favouring the concentration of the pollutant at the semiconductor interface, the photocatalytic activity of RE-doped TiO₂ may be enhanced, either under visible or UV irradiation. For instance, lanthanide (Eu³⁺, Pr³⁺, Yb³⁺)-doped TiO₂ showed a significantly higher photocatalytic activity in the mineralization of different chlorinated aromatic compounds, carboxylic acids, and amines, attributed to an enhanced adsorption of the target molecule on the catalyst surface, favoured by the formation of Lewis acid–base complexes (Ranjit et al. 1999, 2001). Analogous results were observed for La³⁺-doped titania in the photocatalytic degradation of 2-mercaptobenzothiazole, which were justified by an improvement in the adsorption properties, due to the formation of Lewis acid–base complexes between La³⁺ and the –SH groups (Li et al. 2004).

As in the case of transition metal ions, the presence of lanthanide dopants in the TiO₂ lattice can produce other effects, such as hindering the anatase-to-rutile transition or restraining the crystal growth and, consequently, increasing the surface area of the material (Ranjit et al. 2001; Li et al. 2004; Zhang et al. 2005; Baiju et al. 2010; Anandan et al. 2012). Setiawati and co-workers estimated that the anatase growth rate was decelerated from 0.1 nm/°C in pure TiO₂ to 0.03 nm/°C in 1 mol % Sm- and Eu-doped titania (Setiawati and Kawano 2008). In another

example, a considerable inhibitory effect of the transition from anatase to rutile was observed for 1–2 at.% Nd³⁺-, Pr³⁺-, Er³⁺-, and Dy³⁺-doped titania, attributed to the presence of Ti–O–RE bonds. The reduction in the crystallite size also observed in these doped materials was proposed to be caused by the segregation of the lanthanide cations at the grain boundaries, which would inhibit grain growth by restricting direct contact among grains. While increasing the calcination temperature was detrimental for the photoactivity of bare TiO₂, it was beneficial in the case of doped photocatalysts, due to the higher stability of the anatase phase in these materials and to the role of the dopants in preventing the agglomeration and sintering of titania nanoparticles. This will affect, accordingly, the BET surface area and, hence, the population of hydroxyl groups and adsorbed oxygen on the surface of the photocatalysts (Zhang et al. 2005). These effects have been also observed in lanthanide-doped mesoporous titania. The incorporation of Ce^{3+/4+} and La³⁺ resulted in an increase in the surface area, pore volume, and average pore size with respect to the undoped mesoporous TiO₂. Furthermore, the doping was demonstrated to inhibit the collapse of the mesoporous structure upon calcination (Nguyen-Phan et al. 2009). Doping with Gd³⁺ also proved to be able to yield high surface area materials with well-defined mesopores, even at calcination temperatures as high as 800 °C, while bare TiO₂ showed practically null surface area (Baiju et al. 2010).

The promising photocatalytic results obtained so far encourage further investigation on rare-earth-doped TiO₂-based materials. Co-doping of rare-earth metals with other elements and the development of new preparation techniques are also being matter of research (Bingham and Daoud 2011).

13.4 Incorporation of Other Elements

Although not very frequently, the photocatalytic efficiency of alkaline and alkaline-earth-doped TiO₂ has also been explored. The reported results of photoactivity are contradictory. For instance, a poisoning effect is usually attributed to the presence of Na⁺ in the lattice of calcined glass-supported TiO₂, which may act as recombination centre in the thin films (Fernández et al. 1995). However, other authors have observed that the inhibitory or promoting effect of doping on the photocatalytic activity is not only dependent on the dopant nature and its concentration, but also on the preparation method and, of course, on the nature of the target pollutant. For instance, it was reported that the photocatalytic efficiency of alkaline-doped TiO₂ prepared by a sol–gel procedure was lower than that of the analogous materials prepared by impregnation. Furthermore, the authors observed that the presence of small concentrations of Na⁺ improved the photocatalyst efficiency (Bessekhouad et al. 2004). Contradictory results have been also reported for Li⁺- or Mg²⁺-doped titania. While a beneficial effect is observed in some studies (Bessekhouad et al. 2004; Venkatachalam et al. 2007), ascribed to modifications in the adsorption and electronic properties of the doped materials, other

authors correlate a decrease in the photoactivity of titania to the presence of these cations (López et al. 2001). The influence of Be^{2+} doping on the photocatalytic activity of TiO_2 has also been evaluated. Due to its small size, Be^{2+} cations are expected to enter into the interstitial sites of the titania lattice. The authors found that the presence of this alkaline earth element at the shallow surface of the photocatalyst was beneficial for the photocatalytic activity, while its incorporation into the deep bulk was detrimental (Peng et al. 2004). An enhanced photocatalytic activity of Be^{2+} -doped TiO_2 has been also observed under visible light irradiation, attributed to a more efficient electron–hole separation (Avasarala et al. 2010). Doping TiO_2 with Ca^{2+} , Sr^{2+} , and Ba^{2+} was also found to be beneficial for the photocatalytic activity of anatase. The presence of these alkaline earth cations proved to limit the crystal growth and, consequently, increase the surface area of the doped materials. The slightly higher band gap of these samples was also attributed to the reduction in the particle size (Al-Salim et al. 2000).

Incorporation of metallic elements from the p-block has also been considered as an approach to improve the photocatalytic efficiency of TiO_2 . For instance, as it occurs with other dopants, the presence of Al and Ga has proved to retard the anatase-to-rutile transformation (Fernández-García et al. 2004) and lead to the creation of oxygen vacancies to compensate the charge imbalance caused by the location of trivalent cations at Ti^{4+} sites (Song et al. 2011). As previously commented, these oxygen vacancies can act as electrons traps, delaying the recombination processes. Besides, it has been observed that the presence of Al_2O_3 , Ga_2O_3 , or In_2O_3 induces an increase in the surface area and the surface acidity of titania that may favour the adsorption of organic compounds, thus contributing to enhance the photocatalytic activity of these materials (Deshpande et al. 2005). In indium-doped TiO_2 , the improved performance reported with respect to undoped titania has also been attributed to the narrowing of the band gap caused by the contribution of the 5s5p orbitals to the conduction band of TiO_2 (Ti 3d) (Yang et al. 2008; Sasikala et al. 2010).

Among the post-transition elements, it is also worth remarking the role of Sn^{4+} as a TiO_2 dopant. Sn^{4+} is expected to occupy a substitutional position in the TiO_2 lattice, since the electronegativity and ionic radius approach those of Ti^{4+} . Nevertheless, the slightly larger ionic radius of Sn^{4+} with respect to Ti^{4+} induces an increment in the cell volume and a distortion of the lattice, which is translated in a shift of the diffraction peaks of the XRD pattern of Sn^{4+} -doped titania to lower angles. An expansion of the unit cell takes place with increasing tin concentration, as it was observed for $\text{Ti}_{1-x}\text{Sn}_x\text{O}_2$ solid solutions with rutile structure (Fig. 13.7) (Sensato et al. 2003). This distortion may result in the formation of more surface defects that can contribute to a more effective adsorption of reactants. Since SnO_2 presents a rutile structure, and it can induce the nucleation of rutile crystallites of TiO_2 , the reported studies on Sn-doped TiO_2 indicate that most of these samples present this structure. Theoretical calculations suggest that the presence of tin transforms the rutile electronic transition from direct to indirect, as it is for anatase. Since indirect transitions are less prone to electron–hole recombination, as they cause that the lowest energy transition is forbidden, this transformation results

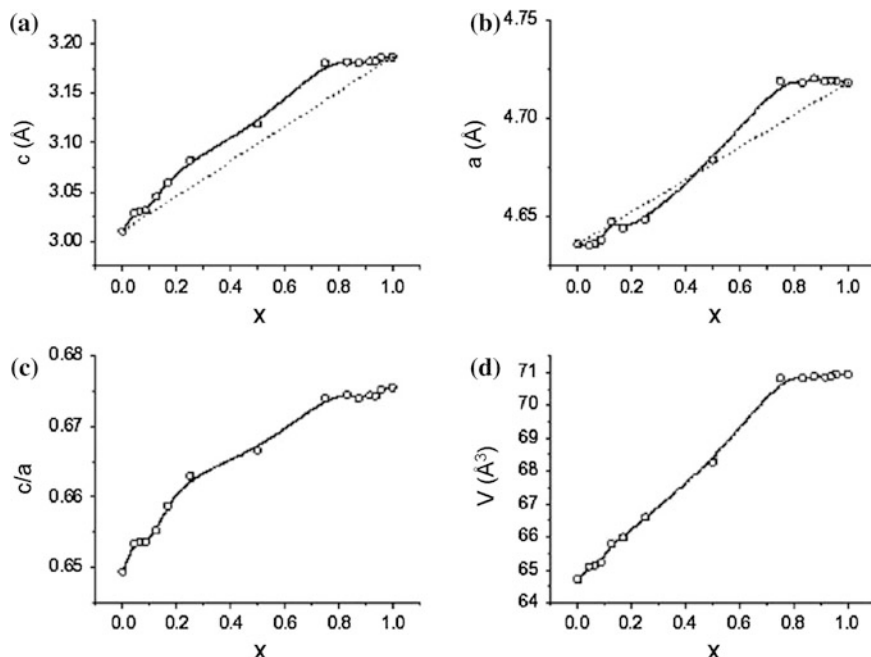


Fig. 13.7 Calculated lattice parameters of rutile as a function of x for $\text{Ti}_{1-x}\text{Sn}_x\text{O}_2$ solid solution with rutile structure: (a) c ; (b) a ; (c) axial ratio c/a ; and (d) unit cell volume (reproduced with permission from Sensato et al. 2003. Copyright Elsevier)

beneficial for the photocatalytic activity. Besides, Ti-Sn solid solutions with rutile structure show an increased band gap that contributes as well to increase the lifetime of the photogenerated charges (Lin et al. 1999; Tudela et al. 2010).

The number of studies on tin-doped anatase is more limited. Unlike the blue shift observed in rutile samples, a red shift in the absorption spectrum has been observed in Ti-Sn solid solutions with anatase structure, attributed to the Sn^{4+} electronic states situated about 0.4 eV below the anatase TiO_2 conduction band. These doping energy levels allow a more efficient separation and transfer of the photogenerated charge carriers. An enhanced photocatalytic performance has been reported for Sn-doped anatase photocatalysts compared to pure titania, both under UV and visible light. The activity has shown to increase with the Sn content up to an optimum value, decreasing at higher doping contents (Yang et al. 2002; Cao et al. 2004; Martínez et al. 2005; Fresno et al. 2009). Even higher photocatalytic activities have been obtained with Ti-Sn samples containing both anatase and rutile phases, attributed to a lower electron-hole recombination due to the anatase/rutile coupling (Fresno et al. 2005; Liqiang et al. 2006). Nevertheless, the presence of a high content of rutile can be detrimental for the photocatalytic activity (Yang et al. 2002).

Besides Ti-Sn solid solutions, the segregation of an SnO₂ phase gives rise to coupled TiO₂/SnO₂ photocatalysts. This situation can lead to an interaction between the two phases, with the formation of Sn-doped TiO₂ and Ti-doped SnO₂ at the interphase. The photocatalytic activity of these coupled systems has been tested both in gas- and liquid-phase reactions. The higher efficiency generally observed for these materials has been ascribed to the improved charge separation process. The junction between the two semiconductors, as it will be further described in [Chap. 15](#), may favour the separation of the photogenerated charge carriers since the excited electrons can migrate from the conduction band of titania to the conduction band of SnO₂, located at a lower energy than the former. Furthermore, since the valence band of SnO₂ is also lower in energy than that of TiO₂, the holes can accumulate on the latter (Tudela et al. 2010).

References

- Adán C, Bahamonde A, Fernández-García M, Martínez-Arias A (2007) Structure and activity of nanosized iron-doped anatase TiO₂ catalysts for phenol photocatalytic degradation. *Appl Catal B-Environ* 72:11–17
- Al-Salim NI, Bagshaw SA, Bittar A, Kemmitt T, McQuillan AJ, Mills AM, Ryan MJ (2000) Characterisation and activity of sol-gel-prepared TiO₂ photocatalysts modified with Ca, Sr or Ba ion additives. *J Mater Chem* 10:2358–2363
- Anandan S, Ikuma Y, Murugesan V (2012) Highly active rare-earth-metal la-doped photocatalysts: fabrication, characterization, and their photocatalytic activity. *Int J Photoenergy*. Article ID 921412: 10
- Anpo M, Takeuchi M (2003) The design and development of highly reactive titanium oxide photocatalysts operating under visible light irradiation. *J Catal* 216:505–516
- Avasarala BK, Tirukkovalluri SR, Bojja S (2010) Enhanced photocatalytic activity of beryllium doped titania in visible light on the degradation of methyl orange dye. *Int J Mater* 101:1563–1570
- Baiju KV, Periyat P, Shajesh P, Wunderlich W, Manjumol KA, Smitha VS, Jaimy KB, Warriar KGK (2010) Mesoporous gadolinium doped titania photocatalyst through an aqueous sol-gel method. *J Alloy Compd* 505:194–200
- Bessekhouad Y, Robert D, Weber J-V, Chaoui N (2004) Effect of alkaline-doped TiO₂ on photocatalytic efficiency. *J Photoch Photobio A* 167:49–57
- Bingham S, Daoud WA (2011) Recent advances in making nano-sized TiO₂ visible-light active through rare-earth metal doping. *J Mater Chem* 21:2041–2050
- Cao Y, Yang W, Zhang W, Liu G, Yue P (2004) Improved photocatalytic activity of Sn⁴⁺ doped TiO₂ nanoparticulate films prepared by plasma-enhanced chemical vapor deposition. *New J Chem* 28:218–222
- Carp O, Huisman CL, Reller A (2004) Photoinduced reactivity of titanium dioxide. *Prog Solid State Chem* 32:33–177
- Chen X, Mao SS (2007) Titanium dioxide nanomaterials: synthesis, properties, modifications, and applications. *Chem Rev* 107:2891–2959
- Chen X, Shen S, Guo L, Mao SS (2010) Semiconductor-based photocatalytic hydrogen generation. *Chem Rev* 110:6503–6570
- Choi W, Termin A, Hoffmann MR (1994) The role of metal ion dopants in quantum-sized TiO₂: correlation between photoreactivity and charge carrier recombination dynamics. *J Phys Chem* 98:13669–13679

- Choi J, Park H, Hoffmann MR (2010) Effects of single metal-ion doping on the visible-light photoreactivity of TiO₂. *J Phys Chem C* 114:783–792
- Deshpande AS, Shchukin DG, Ustinovich E, Antonietti M, Caruso RA (2005) Titania and mixed titania/aluminum, gallium, or indium oxide spheres: sol-gel/template synthesis and photocatalytic properties. *Adv Funct Mater* 15:239–245
- Di Paola A, Marci G, Palmisano L, Schiavello M, Uosaki K, Ikeda S, Ohtani B (2002) Preparation of polycrystalline TiO₂ photocatalysts impregnated with various transition metal ions: characterization and photocatalytic activity for the degradation of 4-nitrophenol. *J Phys Chem B* 106:637–645
- Di Paola A, García-López E, Marci G, Martín C, Palmisano L, Rives V, Venezia AM (2004) Surface characterisation of metal ions loaded TiO₂ photocatalysts: structure–activity relationship. *Appl Catal B-Environ* 48:223–233
- El-Bahy ZM, Ismail AA, Mohamed RM (2009) Enhancement of titania by doping rare earth for photodegradation of organic dye (direct blue). *J Hazard Mater* 166:138–143
- Fernández A, Lassaletta G, Jiménez VM, Justo A, González-Elipe AR, Herrmann JM, Tahiri H, Ait-Ichou Y (1995) Preparation and characterization of TiO₂ photocatalysts supported on various rigid supports (glass, quartz and stainless steel). Comparative studies of photocatalytic activity in water purification. *Appl Catal B-Environ* 7:49–63
- Fernández-García M, Martínez-Arias A, Hanson JC, Rodríguez JA (2004) Nanostructured oxides in chemistry: characterization and properties. *Chem Rev* 104:4063–4104
- Fresno F, Coronado JM, Tudela D, Soria J (2005) Influence of the structural characteristics of Ti_{1-x}Sn_xO₂ nanoparticles on their photocatalytic activity for the elimination of methylcyclohexane vapors. *Appl Catal B-Environ* 55:159–167
- Fresno F, Hernández-Alonso MD, Tudela D, Coronado JM, Soria J (2008) Photocatalytic degradation of toluene over doped and coupled (Ti, M)O₂ (M = Sn or Zr) nanocrystalline oxides: Influence of the heteroatom distribution on deactivation. *Appl Catal B-Environ* 84:598–606
- Fresno F, Tudela D, Coronado JM, Soria J (2009) Synthesis of Ti_{1-x}Sn_xO₂ nanosized photocatalysts in reverse microemulsions. *Catal Today* 143:230–236
- Fu X, Clark LA, Yang Q, Anderson MA (1996) Enhanced photocatalytic performance of titania-based binary metal oxides: TiO₂/SiO₂ and TiO₂/ZrO₂. *Environ Sci Technol* 30:647–653
- Fuerte A, Hernández-Alonso MD, Maira AJ, Martínez-Arias A, Fernández-García M, Conesa JC, Soria J (2001) Visible light-activated nanosized doped-TiO₂ photocatalysts. *Chem Commun* 24:2718–2719
- Fuerte A, Hernández-Alonso MD, Maira AJ, Martínez-Arias A, Fernández-García M, Conesa JC, Soria J, Munuera G (2002) Nanosize Ti–W mixed oxides: effect of doping level in the photocatalytic degradation of toluene using sunlight-type excitation. *J Catal* 212: 1–9
- Hernández-Alonso MD, Tejedor-Tejedor I, Coronado JM, Soria J, Anderson MA (2006) Sol-gel preparation of TiO₂–ZrO₂ thin films supported on glass rings: influence of phase composition on photocatalytic activity. *Thin Solid Films* 502:125–131
- Hernández-Alonso MD, Coronado JM, Bachiller-Baeza B, Fernández-García M, Soria J (2007) Influence of structural and surface characteristics of Ti_{1-x}Zr_xO₂ nanoparticles on the photocatalytic degradation of methylcyclohexane in the gas phase. *Chem Mater* 19:4283–4291
- Hernández-Alonso MD, Almeida AR, Moulijn JA, Mul G (2009) Identification of the role of surface acidity in the deactivation of TiO₂ in the selective photo-oxidation of cyclohexane. *Catal Tod* 143:326–333
- Herrmann JM, Disdier J, Pichat P (1984) Effect of chromium doping on the electrical and catalytic properties of powder titania under UV and visible illumination. *Chem Phys Lett* 108:618–622
- Karakitsou KE, Verykios XE (1993) Effects of altrivalent cation doping of titania on its performance as a photocatalyst for water cleavage. *J Phys Chem* 97:1184–1189
- Kubacka A, Fernández-García M, Colón G (2008) Nanostructured Ti–M mixed-metal oxides: toward a visible light-driven photocatalyst. *J Catal* 254:272–284

- Kubacka A, Fernández-García M, Colón G (2012) Advanced nanoarchitectures for solar photocatalytic applications. *Chem Rev* 112:1555–1614
- Li W, Wang Y, Lin H, Shah SI, Huang CP, Doren DJ, Rykov SA, Chen JG, Barteau MA (2003) Band gap tailoring of Nd³⁺-doped TiO₂ nanoparticles. *Appl Phys Lett* 83:4143–4145
- Li FB, Li XZ, Hou MF (2004) Photocatalytic degradation of 2-mercaptobenzothiazole in aqueous La³⁺-TiO₂ suspension for odor control. *Appl Catal B-Environ* 48:185–194
- Lin J, Yu JC, Lo DL, Am SK (1999) Photocatalytic activity of rutile Ti_{1-x}Sn_xO₂ solid solutions. *J Catal* 183:368–372
- Liqiang J, Honggang F, Baiqi W, Dejun W, Baifu X, Shudan L, Jiazhong S (2006) Effects of Sn dopant on the photoinduced charge property and photocatalytic activity of TiO₂ nanoparticles. *Appl Catal B-Environ* 62:282–291
- López T, Hernández-Ventura J, Gómez R, Tzompantzi P, Sánchez E, Bokhimi X, García A (2001) Photodecomposition of 2,4-dinitroaniline on Li/TiO₂ and Rb/TiO₂ nanocrystallite sol-gel derived catalysts. *J Mol Catal A-Chem* 167:101–107
- Martínez AI, Acosta DR, Cedillo G (2005) Effect of SnO₂ on the photocatalytic properties of TiO₂ films. *Thin Solid Films* 490:118–123
- Nguyen-Phan T-D, Song MB, Kim EJ, Shin EW (2009) The role of rare earth metals in lanthanide-incorporated mesoporous titania. *Micropor Mesopor Mat* 119:290–298
- Peng S, Li Y, Jiang F, Lu G, Li S (2004) Effect of Be²⁺ doping TiO₂ on its photocatalytic activity. *Chem Phys Lett* 398:235–239
- Piera E, Tejedor-Tejedor MI, Zorn ME, Anderson MA (2003) Relationship concerning the nature and concentration of Fe(III) species on the surface of TiO₂ particles and photocatalytic activity of the catalyst. *Appl Catal B-Environ* 46:671–685
- Ranjit KT, Cohen H, Willner I, Bossmann SH, Braun AM (1999) Lanthanide oxide-doped titanium dioxide: Effective photocatalysts for the degradation of organic pollutants. *J Mater Sci* 34:5273–5280
- Ranjit KT, Willner I, Bossmann SH, Braun AM (2001) Lanthanide oxide-doped titanium dioxide photocatalysts: novel photocatalysts for the enhanced degradation of p-chlorophenoxyacetic acid. *Environ Sci Technol* 35:1544–1549
- Rehman S, Ullah R, Butt AM, Gohar ND (2009) Strategies of making TiO₂ and ZnO visible light active. *J Hazard Mater* 170:560–569
- Sasikala R, Shirole AR, Sudarsan V, Sudakar C, Naik R, Rao R, Bharadwaj SR (2010) Enhanced photocatalytic activity of indium and nitrogen co-doped TiO₂-Pd nanocomposites for hydrogen generation. *Appl Catal A-Gen* 377:47–54
- Sensato FR, Custodio R, Longo E, Beltrán A, Andrés J (2003) Electronic and structural properties of Sn_xTi_{1-x}O₂ solid solutions: a periodic DFT study. *Catal Tod* 85(145):152
- Setiawati E, Kawano K (2008) Stabilization of anatase phase in the rare earth; Eu and Sm ion doped nanoparticle TiO₂. *J Alloy Compd* 451:293–296
- Shannon RD, Pask JA (1965) Kinetics of the anatase-rutile transformation. *J Am Ceram Soc* 48:391–398
- Shi JW, Zheng JT, Hu Y, Zhao YC (2008) Photocatalytic degradation of methyl orange in water by samarium-doped TiO₂. *Environ Eng Sci* 25:489–496
- Song S, Wang C, Hong F, He Z, Cai Q, Chen J (2011) Gallium- and iodine-co-doped titanium dioxide for photocatalytic degradation of 2-chlorophenol in aqueous solution: role of gallium. *Appl Surf Sci* 257:3427–3432
- Tanabe K, Sumiyoshi T, Shibata K, Kiyoura T, Kitagawa J (1974) A new hypothesis regarding the surface acidity of binary metal oxides. *Bull Chem Soc Jpn* 47:1064–1066
- Tudela D, Fresno F, Coronado JM (2010) Tin-doped nanocrystalline TiO₂ photocatalysts. In: Chen W (ed) *Doped nanomaterials and nanodevices*. American Scientific Publishers, California. ISBN: 1-58883-110-8
- Umabayashi T, Yamaki T, Itoh H, Asai K (2002) Analysis of electronic structures of 3d transition metal-doped TiO₂ based on band calculations. *J Phys Chem Solids* 63:1909–1920

- Venkatachalam N, Palanichamy M, Murugesan V (2007) Sol-gel preparation and characterization of alkaline earth metal doped nano TiO₂: Efficient photocatalytic degradation of 4-chlorophenol. *J Mol Catal A-Chem* 273:177–185
- Wang C, Böttcher C, Bahnemann DW, Dohrmann JK (2003) A comparative study of nanometer sized Fe(III)-doped TiO₂ photocatalysts: synthesis, characterization and activity. *J Mater Chem* 13:2322–2329
- Xu YL (1991) The basics of semiconducting oxides and compounds. Press of Xi'an Electronic Science and Technology University, Xi'an
- Xu A-W, Gao Y, Liu H-Q (2002) The preparation, characterization, and their photocatalytic activities of rare-earth-doped TiO₂ nanoparticles. *J Catal* 207:151–157
- Yamashita H, Ichihashi Y, Takeuchi M, Kishiguchi S, Anpo M (1999) Characterization of metal ion-implanted titanium oxide photocatalysts operating under visible light irradiation. *J Synchrotron Radiat* 6:451–452
- Yamashita H, Harada M, Misaka J, Takeuchi M, Neppolian B, Anpo M (2003) Photocatalytic degradation of organic compounds diluted in water using visible light-responsive metal ion-implanted TiO₂ catalysts: Fe ion-implanted TiO₂. *Catal Today* 84:191–196
- Yang J, Li D, Wang X, Yang X, Lu LD (2002) Rapid synthesis of nanocrystalline TiO₂/SnO₂ binary oxides and their photoinduced decomposition of methyl orange. *J Solid State Chem* 165:193–198
- Yang X, Wang Y, Xu L, Yu X, Guo Y (2008) Silver and indium oxide codoped TiO₂ nanocomposites with enhanced photocatalytic activity. *J Phys Chem C* 112:11481–11489
- Yu JC, Lin J, Kwok RWM (1998) Ti_{1-x}Zr_xO₂ solid solutions for the photocatalytic degradation of acetone in air. *J Phys Chem B* 102:5094–5098
- Zhang Y, Xu H, Xu Y, Zhang H, Wang Y (2005) The effect of lanthanide on the degradation of RB in nanocrystalline Ln/TiO₂ aqueous solution. *J Photoch Photobio A* 170:279–285
- Zorn ME, Tompkins DT, Zeltner WA, Anderson MA (1999) Photocatalytic oxidation of acetone vapor on TiO₂/ZrO₂ thin films. *Appl Catal B-Environ* 23:1–8

Chapter 14

Non-metal Doping for Band-Gap Engineering

Raquel Portela

As mentioned in [Chap. 5](#), the lower edge of the conduction band in pristine TiO_2 (both anatase and rutile) is formed by Ti 3d states and the upper edge of the conduction band by O 2p states, resulting in a wide band gap ($E_{\text{g anatase}}$ ca. 3.2 eV; $E_{\text{g rutile}}$ ca. 3.0 eV). Therefore, one of the main challenges for photocatalytic materials engineering since the late 1980s has been to red shift the absorption edge of the semiconductor (387 nm for anatase, 413 nm for rutile), so that visible light, either from the sun or from interior illumination, can be harnessed for photocatalytic applications. The first approaches explored to reach this goal have been the photosensitization of TiO_2 with dyes ([Chap. 16](#)), which act as visible light harvesters, and the metal doping, described in the previous chapter. Only in 2001, one decade after the first studies on the incorporation of anions into the titania matrix (Saha and Tompkins 1992), non-metal Doping of TiO_2 appeared as an alternative strategy for photocatalytic applications (Asahi et al. 2001); since then, the anionic doping of titania has been intensively investigated, and interesting photocatalysts with promising results under visible light have been obtained.

In metal-doped TiO_2 , the cations replace titanium atoms; meanwhile in the non-metal-doped TiO_2 , the anionic dopants are expected to substitute the oxygen atoms, although cationic substitutions may take place as well with some non-metals. Even though titania with partial substitution at the oxygen sites is usually represented in the literature as $\text{TiO}_{2-x}\text{A}_x$, where A is the anion, this representative formula must be carefully employed and seems questionable for very low A/Ti ratios.

In order to achieve a good coupling between the matrix and the anion, a homogeneous distribution of the dopant at atomic level is required, without the loss of the crystal structure of the semiconductor. Additionally, the aim of adsorbing radiation less energetic than UV-A requires the band-gap narrowing, by the elevation of the valence band maximum, the lowering of the conduction band minimum or the introduction of localized energy levels. Furthermore, only when

R. Portela (✉)

Institute of Catalysis and Petrochemistry, CSIC, Calle Marie Curie 2 E-28049 Madrid, Spain
e-mail: raquel.portela@csic.es

the redox potentials of the charge carriers created by visible light excitation are capable of inducing subsequent photocatalytic reactions, the visible light absorption achieved by doping is effective. For instance, in the case of overall water-splitting applications, the TiO_2 conduction band minimum, just above the $\text{H}_2/\text{H}_2\text{O}$ redox potential level, can be only slightly modified for the photoreduction activity to be ensured, so that the energy level of the optically excited electrons is low enough for H_2 evolution. On the other hand, the valence band maximum of the doped semiconductor must not be far from that of TiO_2 , so that the generated holes are oxidative enough for O_2 evolution.

So far, nearly all non-metals have been explored as dopants for the modification of the electronic structure of TiO_2 to improve the photocatalytic activity, especially under visible light. However, TiO_2 is generally a stable compound and not easily doped by a non-metal element. As a result, surface doping has been more commonly studied than the homogeneous incorporation of the anionic dopant into the bulk. The differences between both approaches are summarized in Table 14.1.

The chemical state, amount, and location of the non-metal depend on the dopant selection and on the method of preparation of the doped material, giving rise to the contradictory theories explaining the origin of the doping-induced visible light absorption found in the literature that will be commented in the following sections.

Doped TiO_2 nanostructures can typically be prepared by treatment or growth of TiO_2 in a solution of the dopant precursors, thermal treatment or sputtering in an atmosphere of the doping species, or ion implantation. In general, the distribution and concentration of the dopant atoms obtained by chemical methods can be improved by several approaches. One option is rendering the diffusion length for the dopant short enough. This can be achieved either by reducing the size of TiO_2 particles or by facilitating the diffusion, for example, with a layered structure. Other option is employing high-energy physical doping methods.

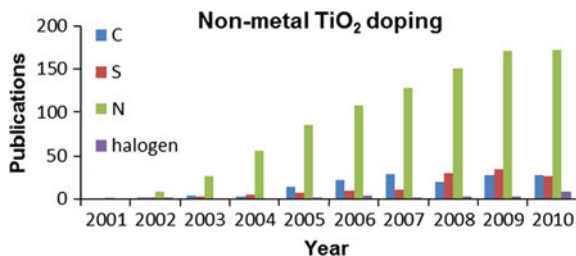
The main requirements for the anionic dopant to elevate the valence band maximum are the following (Liu et al. 2010):

1. Lower electronegativity than oxygen, so that the dopant states can be involved in the formation of a new valence band at a higher energy level. The Pauling electronegativity of O is 3.4, higher than that of all non-metals, except F, with electronegativity of 3.98.

Table 14.1 Comparison between surface and homogeneous TiO_2 -doping with non-metals. Adapted from Liu et al. (2010)

Property	Surface doping	Homogeneous doping
Visible light absorbance	Low	High
Absorption edge shape	Wide	Steep
Mobility of charge carriers	Low	High
Redox potential of charge carriers	Visible light > UV light	Visible light = UV light
Modulation of the chemical state	More flexible	Less flexible
Difficulty	Lower	Higher

Fig. 14.1 Number of publications during the last decade on non-metal-doped TiO₂ for photocatalytic applications with carbon, nitrogen, sulfur, and halogen elements as dopants. *Source* Scopus



2. Similar size to that of lattice O atoms, so that the substitutional anions do not alter the structure uniformity and, thus, the intrinsic properties of the semiconductor. N presents the most similar anionic radius.

Taking this into account, and according to the calculated electronic band structures of the semiconductor with carbon, nitrogen, fluorine, phosphorus, or sulfur as substitutional dopants, it has been suggested that N is the most favorable dopant (Asahi et al. 2001). However, the tremendous effort put into TiO₂ materials has resulted in a lot of theoretical and experimental data on the synthesis, properties, modifications, and applications for several non-metal dopants. In Fig. 14.1, the number of research works in terms of scientific publications concerning the modification of the semiconductor with the main non-metallic elements during the last decade is presented.

Many successful photocatalysts have been synthesized. The main challenge remains achieving higher photocatalytic activity under visible than under ultraviolet light. Therefore, the optimization of the dopants choice and doping strategies continues.

14.1 Nitrogen Doping

N-doped TiO₂ has been synthesized by several methods, such as the hydrolysis of titanium tetraisopropoxide or titanium sulfate with amine or ammonia as nitrogen source; decomposition of gaseous TiCl₄ by an atmospheric microwave plasma torch; sputtering/ion implantation techniques with N₂ or N₂⁺ gas flux; dispersion of TiO₂ in an NH₃-H₂O solution; heating TiO₂ under NH₃ flux; directly from a Ti-bipyridine complex, etc. In low-temperature methods where the oxygen anions of the precursor are adjacent to the titanium cation, the amount of doped nitrogen is limited, because the Ti–O bond is quite stable. The N content may be increased using precursors with Ti–N instead of Ti–O bonds, or with high-energy methods.

Among all non-metals, nitrogen has been the most widely investigated dopant for photocatalytic applications of titanium dioxide. Ought to the similarity of the ionic radii of nitrogen and oxygen, and of the energies of the N 2p states and O 2p states, their mixing in the valence band is favoured. This hybridization entails a raise of the valence band upper edge and, thus, the narrowing of the inherent band gap of TiO₂ (Fig. 14.2c), which has been attributed to be the origin of the visible

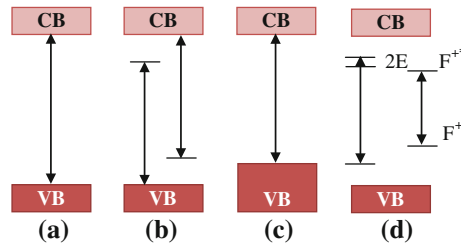
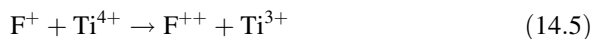
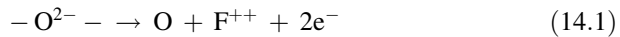


Fig. 14.2 a Band gap of anatase TiO_2 ; b–e possible changes in the band-gap electronic structure due to non-metal Doping explaining the visible light absorption: **b** localized dopant levels near the VB or the CB; **c** broadening of the VB; **d** formation of Ti^{3+} and F^+ centers

light adsorption observed with N-doped TiO_2 in many theoretical and experimental studies (Asahi et al. 2001). However, this attribution has been widely discussed. Some studies point out the formation of isolated N 2p states above the TiO_2 valence band maximum (Irie et al. 2003b). Others hypothesize the formation of localized states below the conduction band minimum, which would be due to the oxygen deficiencies caused by the doping (Ihara et al. 2003), rather than to the dopant itself (Fig. 14.2b). Furthermore, other authors point out the formation of localized states above the valence band maximum due to atomic nitrogen impurities in the bulk of TiO_2 samples (Livraghi et al. 2006). Serpone affirms that the red shift of the absorption edge is due to the color centers (Fig. 14.2d), related to the oxygen vacancies (F , F^+ , F^{++} , and Ti^{3+}), unless heavy doping of the metal oxide semiconductor, which gives rise to the formation of totally different band-gap electronic structures due to the different chemical composition (Serpone 2006). The formation of the color centers is explained in the following equations:



The loss of an O atom in TiO_2 leaves an electron pair trapped in the cavity, an anion vacancy referred to as F^{++} center (Eq. 14.1), that upon interaction with the electrons gives rise to the formation of F^+ (Eq. 14.1) and F (Eq. 14.2) centers. The trapped electrons can also interact with adjacent Ti^{4+} cations to give Ti^{3+} centers (Eqs. 14.4 and 14.5).

While a narrowed band gap would result in steep and parallel absorption edges, as observed for oxynitrides, which are object of Section 14.5, localized states in the band gap would produce an absorption tail, and the latter is usually observed in N-doped materials.

Except for a few works, where the presence of interstitial nitrogen species was proposed (Di Valentin et al. 2005b; Shinri 1986), the N-dopant is generally found in substitutional positions.

The results obtained with these materials are very promising. For instance, in the early work of Asahi and coworkers, undoped and N-doped films were prepared by sputtering of the TiO₂ target in an O₂(20 %)/Ar or an N₂(40 %)/Ar gas mixture and annealing at 550 °C in oxygen or nitrogen, respectively. On the other hand, N-doped powders were prepared by annealing of anatase TiO₂ samples in NH₃(67 %)/Ar atmosphere at 550–600 °C. The samples showed similar activity under UV radiation, but N-doping led to the improvement in the optical and photocatalytic properties under irradiation at wavelengths <500 nm. Therefore, more efficient visible light photodegradation of methylene blue, in the case of the film, and of gaseous acetaldehyde, in the case of the powder, were observed, together with higher hydrophilicity of the titania film (Asahi et al. 2001). In a more recent study, the photocatalytic activity under solar irradiation of P25 and other three commercial titania, A_287 (Alfa Aesar), PC105 (Millennium Inorganic Chemicals), and NanoActive (NanoScale Corporation), was found to be lower than that of homemade N-doped TiO₂ for the degradation of toluene in gas phase. The samples were prepared from TiCl₃ solutions at different pH, and the highest degradation rates were achieved at higher pH, corresponding to the largest amount of paramagnetic centers, as reported by EPR results (Bianchi et al. 2009). Only the lowest pH led to worse samples than the commercial ones. N-doped titania has been found to photocatalytically degrade many other compounds under visible light irradiation, such as gaseous formaldehyde (Qu et al. 2009) or NO_x (Shu et al. 2004), or aqueous bisphenol-A (Subagio et al. 2010). Nitrogen-doped TiO₂ hollow spheres, synthesized through polystyrene sphere templating and treatment with ammonia, exhibited significant increase in bisphenol-A degradation and mineralization under blue, green, and yellow LEDs as compared to the undoped TiO₂ hollow spheres, powder TiO₂, and Hombikat UV100. The success can be ascribed to the extension of the absorption properties to 550 nm ($E_g = 2.26$ eV) and the high porosity and specific surface area of the hollow spheres.

14.2 Incorporation of Carbon, Sulfur, and Other Non-metallic Elements

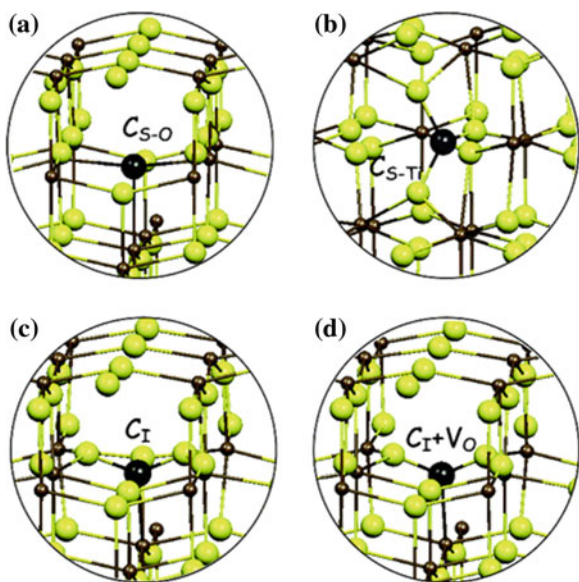
Carbon has received considerable interest as a non-metallic dopant in titania, being the second most used approach after N-doping. The valence shell of the C atom contains four electrons (2s² 2p²), as does the one of the Ti atom (4s² 3d²), although the former can also host up to four excess electrons. The incorporation of carbon into the semiconductor has been suggested to occur with the carbon atoms in an oxidation state ranging from –4, if replacing an oxygen atom, to +4, if forming carbonate species. The first studies concerning the doping of TiO₂ with C

were performed in 2002 by Khan et al. who synthesized rutile by pyrolysis of Ti metal in a natural gas flame with controlled amount of oxygen in the presence of combustion products (CO_2 and H_2O), obtaining a substitutional-type doped material with visible light absorption and activity for photochemical water splitting under irradiation with an Xe-lamp (Khan et al. 2002). On the contrary, the hydrolysis of titanium tetrachloride with tetrabutylammonium hydroxide followed by calcination resulted in the formation of elemental carbon or carbonate species (Sakthivel and Kisch 2003). The Ti-C bond in C-doped titania has been commonly obtained by flame pyrolysis, annealing of TiC powders or ion-assisted electron beam evaporation, while the C-O bond is usually formed via sol-gel or hydrothermal syntheses. The synthesis routes reported in the literature have been thoroughly reviewed by Leary and Westwood (2011).

The substitutional and interstitial carbon doping of TiO_2 , schematized in Fig. 14.3, has been investigated from a theoretical perspective, mainly using density functional theory (DFT) calculations. According to Di Valentin and coworkers, for both rutile and anatase TiO_2 , the substitution of oxygen by carbon atoms and the formation of oxygen vacancies are favored at low partial pressures of oxygen (Di Valentin et al. 2005a). Under oxygen-rich conditions, the substitution of titanium and the incorporation of interstitial carbon are preferential.

Except for the substitution of Ti, the presence of carbon dopants causes the formation of localized occupied band-gap states with different energy depending on the dopant type, the presence of oxygen vacancies, and the partial pressure of oxygen. These states may induce the absorption edge shift toward the visible that has been experimentally observed, with a magnitude varying between around 0.1 and 1.05 eV (Leary and Westwood 2011).

Fig. 14.3 Partial geometry of the models for **a** substitutional C atom to O ($\text{C}_{\text{S-O}}$), **b** substitutional C atom to Ti ($\text{C}_{\text{S-Ti}}$), **c** interstitial C atom (C_{I}), and **d** interstitial C atom nearby an oxygen vacancy ($\text{C}_{\text{I}} + \text{V}_{\text{O}}$) in anatase TiO_2 . The *yellow spheres* represent O atoms, the *small brown spheres* represent Ti atoms, and the *black sphere* represents the carbon impurity (Di Valentin et al. 2005a). Reproduced with permission. Copyright American Chemical Society



A noticeable photocatalytic activity of these modified photocatalysts has been observed in the decomposition of methylene blue, 2-propanol (Irie et al. 2003a), or trichloroacetic acid (Shen et al. 2006), as well as in water splitting (Park et al. 2005). However, there is some controversy concerning whether visible light water splitting using C-doped TiO₂ is actually feasible at all (Murphy 2008). The mechanism of the photocatalytic activity enhancement observed has been attributed in the literature to the existence of the Ti–C, O–Ti–C, C–O, or C–C bonds, or to the existence of mid-gap states related to oxygen vacancies, C 2p, or, more commonly and also questioned, the mixing of C 2p and O 2p.

The anionic doping with elements from the third period, such as sulfur and phosphorus, is particularly difficult, due to the large size of these atoms compared to that of oxygen and the associated increase in the formation energy for the bond with titanium; the substitution at the O sites may significantly modify the electronic structure of TiO₂. For that reason, not only anionic but also cationic doping has been observed when these non-metals have been incorporated into the semiconductor network.

The effective ionic radius of sulfur species is 1.84 Å for S²⁻ anion and 0.37 Å and 0.29 Å for S⁴⁺ and S⁶⁺ cations, respectively. The resultant ionic state in sulfur-doped TiO₂ depends essentially on the synthesis conditions and the precursors. In both anionic and cationic substitutions, the optical absorption edge experienced a red shift, promoting the photonic response of the doped oxide to the visible range. The photocatalytic activities obtained are variable, due to the different carrier behavior in these samples, although frequently, the S-doped TiO₂ was found to display a higher photocatalytic activity in the visible region but a lower photocatalytic activity in the UV region, compared to the undoped oxide.

The first successful attempt of S-doping for photocatalytic applications of TiO₂ was reported in 2002 by Umebayashi, who observed the formation of anatase and the presence of S²⁻ by oxidation of TiS₂ at 600 °C (Umebayashi et al. 2002). Their calculations concluded that the mixing of the S 3p states with the valence band contributed to the band-gap narrowing. The formation of the anionic species in the oxide can be obtained as well by sputtering with S⁺, or grinding the mixture of sulfur and TiO₂ powders and calcining at 400 °C in an inert gas flow (Zhang et al. 2004). The annealing of TiO₂ nanotubular arrays in an H₂S flow at 380 °C has also resulted in the formation of S²⁻ (Tang and Li 2008).

On the contrary, the incorporation of S into the titania network by liquid phase methods, using as precursors thiourea or sulfate, resulted in the formation of S⁴⁺ (Ohno et al. 2004) or S⁶⁺ (Ohno et al. 2003) species. When sulfur exists as S⁴⁺, replacing Ti⁴⁺ cations, S 3s states lie just above the O 2p valence states, and S 3p states contribute to the conduction band of TiO₂. The band-gap narrowing obtained with S⁶⁺ could be produced, in a similar process to that of conventional transition-metal doping by means of intra-band-gap states formed close to the conduction band, as suggested by Yu et al. and the charge imbalance would be neutralized by the hydroxide ions (Yu et al. 2005). Additionally, the sulfur cations generated by some preparations might not actually substitute the Ti⁴⁺ in the titania lattice but form sulfate groups on the surface. The latter species may substantially enhance

the surface acidity or the charge separation in TiO_2 . For instance, in visible light-activated sulfur-doped TiO_2 films synthesized by a sol-gel method with H_2SO_4 as a sulfur source, the uniformly distributed sulfur species identified were both S^{2-} ions, related to anionic substitution, and $\text{S}^{6+}/\text{S}^{4+}$ cations, attributed mainly to the presence of surface sulfate groups (Han et al. 2011a).

Phosphorous species are recently attracting an increasing interest owing to their ability to increase the thermal stability and acidity of mesoporous structures. With this aim, phosphorus from H_3PO_4 was directly incorporated into mesoporous TiO_2 in a work performed in 2003 by Yu and coworkers. Although the dopant incorporation did not induce visible light absorption, an increased photocatalytic activity was observed (Yu et al. 2003). However, P and S are adjacent in the periodic table, and as published in 2005, P-doping in TiO_2 may have a similar red-shifting effect (Lin et al. 2005). With first-principle calculations, the critical phosphorus concentration for the maximization of solar radiation absorption has been set to ca. 0.7 %, and it has been concluded that the P-dopant tends to occupy the cation sites in the TiO_2 lattice (Peng et al. 2011). Nevertheless, both anionic and cationic substitutions have been experimentally observed; in the latter case, the phosphorus atoms presented pentavalent oxidation states. P-doped TiO_2 can be prepared by sol-gel techniques using tetra-n-butyl titanium and H_2PO_4^+ as precursors of TiO_2 and P, respectively (Shi et al. 2006; Lin et al. 2007).

More recent is the interest in the incorporation of a metalloid, boron, into the TiO_2 network aiming at photocatalytic applications of the semiconductor, although already in 1996, it was observed that the reduction of rutile TiO_2 in the presence of borate flux led to interstitial boron incorporation accompanied by reduction of titanium cation to the trivalent state (Grey et al. 1996). According to first-principle calculations, the boron atom would either replace an oxygen atom or sit in the interstitial position, but unlikely replace Ti atoms (Geng et al. 2006). In 2004, it was observed that doping with boron could extend the spectral response of TiO_2 to the visible region, but its photocatalytic activity was limited, and the addition of nickel oxide (Ni_2O_3) was necessary to facilitate the photogenerated electrons transfer, and hence reduce the electron-hole recombination (Zhao et al. 2004). However, visible light photocatalytically active B-doped TiO_2 has been recently synthesized. One synthesis route has been the reaction of a solution of BH_3 in tetrahydrofuran with TiCl_4 under nitrogen atmosphere. In this case, it has been observed that the maximum photoactivity occurred at 1.13 % B content, a part of which was active and substituted oxygen atoms, and another part was inactive and present as boric oxide-like material (In et al. 2007). Another synthesis method has been the surface impregnation of titania using boric acid triethyl ester as boron precursor. This approach introduced boron as B-O-Ti species in the surface of TiO_2 grains (Zaleska et al. 2009). Moreover, mesoporous $\text{TiO}_{2-x}\text{B}_x$ has been very recently synthesized by addition of boron hydroxide to a $\text{Ti}(\text{OC}_4\text{H}_9)_4$ solution which contained sulfuric acid and glucose. A porous carbon hard template was generated by dehydration and further eliminated by calcination. The mesoporous B-doped sample obtained showed visible light absorption (460 nm) and exhibited high photocatalytic activity on phenol degradation (Xiong et al. 2011).

14.3 Doping with Halogen Elements

Recently, doping with halogen elements has received much attention. In principle, a halogen dopant X (X = F, Cl, Br, I) can occupy an O or a Ti site in TiO₂. The effective anionic radius of oxygen and halogen elements at a six-coordinate site increases in the following order: F⁻ (1.33 Å) < O²⁻ (1.40 Å) < Cl⁻ (1.81 Å) < Br⁻ (1.96 Å) < I⁻ (2.20 Å), and the Mulliken's electronegativity of oxygen and halogens decreases in the following order: F (3.91) > O (3.41) > Cl (3.10) > Br (2.95) > I (2.74). Therefore, regarding both the ionic radius and the electronegativity, the substitutional doping at an O site should be favoured in the order F < Cl < Br < I and the contrary when a Ti site is occupied. In the substitution of O²⁻, the halogen atom is present as anionic X⁻, which requires one electron less than oxygen. In the substitution of Ti, however, the halogen atom must exist as a cation. F, Cl, Br, and I atoms are expected to be present as F³⁺ (s²p²), Cl⁴⁺ (s²p¹), Br⁴⁺ (s²p¹), and I⁵⁺ (s²) ions at a Ti⁴⁺ (d⁰) site, respectively. The doped TiO₂ is overall electrically neutral. However, replacing a TiO₂ site with an element of different oxidation state can induce a charge imbalance, which can result in the formation of a crystallographic point defect (e.g., an oxygen or Ti vacancy) or can be compensated by a change in the oxidation state of the dopant, the titanium, or the oxygen.

F-doped rutile electrodes with increased photoelectrochemical response have been synthesized by treating TiO₂ at high temperature under HF flow (Subbarao et al. 1979) or by ion implantation with F⁺ ion flux at room temperature (Yamaki et al. 2002). The first photocatalytic degradation tests with fluorinated TiO₂ were performed in gas phase, exploring the oxidation of CH₃CHO with a photocatalyst prepared by fluorine diffusion into a TiO₂ film from a F:SiO₂ underlayer (Hattori et al. 1999). In aqueous solution, the first tests used commercial TiO₂ where NaF was added. The phenol degradation rate enhancement was attributed to the formation of homogenous free OH radicals (Minero et al. 2000). F-doped TiO₂ photocatalysts with promoted activity have been synthesized by sol-gel, using titanium tetraisopropoxide and an NH₄F-H₂O solution as precursors (Yu et al. 2002), by spray pyrolysis from an aqueous solution of H₂TiF₆ (Li et al. 2005c) or by microwave-assisted hydrothermal treatment using NaF and TiO₂ microspheres as precursors (Zhu et al. 2011). Moreover, F-doped flower-like TiO₂ nanostructures, which besides efficiency in the photodegradation of organic pollutants exhibit high photoelectrochemical activity for water splitting, have been directly grown in HF solutions using a low-temperature hydrothermal method (Wu et al. 2008). The improved photocatalytic activity of F-doped TiO₂ has been attributed to the increase in the surface acidity and anatase crystallinity and the creation of oxygen vacancies and active sites. The photocatalytic activity observed under visible light in some experimental studies has been attributed to the creation of surface oxygen vacancies rather than the change in the optical absorption edge of bulk titania (Li et al. 2005c; Yamaki et al. 2002). Actually, only a small (about 0.05 eV) (Yu et al. 2002) or no (Li et al. 2005c) red shift of the absorption edge

after F-doping has been experimentally observed, according to theoretical studies that indicate that the F 2p states are localized below the O 2p valence states without any mixing with the valence or conduction band. Additional states appeared just below the conduction edge, due to the electron-occupied level composed of the t_{2g} state of the Ti 3d orbital (Yang et al. 2008).

A more pronounced band-gap narrowing is theoretically expected after doping with chlorine (0.2 eV) and bromine (0.3 eV), corresponding to the optical absorption edges of 413 and 428 nm, respectively, so they should exhibit a green-yellow color. The theory is in agreement with the reduction of 0.2–0.3 eV experimentally observed in Cl/Br-codoped TiO₂ (Luo et al. 2004). However, only few scientific studies have dealt with the doping of the oxide with these halogen elements. Chlorine-doped anatase with visible light absorption has been prepared by hydrolysis of tetrabutyl titanate in hydrochloric acid and showed good photocatalytic activity in the degradation of phenol. According to X-ray photoelectron spectroscopy chlorine was present as an anion (Long et al. 2007). In a different approach, the soft interface of water and chloroform was utilized as platform to synthesize chlorine-doped rutile spherical clusters by a hydrothermal method using TiCl₄ as the starting material (Xu et al. 2008a). Peichang et al. have reported the hydrothermal synthesis of photocatalytically active Br-doped TiO₂ from potassium bromide and titanium sulfate (Peichang et al. 2010).

Even more pronounced is the theoretical band-gap narrowing predicted for iodine doping at O sites, about 0.7 eV, so that a significant red shift of the absorption edge and a yellow color of the samples are expected (Yang et al. 2008) and have been empirically observed (Song et al. 2010). However, there are few experimental works involving anionic iodine doping. One example is the I-doped TiO₂ obtained by a hydrothermal method using Ti(SO₄)₂ and KIO₃ as precursors, where the iodine existed in both I⁷⁺ and I⁻ chemical states (Su et al. 2008). The substitution of Ti⁴⁺, with an ionic radius of 0.64 Å, by I⁵⁺, with an ionic radius of 0.62 Å, is also favorable, and has proven to be a way of extending the photocatalytic activity in the visible light range (Song et al. 2010). Hong et al. reported for the first time this substitution. They synthesized I-doped TiO₂ with optical absorption in the visible region using an iodic acid aqueous solution (Hong et al. 2005). The investigation of the transient behavior of the photogenerated charge carriers of I-doped titania using time-resolved diffuse reflectance spectroscopy (Tojo et al. 2008) suggests that the recombination of e⁻-h⁺ pairs is inhibited because the I sites act as h⁺ trapping (Fig. 14.4). On the other hand, iodine-doped mesoporous TiO₂, as well as nanotubes or nanospheres, has also been synthesized by hydrothermal methods (He et al. 2011; Long et al. 2009).

14.4 Codoping

The visible light photocatalytic activity of TiO₂ is far from being high, despite the research efforts and the promising results obtained by doping. A way to improve the performance of the doped semiconductor that is attracting increasing attention

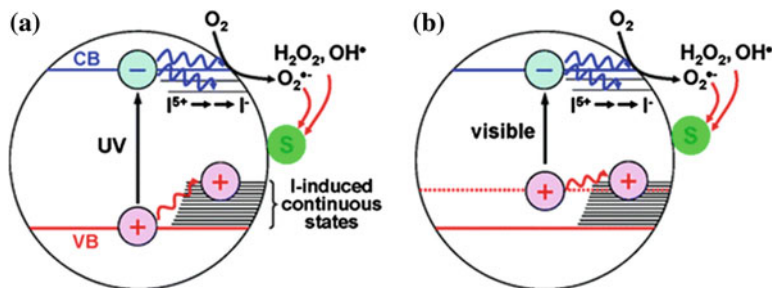


Fig. 14.4 Schematic illustrations of the photocatalytic reaction processes over I-doped TiO_2 under UV **a** and visible light **b** irradiation. Short *solid lines* represent the I-induced continuous states, which are derived from the mixture of I 5s, I 5p, and O 2p orbitals, and intrinsic defect states (Tojo et al. 2008). Copyright American Chemical Society

at the moment is to introduce two or more different dopants into the titania matrix, so that a synergistic effect is obtained. However, the success of the codoping strategy depends on the choice, amount, and position of the elements introduced, and therefore, a big amount of theoretical and experimental research is underway. Many are the possibilities explored with a non-metallic element as one of the dopants, which include codoping with different types of other non-metal elements, a metal—commonly a transition metal—or even a metalloid.

14.4.1 Non-metal/metal

Donor–acceptor or n–p codoping with metals may be a advantageous route, since the recombination may be reduced, the absorption edge red-shifted and, besides, the columbic attraction between the donor–acceptor pair may enhance the incorporation of both dopants, especially the non-metal, into the TiO_2 lattice.

According to first-principle calculations, it has been proposed that these effects are obtained in compensated (or passivated) n–p codoping with transition metals, where the electrons in the donor levels compensate the same amount of holes in the acceptor levels (Gai et al. 2009). Among V, Cr, Nb, and Mo (3d the former two, 4d the latter two) replacing the Ti as n-type dopants, and N and C substituting the O as p-type dopants, it has been suggested that C, Mo–codoped TiO_2 could be a good candidate for photocatalytic water splitting. This material has been obtained by thermal oxidation of the mixture TiC-MoO_3 in air (Zhang et al. 2010). Nevertheless, with high 4d and 5d atomic orbital energies, Nb and Ta are good choices as donors. It has been calculated that Nb or Ta impurities facilitate the concentration of p-type dopants (N and C) in the host lattice. In the case of 1:2 compensated Nb/C/Nb and Ta/C/Ta the codoping not only reduces the band gap and eliminates the local trapping, improving the carriers mobility and conversion efficiency, but also maintains the reduction potential (Ma et al. 2011).

On the other hand, it has been also proposed that in non-compensated n-p codoping, there exists an extra charge that can ensure the creation of intermediate bands in the gap region of TiO_2 , narrowing its band gap. The position and magnitude of the intermediate bands can be tuned by choosing different combinations and concentrations of codopants. In a theoretical study with V or Cr as n-type dopant and C or N as p-type dopant, it was concluded that the non-compensated codopant pair of Cr and N was the most convenient; N, Cr-codoped TiO_2 has been prepared by hydrolysis of titanium isopropoxide in the presence of ethylenediamine and chromium acetylacetonate (Zhu et al. 2009). However, N, Cr-codoped TiO_2 synthesized by different methods has shown lower photoactivity than either Cr- or N-monodoped TiO_2 (Li et al. 2011; Pan and Wu 2006), while N, V-codoped titania showed a photocatalytic activity enhancement for the degradation of methylene blue under visible light irradiation compared with the V- or N-monodoped TiO_2 . The positive effect of the codoping was attributed to the enhanced absorption in the visible light region and the improved quantum efficiency. The existence of V ions facilitated the incorporation of substitutional and interstitial N into the anatase lattice (Gu et al. 2008).

Theoretical studies centered in other 5d transition metals such as W, Re, and Os concluded that codoped systems with C present a slightly narrower band gap than those with N, although N, W-codoped TiO_2 is considered the most attractive photocatalyst because of the relatively small formation energies and large binding energies (Long and English 2010b). N, W-codoped anatase has been prepared by a microemulsion method subjecting the W-Ti-containing precursor to a heating ramp in NH_3/N_2 . The resulting material presented high activity and selectivity in the partial oxidation of aromatic hydrocarbons to fine chemical oxygenates using sunlight (Kubacka et al. 2009). Another example of codoping with an element of the sixth period is the addition of nitrogen and platinum to commercial TiO_2 powders by impregnation with ammonium carbonate and photodeposition of platinum (Zhou et al. 2007).

Other transition metals employed for codoping with non-metals have been iron, zinc, or zirconium, from the fourth period. For instance, P, Zn-codoped TiO_2 nanoparticles with high thermal stability and photoactivity have been synthesized by sol-gel (Yu et al. 2008). The iodine and zirconium codoped oxide has been prepared by hydrolysis of tetrabutyl titanate mixed with zirconium nitrate in an iodic acid aqueous solution. The zirconium has been found to increase the number of reactive sites, by promoting the presence of small-sized crystalline domains and a large surface area, but the inhibition of the electron-hole pair recombination by e^- trapping with Zr^{4+} was not significant (Song et al. 2011a). N, Fe-codoped nanoparticles of titanium dioxide have been prepared by a homogeneous precipitation-hydrothermal method. Fe^{3+} species were incorporated into the lattice of titania; on the other hand, the nitrogen doping was reported to inhibit the growth and aggregation of the particles. The degradation efficiency for rhodamine B was 75 and 5 % higher than pure titania under visible and ultraviolet irradiation, respectively. Yet, their performance has not been compared with that of the corresponding monodoped materials (Cong et al. 2007).

Although less frequently, also lanthanides have been studied as codopants for TiO_2 photocatalysts with enhanced photocatalytic activity. Codoping with iodine and rare earths has been lately achieved in liquid phase using tetrabutyl titanate as titania precursor, and in addition to iodate or iodic acid, and the nitrate of the rare earth dopant, in a similar procedure to that used for titanium dioxide codoping with iodine and transition metals. The codoped materials with cerium (Song et al. 2008) and lanthanum (He et al. 2008) have been successfully tested in the degradation of oxalic acid, and with neodymium (Jiang et al. 2010) in the oxidation of methylene blue or bovine serum albumin, and also for disinfection. Their high photocatalytic activity under visible light was attributed to the f-electron structure and multiple energy levels of the rare-earth element, as well as to the sub-band-gap transition corresponding to the doped iodine species.

The same preparation method has been employed to obtain I, Ga-codoped TiO_2 (Song et al. 2011b) with improved activity for the degradation of 2-chlorophenol. Gallium, a post-transition metal, was found to play a decisive role in inhibiting the anatase–rutile phase transformation, extending the absorption response, and creating oxygen vacancies for photoelectron trapping to prevent the e^-h^+ recombination process.

14.4.2 Non-metal/non-metal

The codoping of titanium dioxide with different non-metals may be beneficial for the photocatalytic activity as well, and is currently being widely explored.

All the possible pairs combining two of the C, N, and S elements have been explored. Even C, N, S-tridoped titania has been prepared by calcination of a TiO_2 xerogel and thiourea (Zhou and Yu 2008) or by a novel biomolecule-controlled hydrothermal method. In this method, L-cysteine was employed as a common source of the three dopants, due to its three functional groups with strong tendency to coordinate with inorganic cations: $-\text{NH}_2$, $-\text{COOH}$, and $-\text{SH}$ (Wang et al. 2009). Thiourea and urea have often been used as sources of the non-metallic element, because they can supply nitrogen and carbon, and sulfur in the case of thiourea. C, S-codoped TiO_2 was synthesized by hydrolysis of tetrabutyl titanate in a mixed aqueous solution containing thiourea and urea, although the activity remained below that of pure TiO_2 (Sun et al. 2006). Similarly, Tachikawa et al. reported a complete loss of the photocatalytic activity for the codoped material, while the activity for the C- or S-monodoped oxide was higher than that of the bare semiconductor (Tachikawa et al. 2004). On the contrary, N, C-codoped TiO_2 obtained by sol–gel showed higher photocatalytic activity under visible light than the material doped with solely carbon or nitrogen. This effect has been attributed to the enhanced adsorption of the carbonate species formed on the surface and the visible light absorption induced by N-doping into the TiO_2 lattice (Chen et al. 2007). The same synergistic effect has been observed for N, S-codoping. The high activity of the resulting mesoporous material prepared by hydrolysis of the Ti

precursor in the presence of ammonia/ammonium was attributed to a stronger radiation absorption in the UV–Vis region, the red shift of the band-gap transition, high crystallinity, large surface area, and the formation of a two-phase structure, constituted by undoped and codoped TiO₂ (Yu et al. 2006; Xu et al. 2008b).

Phosphorus has also been recently employed as codopant. In a study on the influence of N, P, and S as codopants for TiO₂ prepared by a hydrothermal method, N, P–codoped TiO₂ powders exhibited the best photocatalytic activity for the degradation of methylene blue employing a solar simulator (Han et al. 2011b). Theoretically, no obvious band-gap energy reduction is achieved at low dopant concentrations in the bulk, but a significant narrowing can be obtained at increased P/N concentration ratios. On the other hand, synergistic effects are predicted when one of either N or P is present as a substitutional dopant and the other acts as a surface dopant (Long and English 2010a).

The combination of one of the aforementioned non-metals with a halogen has also been successfully explored, especially of N with F. N, F–codoped nanostructured TiO₂, prepared via spray pyrolysis with a mixed solution of TiCl₄ and NH₄F, showed high visible light photocatalytic activity for the degradation of acetaldehyde and trichloroethylene. The good results were ascribed to a synergistic effect consisting in the creation of surface oxygen vacancies, the improvement in optical absorption properties, the enhancement of surface acidity and porosity, and the formation of Ti³⁺ ions (Li et al. 2005a, b). In another approach, high absorbance and water-splitting activity under visible light were demonstrated using (NH₄)₂TiF₆ as precursor (Nukumizu et al. 2003). Theoretical calculations confirmed the experimental results: N, F-codoping reduced the energy cost of doping and the amount of defects (oxygen vacancies) in the lattice, as a consequence of the charge compensation between the nitrogen (p-dopant) and the fluorine (n-dopant). The incorporation of nitrogen is favored in the presence of fluorine, and the visible light absorption and photocatalytic activity are enhanced with respect to the monodoped oxide (Di Valentin et al. 2008). In Ti₆₄N₂O₁₂₄F₂, prepared by thermal treatment of NH₄TiOF₃ with either NH₃ or N₂, the use of NH₃ as a reactant gas appeared to be indispensable to obtain a broad absorption band in the visible region and high photocatalytic activity for the water oxidation reaction (Maeda et al. 2009). Codoping with N and other halogens (Cl, Br, or I) was explored through a direct reaction between a TiO₂ sol and the corresponding cetyltrimethylammonium halide (chloride, bromide, or iodide), and according to X-ray photoelectron spectroscopy results, only the combination of N and Br, both as oxygen substituents, was successful (Sheng et al. 2011). An example of codoped material with a halogen and a non-metal different than N is the mesoporous S, I–codoped TiO₂ that has been synthesized by hydrolysis of titanium isopropoxide with thiourea and iodic acid as sources for the S⁶⁺ and I⁵⁺ cations introduced in titanium sites. The visible light activity, far superior to that of single S- or I-doped TiO₂, was ascribed to the strong absorption of light, the well-crystallized anatase phase, and the mesoporous structure (Yu 2010a).

The combination of two different halogens has shown to be another option for improving the photoactivity. For instance, Cl, Br–codoped nanomaterials have

been synthesized by addition of TiCl_4 to ethanol-containing HBr , and displayed a much higher photocatalytic activity than only chlorine- or bromine-doped TiO_2 (Luo et al. 2004). The same positive synergy has been observed in I–F–codoped titania. These photocatalysts have been prepared by a sol–gel impregnation method, using tetrabutyl orthotitanate in a mixed NH_4I – NH_4F aqueous solution (Wen et al. 2009).

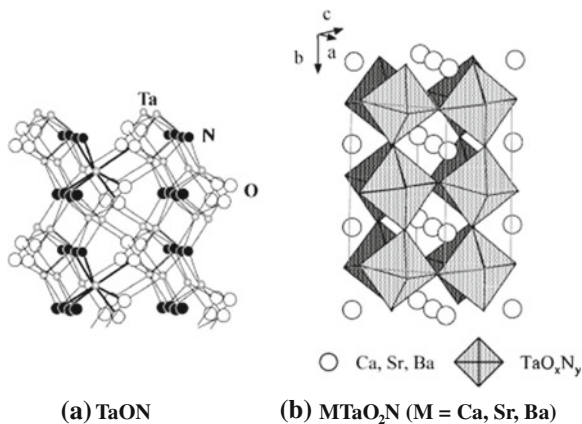
14.4.3 Non-metal/metalloid

The metalloid boron has been widely employed as codopant due to its similarity with the oxygen atom. For instance, F, B–codoped TiO_2 nanotubes have been obtained by chemical vapor deposition, where boron and fluorine impurities retarded the anatase to rutile transition and induced a remarkably strong absorption in both UV and visible ranges. The photoelectrocatalytic activity observed was higher than that of F-doped and B-doped samples (Su et al. 2007). The synergistic effect of N and B is unclear. It has been refused, for photocatalysts obtained via sequential reaction of BH_3 in THF with TiCl_4 (In 2007), and confirmed, for N, B–codoped TiO_2 obtained by either a one-step aerosol-assisted flow synthetic method (Ding et al. 2011) or a two-step hydrothermal process (Liu et al. 2008). In the latter case, it has been observed that the O–Ti–B–N structure formed on the surface of the photocatalyst is highly active in trapping and separating the charge carriers, thereby greatly enhancing the visible light photocatalytic activity. Another metalloid, silicon, has been employed as codopant in P, Si– TiO_2 nanoparticles. The nanoparticles were synthesized by a sol–gel method using tetraethylorthotitanite, tetraethylorthosilicate, and phosphoric acid as precursors, presenting enhanced thermal stability and photocatalytic activity (Yu 2010b).

14.5 Stoichiometric Nitrides and Oxynitrides

As it has been commented, the presence of anionic dopants in the titania matrix may induce a red shift and an increase in the light absorption. A number of anion-doped TiO_2 -based materials have proved to exhibit visible light photocatalytic activity for the degradation of multiple compounds and even disinfection. However, the activity should be further improved. The impurity levels created are usually discrete, which does not favor the charge transfer, and the oxygen vacancies can act as recombination centers. Especially for water splitting, the activity is still low, even though the conduction and valence bands of these materials may have adequate potentials for the reduction of H^+ to H_2 and the oxidation of water to O_2 . In contrast to what happens in doped materials, in oxynitrides or oxysulfides, the anion is a constituent element that forms the top of the valence band and the photogenerated charges can easily migrate. This advantage is particularly interesting for water splitting.

Fig. 14.5 Schematic structures of TaON and MTaO₂N (Yamasita et al. 2004). Figure reprinted with permission. Copyright Elsevier



Metal nitrides or oxynitrides of several transition metals may be obtained by introduction of nitrogen into the oxide network. The negative charge generated may be compensated by cationic substitutions. The structure of tantalum oxynitride is shown in Fig. 14.5.

The improvement in the synthesis method, so that the density of defects is reduced, is one of the present challenges to enhance the performance of these materials. The oxidation state of the metallic element in such photocatalysts is the highest, that is, Ti⁴⁺, Zr⁴⁺, Nb⁵⁺, Ta⁵⁺, or W⁶⁺ in the d⁰ group (with empty d orbitals), and Ga³⁺, In³⁺, Ge⁴⁺, Sn⁴⁺, or Sb⁵⁺ in the d¹⁰ group (with filled d orbitals). Oxynitride and oxysulfide photocatalysts having the ability to reduce and/or oxidize water under visible light usually contain d⁰ transition metal cations. In most of these catalysts, some N₂ evolution is observed in the initial stages of the photocatalytic reaction, indicating that the oxynitride is partially decomposed by the photogenerated holes, but the production of N₂ is suppressed as the reaction progresses (Maeda and Domen 2007). Nevertheless, the best expectations in the overall water-splitting research lay on oxynitrides and oxysulfides with d¹⁰ configurations. In these materials, the top of the valence band is composed of sp hybrid orbitals that possess large dispersion, facilitating the mobility of the photogenerated charges and, consequently, the photocatalytic activity. Among them, the most investigated is a solid solution of GaN and ZnO (Ga_{1-x}Zn_x) (N_{1-x}O_x) that, when loaded with an appropriate cocatalyst, has achieved a quantum efficiency of ca. 5.9 % at 420–440 nm in overall water splitting under visible light (Maeda et al. 2008).

Among the transition metals with empty d orbitals, tantalum has been the most researched for nitride and oxynitride photocatalysts. For instance, Ta₃N₅ has been prepared by nitridation of Ta₂O₅ or Ta metal particles, ammonolysis of TaCl₅ or TaS₂, or thermal decomposition of organic tantalum compounds (Yuliaty et al. 2010; Fischer et al. 2007). TaON, MTaO₂N (M = Ca, Sr, Ba), and LaTaON have been prepared by nitridation of the corresponding oxides. Under visible radiation, these oxynitrides, when loaded with Pt, show stable but low activity for H₂

evolution from a methanol solution; however, the photocatalytic activity can be improved by photodeposition of Ru nanoparticles. On the other hand, for TaN_3 and TaON , it was observed O_2 evolution using silver nitrate as electron acceptor, with activities about an order of magnitude higher than those obtained for H_2 evolution (Yamasita et al. 2004).

Ti is cheaper than Ta and most Ti-based oxides are able to evolve H_2 and O_2 under UV-A radiation. Furthermore, some of them photocatalyze the overall water-splitting reaction. As a consequence, several Ti-based nitrides and oxynitrides have been synthesized, being expected to present activity in the visible range. Nanoparticles of LaTiO_2N with perovskite structure, which has been observed to be indispensable for the photoreactivity of these materials, have been obtained by heat treatment of $\text{La}_2\text{Ti}_2\text{O}_7$ in an NH_3 flow. These oxynitrides have been tested for the decomposition of acetone and for H_2 and O_2 evolution under visible light (Kasahara et al. 2002; Aguiar et al. 2008). The high visible light absorption and the dependence of the evolution rate on the nitridation time are shown in Fig. 14.6. DFT calculations indicate that the top of the valence band consists predominantly of N 2p orbitals with a small contribution by O 2p orbitals, while the bottom of the conduction band is made up mainly of empty Ti 3d orbitals.

Some cation substitutions have been explored in Ti-based oxynitrides. For example, Ca^{2+} substitution in the aforementioned LaTiO_2N allowed the adsorption of IrO_2 as cocatalyst, otherwise not possible (Kasahara et al. 2002). The resulting $\text{Ca}_{0.25}\text{La}_{0.75}\text{TiO}_{2.25}\text{N}_{0.75}$ presented the same O_2 evolution rate as the non-substituted material, but the stability and activity were greatly enhanced in the presence of the cocatalyst. Another example is $\text{Sr}_{1-x}\text{La}_x\text{TiO}_{3-x}\text{N}_x$. This material displayed better activity for the photocatalytic oxidation of 2-propanol under UV and visible

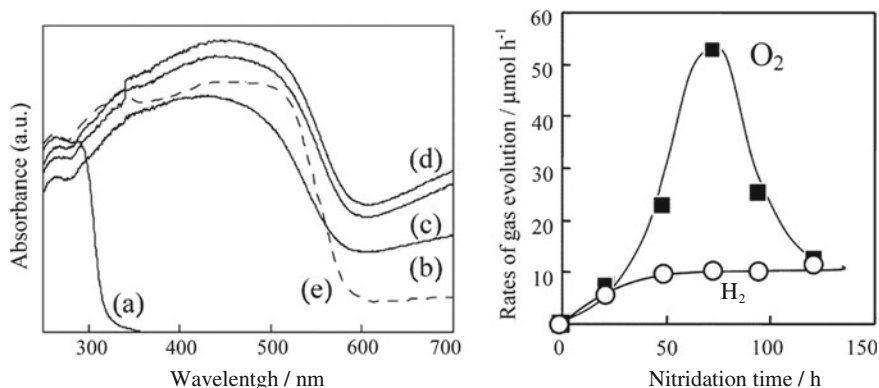


Fig. 14.6 On the left, UV-Vis DR spectra of **a** $\text{La}_2\text{Ti}_2\text{O}_7$, **b-d** LaTiO_2N obtained by nitridation at 1,123 K for 22, 48 and 72 h, and **e** sample **d** after heating in air at 573 K for 24 h. On the right, rates of evolution of H_2 , using Pt-coated LaTiO_2N in a methanol solution, and of O_2 , using LaTiO_2N and La_2O_3 in an AgNO_3 solution, as a function of the nitridation time (Kasahara et al. 2002). Copyright American Chemical Society

radiation than $\text{SrTiO}_{3-2x}\text{N}_x$. This effect was attributed to the lower number of oxygen vacancies and, therefore, lower recombination rate (Miyachi et al. 2003).

Similarly to oxynitrides, some Ti-based oxysulfides and oxyfluorides have deserved the researchers' attention. For instance, stable and active oxysulfides with the formula $\text{Ln}_2\text{Ti}_2\text{S}_2\text{O}_5$ (with Ln being a lanthanide: Pr, Nd, Sm, Gd, Tb, Dy, Ho, or Er) have been synthesized by sulfurization of the lanthanide titanate in a H_2S flow (Ishikawa et al. 2004). Among them, $\text{Sm}_2\text{Ti}_2\text{S}_2\text{O}_5$ was found to have the highest activity for O_2 evolution. All the oxysulfides presented a layered perovskite structure, distorted in the case of Pr, Nd, and Er.

References

- Aguiar R, Kalytta A, Reller A, Weidenkaff A, Ebbinghaus SG (2008) Photocatalytic decomposition of acetone using LaTi (O, N)₃ nanoparticles under visible light irradiation. *J Mater Chem* 18(36):4260–4265
- Asahi R, Morikawa T, Ohwaki T, Aoki K, Taga Y (2001) Visible-light photocatalysis in nitrogen-doped titanium oxides. *Science* 293(5528):269–271
- Bianchi CL, Cappelletti G, Arizzone S, Gialanella S, Naldoni A, Oliva C, Pirola C (2009) N-doped TiO_2 from TiCl_3 for photodegradation of air pollutants. *Catal Today* 144(1–2):31–36
- Chen D, Jiang Z, Geng J, Wang Q, Yang D (2007) Carbon and nitrogen co-doped TiO_2 with enhanced visible-light photocatalytic activity. *Ind Eng Chem Res* 46(9):2741–2746
- Cong Y, Zhang J, Chen F, Anpo M, He D (2007) Preparation, photocatalytic activity, and mechanism of nano- TiO_2 Co-Doped with nitrogen and iron (III). *J Phys Chem C* 111(28):10618–10623
- Di Valentin C, Pacchioni G, Selloni A (2005a) Theory of carbon doping of titanium dioxide. *Chem Mater* 17(26):6656–6665
- Di Valentin C, Pacchioni G, Selloni A, Livraghi S, Giamello E (2005b) Characterization of paramagnetic species in N-doped TiO_2 powders by EPR spectroscopy and DFT calculations. *J Phys Chem B* 109(23):11414–11419
- Di Valentin C, Finazzi E, Pacchioni G, Selloni A, Livraghi S, Czoska AM, Paganini MC, Giamello E (2008) Density functional theory and electron paramagnetic resonance study on the effect of N–F Codoping of TiO_2 . *Chem Mater* 20(11):3706–3714
- Ding X, Song X, Li P, Ai Z, Zhang L (2011) Efficient visible light driven photocatalytic removal of NO with aerosol flow synthesized B, N-codoped TiO_2 hollow spheres. *J Hazard Mater* 190(1–3):604–612
- Fischer A, Antonietti M, Thomas A (2007) Growth confined by the nitrogen source: synthesis of pure metal nitride nanoparticles in mesoporous graphitic carbon nitride. *Adv Mater* 19(2):264–267
- Gai Y, Li J, Li SS, Xia JB, Wei SH (2009) Design of narrow-gap TiO_2 : a passivated codoping approach for enhanced photoelectrochemical activity. *Phys Rev Lett* 102 (3)
- Geng H, Yin S, Yang X, Shuai Z, Liu B (2006) Geometric and electronic structures of the boron-doped photocatalyst TiO_2 . *J Phys: Condens Matter* 18(1):87–96
- Grey IE, Li C, MacRae CM, Bursill LA (1996) Boron incorporation into rutile. phase equilibria and structure considerations. *J Solid State Chem* 127 (2):240–247
- Gu D-E, Yang B-C, Hu Y-D (2008) V and N co-doped nanocrystal anatase TiO_2 photocatalysts with enhanced photocatalytic activity under visible light irradiation. *Catal Commun* 9(6):1472–1476

- Han C, Pelaez M, Likodimos V, Kontos AG, Falaras P, O'Shea K, Dionysiou DD (2011a) Innovative visible light-activated sulfur doped TiO₂ films for water treatment. *Appl Catal B* 107(1–2):77–87
- Han S, Guo S, Xiang W, Wang H, Yang L, Wang F (2011b) Discussion the influence of nonmetal doped TiO₂. *Adv Mater Res* 287–290:1771–1774
- Hattori A, Shimoda K, Tada H, Ito S (1999) Photoreactivity of Sol-Gel TiO₂ films formed on soda-lime glass substrates: effect of SiO₂ underlayer containing fluorine. *Langmuir* 15(16):5422–5425
- He Z, Xu X, Song S, Xie L, Tu J, Chen J, Yan B (2008) A visible light-driven titanium dioxide photocatalyst codoped with lanthanum and iodine: an application in the degradation of oxalic acid. *J Phys Chem C* 112(42):16431–16437
- He Z, Zhan L, Hong F, Song S, Lin Z, Chen J, Jin M (2011) A visible light-responsive iodine-doped titanium dioxide nanosphere. *J Environ Sci* 23(1):166–170
- Hong X, Wang Z, Cai W, Lu F, Zhang J, Yang Y, Ma N, Liu Y (2005) Visible-light-activated nanoparticle photocatalyst of iodine-doped titanium dioxide. *Chem Mater* 17(6):1548–1552
- Ihara T, Miyoshi M, Iriyama Y, Matsumoto O, Sugihara S (2003) Visible-light-active titanium oxide photocatalyst realized by an oxygen-deficient structure and by nitrogen doping. *Appl Catal B* 42(4):403–409
- In S, Orlov A, Berg R, García F, Pedrosa-Jimenez S, Tikhov MS, Wright DS, Lambert RM (2007) Effective visible light-activated B-doped and B, N-Codoped TiO₂ photocatalysts. *J Am Chem Soc* 129(45):13790–13791
- Irie H, Watanabe Y, Hashimoto K (2003a) Carbon-doped Anatase TiO₂ Powders as a visible-light sensitive photocatalyst. *Chem Lett* 32(8):772–773
- Irie H, Watanabe Y, Hashimoto K (2003b) Nitrogen-concentration dependence on photocatalytic activity of TiO_{2-x} powders. *J Phys Chem B* 107(23):5483–5486
- Ishikawa A, Takata T, Matsumura T, Kondo JN, Hara M, Kobayashi H, Domen K (2004) Oxysulfides Ln₂Ti₂S₂O₅ as stable photocatalysts for water oxidation and reduction under visible-light irradiation. *J Phys Chem B* 108(8):2637–2642
- Jiang X, Yang L, Liu P, Li X, Shen J (2010) The photocatalytic and antibacterial activities of neodymium and iodine doped TiO₂ nanoparticles. *Colloids Surf B: Biointerfaces* 79(1):69–74
- Kasahara A, Nukumizu K, Takata T, Kondo JN, Hara M, Kobayashi H, Domen K (2002) LaTiO₂N as a visible-light (≤600 nm)-driven photocatalyst (2). *J Phys Chem B* 107(3):791–797
- Khan SUM, Al-Shahry M, Jr WBI (2002) Efficient photochemical water splitting by a chemically modified n-TiO₂. *Science* 297(5590):2243–2245
- Kubacka A, Bachiller-Baeza Bn, Colón G, Fernández-García M (2009) W, N-Codoped TiO₂-anatase: a sunlight-operated catalyst for efficient and selective aromatic hydrocarbons photo-oxidation. *J Phys Chem C* 113(20):8553–8555
- Leary R, Westwood A (2011) Carbonaceous nanomaterials for the enhancement of TiO₂ photocatalysis. *Carbon* 49(3):741–772
- Li D, Haneda H, Hishita S, Ohashi N (2005a) Visible-light-driven NF-Codoped TiO₂ photocatalysts. 1. synthesis by spray pyrolysis and surface characterization. *Chem Mater* 17(10):2588–2595
- Li D, Haneda H, Hishita S, Ohashi N (2005b) Visible-light-driven NF-Codoped TiO₂ photocatalysts. 2. optical characterization, photocatalysis, and potential application to air purification. *Chem Mater* 17(10):2596–2602
- Li D, Haneda H, Hishita S, Ohashi N, Labhsetwar NK (2005c) Fluorine-doped TiO₂ powders prepared by spray pyrolysis and their improved photocatalytic activity for decomposition of gas-phase acetaldehyde. *J Fluorine Chem* 126(1):69–77
- Li Y, Wang W, Qiu X, Song L, Meyer III HM, Paranthaman MP, Eres G, Zhang Z, Gu B (2011) Comparing Cr, and N only doping with (Cr, N)-codoping for enhancing visible light reactivity of TiO₂. *Appl Catal B* 110:148–153
- Lin L, Lin W, Zhu Y, Zhao B, Xie Y (2005) Phosphor-doped titania—a novel photocatalyst active in visible light. *Chem Lett* 34(3):284–285

- Lin L, Lin W, Xie JL, Zhu YX, Zhao BY, Xie YC (2007) Photocatalytic properties of phosphor-doped titania nanoparticles. *Appl Catal B* 75(1–2):52–58
- Liu G, Zhao Y, Sun C, Li F, Lu GQ, Cheng H-M (2008) Synergistic effects of B/N doping on the visible-light photocatalytic activity of mesoporous TiO₂. *Angew Chem Int Ed* 47(24):4516–4520
- Liu G, Wang L, Yang HG, Cheng H-M, Lu GQ (2010) Titania-based photocatalysts-crystal growth, doping and heterostructuring. *J Mater Chem* 20(5):831–843
- Livraghi S, Paganini MC, Giamello E, Selloni A, Di Valentin C, Pacchioni G (2006) Origin of photoactivity of nitrogen-doped titanium dioxide under visible light. *J Am Chem Soc* 128(49):15666–15671
- Long R, English NJ (2010a) First-principles calculation of synergistic (N, P)-codoping effects on the visible-light photocatalytic activity of anatase TiO₂. *J Phys Chem C* 114(27):11984–11990
- Long R, English NJ (2010b) Synergistic effects on band gap-narrowing in titania by codoping from first-principles calculations. *Chem Mater* 22(5):1616–1623
- Long M, Cai W, Chen H, Xu J (2007) Preparation, characterization and photocatalytic activity of visible light driven chlorine-doped TiO₂. *Front Chem China* 2(3):278–282
- Long R, Dai Y, Huang B (2009) Structural and electronic properties of iodine-doped anatase and rutile TiO₂. *Comput Mater Sci* 45(2):223–228
- Luo H, Takata T, Lee Y, Zhao J, Domen K, Yan Y (2004) Photocatalytic activity enhancing for titanium dioxide by Co-doping with bromine and chlorine. *Chem Mater* 16(5):846–849
- Ma X, Wu Y, Lu Y, Xu J, Wang Y, Zhu Y (2011) Effect of compensated codoping on the photoelectrochemical properties of anatase TiO₂ photocatalyst. *J Phys Chem C* 115(34):16963–16969
- Maeda K, Domen K (2007) New non-oxide photocatalysts designed for overall water splitting under visible light. *J Phys Chem C* 111(22):7851–7861
- Maeda K, Teramura K, Domen K (2008) Effect of post-calcination on photocatalytic activity of (Ga_{1-x}Zn_x)(N_{1-x}O_x) solid solution for overall water splitting under visible light. *J Catal* 254(2):198–204
- Maeda K, Lee B, Lu D, Domen K (2009) Physicochemical effects on photocatalytic water oxidation by titanium fluorooxynitride powder under visible light. *Chem Mater* 21(11):2286–2291
- Minero C, Mariella G, Maurino V, Pelizzetti E (2000) Photocatalytic transformation of organic compounds in the presence of inorganic anions. 1. hydroxyl-mediated and direct electron-transfer reactions of phenol on a titanium dioxide—fluoride system. *Langmuir* 16(6):2632–2641
- Miyauchi M, Takashio M, Tobimatsu H (2003) Photocatalytic activity of SrTiO₃ codoped with nitrogen and lanthanum under visible light illumination. *Langmuir* 20(1):232–236
- Murphy AB (2008) Does carbon doping of TiO₂ allow water splitting in visible light? Comments on “Nanotube enhanced photoresponse of carbon modified (CM)-n-TiO₂ for efficient water splitting”. *Sol Energy Mater Sol Cells* 92(3):363–367
- Nukumizu K, Nunoshige J, Takata T, Kondo JN, Hara M, Kobayashi H, Domen K (2003) Ti_{Nx}O_yF_z as a stable photocatalyst for water oxidation in visible light (<570 nm). *Chem Lett* 32(2):196–197
- Ohno T, Mitsui T, Matsumura M (2003) Photocatalytic activity of S-doped TiO₂ photocatalyst under visible light. *Chem Lett* 32(4):364–365
- Ohno T, Akiyoshi M, Umebayashi T, Asai K, Mitsui T, Matsumura M (2004) Preparation of S-doped TiO₂ photocatalysts and their photocatalytic activities under visible light. *Appl Catal A* 265(1):115–121
- Pan C-C, Wu JCS (2006) Visible-light response Cr-doped TiO₂-XNX photocatalysts. *Mater Chem Phys* 100(1):102–107
- Park JH, Kim S, Bard AJ (2005) Novel carbon-doped TiO₂ nanotube arrays with high aspect ratios for efficient solar water splitting. *Nano Lett* 6(1):24–28
- Peichang D, Jiezhen H, Haizeng W, Baowei S (2010) Hydrothermal preparation and comparative study of halogen-doping TiO₂ photocatalysts. *J Adv Oxid Technol* 13(2):200–205

- Peng Y, He J, Liu Q, Sun Z, Yan W, Pan Z, Wu Y, Liang S, Cheng W, Wei S (2011) Impurity concentration dependence of optical absorption for phosphorus-doped anatase TiO₂. *J Phys Chem C* 115(16):8184–8188
- Qu X-G, Liu W-X, Ma J, Cao W (2009) Research on photodegradation of formaldehyde by nanocrystalline N-TiO₂ powders under visible light irradiation. *Res Chem Intermed* 35(3):313–320
- Saha NC, Tompkins HG (1992) Titanium nitride oxidation chemistry: an x-ray photoelectron spectroscopy study. *J Appl Phys* 72(7):3072–3079
- Sakthivel S, Kisch H (2003) Daylight photocatalysis by carbon-modified titanium dioxide. *Angew Chem-Int Edit* 42(40):4908–4911
- Serpone N (2006) Is the band gap of pristine TiO₂ narrowed by anion- and cation-doping of titanium dioxide in second-generation photocatalysts? *J Phys Chem B* 110(48):24287–24293
- Shen M, Wu Z, Huang H, Du Y, Zou Z, Yang P (2006) Carbon-doped anatase TiO₂ obtained from TiC for photocatalytic under visible light irradiation. *Mater Lett* 60(5):693–697
- Sheng YG, Liu HY, Luo L, Ren BY (2011) Sol-gel preparation of visible-light-driven N-halogen-codoped TiO₂ photocatalysts. *Gongneng Cailiao/Journal of Functional Materials* 42 (SUPPL. JUNE):497–501
- Shi Q, Yang D, Jiang Z, Li J (2006) Visible-light photocatalytic regeneration of NADH using P-doped TiO₂ nanoparticles. *J Mol Catal B Enzym* 43(1–4):44–48
- Shinri S (1986) Photocatalytic activity of NO_x-doped TiO₂ in the visible light region. *Chem Phys Lett* 123(1–2):126–128
- Shu Y, Yamaki H, Zhang QW, Komatsu M, Wang JS, Qing T, Saito F, Sato T (2004) Mechanochemical synthesis of nitrogen-doped titania and its visible light induced NO_x destruction ability. *Solid State Ionics* 172(1–4):205–209
- Song S, Tu J, Xu L, Xu X, He Z, Qiu J, Ni J, Chen J (2008) Preparation of a titanium dioxide photocatalyst codoped with cerium and iodine and its performance in the degradation of oxalic acid. *Chemosphere* 73(9):1401–1406
- Song S, Tu J, He Z, Hong F, Liu W, Chen J (2010) Visible light-driven iodine-doped titanium dioxide nanotubes prepared by hydrothermal process and post-calcination. *Appl Catal A* 378(2):169–174
- Song S, Hong F, He Z, Wang H, Xu X, Chen J (2011a) Influence of zirconium doping on the activities of zirconium and iodine co-doped titanium dioxide in the decolorization of methyl orange under visible light irradiation. *Appl Surf Sci* 257(23):10101–10108
- Song S, Wang C, Hong F, He Z, Cai Q, Chen J (2011b) Gallium- and iodine-co-doped titanium dioxide for photocatalytic degradation of 2-chlorophenol in aqueous solution: Role of gallium. *Appl Surf Sci* 257(8):3427–3432
- Su Y, Zhang X, Han S, Chen X, Lei L (2007) F-B-codoping of anodized TiO₂ nanotubes using chemical vapor deposition. *Electrochem Commun* 9(9):2291–2298
- Su W, Zhang Y, Li Z, Wu L, Wang X, Li J, Fu X (2008) Multivalency iodine doped TiO₂: preparation, characterization, theoretical studies, and visible-light photocatalysis. *Langmuir* 24(7):3422–3428
- Subagio DP, Srinivasan M, Lim M, Lim T–T (2010) Photocatalytic degradation of bisphenol-A by nitrogen-doped TiO₂ hollow sphere in a vis-LED photoreactor. *Appl Catal B* 95(3–4):414–422
- Subbarao SN, Yun YH, Kershaw R, Dwight K, Wold A (1979) Electrical and optical properties of the system TiO₂–xFx. *Inorg Chem* 18(2):488–492
- Sun H, Bai Y, Cheng Y, Jin W, Xu N (2006) Preparation and characterization of visible-light-driven carbon-sulfur-codoped TiO₂ photocatalysts. *Ind Eng Chem Res* 45(14):4971–4976
- Tachikawa T, Tojo S, Kawai K, Endo M, Fujitsuka M, Ohno T, Nishijima K, Miyamoto Z, Majima T (2004) Photocatalytic oxidation reactivity of holes in the sulfur- and carbon-doped TiO₂ powders studied by time-resolved diffuse reflectance spectroscopy. *J Phys Chem B* 108(50):19299–19306
- Tang X, Li D (2008) Sulfur-doped highly ordered TiO₂ nanotubular arrays with visible light response. *J Phys Chem C* 112(14):5405–5409

- Tojo S, Tachikawa T, Fujitsuka M, Majima T (2008) Iodine-doped TiO₂ photocatalysts: correlation between band structure and mechanism. *J Phys Chem C* 112(38):14948–14954
- Umebayashi T, Yamaki T, Itoh H, Asai K (2002) Band gap narrowing of titanium dioxide by sulfur doping. *Appl Phys Lett* 81(3):454–456
- Wang Y, Huang Y, Ho W, Zhang L, Zou Z, Lee S (2009) Biomolecule-controlled hydrothermal synthesis of C-N-S-tridoped TiO₂ nanocrystalline photocatalysts for NO removal under simulated solar light irradiation. *J Hazard Mater* 169(1–3):77–87
- Wen C, Zhu YJ, Kanbara T, Zhu HZ, Xiao CF (2009) Effects of I and F codoped TiO₂ on the photocatalytic degradation of methylene blue. *Desalination* 249(2):621–625
- Wu G, Wang J, Thomas DF, Chen A (2008) Synthesis of F-doped flower-like TiO₂ nanostructures with high photoelectrochemical activity. *Langmuir* 24(7):3503–3509
- Xiong L, Zheng L, Xu J, Zheng D, Li J, Li X, Sun J, Liu Q, Niu L, Yang S, Xia J (2011) Photocatalytic degradation of phenol with mesoporous TiO_{2-x}Bx. *Environ Chem Lett* 9(2):251–257
- Xu H, Zheng Z, Zhang L, Zhang H, Deng F (2008a) Hierarchical chlorine-doped rutile TiO₂ spherical clusters of nanorods: large-scale synthesis and high photocatalytic activity. *J Solid State Chem* 181(9):2516–2522
- Xu J-H, Li J, Dai W-L, Cao Y, Li H, Fan K (2008b) Simple fabrication of twist-like helix N, S-codoped titania photocatalyst with visible-light response. *Appl Catal B* 79(1):72–80
- Yamaki T, Sumita T, Yamamoto S (2002) Formation of TiO_{2-x}Fx compounds in fluorine-implanted TiO₂. *J Mater Sci Lett* 21(1):33–35
- Yamasita D, Takata T, Hara M, Kondo JN, Domen K (2004) Recent progress of visible-light-driven heterogeneous photocatalysts for overall water splitting. *Solid State Ionics* 172(1–4):591–595
- Yang K, Dai Y, Huang B, Whangbo MH (2008) Density functional characterization of the band edges, the band gap states, and the preferred doping sites of halogen-doped TiO₂. *Chem Mater* 20(20):6528–6534
- Yu H-F, Yang S-T (2010b) Enhancing thermal stability and photocatalytic activity of anatase-TiO₂ nanoparticles by co-doping P and Si elements. *J Alloys Compd* 492(1–2):695–700
- Yu JC, Yu J, Ho W, Jiang Z, Zhang L (2002) Effects of F-doping on the photocatalytic activity and microstructures of nanocrystalline TiO₂ powders. *Chem Mater* 14(9):3808–3816
- Yu JC, Zhang L, Zheng Z, Zhao J (2003) Synthesis and characterization of phosphated mesoporous titanium dioxide with high photocatalytic activity. *Chem Mater* 15(11):2280–2286
- Yu JC, Ho W, Yu J, Yip H, Wong PK, Zhao J (2005) Efficient visible-light-induced photocatalytic disinfection on sulfur-doped nanocrystalline titania. *Environ Sci Technol* 39(4):1175–1179
- Yu J, Zhou M, Cheng B, Zhao X (2006) Preparation, characterization and photocatalytic activity of in situ N, S-codoped TiO₂ powders. *J Mol Catal A: Chem* 246(1–2):176–184
- Yu H-F, Zhang Z-W, Hu F-C (2008) Phase stabilities and photocatalytic activities of P/Zn-TiO₂ nanoparticles able to operate under UV-vis light irradiation. *J Alloys Compd* 465(1–2):484–490
- Yu C, Cai D, Yang K, Yu JC, Zhou Y, Fan C (2010a) Sol-gel derived S, I-codoped mesoporous TiO₂ photocatalyst with high visible-light photocatalytic activity. *J Phys Chem Solids* 71(9):1337–1343
- Yuliati L, Yang J-H, Wang X, Maeda K, Takata T, Antonietti M, Domen K (2010) Highly active tantalum (v) nitride nanoparticles prepared from a mesoporous carbon nitride template for photocatalytic hydrogen evolution under visible light irradiation. *J Mater Chem* 20(21):4295–4298
- Zaleska A, Grabowska E, Sobczak JW, Gazda M, Hupka J (2009) Photocatalytic activity of boron-modified TiO₂ under visible light: the effect of boron content, calcination temperature and TiO₂ matrix. *Appl Catal B* 89(3–4):469–475
- Zhang Q, Wang J, Yin S, Sato T, Saito F (2004) Synthesis of a visible-light active TiO_{2-x}Sx photocatalyst by means of mechanochemical doping. *J Am Ceram Soc* 87(6):1161–1163

- Zhang J, Pan C, Fang P, Wei J, Xiong R (2010) Mo + C Codoped TiO₂ using thermal oxidation for enhancing photocatalytic activity. *ACS Appl Mater Interfaces* 2(4):1173–1176
- Zhao W, Ma W, Chen C, Zhao J, Shuai Z (2004) Efficient degradation of toxic organic pollutants with Ni₂O₃/TiO_{2-x}B_x under visible irradiation. *J Am Chem Soc* 126(15):4782–4783
- Zhou M, Yu J (2008) Preparation and enhanced daylight-induced photocatalytic activity of C, N, S-tridoped titanium dioxide powders. *J Hazard Mater* 152(3):1229–1236
- Zhou L, Tan X, Zhao L, Sun M (2007) Photocatalytic degradation of NO_x over platinum and nitrogen codoped titanium dioxide under visible light irradiation. *Collect Czech Chem Commun* 72(3):379–391
- Zhu WG, Qiu XF, Iancu V, Chen XQ, Pan H, Wang W, Dimitrijevic NM, Rajh T, Meyer HM, Paranthaman MP, Stocks GM, Weiering HH, Gu BH, Eres G, Zhang ZY (2009) Band gap narrowing of titanium oxide semiconductors by non-compensated anion-cation codoping for enhanced visible-light photoactivity. *Phys Rev Lett* 103:226401
- Zhu ZF, Zhou JQ, He ZL, Li JQ, Liu H (2011) Preparation, characterisation and activity of TiO₂-x F_x spherical photocatalyst: influence of sodium fluoride on methyl orange degradation. *Mater Res Innovations* 15(2):78–82

Chapter 15

Heterojunctions: Joining Different Semiconductors

Fernando Fresno

Coupling different semiconductors is one of the strategies that have been successfully followed in order to obtain more active photocatalysts. Differently to the case of doping described in Chaps. 13 and 14, here we will concentrate on materials composed of clearly distinct crystalline phases and, especially on the role of the interface between these different phases, which is the feature that characterizes this type of systems and provides improved photocatalytic (and other) properties. As it has been highlighted throughout this book regarding most aspects of photocatalysis, TiO₂-based coupled systems are by far the most studied ones, and hence, they will be covered to a higher extent. A special case of these systems would be represented by quantum dots, which will be described in the following chapter.

15.1 The Electronic Characteristic of Heterojunctions

Coupling between different semiconductors in photocatalytic systems was designed to alleviate the charge carrier recombination. This is the main process invoked to lead to improved photocatalytic activity in composite semiconductors, although other factors that will be mentioned in specific examples may also play an important role. Provided that the relative energies of the bands and the contact between the two components are adequate, the junction between the two semiconductors may lead to the physical separation of the photogenerated charge carriers (Carp et al. 2004; Zhang et al. 2009). This process implies the formation of a p–n junction, analogous to those established in photovoltaic cells, in which the energy gap between corresponding band levels drives the charge carrier from one phase to the other. These junctions imply the equilibration of the Fermi levels. In this way, electrons migrate from the most energetic conduction band to the less

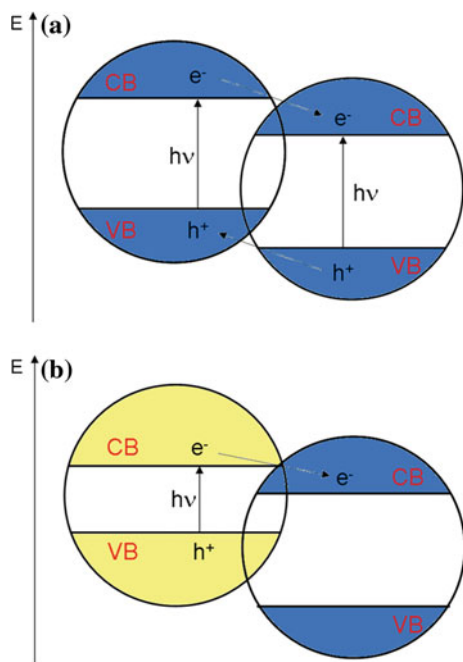
F. Fresno (✉)

Laboratory for Environmental Research, University of Nova Gorica, Nova Gorica, Slovenia
e-mail: fernando.fresno@ung.si

energetic one, while, conversely, holes formally move from the lower valence band to the higher energy one. This process is schematically depicted in Fig. 15.1. Two different cases can be distinguished: (a) both components are excited (Fig. 15.1a), or (b) only one semiconductor is excited and the second is not (Fig. 15.1b). When both semiconductors are excited, a vectorial transfer of electrons and holes from one semiconductor to another occurs: electrons accumulate at the lower-lying conduction band of one semiconductor, while the holes accumulate at the valence band of the other one. In the second case, an electron photo-generated on the activated semiconductor with a more negative conduction band is injected into the conduction band of the non-excited semiconductor, while the hole remains on the former one. This yields vectorial electron transfer, which is irreversible under certain conditions. In both cases, the physical separation of charges is expected to diminish the recombination rate and thus improve photocatalytic performance by increasing the lifetime of charge carriers. This approach may be also employed for sensitization of a wide band gap photocatalyst towards the visible light region by coupling it with a visible light-sensitive semiconductor. The possible semiconductor combinations and their mode of coupling can therefore be predicted from their band energies or potentials. The band schemes corresponding to some common semiconductors can be seen in Fig. 2.11.

Regarding the geometric aspects of coupled semiconductors, different configurations have been approached. In an “external” coupling, both components are exposed at the surface, while “core-shell” configurations consist of one

Fig. 15.1 Charge separation in coupled semiconductors with (a) both components excited and (b) only one component excited



semiconductor phase surrounding the particles of the second one. In addition, alternating layers of the single components have been also employed, which, if carefully controlled synthesis conditions are obtained, may also lead to both semiconductors exposed to the surface in a “patterned” configuration. Size effects must also be taken into account since, as seen in [Chap. 11](#), crystal size influences the electronic states of semiconductors through confinement effects. Thus, the adequate relative positions of the single semiconductors may depend on their crystallite sizes and, moreover, may be tuned by means of size control.

The interparticle electron transfer was first reported by Serpone et al. (1984) from improved splitting of water in the presence of hydrogen sulphide by CdS/TiO₂ colloids. The current understanding of the electronic mechanisms of this process, however, is far from complete (Kubacka et al. 2012), and other factors than relative band positions may affect the efficiency of coupled photocatalysts, such as surface area, defect density, crystallinity and quantum size effects (Zhang et al. 2009). In addition, the surface contact between the single components is strongly dependent on the preparation method. In any case, charge separation has been experimentally proved by several techniques. Particularly, an elegant experiment of Ag photodeposition followed by SEM observation was used by Tada and co-workers (Tada et al. 2000) to demonstrate the electron migration from TiO₂ to SnO₂ in patterned bilayer photocatalysts. [Figure 15.2](#) shows images of the patterned TiO₂/SnO₂/glass photocatalyst after the photodeposition experiment. [Figure 15.2a](#) is a SEM image after illumination. An X-ray image of Ti in the same region ([Fig. 15.2b](#)) reveals that the zone on the left (light area) is covered with TiO₂, and the SnO₂ layer is exposed on the right (dark area). An X-ray image of Ag in the same region ([Fig. 15.2c](#)) demonstrates the preferential deposition of Ag particles on the surface of SnO₂. Comparison of [Fig. 15.2c](#) and [d](#) (X-ray image of non-patterned TiO₂/SnO₂/glass after photodeposition) indicates that the patterning effect also enhances the photodeposition of Ag. These data show that most of the excited electrons generated by the band gap transition of TiO₂ flow towards the conduction band of SnO₂, as depicted in [Fig. 15.1](#), where they are consumed by the reduction process. These experiments were also employed to prove a similar charge separation in patterned TiO₂(anatase)/TiO₂(rutile) bilayer photocatalysts (Kawahara et al. 2002), as mentioned in [Chap. 5](#). Also in the TiO₂/SnO₂ system, time-resolved photocharge measurements demonstrated the presence of a contact potential between the two semiconductors, which leads to a flow of photoelectrons towards the SnO₂/TiO₂ interface (Levy et al. 1997). Accordingly, the incident photon-to-current efficiencies (IPCE) in coupled electrodes are higher than those obtained with the single components (Vinodgopal et al. 1996). In addition, improved charge separation has been demonstrated by means of laser flash photolysis experiments (Gopidas et al. 1990; Bedja and Kamat 1995), while EPR spectra have shown the formation of Ti³⁺ centres in visible light-irradiated CdS/TiO₂ samples, which demonstrates the mechanism depicted in [Fig. 15.1b](#) (Wu et al. 2006).

Finally, not only the electronic issue of charge separation has been invoked to explain the higher performance, but also surface modifications such as increased surface acidity and different water adsorption properties have been reported. The

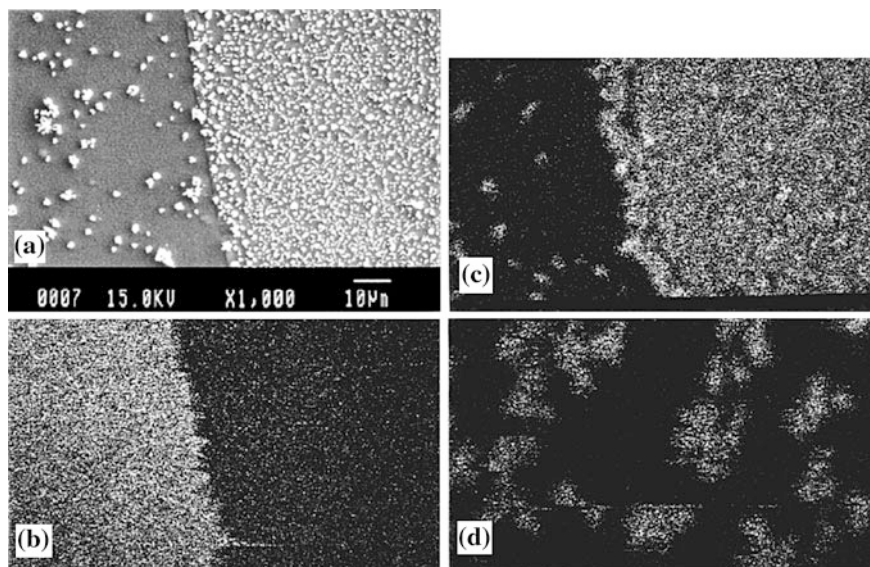


Fig. 15.2 **a** SEM micrograph of patterned $\text{TiO}_2/\text{SnO}_2/\text{glass}$ after Ag photodeposition. **b** X-ray image of Ti for the same region as **(a)**. **c** X-ray image of Ag for the same region as **(a)**. **d** X-ray image of Ag for $\text{TiO}_2/\text{SnO}_2/\text{glass}$. Reproduced with permission from Tada et al. (2000). Copyright American Chemical Society

former is a critical point in catalytic processes since it directly affects the adsorption of the reactant molecules. In the particular case of photocatalysis, the modification of the surface water may also play a key role in the photocatalytic activity of the final material (Soria et al. 2010). The following sections describe specific examples of the use of coupled systems in photocatalysis.

15.2 Coupling of Oxides

15.2.1 The $\text{TiO}_2(\text{anatase})/\text{TiO}_2(\text{rutile})$ System

As already mentioned in Chap. 5, the two most commonly used polymorphs of TiO_2 , anatase and rutile, present different electronic structures as a result of the different arrangements of the TiO_6 octahedra. Thus, both the valence and conduction bands of rutile have lower energy than those of anatase, in such a way that a heterojunction like that described in Fig. 15.1a is possible to occur. Interestingly, this heterojunction occurs in the still benchmark TiO_2 photocatalyst P25, a material with the anatase and rutile crystalline phases. Charge separation due to the heterojunctions formed between these two phases has been invoked to explain the high activity of this commercial catalyst (Bickley et al. 1991; Ohno et al. 2003). In

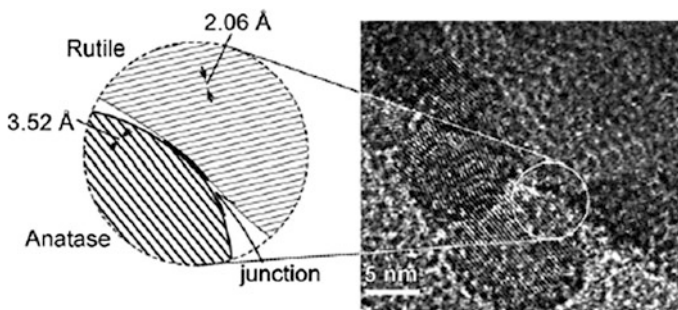


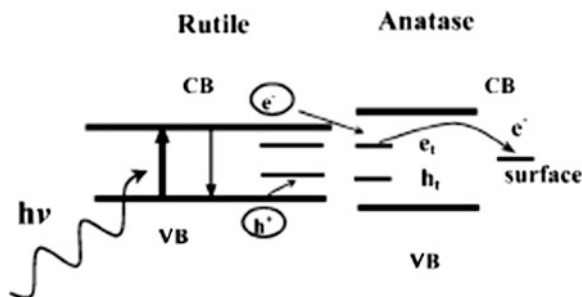
Fig. 15.3 Junction structure formed between the anatase and rutile phases of TiO_2 in a composite sample. Reproduced with permission from Zhang et al. (2008). Copyright Wiley-VCH

P25, anatase nanocrystals are supported on larger rutile ones, and specific structural features exist at a narrow interface layer, with different characteristics than those found in the bulk of both phases (Kubacka et al. 2012). Direct evidence of the formation of an anatase–rutile junction in an anatase–rutile composite system has been obtained by HRTEM (Zhang et al. 2008), as shown in Fig. 15.3.

As mentioned in the preceding section, charge separation in the anatase–rutile junction was demonstrated by SEM observation of a patterned $\text{TiO}_2(\text{anatase})/\text{TiO}_2(\text{rutile})$ photocatalyst after silver photodeposition from aqueous AgNO_3 (Kawahara et al. 2002). Revealing the different photoactivities of both phases separately, Ag particles are scarcely observed on the rutile section of the photocatalyst in low magnification images (see Fig. 5.4). However, the situation is reversed in the interface region, where deposition preferentially occurs on the rutile layer. From these data, the diffusion length of electrons across the phase boundary has been estimated at 10 nm, which is in fairly good accordance with that calculated from their mobility and lifetime in TiO_2 . Possessing a band gap at the limit between UV and visible light regions, rutile has also been proposed as a photon “antenna” leading to visible light activity by charge injection (Hurum et al. 2003). According to this model, the presence of small rutile crystallites would create a structure where rapid electron transfer from rutile to lower energy anatase lattice trapping sites would lead to a more stable charge separation under visible illumination. Transfer of the photogenerated electron to the anatase lattice trapping sites would allow holes that would have been lost in recombination to reach the surface. Subsequent electron transfer would move the electron from anatase trapping sites to surface trapping sites, further separating the electron/hole pair (Fig. 15.4). Another proposed model is based on the band gap variation in the connected nanocrystallites as a function of the size distribution (Zachariah et al. 2008).

A superior photocatalytic activity of $\text{TiO}_2(\text{anatase})/\text{TiO}_2(\text{rutile})$ photocatalysts with respect to the sole anatase phase has been reported in many works. However, other factors than charge separation must be taken into account given that some anatase samples have shown higher photocatalytic activity than P25 in the same conditions (Fresno et al. 2005; Ohtani 2010). As in any composite system, an

Fig. 15.4 Proposed photon “antenna” mechanism for anatase–rutile junctions under visible light irradiation. Reproduced with permission from Hurum et al. (2003). Copyright American Chemical Society



optimum anatase-to-rutile ratio is expected to achieve maximum photocatalytic activity. This ratio, however, must be strongly dependent on the extent of the contact between the different phases and hence on the preparation method, and considerably different figures regarding this issue can be found in the literature (Kubacka et al. 2012). These considerations point out to the need of additional studies to confirm these aspects and to further define the details of the electronic interactions between TiO_2 phases.

15.2.2 $\text{TiO}_2/\text{SnO}_2$ Photocatalysts

As mentioned in Chap. 6, SnO_2 is generally considered a poor photocatalyst. However, it has been quite extensively used in coupled systems in combination with TiO_2 (Zhang et al. 2009; Tudela et al. 2010). Since both the conduction and valence bands in SnO_2 are lower in energy than the corresponding ones in TiO_2 , a junction like that described in Fig. 15.1a may occur provided that the contact between the two phases is adequate. As described in the first section of this chapter, charge separation in the $\text{TiO}_2/\text{SnO}_2$ system has been demonstrated with different techniques. This mechanism has led to improved photocatalytic activity for different reactions with respect to the single phases, especially when an external bias potential is applied. Consistently with the vectorial charge carrier transfer model, photoelectrocatalytic oxidation reactions have been shown to be more efficient over $\text{TiO}_2/\text{SnO}_2$ electrodes than on pure TiO_2 , while the opposite effect is found for reduction processes. For the preparation of $\text{TiO}_2/\text{SnO}_2$ photocatalysts, several synthetic procedures have been followed, including sol–gel, co-hydrolysis, and chemical vapour deposition among others (Tudela et al. 2010). Using these methods, different configurations can be obtained, exerting a strong influence on the behaviour of the material. For instance, patterning alternate layers of TiO_2 and SnO_2 , with both semiconductors exposed to the surface, as shown in Fig. 15.5, seem to positively influence the photocatalytic performance with respect to a simple bilayer system (Kawahara et al. 2001).

In most of the $\text{TiO}_2/\text{SnO}_2$ composites used in photocatalysis, TiO_2 is found to be in the anatase phase, while SnO_2 crystallizes with the rutile-type cassiterite

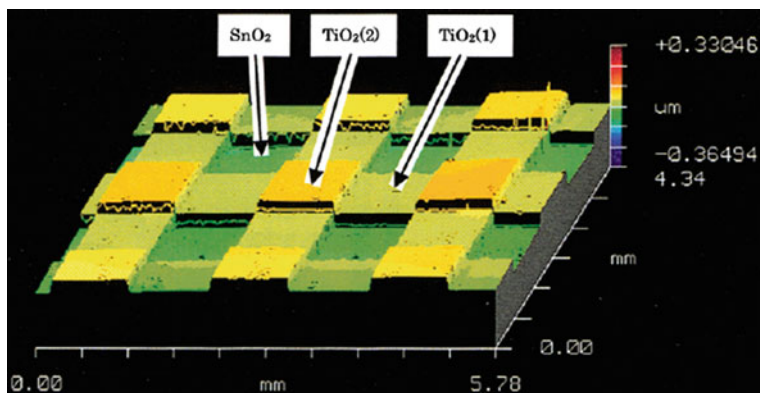


Fig. 15.5 Three-dimensional imaging surface structure of a cross-patterned $\text{TiO}_2/\text{SnO}_2$ film. Reproduce with permission from Kawahara et al. (2001). Copyright American Chemical Society

structure. In these systems, concentration depth profiles reveal that the percentage of Sn atoms start to increase at the same position that Ti begins to increase, revealing the existence of an interface layer between TiO_2 and SnO_2 , similarly to the case of anatase/rutile catalysts.

The performance of $\text{TiO}_2/\text{SnO}_2$ photocatalysts has been tested in both gas and liquid phase reactions, not only in pure photocatalytic but also in electrochemically assisted photocatalytic systems. Thus, the photoelectrocatalytic degradation of the acid orange 7, naphthol blue black and methylene blue dyes on $\text{TiO}_2/\text{SnO}_2$ photoanodes has been satisfactorily carried out, with disappearance rates considerably higher than those obtained with TiO_2 or SnO_2 alone (Vinodgopal et al. 1996). In pure photocatalytic processes, several molecules like methanol, formic acid, phenol and different dyes have been used for testing the improved activity of $\text{TiO}_2/\text{SnO}_2$ samples for the degradation of aqueous pollutants. Furthermore, aldehydes, isopropanol and benzene, for instance, have been degraded in the gas phase over these mixed systems with increased rates with regard to TiO_2 (Tudela et al. 2010). Compared to other coupled systems like $\text{TiO}_2(\text{anatase})/\text{TiO}_2(\text{rutile})$ and WO_3/TiO_2 , $\text{TiO}_2/\text{SnO}_2$ photocatalysts have shown a superior performance. This may be related to the long separation distance encountered for charge carriers in the latter heterojunction (Kawahara et al. 2002). Since SnO_2 itself is considerably less photocatalytically active than TiO_2 , it may be expected that the maximum enhancement of the activity will be achieved in the coupled system for a certain $\text{SnO}_2/\text{TiO}_2$ ratio. Of course, this amount must depend on many factors like phase contact, geometry of the catalyst, etc., but for purely photocatalytic reactions, the figure seems to be between 10 and 20 % weight of SnO_2 (Tudela et al. 2010).

As mentioned at the beginning of the chapter, not only the charge separation at the interface of coupled semiconductors has called the attention of researchers. In the specific case of $\text{TiO}_2/\text{SnO}_2$ systems, surface modifications have also been invoked to explain the improved properties of these materials. Increased hydrophilicity of TiO_2 when coupled with small quantities of SnO_2 has been related to

its improved photocatalytic activity by several authors (Tudela et al. 2010). Indeed, an enhanced photoinduced superhydrophilic effect has been found in $\text{TiO}_2/\text{SnO}_2$ composites, with water contact angles close to 0° after illumination with natural light (Liu et al. 2002). This effect has been related to an increased amount of surface hydroxyls and can be maintained for long periods in the dark. Also related to surface characteristics, resistance to deactivation in the gas phase photocatalytic degradation of toluene has been obtained in TiO_2 by coupling with SnO_2 (Fresno et al. 2008). This deactivation is generally related to the accumulation of stable, recalcitrant intermediates on the surface of the catalyst. In $\text{TiO}_2/\text{SnO}_2$ samples, a different structure of the surface water was proposed, which resulted in a lower accumulation of these intermediates. The modification of surface characteristics such as water adsorption and surface acidity has been also considered to account for the observed improvement in TiO_2 performance when coupled to ZrO_2 (Hernández-Alonso et al. 2006; Fresno et al. 2008)

15.2.3 TiO_2/WO_3 Photocatalysts

As mentioned in Chap. 6, WO_3 is a semiconductor with a relatively narrow (2.7 eV) band gap. Its coupling scheme with TiO_2 is somewhat different to those depicted as general examples in Fig. 15.1. In the bulk crystalline form (frequently monoclinic or orthorhombic), the conduction band of WO_3 has lower energy than that of anatase, whereas the valence band is higher, so that both electrons and holes can migrate from TiO_2 to WO_3 upon excitation of the former, but the opposite migration is not permitted from excited WO_3 . This scheme is modified for small crystallite sizes of WO_3 due to size quantization effects, as shown in Fig. 15.6, so that below a certain value, a junction equivalent to that in Fig. 15.1a is formed. Once this point is reached, and after simultaneous excitation, electrons migrate from TiO_2 to WO_3 and holes follow the opposite path (Zhang et al. 2009). Of these two configurations, the use of nanostructured WO_3 appears to be more favourable for charge separation. However, at these sizes, the band gap of WO_3 becomes too large to absorb visible photons. In addition, for particles well below 10 nm, WO_3 is considered to be mainly amorphous, and hence, the capability to handle charge carriers to produce chemical reactions is essentially lost. Therefore, positive effects arising from interface charge transfer can only be envisaged in a narrow size range mainly governed by WO_3 characteristics (Kubacka et al. 2012).

The electron transfer from TiO_2 to WO_3 has been described to proceed via the formation of an intermediate W(V) species, increasing the surface acidity of the coupled material, which can be beneficial for transfer of electrons from the CB of TiO_2 to adsorbed oxygen molecules and for the adsorption of organic reactants. In addition, similarly to the case of SnO_2 , an increased hydrophilicity of TiO_2 when coupled to WO_3 has been reported. Therefore, the beneficial effect of coupling WO_3 to TiO_2 on photocatalytic activity relies not only on improved charge carrier separation but also on surface modifications; in fact, this latter effect may be

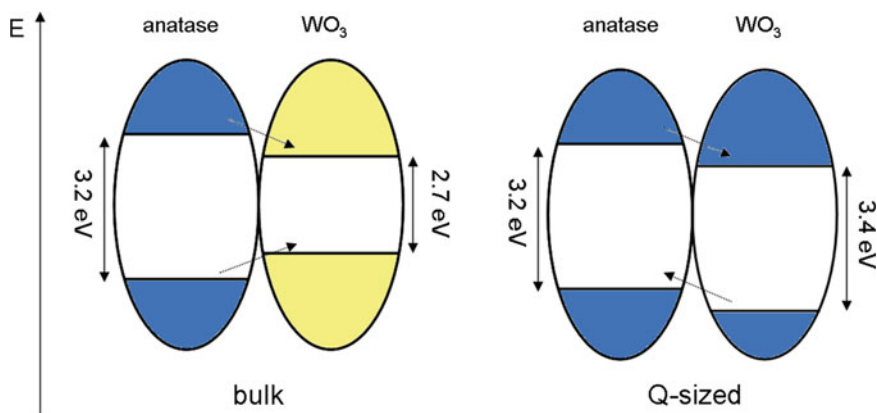


Fig. 15.6 Energetic diagram of the coupling between anatase and bulk or quantum-sized WO_3 . Based on Kubacka et al. (2012)

predominant under certain circumstances (Zhang et al. 2009). The structural details of the WO_3/TiO_2 interface, however, are essentially unknown. The presence of several W oxidation states, anion vacancies, and corresponding WO_3 phases (with a certain degree of amorphization) illustrate the complexity of the situation that can be encountered in this system (Kubacka et al. 2012).

The beneficial effect of coupling WO_3 with TiO_2 has been explored for the photocatalytic degradation of several organic pollutants (Robert 2007; Zhang et al. 2009), as well as for water splitting (Chen et al. 2010). Under visible light, it has been observed that coupling N-doped TiO_2 with WO_3 leads to higher hydrogen production than either $\text{TiO}_{2-x}\text{N}_x$ or WO_3 alone.

15.2.4 Other Oxide/Oxide Couplings

Some other oxides in combination with TiO_2 are worth mentioning. In addition to those already described, archetypical examples are ZnO –, Bi_2O_3 –, Fe_2O_3 –, Fe_3O_4 –, CeO_2 – and Cu_2O – TiO_2 composites. However, the list is shortened when limited to active and reasonably stable systems (Kubacka et al. 2012).

The bulk-type contact between anatase and Cu_2O has not been well studied, but the band energy levelling would be only adequate for enhancing charge separation under UV illumination. Taking the size to the nanoscale, however, drastically changes the situation. Around 10 nm, the modification of the Cu_2O band gap and the position of the Fermi level of the nanocomposite provides an effective way to transfer visible light-excited electrons from the copper oxide to anatase and to promote electron-hole separation. This should lead to highly active sunlight-driven photocatalysts which, however, have been scarcely analysed up to date. Below 10 nm, the band gap is expected to reach a value close to 3.0 eV, which limits the

absorption of visible light photons, although the system would be still adequate under UV irradiation. According to the VB position, holes at the Cu_2O phase can be used to attack organic molecules, or to oxidize Cu_2O to CuO in the presence of water. However, in this case, photocorrosion is kinetically limited at room temperature, and the Cu^+ state appears as the stable one under irradiation conditions.

Other possible candidate system could be the $\alpha/\gamma\text{-Fe}_2\text{O}_3/\text{TiO}_2$ couple, although this combination appears to be somewhat limited (Kubacka et al. 2012). Upon UV excitation, electrons in the conduction band of TiO_2 may be transferred to Fe_2O_3 and so may be the holes in the valence band of anatase, in a similar manner as that described for bulk WO_3 . Therefore, bulk Fe_2O_3 lacks the adequate electronic structure to be used as a visible light sensitizer for TiO_2 . Some changes may be expected with decreasing crystallite sizes, where visible light-excited electrons in Fe_2O_3 could migrate to TiO_2 . However, only a few reports have analysed this nanocomposite system for visible or UV/visible light excitation. Other oxides such as CeO_2 or Bi_2O_3 are also useful regarding their interaction with titania. The latter is particularly well suited as the relative positions of the valence and conduction bands should promote (visible-photon generated) electron transfer from Bi_2O_3 to anatase and (UV-photon generated) hole transfer from anatase to Bi_2O_3 . However, Bi_2O_3 lacks the necessary stability under photocatalytic reaction conditions. On the other hand, more stable bismuth oxyhalides (see Chap. 7) have been tested in combination with TiO_2 in the recent years (Li et al. 2011b).

Regarding more complex oxides, a wide range of metallates like those described in Chap. 7 have been explored as candidates to improve the photocatalytic properties of TiO_2 via coupling, with special attention to those capable of acting as inorganic visible light sensitizers. In this respect, it is worth mentioning the use of BiVO_4 (Hu et al. 2011), Bi_2WO_6 (Colón et al. 2010) and other titanium-, vanadium- and bismuth-based oxides (Kubacka et al. 2012). However, more studies are required to establish the behaviour of these systems.

Oxidic coupled systems not containing TiO_2 are scarcer but some of them have also been assayed as photocatalysts. In order to mention a few examples, Cr-doped $\text{Ba}_2\text{In}_2\text{O}_5/\text{In}_2\text{O}_3$ turned out to have enhanced photocatalytic activity for water splitting with regard to the individual components (Cr-doped $\text{Ba}_2\text{In}_2\text{O}_5$ and Cr-doped In_2O_3) because of interface charge carrier separation and migration. On the same basis, $\text{In}_2\text{O}_3/\text{NaNbO}_3$ has also been found advantageous for sacrificial hydrogen evolution under visible light and for stoichiometric water splitting under UV (Chen et al. 2010). In depollution applications, $\text{BiVO}_4/\text{Bi}_2\text{O}_3$ core-shell materials have shown interesting photocatalytic properties under visible light (Guan et al. 2011), and combining bismuth-based oxides with bismuth oxyhalides (BiOX), or two different BiOX , are other recently explored possibilities (Li et al. 2011a).

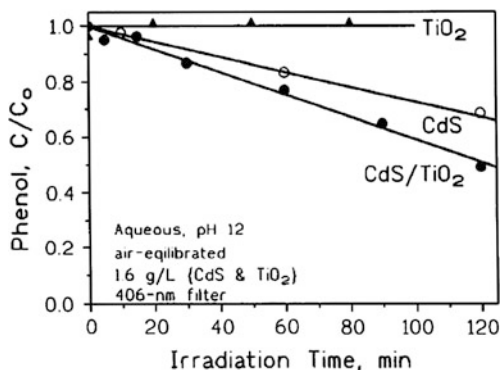
15.3 Combining Oxides with Chalcogenide and Other Semiconductors

15.3.1 CdS/TiO₂ Photocatalysts

Both the CB and the VB energies of CdS (see Chap. 8) are above the corresponding ones in TiO₂. Therefore, upon excitation, electrons in the CB of CdS can migrate to TiO₂ leaving the holes behind, as depicted in Fig. 15.1b. If we add the fact that CdS is capable of absorbing visible light and that the mobility and lifetime of charge carriers are adequate for photocatalytic reactions, we have a paradigmatic example of inorganic sensitization of TiO₂ to visible light. Indeed, this system has been widely used since the 1980s in photo(electro)catalytic reactions for pollutant degradation, hydrogen production, CO₂ reduction, as well as in solar cells (Usubharatana et al. 2006; Zhang et al. 2009; Roy et al. 2010). As mentioned above, interfacial charge separation in this system was demonstrated by the detection of Ti³⁺ upon visible light irradiation with EPR. Under UV or UV–vis irradiation, the scheme depicted in Fig. 15.1a may also occur, with electron transference from CdS to TiO₂ and hole migration in the opposite direction. In addition, this approach has also been employed to protect CdS from photocorrosion in CdS(core)/anatase(shell) materials. In this last respect, however, a more satisfactory solution has been found in ternary Au/CdS/TiO₂ systems in which a constant electron supply from the metallic phase minimizes the hole attack to CdS (Kubacka et al. 2012).

Early research on CdS/TiO₂ coupled photocatalysts was mostly limited to colloidal systems in which the former was the dominant component. This trend changed into the reverse situation in more recent years, when CdS has been used with a closer role to that of a sensitizer. Many tests on the photocatalytic activity of this system under visible light, however, have been carried out using dyes as probe molecules (Robert 2007; Zhang et al. 2009), which, as mentioned elsewhere in this book, does not guarantee TiO₂ sensitization by CdS since a dye-sensitized mechanism (see Chap. 16) cannot be ruled out (Herrmann 2010). In any case, regardless of the actual mechanism, increased rates for the decolouration of dyes under visible light have been reported with CdS/TiO₂ catalysts with respect to the individual components. Degradation of other non-visible light-absorbing organic molecules, or water reduction to H₂, are more prone to occur via electron transfer from visible light-excited CdS. Regarding the first case, the photocatalytic degradation of phenols with CdS/TiO₂ composites under purely visible light was reported almost two decades ago (Serpone et al. 1995), with improved results with respect to the single photocatalysts. Sacrificial hydrogen production in the same irradiation conditions was reported earlier (Serpone et al. 1984) and has been a matter of research since then (Osterloh 2008; Chen et al. 2010). Thus, the positive effect of the scheme shown in Fig. 15.1b on photocatalytic activity in the CdS/TiO₂ system appears well documented. Under UV–vis irradiation, however, an improvement of the photocatalytic activity of TiO₂ by the CdS/TiO₂ couple is not

Fig. 15.7 Photocatalytic removal of phenol in water over TiO_2 , CdS and the coupled system. Reproduced with permission from Serpone et al. (1995). Copyright Elsevier



so clear. Indeed, lower reaction rates have been obtained with the composite system for different reactions (Serpone et al. 1995; Robert 2007), suggesting that the separation scheme of Fig. 15.1a for this specific example may play a negative role with respect to TiO_2 alone. On the other hand, higher photocatalytic activities are obtained with CdS/ TiO_2 materials than with CdS under UV–vis or solar irradiation (Serpone et al. 1995; Robert 2007), an example of which is shown in Fig. 15.7. In any case, it is worth mentioning that the toxicity of Cd can be a serious limitation for an extensive use of these composites, especially taking into account that photocorrosion of the sulphide (see Chap. 8) is not prevented by the interfacial charge separation depicted in Fig. 15.1a.

15.3.2 Other Sulphide/Oxide Couples

Bi_2S_3 is a narrow band gap (1.3 eV) used in photodiode arrays and photovoltaic devices. In photocatalysis, it has been tested not only on its own for sacrificial hydrogen production, but also coupled to TiO_2 in order to induce visible light activity. Indeed, this couple has shown, for instance, photocatalytic activity under visible light for the degradation of 4-hydroxybenzoic acid and benzamide, giving rise to higher degradation rates than Bi_2S_3 and, as expected, than TiO_2 (P25) itself. Under UV–vis irradiation, however, similar degradation rates are obtained with TiO_2 and $\text{Bi}_2\text{S}_3/\text{TiO}_2$ catalysts, while the use of sulphide on its own results in a reduced degradation efficiency, probably due to its low band gap energy (Bessekhouad et al. 2004).

Molybdenum and tungsten sulphides are also interesting for the photocatalytic approach issued here, because of the good matching of their band gaps (1.1–1.7 eV) with the solar spectrum and their stability against photocorrosion (Robert 2007). In the bulk form, the conduction band levels of MoS_2 and WS_2 are lower in energy than that of TiO_2 , so that no injection of electrons into the latter is to be expected. However, as a common feature of chalcogenide materials, a high morphological control can be achieved (Kubacka et al. 2012), so that

nanostructured MoS₂ and WS₂ having higher conduction band levels due to quantum size effect, but still absorbing visible light, have been tested in combination with TiO₂ for visible light photocatalysis. These materials are able to degrade 4-chlorophenol in aqueous solution under irradiation with $\lambda > 400$ nm. The detection of Ti³⁺ in the EPR spectra of the visible light-irradiated couples confirms the electron injection from the MS₂ phase into the otherwise inactive TiO₂ one (Ho et al. 2004).

15.3.3 Selenide/TiO₂ Photocatalysts

CdSe was described as a photocatalyst in Chap. 8. According to its electronic structure, it can be used to sensitize TiO₂ towards visible light absorption in an equivalent scheme to that of CdS, although it presents a considerably narrower band gap (1.74 eV). In combination with other semiconductors like TiO₂ and SnO₂, CdSe has been employed as a visible light harvester for different photonic applications (Kamat 2007). In photocatalysis, it has been tested in combination with TiO₂ for the degradation of organic pollutants. Under visible light, CdSe/TiO₂ photocatalysts have shown activity for the oxidation of 4-chlorophenol in water, although with low substrate disappearance rate and discrete TOC removal (Lo et al. 2004; Ho and Yu 2006). In any case, although low, the system does present activity under visible light and higher than CdSe itself. This fact, together with the detection of Ti³⁺ with EPR under irradiation at 420 nm, indicates that the interparticle charge transfer is occurring to some extent. Upon UV excitation, the situation is rather different, with the coupled system exhibiting higher oxidation and mineralization efficiency than TiO₂ itself. In these conditions, an improved charge separation due to a charge transfer scheme like that in Fig. 15.1a is likely to occur. Nevertheless, the CdSe/TiO₂ system has shown lower photocatalytic efficiency than the CdS/TiO₂ one (Robert 2007). CdSe and other selenides have been also combined with TiO₂ in the form of quantum dots, which will be reviewed in the following chapter.

15.3.4 Coupling TiO₂ with Carbonaceous Materials

Another attractive type of coupling partners for photocatalysts is formed by carbon materials such as graphite, fullerenes, carbon nanotubes and graphene. The delocalized conjugated π electron system present in these carbon allotropes has been proved to cause a rapid photoinduced charge separation in electron-transfer processes (Di Paola et al. 2012). In addition, they can improve the photocatalyst adsorptive properties and/or contribute highly active catalytic sites.

Graphite has been employed to boost the efficiency of TiO₂ in pollutant degradation reactions and have shown, for example, higher photocatalytic activity

than P25 in both gas and liquid phase reactions (Di Paola et al. 2012). This high activity is generally ascribed to charge transfer between the conduction band of TiO₂ and the π system of graphite. This form of carbon has also been proposed as a suitable visible light sensitizer for wide band gap photocatalysts.

Rolled up layers of graphitic carbon form the so-called carbon nanotubes. This carbon species show potential to contribute to photocatalytic activity in several ways, namely increasing surface area, retarding of electron–hole recombination and visible light sensitization (Leary and Westwood 2011). They have been widely reported to enhance the photocatalytic activity of TiO₂ through the retardation of electron–hole recombination, giving better results than bare titania for a variety of photocatalytic applications, such as pollutant degradation, disinfection, CO₂ reduction and water splitting (Di Paola et al. 2012; Leary and Westwood 2011).

Fullerenes are widely known because of their unique electronic properties. They are well established as singlet oxygen sensitizers in organic synthetic photooxidations, in electron donor–acceptor assemblies as part of artificial photosynthetic systems and in photochemical solar cells. However, their application in photocatalysis is much less well explored (Leary and Westwood 2011). In fullerene/TiO₂ photocatalysts reported in the recent literature, the fullerene component has been cited either as an electron acceptor, therefore being expected to provide enhanced photocatalytic activity through a mechanism similar to that depicted in Fig. 15.1a, or as an electron donor, therefore being expected to provide enhanced photocatalytic activity through sensitization of TiO₂ (Fig. 15.1b). Indeed, it has been demonstrated that fullerenes, in their ground or excited states, can interact with TiO₂ in both ways, depending on the environment and the experimental conditions.

Graphene is a new and highly promising material, composed of a one-atom-thick planar sheet of sp²-bonded carbon atoms that is being studied for an increasing number of applications, including photocatalysis. Single-layer graphene is a zero band gap semiconductor or semimetal in which the highest occupied molecular orbital (HOMO) touches the lowest unoccupied molecular orbital (LUMO) at single points called “Dirac points”. For thicker flakes, stacking of multiple layers leads to some overlap of their carrier wave functions and the overall behaviour becomes metallic (Allen et al. 2010). Apart from an extremely high carrier mobility, graphene has several other excellent attributes to be used in catalytic and photocatalytic reactions, such as a large theoretical specific surface area and a high transparency due to its one-atom thickness. Indeed, graphene-based assemblies are gaining attention as a viable alternative to boost the efficiency of various catalytic and storage reactions in energy conversion applications (Kamat 2010). There have been several reports highlighting the improvement in activity obtained by coupling graphene with TiO₂ and other semiconductors for different photocatalytic applications (Di Paola et al. 2012; Leary and Westwood 2011; Xiang et al. 2012). Several reasons are invoked to account for this enhancement. Specifically, the two-dimensional carbon nanostructure may facilitate the dispersion of catalyst particles, improve charge separation within the composite and increase the concentration of organic molecules near the catalyst

surface. However, the mechanisms of photocatalytic enhancement by graphene are partly unclear (Xiang et al. 2012). For example, whether the photocatalytic activity of TiO₂-graphene composites is truly different from other TiO₂-C composite materials. Nevertheless, graphene-based composite photocatalysts are expected to be developed as robust materials to address various environmental and energy-related issues.

References

- Allen MJ, Tung VC, Kaner RB (2010) Honeycomb carbon: a review of graphene. *Chem Rev* 110:132–145
- Bedja I, Kamat PV (1995) Capped semiconductor colloids. synthesis and photoelectrochemical behavior of TiO₂-capped SnO₂ nanocrystallites. *J Phys Chem* 99:9182–9188
- Bessekhouad Y, Robert D, Weber JV (2004) Bi₂S₃/TiO₂ and CdS/TiO₂ heterojunctions as an available configuration for photocatalytic degradation of organic pollutant. *J Photochem Photobiol A Chem* 163:569–580
- Bickley RI, Gonzalez-Carreno T, Lees JS, Palmisano L, Tilley RJD (1991) A structural investigation of titanium dioxide photocatalysts. *J Solid State Chem* 92:178–190
- Carp O, Huisman CL, Reller A (2004) Photoinduced reactivity of titanium dioxide. *Prog Solid State Chem* 32:33–177
- Guan ML, Ma DK, Hu SW, Chen YJ, SM (2011) From hollow olive-shaped BiVO₄ to n-p Core-Shell BiVO₄@Bi₂O₃ microspheres: controlled synthesis and enhanced visible-light-responsive photocatalytic properties. *Inorg Chem* 50:800–805
- Chen X, Shen S, Guo L, Mao SS (2010) Semiconductor-based photocatalytic hydrogen generation. *Chem Rev* 110:6503–6570
- Colón G, Murcia López S, Hidalgo MC, Navío JA (2010) Sunlight highly photoactive Bi₂WO₆-TiO₂ heterostructures for rhodamine B degradation. *Chem Commun* 46:4809–4811
- Di Paola A, García-López E, Marci G, Palmisano L (2012) A survey of photocatalytic materials for environmental remediation. *J Hazard Mater* 211–212:3–29
- Fresno F, Coronado JM, Tudela D, Soria J (2005) Influence of the structural characteristics of Ti_{1-x}Sn_xO₂ nanoparticles on their photocatalytic activity for the elimination of methylcyclohexane vapors. *Appl Catal B-Environ* 55:159–167
- Fresno F, Hernández-Alonso MD, Tudela D, Coronado JM, Soria J (2008) Photocatalytic degradation of toluene over doped and coupled (Ti, M)O₂ (M = Sn or Zr) nanocrystalline oxides: influence of the heteroatom distribution on deactivation. *Appl Catal B-Environ* 84:598–606
- Gopidas KR, Bohorquez M, Kamat PV (1990) Photophysical and photochemical aspects of coupled semiconductors. Charge-transfer processes in colloidal CdS-TiO, and CdS-AgI systems. *J Phys Chem* 94:6435–6440
- Hernández-Alonso MD, Tejedor-Tejedor I, Coronado JM, Soria J, Anderson MA (2006) Sol-gel preparation of TiO₂-ZrO₂ thin films supported on glass rings: influence of phase composition on photocatalytic activity. *Thin Solid Films* 52:125–131
- Herrmann JM (2010) Photocatalysis fundamentals revisited to avoid several misconceptions. *Appl Catal B Environ* 99:461–468
- Ho W, Yu JC (2006) Sonochemical synthesis and visible light photocatalytic behavior of CdSe and CdSe/TiO₂ nanoparticles. *J Mol Catal A: Chem* 247:268–274
- Ho W, Yu JC, Lin J, Yu J, Pui-shan Li P (2004) Preparation and photocatalytic behavior of MoS₂ and WS₂ nanocluster sensitized TiO₂. *Langmuir* 20:5865–5869

- Hu Y, Li D, Zheng Y, Chen W, He Y, Shao Y, Fu X, Xiao G (2011) BiVO₄/TiO₂ nanocrystalline heterostructure: a wide spectrum responsive photocatalyst towards the highly efficient decomposition of gaseous benzene. *Appl Catal B Environ* 104:30–36
- Hurum DC, Agrios AG, Gray KA, Rajh T, Thurnauer MC (2003) Explaining the enhanced photocatalytic activity of Degussa P25 mixed-phase TiO₂ using EPR. *J Phys Chem B* 107:4545–4549
- Kamat PV (2007) Meeting the clean energy demand: nanostructure architectures for solar energy conversion. *J Phys Chem C* 111:2834–2860
- Kamat PV (2010) Graphene-based nanoarchitectures. Anchoring semiconductor and metal nanoparticles on a two-dimensional carbon support. *J Phys Chem Lett* 1:520–527
- Kawahara T, Konishi Y, Tada H, Toghe N, Ito S (2001) Patterned TiO₂/SnO₂ bilayer type photocatalyst. 2. Efficient dehydrogenation of methanol. *Langmuir* 17:7442–7445
- Kawahara T, Konishi Y, Tada H, Tohge N, Nishii J, Ito S (2002) A patterned TiO₂ (Anatase)/TiO₂ (Rutile) bilayer-type photocatalyst: effect of the anatase/rutile junction on the photocatalytic activity. *Angew Chem Int Ed* 41:2811–2813
- Kubacka A, Fernández-García M, Colón G (2012) Advanced nanoarchitectures for solar photocatalytic applications. *Chem Rev* 112:1555–1614
- Leary R, Westwood A (2011) Carbonaceous nanomaterials for the enhancement of TiO₂ photocatalysis. *Carbon* 49:741–772
- Levy B, Liu W, Gilbert SE (1997) Directed photocurrents in nanostructured TiO₂/SnO₂ heterojunction diodes. *J Phys Chem B* 101:1810–1816
- Li TB, Chen G, Zhou C, Shen ZY, Jin RC, Sun JX (2011a) New photocatalyst BiOCl/BiOI composites with highly enhanced visible light photocatalytic performances. *Dalton Trans* 40:6751–6758
- Li Y, Wang J, Liu B, Dang L, Yao H, Li Z (2011b) BiOI-sensitized TiO₂ in phenol degradation: a novel efficient semiconductor sensitizer. *Chem Phys Lett* 508:102–106
- Liu Q, Wu X, Wang B, Liu Q (2002) Preparation and superhydrophilic properties of TiO₂/SnO₂ composite thin films. *Mater Res Bull* 37:2255–2262
- Lo SC, Lin CF, Wu CH, Hsieh PH (2004) Capability of coupled CdSe/TiO₂ for photocatalytic degradation of 4-chlorophenol. *J Hazard Mater* 114:183–190
- Ohno T, Sarukawa K, Tokieda K, Matsumura M (2003) Morphology of a TiO₂ photocatalyst (Degussa, P-25) consisting of anatase and rutile crystalline phases. *J Catal* 203:82–86
- Ohtani B (2010) Photocatalysis A to Z—What we know and what we do not know in a scientific sense. *J Photochem Photobiol C Photochem Rev* 11:157–178
- Osterloh FE (2008) Inorganic materials for photochemical splitting of water. *Chem Mater* 20:35–54
- Robert D (2007) Photosensitization of TiO₂ by M_xO_y and M_xS_y nanoparticles for heterogeneous photocatalysis applications. *Catal Today* 122:20–26
- Roy SC, Varghese OK, Paulose M, Grimes CA (2010) Toward solar fuels: photocatalytic conversion of carbon dioxide to hydrocarbons. *ACS Nano* 4:1259–1278
- Serpone N, Borgarello E, Grätzel M (1984) Visible light induced generation of hydrogen from H₂S in mixed semiconductor dispersions; improved efficiency through inter-particle electron transfer. *J Chem Soc Chem Commun* 342–344
- Serpone N, Maruthamuthu P, Pichat P, Pelizzetti E, Hidaka H (1995) Exploiting the interparticle electron transfer process in the photocatalysed oxidation of phenol, 2-chlorophenol and pentachlorophenol: chemical evidence for electron and hole transfer between coupled semiconductors. *J Photochem Photobiol A Chem* 85:247–255
- Soria J, Sanz J, Sobrados I, Coronado JM, Hernández-Alonso MD, Fresno F (2010) Water-hydroxyl interactions on small anatase nanoparticles prepared by the hydrothermal route. *J Phys Chem C* 114:16534–16540
- Tada H, Hattori AQ, Tokihisa Y, Imai K, Tohge N, Ito S (2000) A patterned-TiO₂/SnO₂ bilayer type photocatalyst. *J Phys Chem B* 104:4585–4587

- Tudela D, Fresno F, Coronado JM (2010) Tin-doped nanocrystalline TiO₂ photocatalysts. In: Chen W (ed) Doped nanomaterials and nanodevices, American Scientific Publishers, California. ISBN: 1-58883-110-8
- Usubharatana P, MacMartin D, Veawab A, Tontiwachwuthikul P (2006) Photocatalytic process for CO₂ emission reduction from industrial flue gas streams. *Ind Eng Chem Res* 45:2558–2568
- Vinodgopal K, Bedja I, Kamat PV (1996) Nanostructured semiconductor films for photocatalysis. Photoelectrochemical behavior of SnO₂/TiO₂ composite systems and its role in photocatalytic degradation of a textile azo dye. *Chem Mater* 8:2180–2187
- Wu L, Yu JC, Fu X (2006) Characterization and photocatalytic mechanism of nanosized CdS coupled TiO₂ nanocrystals under visible light irradiation. *J Mol Catal A: Chem* 244:25–32
- Xiang Q, Yu J, Jaroniec M (2012) Graphene-based semiconductor photocatalysts. *Chem Soc Rev* 41:782–796
- Zachariah A, Baiju KV, Shukla S, Deepa KS, James J, Warriar K GK (2008) Synergistic effect in photocatalysis as observed for mixed-phase nanocrystalline titania processed via sol-gel solvent mixing and calcination. *J Phys Chem C* 112:11345–11356
- Zhang J, Xu Q, Feng Z, Li M, Li C (2008) Importance of the relationship between surface phases and photocatalytic activity of TiO₂. *Angew Chem Int Ed* 47:1766–1769
- Zhang H, Chen G, Bahnemann DW (2009) Photoelectrocatalytic materials for environmental applications. *J Mater Chem* 19:5089–5121

Chapter 16

Sensitizers: Dyes and Quantum Dots

Fernando Fresno and María Dolores Hernández-Alonso

Several approaches aimed at extending the spectral activity range of wide-band-gap semiconductors have been already reviewed in previous chapters of this book. In addition to structural modifications that may lead to different electronic effects, such as anionic or cationic doping and solid solution formation, there is a possibility of modifying the surface of the semiconductor with a substance that absorbs light energy and transfers it, under favourable conditions, to an otherwise photochemically inactive or less active substrate. This substance is referred to as *photosensitizer*. This concept was already introduced in the preceding chapter when dealing with one of the types of coupled photocatalysts. Indeed, that case may be regarded as an *inorganic sensitization* and will be resumed in the third section of this chapter, which will refer to the specific case of quantum-sized *islands* of one semiconductor embedded in different semiconductor matrices, that is, *quantum dots*.

16.1 Electron Transference from Sensitizer

According to the IUPAC definition, photosensitization is “the process by which a photochemical or photophysical alteration occurs in one molecular entity as a result of initial absorption of radiation by another molecular entity called a photosensitizer”. The history of sensitization is nearly as long as that of photography. The silver halides used in photography have band gaps around 2.7–3.2 eV, and thus, they are insensitive to much of the visible spectrum. The first panchromatic film, able to render the image of a scene realistically to black and white, followed

F. Fresno (✉)

Laboratory for Environmental Research, University of Nova Gorica,
Nova Gorica, Slovenia
e-mail: fernando.fresno@ung.si

M. D. Hernández-Alonso

Renewable Energy Division, CIEMAT, Madrid, Spain
e-mail: lolihza@gmail.com

on the work of Vogel in Berlin after 1873, in which he associated dyes with the halide semiconductor grains. The first sensitization of a photoelectrode followed shortly after, using a similar chemistry. However, it was not until 1960s that the recognition of the parallelism between this two procedures and the verification of their mechanism by injection of electrons from the excited dye molecules into the conduction band of the semiconductor occurred (Grätzel 2003). Since then, sensitization of semiconductors (mainly TiO_2) has been applied in many fields, among which the use in photovoltaic devices is prominent, as it has been briefly mentioned in Chap. 2. However, to a lesser extent, sensitized visible-light-promoted photocatalytic degradation of pollutants and water splitting have been reported too (Pei and Luan 2012).

The physical principles of sensitization are related to those introduced in Chap. 15 when referring to charge separation in coupled photocatalysts. In the case of a molecular photosensitizer such as the commonly used dyes, excitation occurs upon absorption of light with the adequate energy, followed by the injection of electrons from the excited state of the sensitizer into the conduction band of the semiconductor. Therefore, when referring to dye-sensitized photocatalysis, in contrast to classical photocatalysis, the conduction band of the semiconductor acts as a mediator for transferring electrons from the sensitizer to substrate electron acceptors on the photocatalyst surface, while the valence band remains unaffected. It is evident that in order for this electron transference to occur, the excited state of the sensitizer must possess higher energy than the conduction band of the semiconductor. The charge injection from the excited sensitizer into the semiconductor nanoparticles must be an ultrafast process occurring on the timescale of picoseconds or below in order to achieve good quantum yields, since it competes with other radiative or radiationless deactivation channels that typically occur with rate constants in the range of 10^3 to 10^{10} s^{-1} . In recent years, molecularly engineered sensitizers that meet these requirements have been developed (Grätzel 2005). With these sensitizers, the injection times are in the pico- or femtosecond range and the quantum yield of charge injection generally exceeds 90 %. Actually, for several sensitizers, the electron transfer to the conduction band of the oxide is so rapid that it occurs from vibrationally hot excited states (Grätzel 2005).

After electron transference, the regeneration of the system is an issue that needs to be taken into account. In the case of dye-sensitized solar cells, the original state of the dye is restored by electron donation from the electrolyte, usually an organic solvent containing a redox system such as the iodide/triiodide couple, which in turn can be regenerated at the counter electrode completing the redox cycle. In a solid-state dye-sensitized solar cell, the electrolyte is replaced by a solid p-type semiconductor which permits charge neutralization of the dye molecules by means of its hole transport properties (Grätzel 2005). On the other hand, a sacrificial electron donor can be used for the regeneration of the sensitizer in the case of photocatalytic reactions. For instance, ethylenediaminetetraacetic acid (EDTA) and triethanolamine (TEOA) have proved to be effective donors in the photocatalytic visible-light-induced production of H_2 over sensitized Pt- TiO_2 (Hirano et al. 2000). Figure 16.1 illustrates a plausible mechanism of the primary electron

pathway in a dye-sensitized semiconductor photocatalyst using the water-splitting reaction as example. In addition to its role as photosensitizer, the dye molecules (S) also serve as a molecular bridge to connect the electron donor (D) to the semiconductor.

Figure 16.1 also illustrates the possible recombination pathways and fluorescence decay of the excited sensitizer (Pei and Luan 2012). Back electron transfer between the injected electron and the oxidized sensitizer plays an important role in controlling the efficiency of net electron transfer. As mentioned above, at each branching point in the chain of electronic transitions, a high quantum yield can be obtained only if the forward electron transfer rate (solid arrows) is faster than the sum of all the reverse rates from the same state of the system. For example, in Fig. 16.1, the forward electron transfer from the semiconductor to the hydrogen evolving from the catalyst must compete effectively with the back transfer to the oxidized dye and also with the electron transfer to the electron donor for water oxidation. In general, the reverse pathways have much greater driving forces than the forward ones, and this makes the reverse reactions faster. However, due to the existence of the interface between the dyes and the photocatalyst, the separated electrons and holes have little possibility to recombine again, regardless of the existence of the charge-capturing species which are mentioned above. This ensures high charge separation efficiency in the hybrid material.

16.2 Organic and Metal–Organic Dyes

As previously mentioned, dye sensitization can also be a plausible alternative to extend the photocatalyst response to the visible range, leading to a more efficient use of solar energy. Thus, this strategy is being frequently used in visible-light-induced water splitting (Youngblood et al. 2009) and photocatalytic degradation processes (Table 16.1). Among the latter, wastewater treatment, and in particular

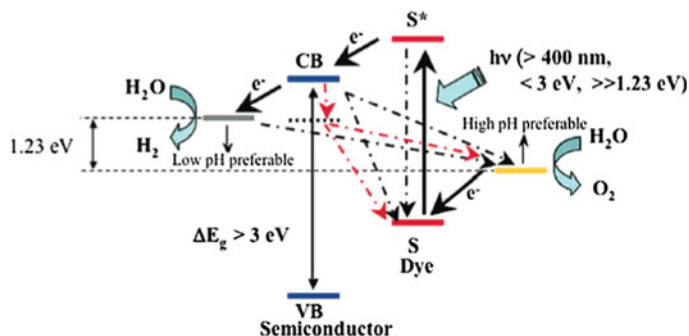


Fig. 16.1 Proposed mechanism of dye-sensitized photocatalysis under visible light irradiation, including forward electron transfer and possible recombination pathways. Reproduced with permission from Youngblood et al. 2009. Copyright American Chemical Society

Table 16.1 Examples of the utilization of sensitized photocatalysts in water splitting and photocatalytic degradation reactions under visible light irradiation (Pei and Luan 2012). Details on the reaction conditions can be found in the corresponding references

Sensitizer	Catalyst	Hydrogen evolution ($\mu\text{mol/h}$)	Apparent quantum efficiency (%)	Reference
Eosin Y	Pt/TiO ₂	65	10	Abe et al. (2000)
Ru complex	Pt/TiO ₂	Max. 132	22.4	Bae and Choi (2006)
Eosin Y	Rh/TiO ₂	14.63	7.10	Jin et al. (2006)
Eosin Y	CuO/TiO ₂	10.56	5.1	Jin et al. (2007)
Eosin Y	Pt/MWCNT ^a	54.20	12.14	Li et al. (2007a)
Eosin Y	Pt/Ti-MCM-41	~ 10	12.01	Li et al. (2007b)
Eosin Y-Fe ³⁺	Pt/TiO ₂	275	19.1	Li et al. (2009)
Sensitizer	Catalyst	Target contaminant	Degradation efficiency	Reference
Ru complex	TiO ₂	Herbicide terbutryn	100 % (4 h)	Lobedank et al. (1997)
Ru complex	TiO ₂	CCl ₄	0.446 $\mu\text{M min}^{-1} \text{g}^{-1}$	Cheung et al. (1998)
Ru complex	TiO ₂	CCl ₄	0.585 $\mu\text{M min}^{-1} \text{g}^{-1}$	Fung et al. (2003)
Polyaniline	TiO ₂	Methylene blue	80 % (1.5 h)	Min et al. (2007)
Poly(flourene-co-thiophene)	TiO ₂	Phenol	74.3 % (10 h)	Song et al. (2007)

^a MWCNT: multiwalled carbon nanotubes

the degradation of colourants, is one of the major niches of application of dye-sensitized TiO_2 (Chatterjee and Dasgupta 2005).

Regardless of the practical application, dye sensitizers have to meet several common requirements. Apart from a desirable wide range of light absorption in the visible and near-IR regions and the energy-level requirements mentioned in the previous section, the dye needs to be grafted onto the host surface. Depending on the sensitizer molecule, this attachment can take place through covalent bonding, electrostatic forces, hydrogen bonding, hydrophobic interactions, van der Waals forces, or physical entrapment. Dye sensitizers often contain anchoring groups such as silyl ($-\text{O}-\text{Si}-$), amide ($-\text{NH}-(\text{C}=\text{O})-$), carboxyl ($-\text{O}-(\text{C}=\text{O})-$), or phosphonate ($-\text{O}-(\text{HPO}_2)-$) groups in their structure, which have proved to spontaneously react with the surface hydroxyl groups of the semiconductor, forming highly stable linkages (Kalyanasundaram and Grätzel 1998). For instance, carboxylic and phosphonic acid derivatives are able to react with the photocatalyst surface, forming the corresponding ester (Fig. 16.2). Likewise, silyl groups have high affinity for the hydroxyl groups on the surface of the semiconductor (Pei and Luan 2012).

The properties and, consequently, the efficiency of the photosensitizer will be influenced by the nature and number of the anchoring groups (Park et al. 2006; Pei and Luan 2012). However, the stability of the linkages may be affected by the pH in aqueous solutions, thus limiting the use of the system to a certain pH range (Lobedank et al. 1997; Robertson 2006). Furthermore, the polarity of the solvent also affects the efficiency of the sensitized systems (Pei and Luan 2012). Within a certain range, the photosensitization effect is enhanced by increasing the dye concentration (Grätzel 2004; Pei and Luan 2012).

Further modification of the sensitized photocatalysts by surface metal deposits (e.g. Pt) has proved to benefit the photocatalytic activity under visible light irradiation. In the case of Pt, for instance, this effect can be ascribed to the fast electron trapping by the metal, inhibiting the back electron transfer to the dye (Pei and Luan 2012).

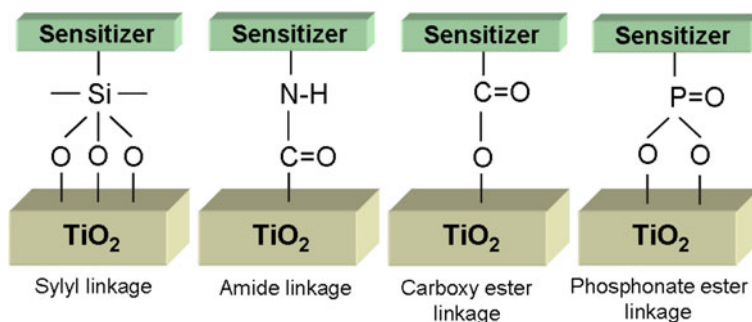


Fig. 16.2 Schematic representation of a sensitizer grafted onto TiO_2 through different anchoring groups (based on Kalyanasundaram and Grätzel 1998)

Organic dyes are the most frequently studied sensitizers, due to a highly efficient light harvesting over a wide spectral region of sunlight. They enclose a wide variety of chemical structures, including porphyrins, coumarins, catechols, polyenes, cyanines, hemicyanines, phthalocyanines, indolines, thiophenes, and polymeric dyes, among many others. Besides, the possibility of incorporating substituents into the organic dye skeleton opens a route to easily tuning their photochemical properties (Ooyama and Harima 2009). The structure of different organic dyes is presented in Fig. 16.3. The use of natural photosensitizers, extracted from fruits, flowers, or leaves, has also been explored. For instance, anthocyanins can be easily obtained from strongly coloured fruits, such as berries and plums. Similarly, the sensitization of semiconductors with chlorophyll and different chlorophyll derivatives has been investigated in an attempt to emulate the efficient light harvesting in natural photosynthesis (Kay and Grätzel 1993). Besides the environmental advantages derived from their cheaper and low-energy production, together with their lower toxicity, natural sensitizers often show an improved dye performance which have been attributed to the presence of a mixture of dyes in these natural extracts (Polo et al. 2004). The strategy of combining different dyes to obtain a broader response in the visible and near-IR region has

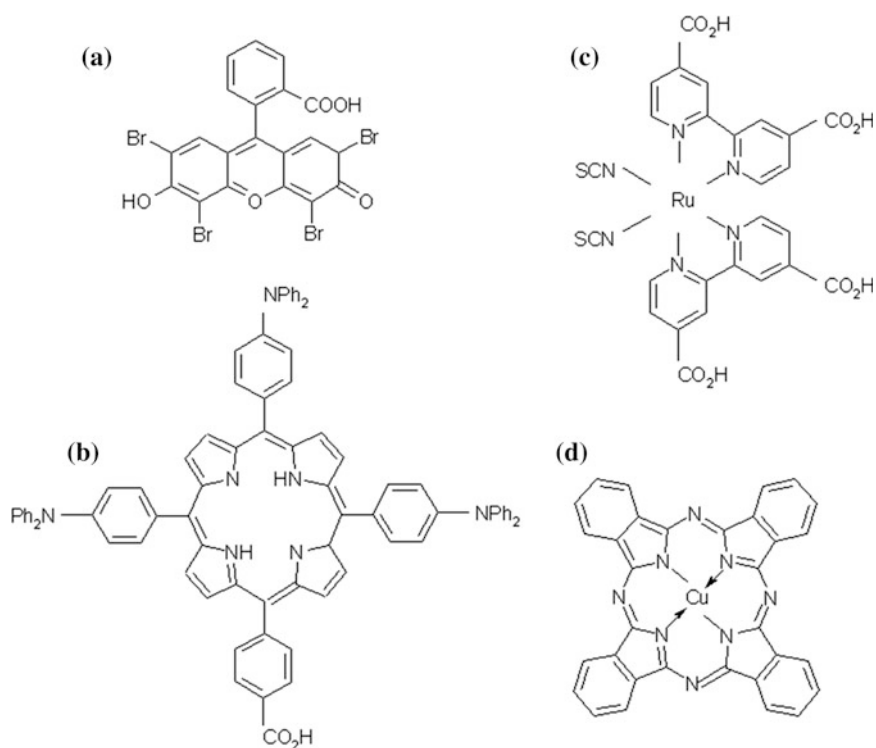


Fig. 16.3 Examples of dyes: **a** Eosin Y; **b** porphyrin dye; **c** N3 dye; **d** copper phthalocyanine

also been investigated in artificial systems, proving that the optical absorption of the dyes in the mixture can be additive (Ehret et al. 2001; Grätzel 2004).

The utilization of organic dye-sensitized TiO₂ for the photocatalytic degradation of pollutants has also been explored. Intentionally hindering the regeneration stage of the sensitizer would lead to the photocatalytic degradation of the organic dye. Most of the dyes are relatively stable under visible light irradiation in the absence of TiO₂, so in this sense, the process of self-sensitized oxidation results to be very useful for degrading coloured pollutants, such as textile dyes, from wastewaters (Zhao et al. 2005; Chatterjee and Dasgupta 2005). In one of the first publications that can be found related to this topic, the photocatalytic oxidation of an herbicide using Rose Bengal-sensitized titania was explored (Ross et al. 1994). The authors found that the herbicide was degraded under solar light exposure only when the sensitizer was present in the solution. However, simultaneous photocatalytic decomposition of the organic sensitizer was also observed. In the photocatalytic oxidation of phenol, performed over Acid Red 44-sensitized TiO₂ under visible light, the decomposition of the dye was only observed after decomposition of phenol, which resulted to be more easily attacked by the photogenerated radicals (Moon et al. 2003). The already mentioned Eosin Y has also been used to sensitize TiO₂ for the photocatalytic degradation of phenol under visible light, with Pt as co-catalyst and TEOA as sacrificial electron donor (Chowdhury et al. 2012). Other organic dyes, such as thionine, rhodamine B, methylene blue, and safranin O, have been employed in the photocatalytic degradation of different pollutants under visible light by dye-sensitized TiO₂ (Chatterjee and Dasgupta 2005). Finally, organic dyes such as Eosin Y (Fig. 16.3a) have been frequently used as photosensitizers for H₂ production under visible light irradiation (Nada et al. 2008, Pei and Luan 2012).

Despite their relatively lower molar absorption coefficients, better results are usually obtained with metal coordination complexes as photosensitizers, among which polypyridine complexes are probably the most widely studied. In these metal-organic dyes, the visible light absorption is originated by metal-to-ligand charge transfer (MLCT) transitions, in which energies depend on the metal and the ligands present in the sensitizer (Meyer 1986). In particular, it is worth mentioning the extensive use of ruthenium complexes, such as tris(bipyridyl)-ruthenium(II) ([Ru(bpy)₃]²⁺) derivatives. These compounds have been used to sensitize modified TiO₂ in water-splitting reactions. High efficient H₂ evolution under solar radiation has also been obtained over tris(bipyrimidine)-ruthenium (II) ([Ru(bpym)₃]²⁺)-sensitized Pt-loaded TiO₂. In every case, an increase in the production of H₂ was observed with the concentration of photosensitizer (Hirano et al. 2000; Polo et al. 2004; Nada et al. 2008). Despite the promising results on the photocatalytic water splitting under visible light, the solar power efficiencies obtained so far are really low, and the development of efficient and durable photocatalytic systems is still a challenge (Youngblood et al. 2009). Ruthenium polypyridyl complexes have been applied to the photocatalytic degradation of pollutants as well. For instance, their presence was proved to be effective in the photocatalytic oxidation of herbicides under sunlight excitation. Reductive regeneration of the oxidized sensitizer could

be achieved using sulphur-containing organic compounds (Lobedank et al. 1997). These Ru(II) complexes have also been employed in the photocatalytic reduction of carbon tetrachloride on dye-sensitized titania (Cho et al. 2001). In this case, 2-propanol was used as electron donor to regenerate the sensitizer. The authors observed that the presence of O₂ had a detrimental effect on the efficiency of the process, since oxygen acts as an electron scavenger. The presence of a thin Al₂O₃ overlayer on [Ru(bpy)₃]²⁺-sensitized TiO₂ has proved to significantly increase the photoactivity, both for H₂ production and for dechlorination of CCl₄, by retarding the charge recombination between the electron injected and the oxidized dye (Kim et al. 2009). In another example, higher yields of methane have been obtained under visible irradiation during the photoreduction of CO₂ on TiO₂ films in the presence of [Ru(bpy)₃]²⁺ dye sensitizers (Ozcan et al. 2007).

Carboxylic derivatives are the most frequently employed anchoring ligands in ruthenium complexes, since carboxyl groups easily react with the oxide surface to form the corresponding ester. This is the case of the photosensitizer known as N3 (Fig. 16.3c), reported by Grätzel and co-workers and usually employed as a reference to compare the performance of other dyes, which is a ruthenium bis(dicarboxylic acid bipyridine) complex (Grätzel 2004). Phosphonic acid groups are also often employed for anchoring Ru-based photosensitizers in titania, due to their strong adsorption to the semiconductor surface via ester formation (Polo et al. 2004).

Recent studies have reported that the presence of electron donor groups in the dye, like the thiocyanate (NCS) ligands present in the N3 photosensitizer, contributes to increase the spatial separation between the positive charge density created on the dye and the injected electrons and, therefore, hinders charge recombination. This effect takes also place, for instance, in the triphenylamine-substituted porphyrin organic dye as shown in Fig. 16.3b (Robertson 2006).

Iron-, ruthenium-, osmium-, zinc-, magnesium-, and aluminium-based systems have also been investigated (Kalyanasundaram and Grätzel 1998; Polo et al. 2004). The replacement of ruthenium by osmium has been observed to extend the light absorption and spectral response of TiO₂ photoelectrodes to higher wavelength (Sauvé et al. 2000). In addition to Ru-based sensitizers, a high efficiency has also been achieved in the photocatalytic H₂ formation using copper phthalocyanine (Fig. 16.3d) on modified TiO₂ photocatalysts (Nada et al. 2008). Cu(II)-phthalocyanines, as well as Cu(II) porphyrins, have also been efficiently applied to the photocatalytic degradation of 4-nitrophenol over sensitized TiO₂, leading to higher conversions than their analogous metal-free complexes (Mele et al. 2003). The photoactivity of Sn(IV)-porphyrin-sensitized TiO₂ has been investigated too, with the advantage of tin being less expensive and more abundant than Ru (Kim et al. 2010).

16.3 Quantum Dots

Quantum dots (QDs) are droplets or nanocrystals of a semiconductor, which excitons are confined in the three spatial dimensions, immersed in a matrix material usually with a higher band gap. The matrix does not need to be a semiconductor as well, but solids with other type of electronic characteristics can be also employed. Quantum-dot-based solar cells have drawn a lot of attention during the past few years because of the possibility of boosting the energy conversion efficiency beyond the traditional Shockley and Queisser energy conversion limit for a cell based on a single n–p junction (about 33.7 % in Si devices). Three different types of solar cells that capitalize prominent properties of semiconductor nanocrystals have emerged: (1) metal–semiconductor or Schottky junction photovoltaic cell, (2) semiconductor nanostructure–polymer solar cell, and (3) semiconductor-sensitized quantum-dot solar cell (Kamat 2008). Schemes of the configuration of these three types are shown in Fig. 16.4. In addition, QDs have been proposed as one of the means for taking into practice the so-called intermediate band (IB) solar cell, in which a partially occupied band is created between the valence and conduction bands in order to extend the energy range of absorbed photons while keeping the potential of the charge carriers (Luque and Martí 2010). In this case, the IB would typically arise from the confined states of the electrons in the CB tridimensional potential wells originated by the CB offset between the dot and the matrix material.

There are not many reports on the application of QDs in photocatalysis, and here, we will exclusively refer to those based on the third type of those mentioned above, which is the only one relevant to photocatalysis. The principle of action of this type of materials is thus similar to that described in Chap. 15 when referring to composite photocatalysts, in which a visible-light-absorbing semiconductor injects electrons upon excitation into the conduction band of a wide-band-gap semiconductor, and the same energy restrictions described there apply. As a differentiating

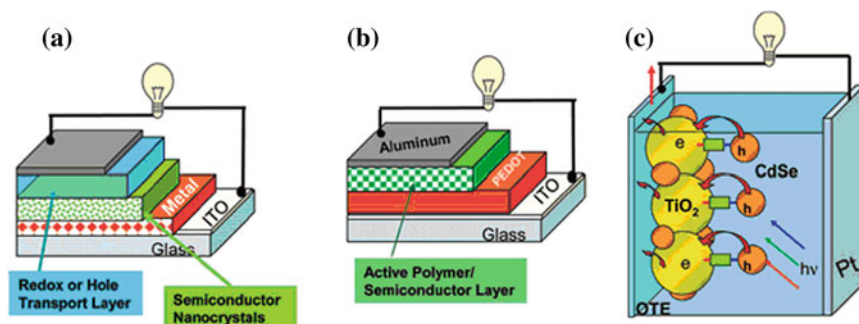


Fig. 16.4 Schematic diagram showing the strategies to develop quantum-dot (semiconductor nanocrystal)-based solar cells: **a** metal–semiconductor junction, **b** polymer–semiconductor, and **c** semiconductor–semiconductor systems. Reproduced with permission from Kamat 2008. Copyright American Chemical Society

fact, here the properties of the semiconductor as sensitizer are size-controlled and in the form of tridimensional nanostructures (rather than mono- and bidimensionally size-confined structures like plate or tubes, see [Chap. 11](#)). In this way, the energetics of the QD particles can be modulated and thus be utilized to promote, suppress, or rectify the electron transfer between two semiconductor nanostructures ([Kamat 2008](#)). In addition, compared to those materials reviewed in the preceding section, inorganic sensitizers have been invoked to be the only ones ensuring long-term stability under a wide range of reaction conditions and lead to more promising results under visible light than those obtained with metal dopants ([Rajeshwar et al. 2001](#); [Kubacka et al. 2012](#)).

Using as an example the typical CdS/TiO₂-coupled system, DFT calculations of bulk and QD semiconductor coupling have been performed to study the different electronic interactions occurring in both cases ([Tada et al. 2011](#)). The conduction band minimum of CdS in the bulk system is only slightly higher than that of TiO₂, whereas in the QD model, both the valence band maximum and the conduction band minimum of the CdS part are raised to higher energies, and the band gap of CdS increases. Thus, the CB offset between CdS and TiO₂ in the QD system is higher, providing a larger $-\Delta G$ value and consequently increasing the rate of interfacial electron transfer.

As mentioned in [Chap. 15](#), metal chalcogenides such as CdS represent a classical example of the use of inorganic sensitizers for the visible light sensitization of wide-band-gap semiconductors. Given the good morphological control that can be attained in their preparation, metal chalcogenides become very suitable to be used for this purpose in the form of QDs. The theoretical approach described above finds experimental corroboration with the increased photocurrent quantum yields that have been measured by combining some quantum-sized metal sulphides like PbS, CdS, Ag₂S, Sb₂S₃, and Bi₂S₃ with oxide semiconductors such as TiO₂, ZnO, SnO, Nb₂O₅, and Ta₂O₅ ([Vogel et al. 1994](#)). When used along with titania, all these sulphides give rise to higher incident photon-to-current efficiencies (IPCEs) under visible light irradiation, although only PbS and CdS show a reasonable stability under illumination. The internal photocurrent quantum yield decreases with increasing QD diameters and is also dependent on the substrate nature, with TiO₂ showing the best performance among the mentioned wide-band-gap oxides for a given sensitizer. This is not only related to the charge mobility properties of the substrate, but also to the relative positions of the CB of sensitizer and substrate. However, as mentioned earlier at the theoretical level, the CB offset can be tuned by means of size control of the QDs, and, for example, the IPCE of the CdS/TiO₂ system increases by ca. 10 % when the CdS particle size is decreased from 6 to 4 nm. This difference is even more noticeable in the case of the CdS/Nb₂O₅ composite, with a 50 % increase in IPCE between the same QD sizes. The CdS (QD)/TiO₂ system has provided good results for sacrificial water splitting with Pt as co-catalyst ([Tada et al. 2011](#)), but also with TiO₂ nanostructures as nanotubes and nanowires. For instance, oxygen-deficient TiO₂ nanowires loaded with CdS QDs have been invoked to be promising catalysts for solar hydrogen production based on IPCE results, although actual photocatalytic tests have not been

performed (Wang et al. 2012). On the other hand, TiO₂ nanotube arrays decorated with CdS QDs (Xie et al. 2010) have given good results in the degradation of methyl orange in aqueous solution under visible light. However, as mentioned earlier in this book, this activity needs to be further assessed using non-coloured target molecules in order to rule out a dye-sensitization mechanism. Indeed, methyl orange and CdS show rather similar absorption maxima. Regarding other sulphide sensitizers, CuS and PbS in the form of QDs have been reported to extend the photocatalytic response of titania to the visible light region. PbS(QD) sensitization increases by a factor of 5 the activity of titania for the photocatalytic reduction of CO₂ to CH₄ and C₂H₆, under light with $\lambda > 400$ nm and using Cu as co-catalyst (Wang et al. 2011), with a QD size of 4 nm showing the best performance. CuS-decorated TiO₂ nanotubes can efficiently degrade malachite green and phenol under irradiation with light filtered at $\lambda < 600$ nm (Ratanatawanate et al. 2011).

As mentioned in Chap. 15, selenides are also good candidates to be used as sensitizers in the form of QDs. Therefore, they have been studied not only for photovoltaic cells (Kamat 2008), but also, although to a lesser extent, for photocatalytic applications. CdSe is the most common selenide QD material, and its size-dependent charge separation properties in combination with wide-band-gap semiconductors (mainly TiO₂) have been extensively studied (Kamat 2008). However, there are not many photocatalytic studies on this system. An example is the application of the Pt/CdSe(QD)/TiO₂ system to the photocatalytic reduction of CO₂, which under visible light ($\lambda > 420$ nm) yields CH₄ as the major product, with CH₃OH, H₂, and CO as secondary products (Wang et al. 2010). In combination with N-doping, CdSe QD sensitization has led to higher IPCE under visible light than those attained with both undoped and N-doped TiO₂ (Lopez-Luke et al. 2008). This enhancement is also observed when this system is used as a photoanode for photoelectrochemical hydrogen production from Na₂S-Na₂SO₃ aqueous solutions. A synergistic effect between CdSe sensitization and N-doping, which facilitates hole transfer/transport from CdSe to TiO₂ through oxygen vacancy states mediated by N-doping, has been proposed (Hensel et al. 2010). PbSe is also a good candidate for this type of systems, and it has been employed in photovoltaic applications (Kamat 2008). However, its feasibility as a QD sensitizer in photocatalysis has still to be deeper studied (Wang et al. 2007).

These chalcogenide QDs, however, can be prone to deactivation due to the photocorrosion process described in Chap. 8, which is pronounced with downsizing the crystals. As mentioned in Chap. 15, coupling with a wide-band-gap semiconductor may already inhibit the occurrence of anodic photocorrosion. Anyway, a loss of activity with usage time is indeed shown in some of the studies cited above. Stabilization by surface modification with sulphur-containing molecules or the use of linkers between the surfaces of the two components of the system has been proposed to alleviate this problem. At a theoretical level, this stabilization has been explained based on a model with H₂S molecules adsorbed at the surface of CdS in the CdS(QD)/TiO₂ system, which cause the surface states to

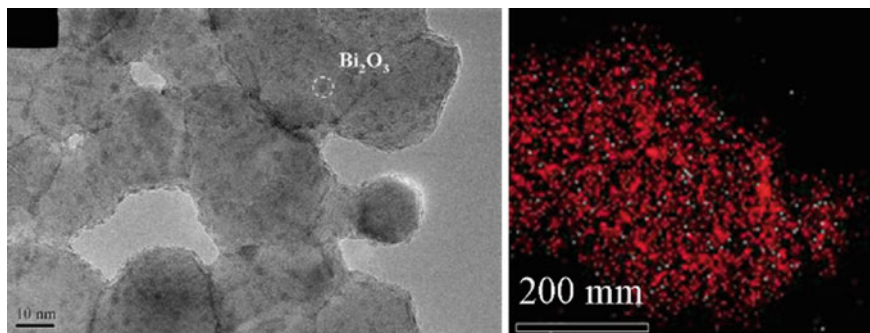


Fig. 16.5 HRTEM image (*left*) and chemical mapping (*right*; red: Ti, blue: Bi) of $\text{Bi}_2\text{O}_3(\text{QD})/\text{TiO}_2$ composite. Adapted with permission from Zhu et al. 2011. Copyright Elsevier

lower in energy and become part of the VB as a consequence of the S–S bond formation between the CdS cluster and the H_2S molecules.

The application of oxidic semiconductors in the form of QDs for spectral sensitization is scarcer than that of the mentioned chalcogenides due to the less pronounced correlation between their primary crystal size and their electronic characteristics (Kubacka et al. 2012). Nevertheless, some examples can be drawn from the literature. Some of them were already mentioned in Chap. 15, regarding nanooxides coupling. Specifically prepared as QDs, flower-like $\text{Bi}_2\text{O}_3/\text{TiO}_2$ composites (Fig. 16.5) have shown a higher photocatalytic activity for the degradation of 4-chlorophenol under visible light than composite samples without this QD configuration. The activity has been correlated with the enhanced photosensitizing effect of Bi_2O_3 when present in this form (Zhu et al. 2011). In the same line, it has been recently proposed that the assembly of a Bi_2WO_6 nanostructure with Bi_2WO_6 QDs dispersed on single crystalline nanosheets has potential in photocatalysis, and the reported enhanced photocatalytic activity for RhB degradation appears to be justified. In addition, the incorporation of TiO_2 units into the Bi_2WO_6 structure leading to a homogeneous heterostructured material has shown that this new photocatalyst can, in principle, function under sun-like irradiation conditions (Kubacka et al. 2012).

Here, it is also worth mentioning graphene, which was already referred to in Chap. 15. Regarding QD composites, graphene has been explored both as host and as guest material (Kamat 2011). Cubic and hexagonal CdSe nanocrystals, with average sizes of 2–4 and 5–7 nm, respectively, have been shown to undergo excited state quenching by reduced graphene oxide. Such excited state interactions have important implications in energy conversion applications such as photovoltaic cells, where CdSe QDs, the light-harvesting material, are supported on the highly conducting flexible graphene electrodes. But also graphene QDs absorb strongly in the visible region, with absorption maxima at around 600 nm. These QDs are able to sensitize TiO_2 films and deliver the photocurrent in a photoelectrochemical cell.

References

- Abe R, Hara K, Sayama K, Domen K, Arakawa H (2000) Steady hydrogen evolution from water on Eosin Y-fized TiO₂ photocatalysts using a silane-coupling reagent under visible light irradiation. *J Photoch Photobio A* 137:63–69
- Bae E, Choi W (2006) Effect of the anchoring group (carboxylate vs phosphonate) in Ru-Complex-sensitized TiO₂ on hydrogen production under visible light. *J Phys Chem B* 110:14792–14799
- Chatterjee D, Dasgupta S (2005) Visible light induced photocatalytic degradation of organic pollutants. *J Photoch Photobio C* 6:186–205
- Cheung STC, Fung AKM, Lam MHW (1998) Visible photosensitization of TiO₂ photodegradation of CCl₄ in aqueous medium. *Chemosphere* 36:2461–2473
- Cho Y, Choi W, Lee C-H, Hyeon T, Lee H-I (2001) Visible light induced degradation of carbon tetrachloride on dye-sensitized TiO₂. *Environ Sci Technol* 35:966–970
- Chowdhury P, Moreira J, Gomaa H, Ray AK (2012) Visible-solar-light-driven photocatalytic degradation of phenol with dye-sensitized TiO₂: parametric and kinetic study. *Ind Eng Chem Res* 51:4523–4532
- Ehret A, Stuhl L, Spittler MT (2001) Spectral sensitization of TiO₂ nanocrystalline electrodes with aggregated cyanine dyes. *J Phys Chem B* 105:9960–9965
- Fung AKM, Chiu BKW, Lam MHW (2003) Surface modification of TiO₂ by a ruthenium (II)-polypyridyl complex via silyl-linkage for the sensitized photocatalytic degradation of carbon tetrachloride by visible irradiation. *Water Res* 37:1939–1947
- Grätzel M (2003) Dye-sensitized solar cells. *J Photoch Photobio C* 4:145–153
- Grätzel M (2004) Conversion of sunlight to electric power by nanocrystalline dye-sensitized solar cells. *J Photoch Photobio A* 164:3–14
- Grätzel M (2005) Solar energy conversion by dye-sensitized photovoltaic cells. *Inorg Chem* 44:6841–6851
- Hensel J, Wang G, Li Y, Zhang JZ (2010) Synergistic effect of CdSe quantum dot sensitization and nitrogen doping of TiO₂ nanostructures for photoelectrochemical solar hydrogen generation. *Nano Lett* 10:478–483
- Hirano K, Suzuki E, Ishikawa A, Moroi T, Shiroishi H, Kaneko M (2000) Sensitization of TiO₂ particles by dyes to achieve H₂ evolution by visible light. *J Photoch Photobio A* 136:157–161
- Jin Z, Zhang X, Lu G, Li S (2006) Improved quantum yield for photocatalytic hydrogen generation under visible light irradiation over Eosin-sensitized TiO₂-Investigation of different noble metal loading. *J Mol Catal* 259:275–280
- Jin Z, Zhang X, Li Y, Li S, Lu G (2007) 5.1 % apparent quantum efficiency for stable hydrogen generation over eosin-sensitized CuO/TiO₂ photocatalysts under visible light irradiation. *Catal Commun* 8:1267–1273
- Kalyanasundaram K, Grätzel M (1998) Applications of functionalized transition metal complexes in photonic and optoelectronic devices. *Coordin Chem Rev* 177:347–414
- Kamat PV (2008) Quantum dot solar cells. Semiconductor nanocrystals as light harvesters. *J Phys Chem C* 112:18737–18753
- Kamat PV (2011) Graphene-based nanoassemblies for energy conversion. *J Phys Chem Lett* 2:242–251
- Kay A, Grätzel M (1993) Artificial photosynthesis. 1. Photosensitization of TiO₂ solar cells with chlorophyll derivatives and related natural porphyrins. *J Phys Chem* 97:6272–6277
- Kim W, Tachikawa T, Majima T, Choi W (2009) Photocatalysis of dye-sensitized TiO₂ nanoparticles with thin overcoat of Al₂O₃: enhanced activity for H₂ production and dichlorination of CCl₄. *J Phys Chem C* 113:10603–10609
- Kim W, Tachikawa T, Majima T, Li C, Kim HJ, Choi W (2010) Tin-porphyrin sensitized TiO₂ for the production of H₂ under visible light. *Energ Environ Sci* 3:1789–1795
- Kubacka A, Fernández-García M, Colón G (2012) Advanced nanoarchitectures for solar photocatalytic applications. *Chem Rev* 112:1555–1614

- Li Q, Chen L, Lu G (2007a) Visible-light induced photocatalytic hydrogen generation on dye-sensitized multiwalled carbon nanotube/Pt catalyst. *J Phys Chem C* 111:11494–11499
- Li Q, Jin Z, Peng Y, Li S, Lu G (2007b) High-efficient photocatalytic hydrogen evolution on Eosin Y-sensitized Ti-MCM41 zeolite under visible-light irradiation. *J Phys Chem C* 111:8237–8241
- Li Y, Guo M, Peng S, Lu G, Li S (2009) Formation of multilayer-Eosin Y-sensitized TiO₂ via Fe₃ + coupling for efficient visible-light photocatalytic hydrogen evolution. *Int J Hydrogen Energ* 34:5629–5636
- Lobedank J, Bellmann E, Bendig J (1997) Sensitized photocatalytic oxidation of herbicides using natural sunlight. *J Photoch Photobio A* 108:89–93
- Lopez-Luke T, Wolcott A, Xu L, Chen S, Wcn Z, Li J, De La Rosa E, Zhang JZ (2008) Nitrogen-doped and CdSe quantum-dot-sensitized nanocrystalline TiO₂ films for solar energy conversion applications. *J Phys Chem C* 112:1282–1292
- Luque A, Martí A (2010) The intermediate band solar cell: progress toward the realization of an attractive concept. *Adv Mater* 22:160–174
- Mele G, Del Sole R, Vasapollo G, García-López E, Palmisano L, Schiavello M (2003) Photocatalytic degradation of 4-nitrophenol in aqueous suspension by using polycrystalline TiO₂ impregnated with functionalized Cu(II)-porphyrin or Cu(II)-phthalocyanine. *J Catal* 217:334–342
- Meyer TJ (1986) Photochemistry of metal coordination complexes: metal to ligand charge transfer excited states. *Pure Appl Chem* 58:1193–1206
- Min S, Wang F, Han Y (2007) An investigation on synthesis and photocatalytic activity of polyaniline sensitized nanocrystalline TiO₂ composites. *J Mater Sci* 42:9966–9972
- Moon J, Yun CY, Chung K-W, Kang M-S, Yi J (2003) Photocatalytic activation of TiO₂ under visible light using Acid Red 44. *Catal Today* 87:77–86
- Nada AA, Hamed HA, Barakat MH, Mohamed NR, Veziroglu TN (2008) Enhancement of photocatalytic hydrogen production rate using photosensitized TiO₂/RuO₂-MV²⁺. *Int J Hydrogen Energ* 33:3264–3269
- Ooyama Y, Harima Y (2009) Molecular designs and syntheses of organic dyes for dye-sensitized solar cells. *Eur J Org Chem* 2903–2934
- Ozcan O, Yukruk F, Akkaya EU, Uner D (2007) Dye sensitized artificial photosynthesis in the gas phase over thin and thick TiO₂ films under UV and visible light irradiation. *Appl Catal B-Environ* 71:291–297
- Park H, Bae E, Lee J-J, Park J, Choi W (2006) Effect of the anchoring group in Ru-bipyridyl sensitizers on the photoelectrochemical behaviour of dye-sensitized TiO₂ electrodes: carboxylate versus phosphonate linkages. *J Phys Chem B* 110:8740–8749
- Pei D, Luan J (2012) Development of visible light-responsive sensitized photocatalysts. *Int J Photoenergy* ID 262831:13
- Polo AS, Itokazu MK, Iha NYM (2004) Metal complexes sensitizers in dye-sensitized solar cells. *Coordin Chem Rev* 248:1343–1361
- Rajeshwar K, de Tacconi NR, Chenthamarakshan CR (2001) Semiconductor-based composite materials: preparation, properties, and performance. *Chem Mater* 13:2765–2782
- Ratanatawanate C, Bui A, Vu K, Balkus KJ (2011) Low-temperature synthesis of copper(II) sulfide quantum dot decorated TiO₂ nanotubes and their photocatalytic properties. *J Phys Chem C* 115:6175–6180
- Robertson N (2006) Optimizing dyes for dye-sensitized solar cells. *Angew Chem Int Ed* 45:2338–2345
- Ross H, Bendig J, Hecht S (1994) Sensitized photocatalytic oxidation of terbuthylazine. *Sol Energ Mat Sol C* 33:475–481
- Sauvé G, Cass ME, Coia G, Doig SJ, Lauermaann I, Pomykal KE, Lewis NS (2000) Dye sensitization of nanocrystalline titanium dioxide with osmium and ruthenium polypyridyl complexes. *J Phys Chem B* 104:6821–6836

- Song L, Qiu R, Mo Y, Zhnag D, Wei H, Xiong Y (2007) Photodegradation of phenol in a polymer-modified TiO₂ semiconductor particulate system under the irradiation of visible light. *Catal Commun* 8:429–433
- Tada H, Fujishima M, Kobayashi H (2011) Photodeposition of metal sulfide quantum dots on titanium (IV) dioxide and the applications to solar energy conversion. *Chem Soc Rev* 40:4232–4243
- Vogel R, Hoyer P, Weller H (1994) Quantum-sized PbS, CdS, Ag₂S, Sb₂S₃, and Bi₂S₃ particles as sensitizers for various nanoporous wide-bandgap semiconductors. *J Phys Chem* 98:3183–3188
- Wang C, Kwon KW, Odlyzko ML, Lee BH, Shim M (2007) PbSe nanocrystal/TiOx heterostructured films: a simple route to nanoscale heterointerfaces and photocatalysis. *J Phys Chem C* 111:11734–11741
- Wang C, Thompson RL, Baltrus J, Matranga C (2010) Visible light photoreduction of CO₂ using CdSe/Pt/TiO₂ heterostructured catalysts. *J Phys Chem Lett* 1:48–53
- Wang C, Thompson RL, Ohodnicki P, Baltrus J, Matranga C (2011) Size-dependent photocatalytic reduction of CO₂ with PbS quantum dot sensitized TiO₂ heterostructured photocatalysts. *J Mater Chem* 21:13452–13457
- Wang H, Wang G, Ling Y, Lepert M, Wang C, Zhang JZ, Li Y (2012) Photoelectrochemical study of oxygen deficient TiO₂ nanowire arrays with CdS quantum dot sensitization. *Nanoscale* 4:1463–1466
- Xie Y, Ali G, Yoo SH, Cho SO (2010) Sonication-assisted synthesis of CdS quantum-dot-sensitized TiO₂ nanotube arrays with enhanced photoelectrochemical and photocatalytic activity. *ACS Appl Mater Interf* 2:2910–2914
- Youngblood WJ, Seung-Hyun AL, Maeda K, Mallouk TE (2009) Visible light water splitting using dye-sensitized oxide semiconductors. *Accounts Chem Res* 42:1966–1973
- Zhao J, Chen C, Ma W (2005) Photocatalytic degradation of organic pollutants under visible light irradiation. *Top Catal* 35:269–278
- Zhu J, Wang S, Wang J, Zhang D, Li H (2011) Highly active and durable Bi₂O₃/TiO₂ visible photocatalyst in flower-like spheres with surface-enriched Bi₂O₃ quantum dots. *App Catal B Environ* 102:120–125

Chapter 17

Future Perspectives of Photocatalysis

Juan M. Coronado, María D. Hernández-Alonso, Fernando Fresno and Raquel Portela

After an already long history, which has experienced remarkable progress in the last 25 years, photocatalysis still has a brilliant future ahead. Thus, it seems pertinent to explore the tendencies of this technology in an attempt to anticipate the developments to come in the following decades. This is obviously not a trivial task because of the considerable uncertainties inherent to any projection, but some trends can be outlined with a reasonable degree of confidence in two main aspects: new applications and design of novel materials.

The bases for the remarkable interest of photocatalysis have been extensively discussed in previous chapters, but, ultimately, they are linked to the exceptional and straightforward connection that this technology establishes between solar energy and chemistry. This feature is crucial in the production of solar fuels, either from H₂O or from CO₂, and it is predictable that this field will increment its relevance in the next years. In fact, a simple survey of the literature indicates that this is already happening: in 2011, the publications related to water splitting were about 21 % of the total, and this represents more than a twofold increase with respect to 2001. Besides, a certain degree of hybridization between niches

J. M. Coronado (✉)
Institute IMDEA Energía, Avenida de Ramón de la Sagra, 3 28935 Móstoles,
Madrid, Spain
e-mail: juanmanuel.coronado@imdea.org

M. D. Hernández-Alonso
CIEMAT, Madrid, Spain
e-mail: lolihza@gmail.com

F. Fresno
Laboratory for Environmental Research, University of Nova Gorica,
Nova Gorica, Slovenia
e-mail: fernando.fresno@ung.si

R. Portela
CSIC, Institute of Catalysis and Petrochemistry, Calle Marie Curie 2. Campus de
Cantoblanco, Madrid, Spain
e-mail: raquel.portela@csic.es

previously separated is conceivable. An example of this is the photocatalytic production of hydrogen using pollutants as sacrificial molecules (Kim et al. 2012). Similarly, the direct combination in a single device of photovoltaic components with oxidation and reduction catalysts for water splitting has been recently proposed. This innovative system is based on amorphous silicon sandwiched between hydrogen-evolving catalysts made from a Ni, Mo and Zn alloy and a cobalt/borate catalyst for oxygen production (Reece et al. 2011). These compact and simple structures still present a modest efficiency, but open up a new direction for future research. Furthermore, other possible hyphenation of technologies may arise in the next few years combining electronic devices such as, for instance, sensors and photochromic systems. In addition to these tendencies in the development of novel applications, photocatalysis is attracting the interest of scientists working on previously unrelated fields such as atmospheric chemistry. In this respect, airborne TiO_2 particles present in dust can play a relevant role in the photochemistry of atmospheric gases, including carbon dioxide, nitrogen oxides, nitric acid, sulphur dioxide, ozone, hydrogen peroxide and VOCs (Chen et al. 2012). These investigations may also have implications in planetary science, and in fact, naturally occurring photocatalytic processes have also been proposed to be possible in Mars soils (Shkrob and Chemerisov 2009). In other way, photocatalysis has been related to the abiotic synthesis and the origin of life (Emeline et al. 2003), and although these studies represent an exploration of the frontiers of science, it cannot be discarded that they may gain further relevance in the future.

Development of alternative photocatalytic materials is a central topic of this book, and the most relevant advances in this area have been presented in previous chapters. Future trends are most likely unpredictable, but some firm directions of innovation can be foreseen. On the one hand, nanotechnology is gaining an unprecedented control of the architecture of functional materials in a bottom-up approach. Examples of the use of multicomponent materials assembled in the nanoscale are becoming common. Figure 17.1 illustrates the degree of control that can be achieved by combining nanostructured semiconductors, such a CdS and



Fig. 17.1 Scheme showing the different behaviour for water splitting of ZnSe/CdS/Pt heteronanostructures when the surface is unmodified (*right side*) or stabilized with electron donor molecules (*left*). The inset at the *bottom* shows the high-resolution image of one of these nanostructures. Reproduced with permission from Acharya et al. 2011. Copyright American Chemical Society

ZnSe, with Pt nanoparticles (Acharya et al. 2011). In particular, this work also highlights the relevance of surface composition on the performance of these heterostructures, because hydrogen production is only possible in the presence of adsorbed donor molecules. On the other hand, joining structures in very different scales to achieve hierarchical materials can also create new opportunities for improving the efficiency of the photocatalyst. A good example of this approach is the development of structures with lattice periodicity in the range of the wavelengths of light, known as photonic crystals, combined with Au nanoparticles with plasmonic properties (Lu et al. 2012). The synergy between these components enhances light harvesting and promotes the visible light activity of these highly structured photocatalysts.

Finally, it is plausible to think that new photocatalytic materials will be successfully used in the future. A good example of the rapid incorporation of new components is the recent scientific revolution associated with the discovery of the fascinating electronic properties of graphene. This development has also influenced photocatalysis as it has been mentioned in Chaps. 15 and 16. These carbon-based materials provide remarkable results in combination with semiconductors such as TiO₂. However, two major hurdles remain in developing large-scale graphene-supported catalytic systems: obtaining solution-processable graphene sheets and achieving a good dispersion of the metal co-catalysts (Kamat 2010). Interestingly, graphene can be hybridized with other carbon-based non-conventional photocatalysts such as graphitic carbon nitride (g-C₃N₄) to achieve a very high efficiency for water splitting under visible light irradiation, using Pt as co-catalysts (Xiang et al. 2011). This type of materials holds a huge potential of improvement, although in order to achieve this, further research efforts will be required.

In summary, it can be concluded that although the particular directions that photocatalysis will take in the next years are still uncertain, they will surely lead to bright technological developments.

References

- Acharya KP, Khnayzer RS, O'Connor T, Diederich G, Kirsanova M, Klinkova A, Roth D, Kinder E, Imboden M, Zamkov M (2011) The role of hole localization in sacrificial hydrogen production by semiconductor–metal heterostructured nanocrystals. *Nano Lett* 11(7):2919–2926
- Chen H, Nanayakkara CE, Grassian VH (2012) Titanium dioxide photocatalysis in atmospheric chemistry. *Chem Rev* 112:5919–5948
- Emeline AV, Otroshchenko VA, Ryabchukc VK, Serpone N (2003) Abiogenesis and photostimulated heterogeneous reactions in the interstellar medium and on primitive earth: relevance to the genesis of life. *J Photochem Photobio C* 3:203–224
- Kamat PV (2010) Graphene-based nanoarchitectures. anchoring semiconductor and metal nanoparticles on a two-dimensional carbon support. *J Phys Chem Lett* 1:520–527

- Kim J, Monllor-Satoca D, Choi W (2012) Simultaneous production of hydrogen with the degradation of organic pollutants using TiO₂ photocatalyst modified with dual surface components. *Energy Environ Sci* 5(6):7647–7656
- Lu Y, Yu H, Chen S, Quan X, Zhao H (2012) Integrating plasmonic nanoparticles with TiO₂ photonic crystal for enhancement of visible-light-driven photocatalysis. *Environ Sci Technol* 46(3):1724–1730
- Reece SY, Hamel JA, Sung K, Jarvi TD, Esswein AJ, Pijpers JJH, Nocera DG (2011). Wireless solar water splitting using silicon-based semiconductors and earth-abundant catalysts. *Science* 334:645–648
- Shkrob IA, Chemerisov SD (2009) Light induced fragmentation of polyfunctional carboxylated compounds on hydrated metal oxide particles: from simple organic acids to peptides. *J Phys Chem C* 113(39):17138–17150
- Xiang Q, Yu J, Jaroniec M (2011) Preparation and enhanced visible-light photocatalytic H₂-production activity of graphene/C₃N₄ composites. *J Phys Chem C* 115:7355–7363